REACTIONS OF IRON- AND ZINC-FUELLED PYROTECHNIC SYSTEMS

THESIS

Submitted in fulfilment of the requirements for the Degree of

DOCTOR OF PHILOSOPHY

of

Rhodes University

by

MICHAEL JOHN TRIBELHORN

May 1994

Department of Chemistry
Rhodes University
Grahamstown

For Robert and Marlene

...and for Sarah

ABSTRACT

A major industrial use of pyrotechnic compositions is as delay fuses in electric detonators. Suitable delay times may be achieved through (i) choice of chemical components (ii) adjustment of composition of the system chosen and, finally, (iii) adjustment of the length of fuse used.

This study forms part of a survey of binary fuel/oxidant combinations in an attempt to provide some fundamental information on the first step above: (i) choice of chemical components. The complete survey has included studies of a single fuel in combination with one of a variety of oxidants, and studies of the oxidation of one of several different fuels separately by barium peroxide and strontium peroxide. This study is part of this second approach and the fuels chosen were iron and zinc powders, mainly for chemical reasons (including the potential for use of thermomagnetometry on the iron systems), but also for possible environmental advantages. The mixed oxide products of pyrotechnic combustion could also have some scientific and/or commercial value.

The techniques used included thermal analyses of mixtures and their individual components, and measurements of temperature-time profiles during combustion. Thermodynamic and kinetic information was obtained under a variety of conditions and scanning electron microscopy and X-ray diffraction and microprobe analyses provided additional information.

Possible mechanisms of reactions are discussed in detail.

The practical conclusions were that any potential use which the Fe/peroxide systems may have as delay compositions, with burning-rates of from 3-30 mm s^{-1}, is offset by the susceptibility of the oxidants to reaction with water and CO_2 in the atmosphere. The Zn/BaO_2 and Zn/SrO_2 systems did not burn under compaction, and combustion of uncompacted powders was erratic. Zinc liquid (and probably zinc vapour) take part in the reaction and the gaseous nature of the combustion makes zinc-fuelled pyrotechnic systems unsuitable for delay applications.

All the techniques used showed the heterogeneity of the solid residues of combustion. If these residues were to be of any value, they would need further conventional treatment involving grinding of the residue, possible adjustment of compositions, and calcining to produce uniform materials.

ACKNOWLEDGEMENTS

The production of a thesis is never a solo attempt, it is supported by the contributions of a number of people either directly or indirectly involved in the researcher's work. I am most grateful to the following people who contributed to this work.

- I should like to thank my supervisor, Professor Michael E. Brown, for the dedication, keen interest, patience and, above all, professional attitude to this work. His constructive suggestions, support and guidance have been a cornerstone of this research.
- Analytical techniques can be fickle at times, and without the constructive suggestions of Professor Desmond Eve, problems associated with XRD equipment might have been substantial.
- The late Doctor Robin English provided excellent suggestions regarding computer modelling on the Vax workstation.
- John Goetsch's assistance with the installation of a network link and Andre Ferreira's assistance with Pascal glitches allowed the writing of computer programs to be as painless as possible.
- The expertise of Mrs Sarah Radloff in the field of BMDP packages allowed me to make a smooth transition from the Cyber based mainframe system to the Sun system.
- The skill of Mr Billy Morgan of the Rhodes University EPMA unit and that of the staff of the Rhodes University EM unit made surface studies possible.
- The service staff of the Department of Chemistry of Rhodes University have always accommodated my requests regarding equipment, and to this end I should particularly like to thank Mr Aubrey Sonemann, Mr Friedl Ranftelshofer and Mr Andre Adriaan for their assistance during my research in the Department.
- The interest of industry in the research resulted in AECI Ltd liaising with the Department on a regular basis. I am particularly grateful to Dr R. Anil Rugunanan and the staff of AECI Explosives Limited for interest and support, and to Mrs Karol Cameron of AECI Chemicals Limited for the interest shown in my work.
- I should like to thank AECI Explosives Limited and the Foundation for Research Development for financial support, and
- Lastly, credit must also go to Steve Taylor and Dean Venables, for their ideas, assistance and encouragement throughout this work, as well as my other colleagues in the department whom I have not mentioned, but who contributed to this work in one way or another.

TABLE OF CONTENTS

LIST OF FIGURES

Section 7:

Section 8:

Section 15:

LIST OF PLATES

Section 14:

Section 15:

LIST OF TABLES

LIST OF SYMBOLS AND UNITS

A	Pre-exponential factor in Arrhenius equation [s^{-1}]
B	Modified rate equation constant
D	Thermal diffusivity [m^2 s^{-1}]
E_a	Activation energy [kJ mol^{-1}]
G	Power function
N_R	Number of contact points
P	Oxygen partial pressure
Q	Heat output [kJ g^{-1}]
R	Universal gas constant [8.314 J K^{-1} mol^{-1}]
T	Temperature [°C or K]
U	Excess temperature [K]
V	Thermocouple output [mV]
b	Reaction zone width [mm]
c	Specific heat capacity [J K^{-1} g^{-1}]
d	Thermocouple diameter [mm]
k	Rate coefficient
m	Order of reaction in modified rate equation
n	Order of reaction
q	Heat of reaction [kJ mol^{-1}]
r	Correlation coefficient
t	Time [s]
v	Linear burning rate [mm s^{-1}]
w	$q(d\alpha/dt)$
y	Oxide film thickness
α	Fractional reaction
ϕ	Heating rate [°C min^{-1}]
ϵ	Porosity factor
λ	Thermal conductivity [W m^{-1} K^{-1}]
ρ	Density [g cm^{-3}]

Subscripts:

calc	Calculated value
exp	Experimental value
ign	Ignition value
obs	Observed value
max	Maximum value
min	Minimum value
TA	Thermal analysis value
th	Thermal relaxation value
TP	Temperature profile value
r	Rise value
d	Decay value
*	Combustion
I	Ignition
0	Initial
a	Ambient value
f	Final value

1.INTRODUCTION:

Explosive materials may be categorised into three main subgroups:

(i) (High) explosives, detonating in the km s^{-1} range

(ii) Propellants, deflagrating in the m s^{-1} range

(iii) Pyrotechnics, burning in the mm s^{-1} range

A pyrotechnic composition consists of at least one initially solid fuel and at least one initially solid oxidant. Binders and other additives are used to increase cohesion and protect the fuels from oxidation by air. These compounds may have an inhibiting effect on the reaction or may act as additional fuels [1].

The fuels used are usually fine powders of reactive metals or other elements such as silicon or carbon. The oxidants are usually metal oxides, peroxides or oxysalts. Even for binary mixtures of one fuel and one oxidant, the number of combinations possible is large and increases greatly when combinations of several fuels and/or oxidants are considered [2].

Prior to World War II, the manufacture of pyrotechnics was an empirical art, and system modification was by trial and error. The applications of pyrotechnics were, however, widespread and included devices producing colour, motion, smoke, sound, electromagnetic radiation (IR decoys and illumination) as well as heat (igniters, incendiaries, metal producers). The study of delay fuses, one of the prime uses of pyrotechnics, has contributed most to the development of theories for pyrotechnic combustion [3].

In 1949, two papers published by Spice and Staveley [4], did much to promote a scientific approach to the study of pyrotechnic reactions. These studies are discussed in Section 3.

It is relatively easy to calculate the adiabatic temperature, T_{ad}, to which the products of a pyrotechnic reaction should be raised as a consequence of the evolution of heat from a proposed chemical reaction, from tables of thermodynamic data [5]. The actual reaction temperature, even if the proposed reaction does occur, is generally lower than T_{ad} due to incomplete reaction and heat loss by conduction, convection and radiation. It is difficult, if not impossible, to predict the kinetic factors which determine the rate of propagation of combustion.

2. AIMS:

For fundamental studies of pyrotechnic combustion, the systems considered should, at least initially, be restricted to binary combinations and, ideally, the fuel should give only one product on oxidation, and the oxidant only one product on reduction.

The alkaline-earth metal peroxides are apparently suitable oxidants since their decompositions are reported to lead to the corresponding oxides:

$$MO_2(s) \rightarrow MO(s) + \tfrac{1}{2}O_2(g)$$

Metal fuel/alkaline-earth metal peroxide pyrotechnic systems are also of interest because of the uncertainty as to whether combustion occurs through solid-solid interaction, or whether the fuel reacts with oxygen gas formed by some decomposition of the oxidant. Drennan [6] has examined the Mo/BaO_2 and Mn/BaO_2 systems, and the closely related Mn/SrO_2 and Mo/SrO_2 systems, in detail. In this study, the same two oxidants are used in binary (and a few ternary) combinations with Fe and Zn fuels.

Fe was chosen as a fuel for several reasons, although it has the disadvantage of yielding a variety of oxides on oxidation. Considerable information is available on the Fe/BaO_2 system from early studies by Spice and Staveley [4,7] (discussed in detail in Section 3.1). Their work could be extended by using thermomagnetometry (TM) to follow the changes in oxidation and structure of the iron during oxidation (in place of the "transformer core" magnetic method used by Spice and Staveley, which required large (typically 10 g) samples and cooling to room temperature before magnetic analysis.) The properties of the Fe/BaO_2 system could also be compared with those of the Fe/SrO_2 system and the other fuel/peroxide systems studied by Drennan [6]. An additional advantage of using Fe was the availability of suitable Fe wire, which permitted some micrographic studies (suggested by Dr A.K. Galwey of the Queen's University of Belfast) to be made of the interaction of the surface of the wire with the oxidants under a variety of conditions (see Section 14).

It was also of interest to examine the behaviour of zinc, as a fuel with a low melting point (420°C), in combination with the peroxides, since the other fuels used in the detailed studies have had much higher melting points (Fe 1535°C; Mn 1244°C; Mo 2610°C). Zinc has a further advantage of existing virtually exclusively in either the 0 or 2+ oxidation states, in comparison with the several possible oxidation states of Fe, Mn and Mo. Both iron and zinc as pyrotechnic fuels also have environmental advantages over systems containing, for example, lead or antimony.

One of the mechanisms considered for pyrotechnic combustion involves rate control by diffusion of fuel atoms, or ions derived from some oxidation of the fuel, into the lattice of the oxidant. Cation vacancies in the BaO_2 and SrO_2 structures can be assumed to accommodate ions of radius less than that of Ba^{2+} (0.136 nm) or of Sr^{2+} (0.058 nm) [8], respectively. In Drennan's study [6], the fuels used were Mn (atom: 0.137 nm; Mn^{2+}: 0.067 nm; Mn^{3+}: 0.058 nm) and Mo (atom: 0.140 nm; Mo^{3+}: 0.067 nm; Mo^{4+}: 0.065 nm; Mo^{6+}: 0.060 nm). This study extends consideration to Fe (atom: 0.126 nm; Fe^{2+}: 0.061 nm; Fe^{3+}: 0.055 nm) and Zn (atom: 0.137 nm; Zn^{2+}: 0.075 nm)

A field with many aspects in common with the study of pyrotechnic delays, is that of the self-propagating high-temperature synthesis (SHS) of materials. An additional aim of this study was to examine the solid products of combustion, which may include ferrates and zincates of barium and strontium, and to determine the conditions required for optimum formation of specific products.

3. PREVIOUS WORK:

3.1 The studies by Spice and Staveley:

Amongst the pyrotechnic systems studied by Spice and Staveley [4] were the iron/barium peroxide and iron/potassium dichromate systems. The occurrence of "pre-ignition reactions" (PIR) in some systems was proposed. A PIR may initiate chemical changes in the layer being heated ahead of the burn front, and need not necessarily be the same reaction as that occurring during combustion. The PIR raises the temperature to a critical level above which the actual combustion reaction can commence.

A magnetic analysis method was used to determine the iron content of the partially reacted compositions, using the transformer principle, whereby the mutual inductance between two coils is significantly enhanced by the insertion of an iron metal core. Pellets were dried at 250°C (no detectable reaction) with continuous evacuation, sealed in Pyrex tubes, heated in the furnace for a pre-determined length of time, and the percentage of metallic iron was determined magnetically using a calibration curve of pellets of known composition. The transformer assembly was not housed in the furnace used to treat the pellets, so pellets had to be cooled prior to being analysed. X-ray analysis showed that no Fe_3O_4 had formed.

Ignition of iron/barium peroxide pellets occurred above 350°C, while no detectable reaction occurred below 300°C. X-ray studies on the system showed that the reaction products were probably Fe_2O_3 and BaO. The mechanism of the PIR was proved, by elimination, to be a genuine solid-solid reaction since (i) direct gaseous oxidation of iron had a smaller temperature coefficient than the PIR and occurred more rapidly; (ii) no decomposition of barium peroxide was recorded for samples kept at 335°C for up to four hours; (iii) iron oxide, a known decomposition catalyst of barium peroxide, actually slowed the reaction; (iv) the extent of oxidation and the initial rate increased with compaction; (v) the rate of oxidation did not decrease with evacuation, but sometimes increased, and (vi) the melting point of barium peroxide was above 400°C and thus no liquid phase was present. Further evidence supporting these observations was that (i) the burning rate and susceptibility to ignition of the iron/barium peroxide system were markedly decreased by pre-heating and (ii) the iron/potassium dichromate system had a PIR beginning at 100°C below the melting point of potassium dichromate.

The study on the iron/potassium dichromate system proceeded along the same lines as on the iron/barium peroxide system. Ignition temperatures (600°C) were closer to the PIR temperatures (300-350°C) than for the iron-barium peroxide system (where combustion temperatures were 1200°C).

The PIR was proposed to be similar to the ignition reaction in the iron/potassium dichromate system.

Oxygen migration was suggested as the mechanism for interaction at the relatively low temperatures involved, due to the low dissociation pressures of the oxidants and the high activation energies associated with movement of atoms/ions through the lattice in a step-wise manner (relative to gaseous oxidation).

The mean ignition temperature for various iron/barium peroxide compositions reached a minimum at 25% iron. This composition gave the most rapid PIR. Increasing the compaction on the pellet increased both the ignition temperature and the PIR. The introduction of Fe_2O_3 was found to decrease the ignition temperature to a minimum, followed by an increase, yet always to decrease the rate of the PIR. This was seen as confirmation that the PIR does not proceed via the gas phase, i.e. the decomposition $BaO_2(s) \rightarrow BaO(s) + \frac{1}{2}O_2(g)$ does not occur significantly prior to reaction with Fe.

In the second paper [7], the heats of reaction and rates of burning were studied. The iron/barium peroxide system was classified as a "class 1" reaction in that Q (the heat of reaction per mole of oxidising agent) remained constant as the percentage of reducing agent was increased beyond the stoichiometric point. This was taken to be an indication that only one reaction was occurring between the oxidant and the fuel.

Of the three possible reactions, namely:

(i) $BaO_2(s) + Fe(s) \rightarrow FeO(s) + BaO(s)$

(ii) $BaO_2(s) + 2Fe(s) \rightarrow Fe_2O_3(s) + 3BaO(s)$

(iii) $BaO_2(s) + 3Fe(s) \rightarrow Fe_3O_4(s) + 4BaO(s)$,

none had a sufficiently high heat of reaction, Q, to match that observed and X-ray studies of the residues failed to show the existence of any Fe_2O_3 or Fe_3O_4, but rather barium ferrite ($BaFe_2O_4$). At the time that the research was performed, no value for the heat of formation of barium ferrite was available to support this finding.

The Maillard-Le Chatelier equation (eqn. 3.1):

$$v = \frac{\lambda q}{bc^2 \rho (T_I - T_0)} \quad \ldots\ldots\ldots \quad 3.1$$

(where v is the linear rate of burning, λ is the thermal conductivity, q the heat of reaction per unit mass, c the specific heat, ρ the density, b the reaction zone width, T_1 the ignition temperature and T_0 the initial temperature) was used to relate the enthalpy of combustion to the burning rate (inversely

related to the zone width, b, above). The enthalpy of combustion was found to have a larger effect on the burning rate than physical factors such as thermal conductivity and specific heat. The systems examined (Table 3.1) always had maximum burning rates at percentages of fuel greater than or equal to those giving a maximum in the heat of burning. Incomplete oxidation of the fuel was thought to be the cause.

An important conclusion of the Spice and Staveley research was that the rate of burning is more sensitive to the chemical nature of the oxidant than to that of the metal/fuel. They explained this in terms of the generally lower melting points of the oxidants in their study, relative to the fuels, and the greater mobility of the ions in solids near the melting point (Tamman effect).

TABLE 3.1: Maxima in burning-rate and Q curves of Fe-fuelled pyrotechnic systems [7]:

System	v_{max}/[mm s^{-1}]	Q/[kJ g^{-1}]	% Fuel	
		at v_{max}	at v_{max}	at Q_{max}
Fe/BaO_2	8.0	1.046	25	<15
$Fe/KMnO_4$	10.6	1.464	55	35
Fe/KNO_3	5.0	1.598	65	<40
$Fe/Sr(NO_3)_2$	2.4	1.226	60	50
$Fe/Ba(NO_3)_2$	1.6	1.305	60	45
$Fe/Pb(NO_3)_2$	3.9	1.192	65	52

Hill *et al* [9] extended the Spice and Staveley study, by studying the relationship between Q and composition. The iron/barium peroxide reaction did not exhibit a peak in the plot of maximum temperature versus composition over the composition range studied (15-55%). The stoichiometric point of the simplest reaction,

$$2Fe(s) + 3BaO_2(s) \rightarrow Fe_2O_3(s) + 3BaO(s)$$

was at 19% iron, yet Q remained constant down to 15% iron - an indication that an additional reaction or a series of reactions occurred. Hill supported Spice and Staveley's finding that the maximum rate is always at a greater percentage of reducing agent than the reaction which gives the maximum heat of reaction.

The ignition temperatures were compared with the activation energies for a variety of systems and showed little correlation. It was concluded that the activation energies for the ignition process were far less (12 to 34 kJ mol^{-1}) than those of the PIR's (about 210 kJ mol^{-1}). Thus the rate-controlling processes for the pre-ignition reactions were concluded to be different from those for the ignition

reactions themselves, and a structural transition or phase change was suggested to be necessary prior to ignition.

3.2 The use of peroxides in pyrotechnic systems:

Drennan [6] mentions that the use of barium and strontium peroxide in pyrotechnic systems is common, but that most of the information is in patent form and little open literature exists. Many systems exist where a peroxide is used in conjunction with other oxidising agents. For example, strontium peroxide is used to give a red flame colour in flares. Barium peroxide finds use chiefly in delay element compositions.

Spice and Staveley [4] studied the Fe/BaO_2, S/BaO_2, Mo/BaO_2 and Mn/BaO_2 systems. Hill [9] published data on the Mo/BaO_2, Fe/BaO_2 and S/BaO_2 systems. Booth [10] used the Fe/BaO_2 system to test his mathematical theory of self-propagating layer-to-layer reactions. Hogan and Gordon [11], whilst studying the Mg/BaO_2/calcium resinate system, extended their study to the binary Mg/BaO_2 system, and proposed a stoichiometry for the system. They also found that the resinate/BaO_2 system had the lowest temperature exotherm of all combinations, and the resinate was directly responsible for lowering the exotherm temperature from 540°C to 299°C. In their TG study of the thermal decomposition of BaO_2, they found a mass loss beginning at 600°C, corresponding to the loss of one oxygen atom, reinforcing the idea of a simple decomposition, yet their DTA study revealed no exotherm for this mass loss. The reaction rate was limited by the particles having the smallest surface area - Mg in this reaction.

Barton *et al* [12], in their study of the Mg/BaO_2/acaroid system, showed the existence of a binder/oxidant reaction in the Mg/BaO_2 system which was responsible for lowering the ignition temperature from above 500°C to 350°C.

Nakahara and Hikita [13,14] studied the temperature and pressure characteristics for a variety of systems including the Fe/BaO_2 and Mo/BaO_2 systems. They concluded that the combustion wave in the iron system is preceded by flowing gas and that this is due chiefly to the endothermic decomposition of the oxidising agent, and not merely the thermal expansion of air.

Johnson [15] investigated the Se/BaO_2 system, used commonly in delays, for the effect of pre-heating and found that the pre-ignition reaction was not self-sustaining. His finding, that the Se diffuses in the lattice to form a surface coating of product prior to ignition, followed by formation of bulk product, was in agreement with the conclusion reached by Hill and Wallace [18] in their study on the $Mo/KMnO_4$ system, and, to a certain extent, Spice and Staveley's research on the Fe/BaO_2 and

$Fe/K_2Cr_2O_7$ systems.

Yoshinaga and co-workers [16] studied the Mo/BaO_2 system, and found that BaO_2 decomposes at 400°C. They also analysed the BaO_2 and found traces of $BaCO_3$ and $Ba(OH)_2$, probably resulting from exposure to air and grinding.

Beyens and Dubois [17] studied the Mg/BaO_2 system and determined that the particle shape played a significant role in the thermal behaviour of BaO_2. They also studied the formation of surface-$BaCO_3$ on burning, as well as noting a decrease in burning rate on exposure to humid air, reaching a limiting value after 3-6 hours.

3.3 Other iron-fuelled pyrotechnic systems:

Hill and Wallace's [18] results for the $Fe/KMnO_4$ system suggested that reaction was similar to that proposed in their more detailed study of the $Mo/KMnO_4$ system, i.e. that two stages are evident in the reaction, the first (occurring at temperatures less than 120°C) involves the most probable migratory species, Mo, coating the internal surfaces with a layer of product by migrating along the grain boundaries, followed by the second reaction in which penetration of the mosaic is energetically possible, and reaction with the bulk material can occur (at 850°C). The Fe-fuelled systems studied by Spice and Staveley appear in Table 3.1.

Martinez *et al* performed a variety of studies [19,20] on BaO_2/FeO reactions as well as reactions between $BaO_2/FeSO_4$, giving barium ferrates as products (discussed in Section 3.11).

3.4 Zinc-fuelled pyrotechnic systems:

Little work has been published on the use of Zn as a fuel in pyrotechnic delays, although the use of Zn in smoke-producing compositions has been investigated. These systems include $Zn/KClO_4$/hexachlorobenzene [21] and Zn/TNT/hexachloroethane [22]. In pyrotechnic reactions, the temperature of the mixture is rapidly raised above the melting point of Zn.

3.5 Summary of relevant pyrotechnic systems:

The pyrotechnic systems previously studied, which have relevance in the present study, are summarised in Table 3.2.

TABLE 3.2: Research previously conducted on similar systems:

Reference	System/s Studied
Drennan [6]	Mn, Mo, BaO_2 and SrO_2
Spice and Staveley [4,7]	Fe, S, Mn, Mo and BaO_2
Hill [9]	Fe, S, Mo and BaO_2
Booth [10]	Fe and BaO_2
Hogan and Gordon [11]	Mg, BaO_2 and Calcium resinate
Barton *et al* [12]	Mg, BaO_2 and acaroid
Nakahara and Hikita [13,14,23]	Fe, Mo and BaO_2
Johnson [15]	Se and BaO_2
Yoshinaga [16]	Mo and BaO_2
Beyens and Dubois [17]	Mg and BaO_2
Hill and Wallace [18]	Fe, $KMnO_4$, $K_2Cr_2O_7$ and BaO_2
Martinez [19,20]	FeO and BaO_2

3.6 Iron and iron oxides

3.6.1 Physical states of iron:

The states of iron [24] include the α-form (below 910°C), the γ-form (between 910°C and 1390°C) and the δ-form (above 1390°C). Both the α and the δ forms have a bcc geometry (the difference between allotropes is related to thermal expansion of the unit cell), while the γ-form has a ccp lattice. The β-form is not a true allotrope. Iron is ferromagnetic up to the Curie point at 768°C, whereafter it becomes paramagnetic, but no change in crystal form occurs until 910°C. Iron is thus known as the β-form between 768°C and 910°C. The melting point of iron is 1539°C and the boiling point 2887°C [8].

TABLE 3.3: The physical states of Fe [25]:

State of iron	Form	Temperature range/[°C]	Packing	Magnetic state
Solid	α	→786	bcc	ferromagnetic
Solid	β	786-910	bcc	paramagnetic
Solid	γ	910-1390	fcc	paramagnetic
Solid	δ	1390-1539	bcc	paramagnetic
Liquid	-	1539-2887	-	-

The change of iron from the ferromagnetic to paramagnetic state is endothermic, and the transition temperature is dependent on the presence of impurities and amount of annealing undergone [24].

3.6.2 The formation of iron oxides:

The reaction of iron with oxygen is sensitive to conditions. Some forms of iron powder are pyrophoric at room temperature, whilst massive iron only begins to oxidise in dry air above 150°C. The oxide scale that forms on iron heated to a high temperature in air consists of three layers: FeO, Fe_3O_4 and Fe_2O_3. The only definite intermediate between FeO and Fe_2O_3 is Fe_3O_4. The oxide formed on Fe powder up to a temperature of 200°C is γ-Fe_2O_3 [26,28]. The rate of the reaction is considered to be controlled by the entry of Fe into the FeO layer. The activation energy for iron oxidation increases from 67 to 167 kJ mol^{-1} as the temperature is raised from 400-1100°C [27]. At high temperatures, the rate is no longer controlled by movement of metal across the metal-oxide interface, but rather by diffusion of the metal through the oxide. The major products are Fe_2O_3 and Fe_3O_4 (in excess oxygen) and FeO above 575°C (in oxygen-deficient atmospheres). FeO is only stable at high temperatures and decomposes into iron and Fe_3O_4 when it is cooled slowly. Crystalline FeO is always deficient in iron (non-stoichiometric), having a formula of $Fe_{0.93}O$ at 575°C. Some Fe^{2+} is replaced by Fe^{3+}, and the resulting stoichiometry arises from charge neutrality considerations. FeO melts at 1368°C. As further oxidation occurs ($Fe^{2+} \rightarrow Fe^{3+}$), Fe_3O_4 results and eventually γ-Fe_2O_3. Fe_3O_4 is a mixed Fe^{2+} - Fe^{3+} oxide, is strongly ferromagnetic, melts at 1538°C and can be oxidised to γ-Fe_2O_3 and eventually α-Fe_2O_3 by heating in air. Fe_3O_4 has the inverse spinel structure $Fe^{2+}(Fe^{3+}O_2)_2$. $\gamma - Fe_2O_3$ is ferromagnetic, and is converted to α-Fe_2O_3 when heated in air above 400°C. Karmazsin *et al* [29] in their study on the $\gamma \rightarrow \alpha$ Fe_2O_3 metastable transition, state that this transformation occurs between 400 and 600°C, and that the Curie point of α-Fe_2O_3 occurs at 627°C. Hellwege [30] claimed that γ-Fe_2O_3 transforms irreversibly to α-Fe_2O_3 at 400°C, and that the Curie temperature of γ-Fe_2O_3 is 675°C. α-Fe_2O_3 (hcp) occurs naturally, is paramagnetic, and melts at 1565°C. The rate of oxidation of iron may be affected by internal magnetic fields [31]. Selected thermochemical data [8] for the iron oxides are presented in Table 3.4.

TABLE 3.4: Thermochemical data for Fe and Fe-oxides:

	ΔH_{melt}/[kJ mol^{-1}]	c/[J K^{-1} mol^{-1}]	mp/[K]	-ΔG/[kJ mol^{-1}]	Temperature/[K]
Fe	14.90	25.104	1539	0	-
FeO	32.2	48.116	1380	269.493+0.0627T	300-1800
Fe_3O_4	138.1	143.428	1596	290.306+0.1163T	300-1800
Fe_2O_3	variable	103.847	1565	309.467+0.2897T	300-1500

Zhigotskii *et al* [32] reported that the heat generated during oxidation of finely-dispersed iron powders can lead to sintering of the bulk of the material, slowing of the oxidation rate and increasing the activation energy of the process.

Kubaschewski and Hopkins [33] studied the oxidation rate of iron in the range 700-950°C, and Rahmel *et al* [34] found the rate to be independent of oxygen pressure if Fe_3O_4 and Fe_2O_3 are present in the surface scale. If only FeO exists on the surface (such as in O_2 deficient environments) the rate becomes:

$$k_l = const[p(O_2)]^{0.7}$$

FeO, being a p-type semi-conductor, has many vacant cation sites, hence diffusion is cationic. In Fe_3O_4, both cations and anions diffuse, whilst in Fe_2O_3, an n-type semi-conductor, diffusion of the anions is the dominant process. Kubaschewski *et al* [33], claimed that the diffusion of Fe in Fe_2O_3 is $2x10^4$ that of O, in the temperature range 930-1270°C. The mechanism of iron oxidation changes from logarithmic below 200°C to parabolic above, with thin film mechanisms, such as that suggested by Hauffe *et al* [35], applying. Ionic movement is not controlled by a concentration gradient, but rather by an electric field. Studies of the effect of water vapour on iron indicate that Fe_3O_4 is the dominant oxide below 700°C, whilst FeO dominates above 700°C, since ΔG for the reaction:

$$Fe_3O_4(s) + H_2(g) \rightarrow 3FeO(s) + H_2O(g)$$

is negative above 700°C. Attack of iron by water vapour may be more rapid than that by air in the region 700-1100°C [36] as the possible absence of Fe_3O_4 allows high rates of diffusion through the vacancy-rich FeO layer.

The formation of FeO scale between 570 and 1550°C is due to the diffusion of Fe, which follows a parabolic oxidation rate [51]. Homogeneity of the field generated across the metal-oxide interface and self-diffusion result in the formation of a broad layer of FeO and thinner layers of the higher oxides. Oxidation mechanisms in the FeO layer are thus most important. The Arrhenius activation energies for diffusion of various species are listed in Table 3.5.

TABLE 3.5: Activation energies for diffusion of mobile species in Fe oxidation:

Research group	Fe oxide	Diffusing species	E_a/[kJ mol^{-1}]	Temperature range/[°C]
Smeltzer *et al*[37]	FeO	Fe	56	570-1550
Smeltzer *et al*[37]	Fe_3O_4	Fe	94	570-1550
Grimes [38]	Fe_3O_4	Fe	231	850-1200
Grimes [38]	Fe_3O_4	O	167	850-1200
Smeltzer *et al*[37]	Fe_2O_3	Fe	208	570-1550
Smeltzer *et al*[37]	Fe_2O_3	O	139	570-1550

The oxidation rate of iron between 220 and 400°C increases as the oxygen pressure is decreased from 100 to 0.01 Torr [39]. The kinetics of oxidation indicate two stages. The oxidation rate is initially

rapid and pressure dependent, followed by a slower, pressure-independent period. In the initial oxidation, the chief product is Fe_3O_4. The subsequent formation of α-Fe_2O_3 slows the reaction [40]. The growth rate of α-Fe_2O_3 appears to be pressure dependent, with rapid formation at "high" oxygen pressures resulting in a decrease in formation of cation vacancies in the Fe_3O_4 layer and a subsequent decrease in the oxidation rate. At low pressures, the rapid oxidation persists for longer and thicker oxide films result.

DTA curves for the oxidation of Fe_3O_4 [41], show exothermic peaks at 250°C and 390°C. The Curie point is evident at 570°C. The Curie temperature of γ-Fe_2O_3 was determined [42] as 675°C. Gallagher *et al* [43], studied the rates of oxidation (by isothermal weight changes) of Fe_3O_4 to Fe_2O_3 in oxygen over the range 500-720°C, and found the Curie point of Fe_3O_4 to be 590°C. The oxidation rate was similar above and below the Curie point, but distinct variation of the rate occurs in the region of the Curie temperature. The finding that the oxidation must be a two-step process disagreed with that of Davies *et al* [44,45], who proposed that Fe_3O_4 oxidation occurs via cation diffusion through the magnetite (Fe_3O_4) and anion diffusion through hematite (Fe_2O_3) layers with combination occurring at the interface and giving rise to further hematite. As this latter oxidation mechanism would generate uniform layers of hematite around magnetite particles (not observed by Gallagher) an alternative mechanism was sought. Yamaguchi and Kimura [46] and Colombo *et al* [47] proposed a two-stage process. In the first stage, Fe_3O_4 is oxidised to form a solid solution of Fe_3O_4/γ-Fe_2O_3. In the second stage, α-Fe_2O_3 is precipitated from the solid solution by nucleation in the supersaturated solution. The first stage of the oxidation was suggested to be diffusion controlled (with an activation energy of 116 kJ mol^{-1} in the range 500-720°C), and microscopic and X-ray observations supported the occurrence of the second stage.

The activation energy for the oxidation of iron is dependent upon both temperature and oxide-layer thickness. The values listed in Table 3.6 have been reported in the literature.

TABLE 3.6: Activation energies reported for the oxidation of Fe:

Reference	Temperature range/[°C]	E_a/[kJ mol^{-1}]
Zhuk and Linchevskii [27]	400-1100	67 → 167
Grimes [38]	850-1200	167
Gallagher [43]	500-720	116
Schumann and Schadler [48]	700-950	94
Stanley *et al* [49]	500-1100	138
Paidassi and Fuller [50]	400-600	153
Paidassi [51]	700-1250	170
Cabrera and Mott [52]	700-900	154

3.7 Thermomagnetometry of iron and iron-oxides

Gallagher *et al* [53] used thermomagnetometry to study the decomposition of siderite ($FeCO_3$). The N_2 used in their experiments contained ppm values of O_2 which they concluded [54] to be sufficient to oxidise FeO or Fe_3O_4 produced during the decomposition. This reaction gave rise to a mass gain observed at 600°C which was not observed in pure O_2 atmospheres, where oxidation of Fe was complete by this temperature. Karmazsin *et al* [55] devised a simple simultaneous thermodilatometry-thermomagnetometry instrument, capable of studying small magnetic fluctuations. They used this technique to study the γ-Fe_2O_3 → α-Fe_2O_3 transition (cell shrinkage) at 470°C. In a similar study on an Fe_3O_4 pellet compacted at 50 MPa, the Fe_3O_4 → γ-Fe_2O_3 transition occurs at ~250°C. The resulting γ-Fe_2O_3 transforms to α-Fe_2O_3 between 320°C and 340°C and the "order point" of α-Fe_2O_3, the temperature at which the Fe_2O_3 lattice shrinks slightly, occurs at 675°C. This technique is suggested for quantitative analysis of the Fe_2O_3 content in compositions. In addition to following magnetic fluctuations in the sample, which occur without corresponding mass changes, it has been suggested that the technique of thermomagnetometry is more sensitive than conventional thermogravimetry [56], and that magnetic saturation of samples provides sensitivity to follow reactions involving less than 1 μg of magnetic material.

Watanabe [57] studied the magnetic behaviour of strontium perovskites of iron and found that electrical conductivity is enhanced by the co-existence of Fe^{3+} and Fe^{4+}. He also found that the level of Fe^{4+} generated in the formation of the perovskites at 900°C in air was 60% of that generated at 1150°C in air.

Work has been performed [58,59] on the effect of a magnetic field on the reaction rate of reduction of magnetic oxides. The reduction of iron oxides is accelerated in the presence of an applied

magnetic field [31], and consequently, the rate of reaction and composition of the final product of oxidation may also be affected by the strength of the magnetic flux applied to a sample of Fe during oxidative heating.

3.8 Zinc and zinc oxide

Zn melts at 419.5°C and boils at 908°C (1 atm). The vapour pressure of zinc increases exponentially with temperature ($\log_{10}p = -6163.14/T + 8.108$) [8], and reaches 100 mm Hg at 734°C [60]. In the presence of oxygen, Zn forms zinc oxide: $Zn + \frac{1}{2}O_2 \rightarrow ZnO$, but, in the presence of other metal oxides, complex oxides may form. Derevyaga *et al* [61] proposed that the combustion of Zn takes place both at the surface and in the surrounding gas space. The kinetics of the oxidation of molten Zn have been examined in detail by Cope [62], who proposed that the oxidation of Zn is controlled by the diffusion of defects associated with the excess metal character of non-stoichiometric zinc oxide. Zn also reacts with H_2O yielding oxides and hydroxides. Mixed oxides form readily, e.g. $BaZnO_2$ [63,64] and $SrZnO_2$ [65] form between 1000°C and 1400°C.

The oxidation of Zn surfaces has been studied extensively. In dry O_2 atmospheres at 25°C, the layer of ZnO formed on a smooth surface is typically 50-200 nm thick [66]. Studies by Evans [67] and Smeltzer *et al* [37] have shown that the oxidation of zinc proceeds via the logarithmic law below between 350°C [67] and 375°C [37], as conditions required for parabolic thickening (such as potential gradients) are absent. This temperature range has been confirmed [68]. Oxidation is believed to occur by the outward passage of interstitial matter through defects or zones of disrupted structure in the outer part of the oxide film. The rate of passage is controlled by the rate of crossing of a less-pervious inner film of constant thickness, and is independent of the thickness of the outer film. As the film thickness increases, so do the number of path obstructions, and hence the rate of growth of the film decreases with film thickness according to the logarithmic law.

At higher temperatures the oxidation follows a parabolic rate law:

$$\frac{dy}{dt} = \frac{k}{y} \quad \text{. . . . . 1.3}$$

where y is the oxide film thickness, but the range of onset temperatures of oxidation obeying the parabolic rate law is variable. The onset temperatures ranges from 200°C to 415°C [69,67], with other researchers [70] estimating the range at between 375°C and 415°C.

The rate constant for oxidation is related to temperature and pressure by a complex rate law above 370°C [69]:

$$k=k_o\frac{jP}{1+jP} \quad \ldots\ldots\ldots\ldots \quad 1.2$$

where k is the rate constant, P is the oxygen partial pressure, k_o=119.2 kJ mol^{-1} and $j=j_o e^{-176.6/RT}$. j_o is a constant.

Thomas [70] has suggested that the rate of oxidation of Zn is controlled by the rate of the process at the oxide-gas interface, while Cabrera and Mott [52] have suggested that the parabolic rate law arises from the rate constant being dependent upon the electric field which develops across the oxide film. Evans [67] (using a similar mechanism to the rift mechanism detailed above) suggested that diffusion of oxygen occurs along grain boundaries in the zinc-oxide film. The oxide has been found to grow as crystallites 30-150 nm in diameter [68], with oxide whiskers growing from the oxide-oxygen interface. The dependence of the rate of oxidation on the partial O_2 pressure is reported [68] to be related to reaction at the oxygen-oxide interface. The two rate-controlling steps are proposed [68] to be (i) incorporation of O^- ions in the lattice, which controls the parabolic kinetics, and (ii) the second ionisation process, $O^- + e^- \rightarrow O^{2-}$, which controls the logarithmic kinetics.

Moore and Lee [69] proposed the following three stages for the mechanism of oxidation: (i) O_2 is adsorbed as O atoms on the surface of the ZnO. (ii) Adsorbed O atoms are converted to adsorbed O^{2-} ions by electrons passing from the metal substrate to the oxide interface. A vacant Zn^{2+} site is formed for each O^{2-} ion adsorbed on the surface. (iii) A new layer of ZnO forms as a Zn^{2+} ion moves through the oxide layer from the metal to fill the vacant site.

Zinc oxide is white when formed, but becomes yellow when heated to 425°C [66]. Parish [71] suggested that the colour is related to the loss of stoichiometry since oxygen is lost during heating, resulting in the establishment of colour centres and the formation of an n-type (excess metal) semi-conductor. The oxide has an hexagonal (wurtzite) lattice [40,66]. ZnO melts at 2000°C, but sublimes at 1720°C at 1 atm in air. Values reported for the Arrhenius activation energy of the $Zn + \frac{1}{2} O_2 \rightarrow ZnO$ reaction are given in Table 3.7.

TABLE 3.7: Activation energies reported for the oxidation of Zn to ZnO:

Reference	E_a / [eV]	E_a / [kJ mol^{-1}]	Temperature range/[°C]
Smeltzer and Young [37]	0.35	34	320-375
Cabrera and Mott [52]	1.50	145	600-700
Cope [62]	1.08	104	440-700
Aylett [66]	1.82	176	300-450
Tuck *et al* [68]	0.95	92	320-370
Tuck *et al* [68]	2.17	209	370-415
Moore and Lee [69]	1.24	119	300-400
Thomas [70]	1.20	116	400

3.9 The alkaline-earth peroxides

3.9.1 Introduction:

The structures of BaO and SrO are of the NaCl type, and BaO_2 and SrO_2 have the CaC_2 structure. This is due to the elongated shape of the O_2^{2-} ion, which deforms the cubic cell to a tetragonal cell. In the dissociation of the peroxide to the oxide, the tetragonal c-axis (the axis to which the peroxide-ions have parallel orientation) shrinks to one of the cubic axes of the oxide.

Although the overall process for the thermal decompositions of BaO_2 and SrO_2 is generally agreed to be:

$$MO_2(s) \rightarrow MO(s) + \tfrac{1}{2}O_2(g)$$

(where M = Ba or Sr), the process shows a high degree of reversibility and hence is influenced by the local and overall partial pressures of O_2 [72]. Thus the reported temperatures of onset of decomposition vary widely. The decompositions are also affected by the presence of impurities. Some of the results reported are discussed below and summarised in Table 3.8.

3.9.2 Thermal stability:

The thermal stability of BaO_2 has been reported to be greater than that of all known metal peroxides [73], including SrO_2 [74]. BaO_2 can occur in a lower temperature, less active α-form, or a higher temperature β-form. No fixed transition temperature has been reported. Decomposition of the β-form gives rise to highly reactive BaO [74,90]. The decomposition of BaO_2 is reported [75] to be accelerated in the presence of CO_2 and H_2O, which result in the formation of carbonates and hydroxides. Onset of decomposition may be at temperatures as low as 200°C [75]. Work has also been performed on the decomposition of $Ba(OH)_2$, $Sr(OH)_2$ and the associated hydrates [76,77], which form as solid solutions in the peroxides at high temperatures [74]. Metal oxides, including Cr_2O_3 and

Fe_2O_3 [78], and CuO [79], have also been reported to accelerate the decomposition.

The values given for the decomposition temperature of BaO_2 vary widely, depending on the atmosphere in which the study was performed, with typical values ranging from 500°C in N_2 [73,80,81], to 840°C in O_2 [82] supported by DTA endotherms at 790°C [83]. Melting has been suggested to occur at 450°C [72].

Nonisothermal studies of the decomposition of SrO_2 [80,81,84], suggest that the decomposition is a two-stage process, occurring in two endothermic steps. This was supported by an isothermal study performed on SrO_2 at 212°C in O_2, which showed that the decomposition proceeds as follows:

$$SrO_2(s) \rightarrow SrO(s) + O(ads)$$

$$O(ads) + SrO_2(s) \rightarrow SrO(s) + O_2(g)$$

The initial rapid dissociation step was separated from the ensuing period of slow dissociation by an interval of re-association. The formation of a solid solution layer of oxygen was seen as a possible explanation for the observed behaviour, whereby further dissociation becomes hindered and dissociation in this layer only becomes apparent at higher temperatures. This mechanism would also account for the two stages of decomposition observed in TG studies.

Azuma and co-workers [75] did not support this two-step process, and reported that the oxide and peroxide can co-exist during the decomposition of SrO_2. They suggested that a linear relationship exists between the logarithm of the oxygen partial pressure and the reciprocal of the decomposition temperature.

The reported decomposition temperatures of SrO_2 vary. Blumenthal [80,81] reported two endothermic stages with onset temperatures of 390 and 525°C. Volnov [85,86] reported a single stage (onset 410°C). Onset temperatures as low as 175°C have been reported [48].

3.9.3 Thermodynamics of dissociation:

Values reported for the enthalpy of dissociation of BaO_2 range from 67.8 kJ mol^{-1} [85,86] to 80.8 kJ mol^{-1} [87]. The entropy of dissociation is 71.5 J K mol^{-1} [88,89], and the enthalpy and entropy of formation 636.4 kJ mol^{-1} and 101.3 J K mol^{-1}, respectively.

The enthalpy of dissociation of SrO_2 has been reported as 48.0 kJ mol^{-1} [75] and 56.5 kJ mol^{-1} [80,81,85,86] for the nonisothermal decomposition, and a value of 41.8 kJ mol^{-1} was reported [80,81] for isothermal decomposition at 212°C in O_2.

3.9.4 Kinetics of dissociation:

The activation energy for the isothermal decomposition of BaO_2 was found [88] to be between 135 kJ mol^{-1} and 141 kJ mol^{-1}, using a variety of kinetic models. The activation energy of the reverse reaction is 51 kJ mol^{-1} [88]. Nonisothermal methods gave a value of 191.6 kJ mol^{-1} [90] for the activation energy. Decomposition of BaO_2 has been suggested to occur in three distinct steps [91]: nucleus formation with an E_a of 12 kJ mol^{-1}; grain growth with an E_a of 104 kJ mol^{-1}; and oxygen diffusion, with an E_a of 2 kJ mol^{-1}.

Kinetie parameters for the decomposition of SrO_2 were not found in the literature surveyed.

TABLE 3.8: Values reported for the enthalpy of dissociation of alkaline-earth metal peroxides

Peroxide	Temperature in N_2/[°C]	Temperature in O_2/[°C]	ΔH_{Diss} /[kJ mol^{-1}]	E_a /[kJ mol^{-1}]	Reference
BaO_2		833	80.8	-	Wiedemann *et al* [87]
	670	844	79.5	140.6	Fahim *et al* [88]
			80.0	-	Till [89]
		790	67.8	-	Volnov [85,86]
	500		70.1	-	Blumenthal [80,81]
SrO_2	390 and 525		56.5	-	Blumenthal [80,81,84]
		480	56.5	-	Volnov [85,86]
			48.0	-	Azuma [75]

3.10 Self-propagating high-temperature synthesis of materials

Self-propagating high-temperature synthesis (SHS) is the term used to describe a class of redox-type chemical reactions which, once initiated, are sufficiently exothermic to be self-propagating, producing useful products from the reagents, i.e. SHS places the emphasis on the nature of the product formed in pyrotechnic reactions.

An expression determining whether a combustion reaction will be stable or unstable, based on the kinetic and thermochemical properties of a system, has been proposed [92]: .

$$\beta = \left(\frac{9.1cRT_{ad}^2}{QE_a}\right)\left(\frac{1-0.27Q}{RT_{ad}}\right) \quad \ldots\ldots\ldots \quad 3.4$$

where c is the heat capacity of the product; Q is the heat of reaction; R is the gas constant; T_{ad} is the adiabatic temperature and E_a is the activation energy. When $\beta > 1$, combustion occurs in a stable mode, while combustion is unstable if $\beta < 0$. SHS processes are thus controlled by three parameters: energy generation, energy distribution and mass transport [5].

Some of the experimental factors which determine the success of SHS reactions [93] are:

i) An increase in the diameter of the sample decreases both the radial heat loss and the amount of unreacted reagent, and thus increases the burning-rate to a maximum, beyond some threshold diameter. In the presence of diluents, this threshold diameter has to be increased to sustain combustion.

ii) The stoichiometric composition usually provides the maximum T_{ad} value.

iii) The specific heat and the thermal conductivity vary with the packing density of the unreacted sample. The usual effect of an increase in packing density is to decrease levels of unreacted reagent in the product and to increase the T_{ad}. When the compaction density is below some threshold value, the heat from the reaction is not effectively conducted ahead of the burn-front, and an unstable reaction or stifling of reaction may result. Similarly if the compaction density is well above the threshold value (usually $>70\%$ theoretical density) [94], heat transfer away from the combustion zone may be too rapid, and unstable reaction may result. Steady-state combustion thus only exists in a specific range of compaction density values (suggested to be between 40 and 65% of the theoretical density [93]).

iv) The particle sizes of the reagents are a major factor. Coarse particles of fuel may act mainly as an inert diluent, leaving large quantities of unreacted fuel in the product, thus affecting the product composition. This change may also decrease the rate of product conversion (forward heat transfer is decreased by particles having a larger thermal mass) and thus broaden the combustion zone. Product formation occurs at a cooler temperature [5], and the rate of combustion [95,96] may be lowered. Decreasing the particle size of the minor component increases the reaction rate by improving the inter-particle contact area. Assuming a typical oxidant particle size range in the lower μm's, optimum particle-size ranges for the fuels in SHS reactions are <80 μm [93].

v) The introduction of an inert diluent, e.g. product, may decrease the rate of combustion and transform a steady-state combustion reaction into an unstable reaction. The quantity of heat energy released per gram of reagent mixture is thus decreased [97]. For confined reactions, the introduction

of inert diluents has little effect on the T_{ad}, until a critical value is reached, where the decrease in T_{ad} becomes linear with proportion of diluent added [97]. For uncontained sample studies, it was found that delamination in the product material (regular separation of the product material into layers orientated perpendicular to the direction of passage of the burn-front) decreases as the concentration of diluent is increased. This is due to a decrease in the temperature gradient across the reaction zone at the lower T_{ad} values and decreased propagation rates, and a decrease in volume change related to the smaller quantity of product being formed [97]. A further effect of increasing the quantity of diluent in a mixture is the associated decrease in cooling time due to decreased reaction temperature, which may adversely affect product formation [97]. In gas-solid reactions, the role of a diluent is often to decrease the reaction temperature below that of the melting-point of one or more of the reagents, as the existence of a liquid phase decreases the penetration of the bulk matrix by the gas phase (decreased permeability) and reaction would be inhibited [98].

vi) Preheating some reactant mixtures may increase their combustion temperatures and the rate of propagation [94].

vii) Slow cooling of the mixture decreases the amount of unreacted reagent.

viii) Packing the sample into a longitudinal container may increase the propagation rate by increasing heat transfer. During SHS the product usually expands, increasing porosity, [97] unlike in sintering, where the sample shrinks. This expansion can be decreased by the container.

Ignitibility limits of compositions are determined by [94]:

i) the proximity of mixtures to the stoichiometric composition, where they are most easily ignited.

ii) the presence of any inert diluents, which decrease the ease of ignition, and

ii) the coexistence of desirable features [93], such as high reaction enthalpy, low activation energy and high initial temperatures.

Five modes of combustion propagation have been observed in SHS reactions [93]. These are steady-state combustion, oscillating combustion (propagation of a planar, pulsating combustion wave), spin combustion, repeated combustion and surface combustion. These five modes correspond to four basic types of temperature profile (Figure 3.1).

Different rate determining steps may operate under ignition and non-ignition conditions [99], as well as in high and low density compacts [100].

Merzhanov [101] suggested a series of thermodynamic equations relating combustion rate to combustion parameters:

$$v = Y(T_*, \alpha_*)\, e^{-\frac{E}{RT_*}} \quad \ldots\ldots\ldots\ldots \quad 3.5$$

where T_* is the combustion temperature, and α_* is the fraction reacted at T_*. Four types of SHS reaction are described in terms of T_* and α_*.

Type I combustion waves (typical of pyrotechnic systems), have a narrow reaction zone with a narrower heated layer and

$$T_* = T_o + \frac{Q}{c} \quad \ldots\ldots\ldots\ldots \quad 3.6$$

and $\alpha_*=1$, which is a simplified version of existing theories [100,132] on intersolid combustion reactions. Type II profiles are characterised by a broad reaction zone (typical of SHS reactions),

$$\left[\frac{d\ln\phi}{d\alpha}\right]_{\alpha*} + \frac{QE}{cRT_*^2} = 0 \quad \ldots\ldots\ldots\ldots \quad 3.7$$

and

$$\alpha_* = \frac{c(T_* - T_0)}{Q} \quad \ldots\ldots\ldots\ldots \quad 3.8$$

with $\phi=(\mathrm{d}\ \ln f(\alpha))/\mathrm{d}\alpha$. Type III profiles are characterised by a step in the temperature profile (derivative = 0) and this indicates the existence of two distinct chemical reaction stages. For type III systems,

$$T_* = T_o + \frac{Q_1}{c_1} \quad \ldots\ldots\ldots\ldots \quad 3.9$$

and $\alpha_*=1$, where Q_1 and c_1 refer to the first stage of the reaction. Type IV profiles are similar, but the isothermal region results from a phase transition. $T_* = T_p$, where T_p is the temperature of the phase transition, and

$$\alpha_* = \frac{c(T_p - T_o)}{Q} \quad \ldots\ldots\ldots\ldots \quad 3.10$$

Studies of the effect of heat loss on the performance of pyrotechnic delay compositions [102] have shown that the effect of radial heat loss on the temperature of the reaction zone is minimal.

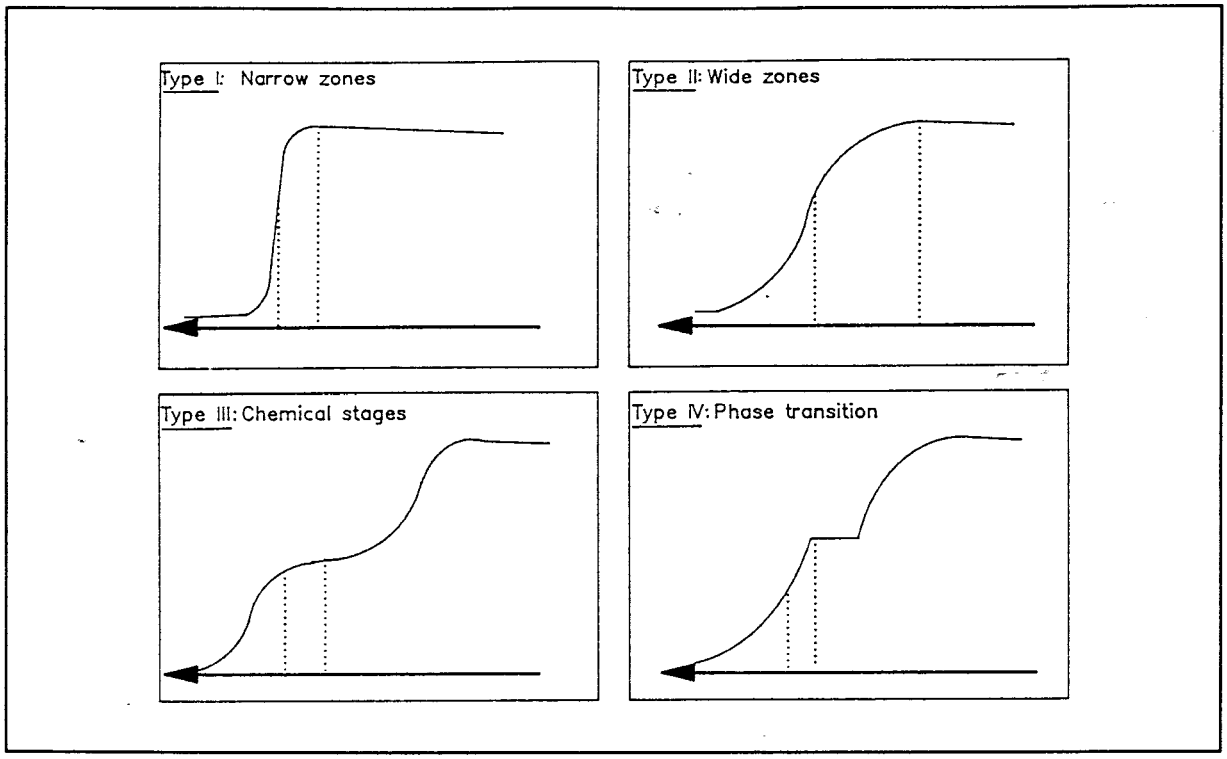

FIGURE 3.1: Types of temperature profiles

In studies of pyrotechnic delays, generally little or no interest has been shown in the nature of the condensed phase products formed, other than their potential as environmental hazards. The formation of gaseous products is generally noted as a factor counting against the practical use of the system being studied in sealed detonator tubes.

The condensed phase products of even binary fuel/oxidant reactions are unlikely to be a mixture of a simple oxidation product of the fuel and a simple reduction product of the oxidant, e.g.

$$AO_2(s) + B(s) \rightarrow AO(s) + BO(s).$$

Mixed oxides, for example ABO_2, are more likely. Because of the rapidity of reaction, a uniform-product is unlikely and the high temperatures reached and rapid cooling mean that the product is often non-crystalline.

3.11 The formation of ferrates

3.11.1 Introduction:

The term "ferrates" (ferrites in some texts) is the collective term for the oxygen compounds of iron in the 4, 5 and 6 valence state. The iron(V) compounds, e.g. K_3FeO_4, do not exist for strontium or barium [103], unlike the iron(IV) and iron(VI) compounds which are discussed below.

No reference was found in the literature to the self-propagating synthesis of ferrates, but much

literature exists on more conventional preparations from mixtures of simple oxides, i.e. the "ceramic route".

The iron(V) species, $MFeO_4$, may be prepared [103] by heating the solid phases of an alkaline earth metal peroxide (MO_2) (or oxide (MO)) with iron (or its oxide) in the ratio M:Fe = 2:1 in a stream of O_2. This method is not satisfactory if pure products are required.

Strontium and barium ferrates are stable in air (with the exception of Ba_3FeO_5 which converts to a red $BaFeO_4$ in moist air) and may be stored as dry crystalline products in closed containers. At room temperature, moist barium ferrate (water content 4-5%) is converted into $BaFeO_3$ with the loss of oxygen. In the dry state (water content of 1-2%) the compound is stable at room temperature. These compounds decompose in two stages: In the first, molecular oxygen is lost, whilst the second involves the formation of trivalent iron compounds. In air, $SrFeO_4$ can decompose over a wide range of temperatures (80-600°C), depending on humidity; and similarly $BaFeO_4$ (105-800°C). The liberation of active oxygen in the thermal decomposition does not imply a single reduction step from 6+ to 3+, but rather that it proceeds through a series of intermediate reduction steps. Strontium and barium ferrates decompose in O_2 as follows: At low temperature (about 200°C) oxygen is liberated and ferrates (3+) are formed. The oxidation of iron from the 3+ to the 4+ state begins at 400°C, reaching a maximum at 700-900°C with the formation of $SrFeO_3$ and $BaFeO_3$. In O_2, all strontium and barium ferrates are stable up to 700-1000°C. Barium and strontium metaferrates begin to decompose in air at 320°C. 34 barium ferrates, 19 strontium ferrates, 4 barium zincates and 1 strontium zincate had been identified by XRD by 1990 [104]. The tetravalent state of iron is known to exist in four types of compound, listed in Table 3.9 [103].

TABLE 3.9: The four varieties of compound formed by tetravalent iron:

Nomenclature	Ratio Ba:Fe	Fe valency	Formula unit	Alkaline earth metal
Metaferrate	1:1	+4	$MFeO_3$	Ba or Sr
Orthoferrate	2:1	+4	M_2FeO_4	Ba or Sr
Pentaoxoferrate	3:1	+4	M_3FeO_5	Ba
Other Ferrate	3:2	+4	$M_3Fe_2O_7$	Ba or Sr

These black, or dark-grey, powdered compounds may be formed by the thermal oxidation of mixtures of two solid phases with M:Fe ratios corresponding to that in the ferrate. Generally the number of cations per formula unit has an effect on the oxidation state of the central atom, albeit small, yet for Fe_2O_3 + BaO mixtures, the iron remains in the quadrivalent state (Table 3.9).

Since the oxidation of iron from the 3+ to the 4+ state seldom proceeds to completion (due to the apparently low thermal stability of the ferrates), nonstoichiometric compounds (or berthollides [8]) containing oxygen lattice vacancies are produced. Studies by Van Hook [105] established that the degree of oxidation in ferrates depends to some extent on the surface area oxidised, a powder giving the maximum oxygen fraction. $BaFeO_{3-x}$ was prepared from $BaCO_3$ and Fe_2O_3, and was found to exist in a high temperature form (up to the melting point at 1370°C) as $BaFeO_{2.50}$, and as a low temperature form with variable oxygen content ($BaFeO_{2.47}$ to $BaFeO_{2.92}$, determined gravimetrically) which transforms to the high temperature form at 915°C in air. $BaFe_2O_4$ and BaO were also detected.

3.11.2 Structural aspects:

$BaFeO_3$ has the $BaTiO_3$ structure [106], but is not a complete structural analogue of the titanate system, since the metaferrate system forms in a single hexagonal structural unit. It appears that the ferrate is the structural analogue of the $CaTiO_3$ system, which has been described by Wyckoff [107] as a tetragonal unit cell of dimensions $a_o=0.398$ nm and $c_o=0.401$ nm. The thermal stability of the hexagonal phase increases with an increase in oxygen pressure. It decomposes at 915°C in air, and melts without decomposing at 50 atm O_2.

The $SrFeO_3$, Sr_2FeO_4 and $Sr_3Fe_2O_7$ ferrates are the structural analogues of the corresponding titanates. These structural types are related to compounds with higher alkaline-earth metal content, which have the basic perovskite structure, with layers of Sr and O ions introduced between single and double perovskite layers.

3.11.3 Preparation:

Studies on the preparation of barium ferrates have been extensive, usually involving the solid phase reaction between $BaCO_3$ and Fe_2O_3 [108,109,110,111], Fe_2O_3 and $BaO.Fe_2O_3$ [112], BaO_2 and FeO [113], or even the reaction between $FeSO_4$ and FeS_2 and BaO_2 [114]. Ferrate compounds may be produced by heating specific mixtures of BaO and Fe_2O_3 at temperatures of 1200-1400°C to form sintered ceramic products [115], or by wet techniques, whereby $BaFeO_3$ (or similar compounds) are prepared in solution and are then calcined (often under pressure) to form the desired ceramic [106]. A further variation on the wet technique is the use of lyophylised gels in the preparation of $BaFe_{12}O_{19}$ by heating at 600°C [116].

Similarly, much work has been performed on the preparation of strontium ferrates from Fe_2O_3 and $SrCO_3$ [117,118,119], and the study of the electrical and magnetic properties of the products formed [119,120]. The formation of strontium ferrates is accompanied by an exotherm at 700°C [117] to

730°C [121] for co-precipitative production, and exothermic activity above 900°C for ceramic preparation. The ferrate formed in the reaction between $SrCO_3$ and Fe_2O_3 [118] (heating to 1000°C) was dependent on the atmosphere under which prepared, and products formed were analogous to those in the Ba-Fe-O system. $SrFe_2O_4$ formed first, and then reacted with excess Fe_2O_3 above 800°C.

Mössbauer and XRD studies [122,123] form the basis of structure and stoichiometry determination of the ferrates.

3.11.4 Applications of ferrates:

Many ferrates which form at 1000-1300°C are only stable at high temperatures [124]. Spinel-type ferrates have found application as catalysts in oxidation processes [125]. Erchak and Ward [126] extended their study of barium ferrates to the catalytic effects of these oxides on the oxidation of CO. Barium ferrates have important electronic application as digital and analog recording media [127]. The technique of laser ablation deposition of thin films of Ba ferrate [128], and the utilisation of the piezo-electric properties of ferrates [129] have also been studied in detail. Sintered ceramic barium ferrate compounds have been produced [115] for use as high frequency magnetic recording material.

4. EXPERIMENTAL:

4.1 Materials:

The specifications of the materials used in this study are listed in Table 4.1.

TABLE 4.1: Materials used in the study:

Reagent	Supplier	Particle Size [μm]	Purity [%]	Chief Impurity
Fuels:				
Fe	Johnson Matthey	<43	>99.9	Fe_2O_3
Zn	Zinchem	<10	94	ZnO
Oxidants:				
BaO_2	Unilab Saarchem	<20	85	BaO
SrO_2	Bernardy Chemie	<20	85	SrO
Additives:				
Al_2O_3	Baird Tatlock	<120	GPR	-
$Ba(OH)_2.8H_2O$	Merck	<120	98	$BaCO_3$
$BaCO_3$	Hopkin Williams	<120	99.5	-
BaO	BDH	<120	Technical	$BaCO_3$
CuO	BDH	<120	Technical	-
Fe_2O_3	Schering Kahlbaum	<120	Spectral	-
Fe_3O_4	BDH	<120	Technical	Fe_2O_3
$Sr(OH)_2.8H_2O$	BDH	<120	97	$SrCO_3$
$SrCO_3$	Unilab Saarchem	<120	Technical	-
SrO	BDH	<120	Technical	$SrCO_3$
ZnO	Hickmann Kleber	<120	Analytical	$ZnCO_3$

The particle-size distribution of the zinc powder was determined by scanning electron microscopy (SEM) and a Malvern Mastersizer, which showed that the zinc consisted mainly of small spheres of less than 8 μm diameter, together with a few large agglomerates which were about 10 μm in diameter. The mean diameter of the particles is 6.0 μm.

The Johnson Matthey (Alfa products division) 99.9% iron (produced by reduction) was purer than the Spice and Staveley material (90%, with the rest of the material being oxide). Iron metal wire (0.4 mm diameter, 99.9% pure) was supplied by Saarchem. The Saarchem barium peroxide, specified as having a purity in excess of 85%, with a particle size <20 μm, was quantitatively similar to the Spice and Staveley material. Mixtures were prepared by tumbling end-over-end in the presence of rubber balls for 1 hour. All mixtures are quoted as the mass percentage of the fuel present in the sample.

4.2 Temperature profile measurement:

The method used in this study for capturing temperature profiles was similar to that used in previous studies [130,131,132] and is based on that developed by the Leeds University research group headed by Boddington and Laye [131]. The channel in which the sample was packed was made from type 304 stainless steel with three vertical slits cut in the sides at intervals of 4, 15 and 28 mm from one end, as shown in Figure 4.1. The end slits are used for measurement of burning-rates using a timing circuit triggered by IR-photodiode detectors. The central slit is used for insertion of an S-type (Pt - 10% Rh/Pt) thermocouple, having an operating temperature range of -50 to 1768°C. The thermocouple was thermally and electrically insulated from the walls of the channel with thin asbestos paper. The ends of the thermocouple were connected to a cold junction compensator unit (model CJR-1 manufactured by Temperature Controls) and a 3140 DC operational amplifier with potentiometer control, having a gain of 256x. Both units were powered by DC cells to avoid mains feedback.

The amplified signal was fed into a PC-26 A/D board interfaced to an 80286 IBM-compatible motherboard, clocked at 20 MHz. The apparatus for the capture of temperature profiles and burning-rates is presented in Figure 4.2. The data were sampled using the software based on the program PC-28 (listed in Appendix 2). Sampling intervals for the system were generally of the order of half a millisecond. Data files containing up to 5000 points were saved and processed as shown below in Section 5.1.

The apparatus and software were modified to allow for data capture from two thermocouples during a single combustion experiment. Figure 4.3 shows the two thermocouple system. Thermocouple signals were passed through individual, isolated cold-junction references and dc-amplifiers (set to the same gain with a tolerance better than 0.05%), before being fed into the A/D board of the PC (channels 0 and 1). The power supplies used were all DC cells, operating independently to avoid feedback. The positioning of both thermocouple junctions about the channel was found to be critical if a conducting phase or product existed in the channel, an electrical circuit could arise, leading to

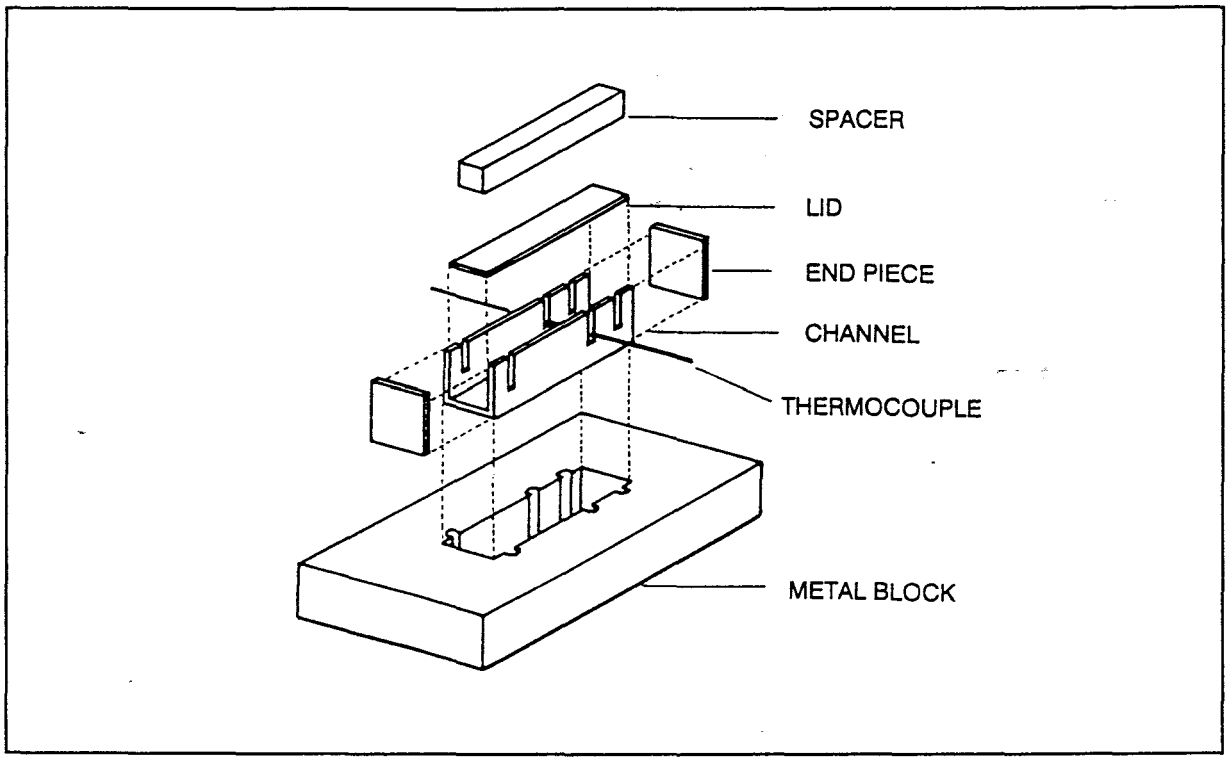

FIGURE 4.1: The stainless steel channel used in combustion experiments

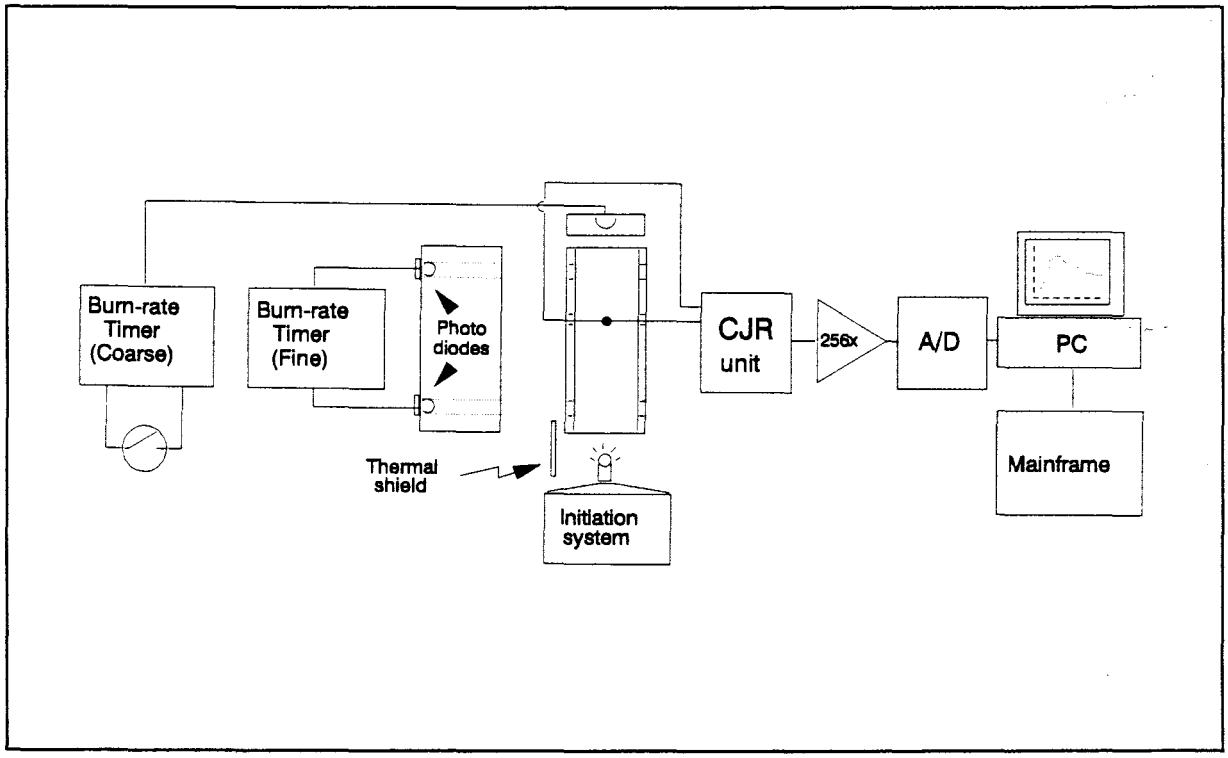

FIGURE 4.2: Apparatus for capture of temperature profiles and burning-rate

spurious results. The stainless-steel channel used in the temperature profile technique described above was thermally and electrically insulated from surrounding apparatus by asbestos paper, and, for some experiments, placed in contact with another thermocouple junction, interleaved between sheets of asbestos paper, to avoid cross-talk and the creation of secondary thermocouple junctions (Figure 4.4).

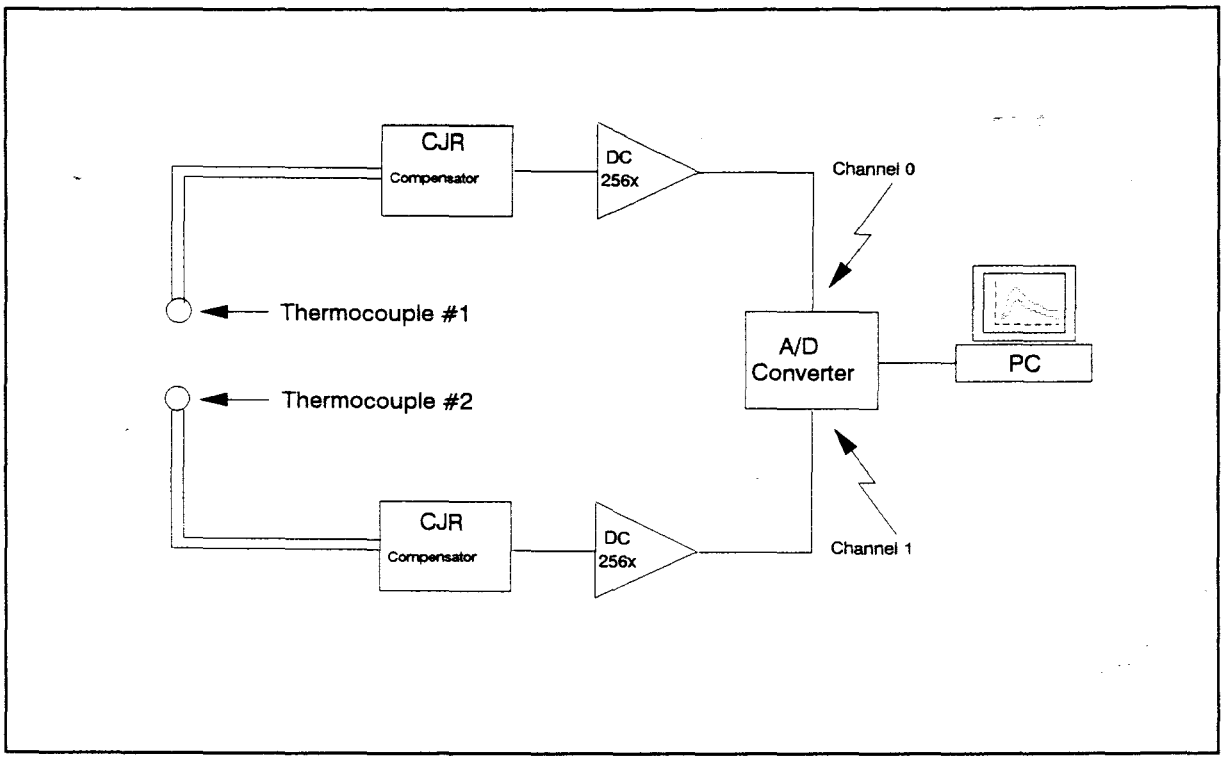

FIGURE 4.3: The dual thermocouple sampling system

Two software routines were used for data capture (see Appendix 2). The first (modtwin.pas) was written to allow both thermocouple channels to be sampled in rapid succession, at a pre-determined rate, allowing for the capture of simultaneous profiles. The trigger signal, which is activated by the primary (channel 0) thermocouple, initiates data capture of both thermocouple signals. This routine was used in conjunction with the apparatus using one thermocouple embedded in the pyrotechnic and one external thermocouple in contact with the channel. Since triggering of the sampling was initiated by the embedded thermocouple, careful positioning of the second thermocouple (in contact with the outside of the channel) was essential to avoid triggering the sampling once the burn-front had passed the location of the second thermocouple, although the use of large sample times eliminated most problems of this nature. Initially the data capture is rapid (rise region), whereafter a second, slower capture takes place (cooling region), as shown in Figure 4.5.

In the second routine, triggering of the first thermocouple results in rapid sampling of only the

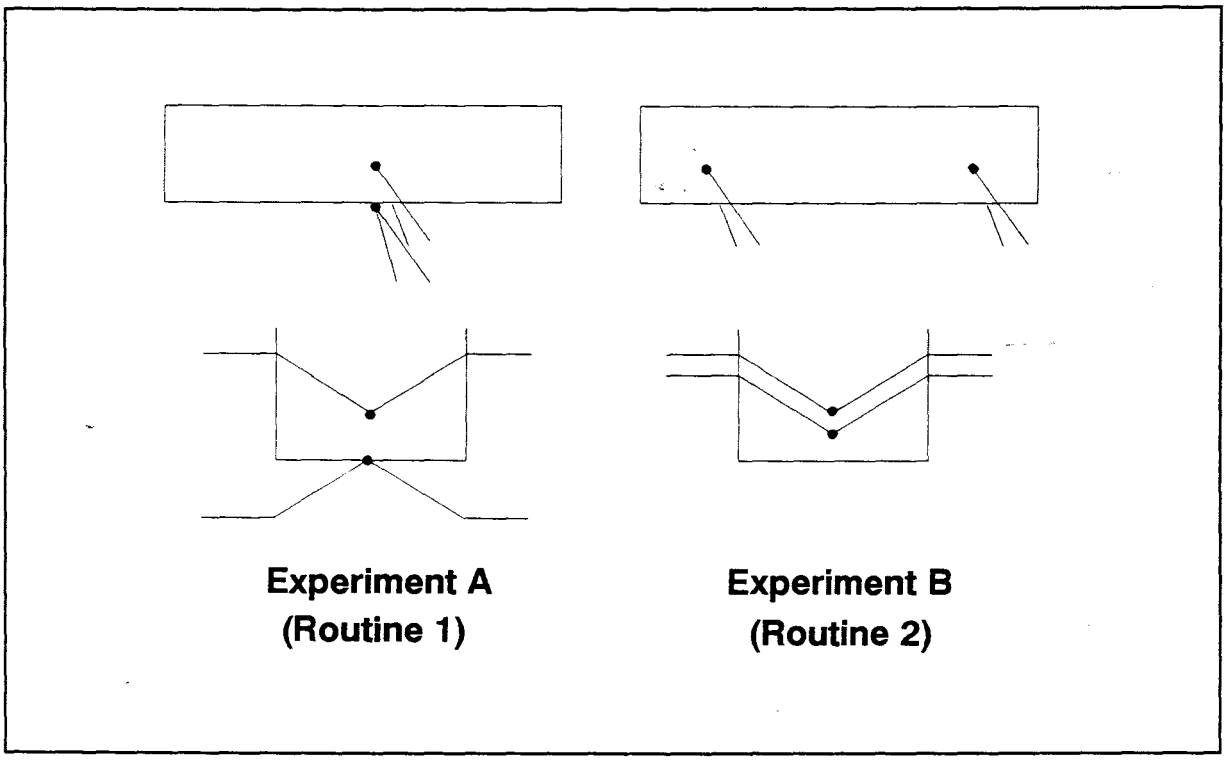

Figure 4.4 Thermocouple junction positions for the twin-thermocouple experiments

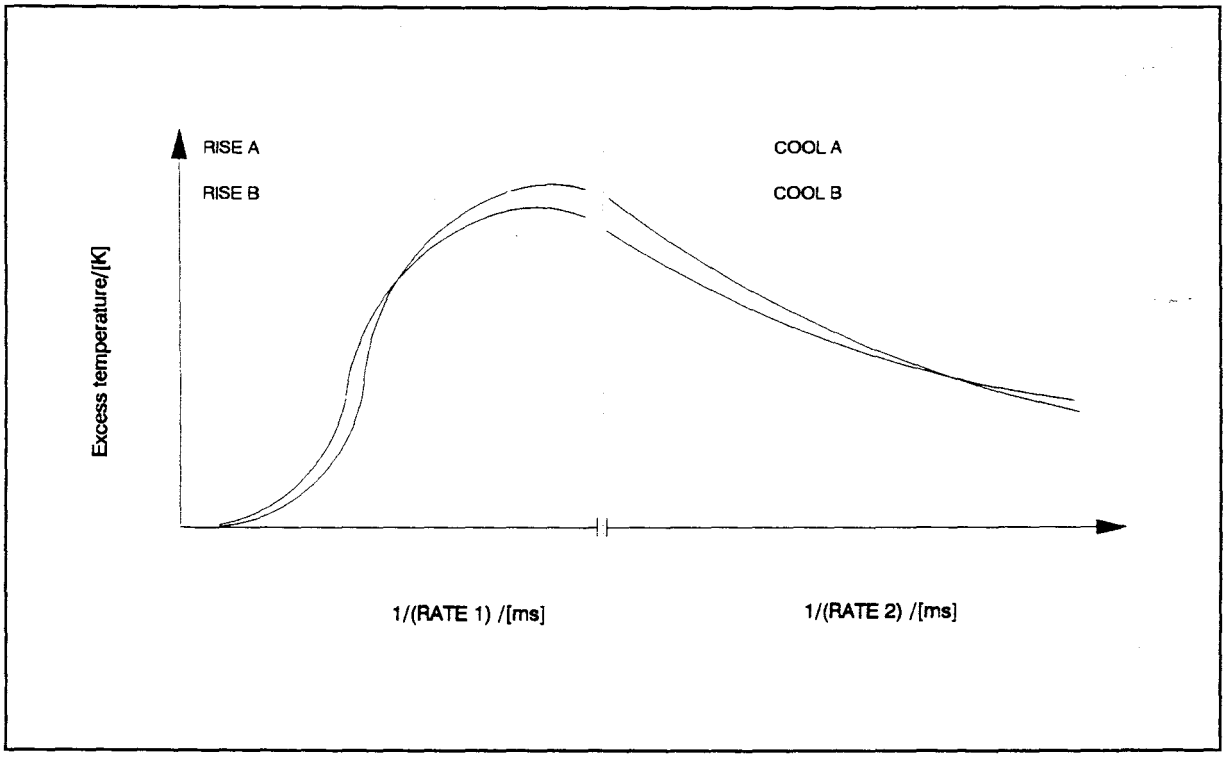

FIGURE 4.5: Schematic of sampling using the first routine

first thermocouple channel, followed by initiation of rapid sampling of the second thermocouple. The software determines the difference between the two initiation times to allow an estimation of the burning-rate to be made, when the separation of the junctions has been determined. Once the rapid sampling of the second thermocouple is complete, a second, slower sampling of the second thermocouple is initiated to determine cooling characteristics of the medium under study. The method of sampling is demonstrated in Figure 4.6.

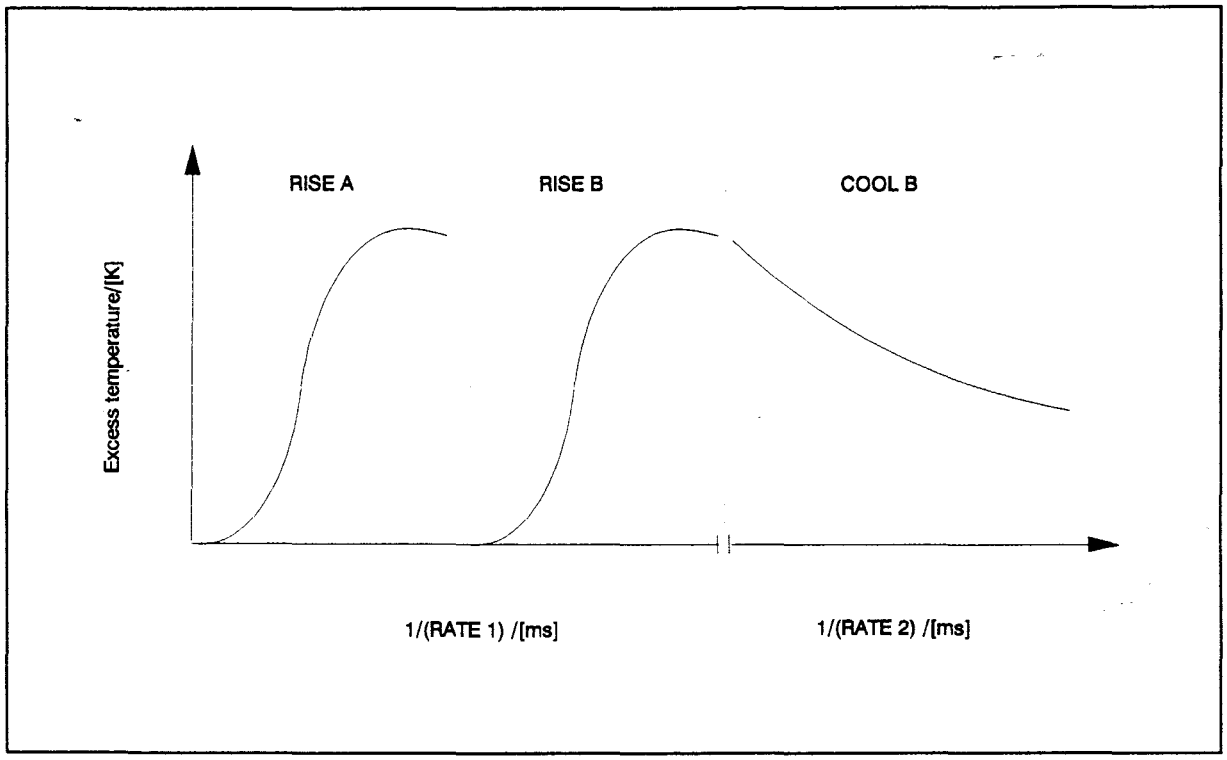

FIGURE 4.6: Schematic of sampling using the second routine

Sampling rates in the two programs were set using a Levell signal generator to generate 15 mV square waves, checked by means of an oscilloscope, at frequencies of between 100 Hz and 1.5 kHz. The two varieties of experiment performed using the twin thermocouple system are detailed below.

The first series of experiments, devised by Beck [133], relied on thermal isolation of the channel and use of the first routine. One thermocouple was positioned in the mixture, and the other was attached to the channel itself. In this manner the temperature rise of the entire ensemble could be determined. Since a rapid response was not needed, a more robust (0.3 mm diameter wire) thermocouple was used to determine the channel temperature. The heat generated in the reaction, $Q=cU_{ad}$, can be estimated from a temperature profile recording the passage of the combustion front, where U_{ad} is the estimated adiabatic temperature rise during combustion and c is the specific heat capacity of the mixture. Alternately Q may be estimated from the profile recorded for a thermocouple placed in contact with the outside of the burn channel.

In this instance,

$$Q_2 = \frac{C_{MIXTURE} m_{MIXTURE} U_{ad2} + C_{CHANNEL} m_{CHANNEL} U_{ad2}}{m_{MIXTURE}}$$

In the second type of experiment, using the second routine, the reproducibility of the two temperature profiles captured at different locations within the same composition during a single combustion experiment was determined. The onset of the rise regions of the two profiles (or similar points on the two profiles, such as U_{max}, together with the separation distance between the thermocouple junctions, allowed an estimation of the burning-rate at the centre of the column and an indication of the uniformity of combustion. The values of the burning-rate determined in this manner were used as confirmation of values obtained using the infrared photodiode detector system. Agreement of values determined by these methods indicate a uniformly shaped burn-front, free from unstable, pulsing reactions.

A channel made from type 304 stainless steel was used in the study, having a heat capacity which ranged from 0.438 J K^{-1} g^{-1} (300 K) to 0.569 J K^{-1} g^{-1} (600 K). The mass of the channel assembly used was constant throughout the study (13.21 g), dominating the mass of the ensemble, with the mass of the mixture approximating 2 g in all experiments conducted. The heat loss to the thermocouples could not be determined.

4.3 Burning rates:

Burning rates were determined using two methods simultaneously. The first method involved a manual initiation of a Racal counter, which stopped on receipt of a signal from an IR sensor placed at the far end of the burn-channel. This system was replaced during the study by an electronic timer using the same circuit as the photo-diode system detailed below, with the initiating diode replaced by a manual switch, but still using the photodiode at the end of the channel to terminate the timing. The second measurement system consisted of two IR-photodiodes which were positioned in line with the two open slits in the side of the channel. A timing circuit was used to determine the time taken for the burning-front to pass from the one slit to the next. The first (manual initiation) method of timing was used as a confirmation of the second (electronic sensor) method, since the second method was susceptible to triggering by ignition flares.

4.4 Thermal analysis apparatus:

Four thermal analysis techniques were used to obtain information about the thermal behaviour of the reagents and the pyrotechnic mixtures. These were thermogravimetry, thermomagnetometry, differential scanning calorimetry and differential thermal analysis.

Three forms of sample were used:

i) powdered pyrotechnic mixtures and reagents;

ii) pellet samples of pyrotechnic mixtures;

and iii) pellets of layered reagents.

Pellet preparation was done in a Ruuc Industries press, with a die diameter of 5mm. Samples were pelleted under a pressure of 55 MPa, and the typical final height of a pellet was 1-1.5 mm. Layered pellets were produced by placing a small quantity of the fuel in the press, compacting the fuel at 25 MPa and blasting the press with compressed air to remove loose fuel particles. The oxidant was added and the entire pellet compacted at 55 MPa, to give a final pellet height of ~ 1 mm. The thicknesses of fuel and oxidant layers were approximately similar in all pellets produced.

Thermogravimetry (TG) was performed using a Perkin-Elmer Delta series TGA7 instrument coupled to a thermal analysis controller, which in turn was coupled to an IBM compatible PC-AT based on an 80286 motherboard, clocked at 12 MHz. This controller was also used to couple the Delta series DSC-7 differential scanning calorimeter to the PC. The software used was that supplied by the manufacturers. The TG furnace was calibrated magnetically using the Curie points of nickel (354°C) and iron (780°C). The operating range of the instrument was from 50°C to 900°C, with high temperatures being avoided wherever possible to limit damage to the furnace. Three different sample atmospheres were used on the TG, namely nitrogen, synthetic air and oxygen, with sample flow rates of from 5 cm^3 min^{-1} to 50 cm^3 min^{-1}. The weighing mechanism was continuously flushed with nitrogen flowing at 6 cm^3 min^{-1}. The nitrogen used in the study contained ppm traces of oxygen. Heating rates of 20°C min^{-1} were used in all thermal analysis experiments, unless stated otherwise.

Flushing via the conventional TG flushing mechanism did not remove all traces of air within a reasonably short time. Reversing the flush by passing the nitrogen through the exhaust and venting the inlet to the atmosphere gave satisfactory results. Increasing the flushing rates to about 25 cm^3 min^{-1}, cut flushing times considerably, although studies on the oxidation of iron powder showed that about three hours of flushing was required before oxidation was completely inhibited. The sample pans used in the TG were platinum. TG studies on the zinc systems were limited to a maximum temperature of 650°C in N_2, due to the damaging effects of zinc vapour on Pt equipment above this temperature.

The TG was also used for thermomagnetometric (TM) experiments, whereby samples were subjected to a heating program whilst in a magnetic field [134,135]. The permanent magnet used for Curie-point determination was similarly placed for TM. The percentage weight changes quoted for thermomagnetometry are for comparative purposes only and no quantitative conclusions should be drawn from them.

Differential scanning calorimetry (DSC) experiments were performed in Al pans (below 575°C) and in Pt pans (below 725°C). Calibration of the DSC was achieved using the melting temperatures of pure (>99.9%) indium (onset 156.60°C) and zinc (onset 419.45°C), and the peak area was calibrated using the enthalpy of fusion of indium (28.45 J g^{-1}). N_2 was used as the purge gas (flow rate 50 cm^3 min^{-1}). DSC studies on the zinc powders were limited to temperatures below 575°C, due to the corrosive nature of zinc vapour (forming above 420°C) on the head of the DSC when using uncrimped Pt pans. DSC studies on zinc, layered zinc+peroxide pellets and zinc/peroxide pellets were performed in crimped aluminium pans, again to a maximum temperature of 575°C.

The use of a Perkin Elmer DTA 1700 high-temperature differential thermal analyser allowed higher temperature studies to be undertaken, extending the temperature range of thermal analysis studies performed previously [6]. The DTA furnace was connected to a Perkin-Elmer system 7/4 controller, and a Perkin-Elmer 3700 data station running a 6809 microprocessor and compiled basic software. The 3700 data capture system was subsequently replaced by an IBM compatible microcomputer and the accompanying PC-software. This instrument could be operated in either DTA or DSC modes to 1400°C (compared to 770°C on the DSC7). The DTA was calibrated using the onset of the melting of gold at 1063°C for high-temperature applications (up to 1300°C), and the onset of the melting of zinc at 420°C for conventional runs (up to 900°C). Although the instrument is intended to operate with alumina sample crucibles and alumina sample containment tubes, the mineral pyrophyllite ("wonderstone") was found to have similar thermal characteristics to alumina (after baking) up to 1300°C and hence some of the above parts were replaced by machined pyrophyllite equivalents, for use below 1300°C. At temperatures above 1450°C, the mineral apparently undergoes a transition accompanied by expansion, hence rendering it unsuitable for use at higher temperatures. Alumina powder was used as the reference material for the DTA.

4.5 Scanning electron microscopy

Scanning electron microscopy (SEM) was used to examine the reactants and solid products of the pyrotechnic reactions. Information about changes occurring on the surfaces of the reacting materials can be obtained, and may thus provide confirmation or otherwise of proposed reaction mechanisms,

for example, the occurrence of solid-solid, solid-liquid or solid-gas reactions. The formation of liquid and/or gaseous intermediates during the reaction may often be deduced from the observation of channels and holes in the surfaces, solidified liquid "flows" and crystalline products different to those in the starting materials. If true solid-solid reactions are involved in these reactions, one would expect the surface to show no solidified melt phases or large channels which indicate the presence of gases.

A JSM-840 scanning electron microscope was used at an acceleration voltage of 20 kV. Samples were prepared by sputter coating under vacuum with gold. The shapes and surface appearance of the individual reactant powders, product residues and surface changes in samples of the iron wire, used in experiments described below, were examined. A study of the microscopic appearance of the reagents and products involved in the reactions was undertaken to (i) ascertain the range of particle sizes involved, thus supplementing data from the Malvern Mastersizer, as well as the manufacturers' claims; and (ii) study the change in surface appearance after the reaction had occurred. Backscattered image studies were also performed.

4.6 Infrared spectroscopy and X-ray diffraction

A Perkin-Elmer 180 infrared spectrophotometer was used to obtain infrared spectra in the 4000-400 cm^{-1} region. Samples examined were BaO_2 and SrO_2 and the combustion residues of mixtures of these peroxides with iron or zinc. Samples were dispersed in KBr discs.

X-ray powder diffraction (XRD) is an essential technique for product identification, although the rapid heating and cooling accompanying combustion can lead to the formation of amorphous glasses. An X-ray powder diffraction study was undertaken on the reactants and products of the binary pyrotechnic systems using a Philips diffractometer. The equipment used incorporated a Philips PW1130 smoothed DC X-ray generator, a PW1349 diffractometer kit, PW1965 proportional detector probe and PW1373 goniometer supply unit. The source used for all studies was a Co Kα gun, filtered by Fe. Results were recorded on a Philips PM8000 flat-bed recorder at 10 mm min^{-1}. The goniometer was geared to move through an angle of 2° min^{-1}. Results were analysed and referenced to the X-ray powder diffraction data files [104,136,137].

Samples were prepared and stored in a desiccator until the XRD analysis could be performed. The initial study was supplemented by studying the entire composition combustion range for both Fe/BaO_2 and Fe/SrO_2, as well as the effects of compaction pressure, to determine whether control of the combustion product could be achieved. Additional X-ray diffraction results were supplied by the Research Department of AECI Ltd, using a Philips PW1050 diffractometer and a Cu-Kα source (filtered by graphite).

4.7 Electron probe micro-analysis

The elemental distribution in a sample may be studied by electron probe micro-analysis (EPMA) [140], which, together with SEM images, provides a method of studying the dispersal of reactants and products. A Jeol 733 Super-probe was used to analyze three series of samples:

i) Elemental distribution across a fuel/peroxide interface in all four pyrotechnic systems.

ii) Elemental distribution in combusted pyrotechnic mixture residues of iron/peroxide systems.

iii) Elemental distribution about an iron wire which had been embedded in an Fe-fuelled pyrotechnic mixture and then combusted.

Samples were prepared and reacted shortly before examination, stored in a desiccator under nitrogen, and set in polyester resin to inhibit reaction with the atmosphere until analysis. These samples were subsequently prepared for analysis by grinding under paraffin and petroleum ether and coated with graphite by sputtering in a vacuum. Data were captured by the probe's software routine, sampled by an A/D board and fed into a ZAF (mass number, atomic number, fluorescence and backscatter) correction routine on an IBM PC-AT, which yielded a set of relative concentrations. The EPMA studies of combustion residues were restricted to the Fe/peroxide systems, as the combustion products of the Zn/peroxide systems did not retain their conformation (a result of the low initial compaction pressures used in the study).

Photographs (both secondary electron and backscattered) were taken at various stages of the study to complement the probe data.

4.8 Crystal structures

PLUTO78 [138], a Fortran program in VMS-system format [139] which takes crystallographic information (space group, cell geometry and dimensions, ionic radii, etc.) as input [141], and produces graphical structures as output, was used to examine various projections of the lattices of the starting materials, and possible reaction intermediates and products.

4.9 Electrical heating of iron wire

Figure 4.7 shows the circuit used to heat Fe wire electrically at fixed temperatures while it is embedded in solid oxidant. A calibration curve was determined using a Fluke 51 K/J digital thermometer to measure wire surface temperatures. The estimation of the temperature of the wire surface was based on temperature-current relationships delivered by the circuit, which fitted an exponential curve. As surface effects were under consideration, heating was performed by a

50 Hz ac circuit, the resulting skin-effect having the advantage that excessive heating of the bulk and possible burn-through was avoided. The wire samples were removed, stored under dry conditions, and the surfaces examined directly after the experiment.

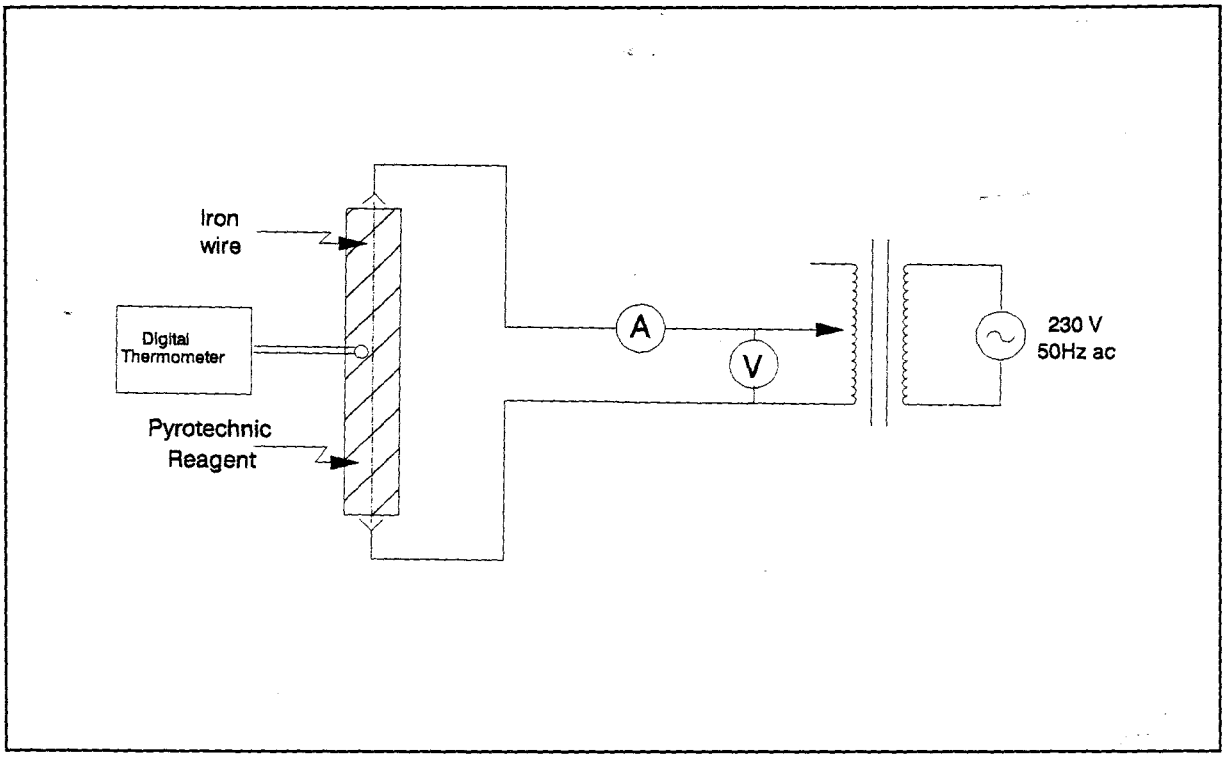

FIGURE 4.7: Circuit used in the electrical heating of the Fe wire

5. DATA TREATMENT:

5.1 Introduction:

A temperature profile consists of three main regions - a rise region, corresponding to heating by conduction from the approaching burn-front; followed by ignition and reaction in the reaction zone; and the decay region, corresponding to the cooling of reaction products as the burn front continues past the thermocouple into the unreacted zone. A schematic of a profile is presented in Figure 5.1. The response of the thermocouple is dependent on many factors, and the variation of the profile with changes in these factors may lead to information about the reaction under study. The use of equations governing heat flow, together with a comprehensive set of (T,t) data (the temperature profile), allows kinetic information to be obtained from an experiment.

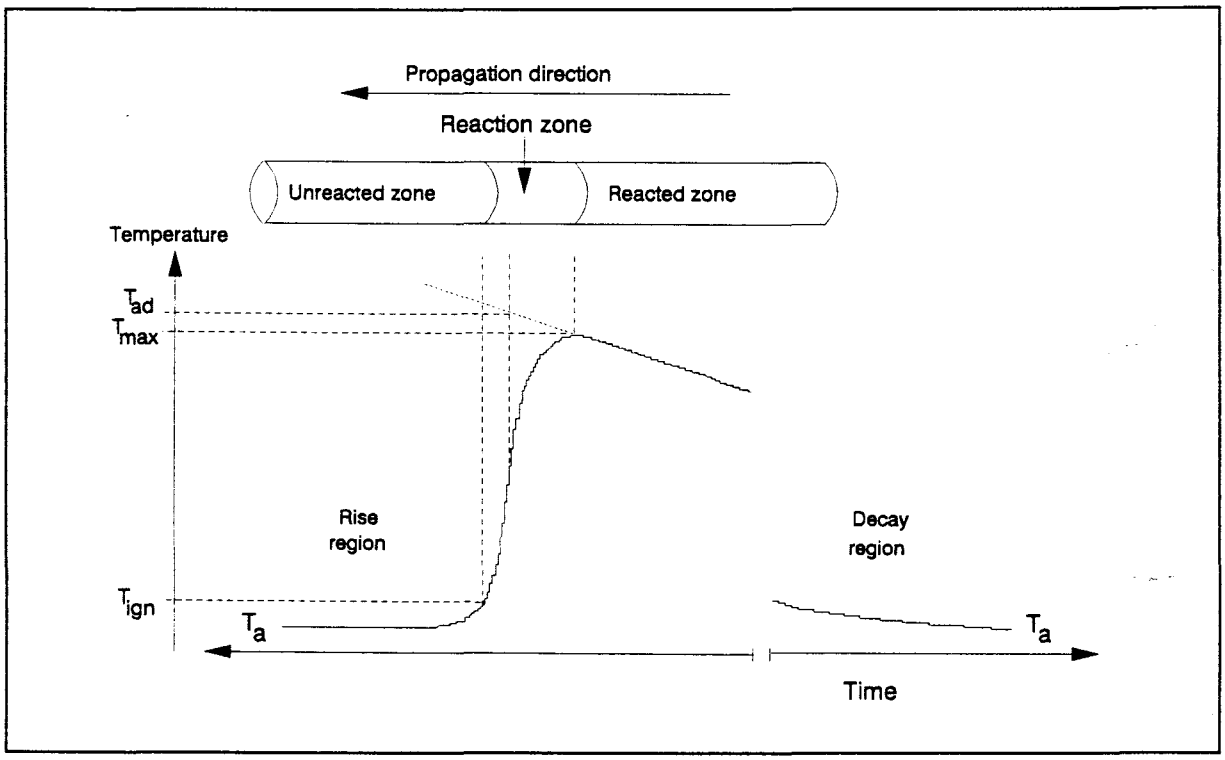

FIGURE 5.1: A temperature profile, showing key regions

The most thorough and comprehensive treatment of the analysis of temperature profiles is that provided by Boddington and Laye's group at the University of Leeds [131,132]. This treatment is more rigorous than earlier treatments such as that of Hill *et al* [9,142]. Detailed descriptions of the theory (referred to as the "Leeds" approach) have been given in the literature [131,132] and in several theses [6,143,144], and will not be repeated here.

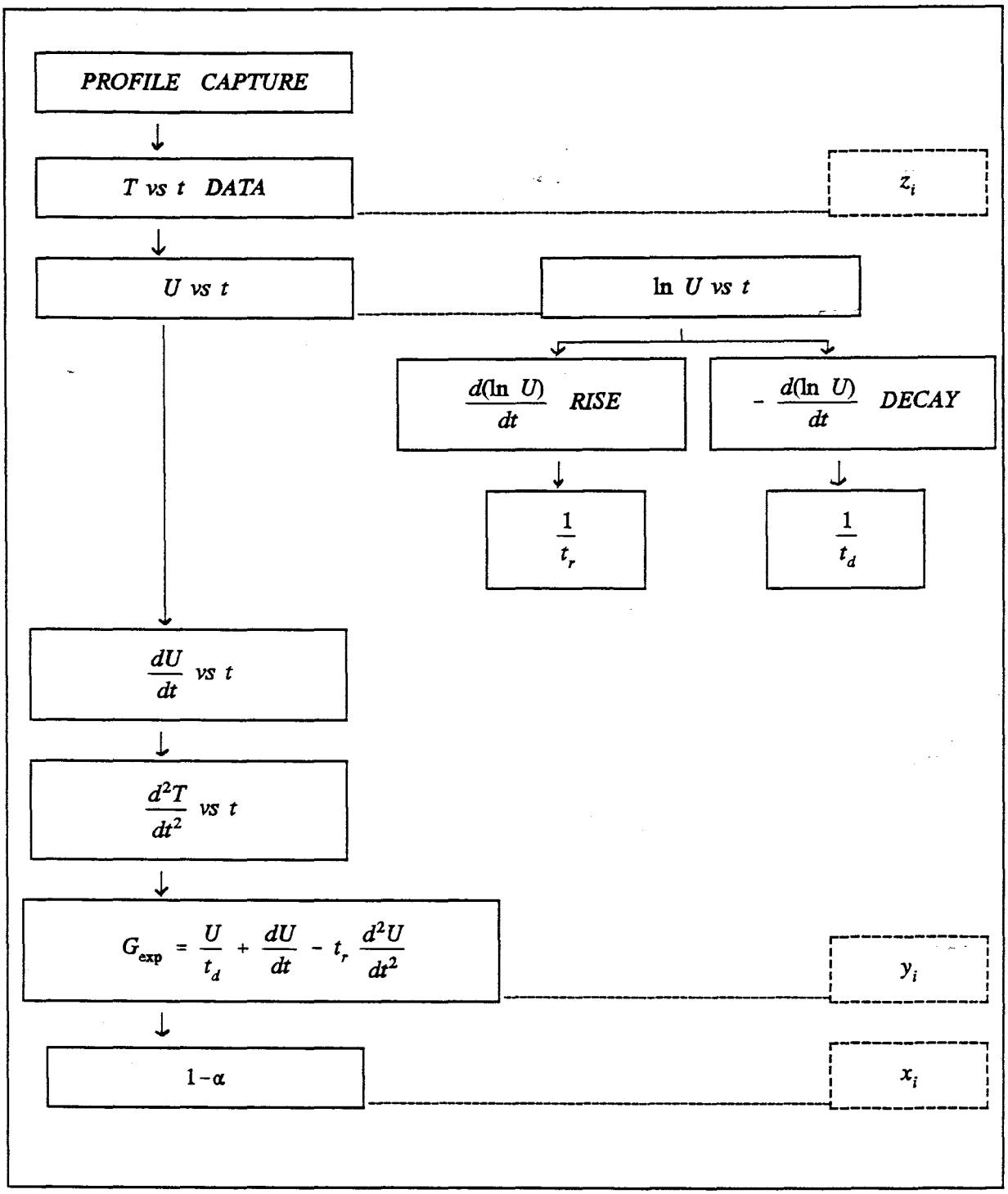

FIGURE 5.2: Flow-diagram of the Leeds approach

A flow diagram of the analysis of temperature profiles, based on the Leeds approach, is given in Figure 5.2. More details of the approach are given in Appendix 12, and symbols are defined on Page xxi. A step-wise example of temperature profile analysis is presented in Section 5.2.

5.2 Temperature profile analysis

5.2.1 Conversion of raw data to temperature values and smoothing:

The thermocouple response, which is registered as a series of time dependent counts in the A/D board, is captured by the PC-28 data capture routine and saved as a LOTUS 123® compatible file. A macro was written, as detailed in Appendix 3, which allowed the data file from the PC-28 routine to be imported into a spreadsheet, where data were converted to millivolts and then to temperature values. The millivolt values were determined by multiplying (i) the counts registered, by (ii) the ratio of the resolution of the 12-bit A/D converter (2.441 mV/count) to the amplification factor of the DC amplifier (253.3x, established using an oscilloscope and DC supply). The temperature values were then determined using correction and calibration factors for S-type thermocouples [145]. Temperature profiles often required smoothing before further analysis. Several methods of smoothing were tested. Savitsky-Golay smoothing [146] was attempted using a 9-point moving-spline convolution procedure. This method provided satisfactory smoothing of the initial profile, but first-derivatives were inadequately smoothed. Use of more points in the smoothing process (up to 15-point smoothing was tried), resulted in loss of data for the terminal points. Where the terminal data were crucial to the analysis, or where few profile points existed, this was unsatisfactory. A published algorithm [147] was incorporated in a Pascal program (detailed in Appendix 2) to produce a matrix of Savitsky-Golay factors which could be used to generate smoothed endpoint data without the loss of crucial endpoints. Although this process succeeded in producing adequate smoothing, the mere bulk of the formulae for the smoothed data caused problems in spreadsheet operation and severely limited the number of data points which could be used. A BASIC routine, "mspline" (see Appendix 2), based on a routine published by Ederer *et al* [148], which uses a cubic-spline function with 12-point smoothing, was thus used to smooth the raw data. Typical raw and smoothed ("mspline") profiles are shown in Figure 5.3. These smoothing techniques are currently being superceded by the use of a software package, GRAFTOOL, which provides a cubic-spline smoothing algorithm with a smoothing factor set by the user. The raw data from the PC-28 package, after conversion to temperature values in the worksheet, are printed to a file in unformatted form (*.prn) for further manipulation. The "mspline" program, which takes the raw data file as input (t,T format), produces smoothed data as output, which is written to disk from where it is later imported back into the worksheet (*.prn).

The first step in the analysis (following the "Leeds" approach) is to convert the temperature values to excess temperatures above ambient, $U=T-T_a$. A plot of the natural logarithm of this excess temperature (ln U) against time yields a linear region where the temperature of the profile rises to the reaction temperature. The slope of a plot of ln U vs t for this rise region is the reciprocal of the rise time, t_r, while the slope of ln U vs t for the decay region of the temperature profile is the negative reciprocal of the decay time, t_d. These two factors are used in the determination of the power

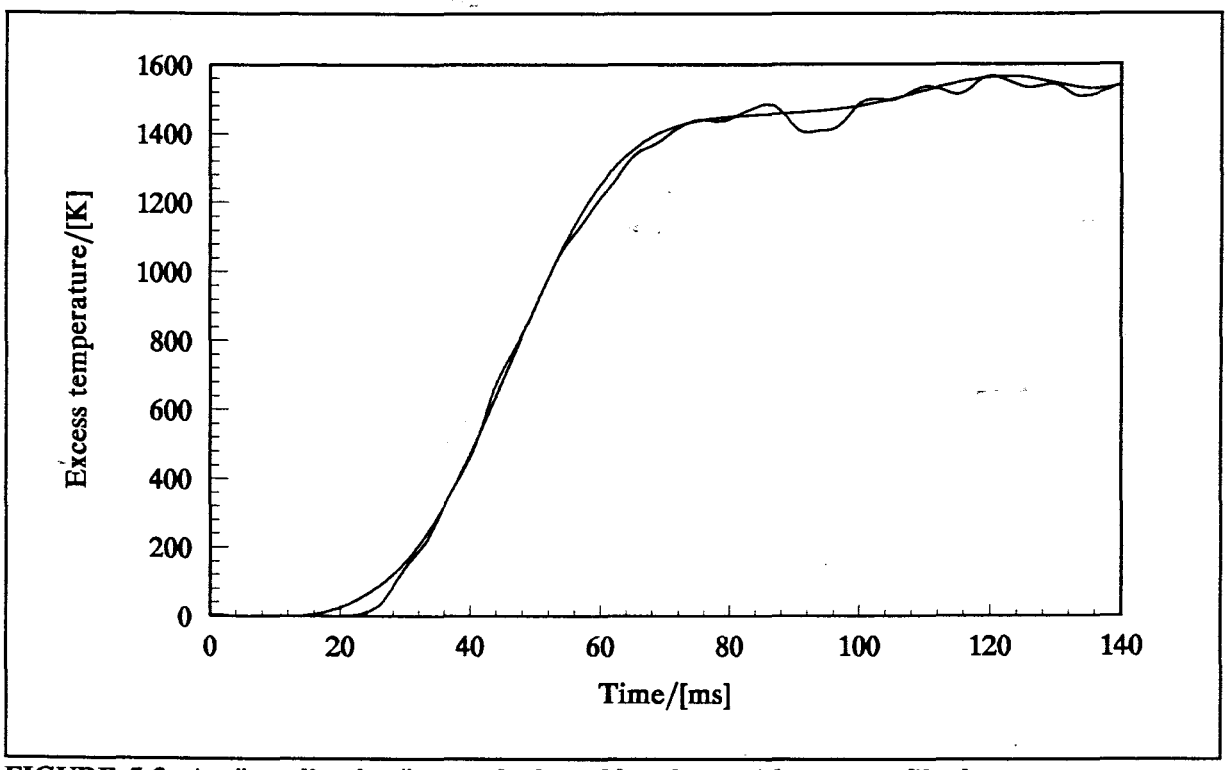

FIGURE 5.3: An "mspline.bas" smoothed profile, along with raw profile data

function, "G". The value calculated for t_d was never less than 2 s and thus the role of cooling was of minor importance in these reactions. A fixed value of t_d=2000 ms was thus used in all analyses. A plot of ln U vs t for a typical profile is shown in Figure 5.4, together with a scaled down version of the profile for comparison. U_{ad} (the adiabatic excess temperature) is generally calculated from the intercept of a graph of $\int$ Udt against U over the rise-region, but when negligible cooling of the reaction products occurs directly after reaction (t_d>2000 ms), it was found that U_{ad} could be approximated to U_{max}.

The Savitsky-Golay [146,147,149] method (using 9 points) was found to be adequate for the determination of first and second derivatives of the smoothed temperature data. Figure 5.5 shows typical first and second derivatives of U vs t data, together with G_{exp} which is explained below.

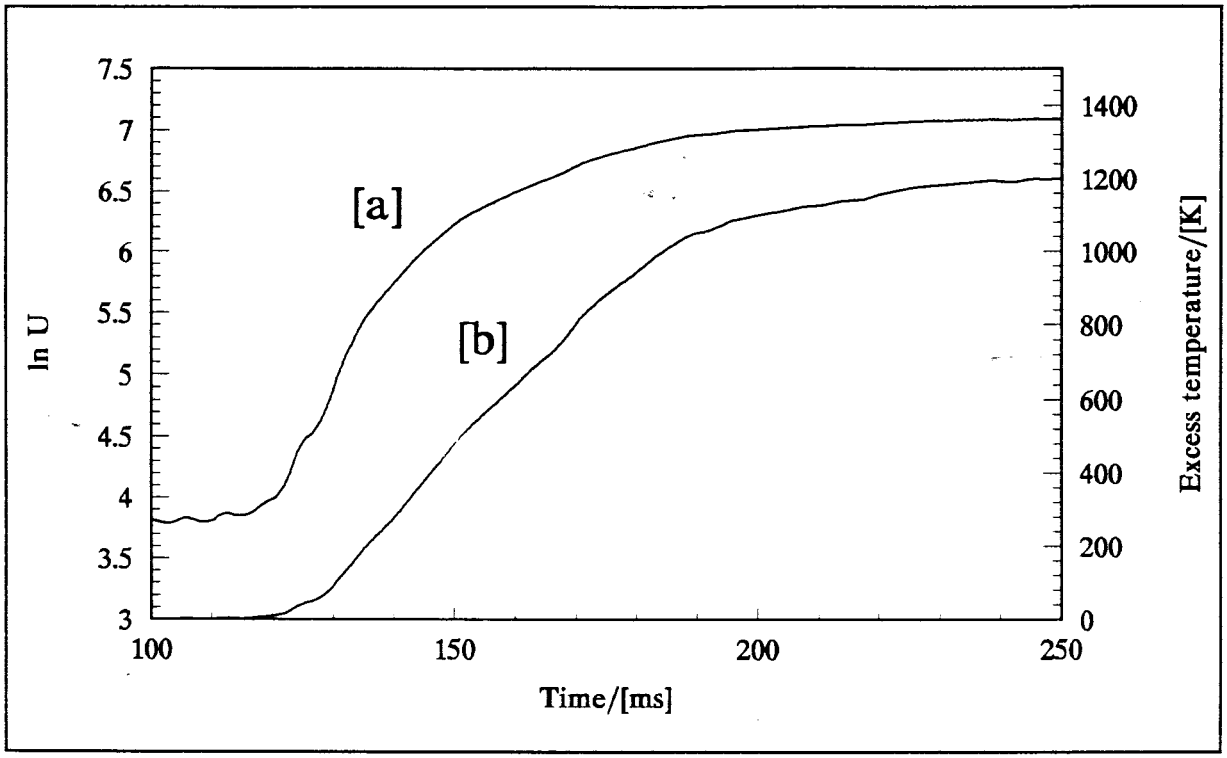

FIGURE 5.4: Excess temperature (U) depicted with ln U
[a]: ln U and [b]: U

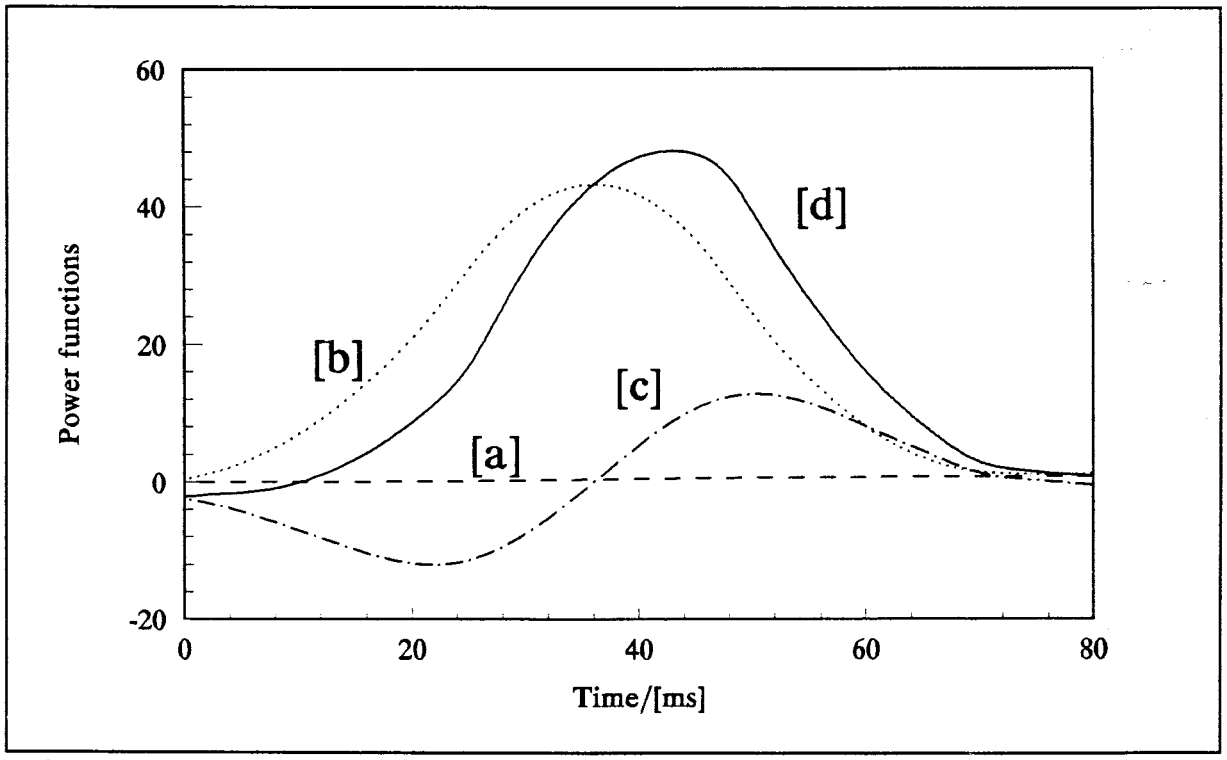

FIGURE 5.5: The terms which constitute the total power function, G
[a]: U/t_d, [b]: $(dU)/(dt)$, [c]: $-t_r(d^2U)/(dt^2)$ and [d]: G_{exp}

5.2.2 The power function, G:

Once t_r, t_d, U, dU/dt and d^2U/dt^2 have been determined, the experimental power function, G_{exp} may be found. The form of G_{exp} used was as follows:

$$G_{exp}=\frac{dU}{dt}-t_r\frac{d^2U}{dt^2}+\frac{U}{t_d} \quad \ldots\ldots\ldots\ldots\ldots\ldots \quad 5.1$$

where dU/dt represents the rate of temperature increase, $-t_r(d^2U/dt^2)$ the heat loss by conduction and $1/t_d(dU/dt)$ the lateral heat loss. The function G_{exp} is plotted against time, providing at least one positive peak. The existence of more than one maximum indicates evolution of heat of reaction in more than one exothermic step. In such circumstances the theory cannot be applied satisfactorily, since a multi-stage reaction is occurring.

The partial areas of the major peak in the G vs t curve were determined at times, t, by integration using the trapezoidal rule (see Appendix 9). The extent of the reaction, α, at time t, is obtained by dividing the partial area by the total area. The analysis is completed by passing three columns of data, namely G_{exp}, $1-\alpha$ and 1/T to a print file in unformatted form, which can be exported to other servers on a network for further processing and optimisation by linear and non-linear techniques [150] (see Appendix 1), by means of the BMDP 1D and 3D statistical packages.

5.2.3 Optimisation of parameters:

The calculated value of G, G_{calc} is given by

$$G_{calc}=U_{ad}\,A(1-\alpha)^n e^{-\frac{E_a}{R}\cdot\frac{1}{T}} \quad \ldots\ldots\ldots\ldots\ldots\ldots \quad 5.2$$

assuming an apparent order of reaction, n, and Arrhenius temperature dependence.

To simplify the optimisation procedures, the following substitutions are made:

$x_i=1-\alpha$, $a=U_{ad}A$ and $b=-E_a/R$.

Thus, G_{calc} has the form:

$$G_{calc} = y = a\,(x)^n\, e^{\frac{b}{T}} \quad \ldots\ldots\ldots\ldots\ldots\ldots \quad 5.3$$

The values of a, b and n are then adjusted to minimise

$$\sum_i (G_{expt} - G_{calc})_i^2 \quad \ldots\ldots\ldots\ldots\ldots\ldots \quad 5.4$$

The optimisation procedure has these three parameters as its output, namely a, b and n. These new parameters are plotted as a curve of G_{calc} for comparison with the G_{exp} curve. Figure 5.6 shows G_{exp} together with the linearly and non-linearly optimised G_{calc} functions for a typical profile.

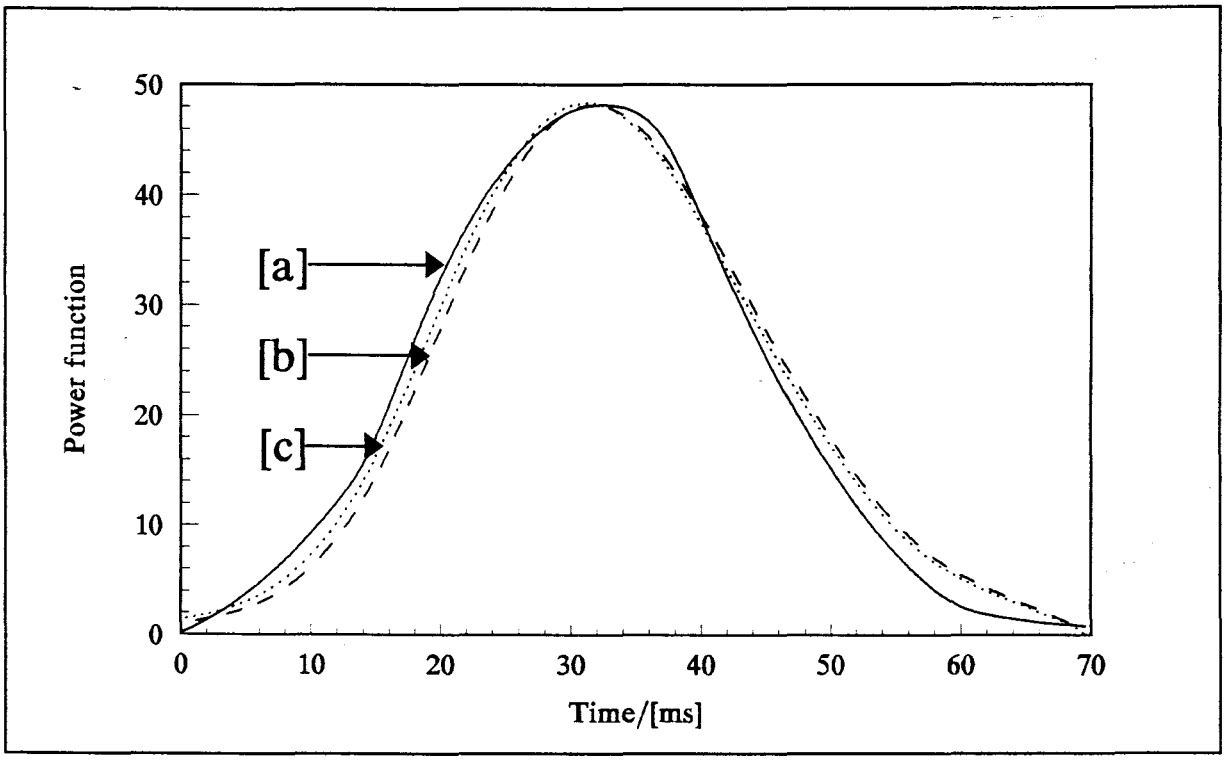

FIGURE 5.6: G from experiment compared to G calculated from optimised parameters [a]: $G_{experiment}$, [b]: $G_{calculated}$ linear and [c]: $G_{calculated}$ non-linear

If the curves are in reasonable agreement, these parameters provide optimised values for the activation energy, E_a, the pre-exponential Arrhenius factor, A, and the apparent reaction order, n.

Since the decay times of the profiles were sufficiently long to allow U_{ad} to be approximated as U_{max}, and $Q = cU_{ad}$, a knowledge of the heat capacities of the mixtures allows determination of the heat of reaction, Q. Heat capacities are temperature dependent, for example [8]:

$$C_p = f + gT + \frac{h}{T^2} \quad \ldots\ldots\ldots\ldots\ldots\ldots \quad 5.5$$

Using Kubaschewski's factors [33] and Weast's tables [8] for the various temperature ranges associated with the T_{max} values for the relevant compositions, the heat capacities of the mixture were estimated.

Burning rates, v, are related to the rise times, t_r, of the profiles, by [132]

$$t_r = \frac{\lambda}{\rho c v^2} \quad \ldots\ldots\ldots\ldots\ldots\ldots\ldots\ldots \quad 5.6$$

where t_r is determined from the slope of a plot of ln U against t over the initial acceleratory region of the profile (as explained above), from

$$\frac{d\ (\ln\ U)}{dt} = \frac{1}{t_r} \quad \ldots\ldots\ldots\ldots\ldots\ldots\ldots\ldots \quad 5.7$$

The heat capacity, c, and density, ρ, are known, allowing determination of any of the three unknowns with knowledge of the remaining two. Burning-rates may be calculated if the thermal conductivity and rise time of a composition are known, and compared with the measured burning rate. Alternatively, an effective thermal conductivity may be calculated and compared with the measured value for the unreacted mixture.

5.3 Kinetics from thermal analysis

Numerous methods have been suggested for obtaining kinetic parameters from isothermal experiments [151-158] and from programmed temperature experiments [159,151,154,160]. Many of these nonisothermal methods require several experiments at different linear heating rates [151]. The Borchardt and Daniels method [159] provides a relatively simple means of extracting kinetic information from a single programmed temperature experiment. The method does, however, require that the thermal analysis curve should be relatively simple. The method makes similar assumptions to those used in temperature profile analysis. The rate equation is assumed to be of the form:

$$\frac{d\alpha}{dt} = k\ (1-\alpha)^n \quad \ldots\ldots\ldots\ldots\ldots\ldots\ldots\ldots \quad 5.8$$

and the rate coefficient, k, is assumed to have an Arrhenius-type temperature dependence,

$$k = Ae^{\frac{-E_a}{RT}} \quad \ldots\ldots\ldots\ldots\ldots\ldots\ldots\ldots \quad 5.9$$

It is also assumed that the derivatives may be separated, so that:

$$\frac{d\alpha}{dt} = (\frac{d\alpha}{dT})(\frac{dT}{dt}) = (\frac{d\alpha}{dT})\phi \quad \ldots\ldots\ldots\ldots\ldots\ldots \quad \mathbf{5.10}$$

where Φ is the constant heating rate (dT/dt).

The first stage of such an analysis involves the determination of the rate constants, k_i, each at a temperature T_i, as follows:

$$k_i = \frac{\left(\frac{d\alpha}{dt}\right)_i}{(1-\alpha_i)^n} \quad \ldots\ldots\ldots\ldots\ldots\ldots\ldots\ldots \quad \mathbf{5.11}$$

Thus in a TG curve, the fractional mass loss is a measure of α_i, and the first derivative (DTG) is proportional to $(d\alpha/dt)_i$. From DSC (or DTA) results, the DSC (DTA) signal is proportional to $(d\alpha/dt)_i$ and the partial area under the DSC curve is a measure of α_i. The value of n is adjusted to give the most linear plot of ln k_i against $1/T_i$ over an appropriate temperature range.

The value of E_a may be obtained from the slope of this Arrhenius plot, $(-E_a/R)$, and that of A may be derived from the intercept, with allowances for any accumulated constants, such as the heating rate, Φ, and any scale factors.

6. THERMAL BEHAVIOUR OF THE FUELS

6.1 Reactions of iron powder:

6.1.1 Behaviour in nitrogen

Since finely-divided metal powders are extremely susceptible to oxidation, thermogravimetric (TG) experiments on metal powders in N_2 are useful for testing the purity of the purge gas and the efficiency of flushing of the balance system (see Section 4.4). The thermomagnetometry (TM) curve for Fe powder in N_2, after lengthy flushing, showed only the Curie transition at 780°C.

6.1.2 Behaviour in air

TG and TM curves for Fe powder in air are shown in Figure 6.1. In the absence of a magnetic field (curve [a]), oxidation begins at about 150°C, accelerates to a maximum rate at 550°C and approaches completion at 900°C at a mass gain of about 43.0% (calculated 42.9% for formation of Fe_2O_3, 38.2% for formation of Fe_3O_4). The TM curve (curve [b]) shows a rapid apparent weight loss at 570°C corresponding to the Curie point of Fe_3O_4. Fe_3O_4 is thus a major intermediate, probably formed in an O_2 deficient atmosphere at the metal/metal oxide interface. A magnetic event at ~340°C may arise from the formation on the surface of some ferromagnetic γ-Fe_2O_3 from Fe_3O_4, which converts to paramagnetic α-Fe_2O_3 at about this temperature (according to Karmazsin *et al* [29], $\gamma \rightarrow \alpha$ at between 400°C and 600°C). The increase in weight above 570°C corresponds to oxidation of Fe_3O_4 to Fe_2O_3. The overall reaction is thus:

$$4Fe(s) + 3O_2(g) \rightarrow 2Fe_2O_3(s)$$

The differential thermal analysis (DTA) curve for Fe in air (Figure 6.1, curve [c]) shows a broad complex exotherm, onset ~180°C, initial shoulder at ~300°C, and maximum at ~500°C, corresponding closely to the DTG curve. This close agreement extends to the occurrence of maxima in the curves, at 340°C (the formation of small quantities of γ-Fe_2O_3 on the surface from Fe_3O_4, which convert to α-Fe_2O_3 at this temperature), 480°C (the dominant process, involving formation of Fe_3O_4 in the bulk, which is oxidised to γ-Fe_2O_3, which in turn becomes α-Fe_2O_3 at 570°C) and 580°C (the formation of small quantities of FeO in the bulk), corresponding to the three oxidation states in the formation of Fe_2O_3 from Fe.

The onset of the reaction:

$$4Fe_3O_4(s) + 5O_2(g) \rightarrow 6Fe_2O_3(s)$$

appears to occur at around 480°C.

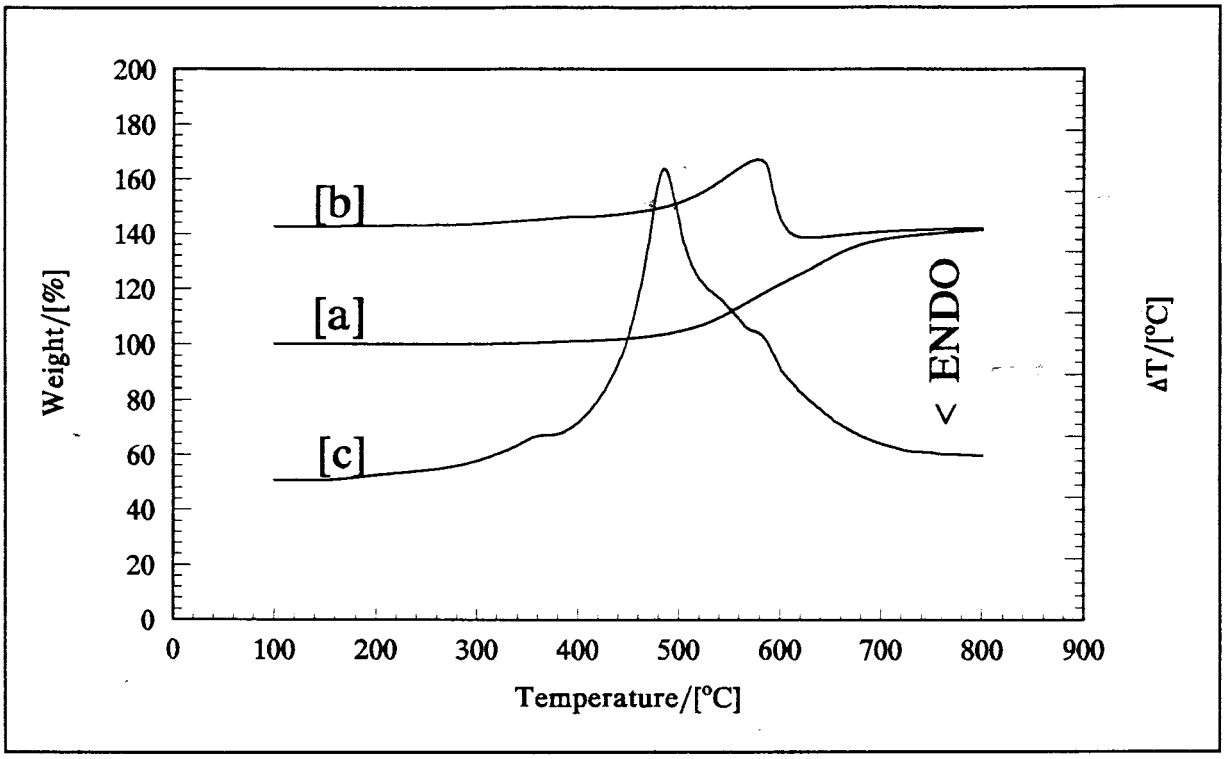

FIGURE 6.1: Thermal behaviour of iron powder
[a]: TG in air, [b]: TM in air and [c]: DTA in air

6.1.3 Behaviour in oxygen:

Two types of behaviour were evident when samples of iron powder were heated in oxygen in the thermobalance at 20°C min^{-1}. Controlled oxidation (Figure 6.2, curve [a]) resulted in a mass gain of 42.8%, with Fe_2O_3 being formed. Shown for comparative purposes in Figure 6.2 are the TG traces of the heated powder (curve [a]) and the cooled resulting oxide (curve [b]), together with the TM traces of the heated powder (curve [c]) and cooled oxide (curve [d]). It can be seen from the confluence of the TG and TM traces of the product above the magnetic transition of Fe_3O_4 at 580°C, that the same compound has formed under both TG and TM conditions.

When the mass of the iron powder sample exceeded about 15 mg (sample pan diameter 6 mm, mass 150 mg), heating the sample at a rate of 20°C min^{-1} or more, resulted in rapid combustion of the iron at ~450°C (Figure 6.3, curve [a]). The resulting mass gain (~38%), agreed well with the formation of Fe_3O_4. Figure 6.3 also shows the rerun TG curve of the cooled product (curve [b]), which shows no thermal events over the range of the experiment. Also shown are the TM traces of the original powder (curve [d]) and the cooled product (curve [e]), both of which demonstrate the Curie transition of Fe_2O_3 as proposed by Karmazsin *et al* [29]. Shown superimposed on these traces is the TM of the product produced by a TG run in the absence of a magnet (curve [c]), showing the Curie transition of Fe_3O_4 at 580°C. It was apparent from curves (b), (c) and (e), that the products formed in the rapid

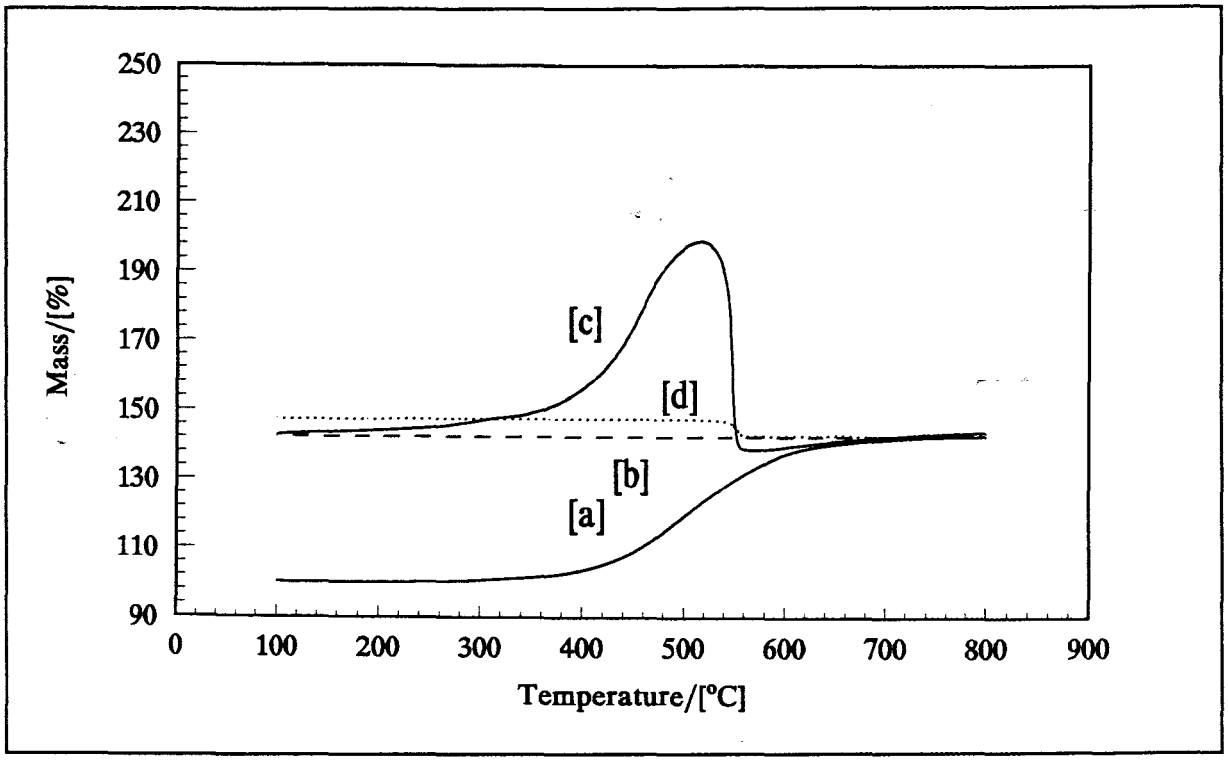

FIGURE 6.2: Controlled oxidation of iron powder in oxygen
[a]:TG original, [b]:TG product, [c]:TM original, [d]:TM product

oxidation experiments differed from one another depending upon whether a magnetic field was present or not.

Close examination of the TM run on the powder (Figure 6.3, curve [d]) showed a feature at between 430°C and 460°C, which was reproducible for a series of experiments (Figure 6.4). Directly before onset of rapid oxidation, the sample temporarily lost magnetic character, to a weight value below that of the final product. Weight gain increased slowly for ~5°C, followed by an immediate rise to a maximum weight value, which exceeded the weight of the cooled TM product. Weight was lost until the Curie transition, where the TM curves for the reactant and product coincided to the instrument limit. The product is different to that formed by regular oxidation as shown in Figure 6.2 - a TG study on this product showed it to be thermally stable in air up to 900°C (Figure 6.3, curve [b]).

6.1.4 Discussion

One of the criteria for rapid oxidation was the sample size. Samples larger than 15 mg heated at 20°C min^{-1} generally ignited, probably because they were incapable of dissipating the heat generated in the oxidation process to the sample pan. The magnetic character of the product is related to the applied magnetic field during the oxidation process.

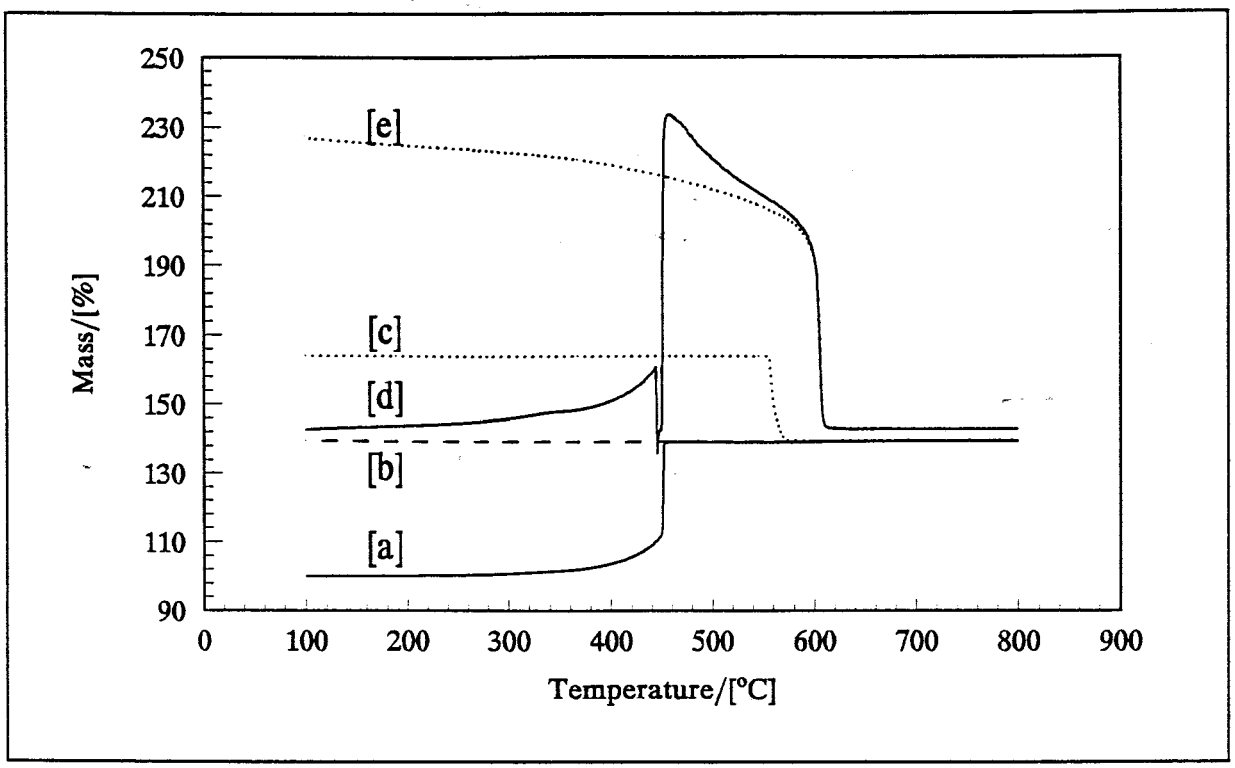

FIGURE 6.3: Rapid oxidation of iron powder in oxygen
[a]: TG original, [b]: TG of TG product, [c]: TM of TG product, [d]: TM original, [e]: TM of TM product

Combustion of the iron powder (observed to be incandescent) will result in local temperatures well in excess of the highest furnace temperatures registered (~450°C). Rapid oxidation may occur at these elevated temperatures, since the shape of the dip in the rescaled curve (Figure 6.4) shows both magnetic and non-magnetic characteristics. The ferromagnetism of the sample returns, however, once it has cooled to the furnace temperature (still at a temperature below the Curie transition), whereafter the programmed heating is resumed and further transitions occur. This behaviour explains why close agreement is found between curves for the reactant and for the product beyond 580°C, as product formation has occurred to completion during the rapid heating stage of the oxidation.

Thermomagnetometry on the product of combustion in the TG (Figure 6.3, curve [b]) indicates a much greater step due to the Curie point of Fe_3O_4 (at ~580°C), than that noted in the regular (non-combustion) oxidation process (Figure 6.2, curve [d]). Fe_3O_4 is thus formed during rapid combustion, possibly by the reactions:

$$Fe + Fe_2O_3 \rightarrow FeO$$

$$4FeO \leftrightarrow Fe_3O_4 + Fe$$

The oxidation of Fe powder may thus generate different final products, dependent on the rate of oxidation and the applied magnetic field and these results have to be kept in mind when attempting to characterize the products generated by intersolid combustion reactions with iron as a constituent.

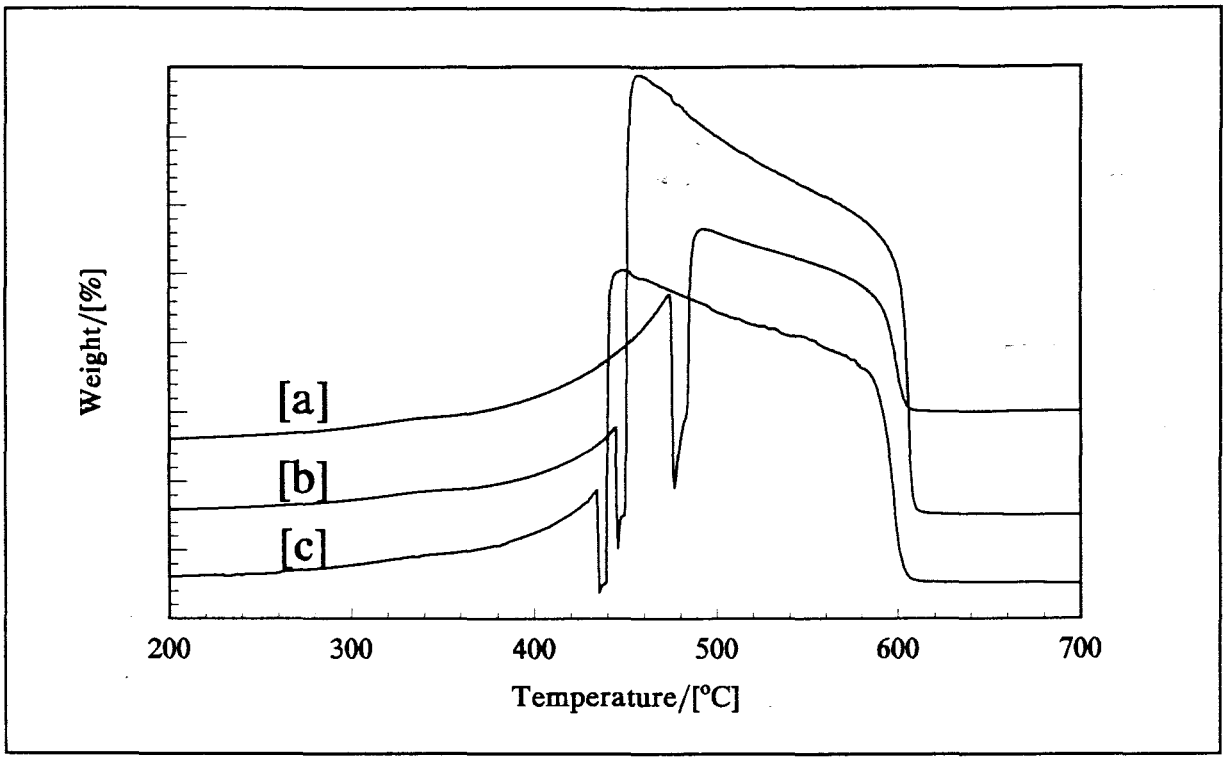

FIGURE 6.4: Reproducible thermal event in rapid oxidation of iron
Approximate initial masses: [a]: 28 mg, [b]: 44 mg and [c]: 49 mg.

6.2 Nonisothermal kinetic analysis

The Borchardt and Daniels [159] method was used to determine the kinetics of oxidation from the thermal analysis data for Fe powder (details of the method are given in Section 4.4 and Appendix 5). TG curves in O_2 and in air, and DTA curves in air were used for the analyses. The Arrhenius plots for various values of the apparent order of reaction, n, are shown in Figure 6.5.

TABLE 6.1: Borchardt and Daniels kinetic analysis for the oxidation of Fe powder:

Atmosphere	T Range/[°C]	n	E_a/[kJ mol^{-1}]	A/[min^{-1}]	r^2
			TG		
O_2	440-600	½	35.8±1.2	(24.1±1.3)x10^0	0.76
		⅔	42.7±1.1	(76.1±3.0)x10^0	0.84
		1	56.5±1.0	(75.4±1.7)x10^1	0.93
		2	97.9±0.6	(73.9±0.5)x10^4	0.99
			DTA		
Air	300-600	½	42.1±0.8	(63.0±1.6)x10^0	0.90
		⅔	45.7±0.7	(12.8±1.9)x10^1	0.93
		1	53.1±0.6	(14.3±1.0)x10^2	0.96
		2	75.2±0.7	(36.4±1.4)x10^3	0.97
			TG		
Air	200-900	½	33.5±0.8	(7.9±2.7)x10^0	0.80
		⅔	38.8±0.6	(22.9±4.1)x10^0	0.89
		1	49.5±0.5	(19.2±3.4)x10^1	0.96
		2	81.6±1.2	(11.4±1.4)x10^4	0.90

The value of E_a depends strongly on the order of reaction, n, chosen. The DTA and TG results in air are in fair agreement, as are the values determined in O_2. Reported values for the E_a of oxidation in the literature depend on the temperature range and atmosphere in which the study was performed. Typical values have been reported in Section 3.6, including the value of 67 kJ mol^{-1} determined [27] at 400°C, which shows closest agreement. The values of E_a determined for diffusion of Fe species range from 56 to 208 kJ mol^{-1} (Table 3.5).

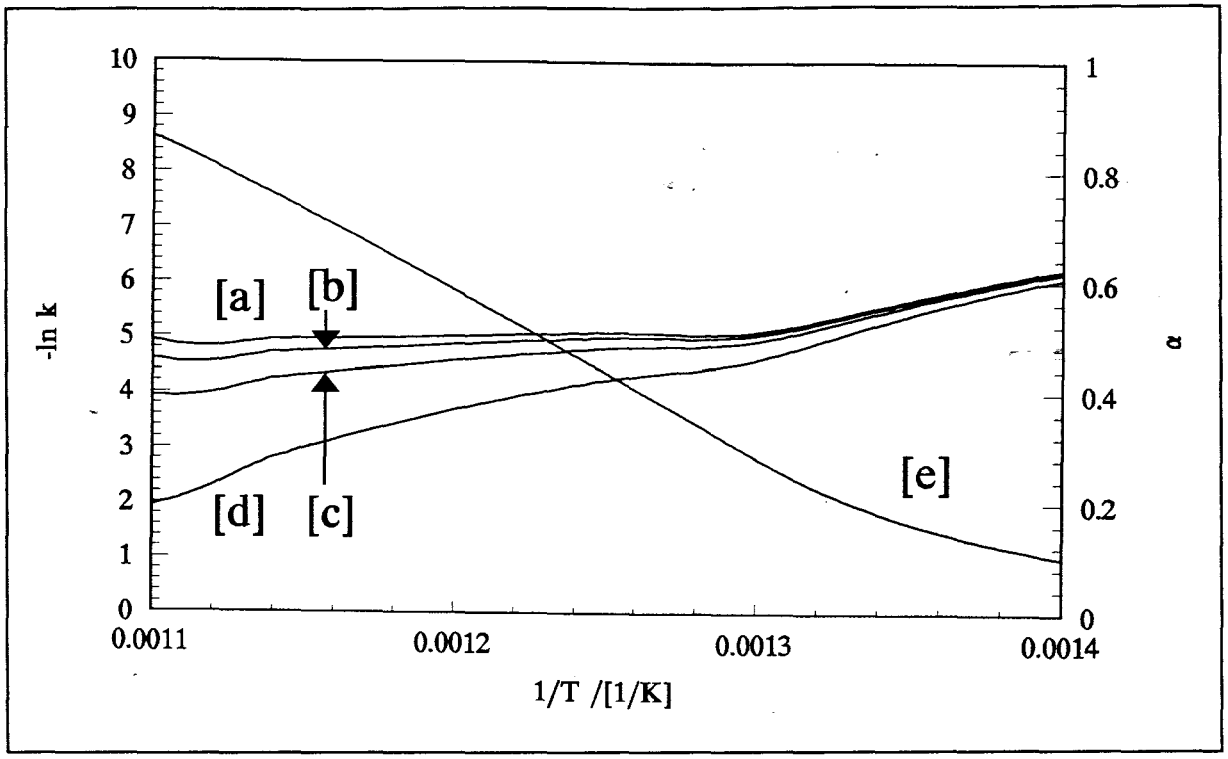

FIGURE 6.5: Borchardt and Daniels kinetic analysis of the oxidation of Fe in O_2 (TG)
[a]: n=½, [b]: n=⅔, [c]: n=1, [d]: n=2 and [e]: α

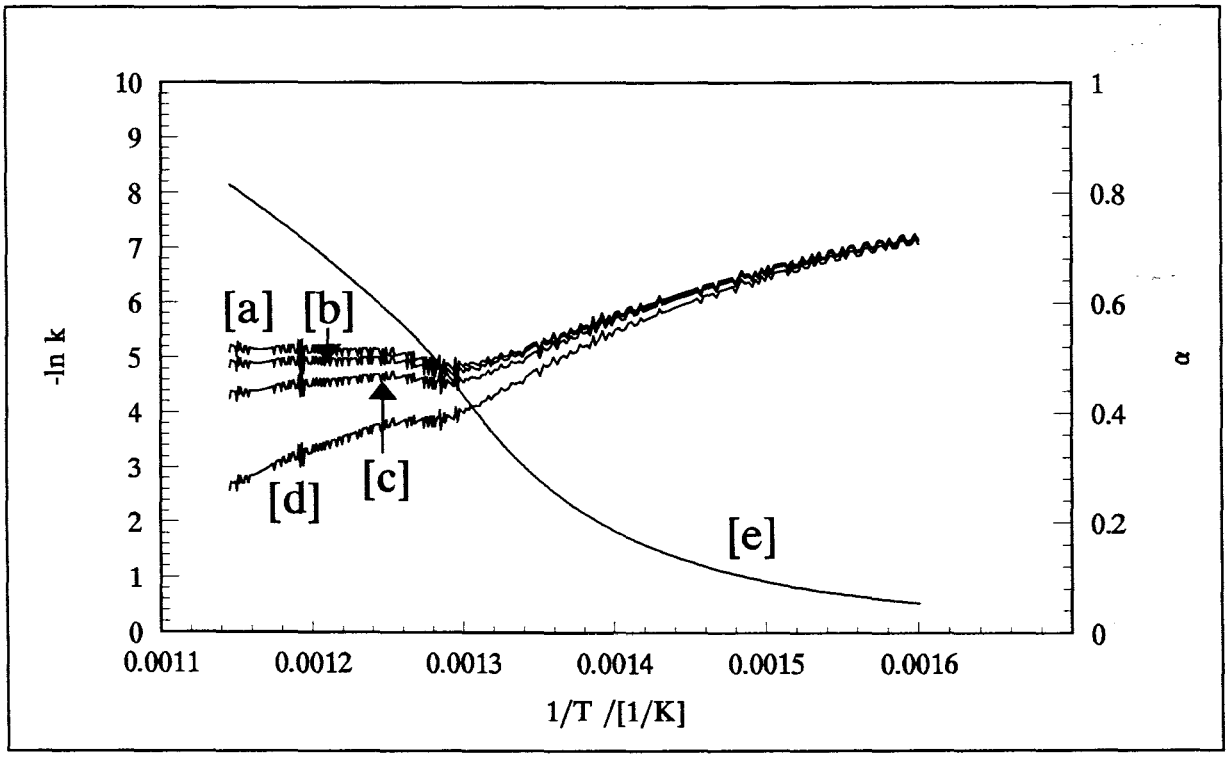

FIGURE 6.6: Borchardt and Daniels kinetic analysis of the oxidation of Fe in air (DTA)
[a]: n=½, [b]: n=⅔, [c]: n=1, [d]: n=2 and [e]: α

6.3 Thermal behaviour of iron oxides:

6.3.1 FeO:

FeO only forms above 575°C in O_2 deficient atmospheres. The proximity of this temperature to that of the Curie temperature for Fe_3O_4, complicates thermomagnetic studies of the iron system.

6.3.2 Fe_3O_4:

Little thermal activity was apparent from TG studies of Fe_3O_4 in O_2 and N_2, with a gradual mass loss occurring to 270°C (0.6%), followed by a mass gain to 390°C and a gradual mass loss continuing to 900°C (1.5%). The calculated mass gain for the oxidation of Fe_3O_4 to Fe_2O_3 is 3.4%. In a magnetic field (TM), weight is gained up to 390°C (~16%) (formation of surface Fe_2O_3), and lost to 680°C (~35%) (formation of bulk Fe_2O_3) in O_2, whereafter the mass is stable to 900°C. DTA (Figure 6.7) showed that a single exotherm occurs in N_2 with an onset temperature of 580°C. This exotherm, which has been observed by other researchers [54], is attributed to oxidation of the Fe_3O_4 by the ppm traces of O_2 in the N_2 purge gas. The temperature at which this occurs corresponds to the loss of magnetism of Fe_3O_4, yet the endothermicity of this magnetic transition is beyond the resolution of the instrument. Two exotherms occur in oxygen. A large, broad exotherm with onset at 260°C and peak at 330°C, due to the transition of Fe_3O_4 to γ-Fe_2O_3, and a further smaller exotherm with onset at 680°C, due to the transition of γ-Fe_2O_3 to α-Fe_2O_3.

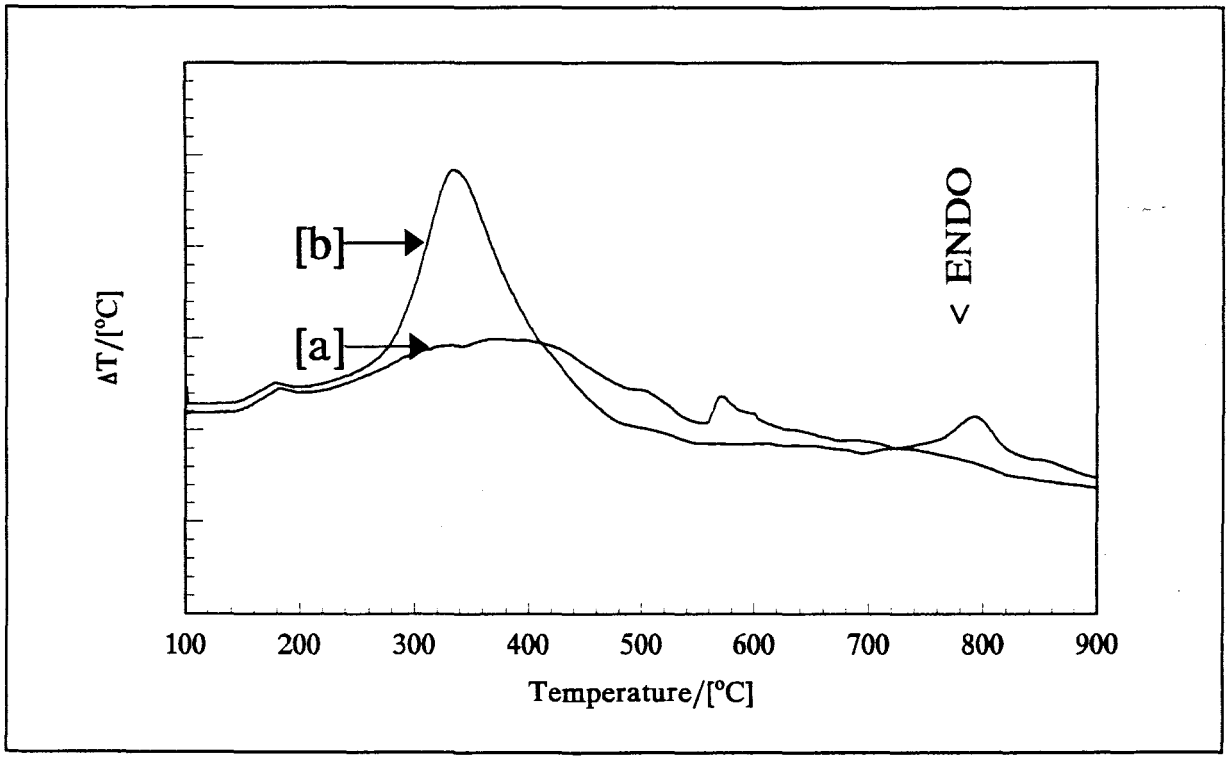

FIGURE 6.7: DTA of Fe_3O_4 in [a]: N_2 and [b]: O_2

6.3.3 Fe_2O_3:

The TG in N_2, TG in O_2, TM in N_2 and TM in O_2 all demonstrate the same behaviour; a gradual, continuous mass loss of less than 0.5% up to 900°C, without any significant thermal events, while the DTA in N_2 and O_2 showed no apparent thermal events up to 1300°C.

6.4 Reactions of zinc powder

6.4.1 Behaviour of zinc in nitrogen

The DSC curve of zinc in nitrogen showed a reproducible fusion endotherm (onset 418.0 ± 2.1 °C) with $\Delta H = 100.8 \pm 2.5$ J g^{-1}. The enthalpy of melting of pure Zn is 108.0 J g^{-1} [161], so this value compared favourably with the value calculated for the reported purity (~94%) of the zinc (101.5 J g^{-1}). The DTA curve of zinc in nitrogen (Figure 6.8, curve [a]) shows the melting endotherm (onset 420°C) and the vaporisation endotherm (onset 685°C). The TG curve in N_2 (Figure 6.9 curve [a]) shows onset of significant vaporisation above ~550°C.

6.4.2 Behaviour of zinc in air and oxygen

The DTA curve in air (Figure 6.8, curve [b]), shows that the melting endotherm is followed immediately by an exotherm attributable to oxidation of the molten metal. The TG curve in air (Figure 6.9, curve [b]) confirmed the onset of the oxidation at 420°C. Oxidation was complete at 900°C (the maximum operating temperature of the instrument) at which stage a mass gain of ~23% had been observed (24.5% calculated for Zn → ZnO, but considering 94% pure zinc, a 23.0% gain is expected). The maximum rate of oxidation was at ~575°C. The DTG curve in air (Figure 6.9, curve [c]) is very similar to the DTA curve in air (Figure 6.8, curve [b]). The oxidation of Zn in air or oxygen showed similar behaviour, unlike the oxidation of iron which reached a sufficiently rapid rate in oxygen to become pyrophoric.

The mass gain during oxidation of zinc was found to vary considerably with changes in the partial pressure of oxygen, due to the high vapour pressure of zinc. In nitrogen, the onset temperature of mass loss was 600°C, after which the mass loss became acceleratory.

6.5 Nonisothermal kinetic analysis:

A Borchardt and Daniels kinetic analysis of the TG and DTA curves for the oxidation of zinc powder yielded the kinetic parameters given in Table 6.2. The best value of the apparent order of the reaction, n, was 2 and E_a was 104.6±0.9 kJ mol^{-1} for the DTA curve in air, and 98.4±0.6 kJ mol^{-1} for the TG curve in O_2. These values compare satisfactorily with each other and the literature values quoted in Section 3.6, namely 67 - 170 kJ mol^{-1}.

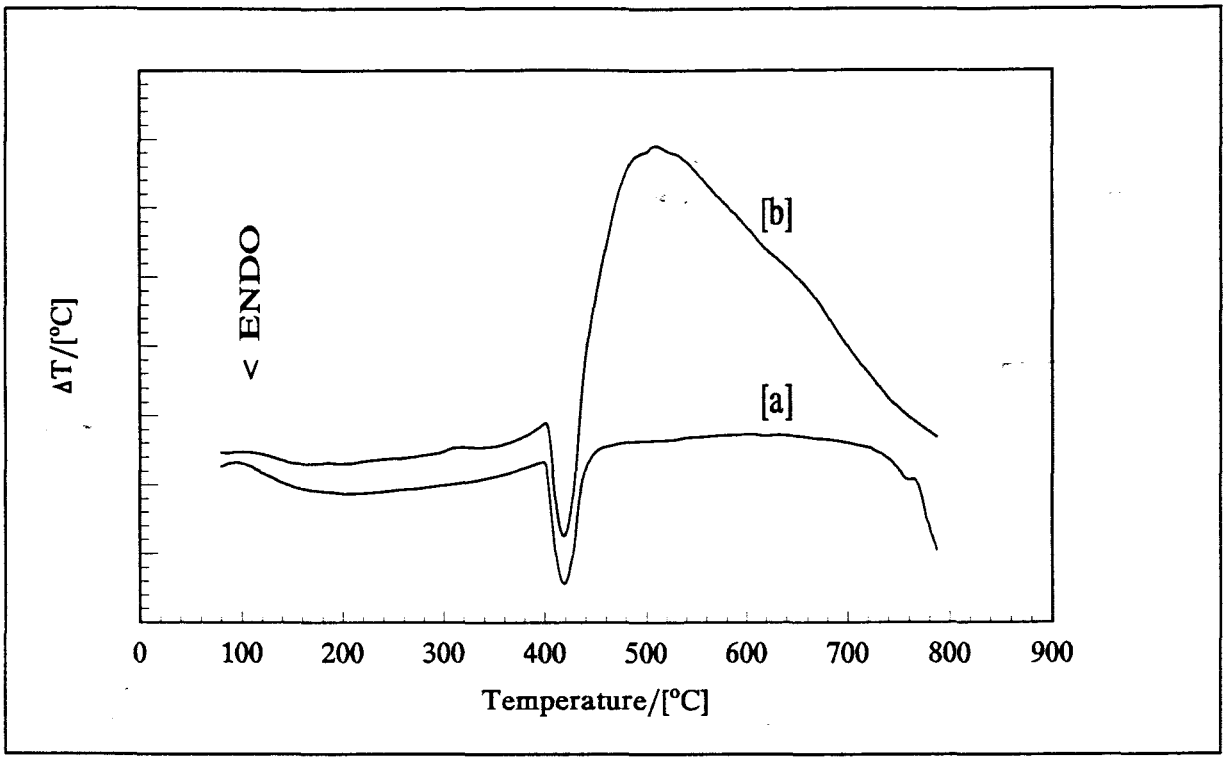

FIGURE 6.8: DTA of zinc powder in [a]: N_2 and [b]: O_2

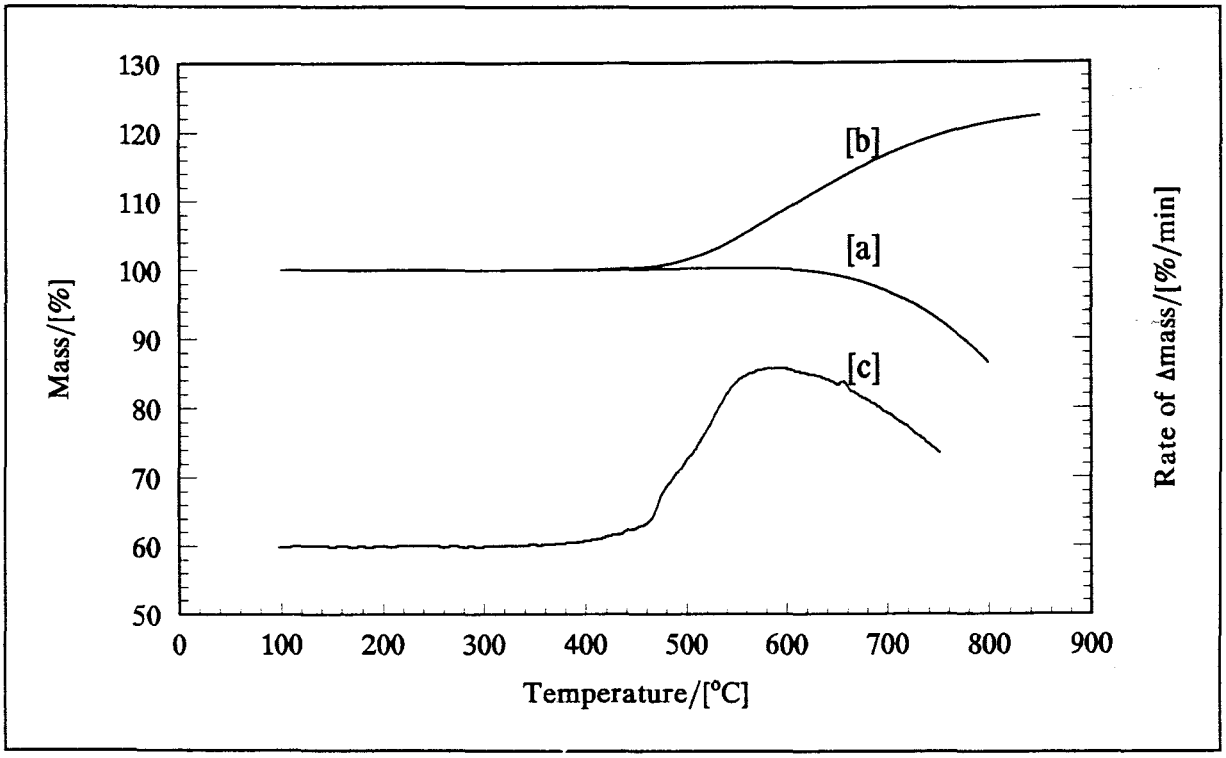

FIGURE 6.9: TG of zinc powder
[a]: Zn in N_2, [b]: Zn in O_2 and [c]: DTG of Zn in O_2

TABLE 6.2: Borchardt and Daniels kinetic analysis for the oxidation of Zn powder:

Atmosphere	T Range[°C]	n	E_a/[kJ mol^{-1}]	A/[s^{-1}]	r^2
			TG		
O_2:	400-725	½	37.5±1.1	(17.5±2.4)x10^0	0.71
		⅔	44.3±1.0	(53.7±4.7)x10^0	0.81
		1	57.8±0.8	(50.2±4.5)x10^1	0.92
		2	98.4±0.6	(41.5±0.9)x10^4	0.98
			DTA		
Air:	437-679	½	25.3±1.2	(04.3±0.2)x10^0	0.52
		⅔	34.1±1.1	(18.0±1.8)x10^0	0.69
		1	51.6±0.9	(30.8±2.8)x10^1	0.87
		2	104.6±0.9	(16.0±0.3)x10^5	0.97
			TG		
Air:	395-815	½	54.2±1.1	(10.2±3.5)x10^1	0.79
		⅔	61.2±1.0	(31.5±5.6)x10^1	0.86
		1	75.1±0.8	(29.8±2.2)x10^2	0.94
		2	117.1±0.7	(25.6±0.7)x10^5	0.98

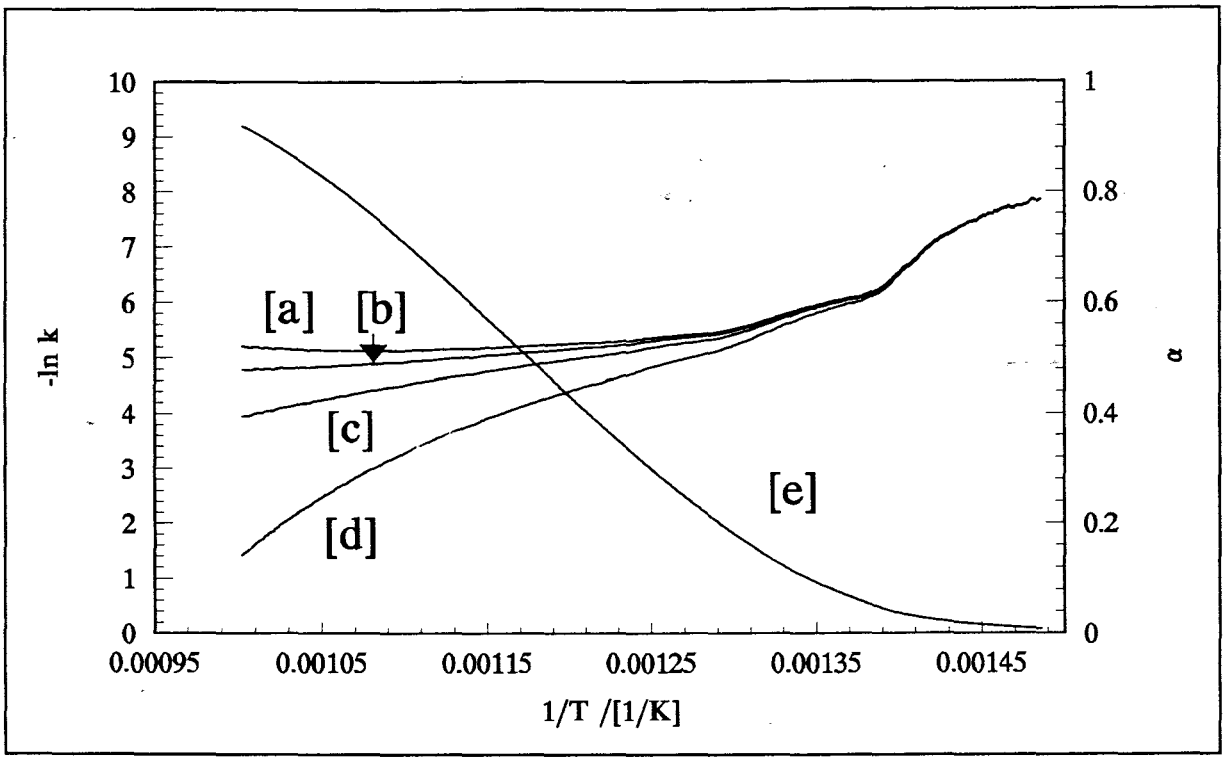

FIGURE 6.10: Borchardt and Daniels kinetic analysis of the oxidation of Zn in O_2 (TG) [a]: n=½, [b]: n=⅔, [c]: n=1, [d]: n=2 and [e]: α

These values of E_a show a strong dependence on the order of reaction, n, chosen. The values determined from the DTA experiments in air are lower than those of the TG experiments in air, but the endotherm corresponding to the fusion of zinc coincides with the onset of the oxidation exotherm and the superposition of these events makes determination of the onset temperature of oxidation difficult. Comparison of data obtained from the TG experiments in air and O_2, shows that the values of E_a are lower in O_2, suggesting a relationship between oxidation rate and the partial pressure of oxygen. Such a relationship was expected from previous studies on the oxidation of zinc (Section 3.8). The values of E_a recorded in the literature range from 34 to 209 kJ mol^{-1} (Table 3.7).

6.6 Thermal behaviour of zinc oxide:

The TG curves for zinc oxide (commercial grade) heated in air and N_2 showed variable mass losses of up to 5.0% (onset at 250°C). No other thermal events were apparent. Comparison of this behaviour with the TG trace of $ZnCO_3$ showed that some ZnO samples formed $ZnCO_3$ on ageing. AR grade ZnO showed no thermal events in the range studied. The DTA curves for commercial grade zinc oxide have an endotherm corresponding to the mass loss apparent in the TG trace present at 250°C, followed by a further smaller endotherm with onset at 380°C in N_2. This second endotherm was not apparent in the run performed in air, and did not correspond to any mass loss in N_2.

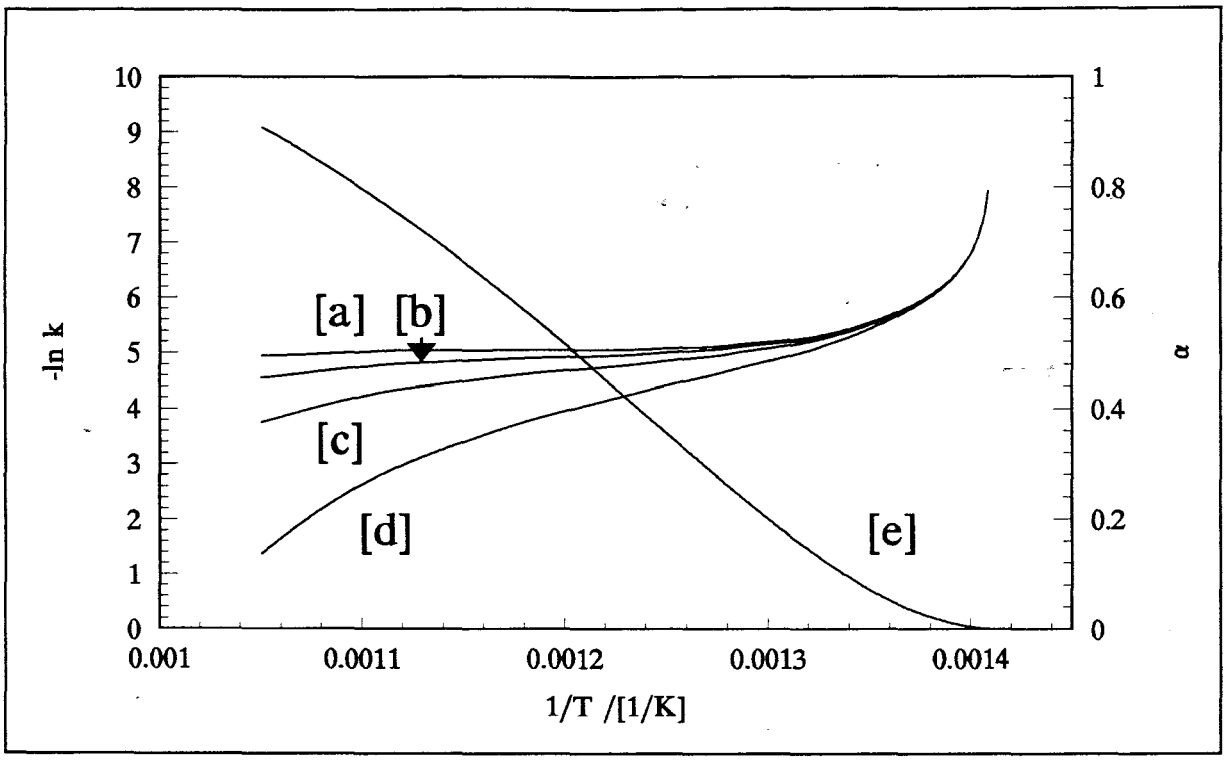

FIGURE 6.11: Borchardt and Daniels kinetic analysis of the oxidation of Zn in air (DTA) [a]: n=½, [b]: n=⅔, [c]: n=1, [d]: n=2 and [e]: α

7. THERMAL BEHAVIOUR OF THE OXIDANTS

7.1 Thermal analysis of BaO_2:

Drennan [6] recorded DSC traces for a variety of different BaO_2 samples, including "dry" and "moist" batches. The traces in N_2 all showed a high temperature endotherm (>600°C) attributed to the decomposition of BaO_2. The expected enthalpy change, calculated from standard enthalpies of formation, was 334 J g^{-1}. The measured value of 382 J g^{-1} for 85% pure BaO_2 (which is corrected to 450 J g^{-1} for 100% BaO_2) compared well with the 473 J g^{-1} recorded by Till [89]. Drennan also reported an endotherm at 360°C, which he ascribed to dehydroxylation of $Ba(OH)_2$, present as an impurity in some of the samples studied by him. The high temperature decomposition endotherm recorded in nitrogen was absent in the traces for all samples heated in O_2 up to the instrument limit of 725°C, indicating that decomposition is shifted to higher temperatures in the presence of O_2.

Runs performed in N_2 on the BaO_2 used in the present study showed a low temperature endotherm due to the loss of adsorbed water (onset 100°C) of variable ΔH, a small endotherm, again of variable ΔH, at 340°C due to the dehydroxylation of $Ba(OH)_2$ formed on ageing, and a high temperature endotherm (onset 625±20°C) which was virtually complete for small samples at the instrument limit of 725°C (but not for large samples), due to the decomposition of the peroxide (with loss of oxygen). ΔH values for the endotherm were found to be in excess of 350 J g^{-1}, with typical values of $\Delta H = 400 \pm 50$ J g^{-1} being obtained (corrected to 470 J g^{-1} for 100% purity). TG curves for BaO_2 heated in N_2 at 20°C min^{-1} (Figure 7.1, curve [a]) showed the removal of small amounts (~0.2%) of moisture at ~100°C and onset of decomposition above 500°C and maximum rate at ~580°C. The 7.7% mass loss found agrees well with the expected loss of 8.0% for decomposition of 85% pure BaO_2 to BaO and O_2. In O_2, onset of decomposition was shifted to ~700°C and the maximum rate to ~730°C (650 and 680°C in air, respectively). Mass loss continued to the instrument limit at 950°C, a finding consistent with previous research [143]. Samples of different masses (15-45 mg) when heated in N_2 in the DTA (one example is shown in Figure 7.2, curve [a]), gave consistent endotherms at 100°C and 680°C (with an onset corresponding closely to the mass loss at 650°C). This endotherm (onset 710°C in O_2) corresponds to the decomposition of BaO_2 to BaO and gaseous O_2. Similar results were obtained for DSC runs in N_2. No further thermal events were recorded up to the instrument limit. For slow flow rates of purge gas (less than 1 ml min^{-1}), the single endotherm accompanying decomposition in air, observed in the above studies, showed broadening into a second peak with onset at 740°C. No additional thermal events up to the 1300°C limit of the DTA were observed.

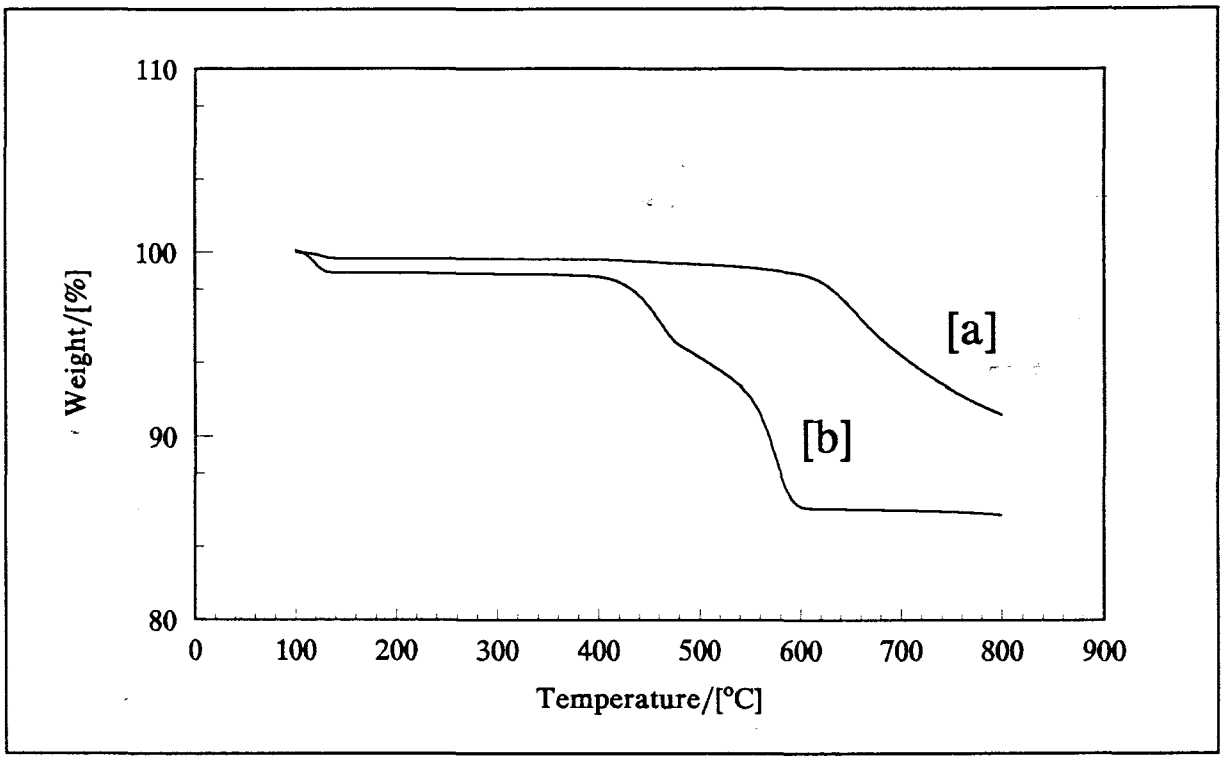

FIGURE 7.1: TG of alkaline-earth peroxides in N_2
[a]: BaO_2 and [b]: SrO_2

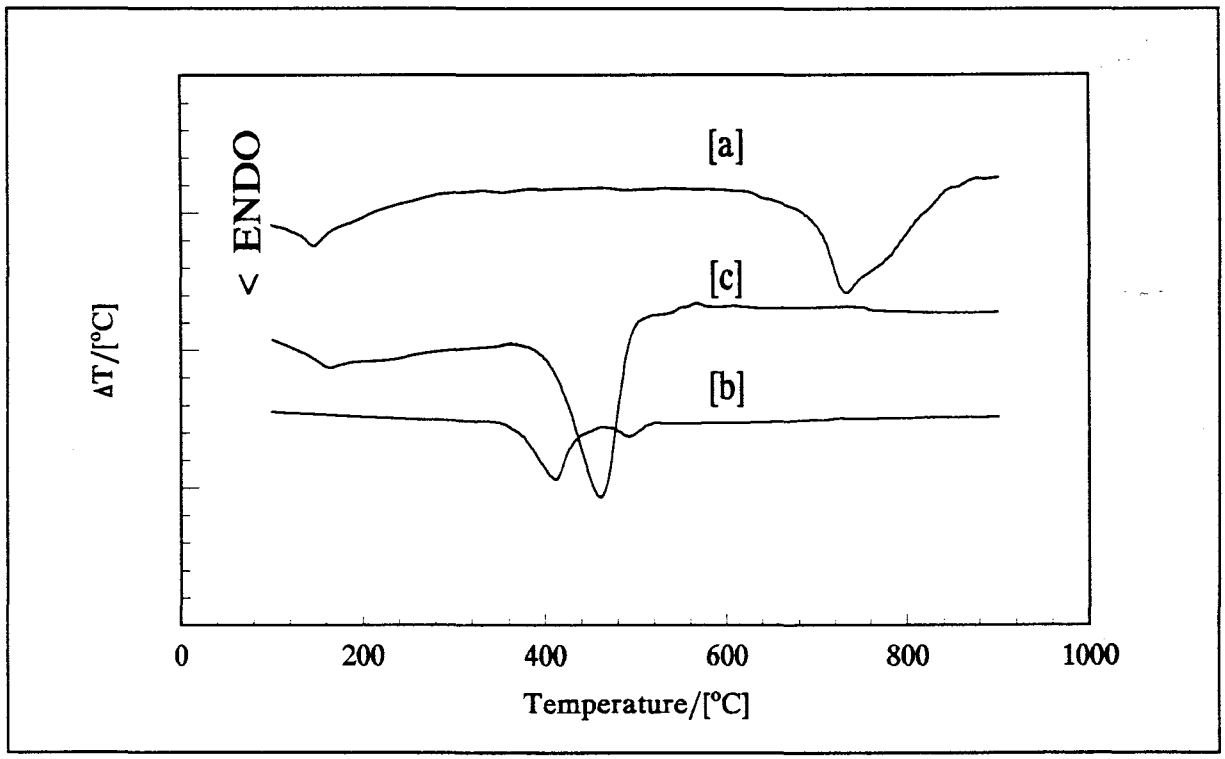

FIGURE 7.2: DTA of alkaline-earth peroxides in N_2
[a]: BaO_2, [b]: SrO_2 two-stage (slow) and [c]: SrO_2 single-stage (rapid heating rates)

7.2 Thermal analysis of SrO_2:

In previous studies [6] of the behaviour of SrO_2 in N_2 by DSC, SrO_2 samples were found to have a varying degree of moisture content. Other than dehydration endotherms with onset around 100°C, two other endotherms with onset temperatures at 390°C (400°C in O_2) and 525°C (550°C in O_2) were observed for dry SrO_2, corresponding to ΔH values of 193 ± 56 J g^{-1} and 133 ± 33 J g^{-1}. The SrO_2 used in this study was also examined by DSC. In addition to the low temperature endotherms due to the loss of adsorbed water, the two endotherms reported in the literature [6] were observed (onset 400 ± 11°C, $\Delta H = 185 \pm 16$ J g^{-1} and onset 521 ± 5°C, $\Delta H = 182 \pm 29$ J g^{-1}), for small sample masses (<1 mg) and 10°C min^{-1} scan rates. The expected enthalpy change for the decomposition of SrO_2 to SrO and O_2 is 427 J g^{-1} [162]. The total ΔH value for the two endotherms recorded is 367 J g^{-1}, which converts to 432 J g^{-1} for 100% purity. Fahim and Ford [88] recorded a value of 402 J g^{-1}. The endotherms were smaller in O_2 (98 ± 30 J g^{-1} and 128 ± 10 J g^{-1}, respectively), due to the inhibition of decomposition by the O_2 atmosphere. As the sample mass was increased and less rapid flushing was used, the first endotherm increased in intensity until the second endotherm virtually disappeared. This endotherm was often preceded by a small exotherm. A study of the thermal behaviour of $Sr(OH)_2$ (see below) yielded a DSC peak with onset at 480°C, corresponding closely with the onset temperature for the large peak in the DSC curve for SrO_2.

The TG curve (Figure 7.1, curve [b]) shows that, after initial loss of adsorbed water (<1%) at 100°C, decomposition of SrO_2 in N_2 occurs in two steps: The first with mass loss ~4.0%, onset 390°C, is followed by loss of a further ~8.0%, onset 525°C (calculated 11.4% for decomposition of 85% pure SrO_2 to SrO and O_2). This value of ~12.0% coincides well with previous studies [6] which recorded a value of 12.7%. A further gradual loss of ~2.0% occurs toward the limit of the instrument at 900°C (decomposition of some $SrCO_3$). In O_2, the relative mass losses in the two stages (8-9% followed by 3-4%) and the onset temperatures are dependent on the pressure of O_2. The DTG curve of the decomposition agrees well with published [6] DSC curves of SrO_2 in N_2.

The DTA curve of SrO_2 in N_2 (Figure 7.2, curve [b]) shows the onset of endothermic decomposition at ~350°C. Two different behaviours were noted, depending on the heating-rate. Either two endotherms were observed (onset ~350°C and ~520°C) (Figure 7.2, curve [b]), or only a single endotherm (Figure 7.2, curve [c]). A single endotherm (onset $\sim 530 \pm 10$°C) usually accompanied a large sample mass, or a low flushing rate, or a high heating-rate. Similar results were obtained using DSC.

The two stages in the mass loss of SrO_2 at 390°C and 490°C are supported by the existence of two endotherms at 405°C and 535°C. Under certain conditions (such as high heating rates) these stages are not readily separable.

7.3 Reaction between BaO_2 and SrO_2:

The TG trace of a 50% by mass BaO_2/SrO_2 mixture showed the combined mass losses of the individual materials, irrespective of the nature of the atmosphere, with the strontium peroxide losses occurring at slightly higher temperatures than usual, and the barium peroxide losses at a lower temperature than usual, as a result of sensitivity of the components to $O_2(g)$. The DTA plot showed the unchanged endotherms characteristic of both substances, which suggests that no interaction occurs between the materials.

7.4 Kinetics of the thermal decompositions of BaO_2 and SrO_2:

7.4.1 Previous studies

Several studies of the decomposition of the alkaline-earth peroxides have been reported [6,11,13,23,72-83,85-89,163-168]. However, only a few of these studies report values for the kinetic parameters. No kinetic parameters for the decomposition of SrO_2 were found in the literature.

The isothermal decomposition of BaO_2 has been reported [88] to obey first-order kinetics, with an activation energy, E_a, of 135 kJ mol^{-1}. The nonisothermal decomposition was also studied [88] and the value of E_a, determined from a plot of $\ln\left(\frac{\ln(1-\alpha)}{T^2}\right)$ versus 1/T, was 141 kJ mol^{-1}. Although the kinetics deviated strongly from first-order behaviour above 800°C, this behaviour was explained in terms of diffusion resistance.

Erofeev *et al* [169] obtained a value of $E_a = 192$ kJ mol^{-1} for the isothermal decomposition of BaO_2 (based on $\alpha = 1-\exp(-kt^n)$). Mayorova *et al* [90] used programmed temperature thermogravimetry and obtained a value for E_a of 360 ± 20 kJ mol^{-1} by assuming first-order behaviour. Brunere *et al* [91] represented the decomposition of BaO_2 by a three-step process: nucleus formation ($E_a = 12$ kJ mol^{-1}); grain growth ($E_a = 104$ kJ mol^{-1}); and oxygen diffusion ($E_a = 2$ kJ mol^{-1}). The details of this research were not available.

7.4.2 Isothermal studies:

Isothermal TG studies were performed on the peroxide systems at a series of different temperatures (490-610°C for BaO_2 and 380-530°C for SrO_2). The TG curves were converted to (α,time) curves (where the fractional decomposition, $\alpha=(m_o-m)/(m_o-m_f)$ and m_o and m_f are the initial and final sample masses, respectively). The value of m_f used was that calculated for complete decomposition to the oxide. The isothermal (α,t) curves at different temperatures are shown in Figure 7.3 (BaO_2) and Figure 7.4 (SrO_2).

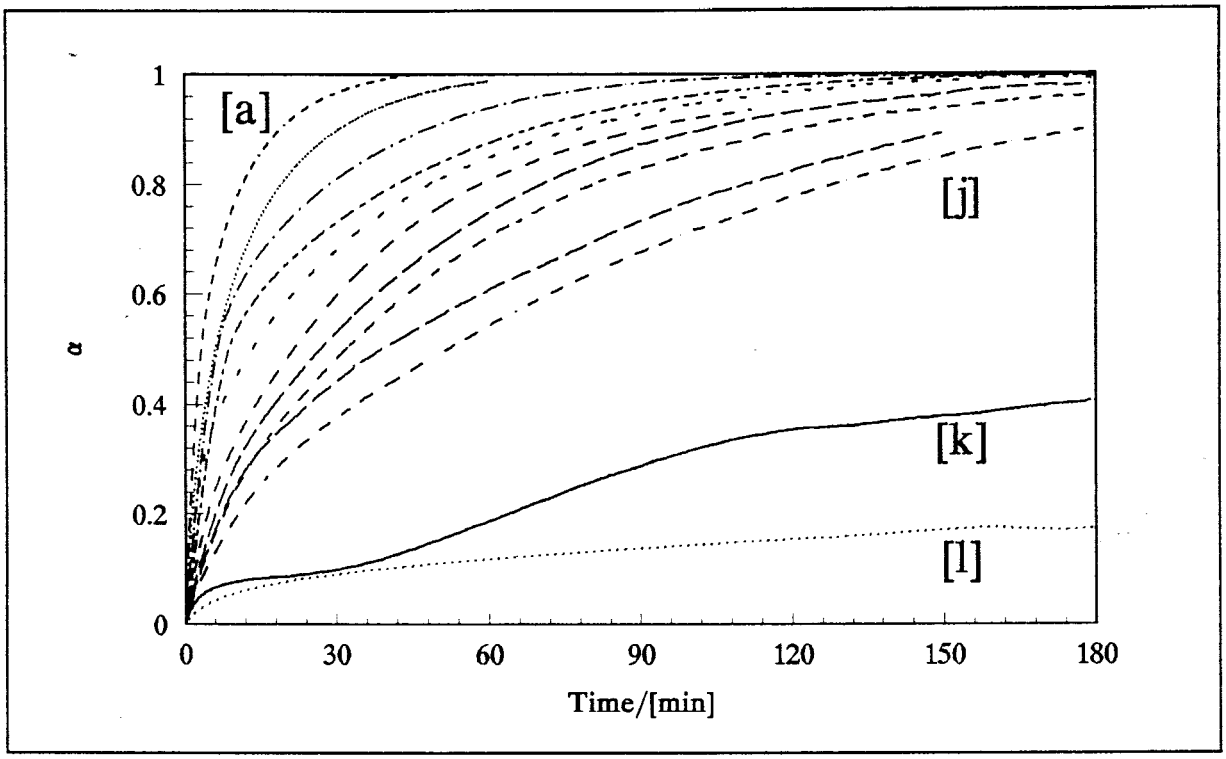

FIGURE 7.3: Isothermal decomposition of BaO_2 in flowing N_2
[a]-[l]: 610, 600, 590, 570, 550, 530, 520, 510, 505, 500, 495 and 490°C.

7.4.2.1 BaO_2:

Decomposition of BaO_2 in N_2, which begins between 490°C and 495°C, is very slow at temperatures below 500°C, and reaction does not approach completion. The low-temperature (495°C) curve for the decomposition of BaO_2 (curve [k]) shows at least four stages:

(i) an initial deceleratory process ($0<\alpha<0.1$);

(ii) an approximately linear segment ($0.1<\alpha<0.25$);

(iii) a second deceleratory process ($0.25<\alpha<0.3$); and

(iv) a very slow approximately linear process which hardly contributes significantly at this temperature, so that the total extent of reaction at low temperatures is only 40% of that expected.

Increasing the temperature to 500°C has a marked effect on all of these stages. Stages (i), (ii) and (iii) become almost linear and the final stage (iv) shows up as a deceleratory process.

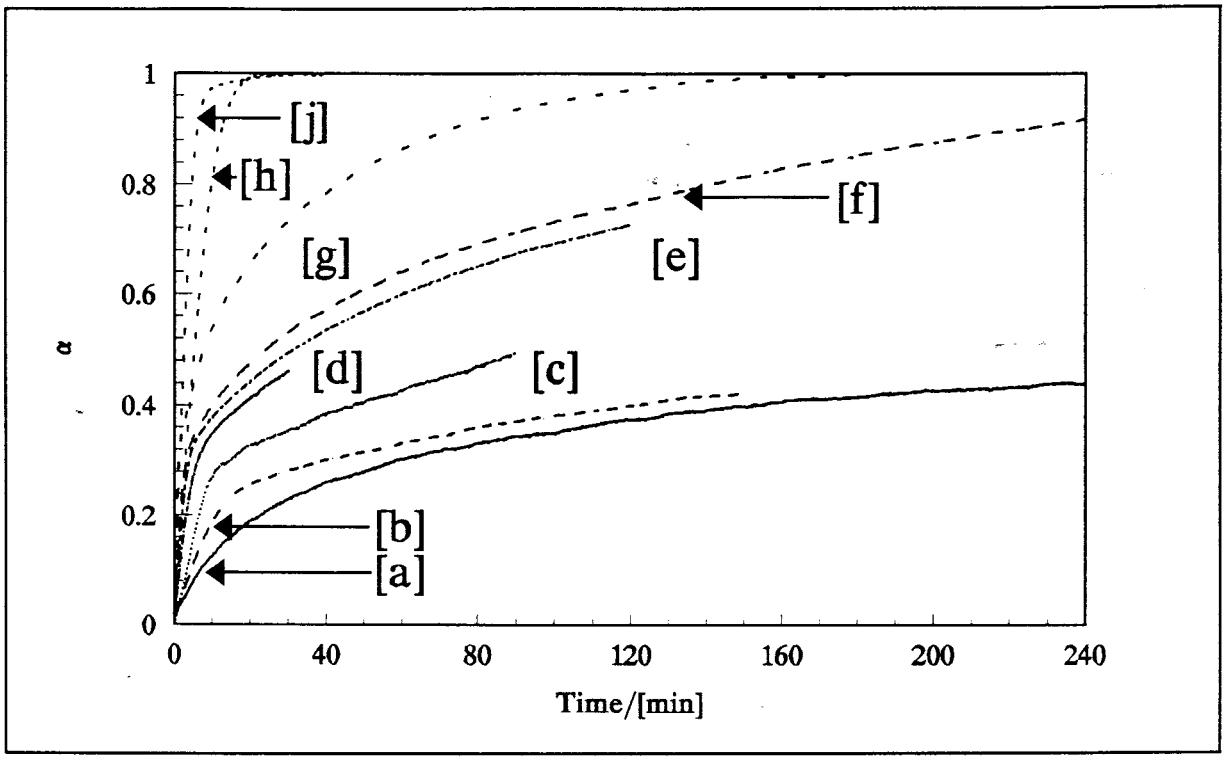

FIGURE 7.4: Isothermal decomposition of SrO_2 in flowing N_2 at various T/[°C] [a]:380, [b]:390, [c]:400, [d]:420, [e]:430, [f]:440, [g]:480, [h]:520, [j]:530

As an approximate kinetic analysis of the first stages of reaction, the initial slopes, s_o, of the α,t curves were measured and ln s_o was plotted against 1/T (Figure 7.5, curve [a]). This assumes that the initial reaction may be treated as a zero-order reaction:

$\frac{d\alpha}{dt} = k = s_o$ (constant over $0<\alpha<0.2$). In general, for a rate equation of the form

$\frac{d\alpha}{dt} = k(1-\alpha)^n$, for $\alpha<<1$, $\frac{d\alpha}{dt} \approx k$, and the influence of the apparent

order, n, is removed. Such a treatment gave Arrhenius plots (Figure 7.5) with two approximately linear regions. For BaO_2 the change in behaviour occurred at about 770 K (496°C) and the E_a values were 109.4 ± 3.8 kJ mol^{-1} for the higher temperature region and a very high apparent value of ~ 1200 kJ mol^{-1} for the lower temperatures.

Kinetic analysis of the full α,t curves in terms of the standard deceleratory kinetic models [170] is illustrated by the plot in Figure 7.6 of f(α) (scaled where necessary) against t.

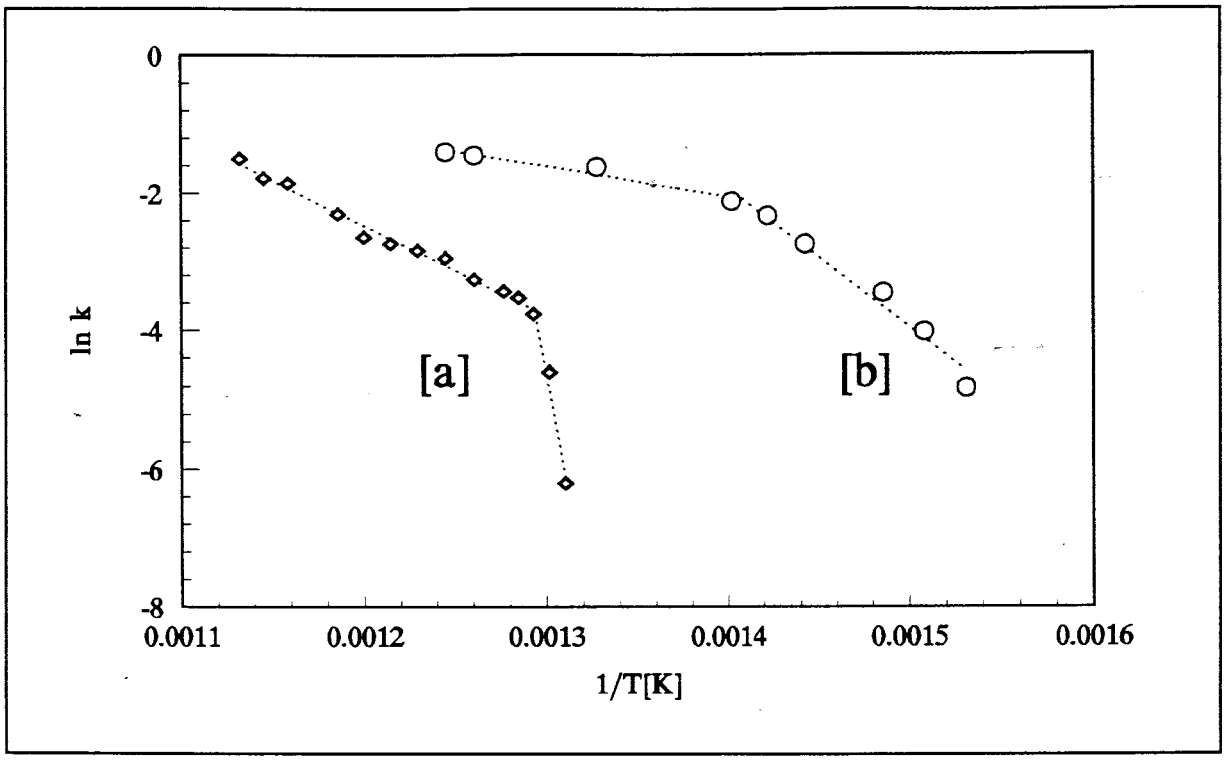

FIGURE 7.5: Arrhenius plots for the decompositions of BaO_2 and SrO_2 based on initial rates [a]: BaO_2 and [b]: SrO_2

The best description of the experimental results was in terms of either the first-order model (F1)

$$f(\alpha) = -\ln(1-\alpha) = k(t-t_o) \quad \ldots\ldots\ldots\ldots\ldots\ldots \quad 7.1$$

or the Ginstling-Brounshtein diffusion model (D4)

$$f(\alpha) = (1-\frac{2}{3}\alpha) - (1-\alpha)^{\frac{2}{3}} = k(t-t_o) \quad \ldots\ldots\ldots\ldots\ldots\ldots \quad 7.2$$

where t_o is a time correction if the model does not apply from t=0. The α-range 0.1 to 0.8 was used for calculation of k values, but the fit of the F1 and D4 models extended to $\alpha \approx 0.95$. The fit of these models to the data is shown in Figure 7.7 and 7.8 for the F1 and D4 models, respectively. The axes in Figure 7.8 have been reversed since the fit of the D4 model cannot be based on a calculation of $\alpha = f(t)$, but rather as $t = f^{-1}(\alpha)$. The Ginstling-Brounshtein model (D4) shows good agreement with the experimental data from very low values of α until α exceeds about 0.8. The fit of the first-order model to the data is satisfactory only at values of α above 0.3.

The Arrhenius parameters of BaO_2 decomposition, calculated from the temperature dependence of the above rate coefficients, are listed in Table 7.1.

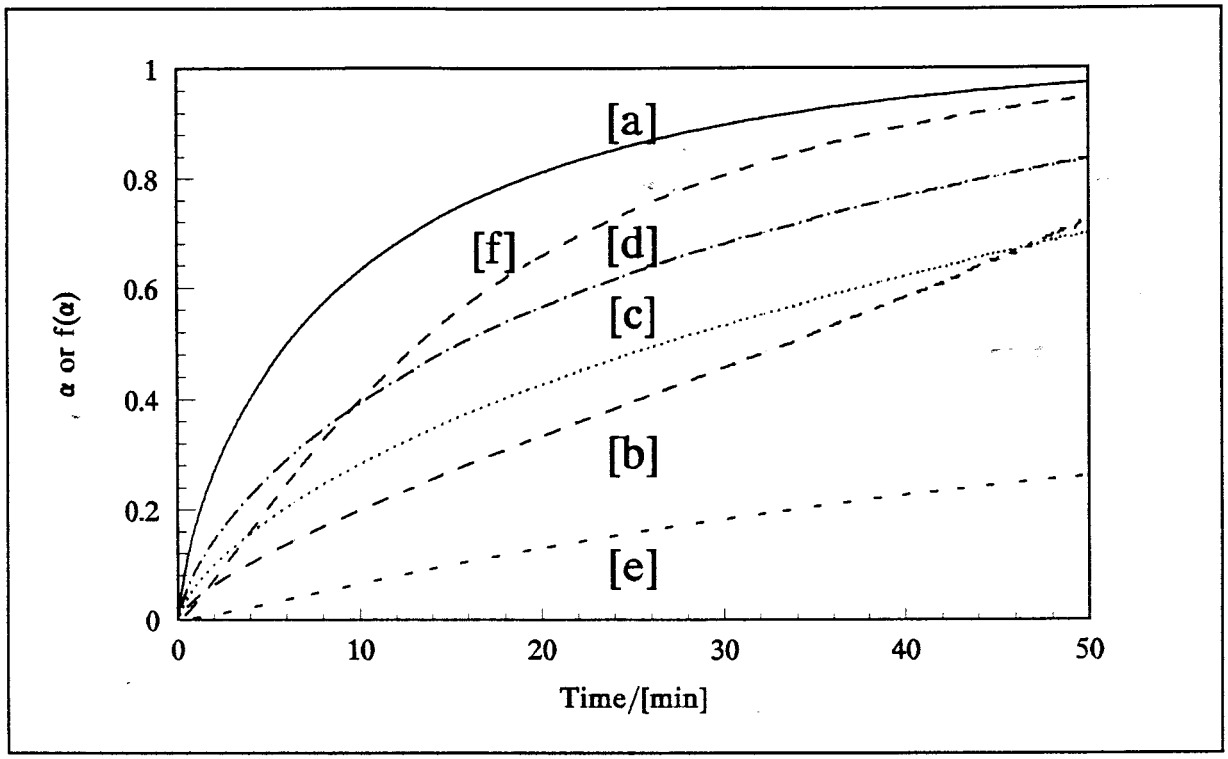

FIGURE 7.6: Application of kinetic models to the decomposition of BaO_2 at 600°C
[a]: α, [b]: (F1) x5, [c]: (R3), [d]: (R2), [e]: (D4) and [f]: (D1)

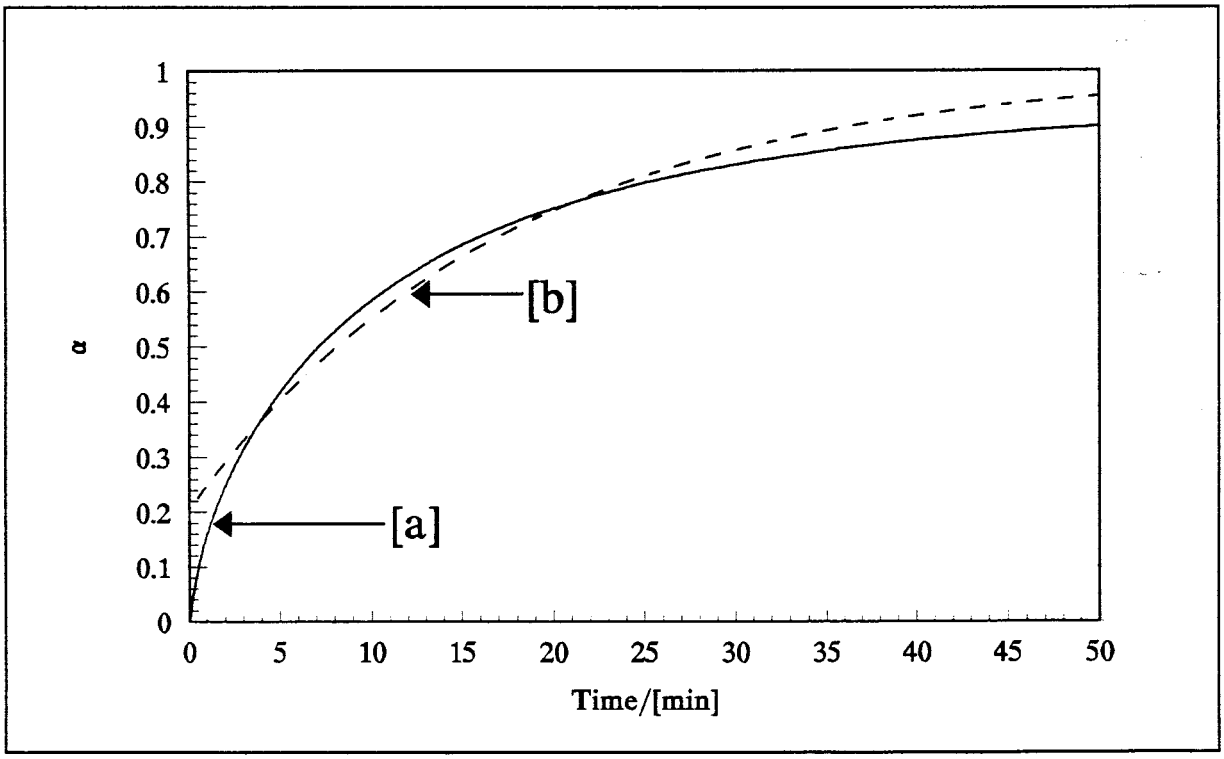

FIGURE 7.7: Correlation between the first-order model prediction and experimental data
[a]: Experimental and [b]: F1 model

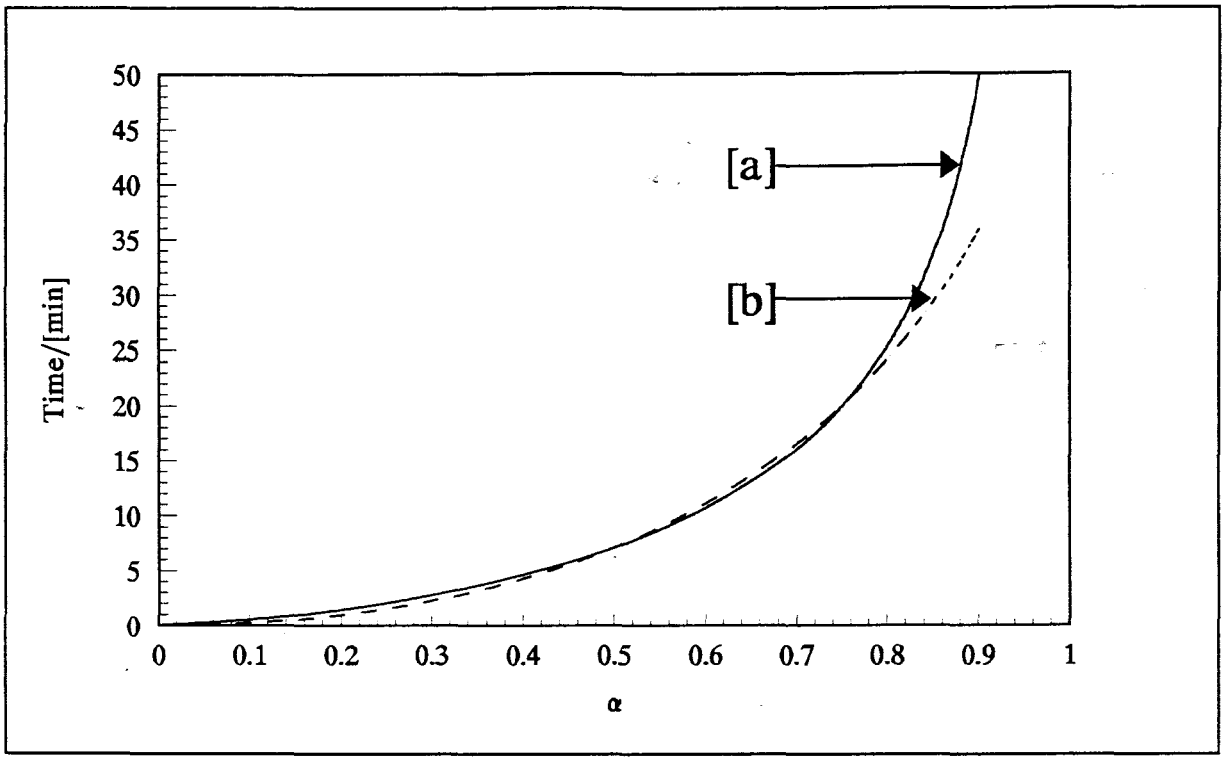

FIGURE 7.8: Correlation between the Ginstling-Brounshtein model prediction and experiment [a]: Experiment and [b]: D4 model

TABLE 7.1: Kinetics of the isothermal decomposition of BaO_2 (560-600°C):

	Kinetic model	f(α)	α Range	E_a/[kJ mol^{-1}]	A/[min^{-1}]
F1	First order (n=1)	-ln(1-α)	0.1 → 0.8	182.8±2.6	(42.3±1.1)x10^9
D4	Ginstling-Brounshtein	(1-⅔α)-(1-α)^{⅔}	0.1 → 0.8	177.9±1.6	(22.6±0.2)x10^7

The applicability of individual deceleratory models is always difficult to determine, especially when the final stages of reactions are slow and the accuracy of the values of m_f are limited. However, the values of E_a determined are not greatly altered by the choice of kinetic model. The value of E_a obtained, 180±3 kJ mol^{-1}, is close to that of 192 kJ mol^{-1} reported by Erofeev [169], but higher than some of the other values reported. The value of E_a for the initial rate process (109.4±3.8 kJ mol^{-1}) is consistent with the findings of Brunere *et al* [91] for grain growth.

Variations in kinetic parameters are to be expected on account of the reversible nature of the decomposition. The conditions used in the above experiments, namely small sample masses and rapid removal of oxygen product, by flushing with nitrogen, would tend to decrease any influence of the reverse reaction. Rate control by removal of oxygen by diffusion is consistent with the D4 model which applies over the major portion of the reaction. Deviation from this model at high values of

α could be explained in terms of some recrystallisation of product oxide at the surface slowing reaction more than predicted.

7.4.2.2 SrO_2:

The isothermal decomposition of SrO_2 (380-530°C) is qualitatively similar to that described above for BaO_2 although the multiple stages at low temperatures are not as clearly defined (Figure 7.4, curve [a]). The marked effect of temperature on the initial stages results in these stages becoming so rapid that initial mass losses at higher temperatures are approximately linear. The increase in rate of the final deceleratory stage, with consequent increase in extent of decomposition within a fixed time, is shown in Figure 7.4.

The Arrhenius plot is shown in Figure 7.5, curve (b). The activation energy for the initial stages, determined, as for BaO_2, from the initial slopes, showed a distinctive change in slope at about 440°C. The value of E_a determined for the lower temperature range was 170 ± 14 kJ mol^{-1}, and that of the higher temperature range a much lower 37.2 ± 6.2 kJ mol^{-1}. These values are both considerably smaller than the values obtained for BaO_2. The low value of E_a at high temperatures suggests diffusion control.

The kinetic models used in the analysis of the BaO_2 results were also applied to the overall α,t curves for the decomposition of SrO_2. Plots of $f(\alpha)$ against t for the F1, R2, R3 and D4 models are shown in Figures 7.9 and 7.10 for the decompositions at 380°C and 480°C, respectively. The low temperature (380°C) behaviour is best described by the D4 model (Figure 7.11), while the F1 and D4 models provided the best description of the kinetic behaviour at the higher temperatures (480°C), as was found for BaO_2. The agreement between these models (predicted values) and the experimental data at 480°C is shown in Figures 7.12 and 7.13. The Ginstling-Brounshtein model agrees well with the data at values of α up to 0.8 (Figure 7.13), as it did for the BaO_2 decomposition. The agreement between the first-order model and the experimental data is reasonable above α values of 0.5 (Figure 7.12).

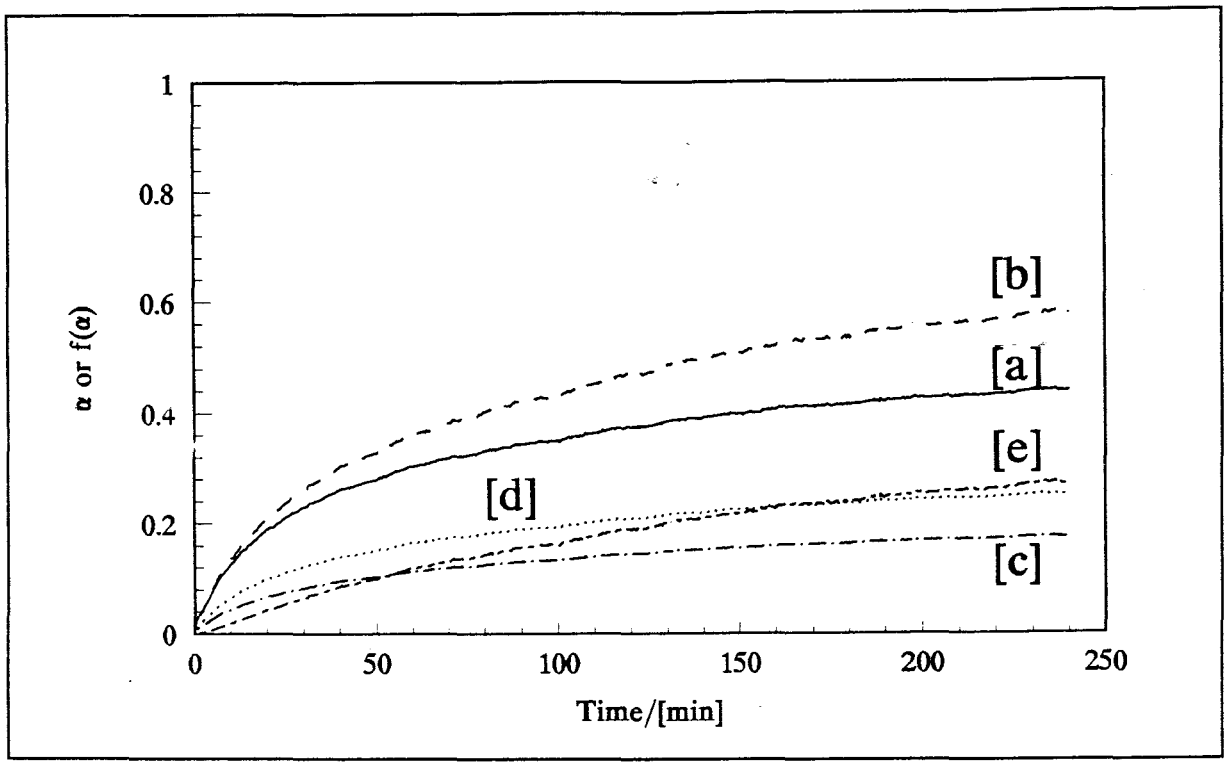

FIGURE 7.9: Application of kinetic models to the decomposition of SrO_2 at 380°C
[a]: α, [b]: (F1), [c]: (R3), [d]: (R2) and [e]: (D4) x10

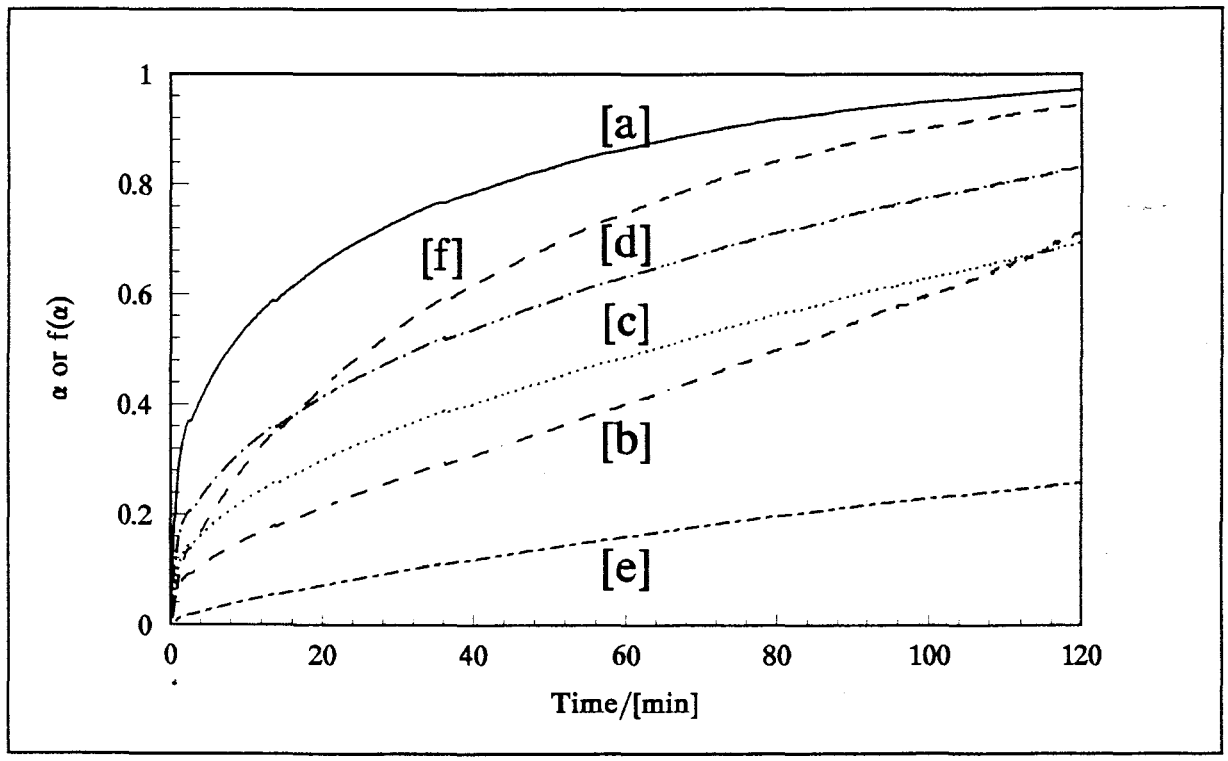

FIGURE 7.10: Application of kinetic models to the decomposition of SrO_2 at 480°C
[a]: α, [b]: (F1) x5, [c]: (R3), [d]: (R2) and [e]: (D4)

At the lower temperatures (380°C to 390°C) the overall extent of reaction is decreased to about 40% of the expected total in more than four hours. These deceleratory curves could also be fitted approximately by the D4 model (Figure 7.9) for $0.1 < \alpha < 0.4$. Comparison of experimental and predicted data is shown in Figure 7.11. The apparent activation energy for this temperature region (Table 7.2) was 250 ± 3 kJ mol^{-1} which is higher than the other values estimated. The practical consequence of a high activation energy is the sensitivity to temperature displayed. TG studies (Section 7.2) support the indications that two different mechanisms occur during decomposition of the peroxide. This would account for the fitting of different models to the initial and the later stages of the decomposition curve.

TABLE 7.2: Kinetics of the isothermal decomposition of SrO_2 (380-390°C):

	Kinetic model	α Range	E_a/[kJ mol^{-1}]	A/[min^{-1}]
D4	Ginstling-Brounshtein	$0 \rightarrow 0.4$	249.6 ± 3.0	$(68.8 \pm 0.1) \times 10^{15}$

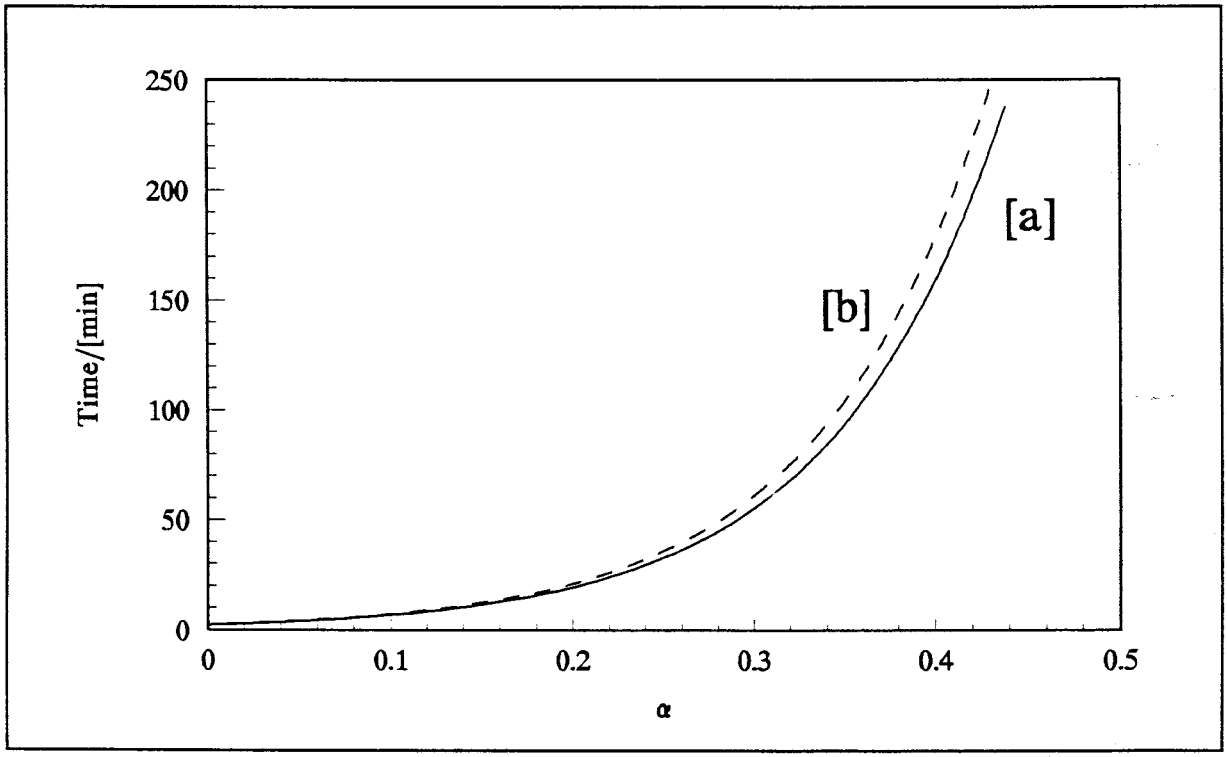

FIGURE 7.11: Correlation between predicted D4 kinetic behaviour and experimental data for the decomposition of SrO_2 at 380°C. [a]: Experiment and [b]: D4 model

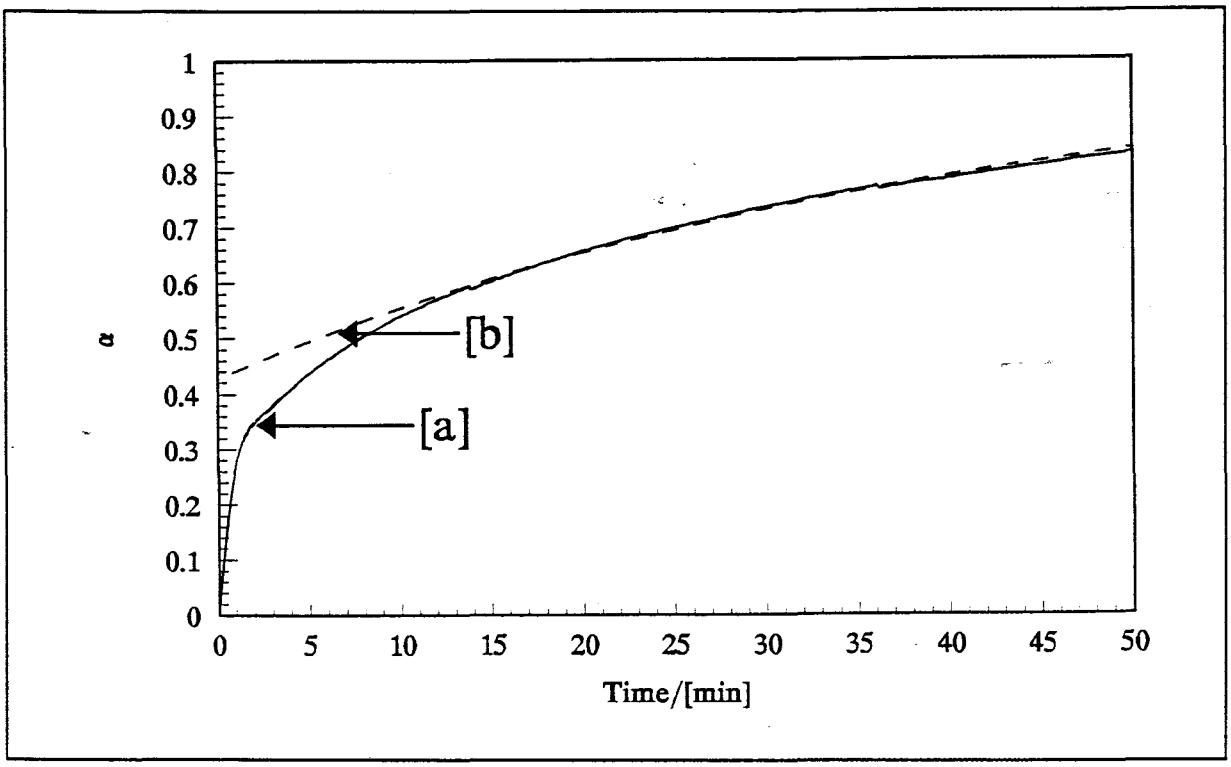

FIGURE 7.12: Correlation between predicted F1 kinetic behaviour and experimental data for the decomposition of SrO_2 at 480°C. [a]: Experimental and [b]: F1 model

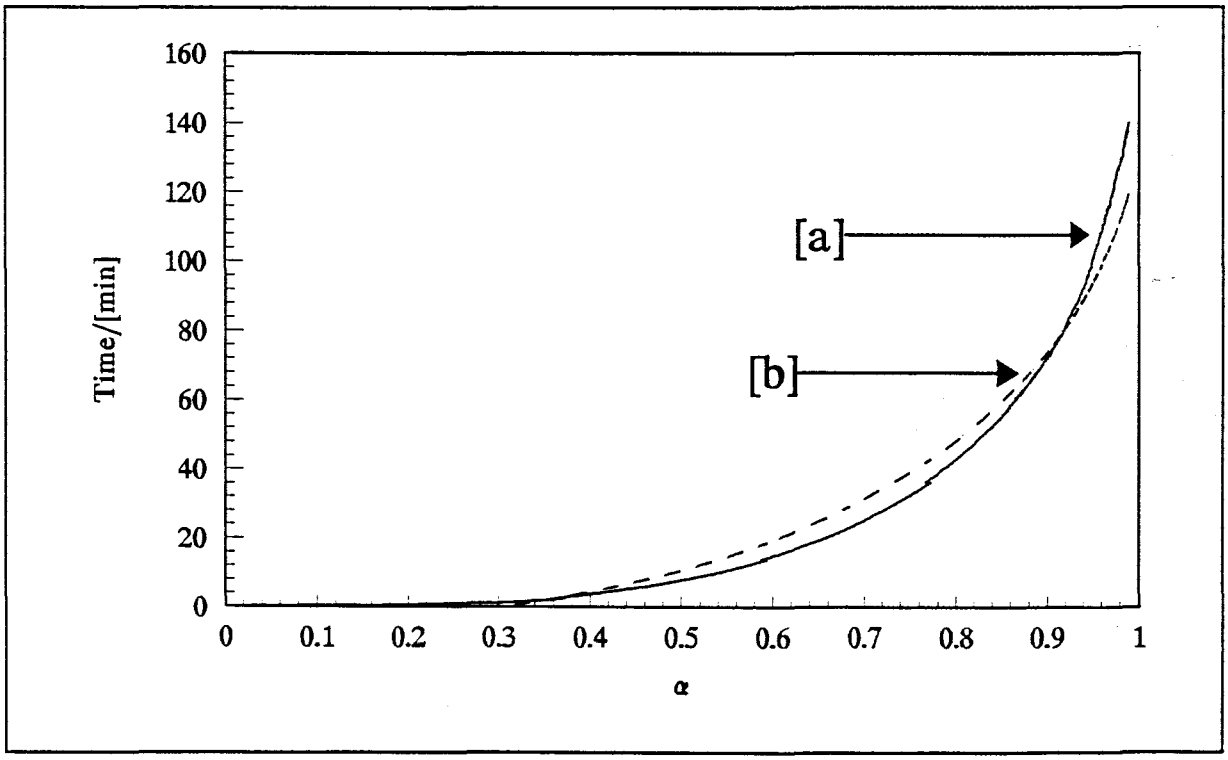

FIGURE 7.13: Correlation between predicted D4 kinetic behaviour and experimental data for the decomposition of SrO_2 at 480°C. [a]: Experiment and [b]: D4 model

TABLE 7.3: Kinetics of the isothermal decomposition of SrO_2 (440-480°C):

	Kinetic model	α Range	E_a/[kJ mol^{-1}]	A/[min^{-1}]
F1	First order (n=1)	0.1 → 0.9	119.7±0.8	(5.10±0.03)x10^6
D4	Ginstling-Brounshtein	0.1 → 0.9	119.3±0.6	(4.42±0.02)x10^5

7.4.3 Nonisothermal kinetic analysis:

The Borchardt and Daniels method [159] was used to obtain kinetic parameters from the programmed temperature thermal analysis studies described in Section 4.4.

The TG curves (in N_2 at 20 K min^{-1}) were converted to α,T curves and plots of α against 1/T and of $\ln\left(\frac{d\alpha/dt}{(1-\alpha)^n}\right)$ against 1/T for various values of n are shown in Figure 7.14 (BaO_2), and Figure 7.15 (SrO_2), respectively. The Arrhenius parameters calculated from the slopes and intercepts of the appropriate linear regions of the plots shown in Figures 7.14 and 7.15, corrected where necessary for the heating rate, for various values of the reaction order, n, are listed in Table 7.4. The apparent activation energies for the of the two peroxides are similar and not very different from the values obtained for BaO_2 from isothermal experiments. The nonisothermal value of SrO_2 lies between the isothermal values for the low and high temperature experiments. Values of E_a do not depend strongly on the value of n in the range n=0.5 to 1.0. Since the mechanism of decomposition of BaO_2 becomes relatively complex beyond $\alpha \sim 0.6$, determination of kinetic data was restricted to this range. Similarly for the SrO_2, the complex behaviour beyond $\alpha \sim 0.4$ (being a combination of the two-decomposition stages, superimposed upon one another) restricts determination of the kinetic data for the initial decomposition to the region $0 < \alpha < 0.4$.

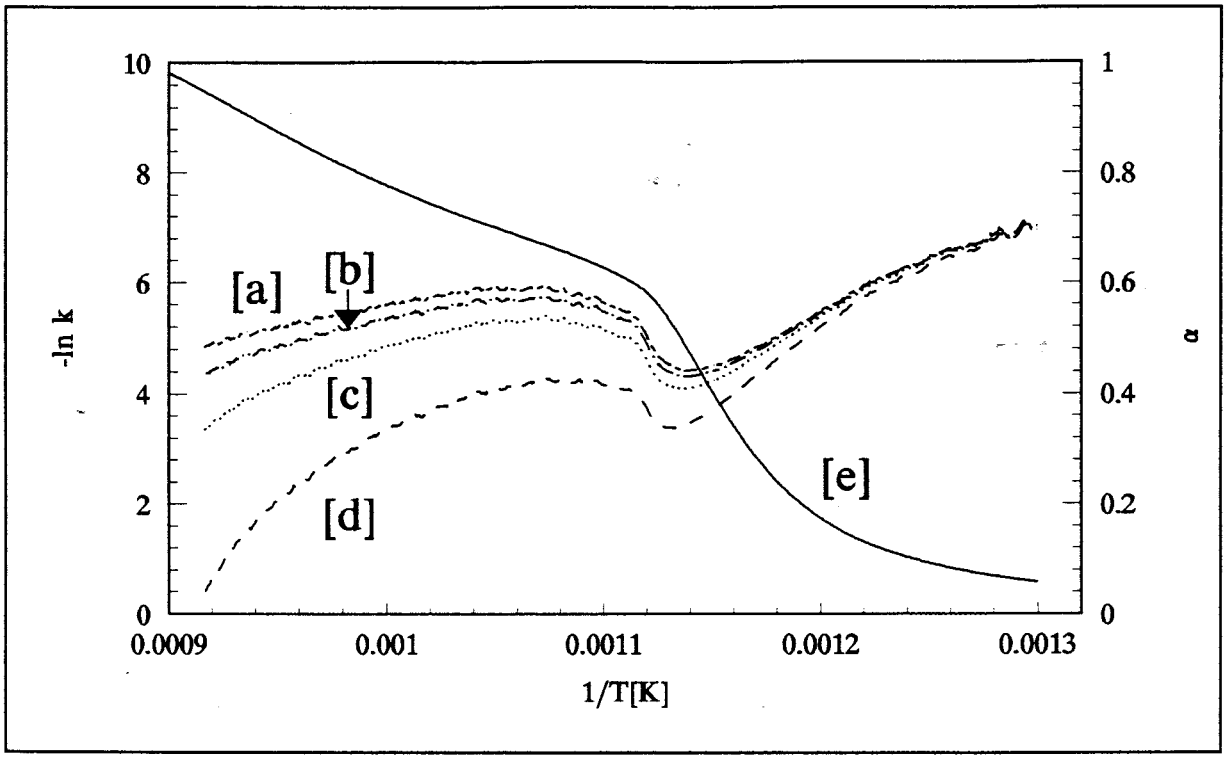

FIGURE 7.14: Borchardt and Daniels method applied to BaO_2 data for various n values [a]: n=½, [b]: n=⅔, [c]: n=1, [d]: n=2 and [e]: α

TABLE 7.4: Nonisothermal decomposition kinetics:

System	Order	E_a/[kJ mol^{-1}]	A/[s^{-1}]	r^2
BaO_2	½	160.0±1.2	(92.0±0.3)x10^7	0.99
	⅔	164.5±1.3	(18.4±0.1)x10^8	0.99
	1	173.5±1.5	(74.0±0.3)x10^8	0.99
SrO_2	½	161.8±2.2	(60.0±0.1)x10^9	0.99
	⅔	164.3±2.2	(93.5±0.1)x10^9	0.99
	1	169.4±2.1	(22.7±0.1)x10^{10}	0.99

7.4.4 Conclusions:

The isothermal decompositions of both of the peroxides, BaO_2 and SrO_2, are deceleratory overall with an initial relatively rapid process followed by the main deceleratory reaction. At temperatures where decomposition to the oxide is complete, the initial process appears as an apparently linear region ($0<\alpha<0.2$) and the temperature dependences of these linear regions give rise to apparent activation energies of ~1200 kJ mol^{-1} at low temperatures (onset of decomposition) and 109.4±3.8 kJ mol^{-1} at higher temperatures for BaO_2; and corresponding values of 169.5±13.5 kJ mol^{-1} and 37.2±6.2 SrO_2 for low and high temperature behaviour of SrO_2.

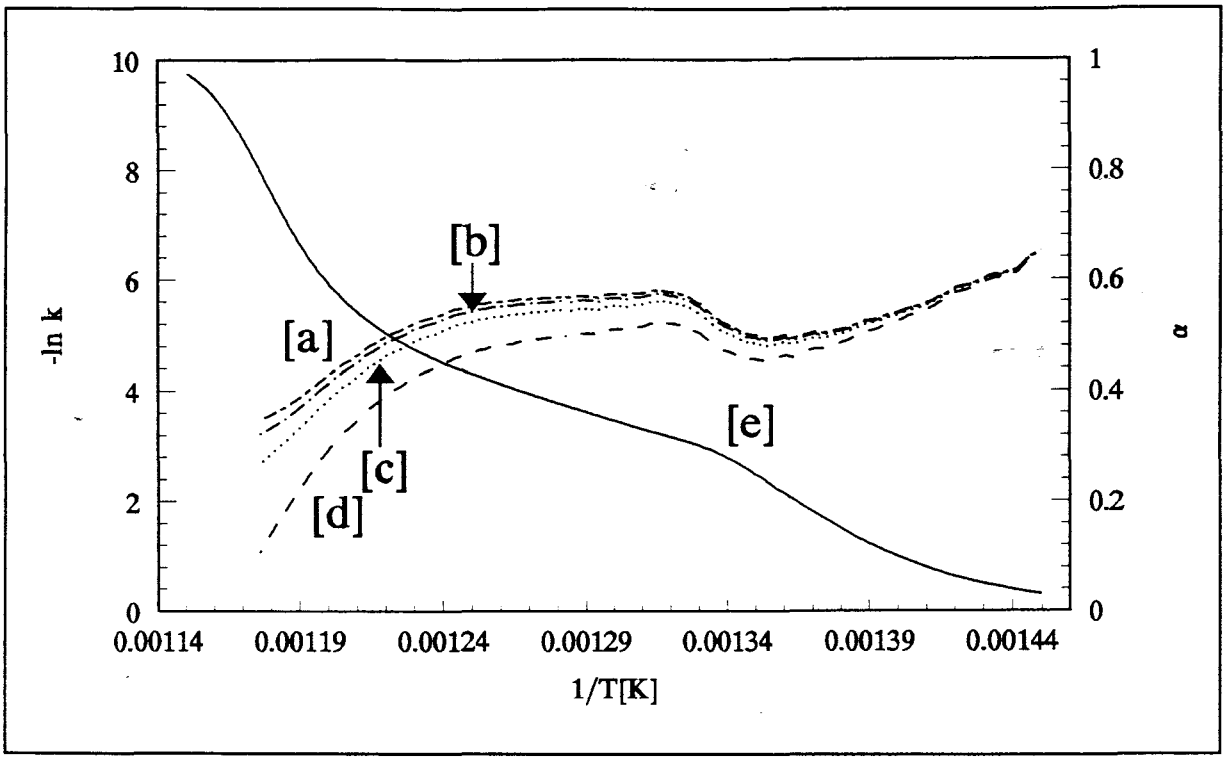

FIGURE 7.15: Borchardt and Daniels method applied to SrO_2 data for various n values [a]: n=½, [b]: n=⅔, [c]: n=1, [d]: n=2 and [e]: α

The main deceleratory process is best described by the diffusion-based Ginstling-Brounshtein model (D4). The activation energy for this stage of the decomposition of BaO_2 is 185±5 kJ mol^{-1}, which is considerably higher than the value of 119±2 kJ mol^{-1} for the deceleratory stage of the SrO_2 decomposition.

The value of 185±5 kJ mol^{-1} for the decomposition of BaO_2 is in good agreement with the value of 192 kJ mol^{-1} reported by Erofeev *et al* [169] (Section 6.3), but higher than that reported by Fahim and Ford [88] of 135 kJ mol^{-1}.

The nonisothermal kinetic analyses gave similar E_a values for the decompositions of both BaO_2 and SrO_2 of 165±5 kJ mol^{-1}. The value for BaO_2 lies between the values mentioned above (Section 7.3.1) and this may be as a result of the averaging effect of the programmed temperature measurements.

It is clear from the above studies of the two peroxides that thermal decomposition is far from the simple process represented by

$$MO_2(s) \rightarrow MO(s) + \tfrac{1}{2}O_2(g).$$

The reversibility is well established, i.e.

$$MO_2(s) \leftrightarrows MO(s) + \tfrac{1}{2}O_2(g)$$

but under the conditions applying in this study, i.e. rapid removal of product gas from small sample masses, the reverse reaction is unlikely to be very significant.

One of the ways of accounting for different decomposition mechanisms for apparently chemically uniform material over one temperature range, is to suggest different reactivities of portions of the sample, determined by differing degrees of imperfection of these portions. Many examples of such behaviour have been reported, for example $KMnO_4$, NH_4ClO_4, etc. [143], and Brunere [91] has suggested that decomposition occurs by the three-step process of nucleus formation, grain growth and oxygen diffusion, with initiation of decomposition occurring at imperfect sites.

When different mechanisms operate over different temperature ranges, either a chemical or a physical explanation may be put forward. A chemical explanation would require the occurrence of different bonding situations within the sample (e.g. dehydration of $CuSO_4.5H_2O$).

Considering the MO_2 structure (Figure 15.3) it is possible that the energy requirements for loss of oxygen via the steps

$$O_2^{2-} \rightarrow O^{2-} + O$$

and

$$2O \rightarrow O_2(g)$$

may be different for different sets of O_2^{2-} ions in the peroxide structure. This aspect is being studied theoretically [205].

The third, and perhaps most likely, explanation for changes of mechanism could be the influence of some recrystallisation of the product oxide on the course of reaction, i.e.

$$MO_2(c) \rightarrow MO(a) + \tfrac{1}{2}O_2(g)$$

and

$$MO(a) \rightarrow MO(c)$$

(where c=crystalline and a=amorphous).

Such processes have been suggested in the dehydration of hydrates and in many decompositions, especially those of alkaline-earth carbonates. The rate of removal of oxygen from the peroxide by diffusion could be drastically altered by the formation of a crystalline layer of oxide on the surface where O_2 gas is eventually to be released.

The study reported here was aimed at characterising the reactivities of the oxidants in their pyrotechnic reactions with powdered metal fuels, so further confirmation of the possible explanations of the complex behaviour discussed above was not pursued.

7.5 $Ba(OH)_2$, $BaCO_3$, BaO, $Sr(OH)_2$, $SrCO_3$ and SrO:

7.5.1 $Ba(OH)_2.xH_2O$:

The TG curve of hydrated $Ba(OH)_2$ showed a sharp mass loss terminating at 200°C (180°C in N_2), due to dehydration, whereafter the mass of the hydroxide remained relatively unchanged in O_2 until 400°C. A slow decomposition ensued (due to the loss of the remaining hydroxide), becoming rapid above 800°C (650°C in N_2). The DTA curve in O_2 showed a series of sharp endotherms below 230°C, corresponding to the loss of adsorbed water. A further endotherm was found at 400°C (380°C in N_2), which corresponded to loss of the last molecule of water [171].

The DSC curve of $Ba(OH)_2$ in N_2 corresponded well with reports [6] that three distinct endotherms exist - a dehydration up to 150°C, another peak at 265°C and a sharp endotherm at 390°C, corresponding well with the DTA trace. ΔH values, which depended upon the H_2O content of the sample, were variable. Typical values for the two higher temperature endotherms were $\Delta H = 9$ J g^{-1} (onset 245°C) for the first and $\Delta H = 56$ J g^{-1} (onset 372°C) for the second.

7.5.2 $BaCO_3$:

A gradual mass loss of 1%, which occurred rapidly at first and slowed down at higher temperatures, occurred in the TG traces in both N_2 and O_2 up to 800°C, due to loss of H_2O adsorbed on the surface of the carbonate. Two distinct, sharp endotherms were characteristic of the DTA trace in O_2 and N_2, including a large endotherm at 830°C, reportedly [172] due to the $\gamma \rightarrow \beta$ transition, and a smaller endotherm at 1000°C, due to the $\beta \rightarrow \alpha$ transition. The second of these peaks was beyond the range of the TG, and probably corresponds to decomposition of $BaCO_3$ to BaO and CO_2. $BaCO_3$ melts [172] at 1380°C, but only under high CO_2 pressures. No thermal events were observed in the range of the DSC in N_2.

7.5.3 $BaO.xH_2O$:

The TG curve of barium oxide heated in air showed a two-step dehydration (terminating at 110°C (variable %) and 170°C (variable %)), whereafter the mass remained constant to 450°C and a gradual mass loss began, which continued to the limit of the instrument. The DTA trace of BaO showed the existence of an endothermic event with onset at 400°C, in addition to the endotherms attributable to the loss of water 100°C. A high temperature exotherm (onset 1200°C, peaking above 1300°C) was also observed, and is probably due to carbonate decomposition, present as an impurity in the oxide.

7.5.4 $Sr(OH)_2.xH_2O$:

In N_2 and O_2, the TG trace showed a mass loss corresponding to dehydration up to 230°C, whereafter the mass remained relatively constant to 450°C. A further mass loss of 7.5% occurred which

terminated at 600°C, whereafter the mass was constant up to 800°C. Three endotherms were apparent in the DTA trace in O_2. The first of these corresponded to dehydration of the hydroxide and had a maximum at 190°C (170°C in N_2). The second endotherm, with onset at 450°C, was complex and appeared to be the superposition of two endotherms, with onset temperatures of 540°C and 570°C, respectively. This multiple endotherm recorded at ~540°C was resolved as a single endotherm at 500°C in N_2. A small endotherm was also observed at 820°C in O_2, but was decreased in size in N_2. Some of the endotherms observed in the DTA study were also observed in the DSC experiment. Onset temperatures were ~75°C for the dehydration, 490°C for the first (sharp) endotherm, and ~545°C for the complex (broad), second endotherm. The ΔH values for the latter two endotherms were variable, but were typically in the range 56 ± 8 J g^{-1} and 158 ± 29 J g^{-1}, respectively.

7.5.5 $SrCO_3$:

The TG trace in N_2 or O_2 showed a gradual mass loss of 2% up to 800°C. The DTA trace showed several thermal events in N_2 and O_2. An endotherm was observed in the low temperature region (up to 300°C), which corresponded to dehydration of the carbonate as evidenced by a corresponding mass loss in the TG. A further small exotherm was observed at ~450°C, probably due to reaction with an impurity. The other peaks in the trace occur above the temperature limit of the TG and hence could not be linked to mass variation. These endotherms, which corresponded to decomposition of the carbonate, had onset temperatures of 820°C (irregular), 950°C (sharp), and 1090°C (broad). Wanmaker and Radielovic [173], who performed a similar study in air, found that decomposition which commenced at 850°C was complete by 1175°C, and deduced that the rate changed from zero to first order at 950°C.

7.5.6 SrO:

The only events recorded were the loss of water around 100°C and decomposition of some $Sr(OH)_2$, present as an impurity, at 450°C.

7.6 Effect of additives:

It has been reported [79,174] that various oxides such as CuO and Fe_2O_3 may catalyse the decomposition of peroxides. The TG curve of BaO_2 + 5% Fe_2O_3 in air showed no major effect (such as onset temperature lowering) on the normal decomposition of BaO_2 (onset 600°C) when heated at 20°C min^{-1}. The reported effect on the decomposition [79] at 200°C was also not observed in TG traces of BaO_2 + 5% CuO in air.

8. THERMAL ANALYSIS OF THE BINARY PYROTECHNIC SYSTEMS

8.1 Thermal analysis of the Fe/BaO_2 system:

8.1.1 Thermal behaviour:

The Fe/BaO_2 system sustained combustion over the range 15 - 50% Fe (see Section 9.2). The stoichiometric composition, based on the reaction

$$2Fe + 3BaO_2 \rightarrow Fe_2O_3 + 3BaO$$

is 18.0% Fe. TG, TM, DTA and DSC were used to study samples of both the fuel-deficient (20% Fe/BaO_2) and fuel-rich (50% Fe/BaO_2) extremes of the combustion range. Onset of oxidation of Fe in air ($\sim$400°C) (Figure 6.1, curve [a]) coincides with the initial slow decomposition of BaO_2 in N_2 (Figure 7.1, curve [a]). The TG curve for 20% Fe/BaO_2 powder in N_2 (Figure 8.1, curve [a]) shows both these processes. Oxidation of Fe by the product and residual O_2 is complete by $\sim$650°C. The residual BaO_2 continues to decompose and at $\sim$900°C (the instrument limit) the overall mass change is approaching the expected 2.2% gain for the simultaneous complete oxidation of Fe to Fe_2O_3 (calculated +8.6%) and decomposition of 85% pure BaO_2 to BaO (calculated -6.4%). The TG curve for a 20% Fe/BaO_2 pellet in N_2 shows only small mass changes up to 800°C (Figure 8.1, curve [c]). TM shows that reaction had commenced by the Curie transition (broad) of Fe_3O_4 (Figure 8.1, curve [d]). The gradual mass gain encountered in studies in N_2 is consistent with that associated with Fe oxidation by residual oxygen in the furnace housing. The degree of conversion of Fe to Fe_3O_4 during the course of the reaction was monitored by observing the magnetic transitions of Fe_3O_4 (585°C) and Fe (780°C). The TM curve for 20% Fe/BaO_2 powder in N_2 (Figure 8.1, curve [b]) shows features similar to the oxidation of Fe in air (Figure 6.1, curve [b]) including the Curie transition of Fe_3O_4 at $\sim$580°C.

DTA studies of the 20% Fe/BaO_2 powder in N_2 (Figure 8.2, curves [c] and [d]) showed the overlap of thermal events of two concurrent processes. The exotherm attributable to the oxidation of Fe (onset 400°C, shown in Figure 8.2, curve [a]) and the endotherm due to peroxide decomposition (onset 600-800°C, dependent upon atmosphere, shown in Figure 8.2, curve [b]), were superimposed upon the reaction exotherm (onset 580°C). As mixtures aged (laboratory conditions for two weeks), a high temperature (onset 900°C), broad exotherm developed, explained [105,121] as the formation of a ferrite phase from Fe_2O_3 and BaO, formed in the reaction. A further endotherm at $\sim$830°C indicated decomposition of residual BaO_2 trapped by product formation.

DSC studies of powdered samples in N_2 showed the same, broad endotherm observed in DTA traces, indicating oxidation of Fe powder. A small dual-peak reaction exotherm (onset 600°C), of variable magnitude, was found superimposed on the Fe oxidation exotherm (Figure 8.3), corresponding closely

to the onset of decomposition of the BaO_2. Pelleted samples were studied in Al pans to a maximum temperature of 575°C (to avoid instrument damage from accidental ignition), and showed no apparent reaction. The absence of exotherms below 575°C was consistent with DTA observations of reaction commencing above 580°C (the temperature of the $\gamma \rightarrow \alpha$-$Fe_2O_3$ transition).

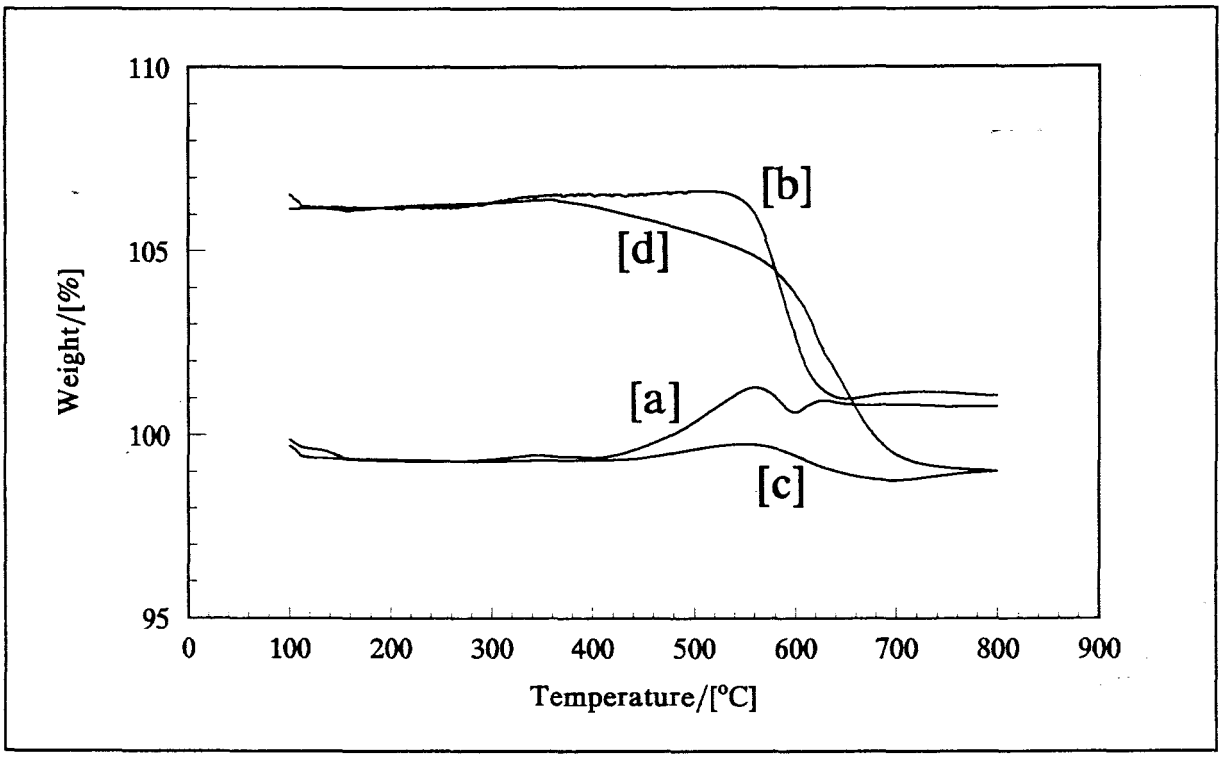

FIGURE 8.1: TG and TM of the 20% Fe/BaO_2 system in N_2
[a]: TG powder, [b]: TM powder, [c]: TG pellet and [d]: TM pellet

The fuel-rich (50% Fe/BaO_2) powdered samples show similar behaviour to the 20% Fe/BaO_2 samples in O_2 and air, with Fe oxidation dominating features of the peroxide decomposition. The TG curve of the fuel-rich composition in O_2 is shown in Figure 8.4, curve [a]. The maximum mass gain of 21% for the trace in O_2 occurs at 700°C, agreeing well with the expected 21.5% for complete oxidation of Fe to Fe_2O_3 with no accompanying peroxide decomposition. At the instrument limit, the overall mass gain was decreased to 18%, agreeing well with the expected 17.5% for simultaneous oxidation of Fe and decomposition of BaO_2. Pelleted samples of the fuel-rich composition showed little reaction in N_2 (as followed by TG), while the oxidation rate of the Fe in the sample increased rapidly in O_2 until the powder became pyrophoric (~600°C), reaching a final mass gain of 15.8%, which remained constant to the instrument limit (Figure 8.4, curve [b]). This gain was intermediate between that expected for FeO (calculated 14.3%) or Fe_3O_4 formation (19.1%), assuming that no decomposition of the BaO_2 occurs. A study performed on another sample of the same material using TM showed that the products are probably mixed oxides, and not unreacted Fe mixed with Fe in

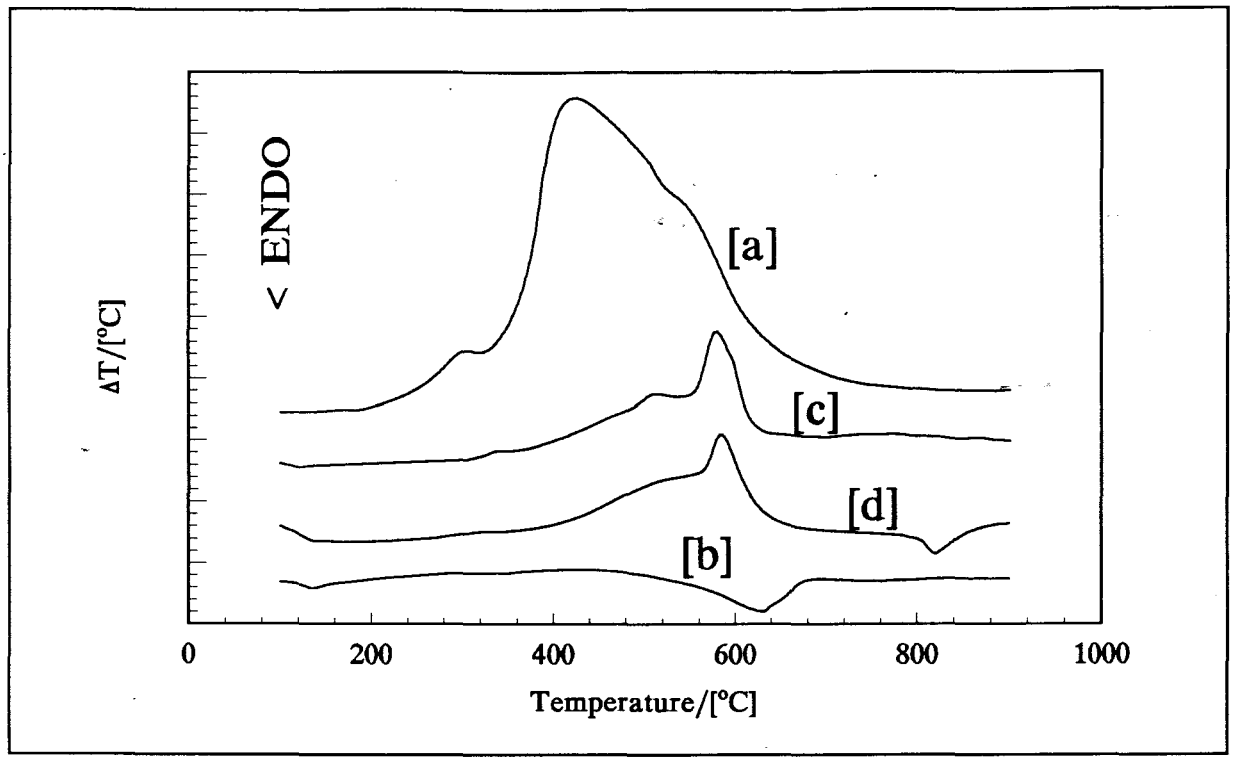

FIGURE 8.2: DTA of the 20% Fe/BaO_2 system
[a]: Fe in air, [b]: BaO_2 in N_2, [c]: powder in N_2 and [d]: powder in O_2

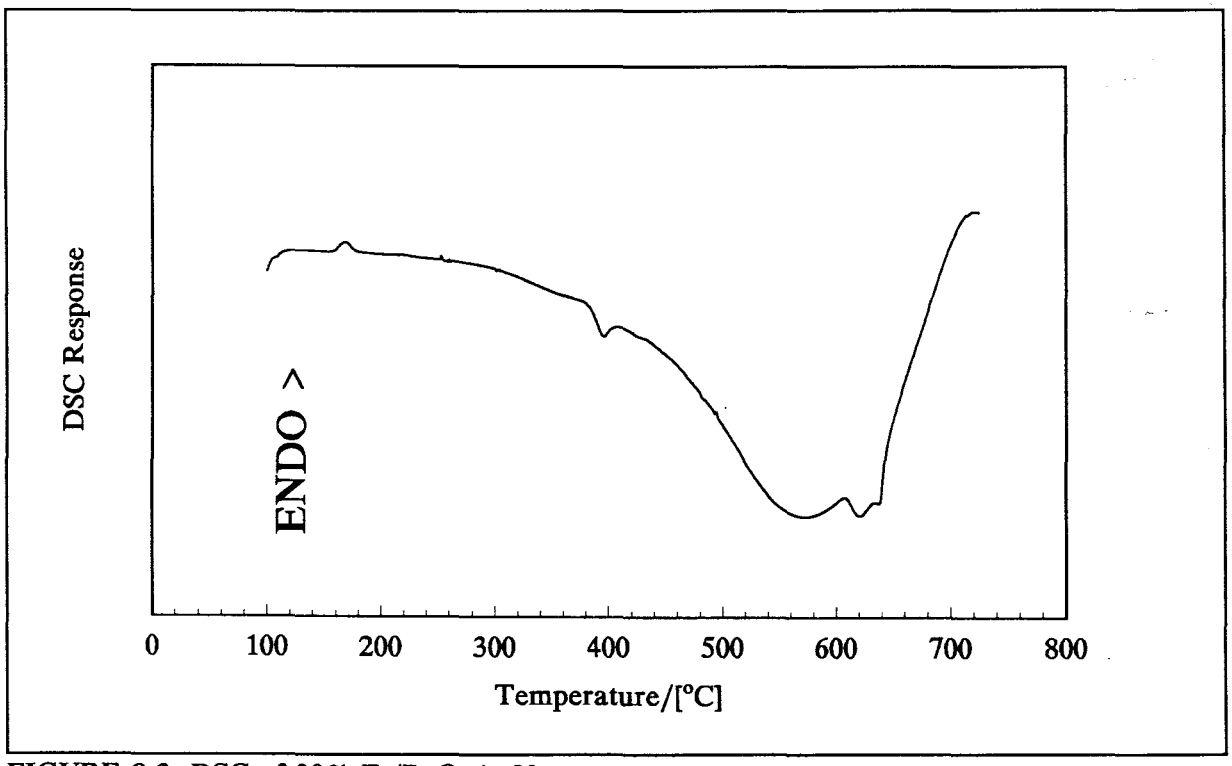

FIGURE 8.3: DSC of 20% Fe/BaO_2 in N_2

various oxidation states, as no Curie transition of Fe occurred at 780°C. The weight gain of pelleted samples reached a maximum at 550°C in O_2, whereafter one of two different reaction routes followed: The magnetic transition at 580°C was usually smooth, as for Fe powder in air (Figure 6.1, curve [a]), with characteristic Fe oxidation and BaO_2 decomposition. If the sample mass exceeded a threshold value (about 32 mg), however, the weight loss associated with the magnetic transition at 580°C was followed directly by a sharp, reproducible weight loss (Figure 8.4, curve [c]) (accompanied by a combustion stage). The product formed in this combustion showed no change in weight at temperatures up to the instrument limit. Reaction by both routes was complete by 730°C, with weight being lost in the Curie transition of Fe at 780°C in the uncombusted sample. DTA of 50% Fe/BaO_2 powders showed the same features as 20% Fe/BaO_2 powders.

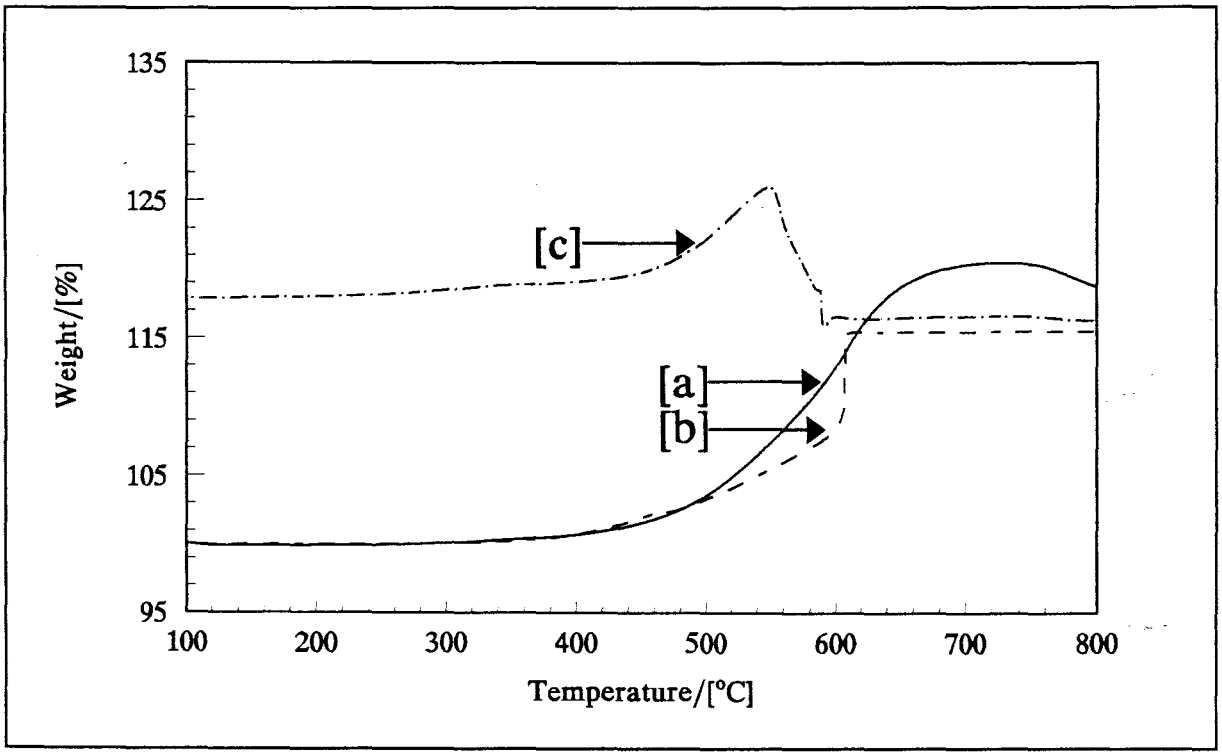

FIGURE 8.4: TG and TM of the 50% Fe/BaO_2 system in O_2
[a]: TG powder, [b]: TG pellet and [c]: TM pellet

8.1.2 Nonisothermal kinetics:

A Borchardt and Daniels analysis (for details see Appendix 5) on the DTA curve for the 20% Fe/BaO_2 composition in N_2 (Figure 8.2, curve [c]) yielded the kinetic information shown in Table 8.1. The DTA curve is complex, which poses problems of interpretation of the kinetic data. In the analysis, the entire reaction exotherm has been used for the calculation of α, as this approach has previously provided data within reasonable limits [55]. The analysis has been performed for comparison on the initial rise region of the endotherm, the rise region of the sharp superimposed

exotherm, and the entire exotherm.

The Borchardt and Daniels plot is shown in Figure 8.5 for various values of apparent order of reaction, n. Also shown is the total extent of reaction α (curve [e]) plotted on the reciprocal temperature scale.

TABLE 8.1: Kinetic parameters obtained by analysis of the DTA curve for Fe/BaO_2 in N_2

Composition	Temperature Range	Order (n)	E_a/[kJ mol^{-1}]	A/[s^{-1}]	r^2
20% Fe/BaO_2	405-750	½	56.0±2.7	(18.8±2.2)x10^1	0.61
	Overall	⅔	74.3±2.0	(34.2±3.7)x10^2	0.83
		1	110.8±1.4	(11.1±0.4)x10^5	0.96
		2	220.3±5.2	(39.0±2.0)x10^{12}	0.86
20% Fe/BaO_2	405-560	½	126.3±4.3	(13.5±0.4)x10^6	0.89
	Initial region	⅔	128.3±4.2	(18.9±0.6)x10^6	0.89
		1	132.4±4.1	(37.3±1.1)x10^6	0.90
		2	144.5±3.7	(29.3±0.7)x10^7	0.93
20% Fe/BaO_2	565-655	½	60.5±8.3	(65.6±5.2)x10^1	0.42
	Sharp exotherm	⅔	84.4±7.8	(20.9±0.8)x10^3	0.61
		1	132.2±6.8	(10.4±0.2)x10^5	0.84
		2	275.7±4.5	(20.4±0.1)x10^{15}	0.98

For the initial region of the DTA peak, which is the least complex and hence should provide the most reliable kinetic parameters, the apparent E_a was not very dependent upon the value of n chosen. The value of E_a of about 130 kJ mol^{-1} (n=1) lies between the value of ~50 kJ mol^{-1} for the oxidation of Fe in air and ~180 kJ mol^{-1} for the decomposition of BaO_2 in N_2.

Over the other temperature intervals, there was a considerable variation of apparent E_a with the value of n chosen, although for a fixed value of n=1, similar E_a values were obtained.

These Arrhenius parameters, estimated from thermal analysis experiments, are compared with those obtained under combustion conditions, in the general discussion in Section 15.5.

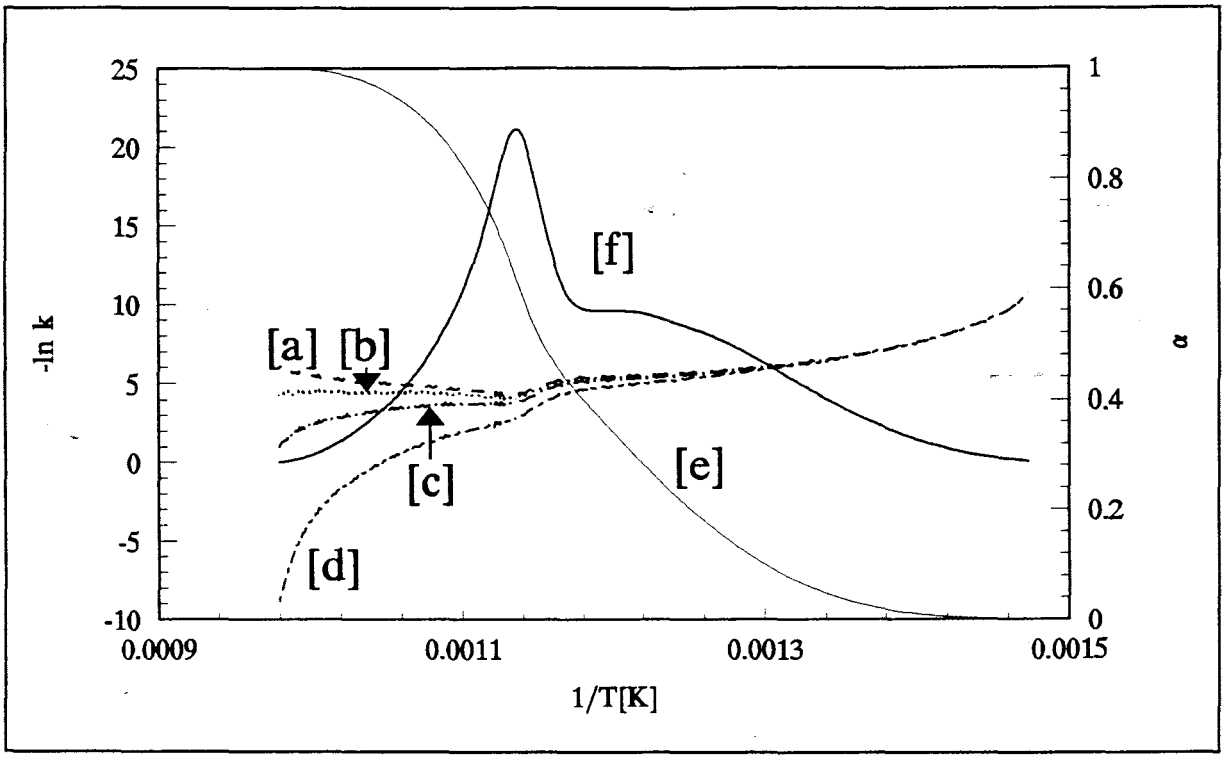

FIGURE 8.5: Borchardt and Daniels kinetic analysis of 20% Fe/BaO_2 DTA for various n values [a]: ½, [b]: ⅔, [c]: 1, [d]: 2, [e]: α and [f]: Rescaled DTA

8.2 Thermal analysis of layered pellets of Fe+BaO_2:

A TG run on a layered pellet in N_2 showed small losses due to a two-stage decomposition (Figure 8.6), with onsets at 490°C (~0.2%) and at 600°C (~0.3%). A TM run in N_2 showed that the weight of the sample increased relatively smoothly (as found for the oxidation of Fe in air or oxygen), with a discontinuity at 320°C and a major weight loss at 575°C (the Curie point of Fe_3O_4). Thereafter the weight remained relatively constant until the Curie point of iron at 780°C. A second TM run on the product of the first run showed no weight change up to the Curie point of Fe_3O_4. Thereafter the TM curve was similar to that of the initial experiment. A DSC trace up to 575°C showed a series of broad thermal events related to the oxidation of Fe and the first stage of decomposition of the barium peroxide. An electron-probe micro-analysis across the boundary between the two reagents is described in Section 14.3.

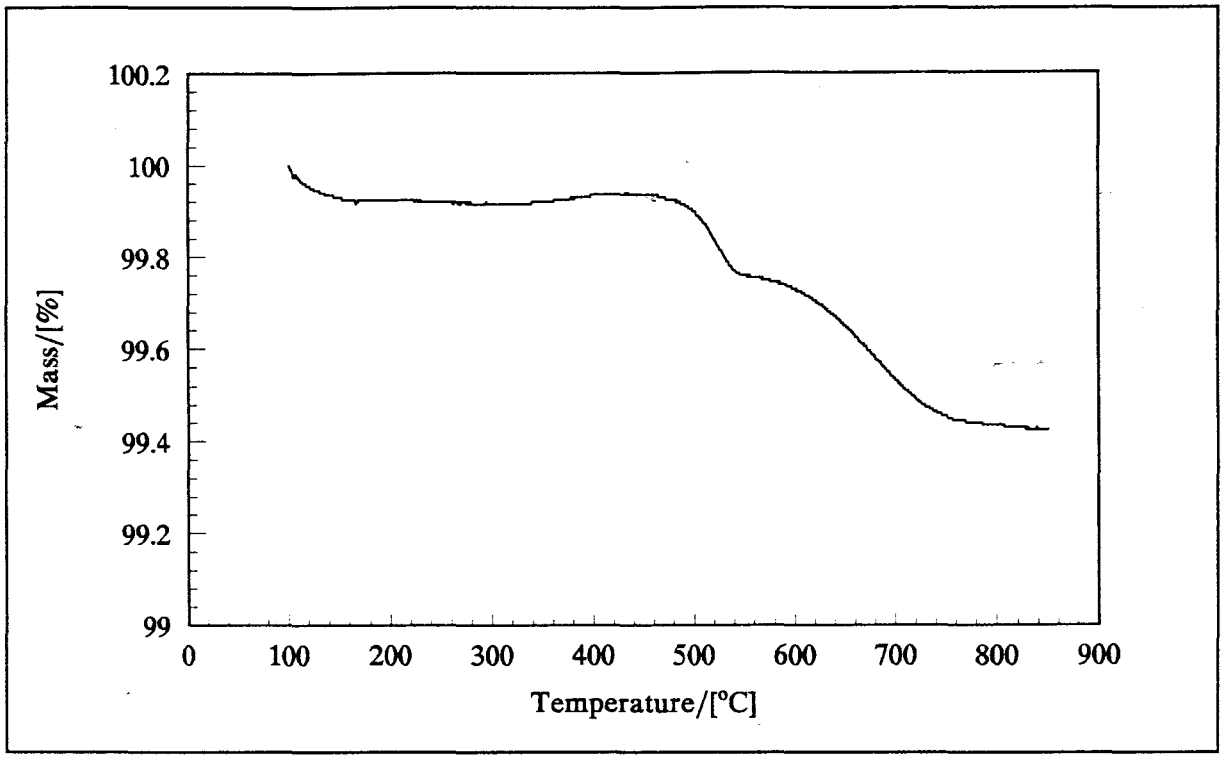

FIGURE 8.6: TG study of Fe+BaO_2 layered pellet in N_2

8.3 Thermal analysis of the Fe/BaO_2 + Zn system:

Work on the zinc/peroxide systems (Sections 11 and 12) suggested a study of the effects of the addition of Zn to the Fe/BaO_2 system. Powdered and pelleted samples of a mixture of 20% Fe/BaO_2 + 5% Zn (by mass) mixture were studied using TG, TM and DSC. The TG and TM responses showed no effects of the zinc in the composition, in either pellet or powdered samples, but DSC showed that, although the fusion endotherm of the zinc in the powdered system was complete (5.4 J g^{-1}, onset 419°C), the endotherm was interrupted by a reaction exotherm in the pellet sample, with onset 422°C, due to the reaction of zinc with BaO_2 (ΔH=-6.25 J g^{-1}).

8.4 Thermal analysis of the Fe/SrO_2 system:

8.4.1 Thermal behaviour

The Fe/SrO_2 system sustained combustion over the range 20-55% Fe (Section 10.2). The stoichiometric composition, based on the reaction

$$2Fe + 3\ SrO_2 \rightarrow Fe_2O_3 + 3SrO$$

is 23.7% Fe. TG results for Fe/SrO_2 powder differ from those of Fe/BaO_2 in that the decomposition of SrO_2 (Figure 7.1, curve [b]) begins at a lower temperature than for BaO_2 (Figure 7.1, curve [a]) and thus precedes the onset of oxidation of Fe (Figure 6.1, curve [a]). The TG curve for 20% Fe/SrO_2 powder in N_2 (Figure 8.7, curve [a]) shows a two-stage mass loss beginning at ~380°C which completely overshadows any concurrent oxidation of Fe. The slope of the curve is similar to

that for the decomposition of SrO_2 alone in N_2. The oxidation of Fe becomes detectable through the slowing of the mass loss at about 480°C, well into the second stage of the decomposition of SrO_2, and by ~580°C a mass gain is observed with the overall mass change approaching a small mass loss (including the initial water present) of 2% (calculated +8.6% for oxidation of the Fe to Fe_2O_3, and -9.1% for decomposition of the 85% pure SrO_2 to SrO). The TM curve for 20% Fe/SrO_2 powder in N_2 (Figure 8.7, curve [b]) shows a weight increase beginning at ~380°C, indicating formation of Fe_3O_4, followed shortly by the mass loss owing to decomposition of SrO_2. At ~580°C the magnetic transition of Fe_3O_4 leads to a rapid apparent loss of weight. The DTA curve of 20% Fe/SrO_2 powder in N_2 (Figure 8.8, curve [c]) shows an initial fairly strong endotherm, onset ~400°C, rapidly overlapped by a series of exotherms with two sharp maxima (~520°C and ~650°C). These strong, sharp exotherms are typical of ignition processes and are superimposed upon the broad exotherm characteristic of Fe oxidation. The fuel-rich composition study (Figure 7.5, curve [d]) demonstrated that surface oxidation occurs, by the development of a small exotherm in N_2 (390°C). Extensive variation in the intensity of the reaction exotherms at both extremes of the composition range studied, due to ageing of the samples (under laboratory conditions for two weeks) was found. The development of a broad exotherm at 750°C with time, is attributed to the formation of a mixed oxide [105,121] from products generated while the composition aged, as was observed in the Fe/BaO_2 system.

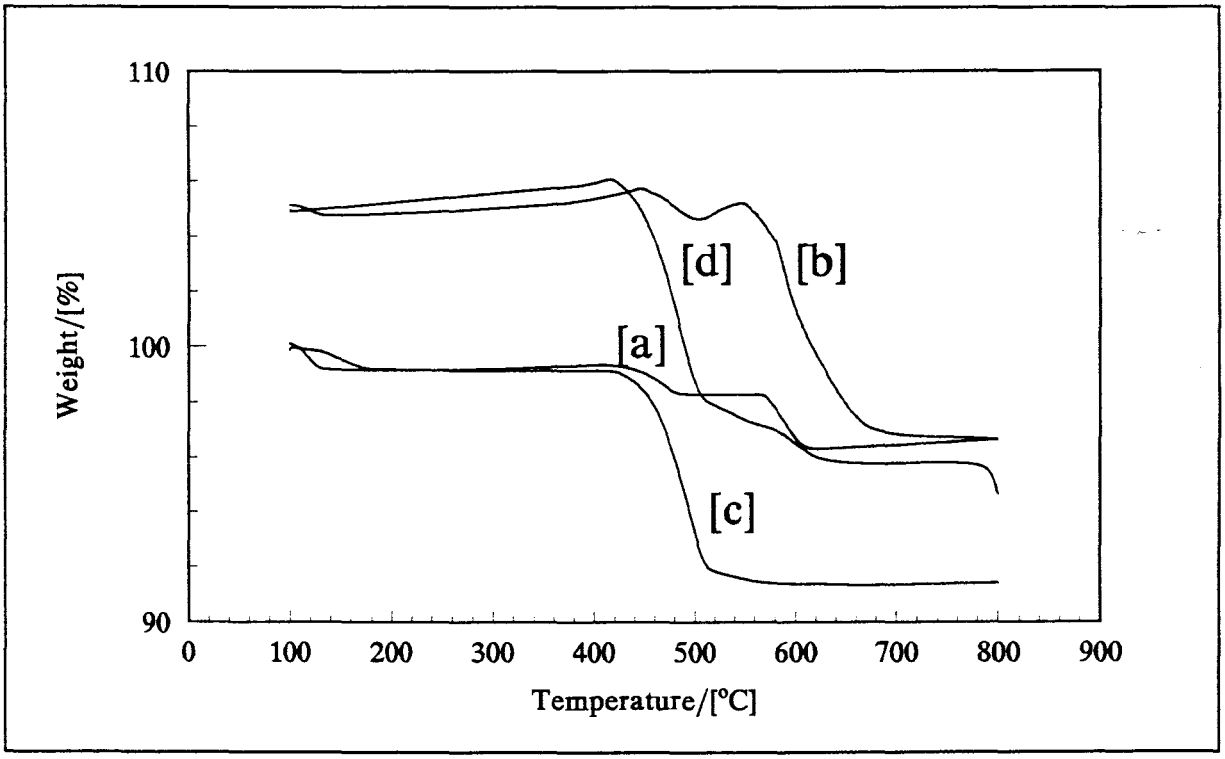

FIGURE 8.7: TG and TM of 20% Fe/SrO_2 in N_2
[a]: TG powder, [b]: TM powder, [c]: TG pellet and [d]: TM pellet

The DSC study of the powder samples exhibited similar behaviour to the DTA study in N_2, in that decomposition of the peroxide (onset 420°C, $\Delta H = 30.4 \pm 1.4$ J g^{-1}) preceded the overlapping reaction exotherm (onset 486±5°C). This first decomposition endotherm is followed by a second endotherm, with onset at 580°C. This second endotherm is extremely variable in intensity, and is related to the degree of reaction of the powdered sample. The trace for a pellet showed a larger, sharper reaction exotherm. The first decomposition stage of the peroxide (onset 424°C) preceded a small endotherm (onset 520°C) indicating further decomposition (the second stage) of unreacted SrO_2. Overlapping thermal peaks and variable degree of reaction, made estimation of the area of the reaction exotherm difficult, however, typical values of ~200 J g^{-1} were obtained for the composition. The TG curve of a 20% Fe/SrO_2 pellet (Figure 8.7, curve [c]) showed only a single-stage mass loss with an onset temperature corresponding to the first-stage of decomposition of SrO_2. Little Fe oxidation was apparent and the mass loss which occurred was that expected for the decomposition of SrO_2 alone. TM (Figure 8.7, curve [d]) showed similar behaviour and a strong magnetic transition of unreacted Fe at 780°C.

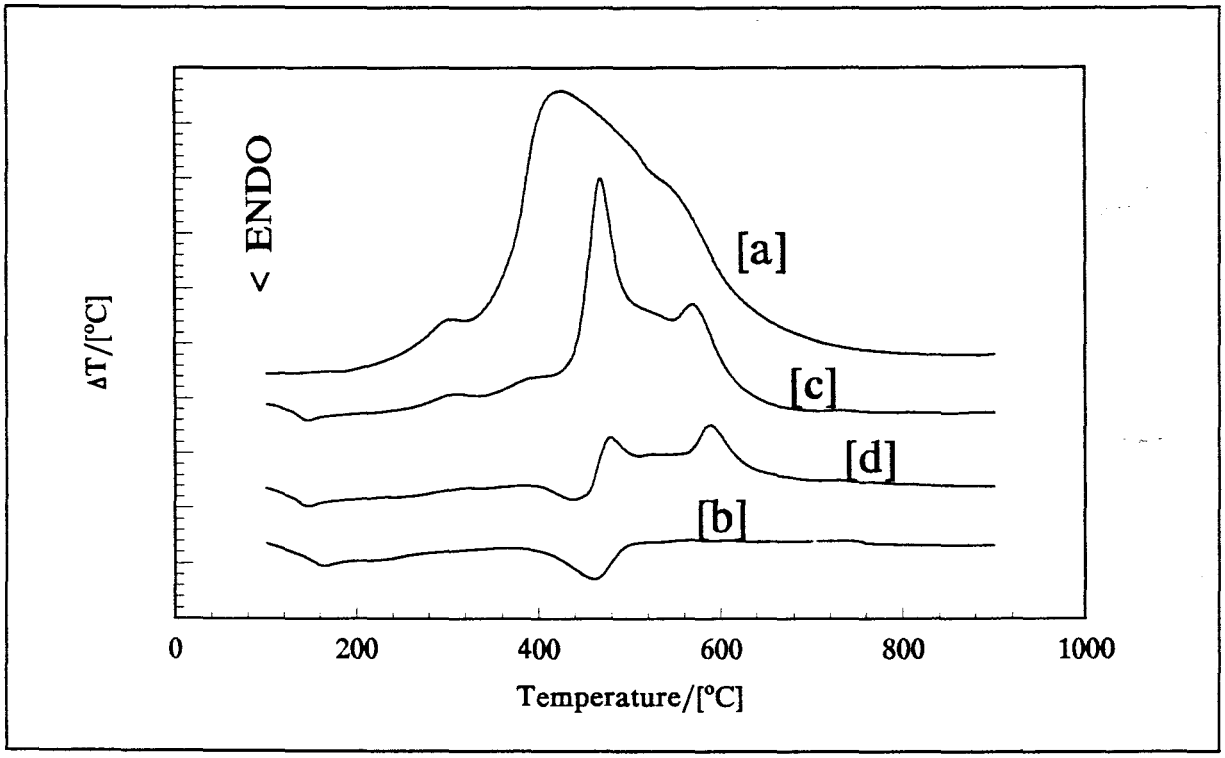

FIGURE 8.8: DTA of Fe/SrO_2 in N_2
[a]: Fe in air, [b]: SrO_2 in N_2, [c]: 20% Fe/SrO_2 and [d]: 55% Fe/SrO_2

In O_2, the mass loss occurring in pellet samples of both fuel-deficient (20% Fe/SrO_2) and fuel-rich (50% Fe/SrO_2) compositions, is followed by a period of acceleratory mass gain, due to the rapid oxidation of Fe in a combustive step. TM showed that in powdered samples of the fuel-rich system which exceed a threshold weight, the thermal events of SrO_2 decomposition (420°C) and the magnetic

transition (580°C) are directly followed by a sudden loss of magnetism as the sample temperature is raised in a combustion reaction.

8.4.2 Nonisothermal kinetics:

A Borchardt and Daniels [159] determination of kinetic parameters of the Fe/SrO_2 system was undertaken using the DTA curve of a 20% Fe/SrO_2 sample in N_2 (Figure 8.8, curve [c]) and yielded the data presented in Table 8.2. A difficulty similar to that encountered for the Fe/BaO_2 system arose, in that the reaction exotherm was not a simple peak, but rather a complex superposition of exothermic events, arising from the overlap of the exothermic reaction with the endothermic first and second stages of decomposition. The entire peak was again used for the calculation of α, and the entire peak, and the individual peak rise regions analyzed for kinetic data.

TABLE 8.2: Kinetic parameters obtained from DTA experiments performed in N_2:

System	Temperature Range	Order (n)	E_a/[kJ mol^{-1}]	A/[s^{-1}]	r^2
20% Fe/SrO_2	495-680	½	36.5±2.1	(26.6±2.1)x10^0	0.60
	Overall	⅔	53.0±1.9	(31.9±2.7)x10^1	0.80
		1	85.9±1.92	(45.0±1.4)x10^3	0.91
		2	184.8±4.2	(12.8±0.3)x10^{10}	0.91
20% Fe/SrO_2	479-508	½	786±28	(60.7±0.1)x10^{50}	0.97
	Initial region	⅔	787±28	(67.8±0.2)x10^{50}	0.97
		1	788±27	(83.9±0.2)x10^{50}	0.97
		2	792±27	(15.9±0.1)x10^{51}	0.97
20% Fe/SrO_2	596-620	½	165±13	(12.5±0.1)x10^8	0.89
	Final exotherm	⅔	180±13	(11.1±0.1)x10^9	0.90
		1	210±13	(88.3±0.3)x10^{10}	0.92
		2	300±14	(44.4±0.1)x10^{16}	0.95

As for the kinetic analysis of the Fe/BaO_2 system, the value of E_a is strongly dependent upon the apparent order of reaction, except over the lowest temperature range, and is here also dependent upon the temperature range under consideration. Again, comparing E_a values for a common value n=1, the value for Fe/SrO_2 (86±2 kJ mol^{-1}) is considerably lower than that for Fe/BaO_2 (111±2 kJ mol^{-1}). The value of E_a determined (Section 7.4) for the decomposition of SrO_2 is ~182 kJ mol^{-1} (for a value of n=1). The unusually high values of E_a recorded over the lowest temperature range may be characteristic of ignition processes (or pre-ignition reactions).

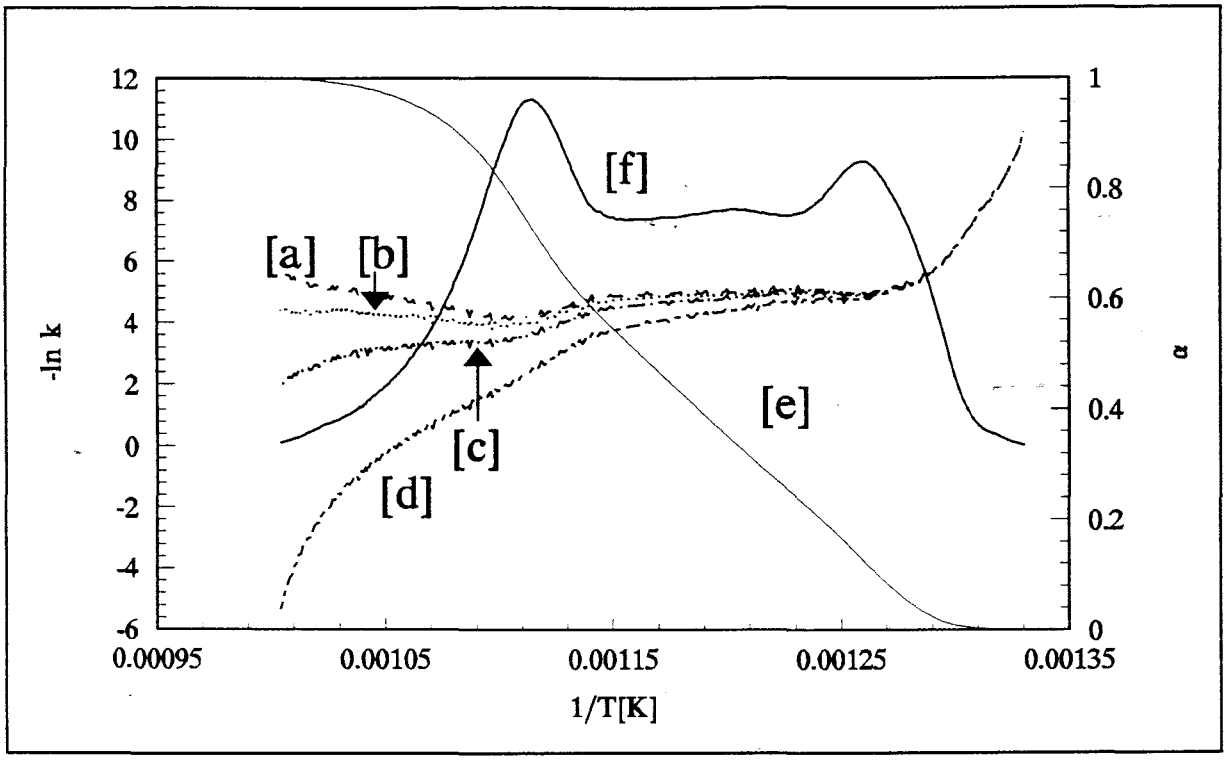

FIGURE 8.9: Borchardt and Daniels kinetic analysis of 20% Fe/SrO_2 for selected values of n [a]: n=½, [b]: n=⅔, [c]: n=1, [d]: n=2, [e]: α and [f]: Rescaled DTA

8.5 Thermal analysis of layered pellets of Fe+SrO_2:

A TG trace of a layered pellet of Fe + SrO_2 in N_2 showed the usual two-step mass loss characteristic of strontium peroxide, with no apparent oxidation of the Fe. The onset temperatures of mass loss were ~375°C and ~520°C, with little overall change in mass. The TM curve in N_2 differed from the TG curve, as was found for the Fe+BaO_2 pellet. The overall behaviour up to 575°C was dominated by the oxidation of Fe, other features being the Curie points of Fe_3O_4 (575°C) and Fe (780°C). The pellet was cooled and a second TM run was done on this product in N_2. No weight variations, other than those due to magnetic transitions were observed. The DSC trace in N_2 showed a broad exotherm, due to the oxidation of Fe (onset 320°C), which overlapped the decomposition endotherm of SrO_2 (onset 420°C), which was incomplete at the instrument limit. In addition, a small reaction exotherm (onset ~480°C) of variable intensity, was observed. An electron microprobe analysis across the boundary between the two reagents in the pellet was performed and is detailed in Section 14.4.

8.6 Thermal analysis of the Fe/SrO_2 + Zn system:

By analogy with the Fe/BaO_2 system, the Fe/SrO_2 + Zn combustion study (Section 10) was complemented by thermal analysis of 20% Fe/SrO_2 + 5% Zn samples in both pellet and powder form. TM and TG curves did not show any unexpected thermal events, whilst the DSC showed the

fusion endotherm of Zn in the powdered sample (onset 419°C), and a reproducible reaction exotherm (onset 475°C, $\Delta H = 95.5 \pm 1.0$ J g^{-1}). This exotherm, which had appeared smaller in pure Fe/SrO_2 experiments (detailed above), extended almost to the instrument limit. The SrO_2 decomposition endotherm (onset 420°C, $\Delta H = 298$ J g^{-1}) was also present.

8.7 Thermal analysis of the Zn/BaO_2 system:

8.7.1 Thermal behaviour

The Zn/BaO_2 system sustained combustion over the range 30 - 50% Zn (see section 11.). The stoichiometric composition, based on the reaction

$$Zn + BaO_2 \rightarrow ZnO + BaO$$

is 27.9% Zn (100% pure) or 29.7% Zn (94% pure). The DTA curves for powdered samples of 30% (Figure 8.10, curve [c]) and 50% Zn/BaO_2, heated at 20°C min^{-1} in N_2, showed the melting of zinc at 418°C, followed immediately by a complex exotherm with a maximum at ~495°C, and a further sharp exotherm (onset 560°C) in the curve for the 50% mixture. In air (Figure 8.10, curve [d]), the complex exotherm was partially resolved into three main peaks with onset temperatures at ~420°C, ~510°C and ~560°C for the 30% mixture, whilst for the 50% mixture only a broad exotherm was obtained. The absence of a high temperature endotherm (onset 700°C) implies that the BaO_2 must have reacted to completion. In nitrogen, the reaction exotherm is less pronounced with a slightly higher onset (425°C), although still directly related to the fusion of zinc. The behaviour of the 30% mixture is very different to the reaction of molten Zn in air and O_2. The DTA curves for Zn in air (curve [a]) and BaO_2 in N_2 (curve [b]) are shown in the same Figure for comparison. The pellet sample of 30% Zn/BaO_2 heated in N_2, showed similar behaviour to that of the powder, displaying the melting endotherm of zinc prior to two reaction exotherms.

In the DSC study in N_2, the powdered sample gave a small endotherm due to the melting of zinc (onset 418°C, $\Delta H = 29.4 \pm 1.0$ J g^{-1}), followed immediately by a broad reaction exotherm (onset 420°C, $\Delta H = 1206.5 \pm 55.7$ J g^{-1}) terminating at ~450°C. Occasionally a further exotherm was found at higher temperatures (onset 540°C, $\Delta H \approx 38$ J g^{-1}). For the pellet however, reaction ensued immediately on the melting of the zinc in a sharp exotherm of variable intensity (onset 419°C, $\Delta H = 58 \pm 12$ J g^{-1}). This result is in contrast to the DTA trace for the pellet in N_2 which shows an endotherm due to the melting of zinc (onset ~420°C), followed by two exotherms, with onsets at 460 and 510°C. These endotherms are decreased in the DSC trace. This contrast in behaviour is probably due to the greater containment of volatile reagents in the DSC run (performed in Al containers with crimped lids), compared to the continuous flushing of the sample in the open crucibles of the DTA.

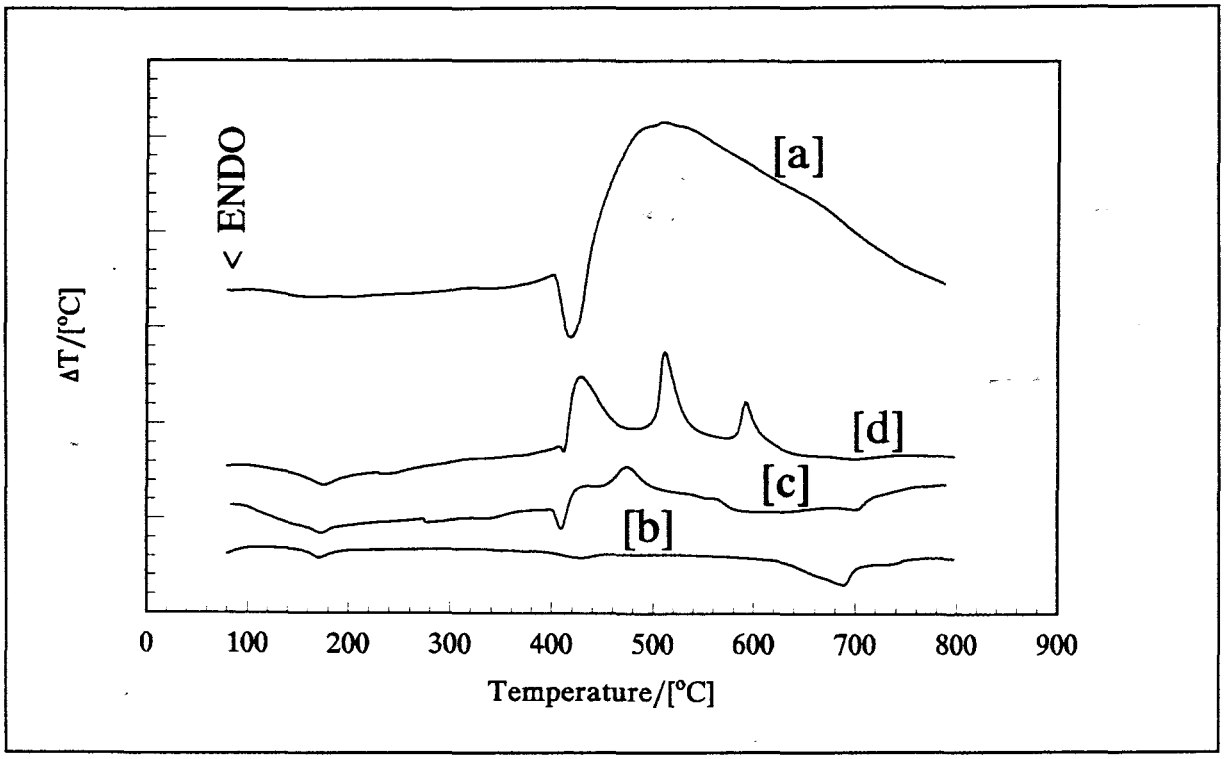

FIGURE 8.10: DTA of Zn/BaO_2
[a]: Zn in air, [b]: BaO_2 in N_2, [c]: 30% Zn/BaO_2 in N_2 and [d]: in air

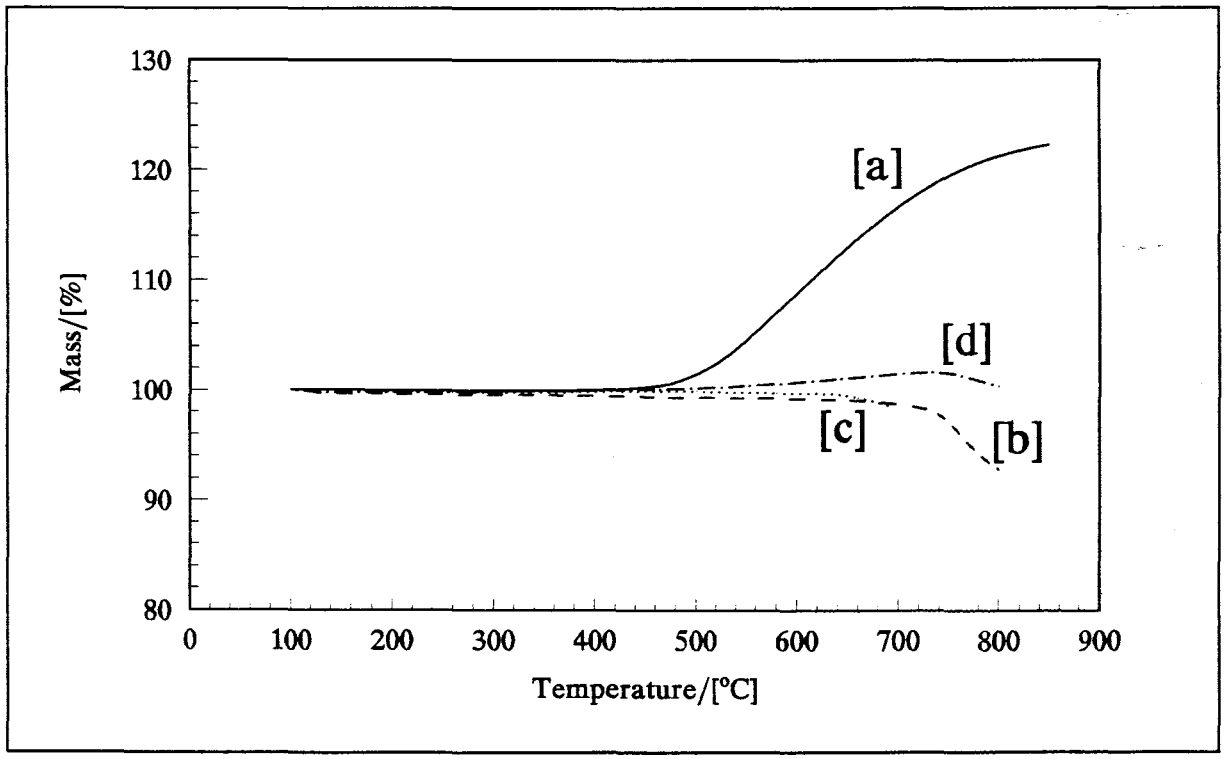

FIGURE 8.11: TG of the Zn/BaO_2 system
[a]: Zn in air, [b]: BaO_2 in air, [c]: 30% Zn/BaO_2 in air and [d]: in N_2

For the 30% Zn/BaO_2 composition, if no external reaction occurred, the overall mass change would be zero and ~78% of the Zn would be oxidised. Independent oxidation of the 30% Zn (94% pure) and decomposition of the 70% BaO_2 (85% pure) would result in a net increase in mass of 1.3%. A TG curve for powdered 30% Zn/BaO_2 composition heated at 20°C min^{-1} in air, showed a regular mass gain up to 700°C, followed by a regular mass loss corresponding to the loss of oxygen during the BaO_2 decomposition. The TG curve for a sample of 30% Zn/BaO_2, heated at 20°C min^{-1} in N_2 (Figure 8.11, curve [c]) showed a mass loss with onset at ~600°C, extending to beyond the limited instrument range of 685°C, reaching a value of -4% at the limit, due to the loss of oxygen in the BaO_2 decomposition. In air, the mass loss was shifted to higher temperatures (onset ~725°C) indicating that reaction was subject to significant inhibition by the presence of one of the products, oxygen. The mass changes observed in the TG in N_2 could be accounted for, at least in part, in terms of the zinc vaporising from the mixture instead of reacting with the peroxide. A study was performed on the Zn/BaO_2 system by heating the mixture in N_2, and then heating the product in air, to establish whether intermediate products had formed. The initial run in N_2 produced a mass loss with onset at 620°C, due partly to the decomposition of BaO_2 and partly to the vaporisation of zinc. Rerunning the product in air (after it had been cooled in N_2) produced a two-step mass loss with onsets at 480°C and 560°C, terminating at ~700°C (Figure 8.12). Since BaO_2 decomposes in a single-step mass loss, this mass loss could be explained by the formation of a layer of zinc on the sample during the initial heating in N_2, formed by the flow of liquid zinc to the surface of the sample when the temperature exceeded the melting point of zinc. This zinc is consequently in a favourable position to vaporise, resulting in the observed mass loss. The second step of mass loss may be attributed to the decomposition of residual BaO_2. The DTA curve of the product of a similar experiment performed on the DTA instrument showed only a small endotherm with an onset at ~490°C.

8.7.2 Nonisothermal kinetics:

The kinetic parameters presented in Table 8.3 were obtained by analysis of the DTA curves of 30% Zn/BaO_2 mixtures in N_2, by the Borchardt and Daniels method [159] of analysis (Figure 8.13). The DTA study in N_2 produced a complex reaction exotherm. The kinetic analysis of this exotherm was performed in the same manner as for the Fe-fuelled systems, by determining the α values from the entire exotherm, and analyzing the initial temperature regions separately, using the overall α values.

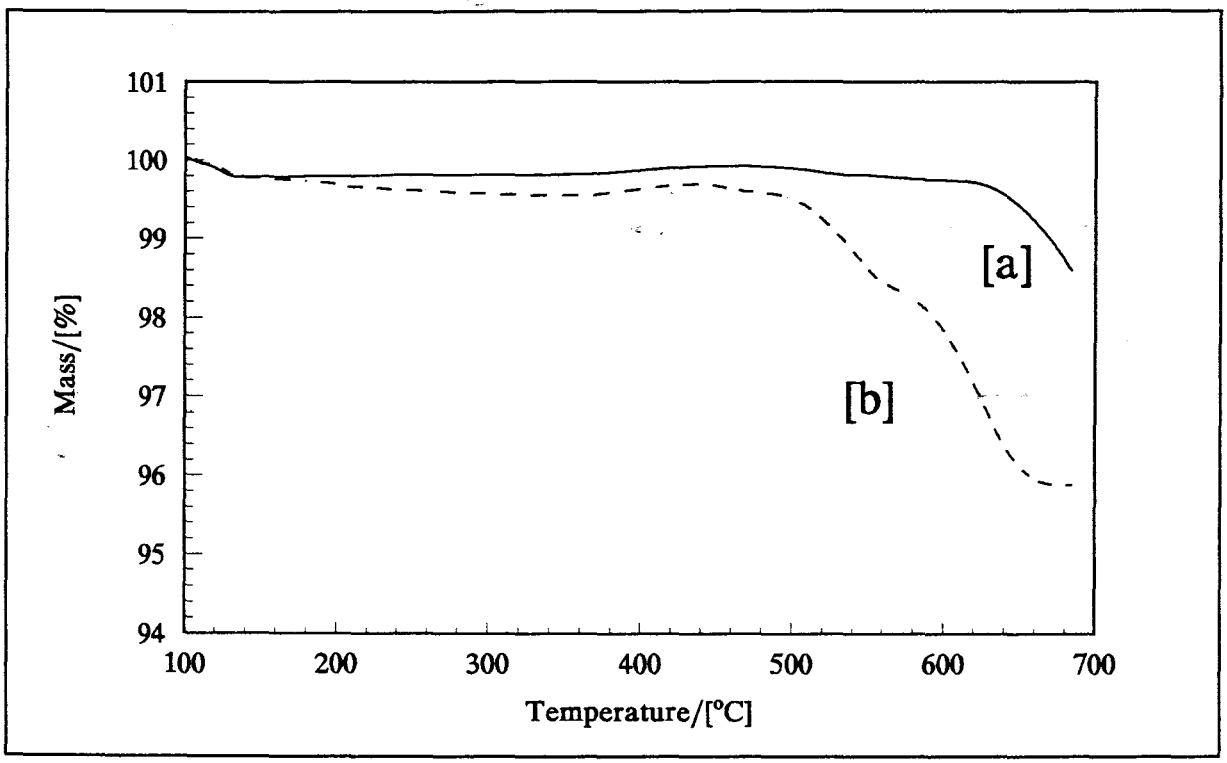

FIGURE 8.12: TG study of intermediate products
[a]: N_2 and [b]: subsequent product of <a> in air

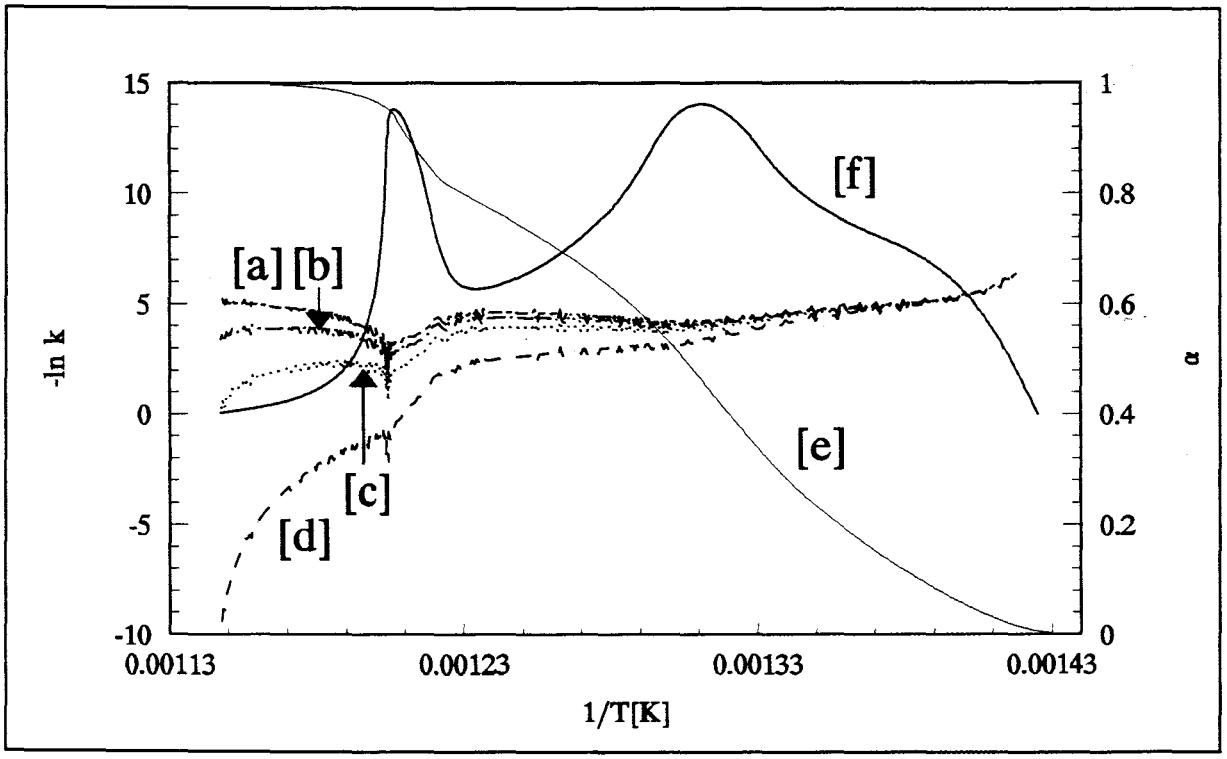

FIGURE 8.13: Borchardt and Daniels kinetic analysis of a 30% Zn/BaO_2 DTA in air
[a]: n=½, [b]: n=⅔, [c]: n=1, [d]: n=2, [e]: α and [f]: Rescaled DTA

TABLE 8.3: Kinetic parameters obtained from DTA experiments:

Atmosphere	T Range[°C]	Order (n)	E_a/[kJ mol^{-1}]	A/[s^{-1}]	r^2
N_2	430-600	1	127.9±2.8	(17.5±0.5)x10^7	0.87
	Overall	2	335.8±8.9	(77.8±2.3)x10^{21}	0.82
N_2	430-495	½	124.7±4.2	(10.9±0.1)x10^7	0.89
	Initial region	⅔	132.4±4.2	(39.9±0.4)x10^7	0.91
		1	147.7±4.0	(52.8±0.5)x10^8	0.93
		2	193.7±3.7	(12.4±0.1)x10^{12}	0.96

The E_a values determined from the initial region are not very dependent on the value chosen for the order of reaction ($0.5 \leq n \leq 1.0$), and a similar value of E_a is obtained. The value of 140 ± 10 kJ mol^{-1} lies between the value of E_a determined for the oxidation of Zn in air (58 kJ mol^{-1}) and the value determined for the decomposition of BaO_2 in N_2 (~ 180 kJ mol^{-1}).

These Arrhenius parameters, estimated under the relatively controlled conditions of thermal analysis, are compared with those estimated from combustion studies, in the general discussion in Section 15.5.

8.8 Thermal analysis of layered pellets of Zn+BaO_2:

The TG study performed in N_2 produced a gradual mass loss (incomplete at 900°C) with an onset temperature ~600°C, due to the decomposition of BaO_2 and vaporisation of zinc. In the DSC trace in N_2, the melting of zinc (onset 418°C) dominated the study, which also detected a small exotherm at 480°C.

8.9 Thermal analysis of the Zn/SrO_2 system:

8.9.1 Thermal behaviour:

The Zn/SrO_2 system sustained combustion over the range 30 - 50% Zn (Section 12). The stoichiometric composition, based on the reaction

$$Zn + SrO_2 \rightarrow ZnO + SrO$$

is 35.3% Zn (100% pure) or 37.6% Zn (94% pure). The DTA curves for powdered samples of 30% (Figure 8.14, curve [c]) and 50% Zn/SrO_2, heated at 20°C min^{-1} in N_2 show two endotherms corresponding to the melting of zinc (418°C) and the decomposition of SrO_2 (onset 425°C), and a subsequent exotherm with onset at 485°C. A broad exotherm ensues in the 50% mixture which has a peak at 790°C in the trace. The DTA trace in air (or O_2) (Figure 8.14, curve [d]) is almost identical to that in nitrogen, which suggests that the reaction may be independent of atmosphere. For a mixture which had aged for 24 h in air at 25°C, the reaction exotherm at 485°C decreased in size

whilst the broad exotherm increased. The DTA curves for Zn in air (curve [a]) and BaO_2 in N_2 (curve [b]) are shown in the same Figure for comparison. The DTA trace of a 30% Zn/SrO_2 pellet in N_2 is similar to that of the powder, with the melting of the zinc preceding the decomposition of the peroxide, with a resultant exotherm occurring immediately. The exotherm is composed of two events, the lower temperature event (onset 450°C) being followed by a sharper exotherm (onset 480°C) possibly corresponding to the second stage of decomposition of the peroxide.

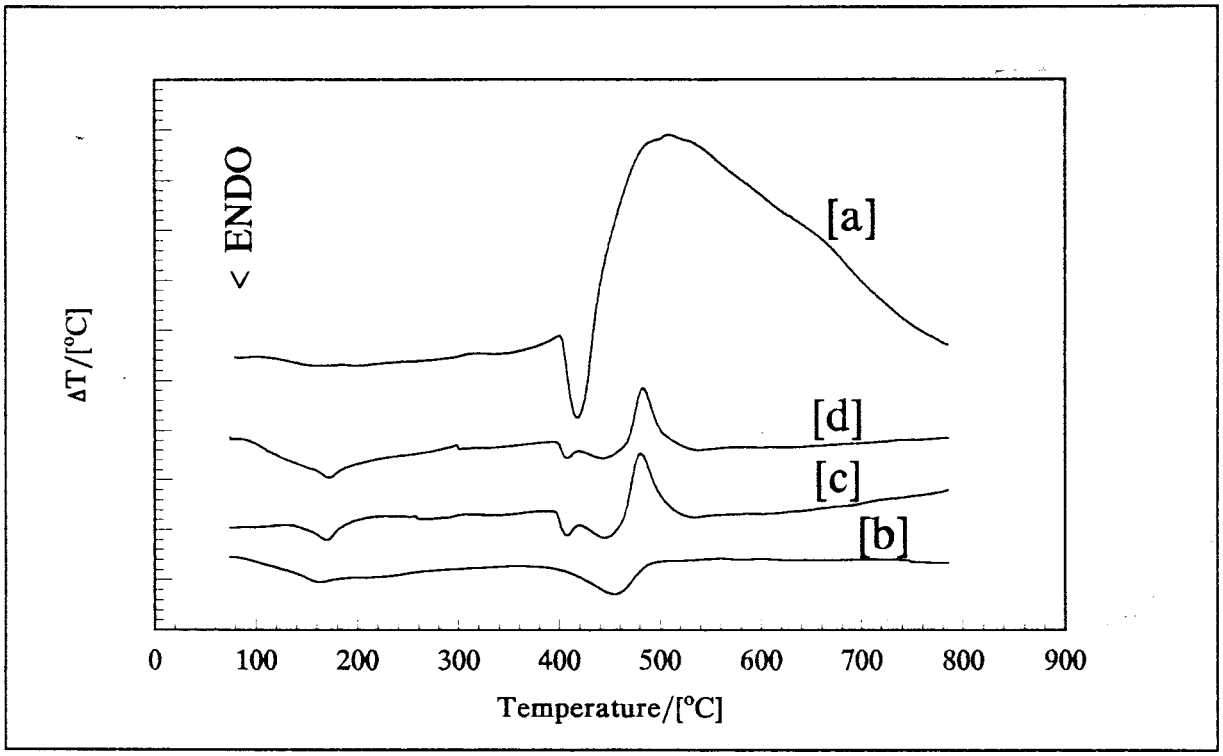

FIGURE 8.14: DTA of Zn/SrO_2
[a]: Zn in air, [b]: SrO_2 in N_2, [c]: 30% Zn/SrO_2 in air and [d]: in N_2

The DTA study on the Zn/SrO_2 system, unlike the Zn/BaO_2 system, shows that the main reaction exotherm does not follow directly after the fusion of the zinc, but rather accompanies the first stage of the decomposition of the peroxide. The behaviour was almost identical in both nitrogen and air, the onset of the decomposition endotherm being 430°C and that of the reaction exotherm 465°C. The only differences noted between 30% Zn and 50% Zn compositions were the increase in intensity of the zinc endotherm (since more zinc was present) and the decrease in the intensity of the reaction exotherm (movement away from the stoichiometric ratio, and less oxygen for reaction).

The DSC study of the powdered sample in N_2 showed dehydration around 100°C, followed by the onset of decomposition of the SrO_2 almost simultaneously with the melting of zinc at 418°C. A reaction exotherm occurred (onset 480°C) midway through the decomposition of the peroxide. This exotherm appeared to be composed of two peaks, the initial being large and sharp ($\Delta H = \sim 93$ J g^{-1}) and the second much smaller but overlapping the first.

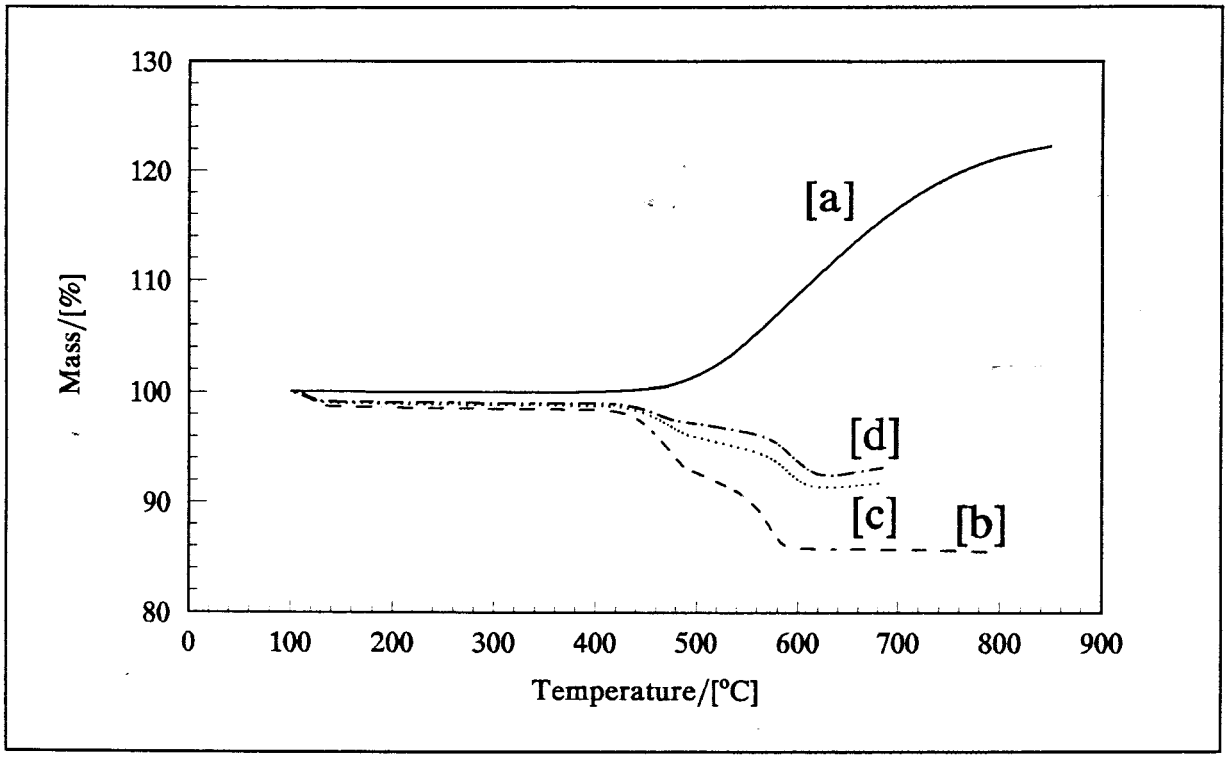

FIGURE 8.15: TG of Zn/SrO_2
[a]: Zn in air, [b]: SrO_2 in N_2, [c]: 30% Zn/SrO_2 in N_2 and [d]: in air

The TG curve for the powdered sample of 30% Zn/SrO_2, heated at 20°C min^{-1} in N_2 (Figure 8.15, curve [c]) records a total mass change of ~7.5% occurring in at least three stages: two of the stages (onsets at ~435°C and ~570°C, appear to be directly related to the decomposition of strontium peroxide, and the final gradual mass gain at the high temperature limit (700°C) is probably the last part of the concurrent oxidation of Zn. In air (curve [d]), the total change is ~6.6%, in similar stages to those in N_2. For the 30% Zn/SrO_2 composition, if no external reaction occurred, the overall mass change would be zero and 100% of the Zn would be oxidised. Independent oxidation of the 30% Zn and decomposition of the 70% SrO_2 (85% pure) would result in a net decrease in mass of 1.1%. Decomposition of the SrO_2 only would give a decrease in mass of 8.0%. The study of the 30% Zn/SrO_2 pellet in N_2 showed a single stage of mass loss of 6.2 ± 0.6% (onset 450°C).

8.9.2 Nonisothermal kinetics:

The kinetic parameters presented in Table 8.4 were obtained (Figure 8.16) from DTA curves of 30% Zn/SrO_2 mixtures in N_2 by the Borchardt and Daniels method of analysis [159]. Only one reaction exotherm was apparent and the analysis refers to the entire peak.

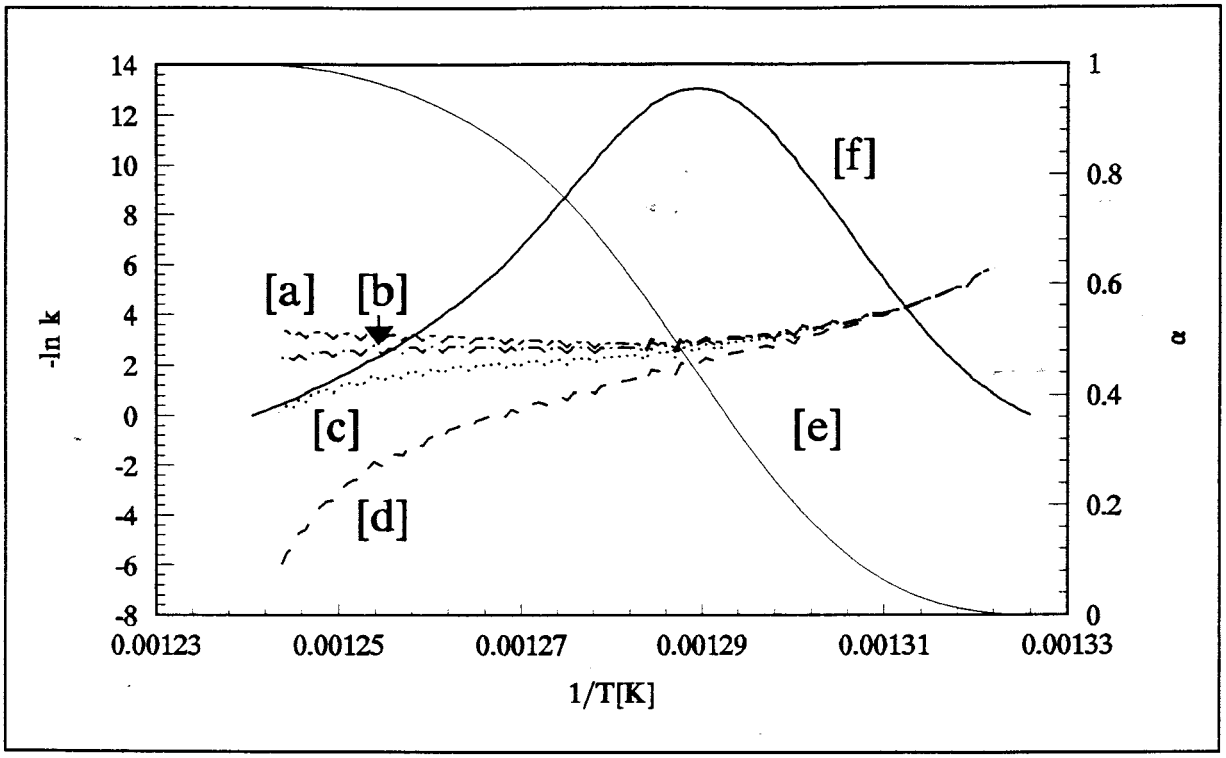

FIGURE 8.16: Borchardt and Daniels kinetic analysis of 30% Zn/SrO_2 in N_2 for selected n [a]: n=½, [b]: n=⅔, [c]: n=1, [d]: n=2, [e]: α and [f]: Rescaled DTA

TABLE 8.4: Kinetic parameters obtained from DTA curves:

Atmosphere	T Range[°C]	Order (n)	E_a/[kJ mol^{-1}]	A/[s^{-1}]	r^2
N_2	484-533	1	302.7±15.1	(18.3±0.2)x10^{19}	0.81
		2	666.0±7.9	(11.8±0.1)x10^{44}	0.99

The analysis shows that the closest correlation exists for a reaction order of 2, giving an E_a of 666 ± 8 kJ mol^{-1}. The values of the kinetic parameters were sensitive to the choice of reaction order, n. The E_a values recorded are all in excess of the value for the oxidation of zinc (~104 kJ mol^{-1}) or the decomposition of the peroxide.

8.10 Thermal analysis of layered pellets of Zn+SrO_2:

The TG trace in N_2 was dominated by the usual two step decomposition associated with the strontium peroxide (onsets 450°C and 650°C), with zinc vaporisation resulting in an increased mass loss toward the instrument limit. The DSC trace was dominated by the melting of zinc, but also showed a small exotherm (onset 480°C), superimposed on the decomposition endotherm of the peroxide (onset 400°C).

9. COMBUSTION OF THE Fe/BaO_2 SYSTEM:

9.1 Reproducibility

Compositions containing from 15 to 50% Fe by mass sustained combustion. Figure 9.1 illustrates the reproducibility of temperature profiles of one composition (20% Fe/BaO_2), at a compaction pressure of 55 MPa. An example of the effect of smoothing on a typical 20% Fe/BaO_2 profile is shown in Figure 9.2. Profiles have been shifted arbitrarily on the time axis since no fixed zero point exists.

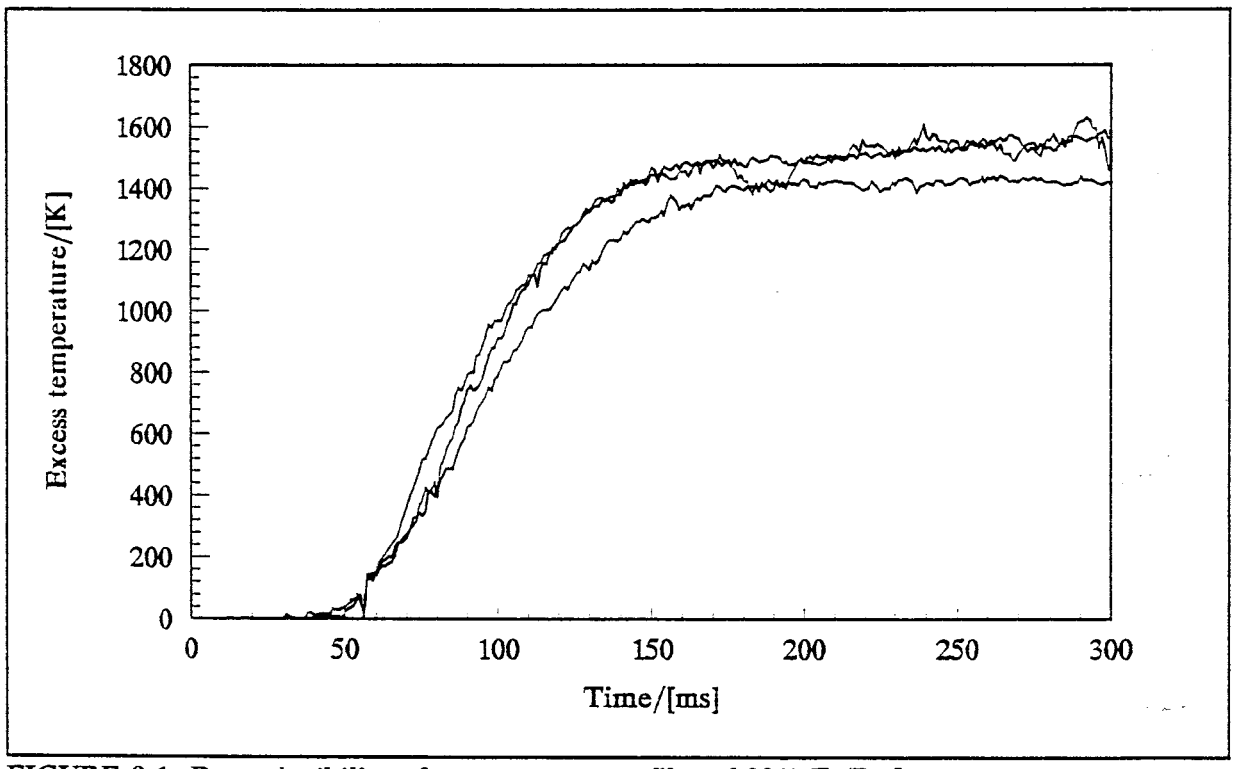

FIGURE 9.1: Reproducibility of temperature profiles of 20% Fe/BaO_2

9.2 Effects of composition and of compaction

The profiles vary in shape (Figure 9.3) with composition (at a constant compaction of 55 MPa) and rise times and maximum temperatures reached are plotted in Figure 9.4. Burning rates ranged from 6 to 42 mm s^{-1}. Figure 9.5 shows that the burning-rate reaches a maximum around 30%. Figure 9.5 also shows that the enthalpy per gram, calculated from the measured maximum temperature rise, U_{max}, and the heat capacity of the mixture, reaches a maximum around 20% Fe. Profiles for samples of 20% Fe/BaO_2 compacted under various pressures are shown in Figure 9.6. Comparison of temperature profiles can be made more quantitative on the basis of rise-times, t_r, (the time taken for the temperature to rise to 1/e of its maximum rise) or the time taken for the temperature to rise from

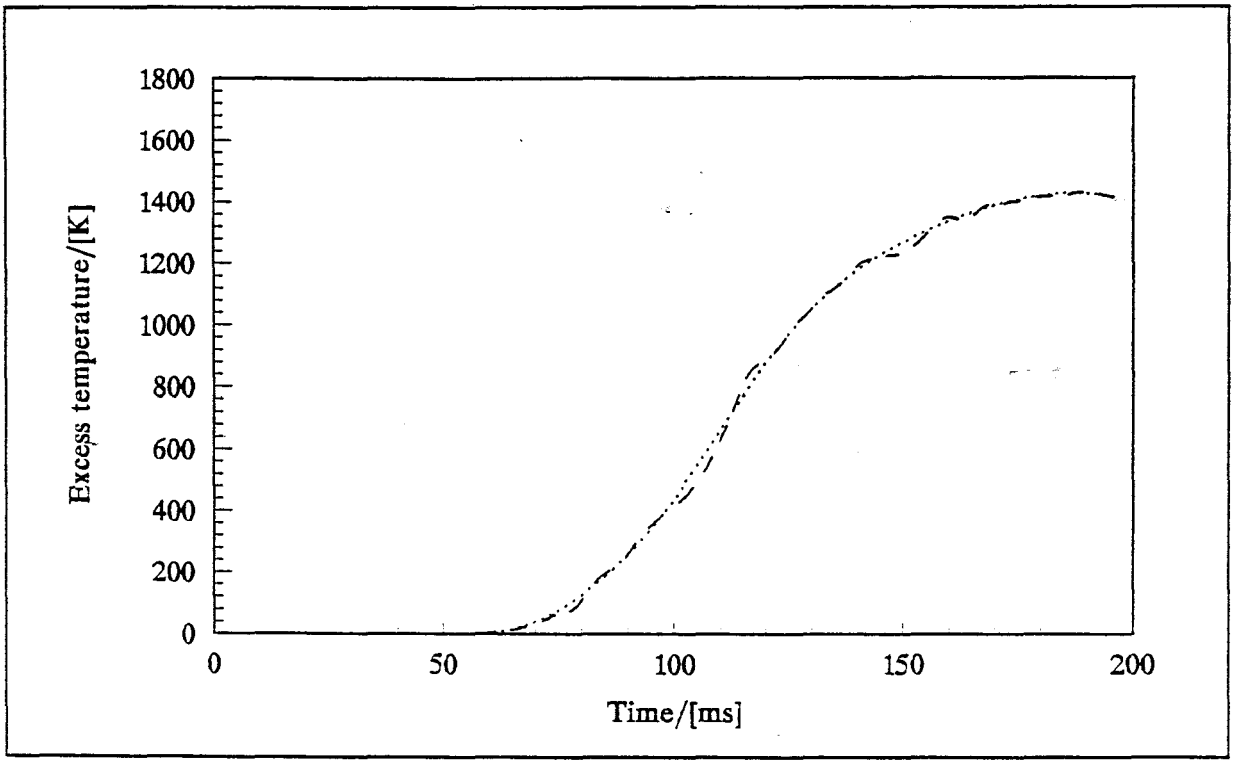

FIGURE 9.2: Effect of smoothing algorithm on a typical temperature profile of 20% Fe/BaO_2

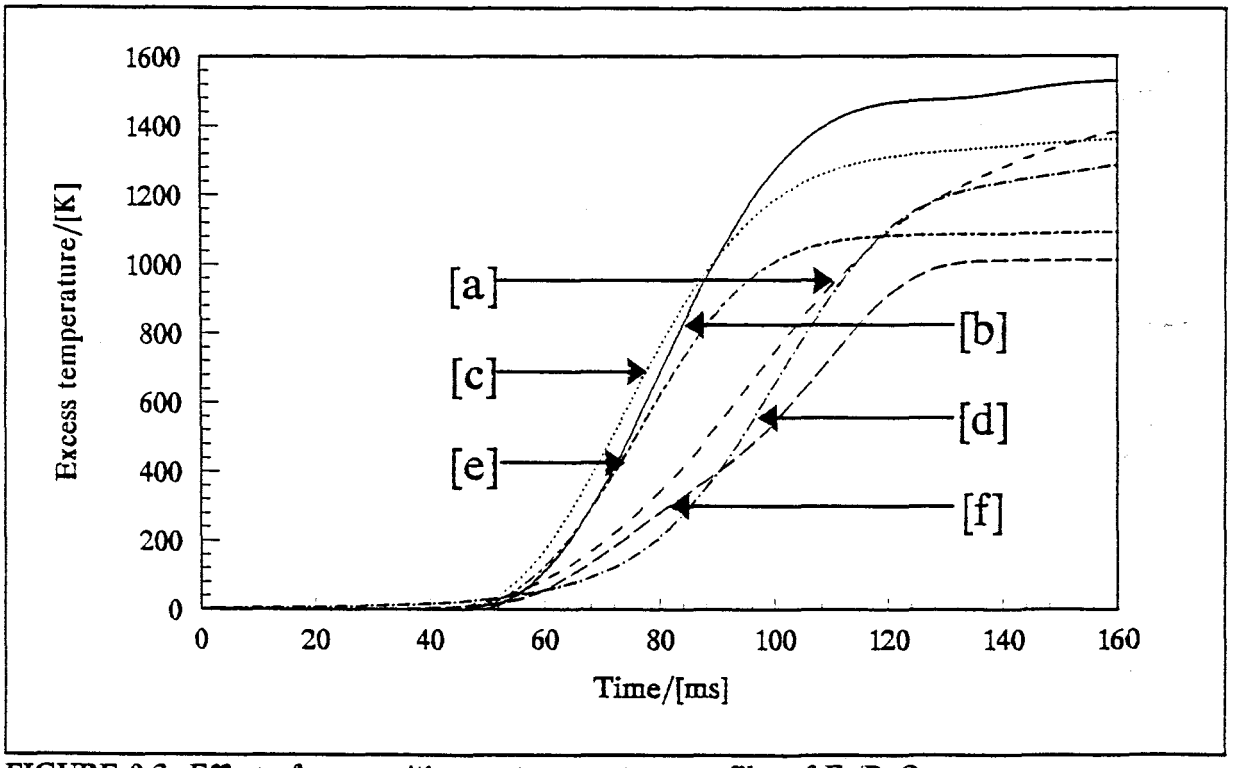

FIGURE 9.3: Effect of composition on temperature profiles of Fe/BaO_2
[a]:15%, [b]:20%, [c]:25%, [d]:30%, [e]:40% and [f]:50%.

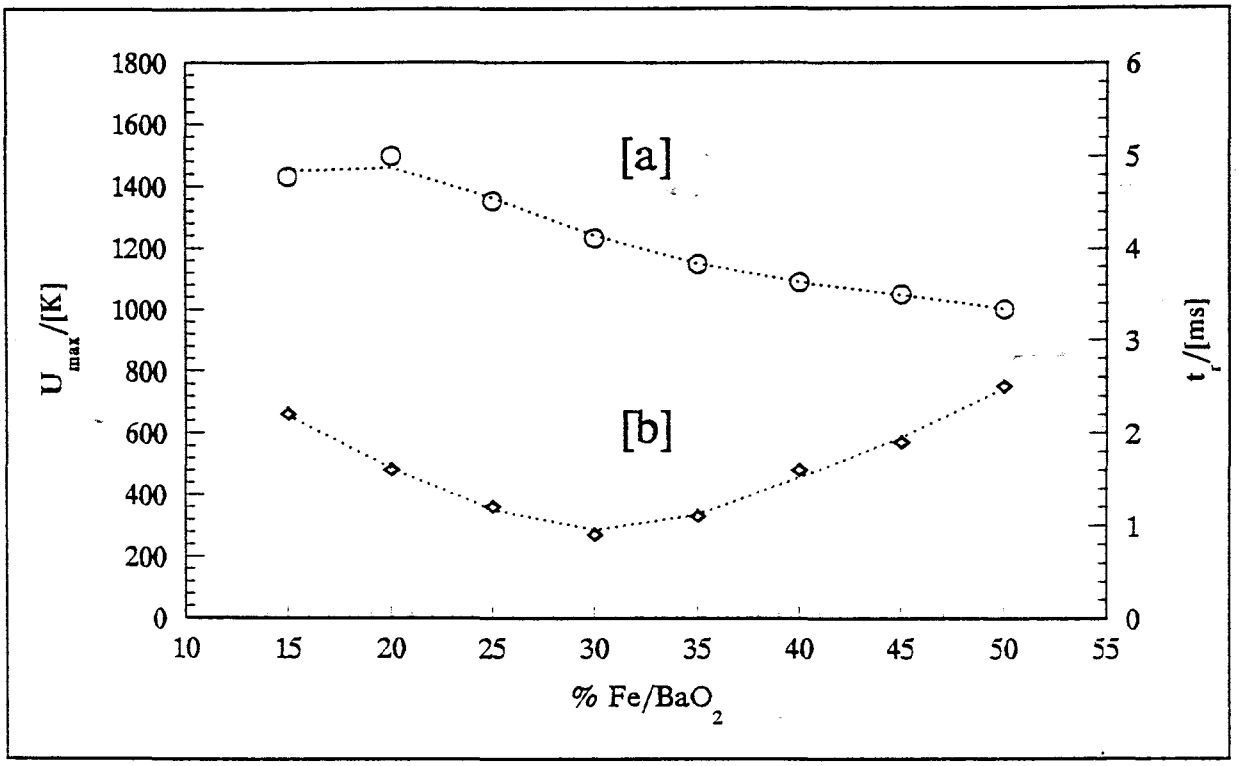

FIGURE 9.4: Effect of composition on [a]: U_{max} and [b]: t_r

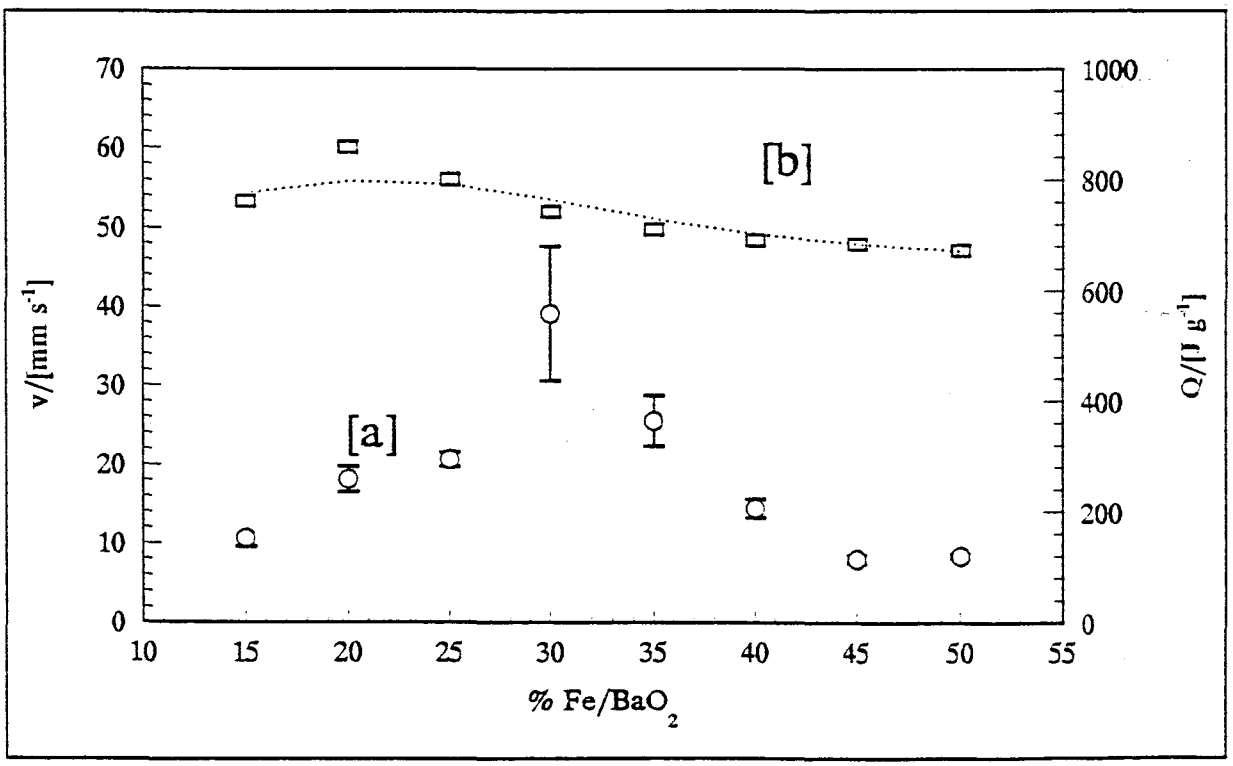

FIGURE 9.5: Effect of composition on [a]: v_{exp} and [b]: enthalpy of reaction of Fe/BaO_2

10% to 90% of its final rise. This time is often used to characterize sigmoid curves [175]. An increase in compaction pressure on the sample increased both the burning-rate (Figure 9.7) and the steepness of the rise region (values of t_r were decreased) of the temperature profile of the 20% Fe/BaO_2 composition. Increases in compaction pressure on the sample (from 55 to 165 MPa) did not increase the burning-rate of the mixture, as had been expected from the previous studies [4,7]. Although the burning-rates increased with compaction pressure up to 55 MPa, an increase beyond 110 MPa decreased the burning-rates (Table 9.1). The effects of compaction and composition are combined in Figure 9.8. Changing the fuel/oxidant ratio gave a graph which was consistent with previous studies on pyrotechnic compositions [143], in that a concave-down curve of burning-rate against composition resulted. Increasing the compaction pressure increases interparticle contact and, hence, the rates of solid-solid reactions, provided that the composition of the mixture is at or near the stoichiometric composition. When solid-gas reactions are involved, increased compaction may decrease the surface of fuel accessible to gas, or compaction may aid in trapping gas which would otherwise move away from fuel surfaces, so simple conclusions cannot be drawn. Fuel/oxidant contact in a solid-solid reaction will be affected far more by composition and particle-size ratios than by compaction (beyond an initial minimum value required) (see Section 15.2 on contact points).

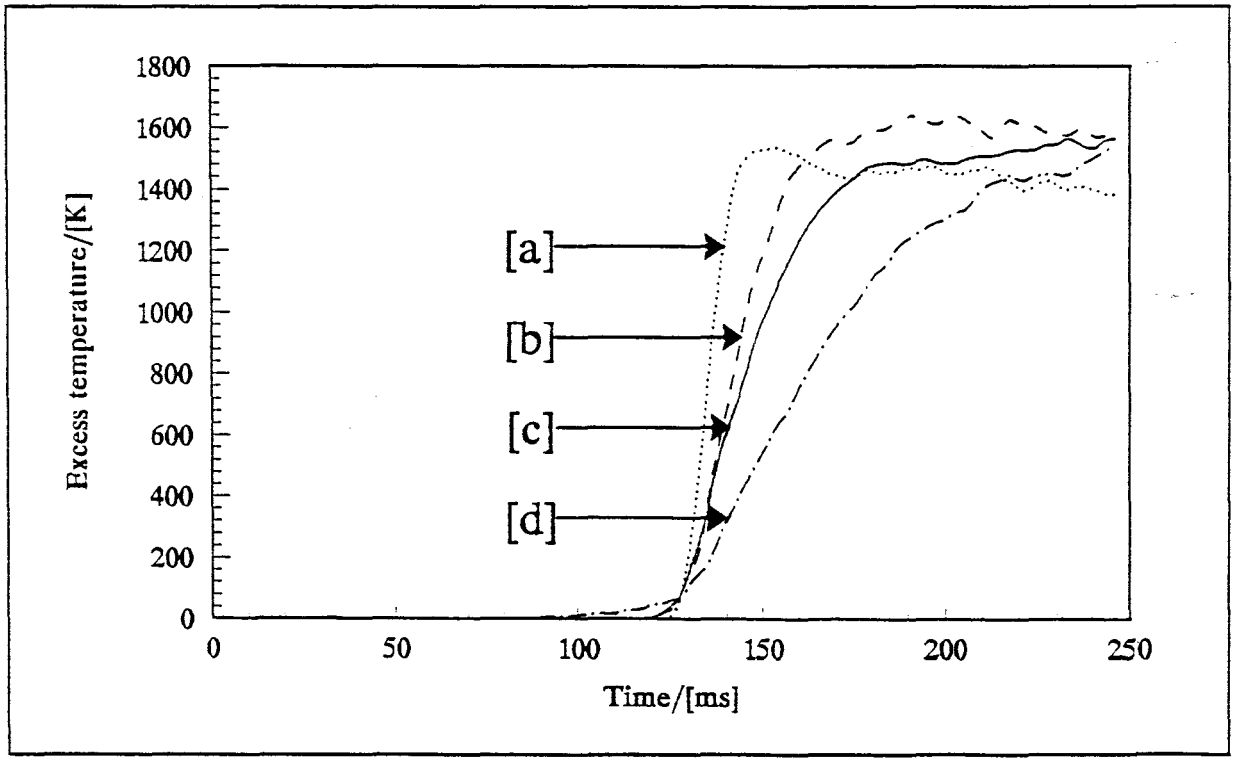

FIGURE 9.6: Effect of compaction on temperature profiles of 20% Fe/BaO_2 [a]: 165 MPa, [b]: 110 MPa, [c]: 65 MPa and [d]: 0 MPa

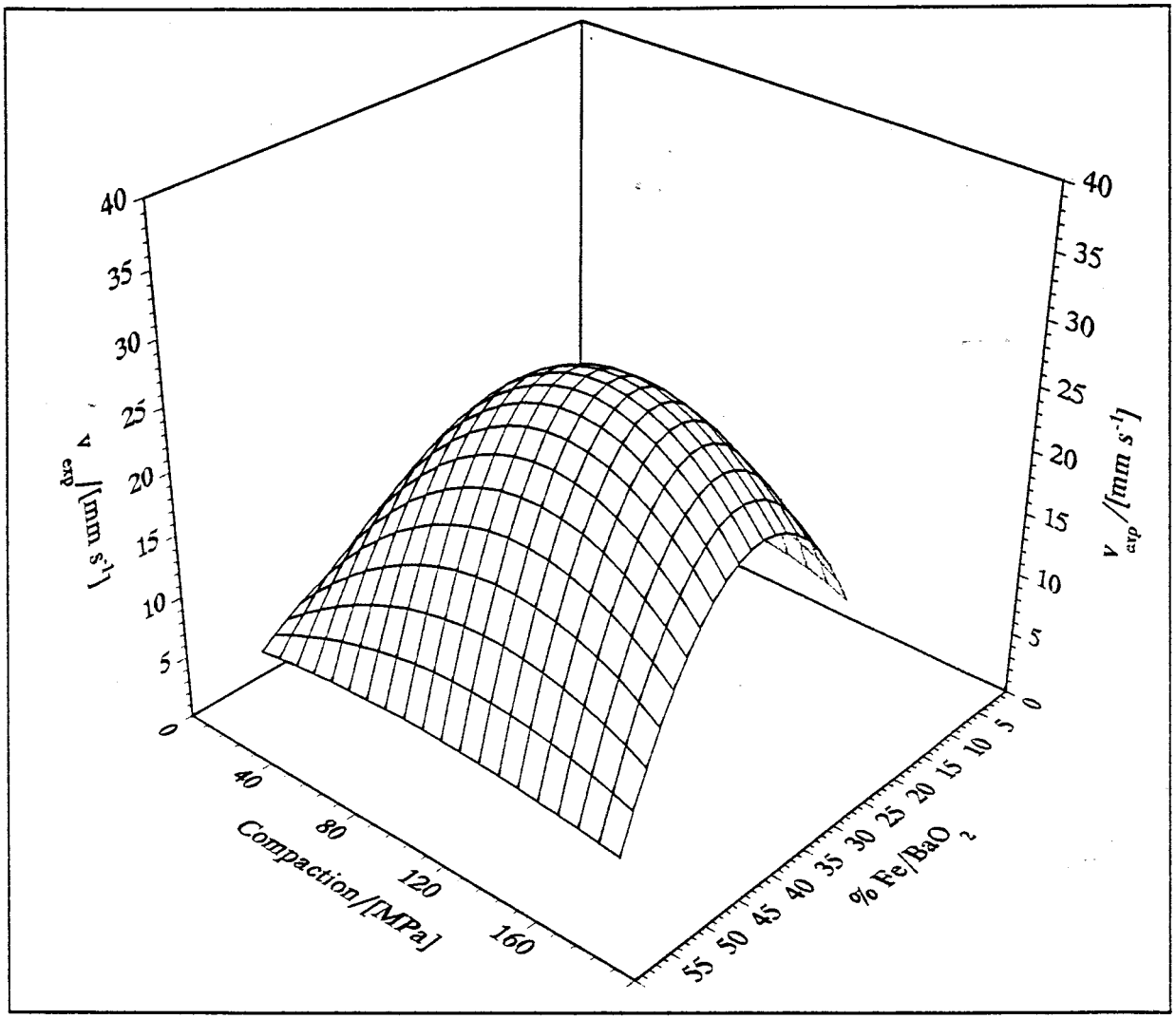

FIGURE 9.7: 3D-surface representation of the effects of compaction and composition on the burning-rates of the Fe/BaO_2 system

The method used for preparing pellets in the Spice and Staveley study [4,7] involved the compaction of the mixture at 124 MPa. The 110 MPa series of burning-rates obtained in this study should thus show closest correlation to their burning-rates, but their values (Table 9.1) are well below those recorded in this study. The Fe powder (<43 μm, 20 μm range) and the barium peroxide (<20 μm) used in this study were of a considerably finer particle-size than the materials used by Spice and Staveley [4,7] (both fuel and oxidant <150 μm) and this may explain their observation that the burning-rates of the Fe/BaO_2 system increased with compaction. The effect of compaction on systems with particles larger than the optimum particle-size [5] is to increase the interparticle contact while still allowing sufficient interstitial volume for gas flow ahead of the burning-front [13,14]. Drennan [6] showed that variation of the particle-size of the peroxide within the range (10 - 36 μm) had negligible effects on temperature profiles for Mn and Mo/peroxide systems. The different thermal environments, different particle sizes and different chemical purities of the materials used in the two

studies could thus explain the lack of agreement of measured burning rates.

TABLE 9.1: The effect of composition and compaction pressure on burning-rates of the Fe/BaO_2 system.

Composition	Burning-rates/[mm s^{-1}] at different compactions				
% Fe	0 MPa	55 MPa	110 MPa	165 MPa	S and S* [124 MPa]
15	2.8±0.9	10.6±1.1	9.1±0.4	9.3±0.1	1.8
20	4.2±1.2	18.1±1.6	16.9±2.4	16.7±2.2	4.6
25	4.7±1.3	20.6±0.9	18.2±0.6	18.0±1.0	6.7
30	5.3±1.1	39.1±8.5	33.6±8.9	26.2±6.2	6.2
35	5.0±0.9	25.5±3.2	18.9±4.1	18.7±2.9	5.3
40	4.3±1.2	14.4±1.2	12.6±2.5	12.5±0.7	4.7
45	3.1±0.8	8.0±0.5	7.8±0.6	7.0±0.5	-
50	2.3±0.9	8.4±0.3	7.0±0.4	3.7±0.3	3.3

* Spice and Staveley [4,7].

9.3 Effect of the diameter of the thermocouple wire

The steepness of the rise region of temperature profiles and the values of U_{max} recorded (Figure 9.8) decreased as the diameter of the thermocouple wire used was increased, owing to the faster response times of the thinner thermocouples and decreased heat losses by conduction along the thermocouple wire. The use of 0.05 mm thermocouples caused practical difficulties, however, in that excessive noise was registered by movement of the junction during passage of the combustion wave. Correction factors for kinetic data were thus obtained by extrapolating data measured with thicker thermocouples, including the U_{max} (Figure 9.9) and t_r (Figure 9.10) values, to zero thermocouple thickness. A factor, for data measured with a 0.1 mm thermocouple, of 1.04 was used for the U_{max} correction, and a factor of 0.35 for the t_r correction.

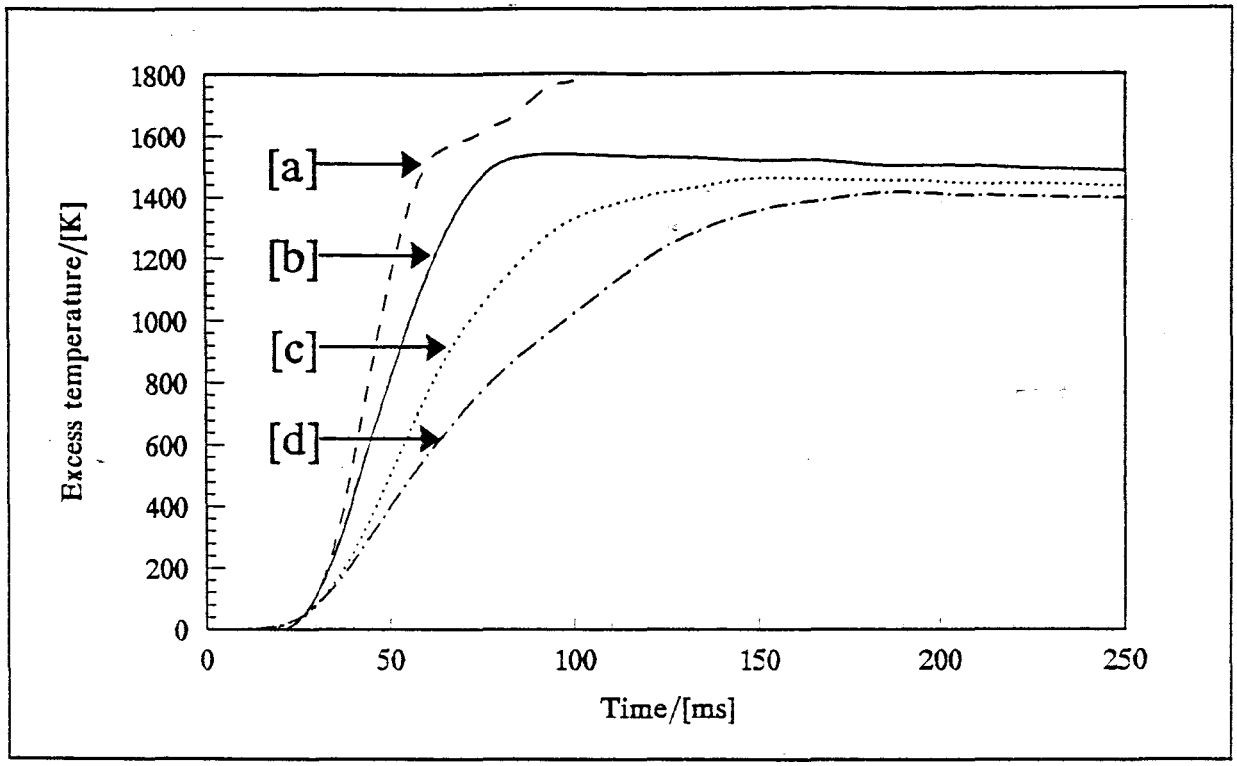

FIGURE 9.8: Effect of thermocouple thickness on temperature profiles of 20% Fe/BaO_2
[a]: 0.05 mm, [b]: 0.1 mm, [c]: 0.2 mm and [d]: 0.3 mm

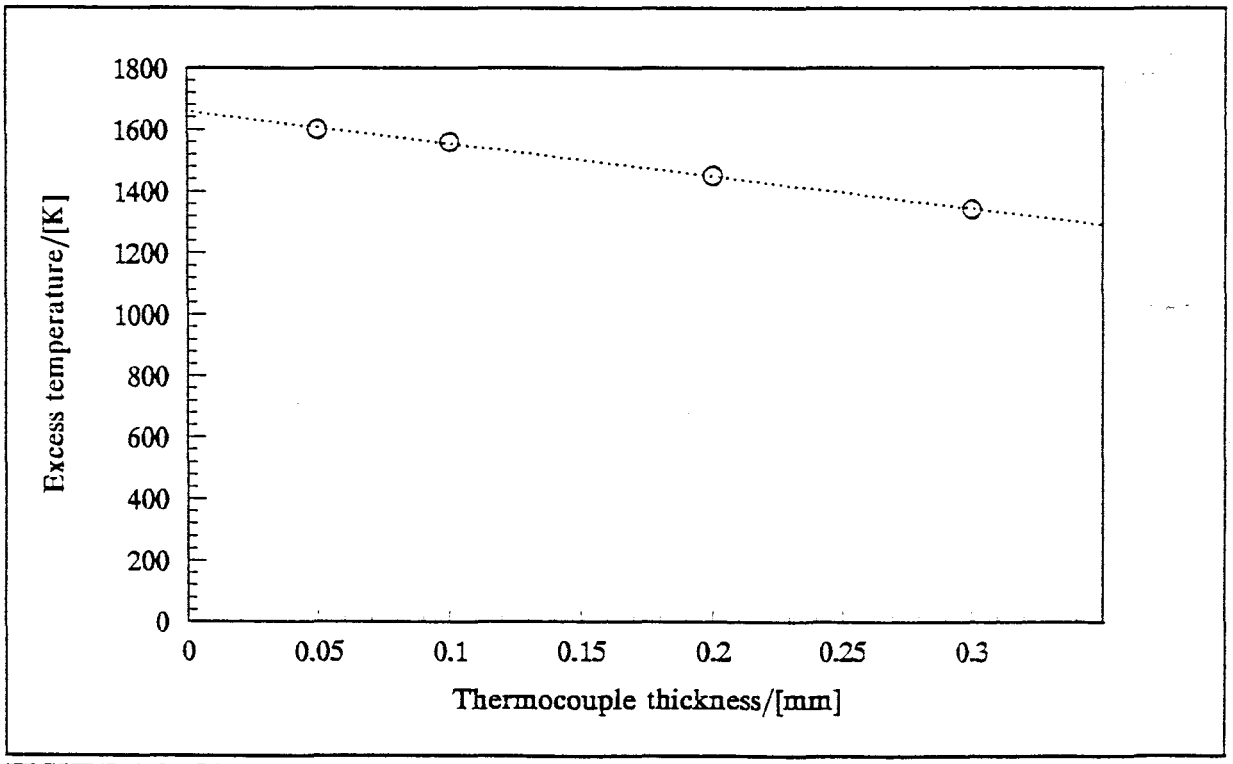

FIGURE 9.9: Effect of thermocouple thickness on U_{max} of 20% Fe/BaO_2

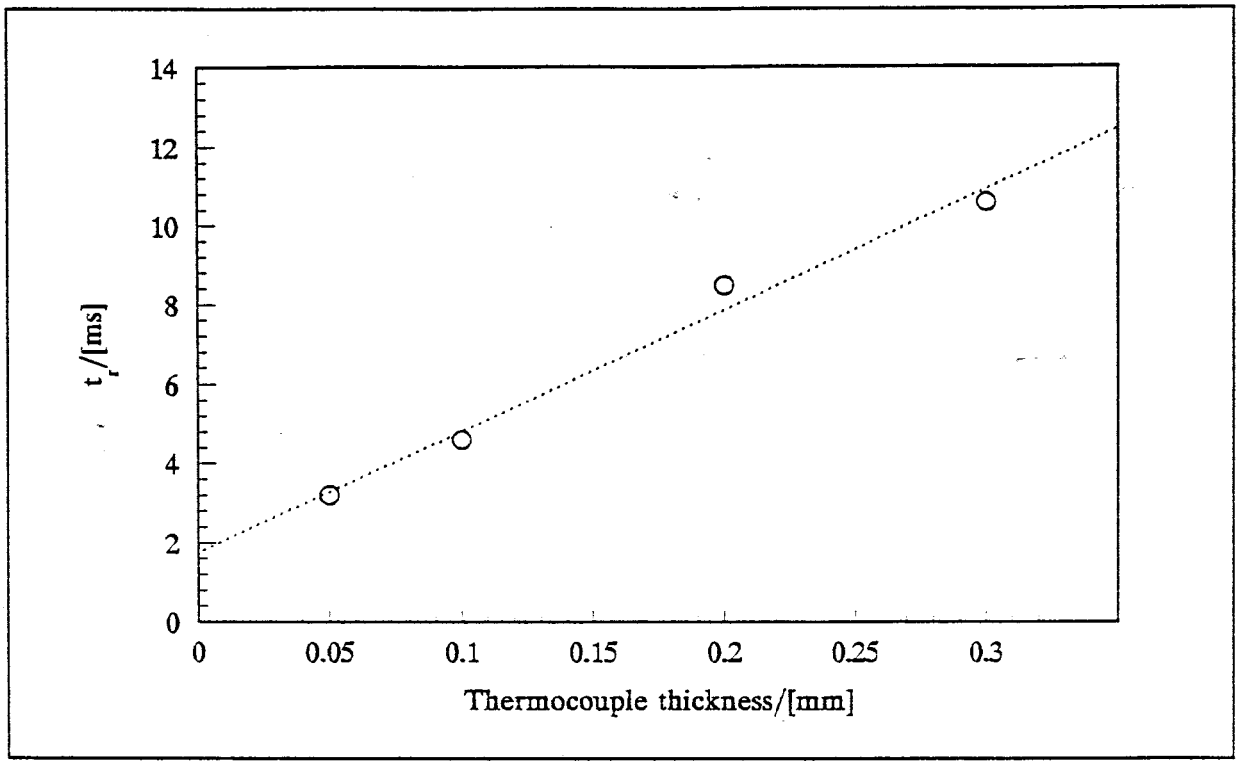

FIGURE 9.10: Effect of thermocouple thickness on t_r of 20% Fe/BaO_2

9.4 Effect of additives

Several substances were introduced separately in small amounts (1 to 10% by mass) into the binary 20% Fe/BaO_2 composition as additives. These substances were: BaO, $Ba(OH)_2$ and $BaCO_3$ (which are likely contaminants of BaO_2); Fe_2O_3 (formed by some oxidation of Fe); water (always present on exposure of compositions to the surrounding atmosphere); and Al_2O_3 (a supposedly inert substance, expected only to affect combustion by its action as a diluent).

Al_2O_3:

Combustion was not supported when more than 10% Al_2O_3 was added to the composition. The addition of Al_2O_3 had a broadening effect on the rise region of the temperature profiles of 20% Fe/BaO_2 (Figure 9.11). The burning-rates at various levels of additive are given in Table 9.2.

BaO:

The burning rate also decreased when BaO was the additive. Up to 10% of oxide was added, after which combustion was not supported. The decreases in U_{max} and the increases in rise times of the temperature profiles (Figure 9.12) were similar to those recorded using Al_2O_3 as an additive.

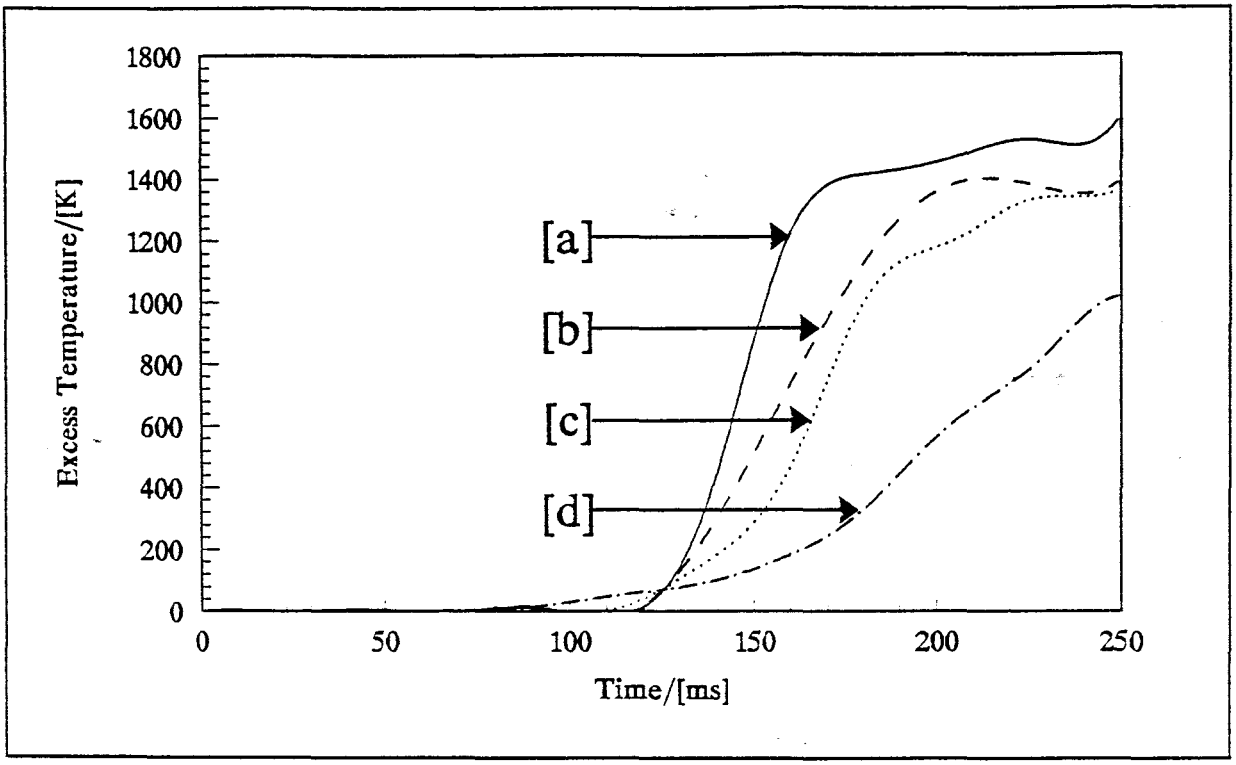

FIGURE 9.11: Effect of Al_2O_3 as additive on temperature profiles of 20% Fe/BaO_2 [a]:0%, [b]:1%, [c]:5% and [d]:10% by mass

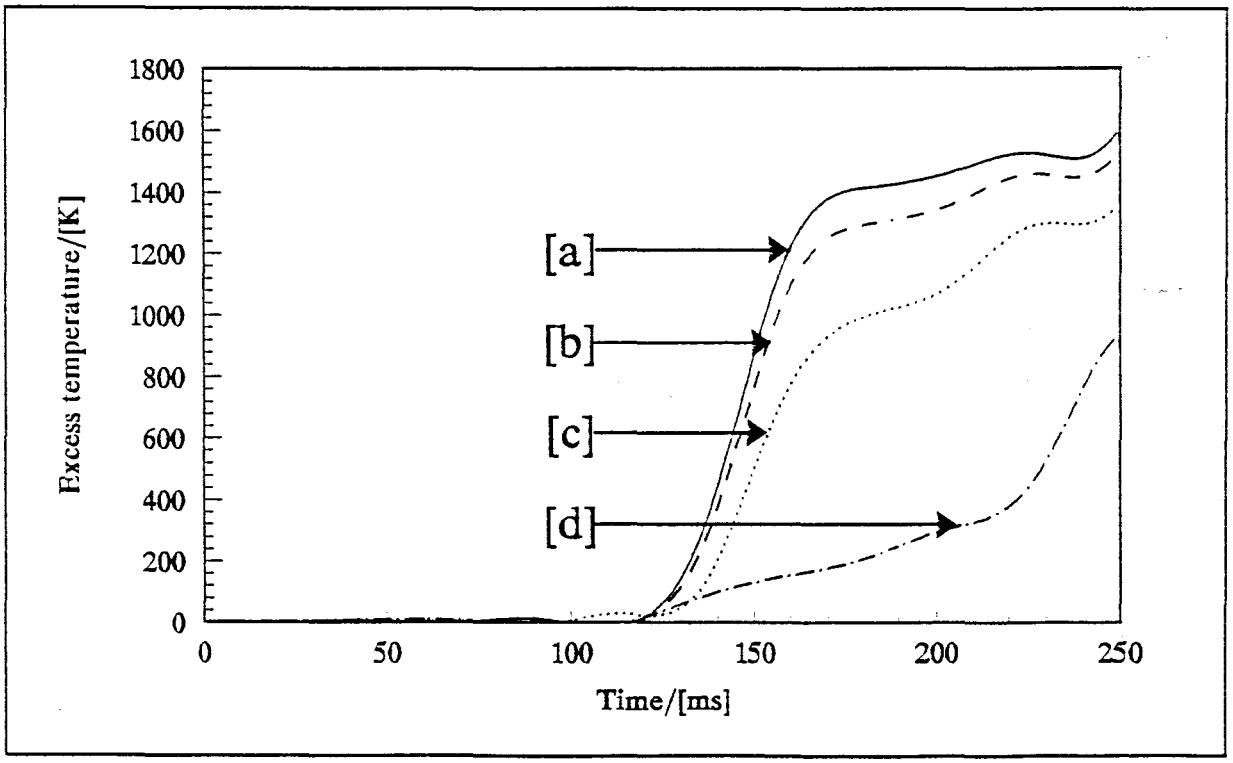

FIGURE 9.12: Effect of BaO as additive on temperature profiles of 20% Fe/BaO_2 [a]:0%, [b]:1%, [c]:5% and [d]:10% by mass

$BaCO_3$:

$BaCO_3$ had the least effect on the profiles of any of the additives used. Even mixtures which contained in excess of 15% $BaCO_3$ were found to support combustion. $BaCO_3$ formation on the surfaces of BaO_2 may, however, have a greater effect on combustion than the presence of separate $BaCO_3$ particles in the mixture. The temperature profiles (Figure 9.13) show that U_{max} and the width of the rise region are not significantly affected by addition of $BaCO_3$. It is also possible that $BaCO_3$ may be involved in a Fe/$BaCO_3$ reaction which parallels the Fe/BaO_2 system (perhaps giving CO(g) as a product), which would account for the continued combustion under conditions of high levels of $BaCO_3$.

$Ba(OH)_2$:

In contrast to the carbonate, the hydroxide has a large effect on temperature profiles. Mixtures containing in excess of 5% of the hydroxide did not support combustion, and the profile of a mixture containing even 1% of the hydroxide showed a marked difference (Figure 9.14) in rise time and U_{max} attained. This effect is related to the sensitivity of the system to the presence of water (see below).

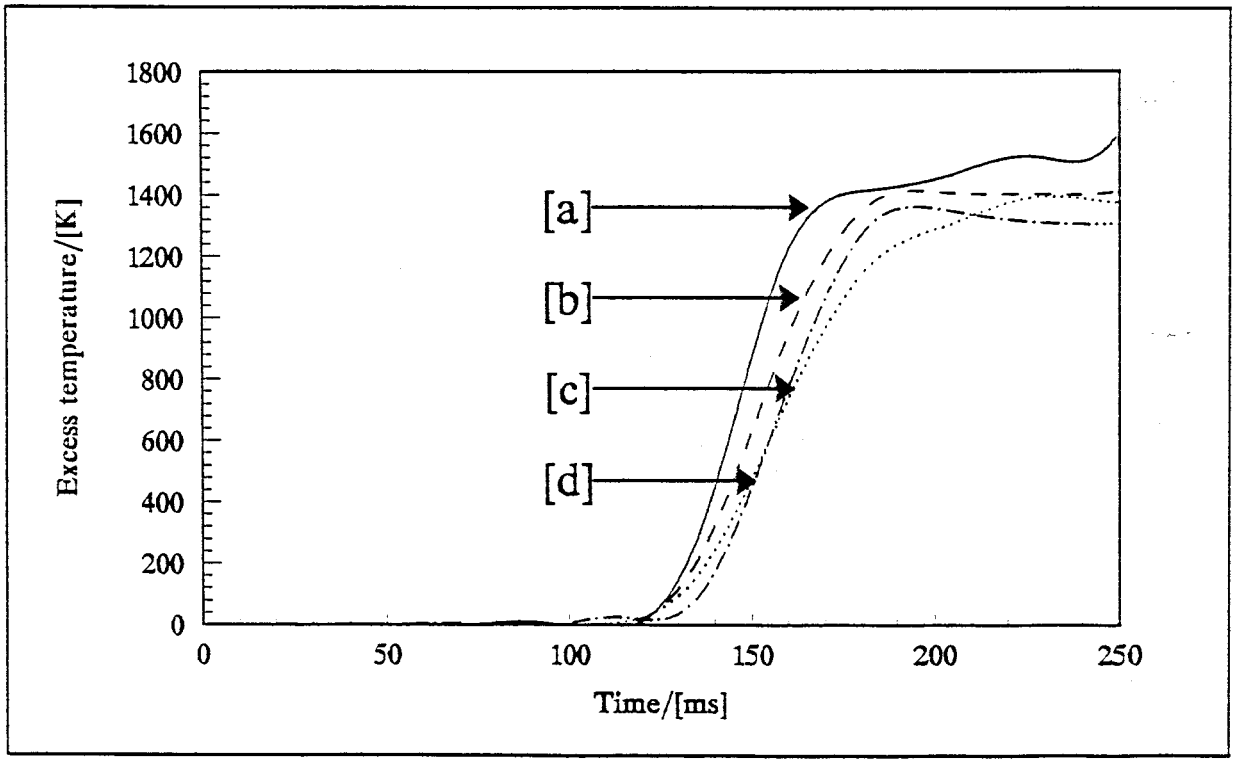

FIGURE 9.13: Effect of $BaCO_3$ as additive on temperature profiles of 20% Fe/BaO_2 [a]:0%, [b]:1%, [c]:5% and [d]:10% by mass

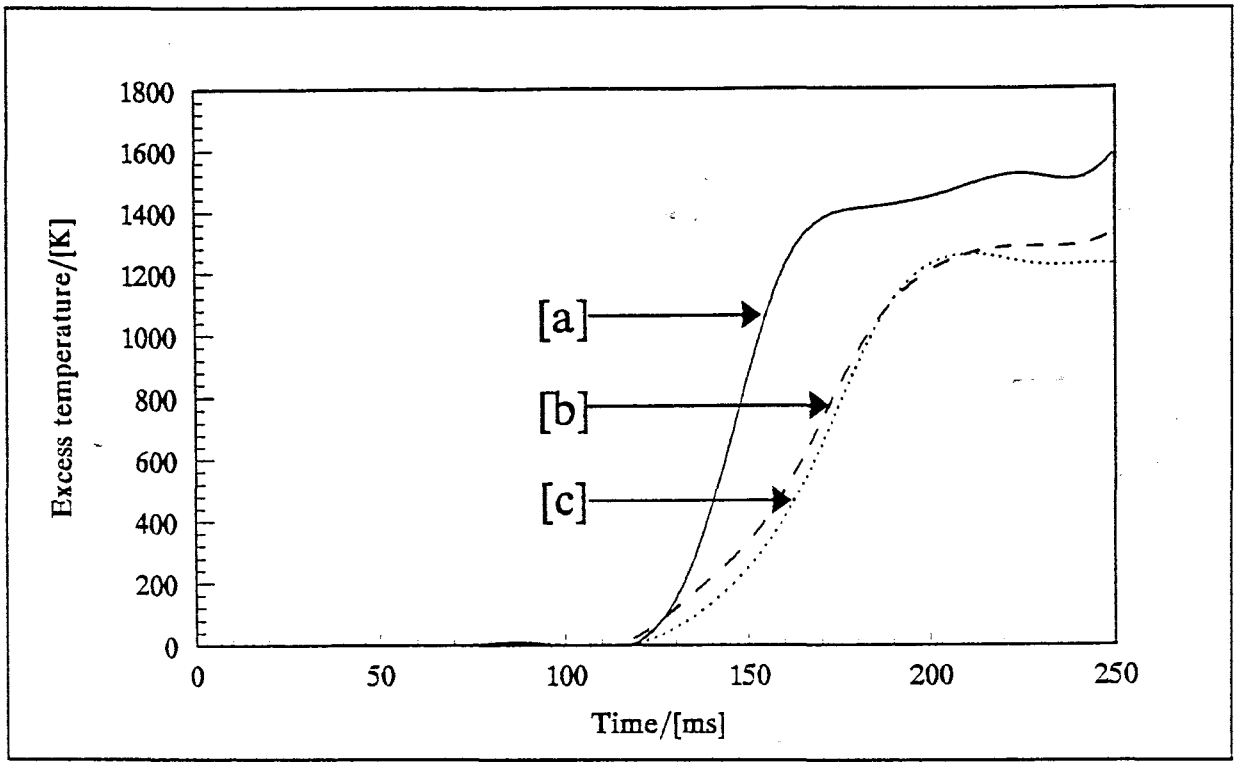

FIGURE 9.14: Effect of $Ba(OH)_2$ as additive on temperature profiles of 20% Fe/BaO_2 [a]:0%, [b]:1% and [c]:5% by mass

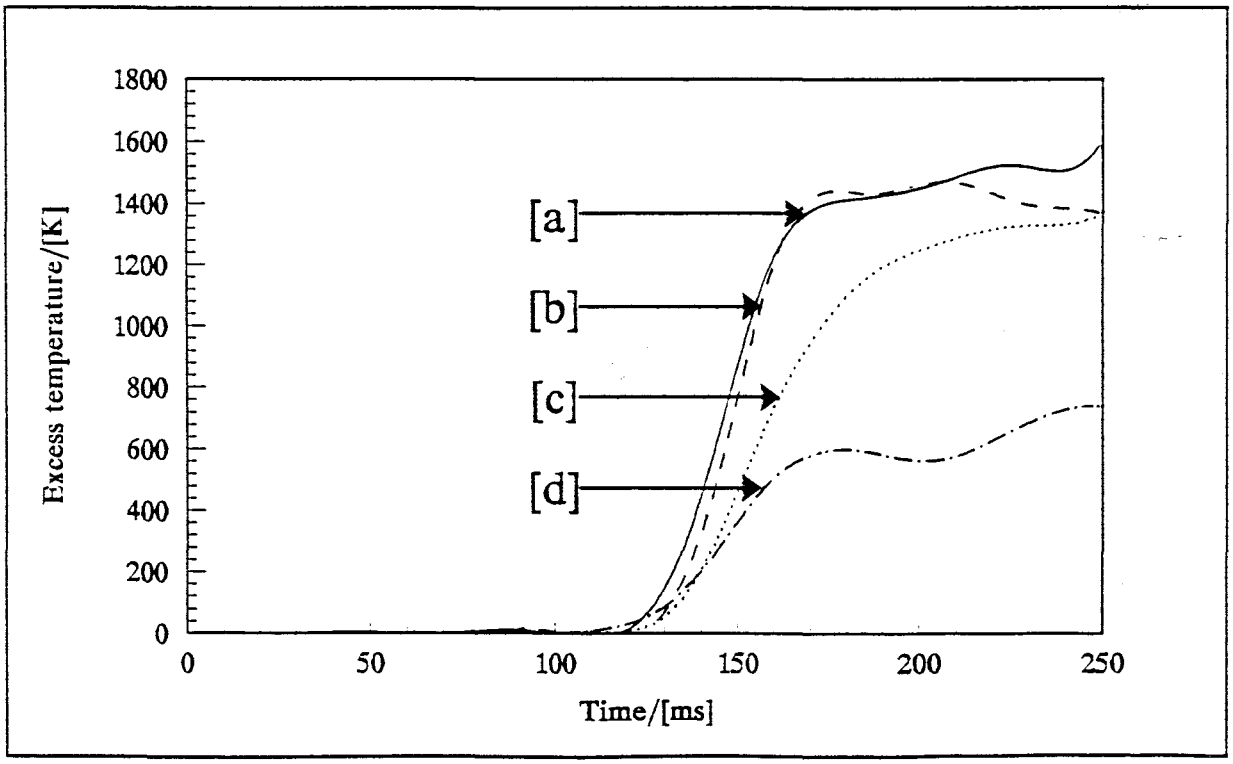

FIGURE 9.15: Effect of Fe_2O_3 as additive on temperature profiles of 20% Fe/BaO_2 [a]:0%, [b]:1%, [c]:5% and [d]:10% by mass

Fe_2O_3:

The addition of Fe_2O_3 to the mixture resulted in an increase in the rise time for the profiles as the percentage of additive increased. The addition of more than 10% Fe_2O_3 led to erratic, unstable combustion of the mixtures. Temperature profiles (Figure 9.15) showed a large difference in profile characteristics (U_{max} and the rise-region).

Water:

Dispersion of water throughout the sample presented difficulties, and a standing time of not less than 12 hours was allowed for complete dispersion. The addition of 5% water to the 20% Fe/BaO_2 mixture resulted in no combustion being initiated. It is suggested that introduction of quantities of water in excess of 1% to the system results in BaO_2 particles being coated in a layer of $Ba(OH)_2$, which inhibits combustion more than having separate particles of $Ba(OH)_2$ interdispersed throughout the mixture. Although the water may be accommodated in the mixture as an amount of $Ba(OH)_2$, during combustion the water will be regenerated by (endothermic) decomposition of the hydroxide and will affect combustion as a gaseous species, disrupting interparticle contact and transferring heat from reaction sites. There is also the possibility of the reaction of H_2O with the surfaces of the iron particles to produce coatings of oxides and hydroxides.

TABLE 9.2: The effect of selected additives on the burning-rates and maximum excess temperatures of the 20% Fe/BaO_2 system.

Additive	Mass %	$v_{observed}$ [mm s^{-1}]	U_{max} [K]
Al_2O_3	0	18.1±1.6	1550±25
	1	15.9±1.4	1420±20
	5	8.7±0.9	1380±30
	10	5.5±0.8	1250±35
	15	-	-
BaO	0	18.1±1.6	1550±25
	1	17.0±1.5	1500±30
	5	9.2±0.9	1350±35
	10	3.3±0.7	1150±45
	15	-	-

Additive	Mass %	$v_{observed}$ [mm s^{-1}]	U_{max} [K]
$BaCO_3$	0	18.1±1.6	1550±25
	1	14.3±1.3	1450±30
	5	11.5±1.2	1400±30
	10	10.4±1.2	1330±45
	15	-	-
$Ba(OH)_2$	0	18.1±1.6	1550±25
	1	12.0±1.2	1350±35
	5	9.8±1.5	1300±40
	10	-	-
	15	-	-
Fe_2O_3	0	18.1±1.6	1550±25
	1	14.4±1.5	1500±30
	5	13.0±1.4	1350±40
	10	9.3±1.2	800±45
	15	-	-
Water	0	18.1±1.6	1550±25
	1	Incomplete	?
	5	-	-

9.5 Thermochemistry

The simplest reactions likely to be involved in combustion of the Fe/BaO_2 system are:

$$2Fe(s) + 3BaO_2(s) \rightarrow Fe_2O_3(s) + 3BaO(s) \quad \text{(i)}$$

$$3Fe(s) + 4BaO_2(s) \rightarrow Fe_3O_4(s) + 4BaO(s) \quad \text{(ii)}$$

$$Fe(s) + BaO_2(s) \rightarrow FeO(s) + BaO(s) \quad \text{(iii)}$$

Assuming 100% pure reactants, the following stoichiometric compositions (% by mass of Fe) were calculated for the above reactions: (i) 18.03%, (ii) 19.83% and (iii) 24.80%. For 85% pure BaO_2, these values decrease to:(i) 15.8%, (ii) 17.4% and (iii) 21.9%. The predicted heat of reaction for reaction (i), using 100% pure reactants, and calculated from tabulated enthalpies of formation [8] is:

$\Delta H^0_{reaction}$ = (-822.2) + 3(-581.6) - 2(0) - 3(-638.1)

= -652.7 kJ for reaction as written

= -326.4 kJ $(mol\ Fe)^{-1}$

= -217.6 kJ $(mol\ BaO_2)^{-1}$

= -1.285 kJ $(g\ BaO_2)^{-1}$

Since the stoichiometric composition is 18.03% Fe, 1 g of mixture contains 0.8199 g BaO_2 (100% pure).

$\therefore$ Heat output, q = 1.285 x 0.8199 kJ (g mixt)$^{-1}$ = 1.05 kJ (g mixt)$^{-1}$

Converting to 85% purity, q = 0.90 kJ (g mixt)$^{-1}$

The following ferrate formation reactions may also occur to some extent, but no enthalpies of formation for the products were found.

$$Fe_2O_3(s) + BaO(s) \rightarrow BaFe_2O_4(s) \quad \ldots\ldots\ldots\ldots\ldots\ldots \text{(iv)}$$

$$FeO(s) + BaO_2(s) \rightarrow BaFeO_3(s) \quad \ldots\ldots\ldots\ldots\ldots\ldots \text{(v)}$$

$$Fe(s) + 2BaO_2(s) \rightarrow Ba_2FeO_4(s) \quad \ldots\ldots\ldots\ldots\ldots\ldots \text{(vi)}$$

$$FeO(s) + 2BaO(s) + BaO_2(s) \rightarrow Ba_3FeO_5(s) \quad \ldots\ldots\ldots\ldots\ldots\ldots \text{(vii)}$$

As the ferrates were suggested to be structural analogs of the titanate systems (Section 3.11), it is probable that the enthalpies of formation are similar; $\Delta H(BaTiO_3)$ = -1663 kJ mol^{-1} [8]. The enthalpies of formation of the corresponding $BaMnO_4$ and $BaMoO_4$ spinel compounds are slightly more negative than the corresponding formation of simple oxides, indicating that formation of mixed oxides may result in more negative enthalpies of formation than those calculated in Table 9.3 for the formation of simple Fe-oxides and BaO.

The values of $\Delta H_{reaction}$, calculated from standard enthalpies of formation, for reaction (i) leading to simple oxide products, and the predicted adiabatic temperature rises calculated using temperature dependent values of heat capacities [8], are compared with the corresponding experimental quantities in Table 9.3.

TABLE 9.3: A comparison of the enthalpies of reaction for the Fe/BaO_2 pyrotechnic system (per g of mixture) determined from temperature profiles with values calculated from standard tables

Composition	$-\Delta H_{reaction}$ [kJ g^{-1}]	$-\Delta H_{reaction}$ [kJ g^{-1}]	$-\Delta H_{reaction}$ [kJ g^{-1}]	U_{ad} [K]	U_{ad} [K]
$\%Fe/BaO_2$	Calculated*	Experiment	S and S	Calculated#	Experiment
15	0.877	0.761	1.134	1652	1458
20	0.874	0.858	1.046	1525	1522
25	0.819	0.800	-	1386	1378
30	0.765	0.743	0.891	1269	1257
35	0.710	0.711	-	1149	1184
40	0.655	0.691	0.757	1033	1115
45	0.601	0.685	-	922	1078
50	0.546	0.693	0.686	811	1055

* From standard enthalpies of formation [8].

From standard enthalpies of reaction and tabulated heat capacities [8].

The maximum heat output predicted from standard enthalpies of reaction is 895 J g^{-1} and occurs at the stoichiometric point of 18% Fe/BaO_2. At higher percentages of fuel the experimental enthalpy of reaction exceeds the predicted values, possibly since additional reactions giving mixed oxide products occur concurrently.

9.6 Twin thermocouple results

A dual-thermocouple system (see Section 4.2) was used to determine the reproducibility of the temperature profiles at various positions in the pyrotechnic mixture down the length of the channel, the associated burning rate of the composition, and the overall heat output.

The reproducibility of profiles at various positions in the 20% Fe/BaO_2 pyrotechnic composition was reasonable and is shown in Figure 9.16. The burning-rates obtained from the time differences of a corresponding point on two profiles and the distance between the thermocouples showed fair agreement with the burning-rates recorded simultaneously by the infrared photodiode system (Table 9.4). The decreased burning-rates of the 20% Fe/BaO_2 system relative to the values indicated in Table 9.1 may be attributed to the ageing of the mixtures prior to combustion.

TABLE 9.4: Comparison of burning-rates obtained by photodiode and twin thermocouple systems

Composition	Twin thermocouple Burning-rate/[mm s^{-1}]	Photodiode Burning-rate/[mm s^{-1}]
20% Fe/BaO_2	12.0 ± 0.6	12.9 ± 1.6
50% Fe/BaO_2	7.7 ± 0.6	6.7 ± 1.1

Calorimetric information determined from the U_{ad} values of the profiles (e.g., Figure 9.17 for 50% Fe/BaO_2) from the thermocouple embedded in the reaction mixture (Profile 1) and from the thermocouple attached to the channel wall (Profile 2) is shown in Table 9.5. Values of Q are averages of three or more experiments.

TABLE 9.5: Comparison of enthalpies of reaction calculated from the different profiles (see text)

Composition	Profile 1 (Expt) U_{ad}/[K]	Profile 1 Q/[J (g mixt)$^{-1}$]	Profile 2 (Expt) U_{ad}/[K]	Profile 2 Q/[J (g mixt)$^{-1}$]	Calculated# [8] Q/[J (g mixt)$^{-1}$]
20% Fe/BaO_2	1460 ± 97	821 ± 17	270 ± 63	834 ± 48	784→874
50% Fe/BaO_2	859 ± 48	524 ± 18	197 ± 39	530 ± 38	490→546

The tabulated values of the enthalpy of formation in the literature are variable (range shown taken from various sources [8,33]). The lower values of the range shown in Table 9.5 have been used in this study.

9.7 Kinetics from temperature profiles

Temperature profiles for Fe/BaO_2 compositions were converted into their component power functions as described in detail in Section 5.1 and Appendix 12. For all the Fe/BaO_2 compositions used, only one major peak was observed for the reaction power function, G. The activation energies and Arrhenius pre-exponential factors and apparent orders of reaction for the compositions are given in Table 9.6.

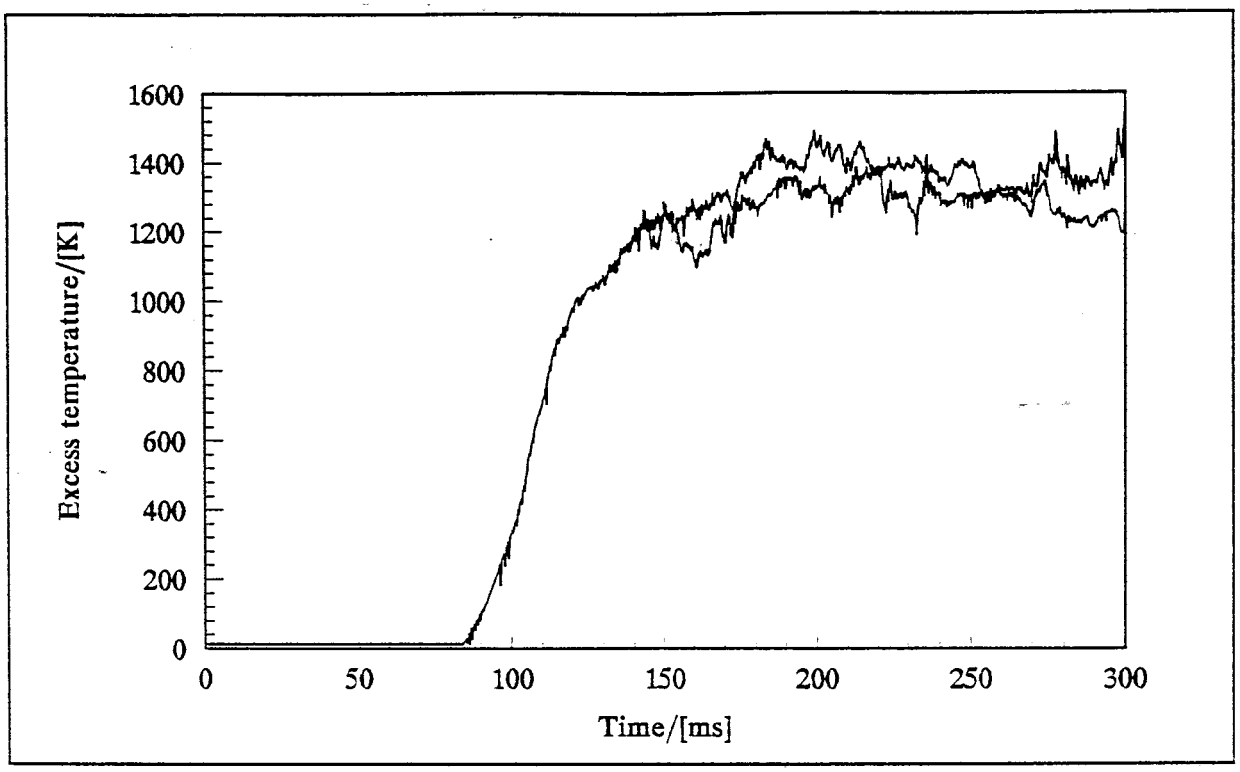

FIGURE 9.16: Reproducibility of temperature profiles at different positions within the combustion channel

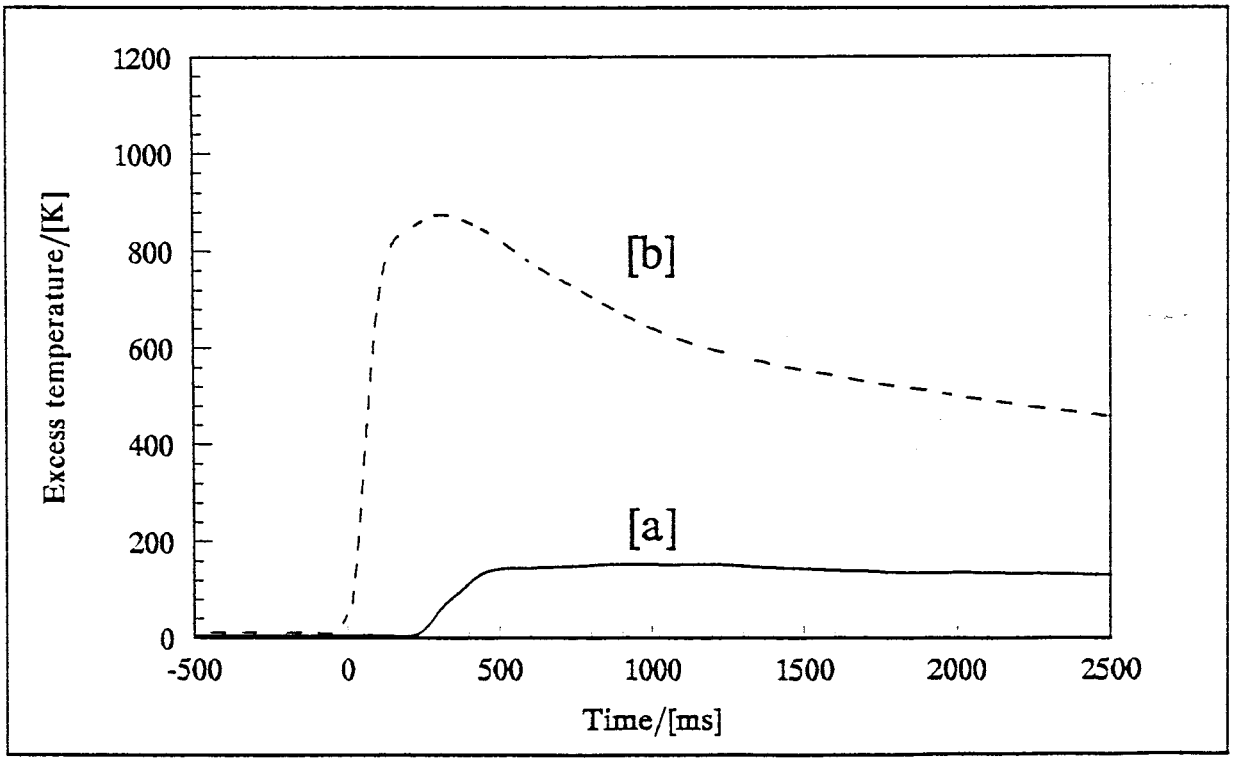

FIGURE 9.17: Temperature profiles captured from thermocouples (a) in contact with the channel, and (b) embedded in the composition during combustion

TABLE 9.6: Kinetic parameters obtained for combustion of the Fe/BaO_2 pyrotechnic system

% Fe	E_a/[kJ mol^{-1}]	A/[s^{-1}]	n
15	13.0±1.5	101±15	0.50±0.06
20	13.8±1.8	165±20	0.72±0.09
25	10.2±0.5	120±3	0.51±0.04
30	13.9±1.7	221±67	0.55±0.07
35	15.5±2.6	218±42	0.58±0.07
40	10.7±2.0	271±72	0.64±0.08
45	7.1±0.8	68±12	0.58±0.10
50	10.2±2.1	110±19	0.71±0.19

The apparent activation energies are all low values characteristic of diffusion-controlled processes, with lowest values at the highest percentages of fuel. The apparent orders of reaction, n, are characteristic of contracting-geometry models of solid state reactions [170].

9.8 Thermal conductivity and burning-rate

The linear burning-rate, v, of a composition is related to the rise-time, t_r, of the corresponding temperature profile by the expression [131]:

$$v = \sqrt{\frac{\lambda}{c\rho t_r}}$$

Where λ is the thermal conductivity, c the heat capacity and ρ the density. Each of these quantities depends upon the composition and, to various extents, on the temperature. Values of c and ρ for the mixtures at 298 K may be calculated from tabulated values for the components [8]. Sometimes sufficient information is available to predict values of c at the combustion temperature. Values of λ are more difficult to estimate, especially at high temperatures, and in this study values were estimated using the Kunii-Smith [176] model (Appendix 13) which has been shown [143] to produce fair agreement with the limited experimental data available.

In Table 9.7, values of λ, c and ρ for the range of Fe/BaO_2 compositions have been estimated. These may be combined to give thermal diffusivities, $D=\lambda/(\rho c)$. The experimental rise-times, $t_{r,exp}$, are then combined with the D values to give the calculated burning-rates, v_{calc}, which are compared with experimental burning-rates, v_{exp}.

TABLE 9.7: Comparison of experimental and predicted burning-rates

Fe/BaO_2	λ	c	ρ	D	$t_{r\,exp}$	v_{exp}	v_{calc}	D_{eff}
%	$W\ m^{-1}\ K^{-1}$	$J\ g^{-1}\ K^{-1}$	$g\ m^{-3}$	$m^2\ s^{-1}$	ms	$mm\ s^{-1}$	$mm\ s^{-1}$	$m^2\ s^{-1}$
15	0.221	0.531	4.10×10^{6}	1.0×10^{-7}	2.2	10.6	6.7	2.5×10^{-7}
20	0.216	0.573	4.01×10^{6}	9.4×10^{-8}	1.6	18.1	7.7	5.2×10^{-7}
25	0.153	0.591	3.67×10^{6}	7.1×10^{-8}	1.2	20.6	7.7	5.1×10^{-7}
30	0.123	0.603	3.50×10^{6}	5.8×10^{-8}	0.9	39.1	8.0	1.4×10^{-6}
35	0.150	0.618	3.80×10^{6}	6.4×10^{-8}	1.1	25.5	7.6	7.2×10^{-7}
40	0.155	0.634	3.92×10^{6}	6.2×10^{-8}	1.6	14.4	6.2	5.3×10^{-7}
45	0.146	0.652	3.88×10^{6}	5.8×10^{-8}	1.9	8.0	5.5	1.2×10^{-7}
50	0.121	0.673	3.46×10^{6}	5.2×10^{-8}	2.5	8.4	4.6	1.8×10^{-7}

Agreement between values of v_{calc} and of v_{exp} is, at best, only fair at the extremes of the composition range. The fact that the experimental and calculated values of the burning-rates are different may be explained if the effective thermal diffusivities, under combustion conditions (see Table 9.7), are greater than those predicted, through increased thermal conductivities and/or decreased heat capacities at higher temperatures.

10. COMBUSTION OF THE Fe/SrO_2 SYSTEM:

10.1 Reproducibility

Compositions containing from 20 to 55% Fe by mass sustained combustion under compaction. This range is similar to that found for Fe/BaO_2 (15 to 50%). Figure 10.1 shows the reproducibility of temperature profiles of the 25% Fe/SrO_2 composition. Comparison of these profiles with those for Fe/BaO_2 (Figure 9.1) shows that U_{max} values are about 200°C lower for the Fe/SrO_2 composition, that the overall temperature rises take place over a longer time scale, and that the initial rise region of the profile may involve at least two stages. The 10-90% times were ~250 ms (compared to ~80 ms for the Fe/BaO_2 system (see Section 9.2)). An example of the effect of smoothing on a typical (25% Fe/SrO_2) raw profile is shown in Figure 10.2. The 25% Fe/SrO_2 composition was studied in preference to the 20% Fe/SrO_2 composition as the combustion behaviour was more reproducible. The rise time values, t_r, and the kinetic parameters were determined from the smoother, more reproducible, temperature profiles since only these profiles gave a single peak in the graph of the power function, G, as required for kinetic analysis. Such an analysis then, may represent an overall process, which, under some (as yet undetermined) conditions, may be resolved into contributing processes, or the continuity of the overall process may be being disrupted by some unpredictable physical effect.

This second interpretation was assumed in this study, in the absence of evidence for the first explanation.

10.2 Effects of composition and of compaction

Variation of the composition changes the shape of the temperature profiles (Figure 10.3) and the maximum temperatures reached by the reaction (Figure 10.4). Linear burning-rates ranged from 4 to 9 mm s^{-1}, compared to 6 to 42 mm s^{-1} for Fe/BaO_2. These burning-rates are of approximately the same magnitude as those measured by Spice and Staveley [4,7] for the Fe/BaO_2 system, suggesting that the coalescense of the SrO_2 particles decreases burning-rates in the same manner as the use of larger particle sizes did in earlier research [4,7]. Figure 10.5 shows that the burning-rate reaches a maximum between 35 and 40%, whilst the heat output reaches a maximum between 20 and 25%.

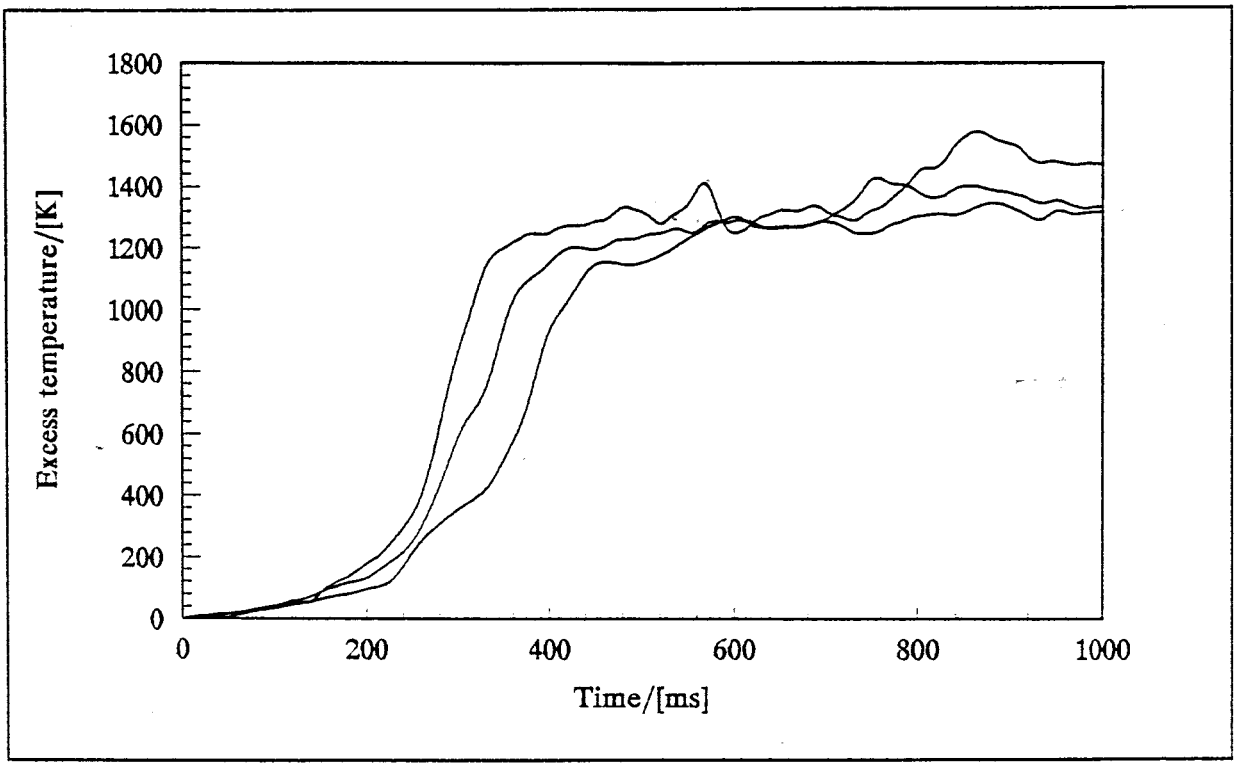

FIGURE 10.1: Reproducibility of temperature profiles of 25% Fe/SrO_2

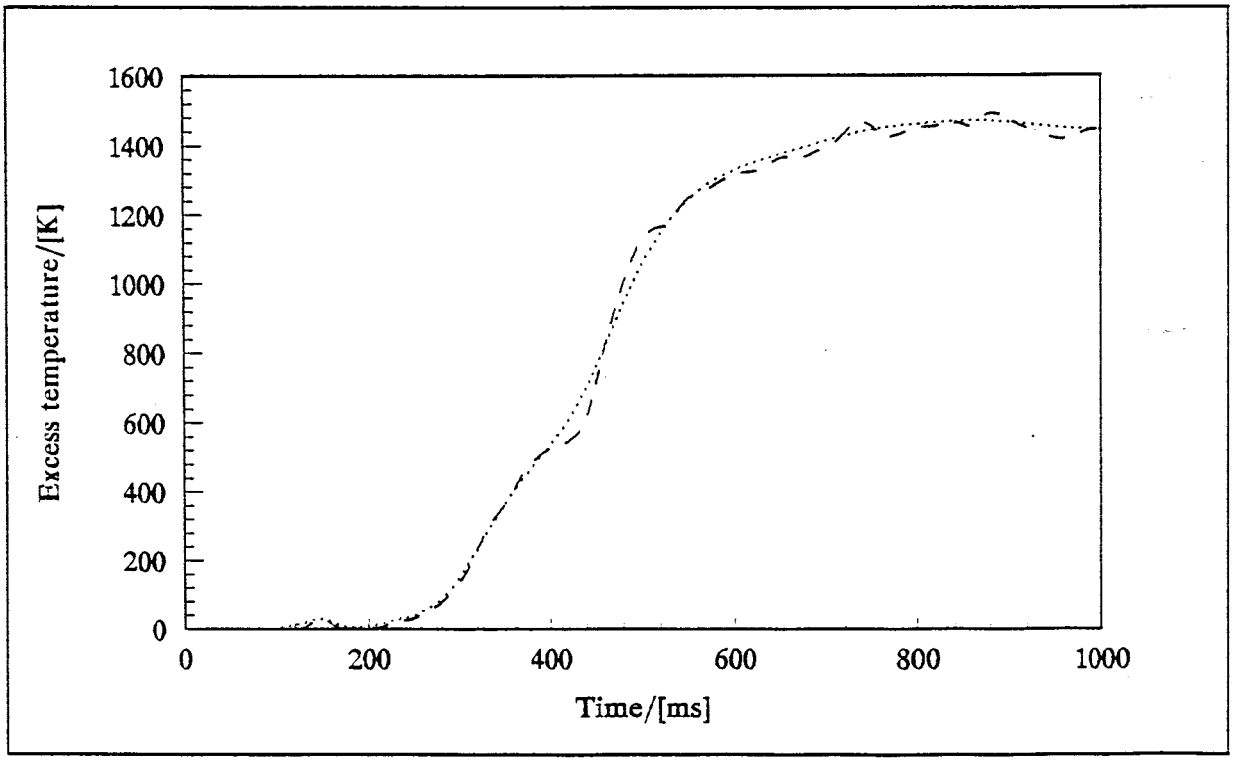

FIGURE 10.2: Effect of smoothing algorithm on a typical temperature profile of 25% Fe/SrO_2

TABLE 10.1: The effects of composition and compaction on the burning-rates of the Fe/SrO_2 system

	Burning-rates/[mm s^{-1}] at different compactions			
% Fe	0 MPa	55 MPa	110 MPa	165 MPa
20	3.3±1.0	3.6±1.1	3.5±0.9	-
25	6.7±1.8	6.8±1.2	7.0±1.3	5.7±1.1
30	6.8±1.7	7.4±2.0	7.4±1.8	6.2±1.3
35	6.8±1.9	7.5±1.8	7.4±1.7	6.7±1.5
40	7.0±2.1	8.3±1.2	7.8±1.5	6.8±1.4
45	6.5±1.1	6.5±0.6	6.0±0.7	5.4±1.1
50	5.8±1.2	6.3±0.8	5.5±1.1	4.8±0.9
55	5.4±1.2	6.0±0.9	5.2±1.0	4.5±1.2

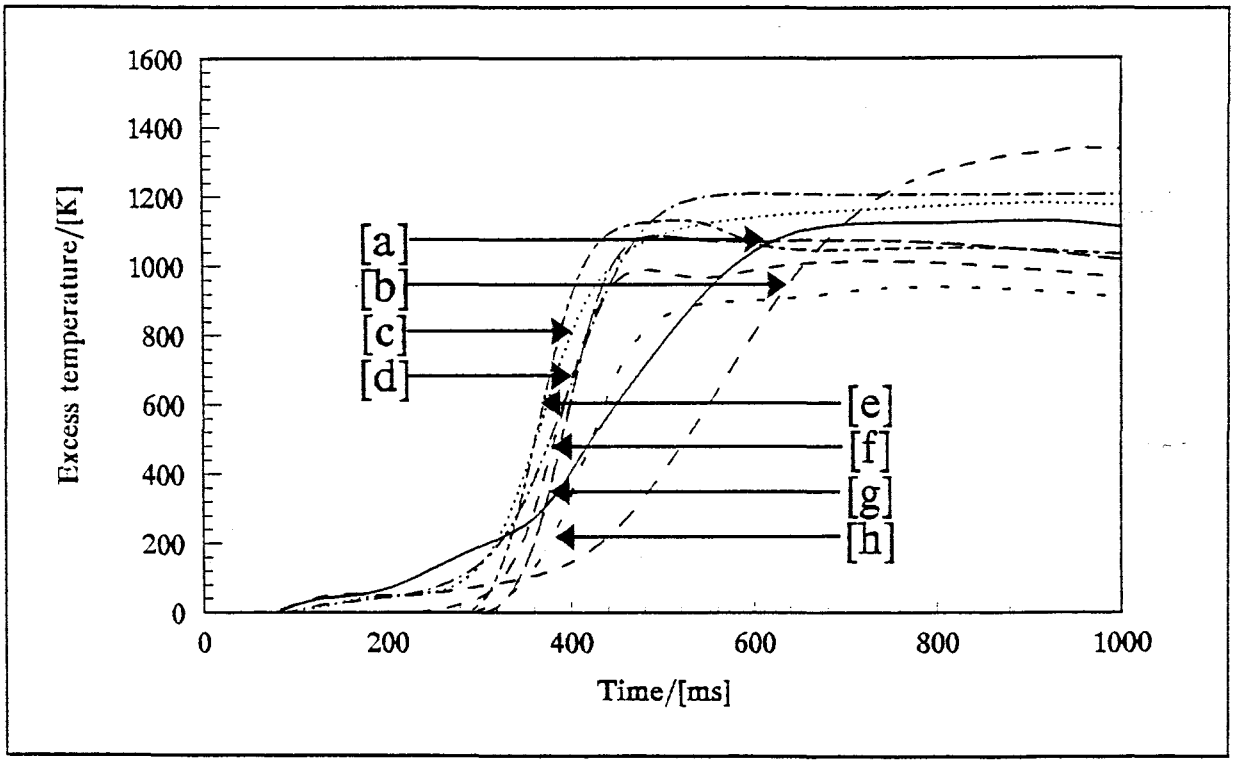

FIGURE 10.3: Effect of composition on temperature profiles of Fe/SrO_2 [a]:20%, [b]:25%, [c]:30%, [d]:35%, [e]:40%, [f]:45%, [g]:50% and [h]: 55%

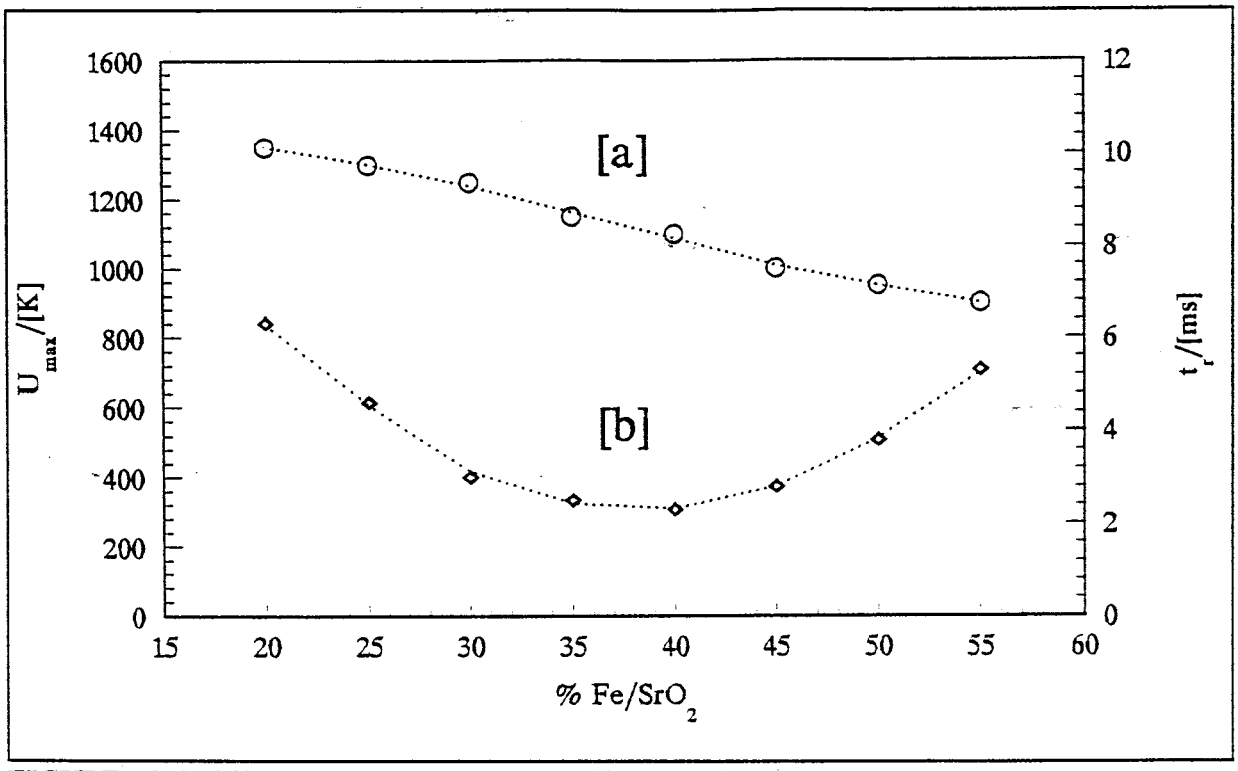

FIGURE 10.4: Effect of composition on [a]: U_{max} and [b]: t_r

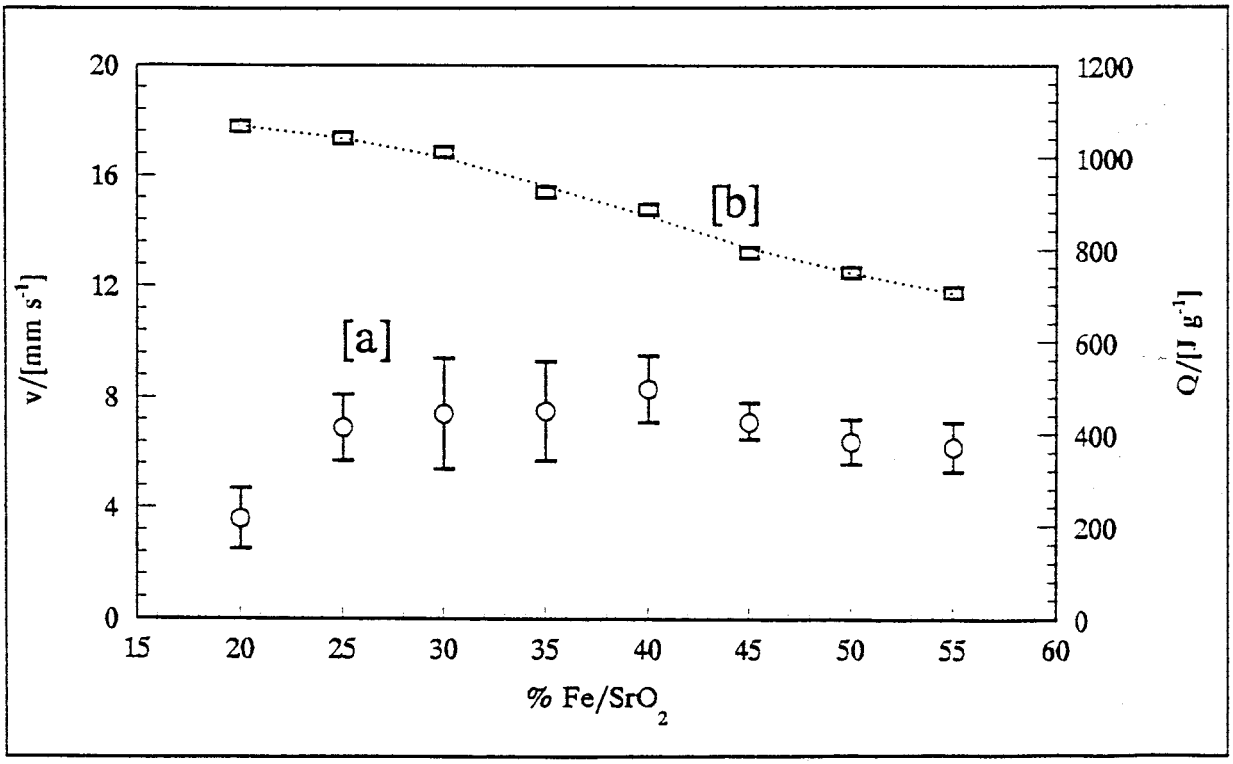

FIGURE 10.5: Effect of composition on [a]: v_{exp} and [b]: Enthalpy of reaction of Fe/SrO_2

Profiles for samples of 25% Fe/SrO_2 compacted under various pressures are shown in Figure 10.6. The complex nature of the rise region is clearly seen. Compaction increased the overall steepness of rise of the temperature profiles, but had relatively little effect on the burning-rate (Figure 10.7), compared with that observed for Fe/BaO_2. The combined effects of composition and compaction are illustrated in Figure 10.7. A tendency of the SrO_2 particles to coalesce on compaction was noted, which could result in uneven dispersal of the peroxide amongst the Fe particles. The effect of compaction on systems with particles larger than the optimum particle-size [5] is to increase the interparticle contact while still allowing sufficient interstitial volume for gas flow ahead of the burning-front [13,14].

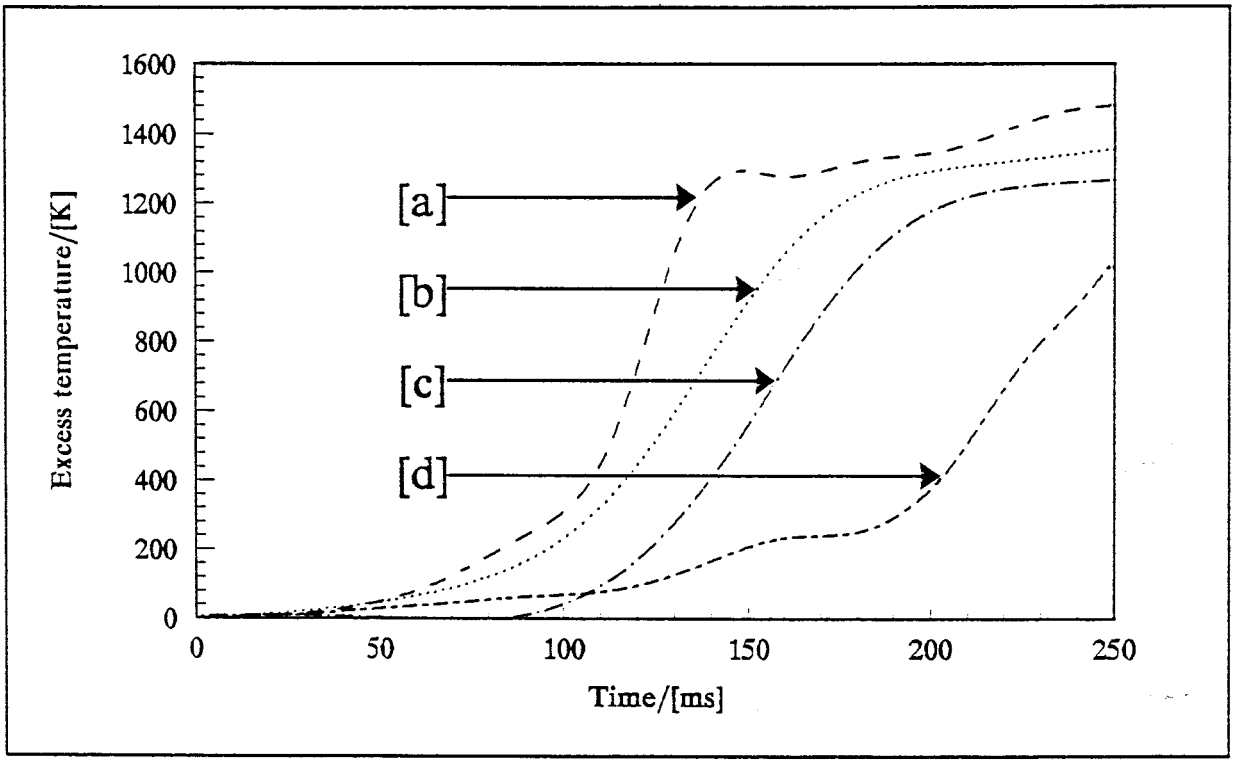

FIGURE 10.6: The effect of compaction on the shape of temperature profiles of 25% Fe/SrO_2 [a]:165 MPa, [b]:110 MPa, [c]:55 MPa and [d]:0 MPa

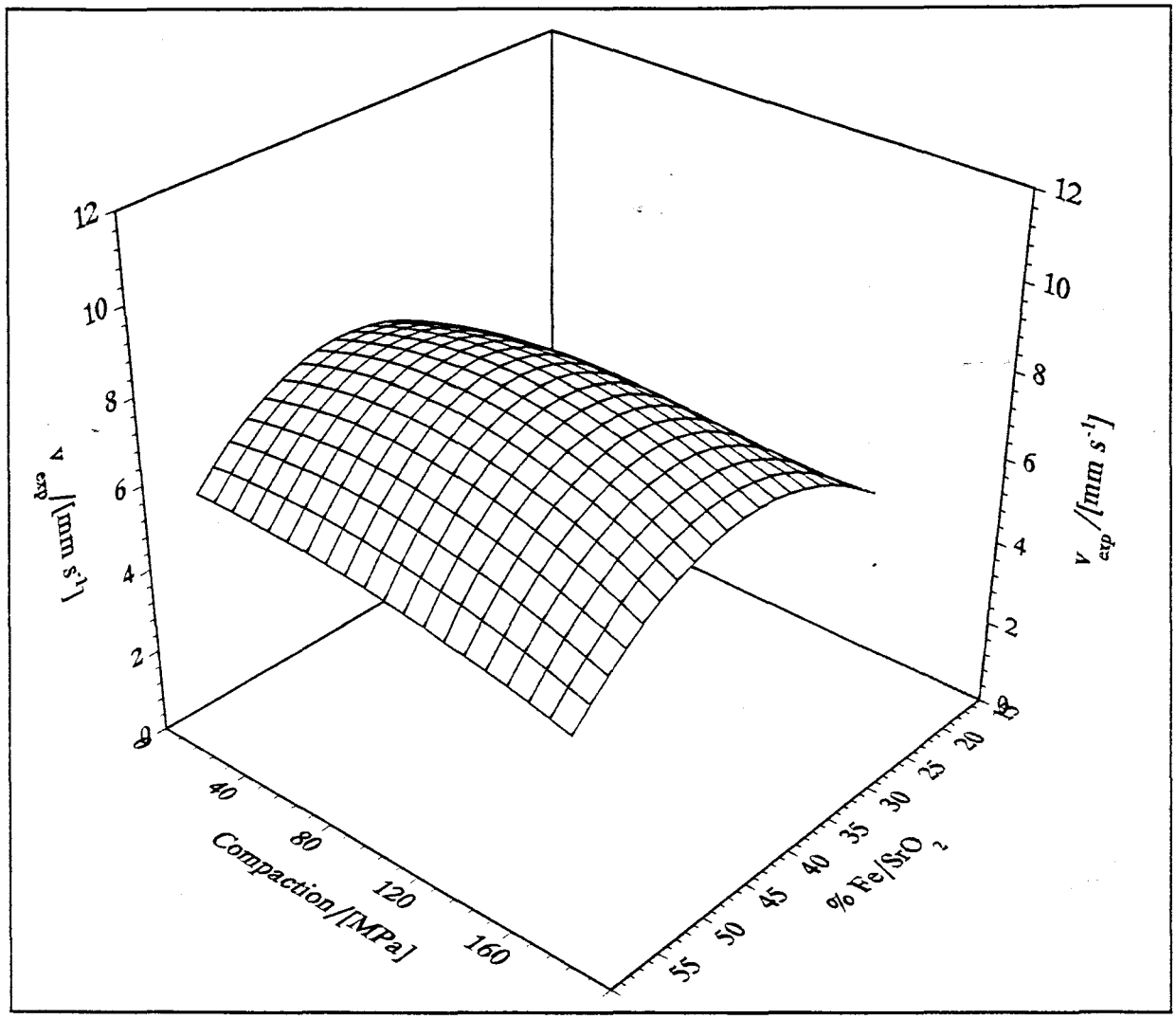

FIGURE 10.7: 3D-surface representation of the effects of compaction and composition on the burning-rates of the Fe/SrO_2 system

10.3 Effect of the diameter of the thermocouple wire

The steepness of the rise region of temperature profiles (Figure 10.8) and the values of U_{max} recorded (Figure 10.9) decreased as the diameter of the thermocouple wire used was increased, owing to the faster response times of the thinner thermocouples and decreased heat losses by conduction along the thermocouple wire. The use of 0.05 mm thermocouples caused practical difficulties, as it had for the Fe/BaO_2 systems, in that excessive noise was again registered from movement of the junction during passage of the combustion wave. Correction factors for determination of kinetic data were thus obtained by extrapolating data measured with thicker thermocouples to zero thermocouple thickness (Figures 10.9 and 10.10). A factor, for data measured with a 0.1 mm thermocouple, of 1.2 was used to correct the U_{max} values, and a factor of 0.17 for the t_r values.

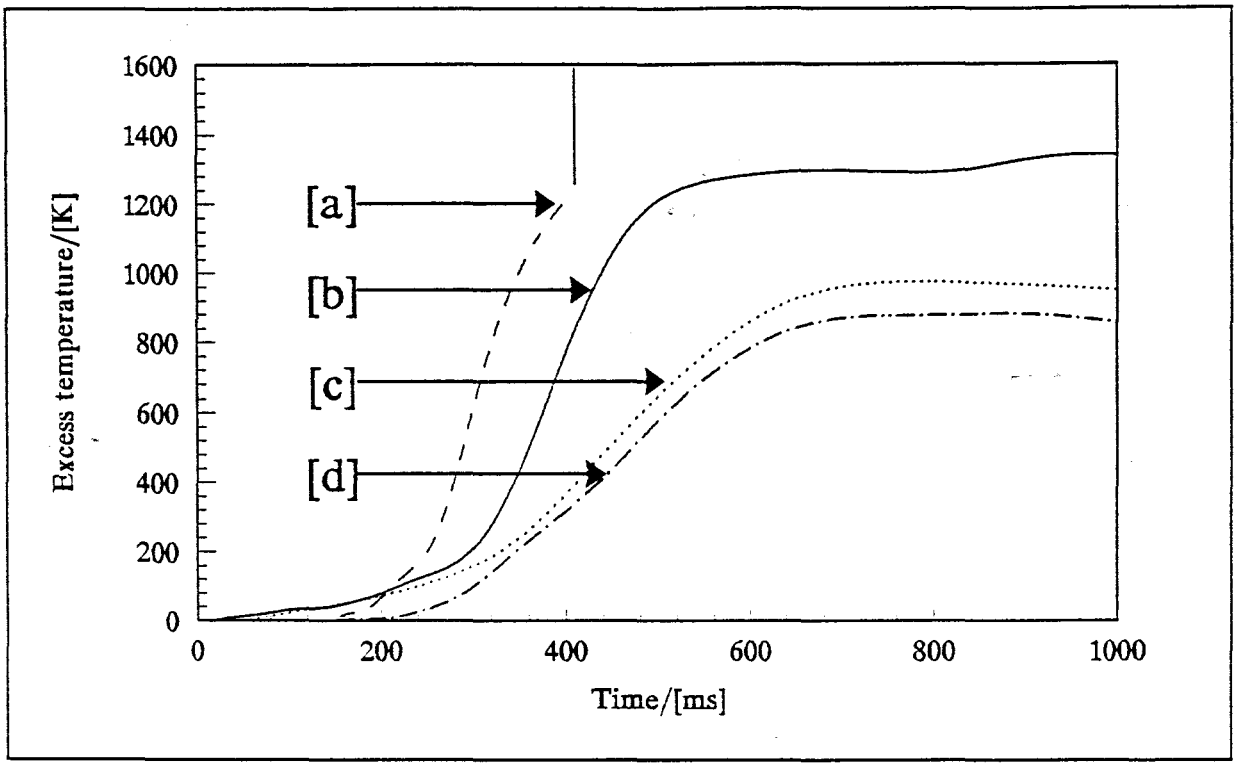

FIGURE 10.8: The effect of thermocouple thickness on temperature profiles of 25% Fe/SrO_2 [a]:0.05 mm, [b]:0.1 mm, [c]:0.2 mm and [d]: 0.3 mm

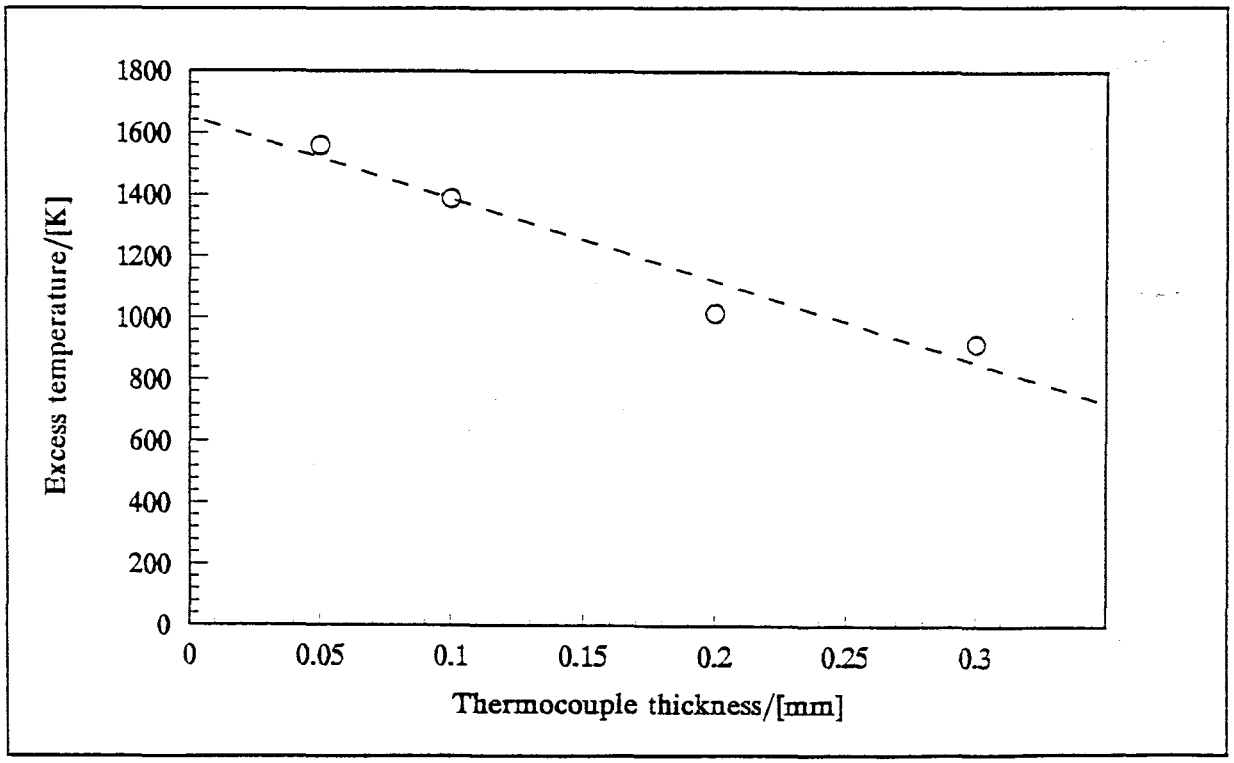

FIGURE 10.9: The effect of thermocouple thickness on U_{max} of 25% Fe/SrO_2 systems

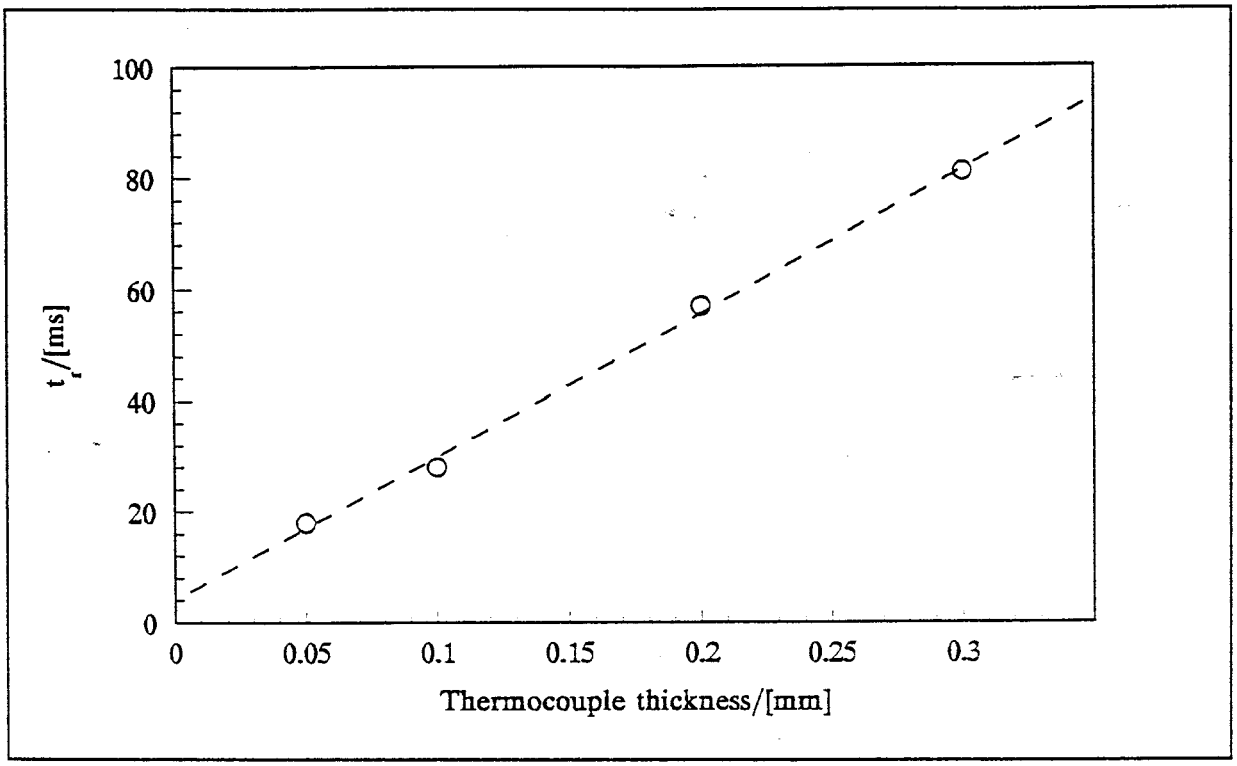

FIGURE 10.10: The effect of thermocouple thickness on t_r of 25% Fe/SrO_2 systems

10.4 Effect of additives

Several substances were introduced separately in small amounts (1 to 10% by mass) into the binary 25% Fe/SrO_2 composition as additives, in a similar manner to the Fe/BaO_2 system study. These substances were: SrO, $Sr(OH)_2$ and $SrCO_3$ (which are likely contaminants of SrO_2); Fe_2O_3 (formed by some oxidation of Fe); water (always present on exposure of compositions to the surrounding atmosphere); and Al_2O_3 (a supposedly inert substance, expected only to affect combustion by its action as a diluent).

Al_2O_3:

Addition of between 1 and 5% Al_2O_3 to the 25% Fe/SrO_2 composition decreased the burning-rate. The temperature profiles are shown in Figure 10.11. Combustion was not supported when more than 5% Al_2O_3 was added.

SrO:

Combustion could still be initiated with up to 5% by mass of SrO as additive. Above this level initiation of combustion failed. The decrease in values of U_{max} and the decrease in rise-time values, was more pronounced than for the addition of Al_2O_3. Profiles are shown in Figure 10.12.

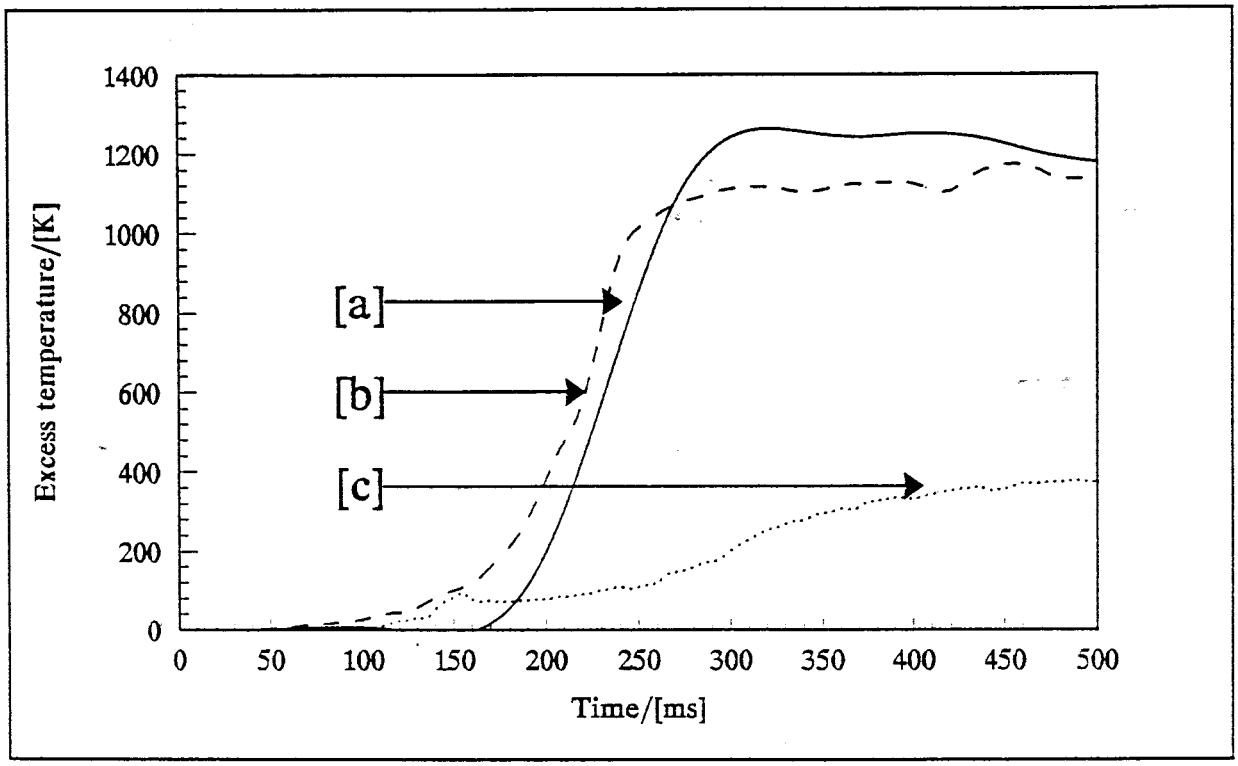

FIGURE 10.11: Effect of Al_2O_3 as additive on temperature profiles of 25% Fe/SrO_2 [a]:0%, [b]:1% and [c]:5% by mass

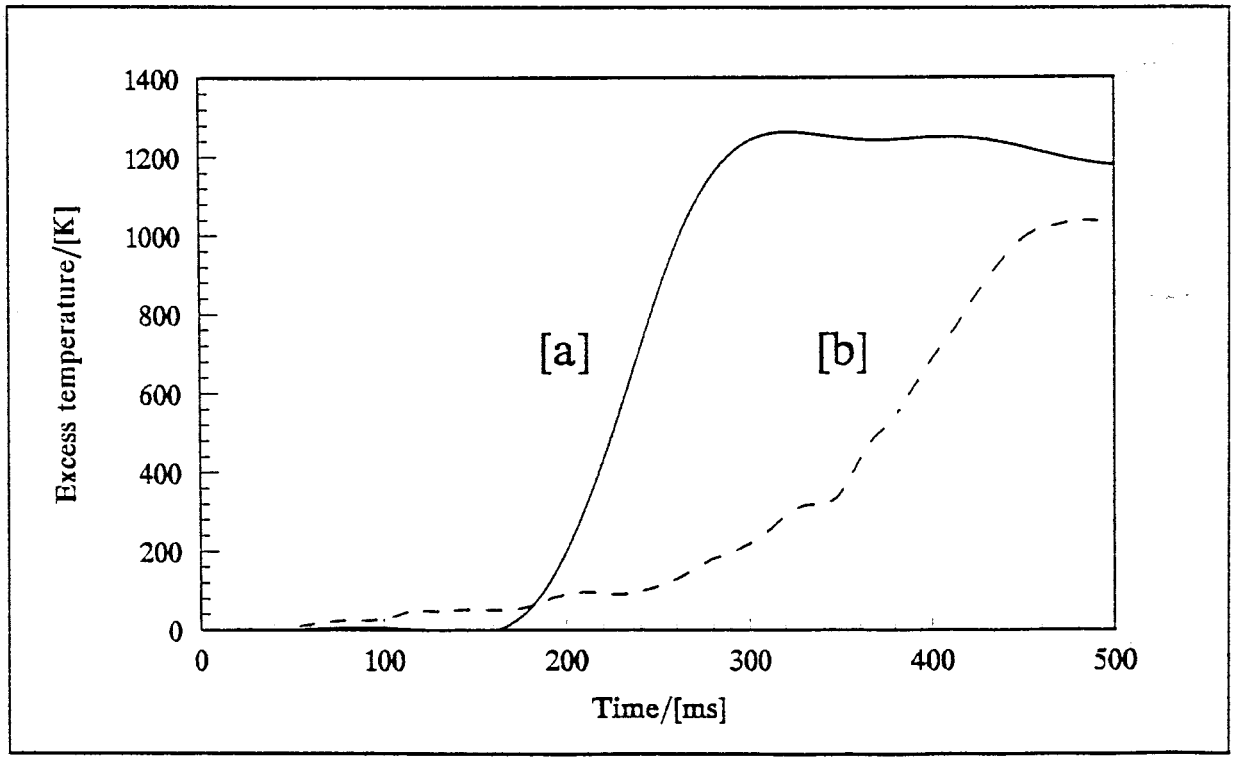

FIGURE 10.12: Effect of SrO as additive on temperature profiles of 25% Fe/SrO_2 [a]:0% and [b]:1% by mass

$SrCO_3$:

Unlike the BaO_2 system, where $BaCO_3$ had the smallest effect on the burning-characteristics of the material, $SrCO_3$ appeared to have a major effect on the burn profile (Figure 10.13). When added in quantities exceeding 1% by mass, mixtures containing $SrCO_3$ failed to support combustion. $SrCO_3$ formation on the surfaces of SrO_2 particles may have an even greater effect on combustion than the presence of separate $SrCO_3$ particles dispersed in the mixture.

$Sr(OH)_2$:

As found for the Fe/BaO_2 system, the presence of the hydroxide has a large effect on temperature profiles. Mixtures containing 1% of the hydroxide did not support combustion. This effect is related to the sensitivity of the system to the presence of water (see below).

Fe_2O_3:

The addition of up to 5% by mass of Fe_2O_3 produced mixtures which still supported combustion. The overall rise times of the temperature profiles (Figure 10.14) for the mixtures steadily increased as the percentage of additive increased. Above 5% Fe_2O_3, the propagation of combustion became uncertain.

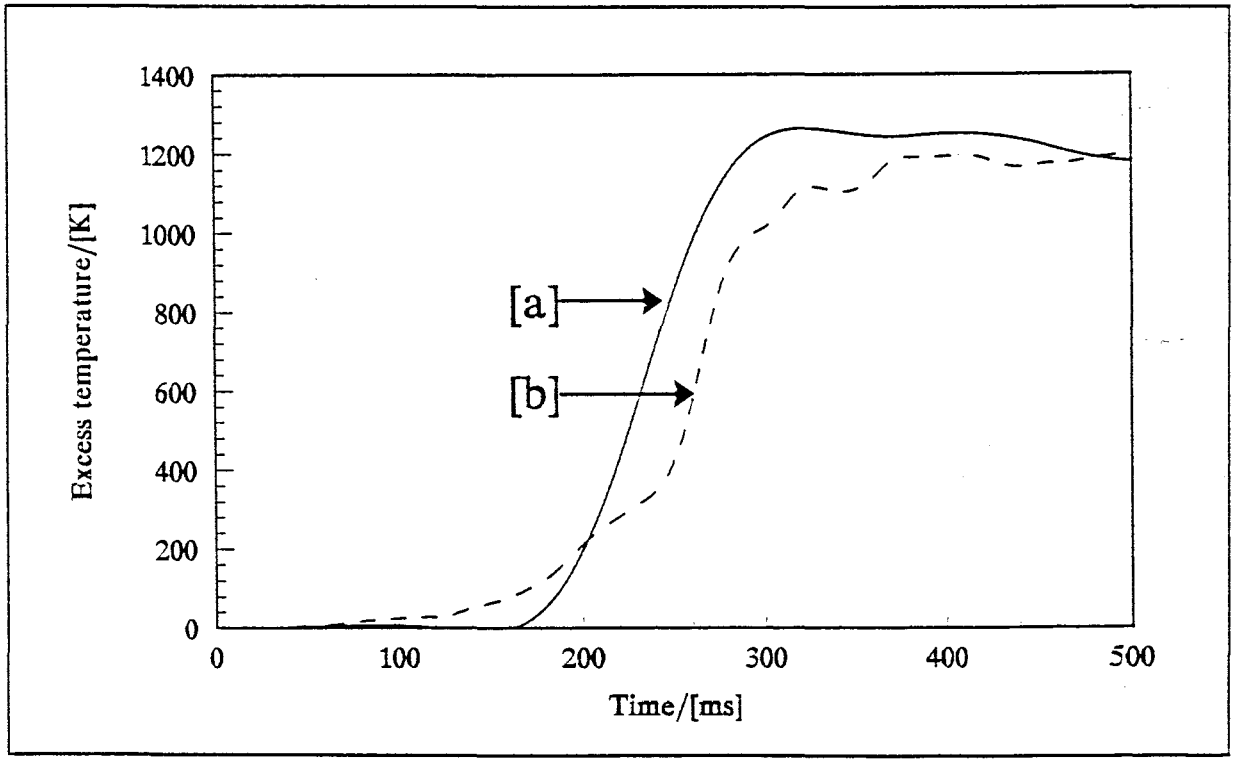

FIGURE 10.13: The effect of $SrCO_3$ as an additive on temperature profiles of 25% Fe/SrO_2 [a]:0% and [b]:1% by mass

Water:

To allow for complete dispersion of water throughout the sample, a standing time of not less than 12 hours was used as was done for the the Fe/BaO_2 system. Combustion could not be initiated in any of the water containing systems (the minimum addition was 1% H_2O by mass). This sensitivity of combustion to the presence of water is similar to that found for the Fe/BaO_2 system and is also supported by the sensitivity of both combustions to the presence of the hydroxides.

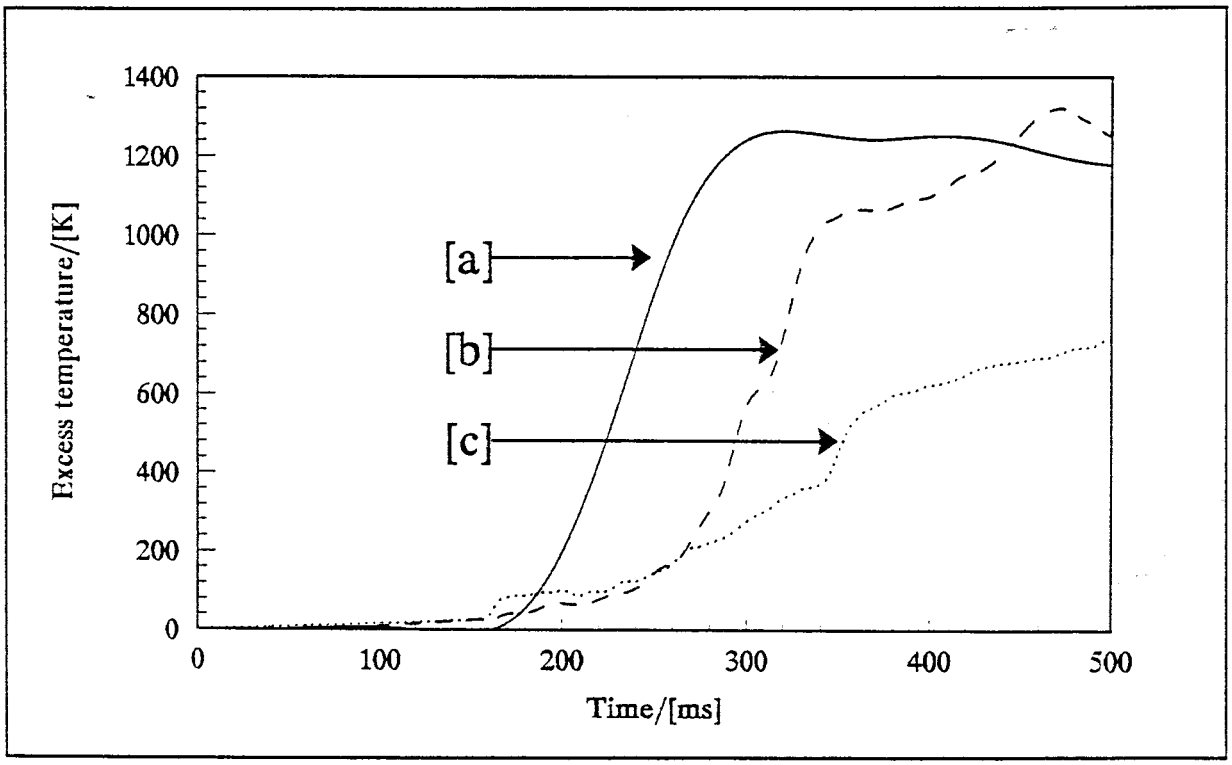

FIGURE 10.14: The effect of Fe_2O_3 as an additive on temperature profiles of 25% Fe/SrO_2 [a]:0%, [b]:1% and [c]:5% by mass

TABLE 10.2: The effect of selected additives on burning-rates and maximum excess temperatures of the 25% Fe/SrO_2 system

Additive	Mass %	$v_{observed}$ [mm s^{-1}]	U_{max} [K]
Al_2O_3	0	6.8±1.8	1265±30
	1	4.5±1.2	1190±35
	5	1.6±0.8	1185±40
SrO	0	6.8±1.8	1265±30
	1	5.8±1.5	1055±40
	5	-	-

Additive	Mass %	$v_{observed}$ [mm s^{-1}]	U_{max} [K]
$SrCO_3$	0	6.8±1.8	1265±30
	1	6.3±1.7	1220±35
	5	-	-
$Sr(OH)_2$	0	6.8±1.8	1265±30
	1	-	-
	5	-	-
Fe_2O_3	0	6.8±1.8	1265±30
	1	5.3±1.4	1090±40
	5	3.2±0.8	710±45
Water	0	6.8±1.8	1265±30
	1	-	-

The additives generally slow the overall rate of temperature rise and hence resolve more clearly the overlapping stages. The greatest slowing effect is on the rise of the initial stage. This rise (see Section 15) is due to conduction of heat ahead of the burning-front, and thermal conduction will be decreased by the presence of inert particles.

10.5 Thermochemistry

The simplest reactions likely to be involved in combustion of the Fe/SrO_2 system are:

$$2Fe(s) + 3SrO_2(s) \rightarrow Fe_2O_3(s) + 3SrO(s) \quad \text{(i)}$$

$$3Fe(s) + 4SrO_2(s) \rightarrow Fe_3O_4(s) + 4SrO(s) \quad \text{(ii)}$$

$$Fe(s) + SrO_2(s) \rightarrow FeO(s) + SrO(s) \quad \text{(iii)}$$

Assuming 100% pure reactants, the following stoichiometric compositions (% by mass of Fe) were calculated for the above reactions: (i) 23.74%, (ii) 25.93% and (iii) 31.83%. For 85% pure SrO_2, these values decrease to:(i) 20.9%, (ii) 22.9% and (iii) 28.4%. The predicted heat of reaction for 100% pure reactants, calculated from tabulated enthalpies of formation [8] for reaction (i) is:

$$\Delta H^0_{reaction} = (-822.2)+3(-603.3) - 2(0)- 3(-654.4)$$
$$= -668.9 \text{ kJ mol}^{-1}$$
$$= -334.5 \text{ kJ (mol Fe)}^{-1}$$
$$= -223.0 \text{ kJ (mol } SrO_2)^{-1}$$
$$= -1.864 \text{ kJ (g } SrO_2)^{-1}$$

Since the stoichiometric mixture is 23.72% Fe, 1 g of mixture contains 0.7628 g SrO_2 (100% pure).

$\therefore$ Heat output, q = 1.864 x 0.7628 kJ (g mixt)$^{-1}$ = 1.42 kJ (g mixt)$^{-1}$

Converting to 85% purity, q = 1.21 kJ (g mixt)$^{-1}$.

It is likely that the simple products of the binary reaction continue to react as a result of the high temperatures present in the reaction (> 1000°C), forming ferrite products in the process. The enthalpies of formation of such products were not available.

$$Fe_2O_3(s) + SrO(s) \rightarrow SrFe_2O_4(s) \quad \text{(iv)}$$

$$FeO(s) + SrO_2(s) \rightarrow SrFeO_3(s) \quad \text{(v)}$$

$$Fe(s) + 2SrO_2(s) \rightarrow Sr_2FeO_4(s) \quad \text{(vi)}$$

$$FeO(s) + 2SrO(s) + SrO_2(s) \rightarrow Sr_3FeO_5(s) \quad \text{(vii)}$$

The tabulated enthalpy of formation of $SrTiO_3$, a structural analog of strontium ferrate, is -1674 kJ mol^{-1} [8]. The enthalpies of formation of the spinels formed with Mn and Mo, viz. $SrMnO_4$ and $SrMoO_4$, are negative [8], and of a similar magnitude to the simple product values.

The values of $\Delta H_{reaction}$, calculated from standard enthalpies of formation, for reaction (i) leading to simple oxide products, and the predicted adiabatic temperature rises calculated using temperature dependent values of heat capacities [8], are compared with the corresponding experimental quantities in Table 10.3.

TABLE 10.3: Comparison of the enthalpies of reaction for the Fe/SrO_2 pyrotechnic system determined from temperature profile analysis

% Fe/SrO_2 composition	ΔH/[kJ g^{-1}] Calculated*	ΔH/[kJ g^{-1}] Experimental	U_{ad}/[K] Calculated**	U_{ad}/[K] Experimental
20	1.197	1.067	1515	1350
25	1.188	1.041	1483	1300
30	1.109	1.011	1371	1250
35	1.030	0.924	1283	1150
40	0.951	0.887	1180	1100
45	0.871	0.793	1098	1000
50	0.792	0.751	1002	950
55	0.713	0.707	908	880

* From tables of standard enthalpies of formation [8]

** From standard enthalpies of reaction and tabulated heat capacities [8]

In the Fe/SrO_2 system, the stoichiometric composition for reaction (i) occurs at about 23%, which corresponds with the maximum heat output. The close agreement between the calculated and experimental values of the enthalpy of reaction support the suggestion that the chief products of the reaction are Fe_2O_3 + 3SrO. The identification of the species (Section 14.3) $Sr_3Fe_2O_{6.16}$ suggests that the enthalpies of reaction of simple oxides → mixed oxides may be small.

10.6 Twin thermocouple results

The dual-thermocouple system (Section 4.2) was used to determine the reproducibility of the temperature profiles at various positions in the pyrotechnic mixture down the length of the channel, the associated burning rate of the composition, and the overall heat output.

There was some lack of reproducibility of the profiles at various positions in the 20% Fe/SrO_2 pyrotechnic composition as shown in Figure 10.15. The burning-rates obtained (see Fe/BaO_2) showed good agreement with the burning-rates recorded simultaneously by the infrared photodiode system (Table 10.4).

TABLE 10.4: Comparison of burning-rates obtained by photodiode and twin thermocouple system

System:	Twin thermocouple Burning-rate/mm s^{-1}	Photodiode Burning-rate/mm s^{-1}
20% Fe/SrO_2	4.3±0.8	3.6±1.1
50% Fe/SrO_2	7.0±1.8	6.3±0.8

Calorimetric information determined from the U_{ad} values of the profiles (e.g., Figure 10.16 for 50% Fe/SrO_2) from the thermocouple embedded in the reaction mixture (Profile 1) and from the thermocouple attached to the channel wall (Profile 2) is shown in Table 10.5. Values of Q are averages of three or more experiments.

TABLE 10.5: Comparison of enthalpies of reaction calculated from the different profiles (see text)

Composition	Profile 1 (Expt) U_{ad}/[K]	Profile 1 Q/[J (g mixt)$^{-1}$]	Profile 2 (Expt) U_{ad}/[K]	Profile 2 Q/[J (g mixt)$^{-1}$]	Calculated† [8] Q/[J (g mixt)$^{-1}$]
20% Fe/SrO_2	1296±83	997±23	204±19	1003±72	1198→1203
50% Fe/SrO_2	860±30	640±22	179±47	672±61	792→796

† Far less variation of the tabulated values of enthalpy of formation was observed between literature sources [8] than for the BaO_2 system.

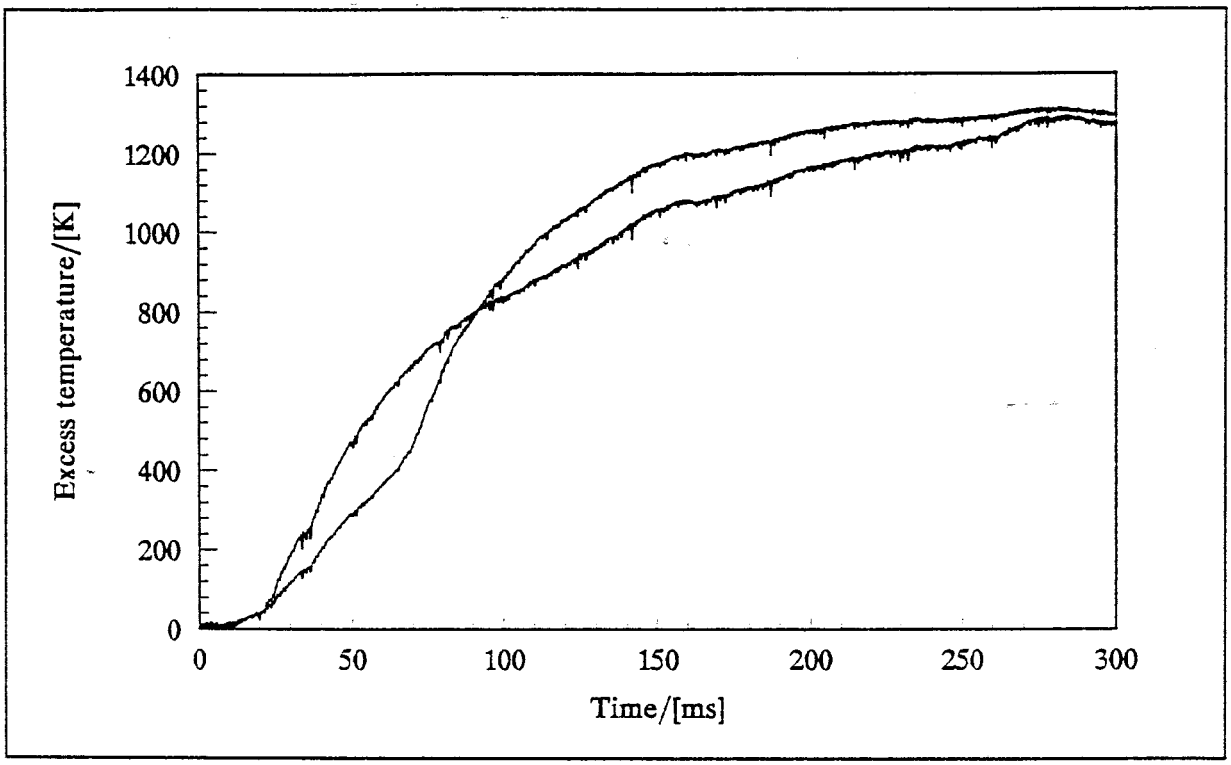

FIGURE 10.15: Reproducibility of temperature profiles at different positions within the combustion channel

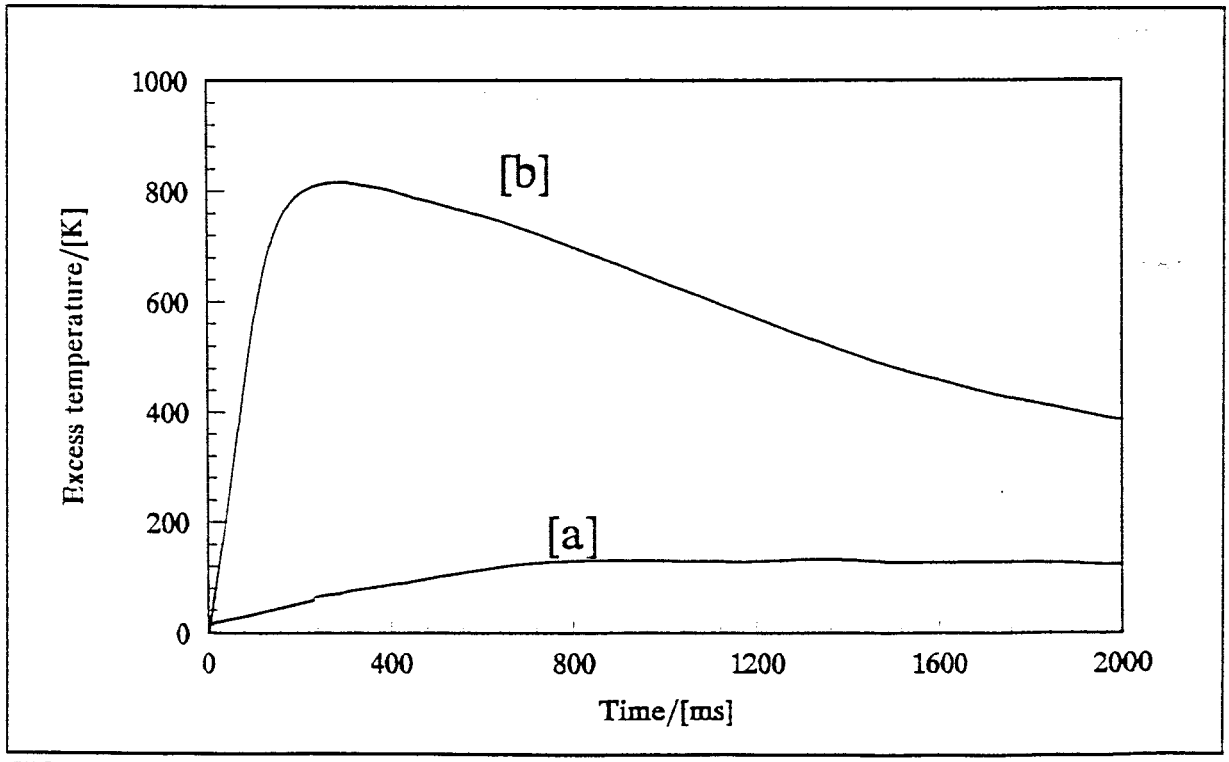

FIGURE 10.16: Temperature profiles captured from thermocouples (a) in contact with the channel and (b) embedded in the composition during combustion

10.7 Kinetics from temperature profiles

Temperature profiles for Fe/SrO_2 compositions were converted into their component power functions as described in detail in Section 5.1 and Appendix 12. For the more reproducible profiles of the Fe/SrO_2 system only one major peak was observed for the reaction power function, G. The activation energies, Arrhenius pre-exponential factors and apparent orders of reaction, n, for the compositions studied are given in Table 10.6.

TABLE 10.6: Optimised kinetic parameters determined for combustion of the Fe/SrO_2 pyrotechnic system

% Fe	E_a/[kJ mol^{-1}]	A/[s^{-1}]	n
20	20.1±2.3	196±30	0.67±0.04
25	27.0±2.4	191±50	0.73±0.12
30	36.7±8.3	190±9	0.67±0.04
35	41.5±9.2	169±37	0.58±0.11
40	43.5±4.4	349±32	0.63±0.06
45	32.8±3.1	349±35	0.56±0.07
50	31.7±7.1	233±21	0.71±0.05
55	27.9±6.7	257±62	0.75±0.18

The apparent activation energies are all low values characteristic of diffusion-controlled processes, and there is little variation with composition. The values of E_a are somewhat larger than those determined for the corresponding Fe/BaO_2 compositions (Table 9.6), and this result is discussed further in Section 15. The apparent orders of reaction, n, lie in a similar range (0.56 to 0.75) to those found for the Fe/BaO_2 compositions.

10.8 Thermal conductivity and burning-rate

In Table 10.7, values of λ, c and ρ for the range of Fe/SrO_2 compositions have been estimated. These may be combined to give thermal diffusivities, $D=\lambda/(\rho c)$. The experimental rise-times, t_{exp}, are then combined with the D values to give the calculated burning-rates, v_{calc}, which are compared with experimental burning-rates, v_{exp}, as was done in Section 9.8 for the Fe/BaO_2 compositions.

TABLE 10.7: Comparison of experimental and predicted burning-rates

Fe/SrO_2	λ	c	ρ	D	$t_{r\,exp}$	v_{exp}	v_{calc}	D_{eff}
%	$W\ m^{-1}\ K^{-1}$	$J\ g^{-1}\ K^{-1}$	$g\ m^{-3}$	$m^2\ s^{-1}$	ms	$mm\ s^{-1}$	$mm\ s^{-1}$	$m^2\ s^{-1}$
20	0.130	0.790	$3.19x10^6$	$5.2x10^{-8}$	6.3	3.6	2.9	$8.2x10^{-8}$
25	0.132	0.801	$3.28x10^6$	$5.0x10^{-8}$	4.6	6.8	3.3	$2.1x10^{-7}$
30	0.115	0.809	$3.22x10^6$	$4.4x10^{-8}$	3.0	7.4	3.8	$1.6x10^{-7}$
35	0.109	0.803	$3.17x10^6$	$4.3x10^{-8}$	2.5	7.5	4.1	$1.4x10^{-7}$
40	0.121	0.806	$3.36x10^6$	$4.5x10^{-8}$	2.3	8.3	4.4	$1.6x10^{-7}$
45	0.115	0.793	$3.37x10^6$	$4.3x10^{-8}$	2.8	6.5	3.9	$1.2x10^{-7}$
50	0.126	0.790	$3.56x10^6$	$4.5x10^{-8}$	3.8	6.3	3.4	$1.5x10^{-7}$
55	0.150	0.785	$3.86x10^6$	$5.0x10^{-8}$	5.3	6.0	3.1	$1.9x10^{-7}$

Agreement between values of v_{calc} and v_{exp} is poor. The fact that the experimental values recorded exceed the calculated burning-rates for all compositions, could be explained if the thermal diffusivities have been underestimated. The effective values of D have been calculated in Table 10.7 and such values could arise from more acute variations of λ (mainly), c and ρ with temperature than the dependence attributed.

11. COMBUSTION OF THE Zn/BaO_2 SYSTEM:

11.1 Effect of composition and compaction:

Zn/BaO_2 compositions supported combustion over a wide range (10-65% zinc) in the uncompacted state, but attempts to initiate combustion of material compacted at 50 MPa failed. Temperature profiles of uncompacted powder (Figure 11.1) showed a rapid rise to U_{max}, but due to the gaseous nature of the reaction, thicker (0.2 mm), less-sensitive thermocouples had to be used to remove effects of noise generated by physical movement of the thermocouple junction. Thermal analysis [Sections 6 to 8] confirmed that the zinc melts prior to reaction. The gaseous nature of the reaction is apparent from the flame generated by the mixture when ignition occurs and the ejection of product from the channel. The burning-rates of uncompacted mixtures, which ranged between 4 and 75 mm s^{-1}, reached a maximum between 45 and 50% zinc (Figure 11.5), while the maximum excess temperature, U_{max}, and enthalpy of reaction, q, reached a maximum below 30% Zn. Enhanced burning-rates of Zn compositions are expected under little or no compaction since the forward convective heat flow over short distances by gaseous Zn probably heats up unreacted powder ahead of the burn-front.

The composition range which supported combustion after compaction under a small amount of pressure (200 kPa) was decreased to 30-55% Zn by mass. The temperature profiles for pressed mixtures were more erratic, and the limited reproducibility of the profiles for 30% Zn/BaO_2 is shown in Figure 11.2. The complex effect of composition on combustion of mixtures compacted at 0.2 MPa is shown in Figure 11.3. Curve [f] is an example of very unstable combustion, possibly caused by the high vapour pressure of zinc in the system. Burning-rates were markedly decreased (Table 11.1). The variations of rise-times and U_{max} values with composition for mixtures compacted at 0.2 MPa are shown in Figure 11.4.

Profiles could only be captured for compositions compacted at 0 to 450 kPa (Figure 11.6). The samples compacted at 450 kPa exhibited unstable combustion, and compaction pressures of 0 and 200 kPa were selected for the study.

Only one range of particle size of zinc powder was used in the study. A major effect of the particle size on the burning-rate is not expected on account of the reaction mechanism (liquid fuel/solid oxidant and some vapour). The particle size of the oxidant was reported [6] to have little noticeable effect, within the limits of reproducibility, on the profiles of Mo and Mn/peroxide systems.

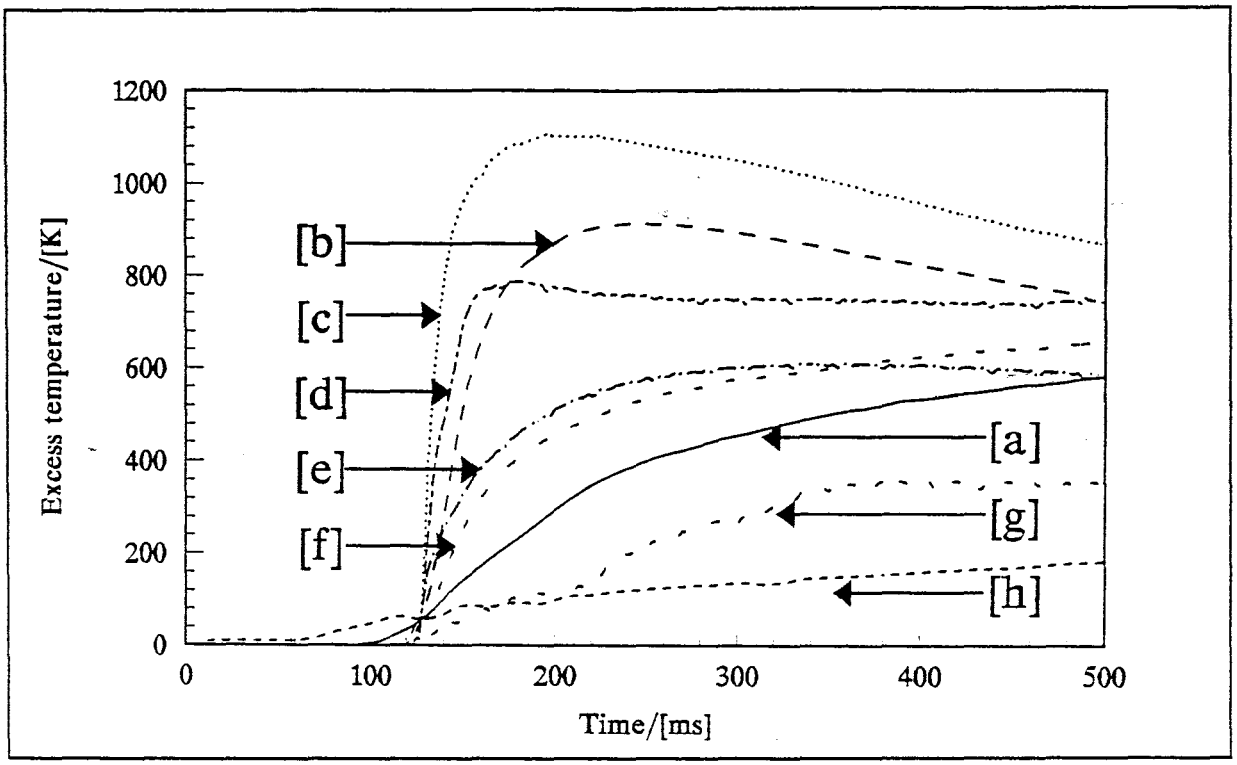

FIGURE 11.1: Effect of composition on temperature profiles of uncompacted Zn/BaO_2 [a]:20%, [b]:30%, [c]:35%, [d]:40%, [e]:45%, [f]:50%, [g]:55% and [h]:60%

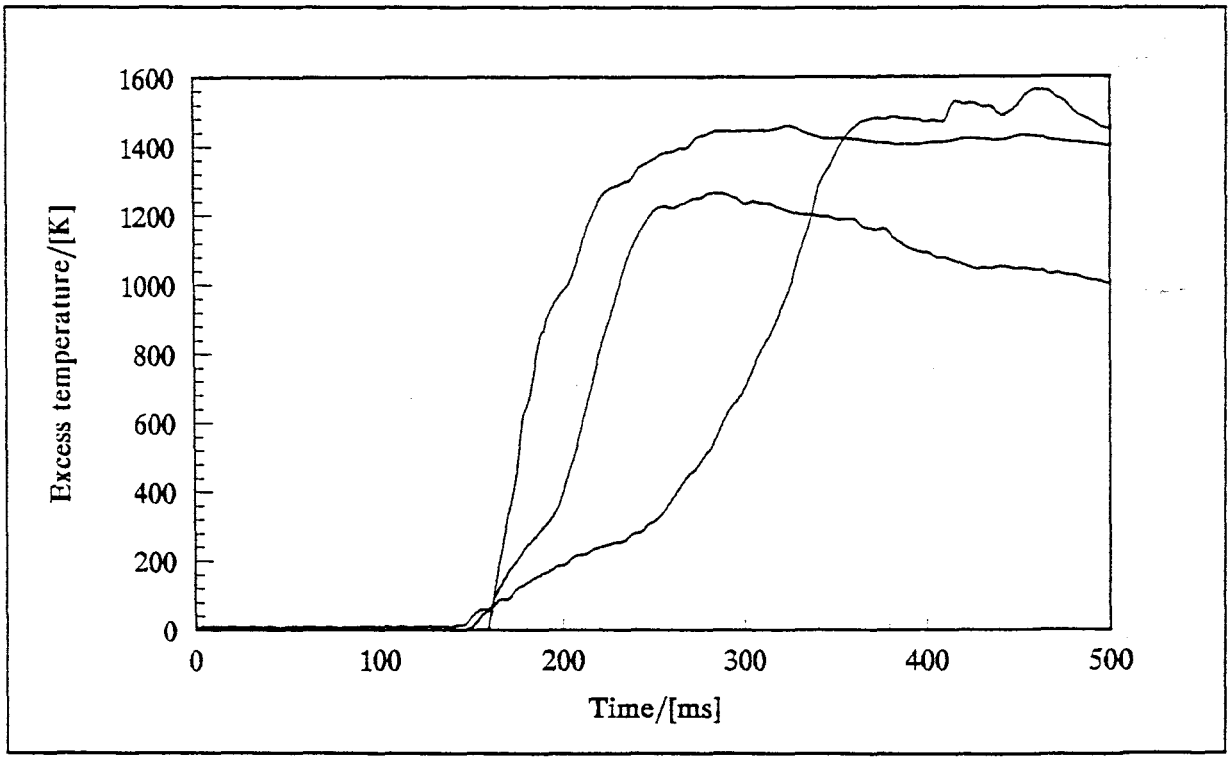

FIGURE 11.2: Reproducibility of temperature profiles of 30% Zn/BaO_2

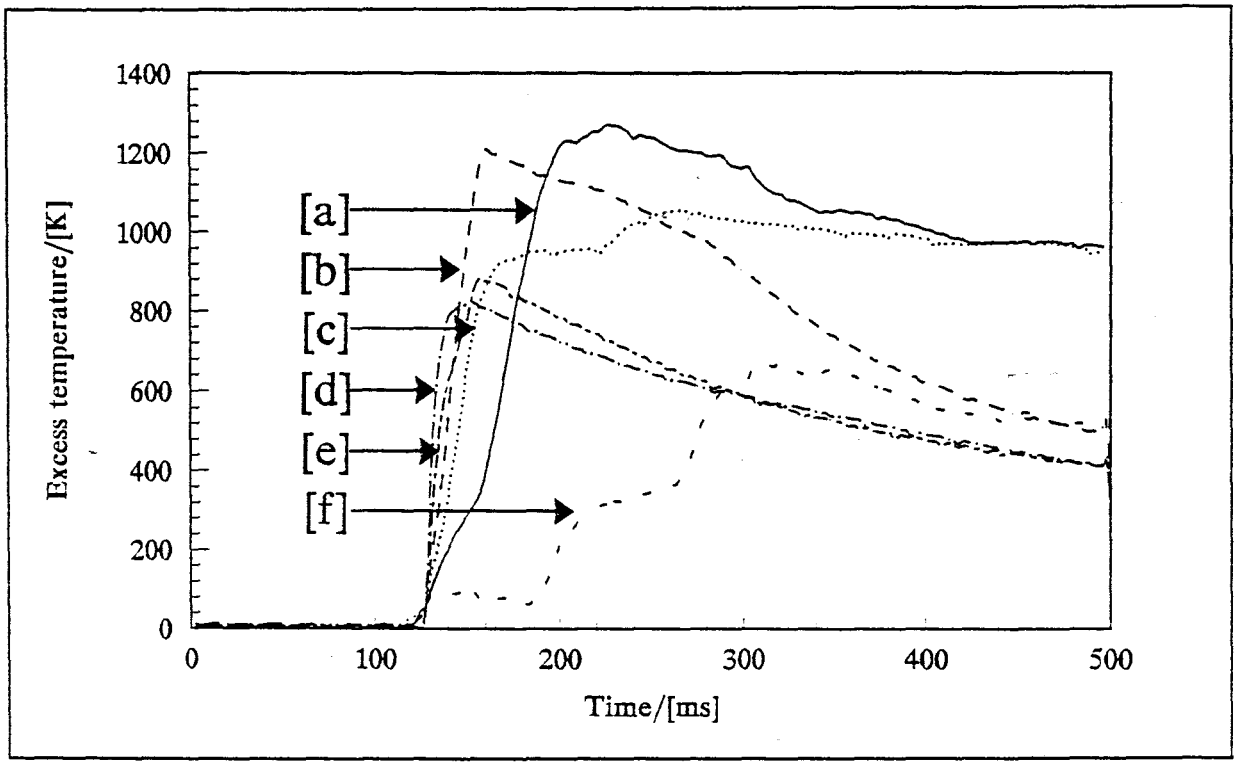

FIGURE 11.3: Effect of composition on profiles of Zn/BaO_2 compacted at 0.2 MPa [a]:30%, [b]:35%, [c]:40%, [d]:45%, [e]:50% and [f]:55%

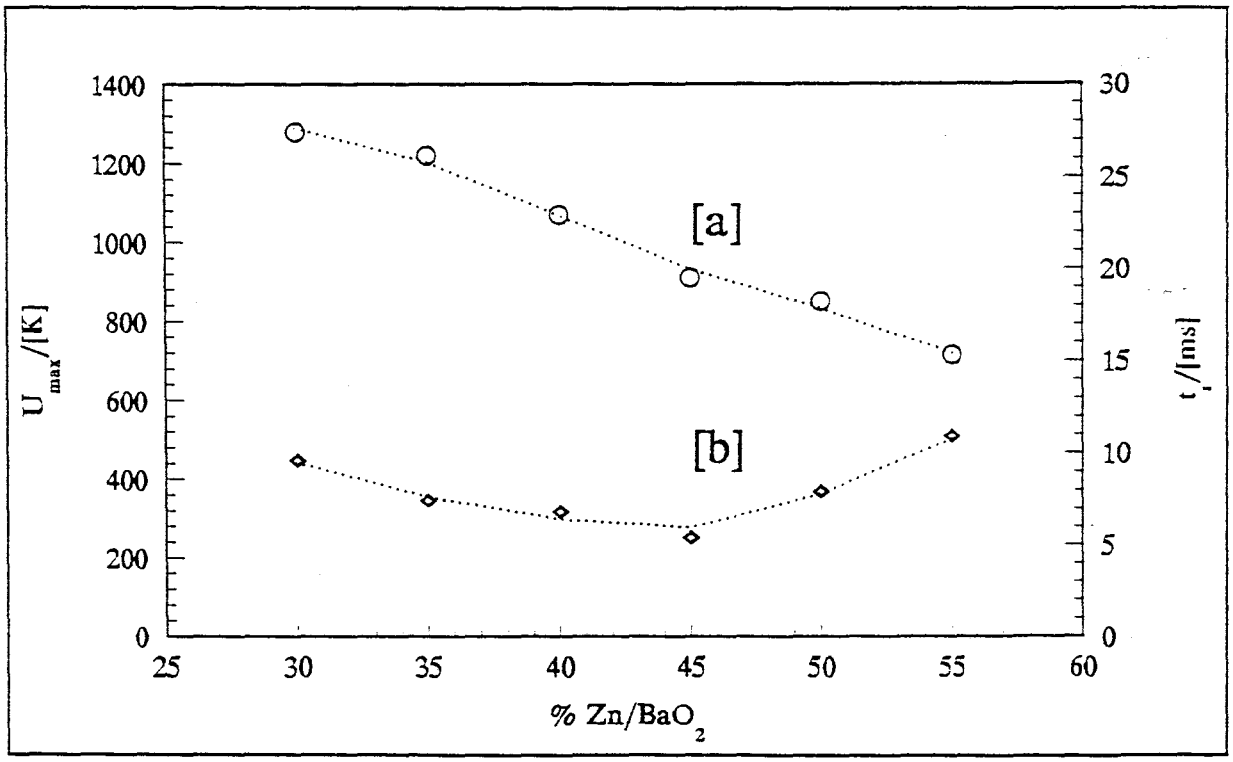

FIGURE 11.4: Effect of composition on [a]: U_{max} and [b]: t_r of Zn/BaO_2 compacted at 0.2 MPa

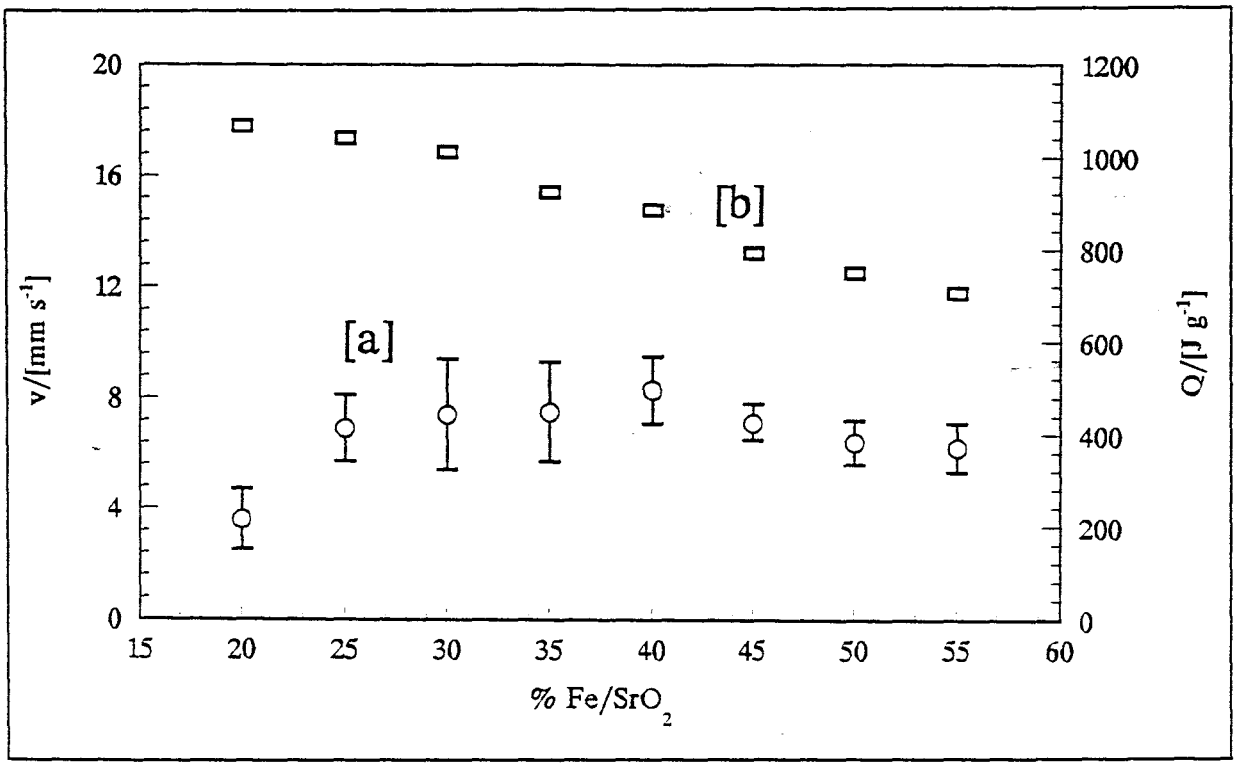

FIGURE 11.5: Effect of composition on [a]: v_{exp} and [b]: enthalpy of reaction of Zn/BaO_2

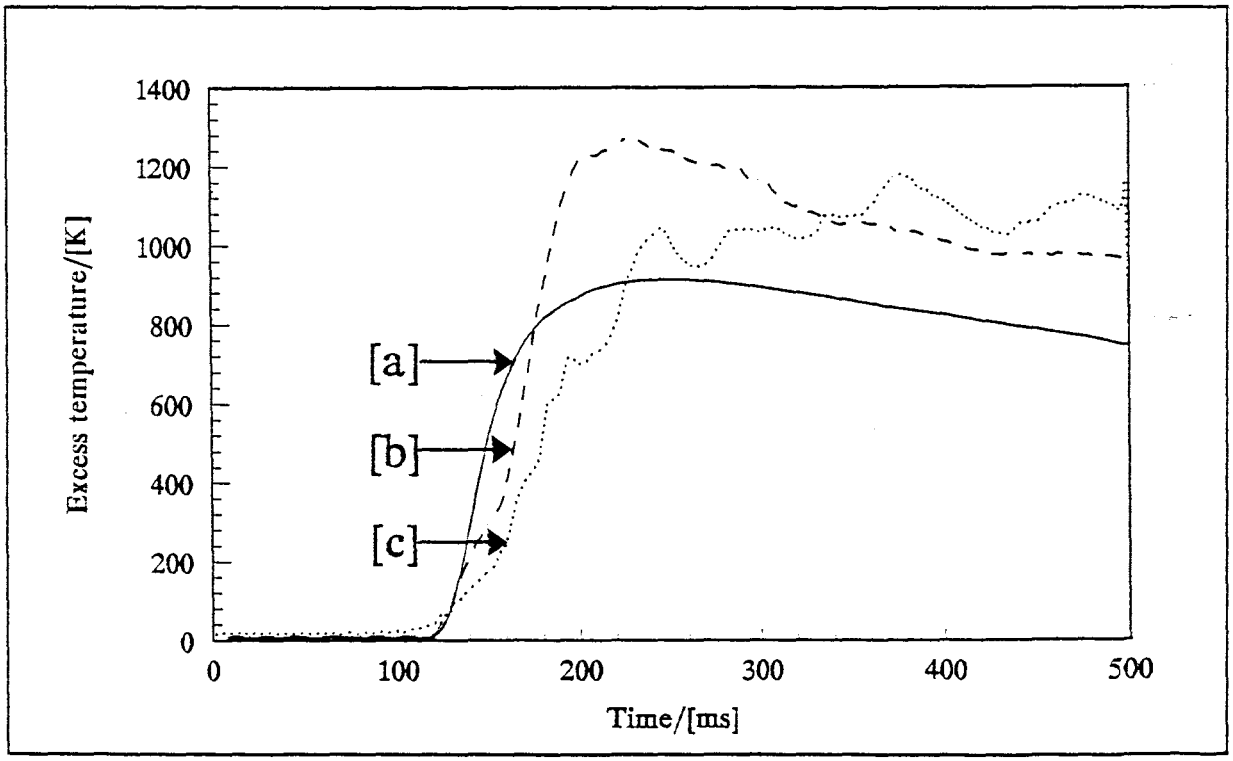

FIGURE 11.6: Effect of compaction on profiles of 30% Zn/BaO_2
[a]: 0 MPa, [b]: 0.2 MPa and [c]: 0.45 MPa

TABLE 11.1: The variation of burning-rates with composition and compaction of Zn/BaO_2:

% Zn/BaO_2	BR/[mm s^{-1}] for 0 Pa	BR/[mm s^{-1}] for 200 kPa
10	4.2±0.1	-
15	5.1±0.2	-
20	9.7±0.6	-
25	14.6±1.4	-
30	21.0±2.9	7.5±0.4
35	37.6±9.4	10.5±0.7
40	58.4±22.7	15.2±1.5
45	75.2±37.7	32.9±7.2
50	42.3±11.9	29.7±5.9
55	29.8±5.9	17.5±2.0
60	12.5±1.0	-
65	4.9±0.2	-

11.2 Effect of thermocouple diameter:

Thicker (0.2 and 0.3 mm) thermocouples had to be used in the study, as described above, with the result that the effects of thermocouple thickness could not be assessed. Based on other studies [6,163] and the Fe/peroxide systems studied here, it is reasonable to assume a correction factor of at least 0.2 for values measured with a 0.2 mm thermocouple, to compensate for the effect of thermocouple thickness on rise-time.

11.3 Effect of additives:

Several substances were introduced separately in small amounts (1 to 10% by mass) into the binary 30% Zn/BaO_2 composition as additives. These substances were: BaO, $BaCO_3$, $Ba(OH)_2$ (likely contaminants of BaO_2; ZnO (formed by some oxidation of Zn); water (always present on exposure of compositions to the surrounding atmosphere); and Al_2O_3 (a supposedly inert substance, expected only to affect combustion by its action as a diluent).

Al_2O_3:

The addition of Al_2O_3, in levels as low as 1%, extinguished combustion in both the 200 kPa and uncompacted systems.

BaO:

Introduction of 1% BaO stifled burning in the 200 kPa compacted material, and resulted in a decrease in the burning-rate of the uncompacted mixture from 21.0 to 4.8 mm s^{-1}.

$BaCO_3$:

The addition of $BaCO_3$, in quantities of 1% or greater, stifled burning, even in uncompacted mixtures.

$Ba(OH)_2$:

The effect of the introduction of 1% $Ba(OH)_2$ was to broaden the rise region of the profiles and decrease the burning rate, with less loss of material from the channel by ejection, and to increase U_{max}. Burning failed when 5% or more $Ba(OH)_2$ was added to mixtures of Zn/BaO_2.

ZnO:

The addition of ZnO in quantities greater than 1% stifled combustion of the compacted material. The burning-rate in the uncompacted mixture was decreased from 21.0 to 5.1 mm s^{-1}. Although the addition of 1% ZnO broadened the rise-region of the temperature profiles, the U_{max} values obtained were the same as those for the pure 30% Zn/BaO_2 system. Addition of 5% ZnO to the system resulted in less vigorous burning of uncompacted powder. Combustion was sustained with difficulty and burning in the channel failed to propagate.

The inhibiting effects of additives on the temperature profiles of the uncompacted mixtures of 30% Zn/BaO_2 and mixtures compacted at 0.2 MPa, are shown in Figures 11.7 and 11.8, respectively. In general, combustion of the binary system is so unstable that the significance of individual additives is probably hidden by the disruption effect of any material of decreased reactivity.

11.4 Thermochemistry:

The simplest reactions likely to be involved in combustion of the Zn/BaO_2 are:

$$Zn(s) + BaO_2(s) \rightarrow ZnO(s) + BaO(s) \quad \ldots\ldots\ldots\ldots\ldots\ldots \text{(i)}$$

$$Zn(l) + BaO_2(s) \rightarrow ZnO(s) + BaO(s) \quad \ldots\ldots\ldots\ldots\ldots\ldots \text{(ii)}$$

$$Zn(g) + BaO_2(s) \rightarrow ZnO(s) + BaO(s) \quad \ldots\ldots\ldots\ldots\ldots\ldots \text{(iii)}$$

The reactant purities are Zn: 94% and BaO_2: 85%. The residual substances are assumed to be inert (which is probably true for the peroxide, but less satisfactory (although less significant) for the metal fuel).

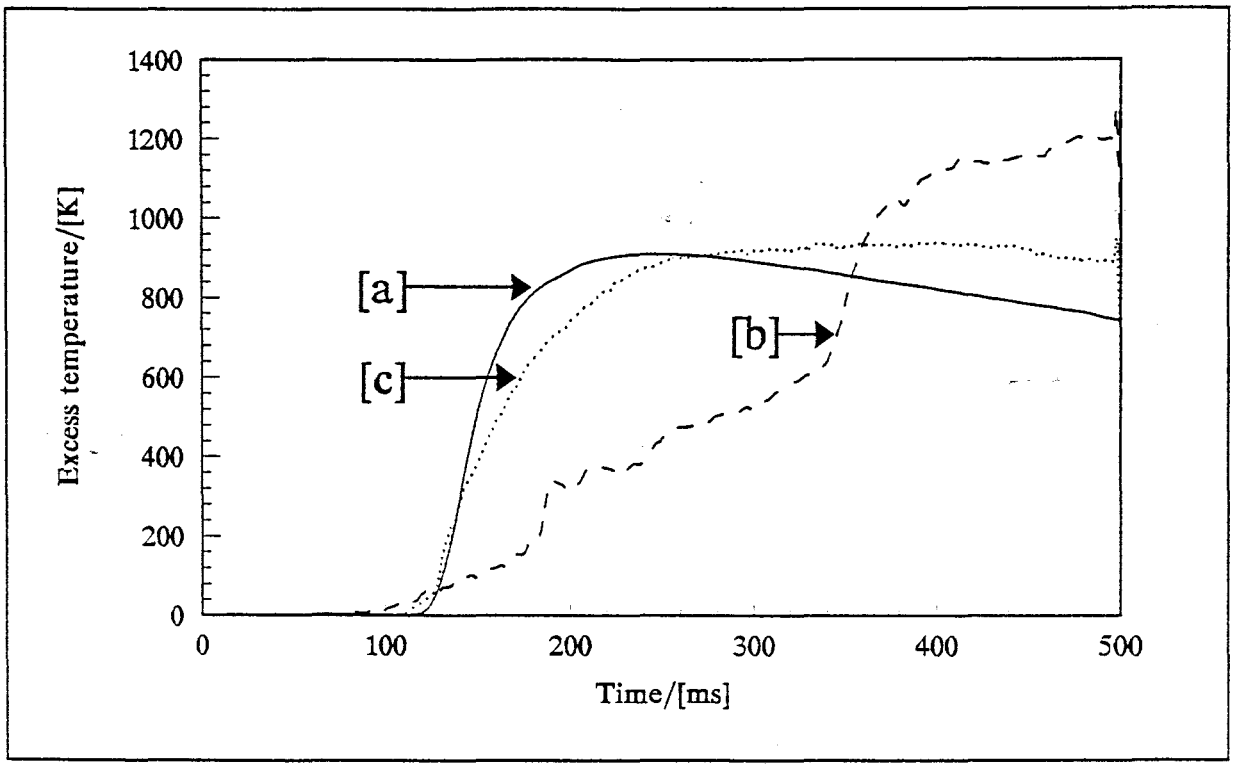

FIGURE 11.7: Effect of additives on temperature profiles of uncompacted 30% Zn/BaO_2 [a]: 0%, [b]: 1% $Ba(OH)_2$ and [c]: 1% ZnO

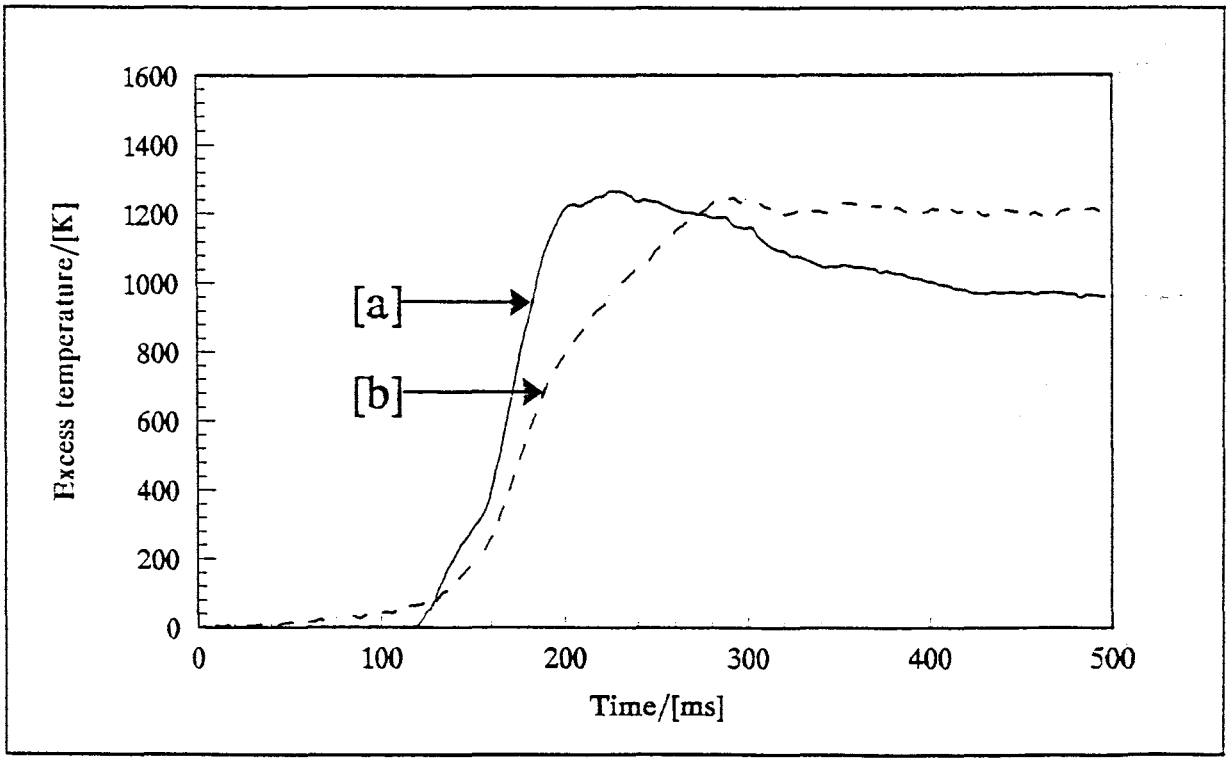

FIGURE 11.8: Effect of additives on profiles of 30% Zn/BaO_2 compacted at 0.2 MPa [a]: 0% and [b]: 1% $Ba(OH)_2$

TABLE 11.2: Standard enthalpies of reaction:

Reaction	ΔH / kJ mol^{-1}
$Zn(s) \rightarrow Zn(l)$	+ 3.5
$Zn(l) \rightarrow Zn(g)$	+ 127.3
$BaO_2(s) \rightarrow BaO(s) + \frac{1}{2}O_2(g)$	+ 84.7
$Zn(s) + \frac{1}{2} O_2(g) \rightarrow ZnO(s)$	- 354.3
$Zn(l) + BaO_2(s) \rightarrow ZnO(s) + BaO(s)$	- 273.1

Assuming 100% pure reactants, the stoichiometric composition (% by mass of zinc) for the Zn/BaO_2 system, based on complete reaction according to (i), (ii) or (iii), is 27.86% Zn. For the 85% pure BaO_2 system, this decreases to 24.7% Zn, and for 94% pure Zn, becomes 25.9%.

The calculated standard enthalpy of reaction for 100% pure reactants, from tables of standard enthalpies of formation at 298K [8] is:

$\Delta H^0_{reaction}$ = -297.8 kJ (mol Zn)$^{-1}$

= -297.8 kJ (mol BaO_2)$^{-1}$

= -1.76 kJ (g BaO_2)$^{-1}$

= -4.55 kJ (g Zn)$^{-1}$

Since the stoichiometric composition is 27.9% Zn, 1 g of mixture contains 0.721 g BaO_2 (100% pure), and so the heat output, q = 1.76 x 0.721 kJ (g mixt)$^{-1}$ = 1.27 kJ (g mixt)$^{-1}$

Converting to 85% purity, q = 1.07 kJ (g mixt)$^{-1}$

It is probable that zincates may form under the conditions present in these reactions, but no enthalpies of formation were found for the following reactions:

$Zn(s) + BaO_2(s) \rightarrow BaZnO_2(s)$ . . . . . (iv)

$Zn(l) + BaO_2(s) \rightarrow BaZnO_2(s)$ . . . . . (v)

$Zn(g) + BaO_2(s) \rightarrow BaZnO_2(s)$ . . . . . (vi)

$ZnO(s) + BaO(s) \rightarrow BaZnO_2(s)$ . . . . . (vii)

The values of ΔH for the binary reactions leading to simple oxide products were calculated using values of heat capacity determined from equations of temperature dependence [8] and values of U_{max}, and are compared to standard values of ΔH.

TABLE 11.3: Comparison of calculated and experimental thermochemistry:

Zn/BaO_2 %	$-\Delta H/[kJ\ g^{-1}]$ Calculated from standard values	$-\Delta H/[kJ\ g^{-1}]$ Experimental	$U_{ad}/[K]$ Predicted from standard ΔH	$U_{ad}/[K]$ Experimental
30	1.041	0.602	2215	1280
35	0.967	0.569	2075	1220
40	0.893	0.492	1941	1070
45	0.818	0.414	1798	910
50	0.744	0.383	1650	850
55	0.669	0.318	1503	715

The maximum value of heat output predicted from standard enthalpies of reaction is 1079 J g^{-1} and occurs at the stoichiometric point of 27.9% Zn/BaO_2. The effects of melting (ΔH = 112.9 J g^{-1}) and vaporisation (ΔH = 1755 J g^{-1}) have not been included in the comparison. The experimental values of ΔH are much lower than calculated for reaction (i) and this most probably arises from incomplete reaction.

Twin-thermocouple studies on the zinc systems were difficult to pursue since the gaseous nature of even the lightly compacted systems resulted in massive ejection of product from the channel. This problem, together with the formation of a liquid reaction phase which shorted the thermocouples, resulted in meaningless data from the use of two thermocouple junctions in the channel.

11.5 Kinetics from temperature profiles:

Temperature profiles for Zn/BaO_2 compositions were converted into their component power functions as described in detail in Section 5.1 and Appendix 12. For the Zn/BaO_2 system only one major peak was observed for the reaction power function, G. The apparent activation energies, pre-exponential factors and reaction orders for the compositions studied are given in Table 11.4.

TABLE 11.4: Kinetic parameters obtained for the Zn/BaO_2 systems

% Zn/BaO_2	$E_a/[kJ\ mol^{-1}]$	$A/[s^{-1}]$	n
30	16.0±3.5	241±54	0.64±0.06
35	13.8±1.6	224±59	0.54±0.06
40	19.0±4.9	522±186	0.63±0.01
45	6.9±1.8	170±10	0.64±0.06
50	6.7±1.1	146±32	0.51±0.03

The activation energies are all low values characteristic of diffusion-controlled processes and are lowest at the higher percentages of fuel (45% and 50%) as shown in Figure 11.9. Reaction orders are in a similar range to those found for the other fuel/peroxide systems.

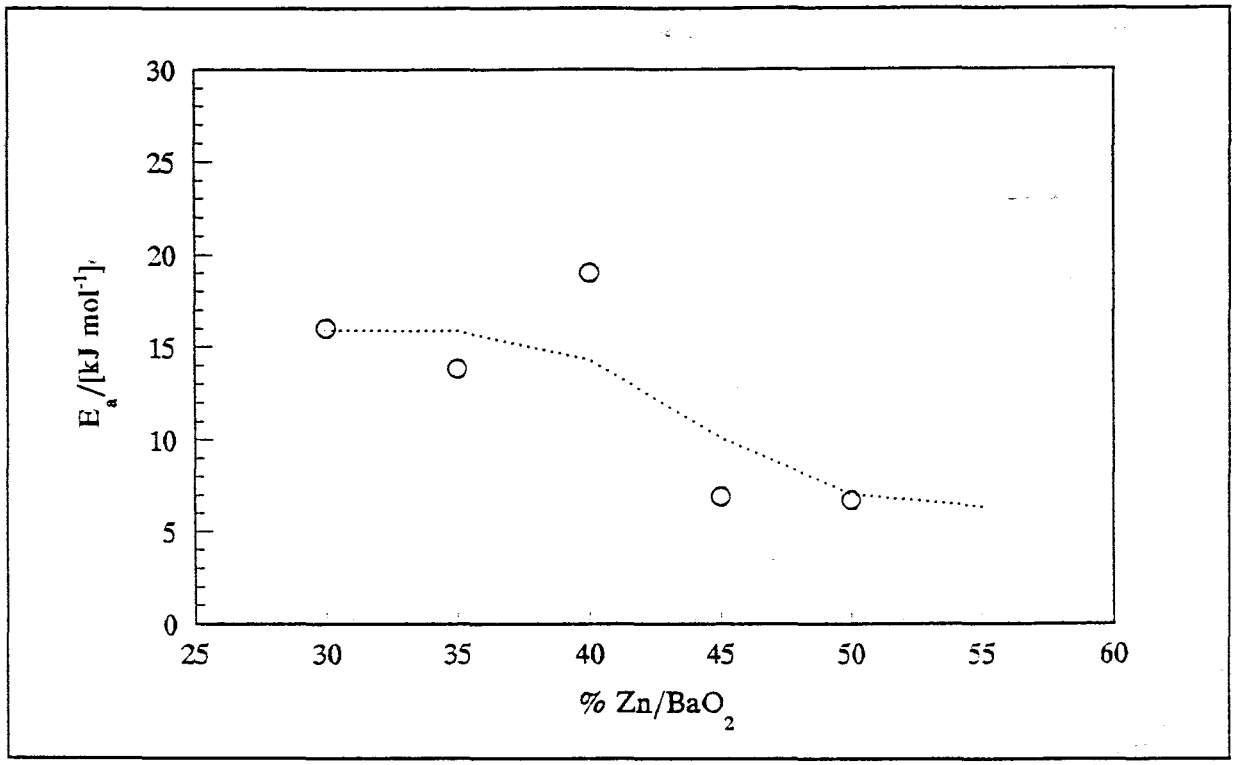

FIGURE 11.9: Effect of composition on the activation energy for combustion of the Zn/BaO_2 system

11.6 Thermal conductivity and burning-rate:

The linear burning-rate, v, of a composition is related to the rise-time, t_r, of the corresponding temperature profile as explained in Section 9.8.

In Table 11.5, values of λ, c and ρ for the range of Zn/BaO_2 compositions have been estimated. These may be combined with the D values to give thermal diffusivities, $D=\lambda/(\rho c)$. The experimental rise-times, $t_{r\,exp}$, are then combined with the D values to give the calculated burning-rates, v_{calc}, which are compared with experimental burning-rates, v_{exp}, as for the Fe/peroxide sections (9 and 10).

Agreement between values of v_{calc} and of v_{exp} is only fair at the low fuel end of the composition range. The fact that the experimental and calculated values of the burning-rates are different may be explained, as for the Fe/peroxide systems, if the effective thermal diffusivities, under combustion conditions (see Table 11.5), are greater than those predicted, through increased thermal conductivities and/or decreased heat capacities at higher temperatures.

TABLE 11.5: Comparison of experimental and predicted burning-rates

Zn/BaO_2	λ	c	ρ	D	$t_{r\,exp}$*	v_{exp}	v_{calc}	D_{eff}
%	$W\ m^{-1}\ K^{-1}$	$J\ g^{-1}\ K^{-1}$	$g\ m^{-3}$	$m^2\ s^{-1}$	ms	$mm\ s^{-1}$	$mm\ s^{-1}$	$m^2\ s^{-1}$
30	0.103	0.470	$3.1x10^6$	$7.1x10^{-8}$	9.5t	7.5	6.1	$4.4x10^{-7}$
35	0.101	0.466	$3.1x10^6$	$7.0x10^{-8}$	6.1t	10.5	7.6	$1.3x10^{-7}$
40	0.098	0.460	$3.1x10^6$	$6.9x10^{-8}$	3.8t	15.2	9.5	$1.8x10^{-7}$
45	0.103	0.455	$3.2x10^6$	$7.1x10^{-8}$	1.3t	29.7	16.5	$2.3x10^{-7}$
50	0.101	0.451	$3.2x10^6$	$7.0x10^{-8}$	2.1t	32.9	12.9	$4.5x10^{-7}$
55	0.101	0.445	$3.2x10^6$	$7.1x10^{-8}$	7.6t	17.5	6.8	$4.7x10^{-7}$

*The correction factor for thermocouple thickness, t, is 0.2. Values of t_r have not been modified, but the factor has been taken account of in calculations.

12. COMBUSTION OF THE Zn/SrO_2 SYSTEM:

12.1 Effect of composition and compaction:

Zn/SrO_2 systems behaved similarly to the Zn/BaO_2 systems, in that uncompacted mixtures burned in the composition range 25-75% Zn by mass (Figure 12.1), compared to the 10-65% Zn range of the Zn/BaO_2 system. The shifting of the burning-range to higher percentages of fuel when SrO_2 was used as the oxidant was also observed in the Fe/peroxide systems. Burning-rates for the compositions ranged between 4 and 25 mm s^{-1}, compared with the 4 to 75 mm s^{-1} range of the Zn/BaO_2 system. The reactions were less vigorous than those of Zn/BaO_2, and values of U_{max} (for the uncompacted compositions) and burning-rates were lower. The reproducibility of the profiles for 30% Zn/SrO_2 is shown in Figure 12.2. The rise-times and 10-90% U_{max} times were similar to those of the Zn/BaO_2 system.

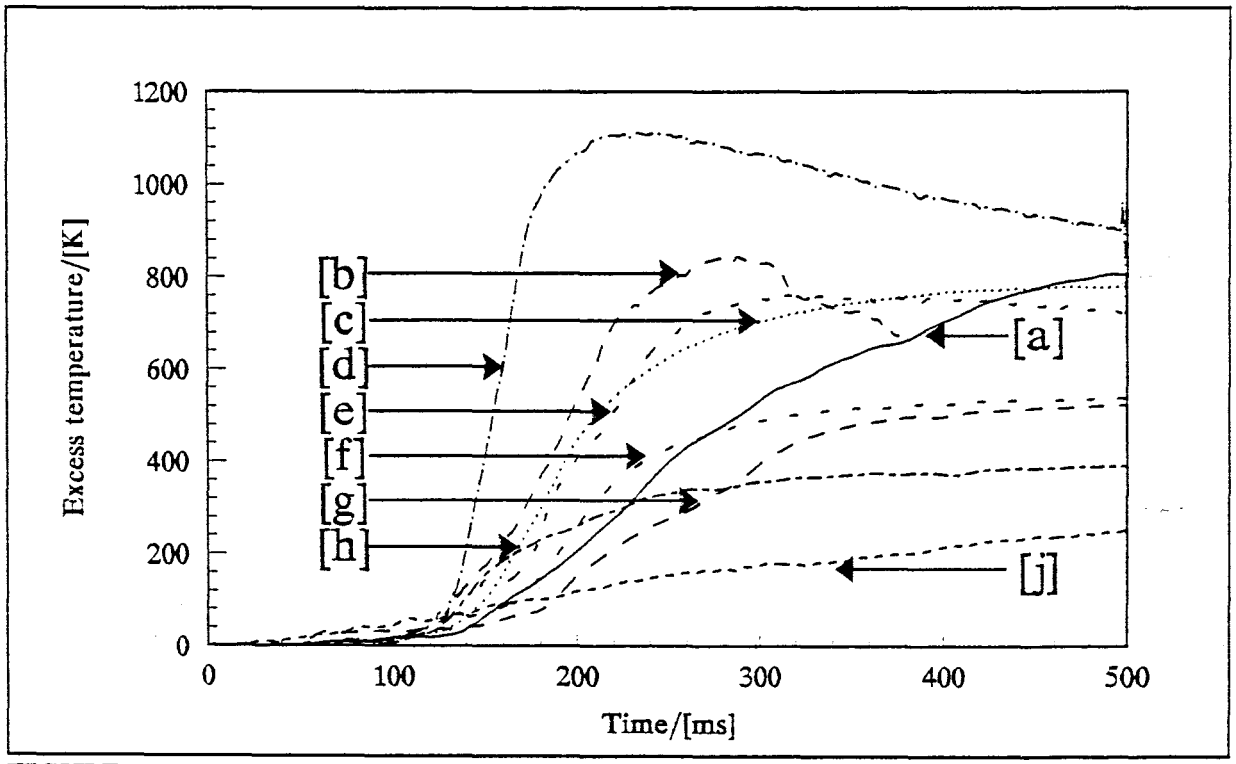

FIGURE 12.1: The effect of composition on temperature profiles of uncompacted Zn/SrO_2 [a]:30%, [b]:35%, [c]:40%, [d]:45%, [e]:50%, [f]:55%, [g]:60%, [h]:70% and [j]:80%

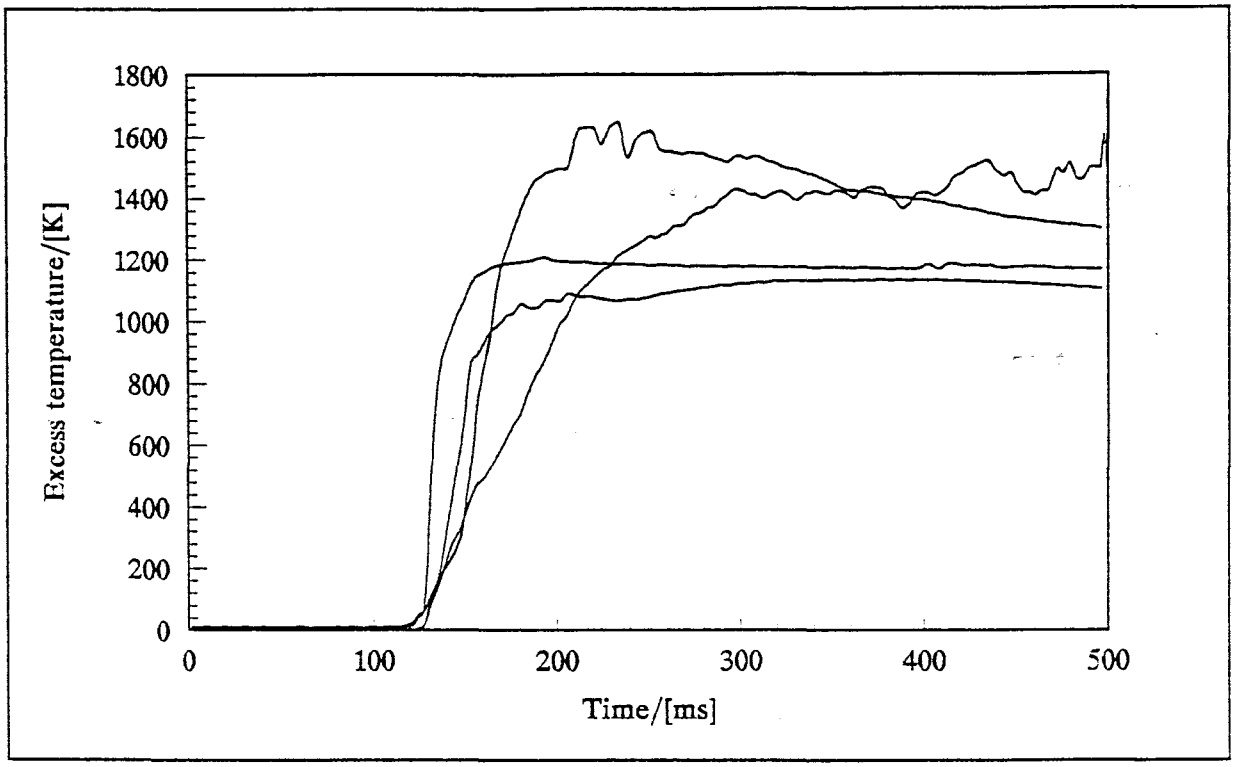

FIGURE 12.2: Reproducibility of temperature profiles of 30% Zn/SrO_2

As found for the Zn/BaO_2 system (Section 11.2), compaction had a marked effect on the combustion. Profiles could only be captured for compositions compacted to less than 450 kPa (Figure 12.6). Mild compaction (200 kPa) decreased the burning-range as shown in Table 12.1, with combustion of the compacted mixtures still being supported over the same range as the Zn/BaO_2 system, viz. 30-55% Zn (Figure 12.3). Figure 12.4 shows the variation of U_{max} and t_r with composition and Figure 12.5 shows that the burning-rate reached a maximum between 45 and 50%, whilst the heat output reached a maximum below 30%.

As for the Zn/BaO_2 system study (Section 11.3), only one range of particle size of zinc powder was used in this study. However, particle size is not expected to affect burning-rate noticeably due to the reaction mechanism (liquid fuel/solid oxidant and some vapour).

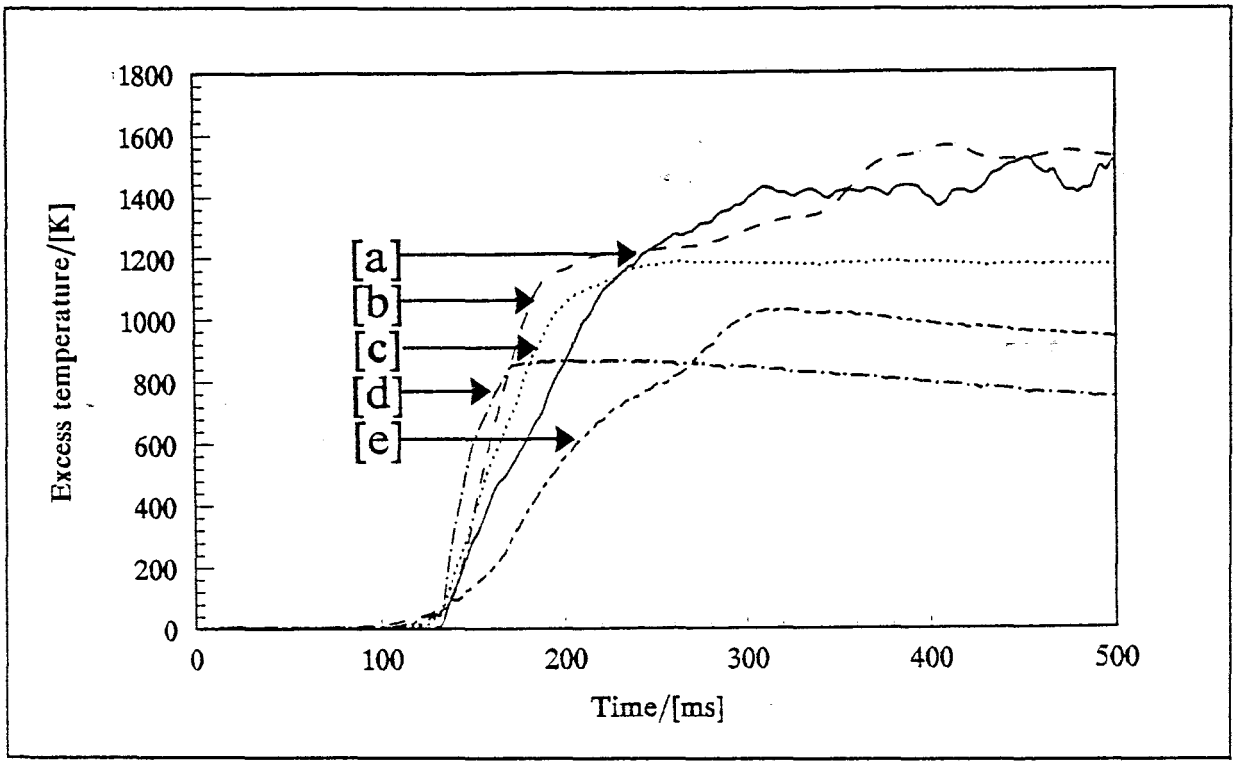

FIGURE 12.3: Effect of composition on profiles of Zn/SrO_2 compacted at 0.2 MPa [a]:30%, [b]:35%, [c]:40%, [d]:45% and [e]:50%

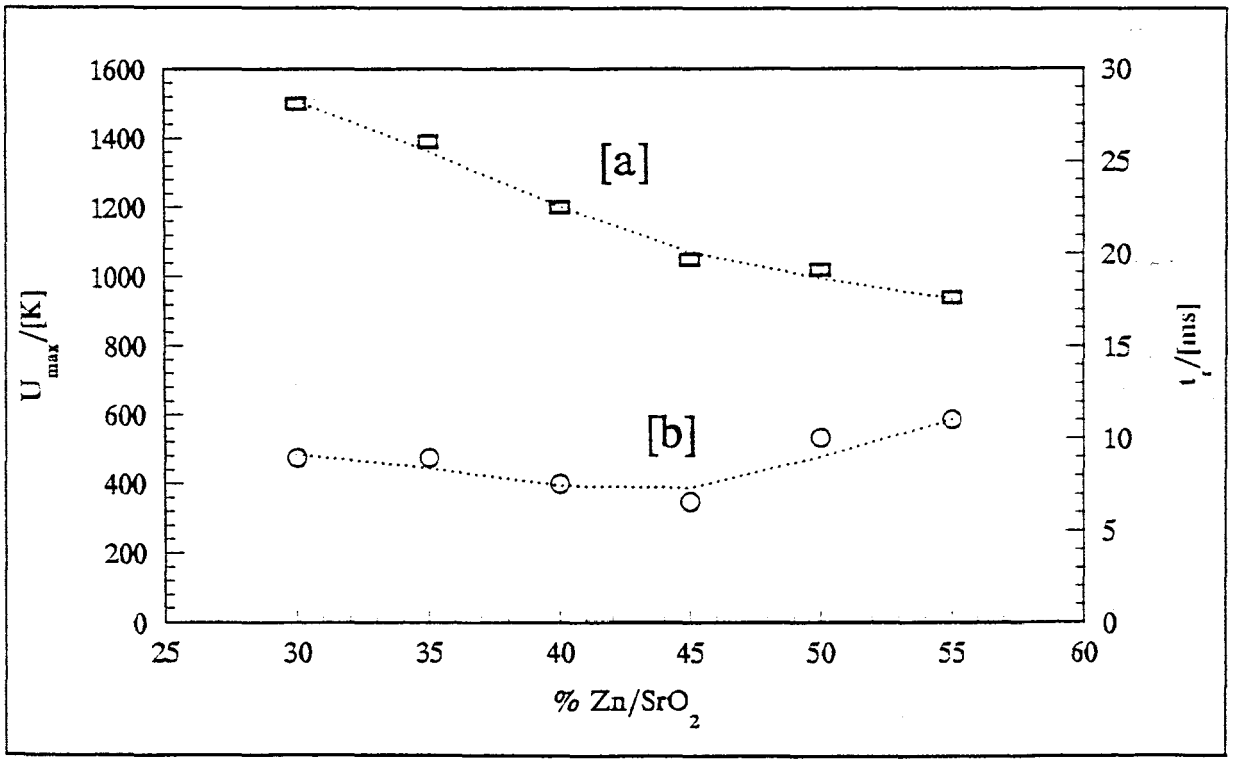

FIGURE 12.4: The effect of composition on [a]: U_{max} and [b]: t_r of Zn/SrO_2

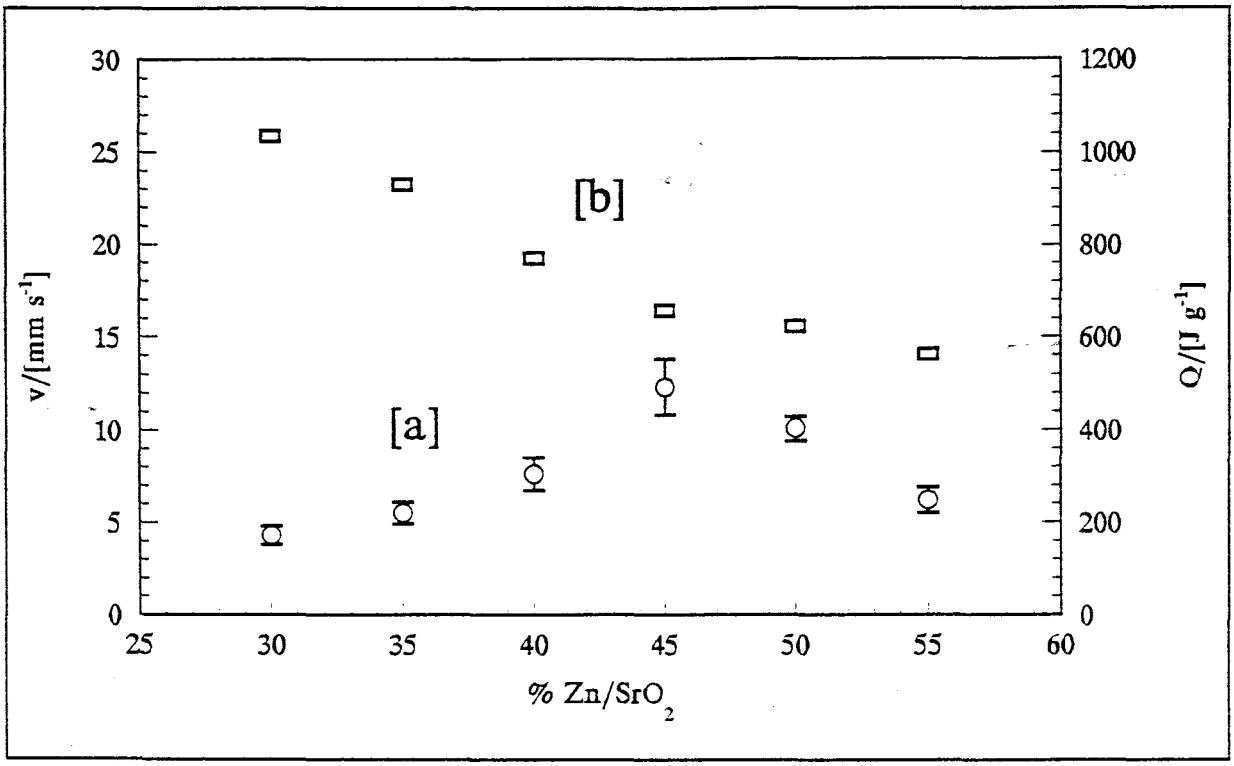

FIGURE 12.5: Effect of composition on [a]:burning-rate and [b]:enthalpy of reaction of Zn/SrO_2

TABLE 12.1: The effect of composition and compaction on burning-rates of Zn/SrO_2 systems:

% Zn/SrO_2	BR/[mm s^{-1}] for 0 Pa	BR/[mm s^{-1}] for 200 kPa
25	5.1±0.2	-
30	10.2±0.7	4.3±0.1
35	15.7±1.6	5.5±0.2
40	20.8±2.9	7.6±0.4
45	24.9±4.1	12.3±1.0
50	22.3±3.3	10.1±0.7
55	19.8±2.6	6.2±0.3
60	15.4±1.6	-
65	9.8±0.6	-
70	6.7±0.3	-
75	4.8±0.2	-

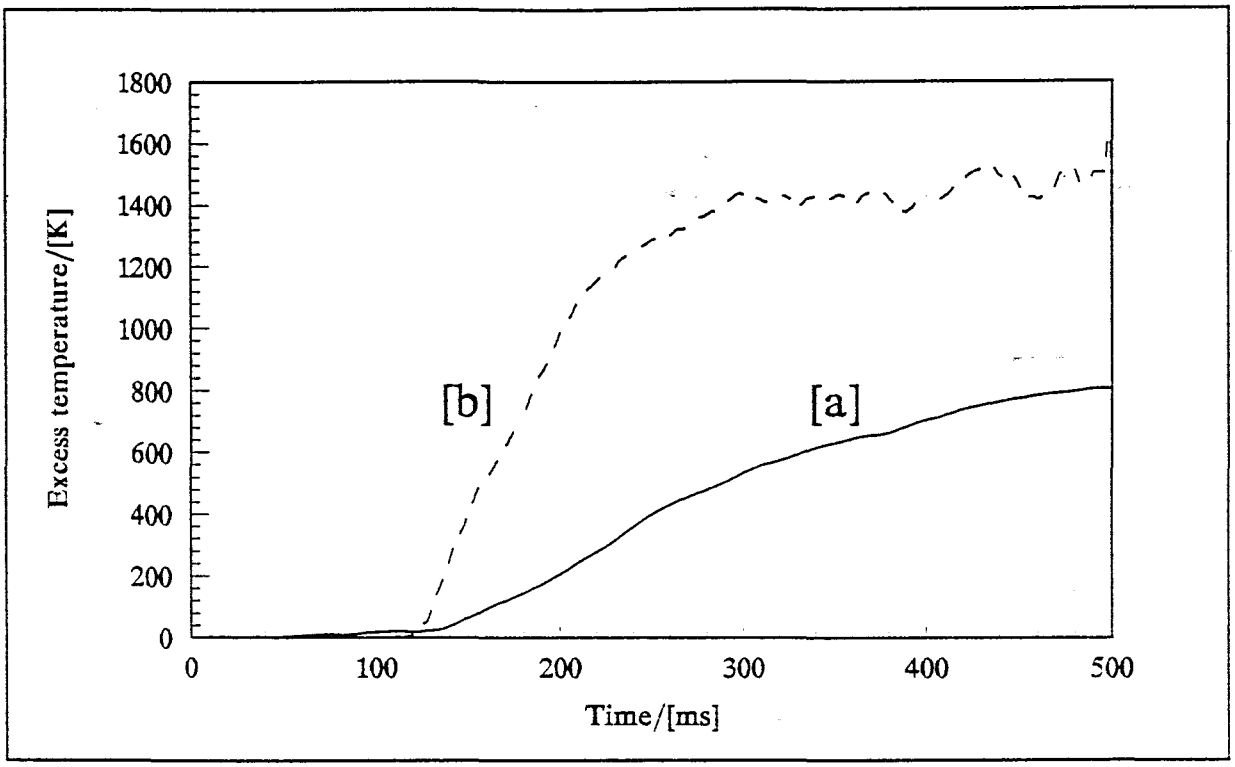

FIGURE 12.6: The effect of compaction on temperature profiles of 30% Zn/SrO_2 [a]: 0.2 MPa and [b]: 0 MPa

12.2 Effect of thermocouple diameter:

Thicker (0.2 and 0.3 mm) thermocouples had to be used in the study, as mentioned in Section 11 (above), with the consequence that the effects of thermocouple thickness could not be assessed in the Zn/SrO_2 system. The same assumptions were made as for the Zn/BaO_2 system, in that a correction factor of about 0.2 was assumed to adjust values measured with a 0.2 mm thermocouple to zero thermocouple thickness, based on previous [6,163] studies and the Fe/peroxide system studies (Sections 9 and 10).

12.3 Effect of additives:

Several substances were introduced separately in small amounts (1 to 10% by mass) into the binary 30% Zn/SrO_2 composition as additives. These substances were: SrO, $SrCO_3$, $Sr(OH)_2$ (likely contaminants of SrO_2; ZnO (formed by some oxidation of Zn); water (always present on exposure of compositions to the surrounding atmosphere); and Al_2O_3 (a supposedly inert substance, expected only to affect combustion by its action as a diluent). The addition of proportions of any of the additives in excess of 1% stifled combustion in both uncompacted and compacted systems. The addition of Al_2O_3, SrO, $SrCO_3$ and H_2O stifled combustion in all systems when quantities of 1% were added. The inhibiting effects of the additives on the temperature profiles of uncompacted 30% Zn/SrO_2 material are shown in Figure 12.7.

$Sr(OH)_2$:

The introduction of $Sr(OH)_2$ resulted in a broadening of the rise region of the temperature profile, and an increased U_{max}. The burning-rate was lowered from 4.3 to 2.1 mm s^{-1}.

ZnO:

Addition of ZnO resulted in similar behaviour, with less broadening of the rise region of temperature profiles than observed for the addition of $Sr(OH)_2$. The burning-rate of the 30% Zn/SrO_2 system decreased from 4.3 to 3.2 mm s^{-1} with the addition of 1% ZnO.

The addition of substances to the 30% Zn/SrO_2 system has more of an effect on combustion than the introduction of similar materials to the 30% Zn/BaO_2 system. The combustions of both binary systems are very unstable and hence easily inhibited. The Fe-fuelled systems showed a similar effect in that combustion of the Fe/BaO_2 system was less affected by the presence of additives than the Fe/SrO_2 system.

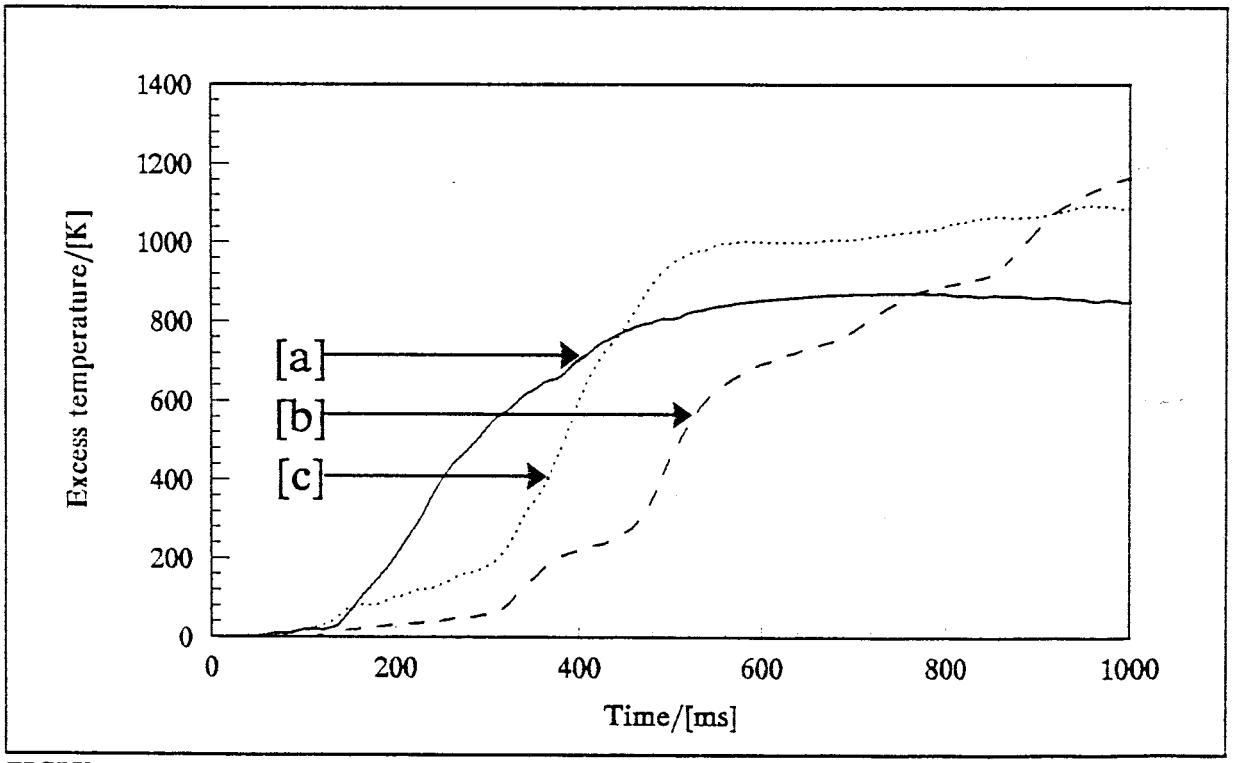

FIGURE 12.7: The effect of additives on temperature profiles of uncompacted 30% Zn/SrO_2 [a]: 0%, [b]: 1% $Sr(OH)_2$ and [c]: 1% ZnO

12.4 Thermochemistry:

The simplest reactions likely to be involved in combustion of the Zn/SrO_2 are:

$$Zn(s) + SrO_2(s) \rightarrow ZnO(s) + SrO(s) \quad \ldots\ldots\ldots\ldots\ldots\ldots \text{(i)}$$

$$Zn(l) + SrO_2(s) \rightarrow ZnO(s) + SrO(s) \quad \ldots\ldots\ldots\ldots\ldots\ldots \text{(ii)}$$

$$Zn(g) + SrO_2(s) \rightarrow ZnO(s) + SrO(s) \quad \ldots\ldots\ldots\ldots\ldots\ldots \text{(iii)}$$

The reactant purities are Zn: 94% and SrO_2: 85%. The residual substances are assumed to be inert (which is probably true for the peroxide, but less satisfactory (although less significant) for the metal fuel).

TABLE 12.2: Standard enthalpies of reaction:

Reaction	ΔH / kJ mol^{-1}
$Zn(s) \rightarrow Zn(l)$	+ 3.5
$Zn(l) \rightarrow Zn(g)$	+127.3
$Zn(s) + \frac{1}{2} O_2(g) \rightarrow ZnO(s)$	-354.3
$SrO_2(s) \rightarrow SrO(s) + \frac{1}{2}O_2(g)$	+ 54.8
$Zn(l) + SrO_2(s) \rightarrow ZnO(s) + SrO(s)$	-303.0

Assuming 100% pure reactants, the stoichiometric composition for the Zn/SrO_2 system, based on complete reaction according to (i), (ii) or (iii), is 35.34%. For 85% pure SrO_2 this decreases to 31.7%, and for 94% pure Zn, becomes 33.1%.

The calculated standard enthalpy of reaction for 100% pure reactants, from tables of standard enthalpies of formation at 298 K [8] is:

$\Delta H^0_{reaction}$ = -303.2 kJ $(mol\ Zn)^{-1}$

= -303.2 kJ $(mol\ SrO_2)^{-1}$

= -2.53 kJ $(g\ SrO_2)^{-1}$

=- 4.64 kJ $(g\ Zn)^{-1}$

Since the stoichiometric composition is 35.3% Zn, 1 g of mixture contains 0.647 g SrO_2 (100% pure), so the heat output, q = 2.53 x 0.647 kJ $(g\ mixt)^{-1}$ = 1.64 kJ $(g\ mixt)^{-1}$

Converting to 85% purity, q = 1.39 kJ $(g\ mixt)^{-1}$.

This value is somewhat greater than that for the Zn/BaO_2 system (1.07 kJ $(g\ mixt)^{-1}$), suggesting higher reaction temperatures should be present in the Zn/SrO_2 system.

It is probable that zincates may form under the conditions present in these reactions, as suggested for the Zn/BaO_2 system, but no enthalpies of formation were found for the following reactions:

$$Zn(s) + SrO_2(s) \rightarrow SrZnO_2(s) \quad \ldots\ldots\ldots\ldots\ldots\ldots \text{(iv)}$$

$$Zn(l) + SrO_2(s) \rightarrow SrZnO_2(s) \quad \ldots\ldots\ldots\ldots\ldots\ldots \text{(v)}$$

$$Zn(g) + SrO_2(s) \rightarrow SrZnO_2(s) \quad \ldots\ldots\ldots\ldots\ldots\ldots \text{(vi)}$$

$$ZnO(s) + SrO(s) \rightarrow SrZnO_2(s) \quad \ldots\ldots\ldots\ldots\ldots\ldots \text{(vii)}$$

Based on the assumption that the binary reactions lead to simple oxide products, the calculated values of ΔH determined using values of heat capacity determined from equations of temperature dependence [8] and values of U_{max}, are compared to standard values of ΔH below.

TABLE 12.3: Comparison of calculated and experimental thermochemistry:

% Zn/SrO_2 system	$-\Delta H/[kJ\ g^{-1}]$ Calculated from standard values	$-\Delta H/[kJ\ g^{-1}]$ Experimental	$U_{ad}/[K]$ Predicted from standard ΔH	$U_{ad}/[K]$ Experimental
30	1.308	1.035	2016	1500
35	1.391	0.931	2086	1390
40	1.290	0.770	2009	1200
45	1.183	0.657	1908	1060
50	1.075	0.622	1762	1020
55	0.968	0.562	1635	940

The maximum value of heat output predicted from standard enthalpies of reaction is 1391 J g^{-1} and occurs at the stoichiometric value of 35.3%. The agreement between calculated and experimental values is best near the stoichiometric composition and decreases as expected for incomplete combustion at higher fuel compositions. The effects of melting (ΔH = 112.9 J g^{-1}) and vaporisation (ΔH = 1755 J g^{-1}) of zinc have not been included in the comparison, but would add to the deviations between experimental and calculated values.

12.5 Kinetics from temperature profiles:

Temperature profiles for Zn/SrO_2 compositions were converted into their component power functions as described in detail in Section 5.1 and Appendix 12. Only one major peak was observed for the reaction power function, G, for the Zn/SrO_2 system. The gaseous nature of the combustion resulted in rather poor profile reproducibility. Optimisation of kinetic data from the 200 kPa profiles yielded the apparent activation energies, pre-exponential factors and apparent orders of reaction shown in Table 12.4.

TABLE 12.4: Kinetic data obtained for the Zn/SrO_2 system

% Zn	E_a/[kJ mol^{-1}]	A/[s^{-1}]	n
30	10.8±0.8	96±13	0.54±0.02
35	9.5±1.5	70±22	0.60±0.08
40	10.2±0.9	94±7	0.71±0.06
45	10.4±1.0	146±30	0.54±0.05
50	16.0±3.3	181±51	0.64±0.07

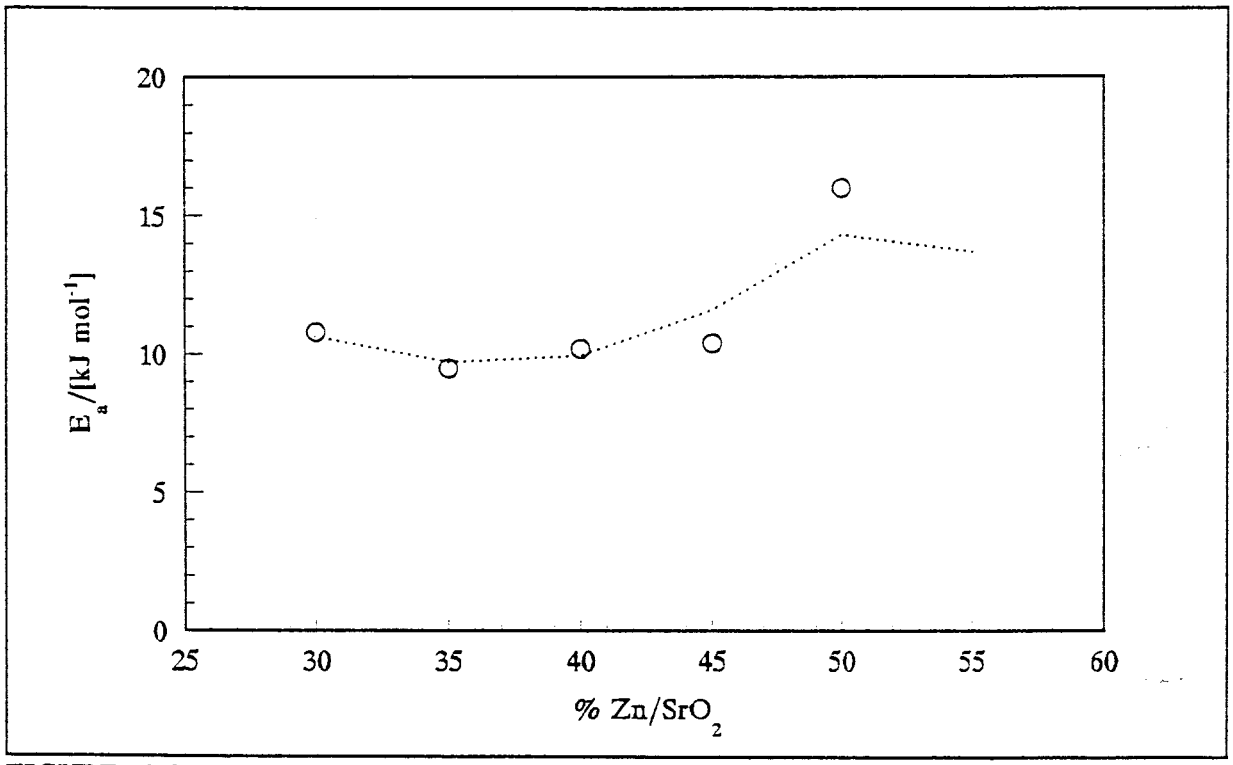

FIGURE 12.8: Effect of composition on activation energy for combustion of the Zn/SrO_2 system

The activation energies are all low values characteristic of diffusion-controlled processes, with an increase at the highest percentage of fuel (50%) (Figure 12.8). These values are similar to those obtained for the Zn/BaO_2 system (E_a from 7 to 19 kJ mol^{-1}).

12.6 Thermal conductivity and burning-rate:

The linear burning-rate, v, of a composition is related to the rise-time, t_r, of the corresponding temperature profile as explained in Section 9.8.

In Table 12.5, values of λ, c and ρ for the range of Zn/SrO_2 compositions have been estimated and thermal diffusivities, $D=\lambda/(\rho c)$, have been calculated. The experimental rise-times, $t_{r\,exp}$, are then combined with these D values to give the calculated burning-rates, v_{calc}, which are compared with

experimental burning-rates, v_{exp}.

TABLE 12.5: Comparison of experimental and predicted burning-rates

Zn/SrO_2	λ	c	ρ	D	$t_{r\,exp}$*	v_{exp}	v_{calc}	D_{eff}
%	W m^{-1} K^{-1}	J g^{-1} K^{-1}	g m^{-3}	m^2 s^{-1}	s	mm s^{-1}	mm s^{-1}	m^2 s^{-1}
30	0.108	0.690	$3.0x10^6$	$5.1x10^{-8}$	15.4b	4.3	4.0	$2.1x10^{-7}$
35	0.114	0.670	$3.1x10^6$	$5.5x10^{-8}$	16.5b	5.5	4.1	$1.0x10^{-7}$
40	0.110	0.642	$3.1x10^6$	$5.5x10^{-8}$	18.2b	7.6	3.9	$2.1x10^{-7}$
45	0.114	0.620	$3.2x10^6$	$5.8x10^{-8}$	15.5b	12.3	4.3	$4.7x10^{-7}$
50	0.110	0.610	$3.2x10^6$	$5.6x10^{-8}$	24.3b	10.1	3.4	$5.0x10^{-7}$
55	0.107	0.592	$3.2x10^6$	$5.7x10^{-8}$	27.0b	6.2	3.2	$2.1x10^{-7}$

* The correction factor for thermocouple thickness effects, b, is 0.2. The t_r values shown above are uncorrected, but the factor has been taken account of in calculations.

Agreement between values of v_{calc} and of v_{exp} is good at the low fuel end of the composition range. The fact that the experimental and calculated values of the burning-rates are different may be explained, as for the Fe/peroxide systems, if the effective thermal diffusivities, under combustion conditions (see Table 9.5), are greater than those predicted, through increased thermal conductivities and/or decreased heat capacities at higher temperatures. The results in Table 12.5 suggest that the increased contribution to the thermal diffusivity probably arises from the presence of excess metal fuel.

Further discussion on the combustion of the pyrotechnic systems discussed in Sections 9 to 12 is provided in Section 15.

13. Ternary Zn, Fe/peroxide systems

13.1 Introduction

The burning characteristics of the binary Fe/peroxide systems are described in Sections 9 and 10. Fe/BaO_2 compositions from 15 to 50% Fe burn with linear burning-rates of from 10.0 mm s^{-1} (15% Fe) to 39.1 mm s^{-1} (30% Fe) and Fe/SrO_2 compositions from 20 to 55% Fe with burning-rates of from 3.6 mm s^{-1} (20% Fe) to 8.3 mm s^{-1} (40% Fe), when compacted at 55 MPa. Similarly, the burning characteristics of the binary Zn/peroxide systems are described in Sections 11 and 12. Zn/BaO_2 compositions support combustion from 10 to 65% Zn with linear burning-rates of from 4.9 mm s^{-1} (65% Zn) to 75.2 mm s^{-1} (45% Zn) in the uncompacted state, while this range is decreased to 30 to 55% Zn with linear burning-rates of from 7.5 mm s^{-1} (30% Zn) to 32.9 mm s^{-1} (45% Zn) when mixtures are compacted to 0.2 MPa prior to combustion. The Zn/SrO_2 compositions support combustion in the range 30 to 80% Zn, with burning-rates of from 4.8 mm s^{-1} (80% Zn) to 24.9 mm s^{-1} (50% Zn), when burned in the uncompacted state. The burning-range is decreased to 30 to 55% Zn when mixtures are compacted at 0.2 MPa prior to combustion, with burning-rates being lowered in the process, giving a range of from 4.3 mm s^{-1} (30% Zn) to 12.3 mm s^{-1} (45% Zn). It was thus of interest to examine the effect of the addition of Zn on the combustion characteristics of the Fe/peroxide systems (which react well above the 908°C boiling point of Zn), and the effect of addition of Fe on the combustion characteristics of Zn/peroxide systems.

13.2 The Zn, Fe/BaO_2 system

Under compaction (55 MPa), the addition of Zn powder in proportions of up to 30% to a 20% Fe/BaO_2 composition, could be followed by successful initiation of combustion. At higher proportions of zinc, reaction was often not sustained or material was ejected from the channel as a result of rapid vaporisation of Zn. Although addition of 5 and 10% Zn by mass to the 20% Fe/BaO_2 system had little effect on the overall shape of the temperature profiles, the addition of more than 15% resulted in a decrease in the U_{max} values recorded by by ~200 K (Figure 13.1), and a broadening in the rise region. The effect of addition of Zn on the burning-rate was an approximately linear decrease up to 30% (Figure 13.2). The results of the addition of Zn to the 20% Fe/BaO_2 system are shown in Table 13.1.

TABLE 13.1: The effect of Zn on burning-rates and U_{max} values of the 20% Fe/BaO_2 system

Proportion of Zn/[%]	$v_{observed}$/[mm s^{-1}]	U_{max}/[K]
0	18.1±1.6	1550±25
1	12.1±1.4	1560±30
5	10.8±1.5	1499±30
10	10.5±1.2	1449±30
15	9.7±1.4	1246±35
20	8.4±1.1	1216±30
25	7.8±0.9	1192±25
30	6.5±1.0	1172±30

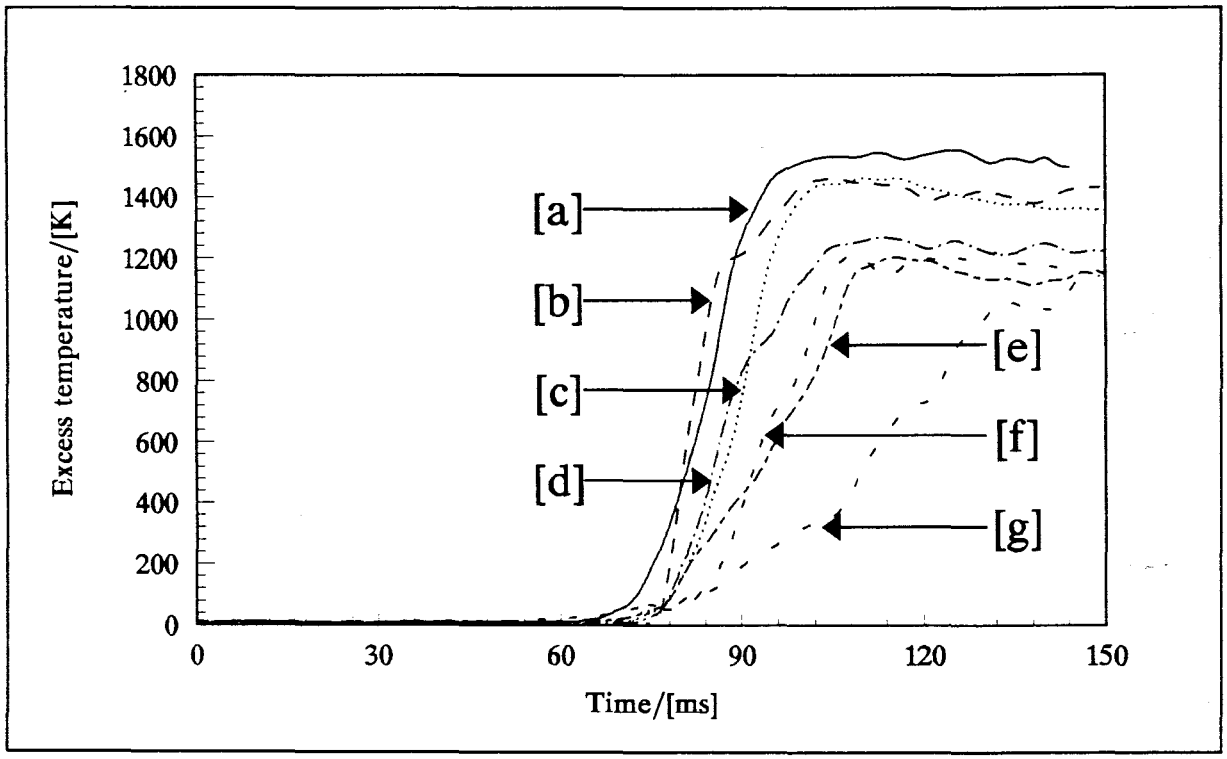

FIGURE 13.1: Effect of zinc on temperature profiles of 20% Fe/BaO_2 [a]:0%, [b]:1%, [c]:5%, [d]:10%, [e]:15%, [f]:20% and [g]:25%

The burning-rates of the ternary systems generated by inclusion of Zn in the Fe/BaO_2 system are represented by the surface shown in Figure 13.3. Since no combustion could be initiated in the Zn/BaO_2 system at compaction pressures of 55 MPa, these burning-rates have been omitted from the diagram.

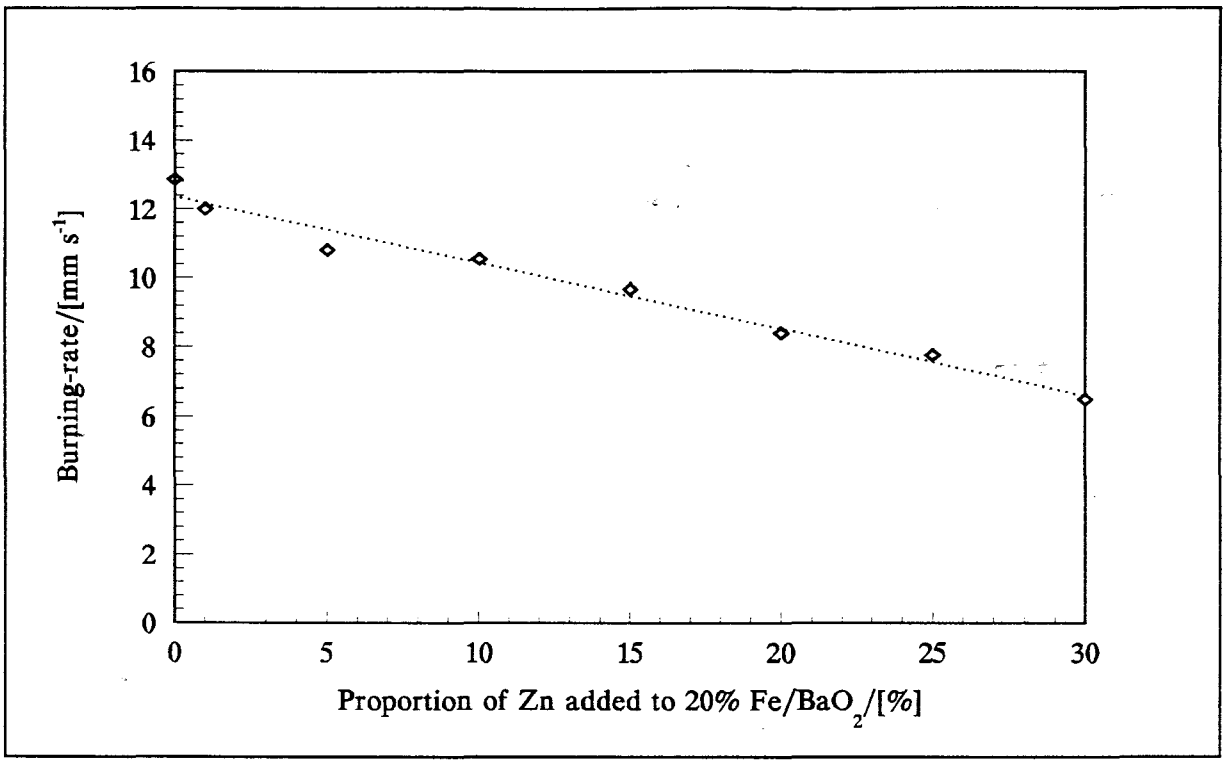

FIGURE 13.2: Effect of zinc on burning-rates of 20% Fe/BaO_2

13.3 The Zn, Fe/SrO_2 system

Under compaction (55 MPa), the addition of quantities of up to 15% Zn to 25% Fe/SrO_2 could be followed by successful initiation of combustion (Figure 13.4), but the zinc vapour generated in systems of high zinc content at the combustion temperatures of the Fe/SrO_2 reaction, often resulted in stifling of reaction and ejection of material from the channel (a similar situation to that observed when Zn was added to the Fe/BaO_2 system). Although the effect on U_{max} was negligible, the rise region of profiles was broadened extensively by the addition of zinc to the system. The 15% Zn system sometimes produced an irreproducible feature of a plateau at 910°C for about 50 ms (not shown), typical of a Type IV temperature profile (Section 3.10). This was the result of vaporisation of the zinc metal in the reaction zone [98]. The variation of burning-rate induced by the introduction of Zn was approximately linear (Figure 13.5). Table 13.2 shows the variation of U_{max} and burning-rate as the proportion of zinc is increased in the system.

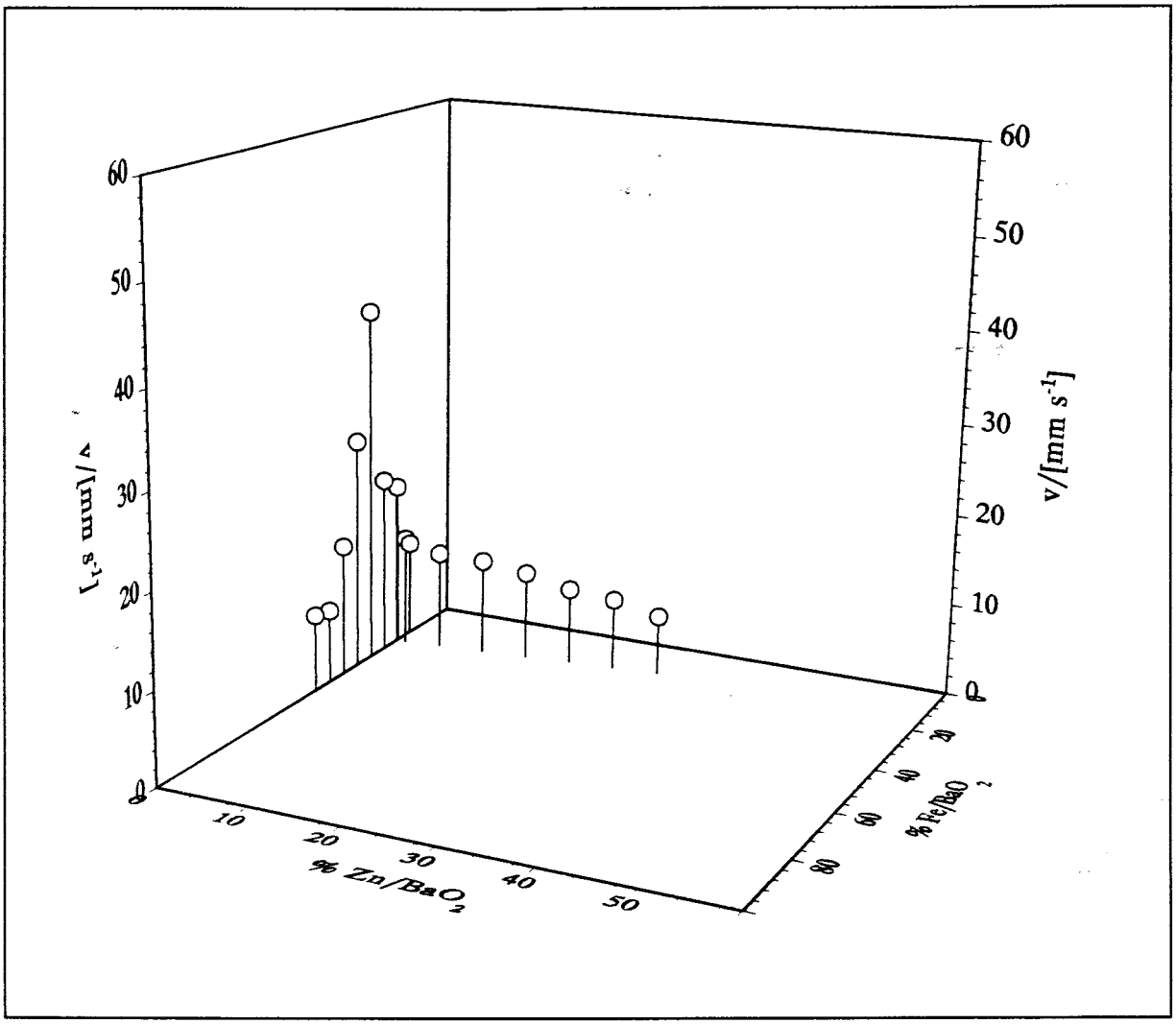

FIGURE 13.3: Burning-rates of the Zn, Fe/BaO_2 system represented as a surface

TABLE 13.2: The effect of Zn on U_{max} and burning-rates of the 25% Fe/SrO_2 system

Proportion of Zn/[%]	$v_{observed}$/[mm s^{-1}]	U_{max}/[K]
0	6.8±1.8	1265±30
1	6.4±1.7	1251±35
5	5.7±1.7	1180±35
10	4.3±1.4	1084±35
15	Incomplete combustion	1037±45
20	Incomplete combustion	1006±50

The ternary system generated by inclusion of Zn in the Fe/SrO_2 system, results in burning-rates represented approximately by the surface shown in Figure 13.6. Since no combustion could be initiated in the Zn/SrO_2 system compacted at 55 MPa, these points have been omitted from the figure.

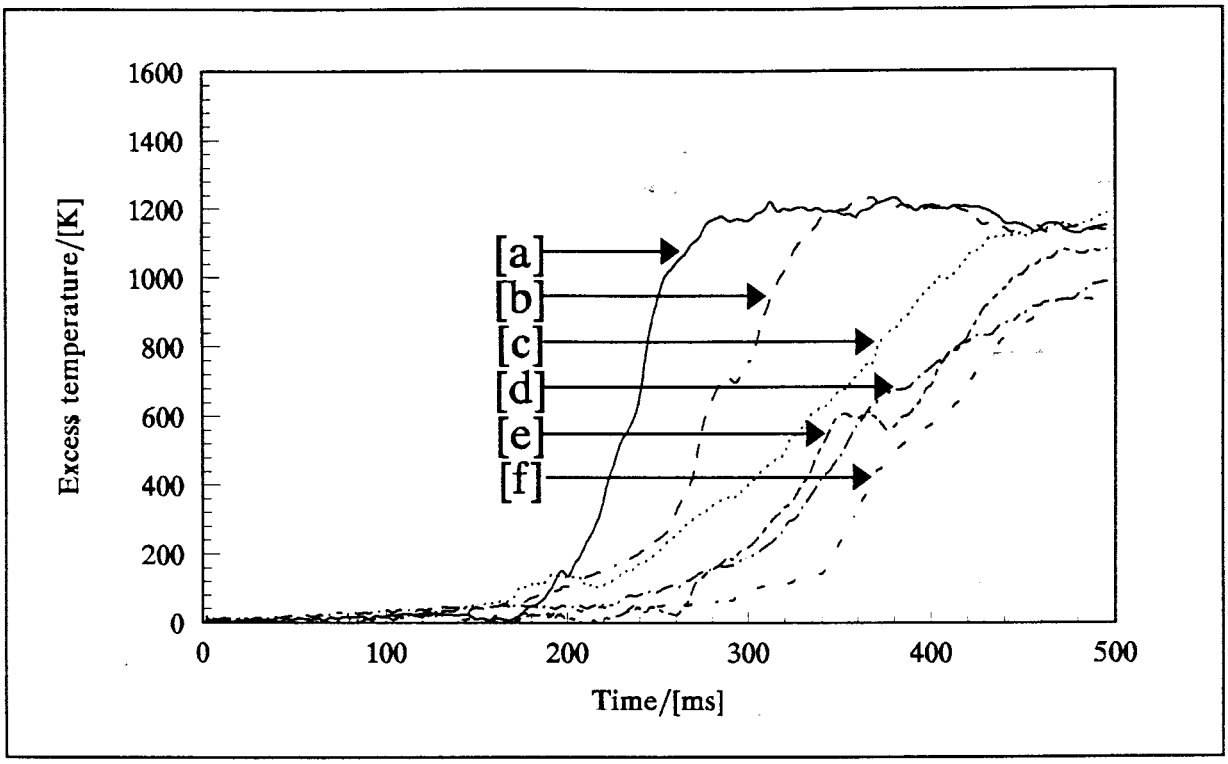

FIGURE 13.4: The effect of zinc on temperature profiles of 25% Fe/SrO_2 [a]:0%, [b]:1%, [c]:5%, [d]:10%, [e]:15% and [f]:20%

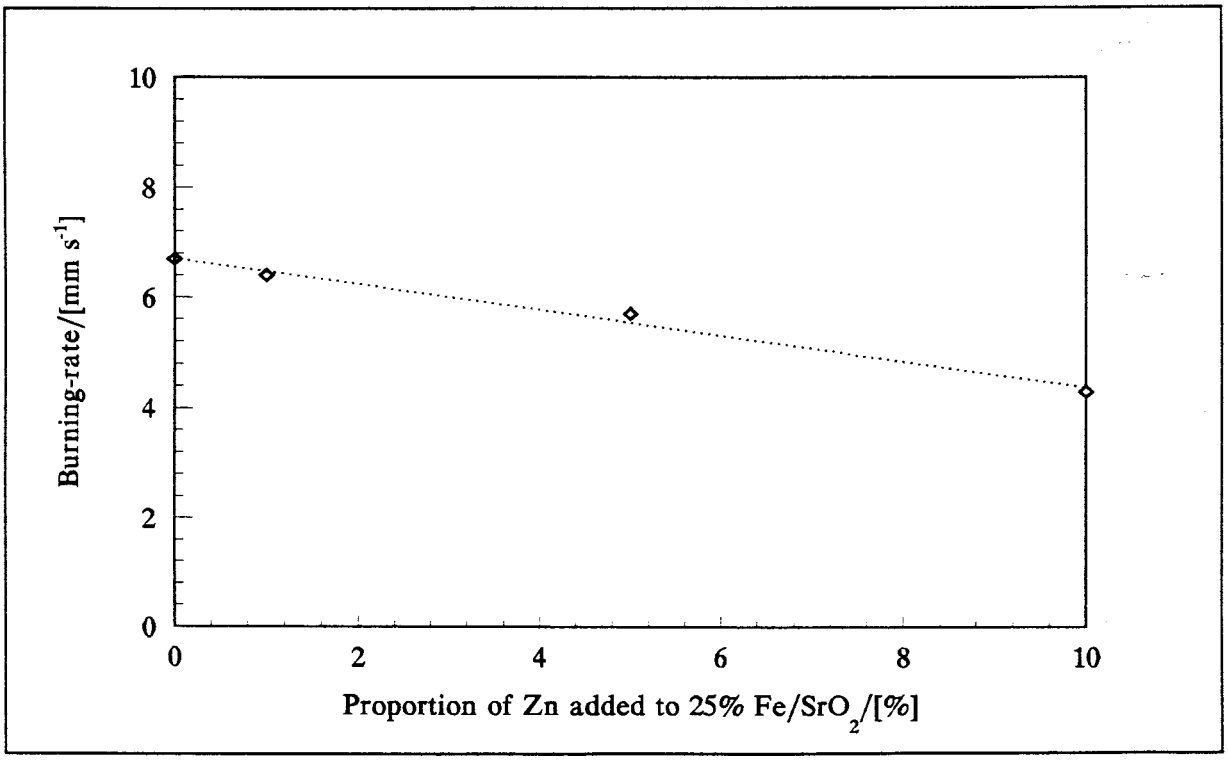

FIGURE 13.5: The effect of zinc on the burning-rates of 25% Fe/SrO_2

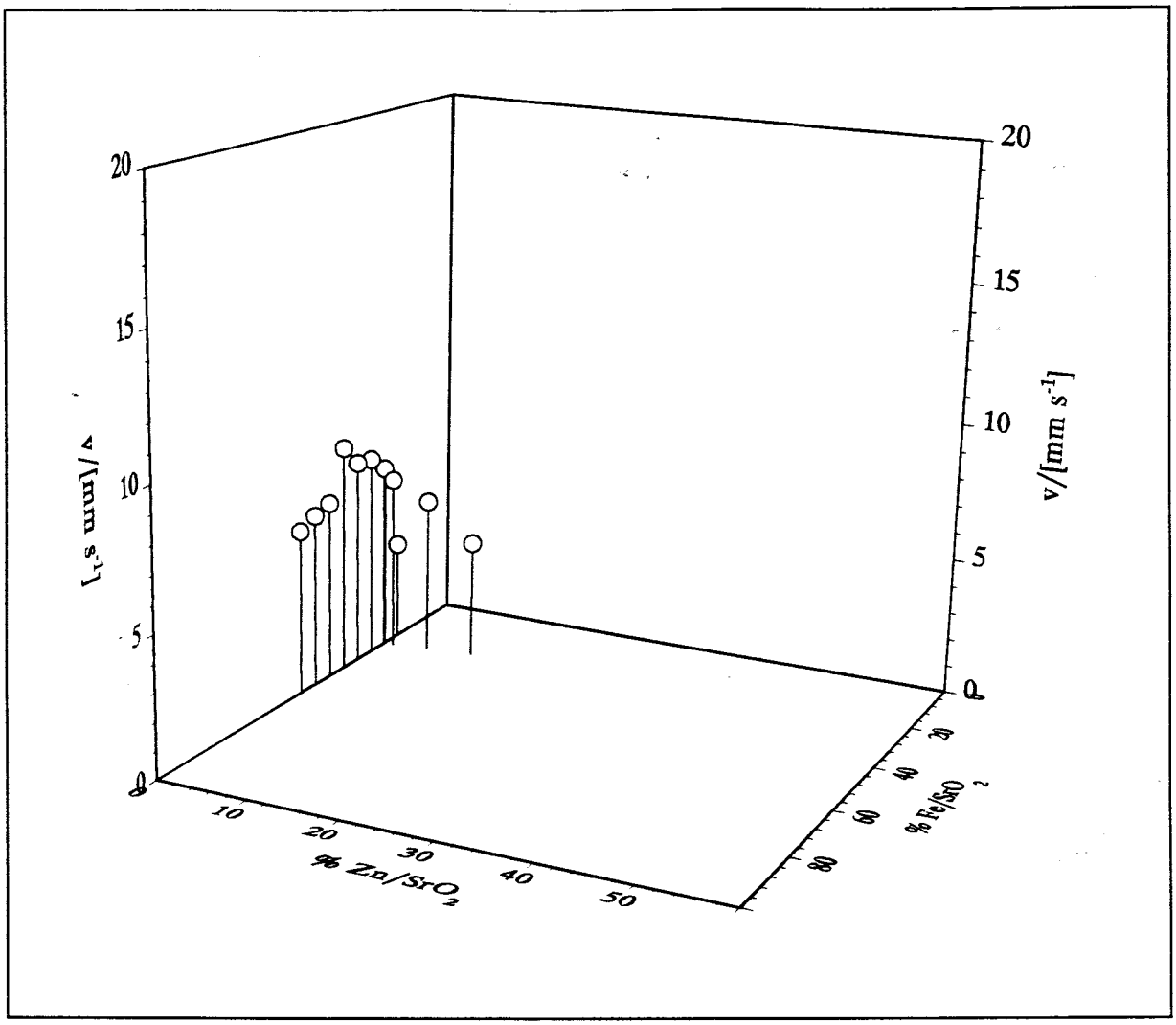

FIGURE 13.6: Burning-rates of the Zn, Fe/SrO_2 system represented as a surface

13.4 The Fe, Zn/BaO_2 system

The introduction of Fe into the system as an additional fuel provided further information on the ternary Zn, Fe/peroxide systems discussed above, where studies on the effect of zinc on the Fe/BaO_2 system revealed that the addition of more than 10% Zn resulted in an almost linear decrease of the burning-rate, lowering of U_{max} and broadening of the rise-region.

Addition of small amounts (1%) of Fe to the compacted Zn/BaO_2 system (Figure 13.8) decreased the burning-rate from 7.5 mm s^{-1} to 4.3 mm s^{-1}. Greater proportions of Fe stifled the 200 kPa compacted mixture, but combustion was still supported for the uncompacted systems, with burning rates of ~30 mm s^{-1} in both the 1% and 5% samples. Temperature profiles of uncompacted mixtures showed an apparent enhancement of reaction (since the width of the rise region decreased), but U_{max} was unchanged (Figure 13.7) suggesting the variation to be due to the irreproducibility of temperature profiles.

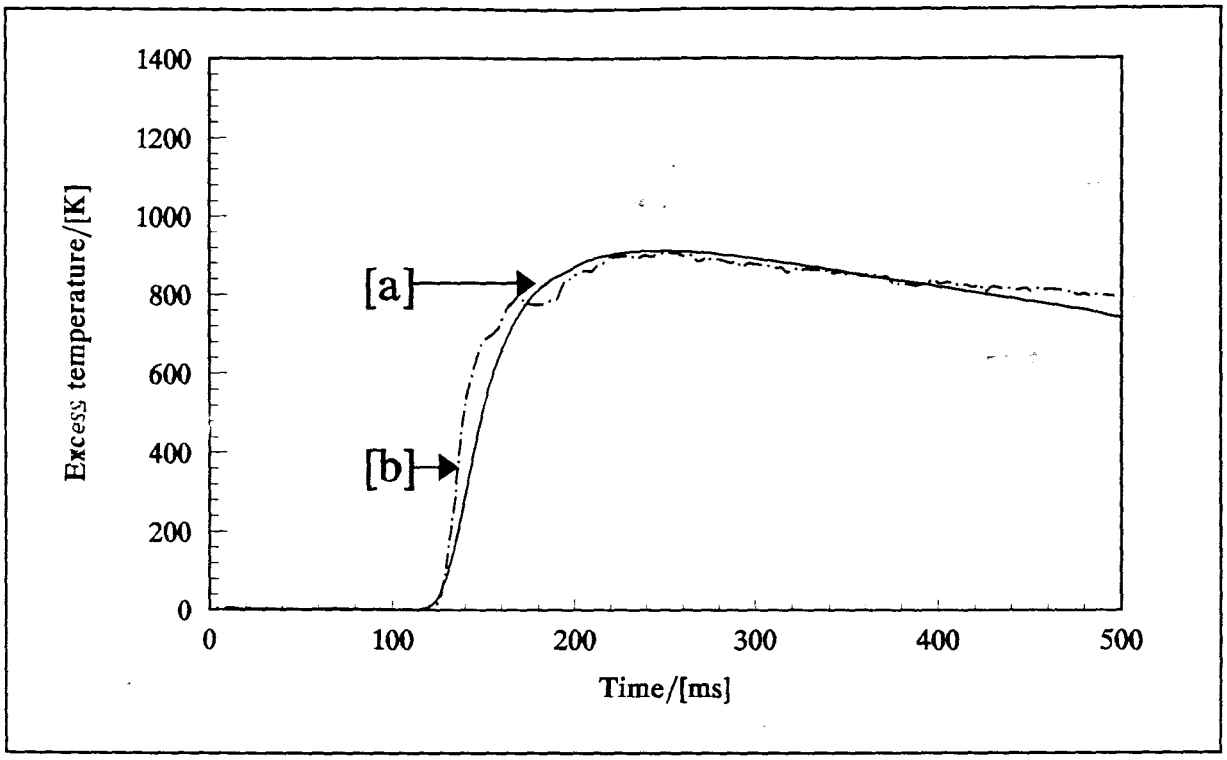

FIGURE 13.7: Effect of Fe on temperature profiles of uncompacted 30% Zn/BaO_2 [a]: 0% and [b]: 1% Fe

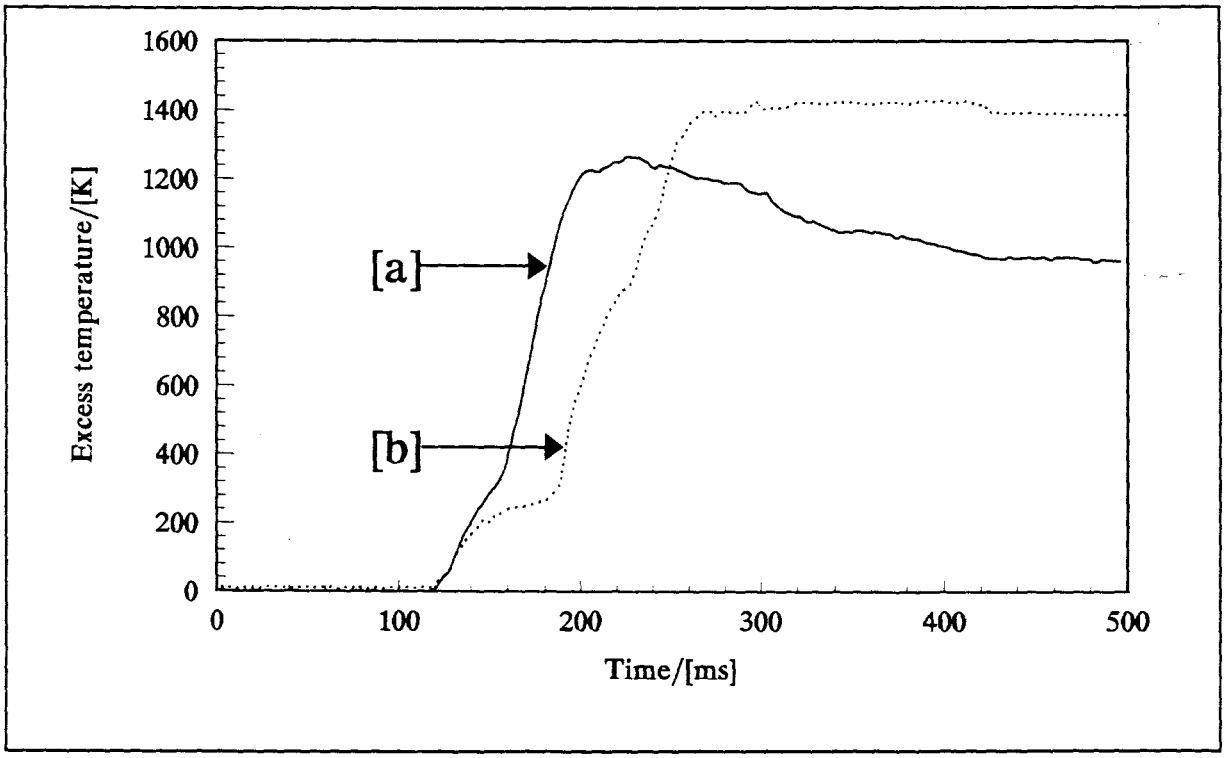

FIGURE 13.8: Effect of Fe on profiles of 30% Zn/BaO_2 compacted at 0.2 MPa [a]: 0% and [b]: 1% Fe

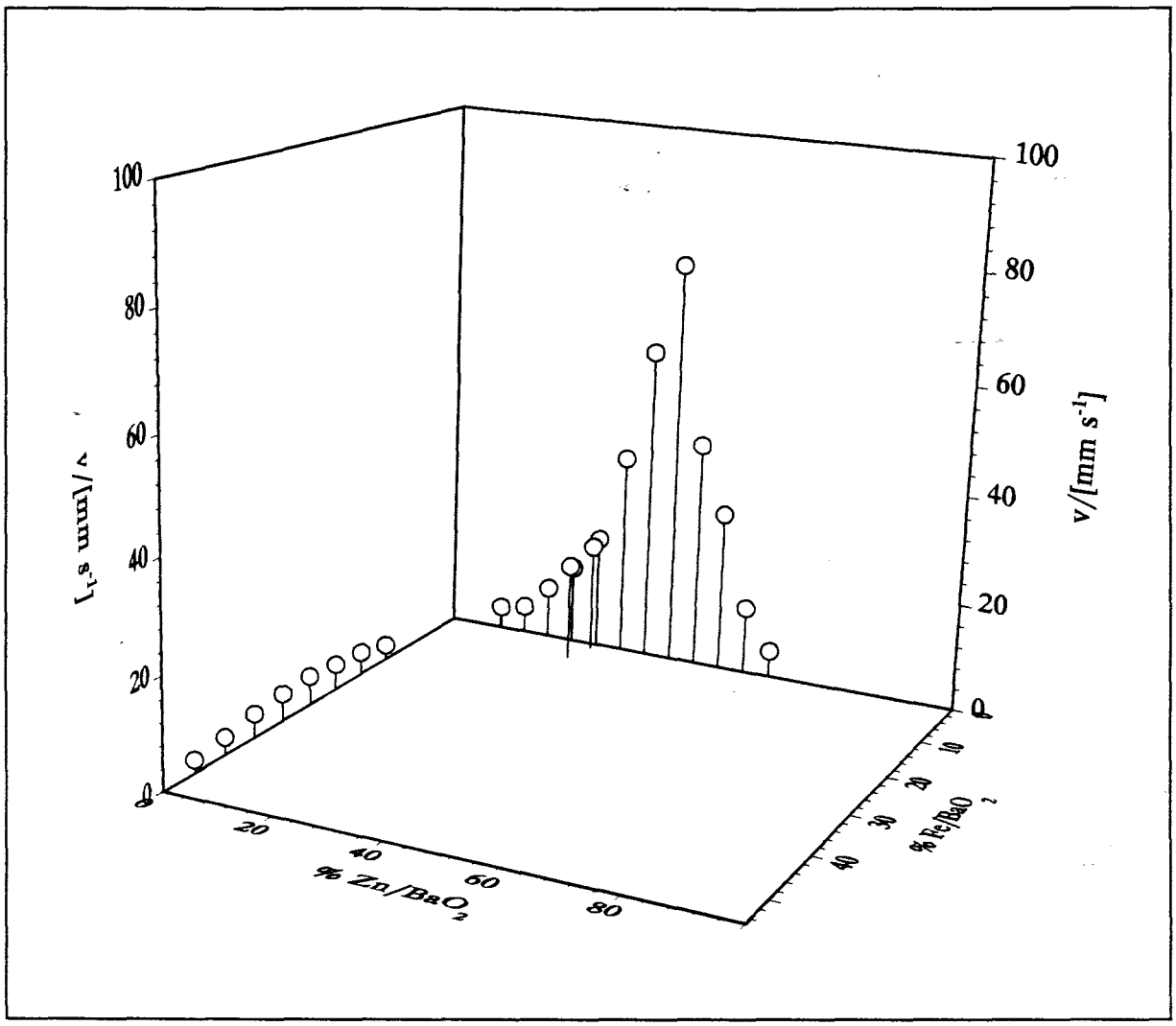

FIGURE 13.9: Burning-rates of the uncompacted Fe, Zn/BaO_2 system as a surface

The burning-rates of the ternary system generated by inclusion of Fe in the Zn/BaO_2 system are represented approximately by the surfaces shown in Figures 13.9 and 13.10.

13.5 The Fe, Zn/SrO_2 system

The ternary system generated by the introduction of Fe as a fuel, was an extension of the system studied in Section 13.3, namely the Zn, Fe/SrO_2 system, and showed a linear decrease in burning-rate with proportion of zinc added to the mixture.

Introduction of Fe into the Zn/SrO_2 system raised U_{max} and narrowed the rise regions of uncompacted profiles (Figure 13.11), yet lowered U_{max} and broadened the rise regions of mixtures compacted under 200 kPa (Figure 13.12). Burning rates were more dependent on compaction than on the proportion of Fe added, as the addition of 1% and 5% Fe by mass resulted in similar burn rates under 200 kPa compaction (2.8 and 2.3 mm s^{-1}) and in the uncompacted state (10.2 and 9.7 mm s^{-1}), respectively.

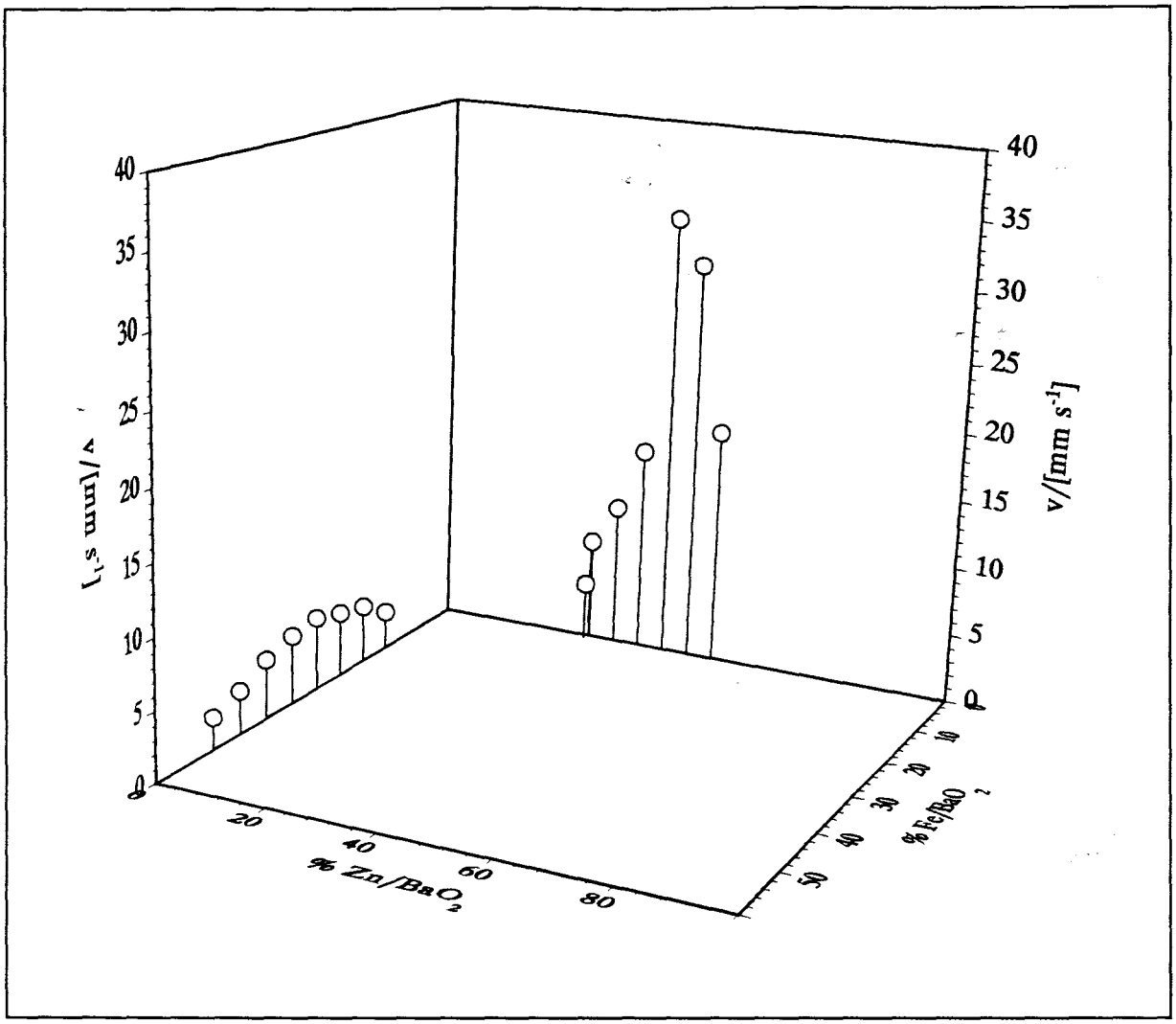

FIGURE 13.10: Burning-rates of the Fe, Zn/BaO_2 system, compacted at 0.2 MPa, as a surface

The ternary system generated by inclusion of Fe in the Zn/SrO_2 system, results in burning-rates represented approximately by the surfaces shown in Figures 13.13 and 13.14. These ternary systems are discussed further in Section 15.

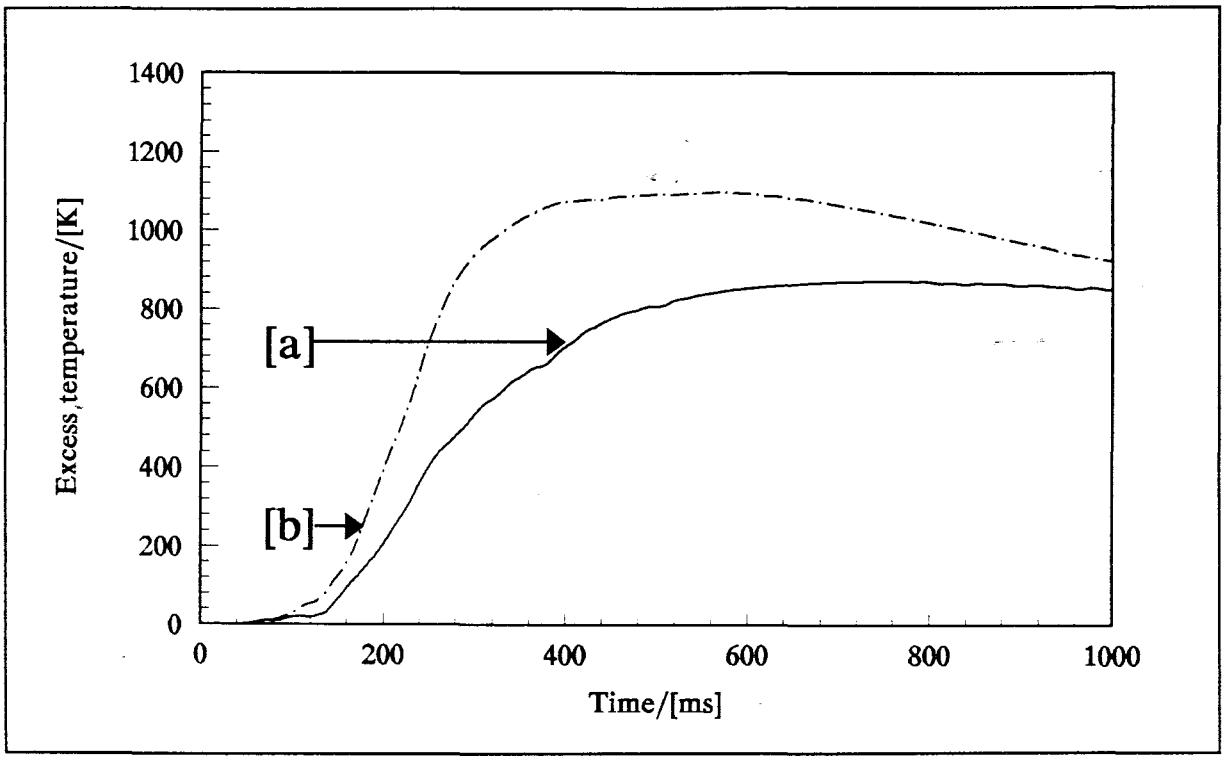

FIGURE 13.11: The effect of Fe on temperature profiles of uncompacted 30% Zn/SrO_2 [a]: 0% and [b]: 1% Fe

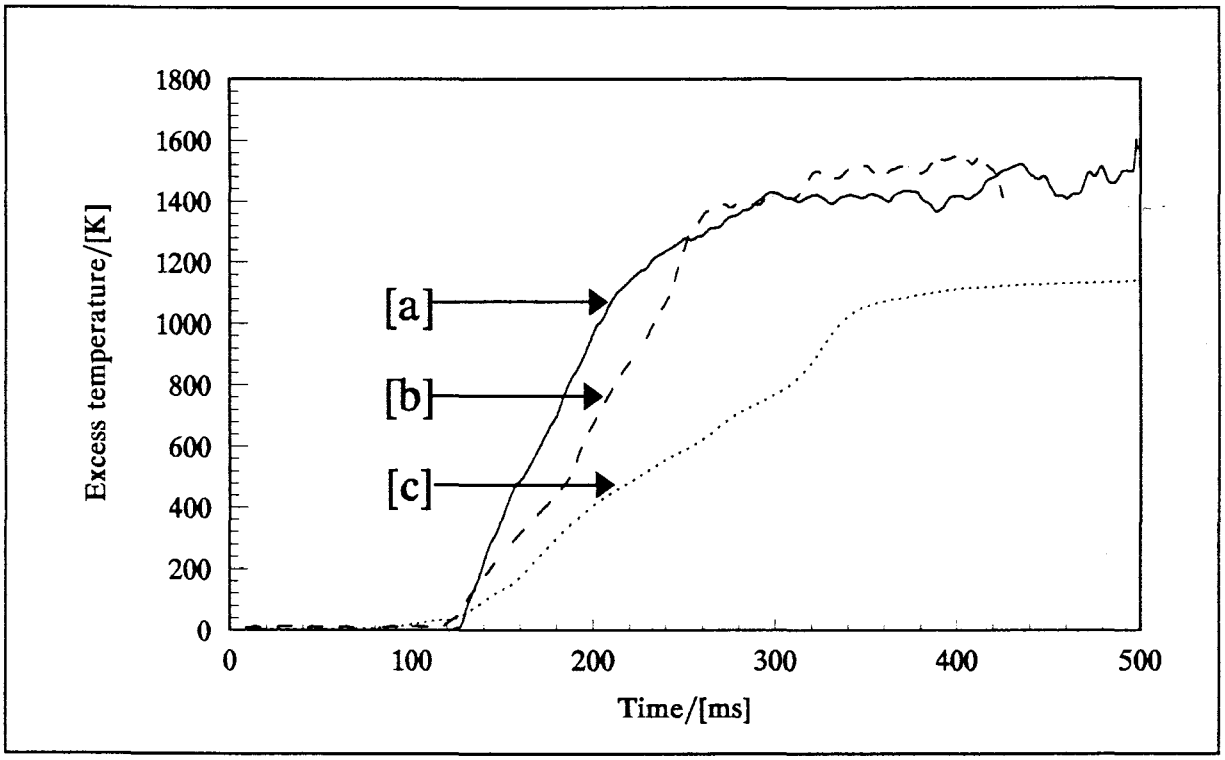

FIGURE 13.12: The effect of Fe on profiles of 30% Zn/SrO_2 compacted at 0.2 MPa [a]: 0%, [b]: 1% Fe and [c]: 5% Fe

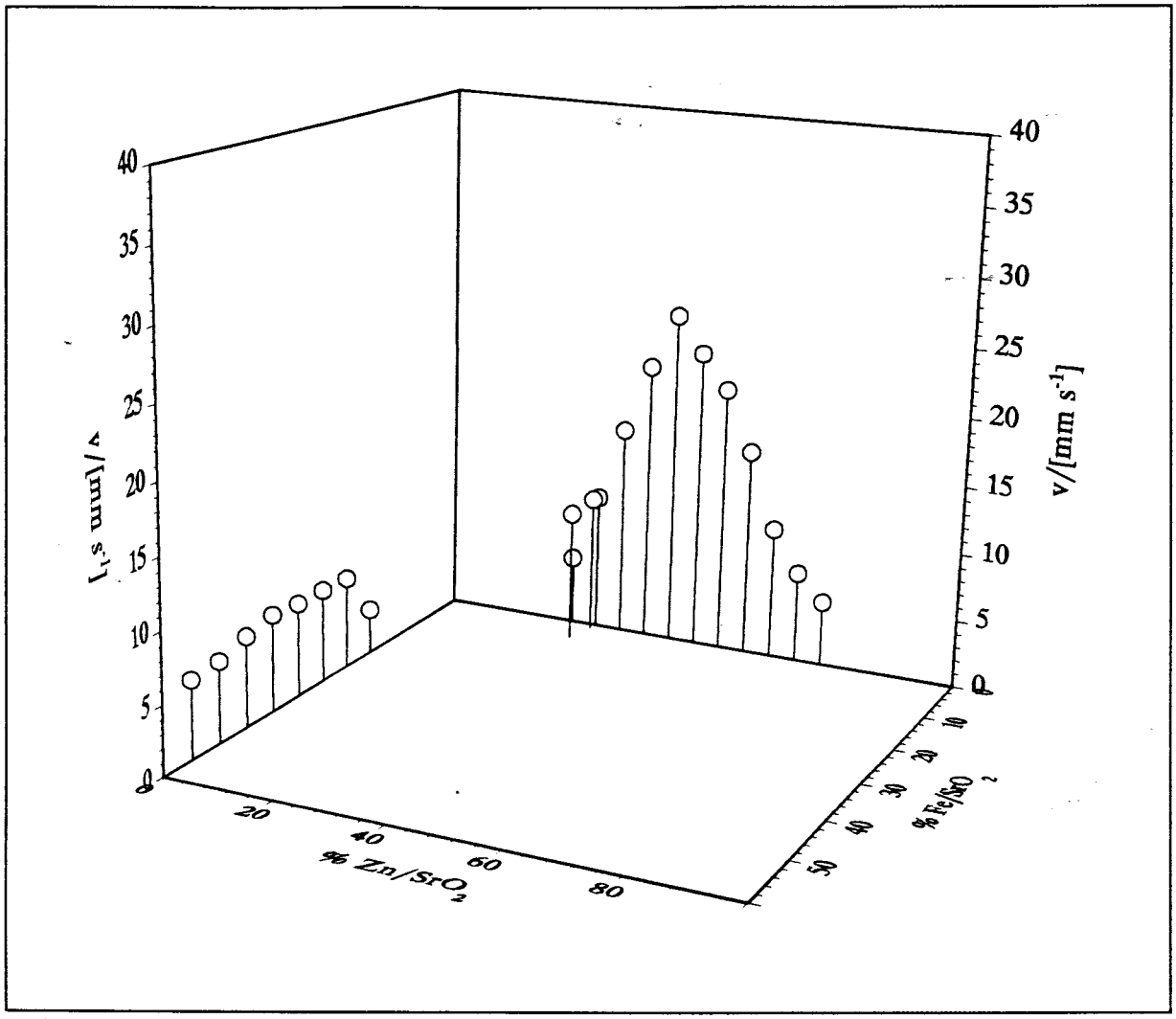

FIGURE 13.13: Burning-rates of the uncompacted Fe, Zn/SrO_2 system, represented as a surface

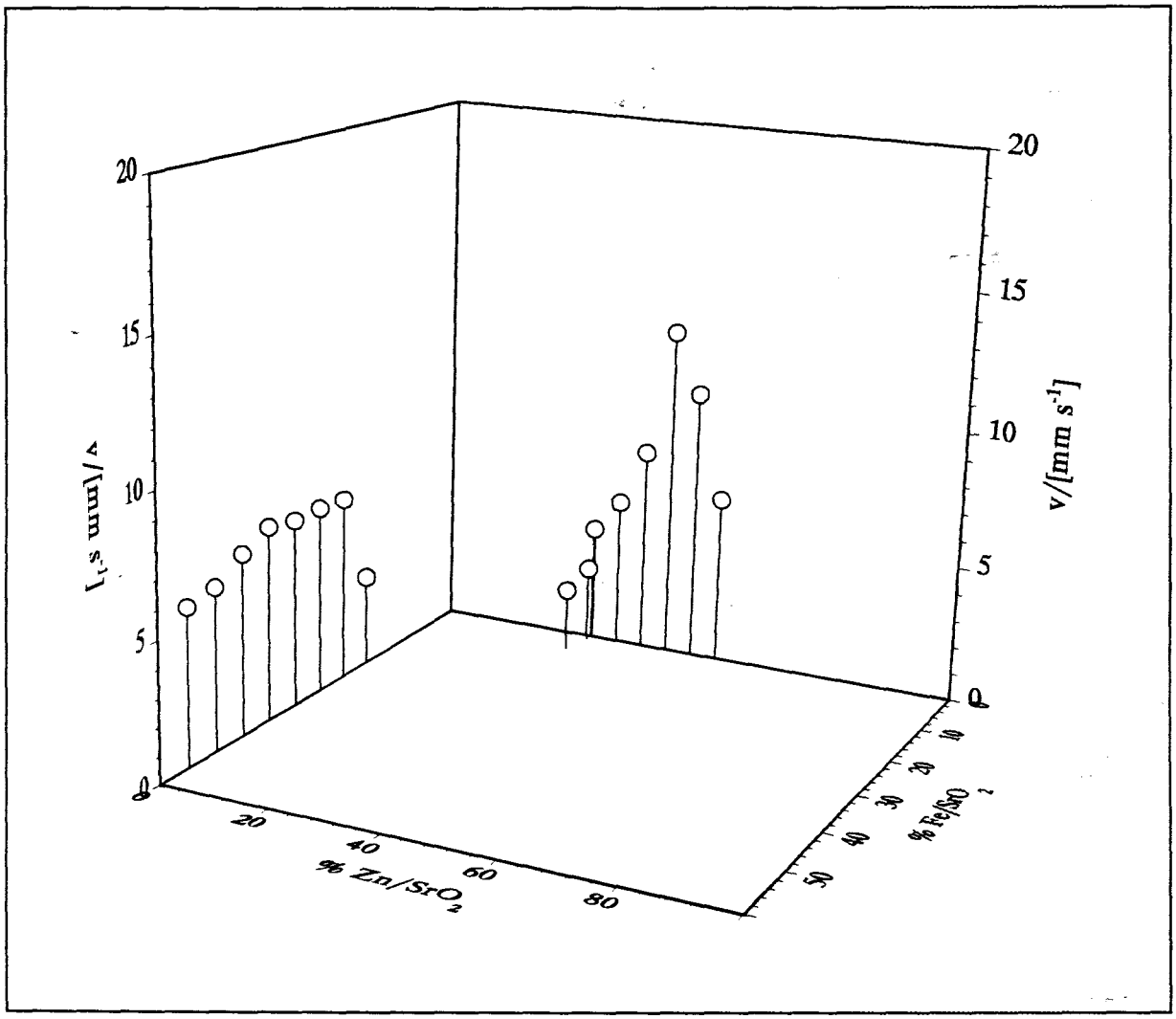

FIGURE 13.14: Burning-rates of the Fe, Zn/SrO_2 system, compacted at 0.2 MPa, as a surface

14. CHARACTERISATION OF MATERIALS:

14.1 SEM and fine-wire studies:

14.1.1 The fuels:

The particle-size distribution of the iron and zinc powders was determined by scanning electron microscopy (SEM). The iron (Plate 14.1) consisted of relatively smooth spherical particles, ranging from 1-5 μm in diameter (mean 4 μm), with some coalescence of particles taking place. The zinc (Plate 14.2) showed a wide range of particle sizes, predominantly smooth spheres in the 2-5 μm range, with a few large agglomerates which were about 10 μm in diameter.

14.1.2 Characterisation of the oxides formed by oxidation of the metal powders:

The iron and zinc powders were oxidised in air or oxygen in the TG thermobalance (Section 6). The product of slow oxidation of Fe showed irregularly-shaped particles of less than 1 μm in diameter (Plate 14.3). Some surface regions had a spongy appearance. The product of combustion in the TG had undergone melting and had a smooth surface with cracks probably caused by cooling (Plate 14.4).

Comparison of the original zinc powder reactant and the product obtained on heating in O_2 (Plate 14.5) showed that the surfaces of the zinc particles are mostly covered by fine needle-like crystallites, which have been reported in the literature [68]. The appearance of the crystallites and the maintenance of the particle shapes support reports [61] of formation of solid ZnO on molten Zn surfaces.

14.1.3 The oxidants:

The BaO_2 used consisted mainly of rough, irregularly-shaped particles (Plate 14.6), with a few more regular crystallites. Previous studies using a Malvern Mastersizer [6] showed that particle sizes were generally less than 20 μm.

Unlike the BaO_2 particles, the SrO_2 particles (Plate 14.7) had a spongy appearance and were generally <5 μm in diameter, giving the peroxide a large specific surface area.

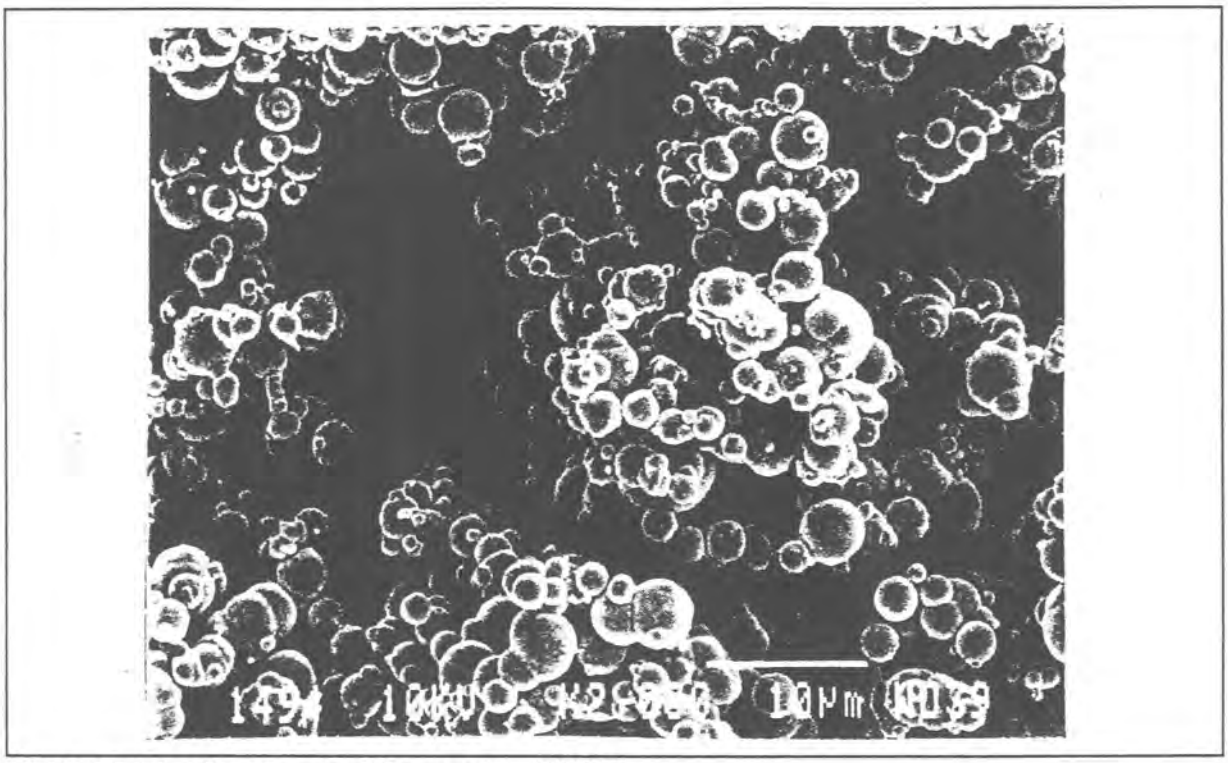

PLATE 14.1: Micrograph of Fe powder (2000X)

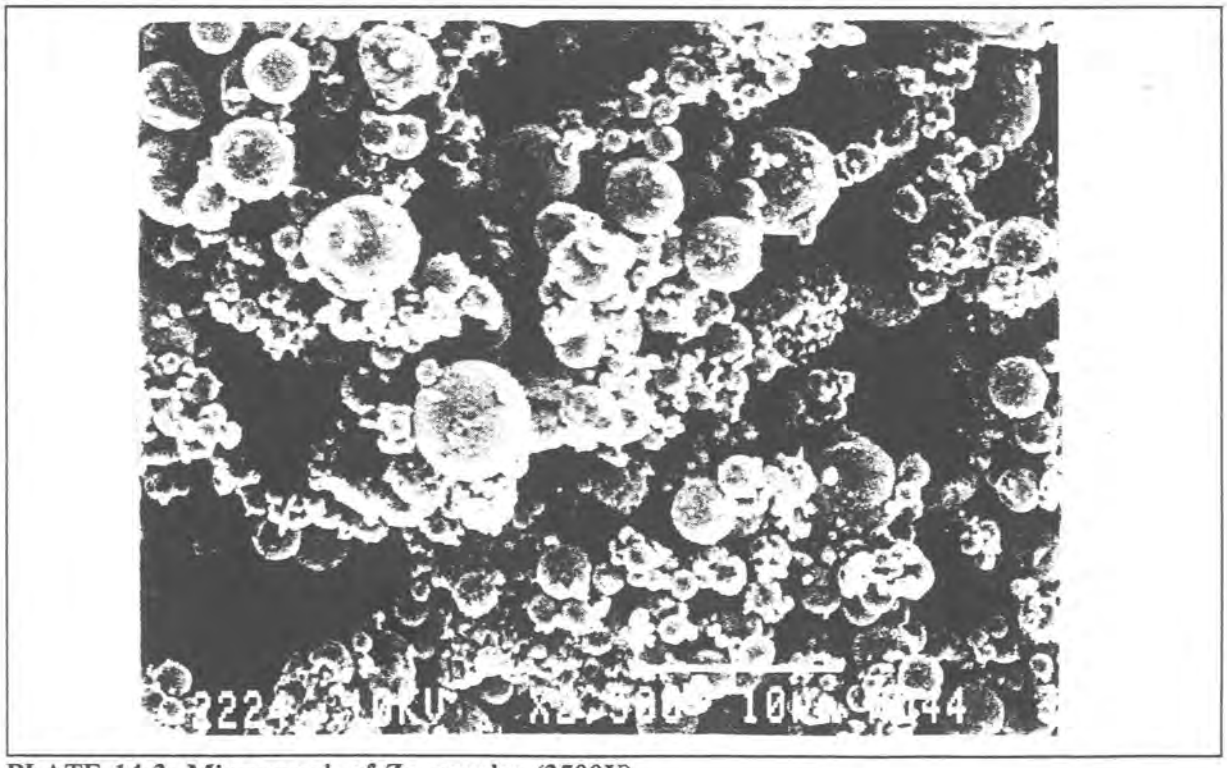

PLATE 14.2: Micrograph of Zn powder (2500X)

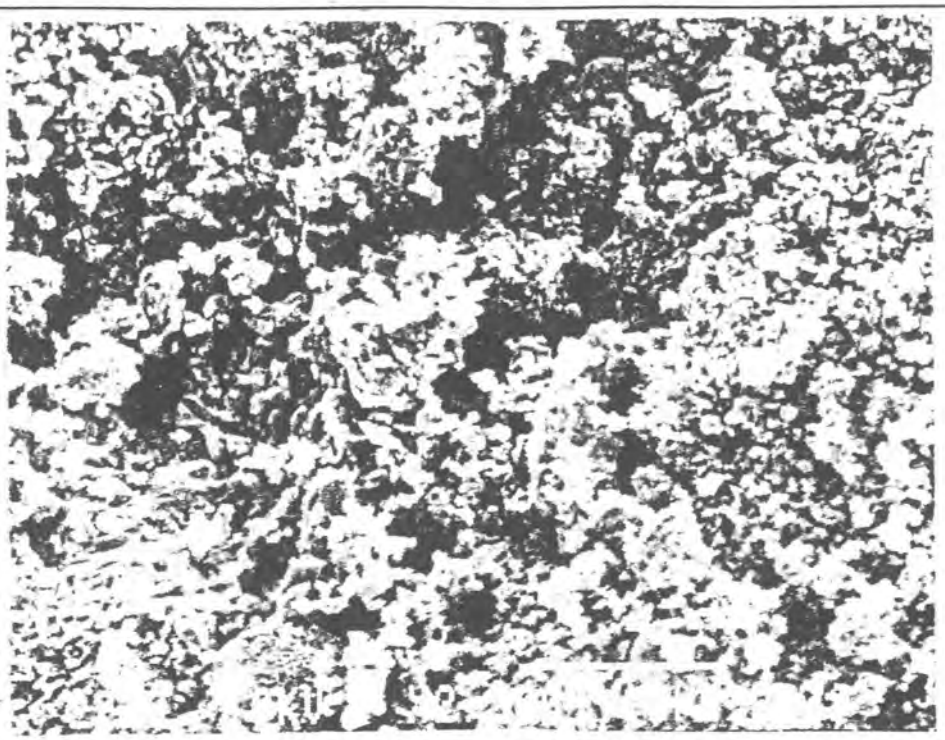

PLATE 14.3: Product of slow oxidation of Fe (2500X)

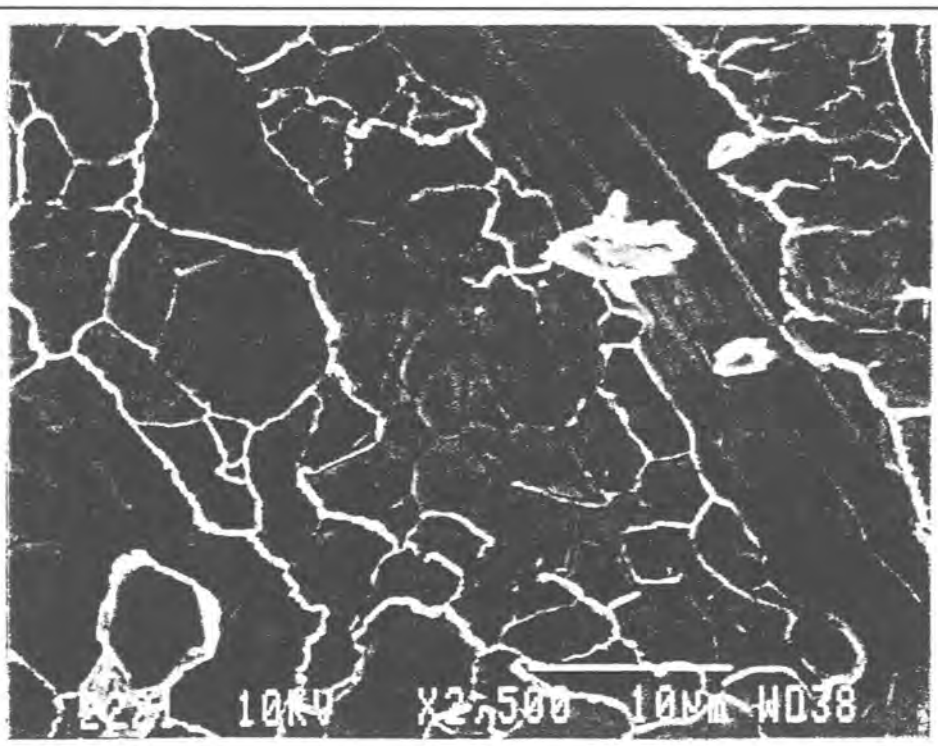

PLATE 14.4: Product of rapid oxidation of Fe (2500X)

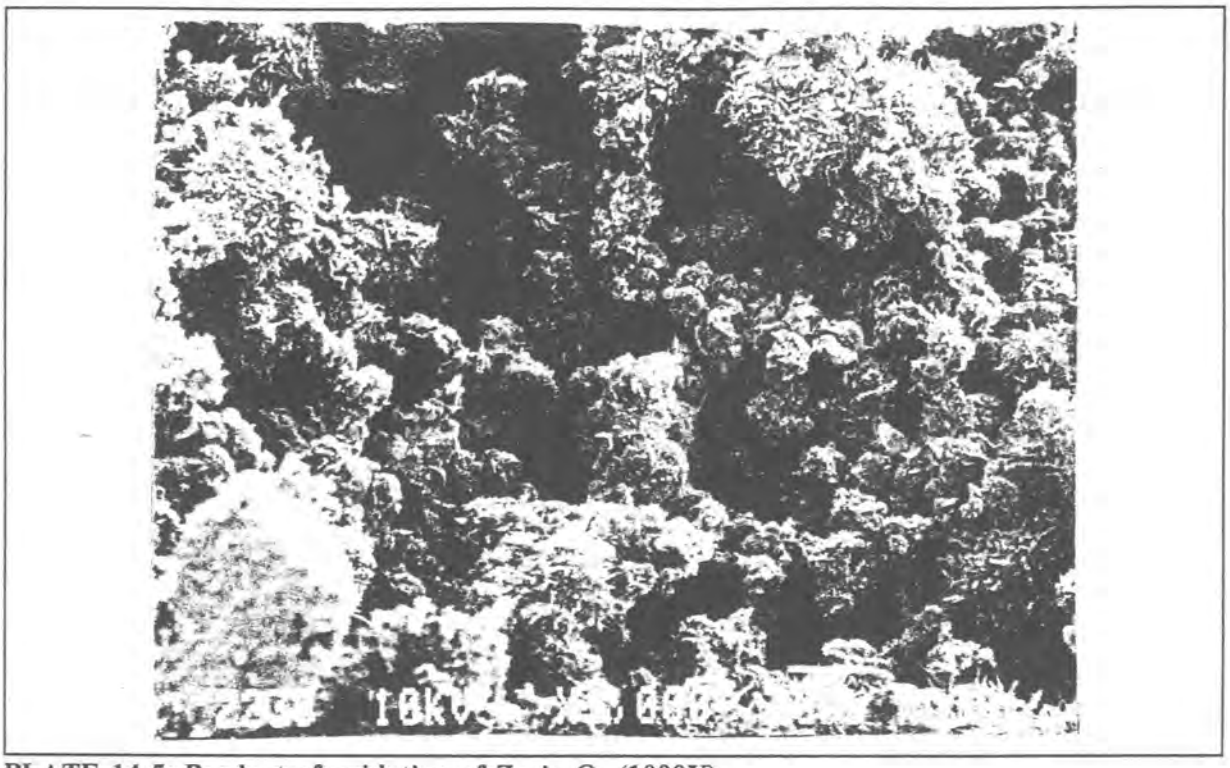

PLATE 14.5: Product of oxidation of Zn in O_2 (1000X)

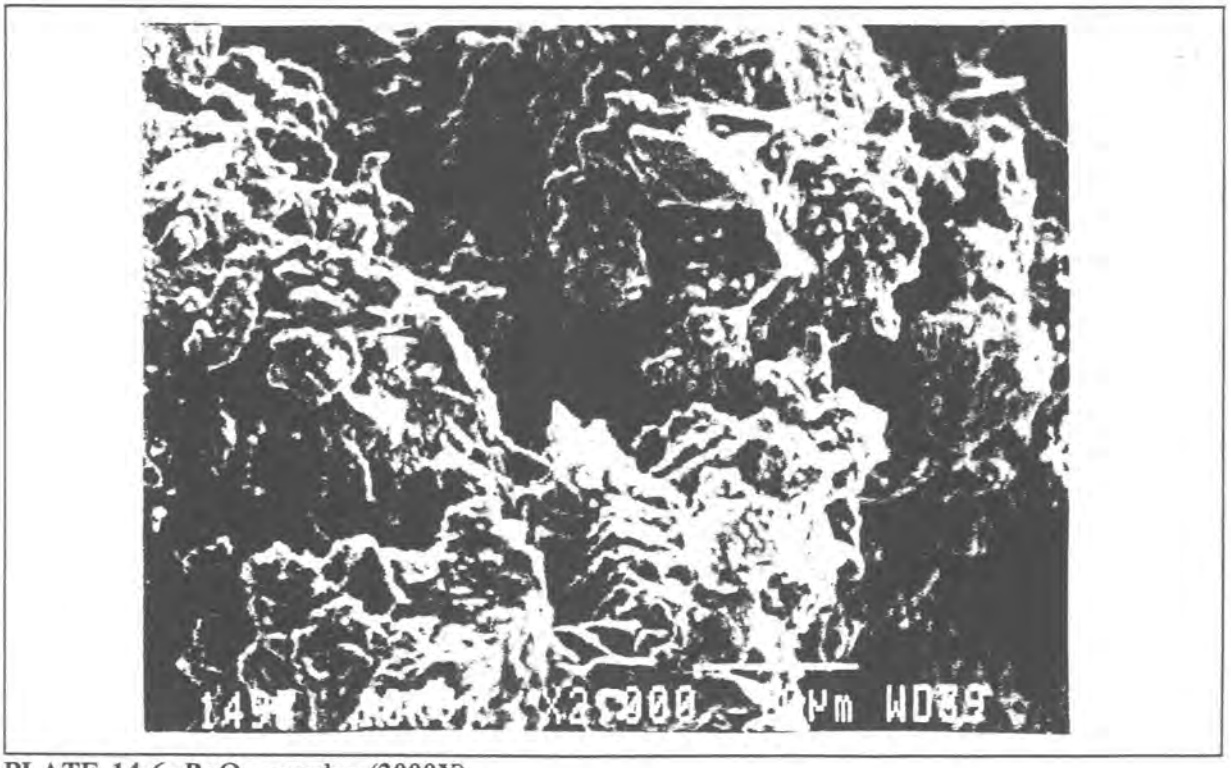

PLATE 14.6: BaO_2 powder (2000X)

14.1.4 The pyrotechnic systems:

The fuel/oxidant mixtures are described in terms of mass percentages of fuel. The mixtures chosen for study were 20% and 50% iron/barium peroxide; 25% and 55% iron/strontium peroxide; 30% and 50% zinc/barium peroxide; and 30% and 50% zinc/strontium peroxide mixtures. The mixtures were combusted and the products were examined. Combustion residues which had been stored in a desiccator for more than 72 hours were compared with fresher material, since reaction of the residues with H_2O and CO_2 in the surrounding atmosphere was difficult to prevent.

14.1.4.1 Fe/BaO_2:

Residues of combustion of 20% Fe/BaO_2 mixtures (Plate 14.8) show extensive melting and trapping of particles in the melt, when compared to the unreacted mixture (Plate 14.9). The stoichiometric ratio for Fe/BaO_2, based on formation of Fe_2O_3 and BaO, is 15.8% for 85% pure BaO_2. Temperature profiles recorded during combustion show that maximum temperatures reached can be in excess of 1600°C, but generally are about 1550°C. The melting point of iron is 1535°C, which could be decreased by the formation of some FeO (m.p. 1369°C). Although it is almost certain that BaO does not undergo melting (m.p. 1918°C), uncertainty exists about the melting of BaO_2. The melt has cracked on cooling and there is evidence of some unchanged spherical iron particles. There were no significant differences in appearance between a freshly prepared sample of the residue and residue which had been aged in a desiccator for more than 72 hours. A composition richer in iron (50% Fe/BaO_2) (Plate 14.10) also shows extensive melting, but the cooled surfaces were not as smooth as was found for 20% Fe/BaO_2. This may indicate more extensive crystallisation from the melt. The high temperatures reached in the combustion process make it possible that barium and strontium ferrates could be formed. The physical appearance of the residues showed that freshly prepared residues were green/grey, while residues which aged in desiccators of silica gel eventually became brown over a period of a few weeks. This finding agreed well with research [110] conducted into the production of $BaFe_2O_4$.

14.1.4.2 Fe/SrO_2:

The residue of combustion of 25% Fe/SrO_2 (Plate 14.11) (stoichiometric ratio for formation of Fe_2O_3 and SrO from 85% pure SrO_2 is 23.4%) also shows extensive melting with inclusion of oxidant, when compared to the unreacted pellet of the mixture (Plate 14.12). The maximum temperatures recorded during combustion were around 1300°C, far below the melting point of SrO (2430°C), which is higher than that for BaO (1918°C). No evidence for the melting of SrO_2 exists. The composition with a higher proportion of iron (55% Fe/SrO_2) (not shown) again shows a less-congealed appearance (opposite to what would be expected if iron melts) and some signs of the original iron particles.

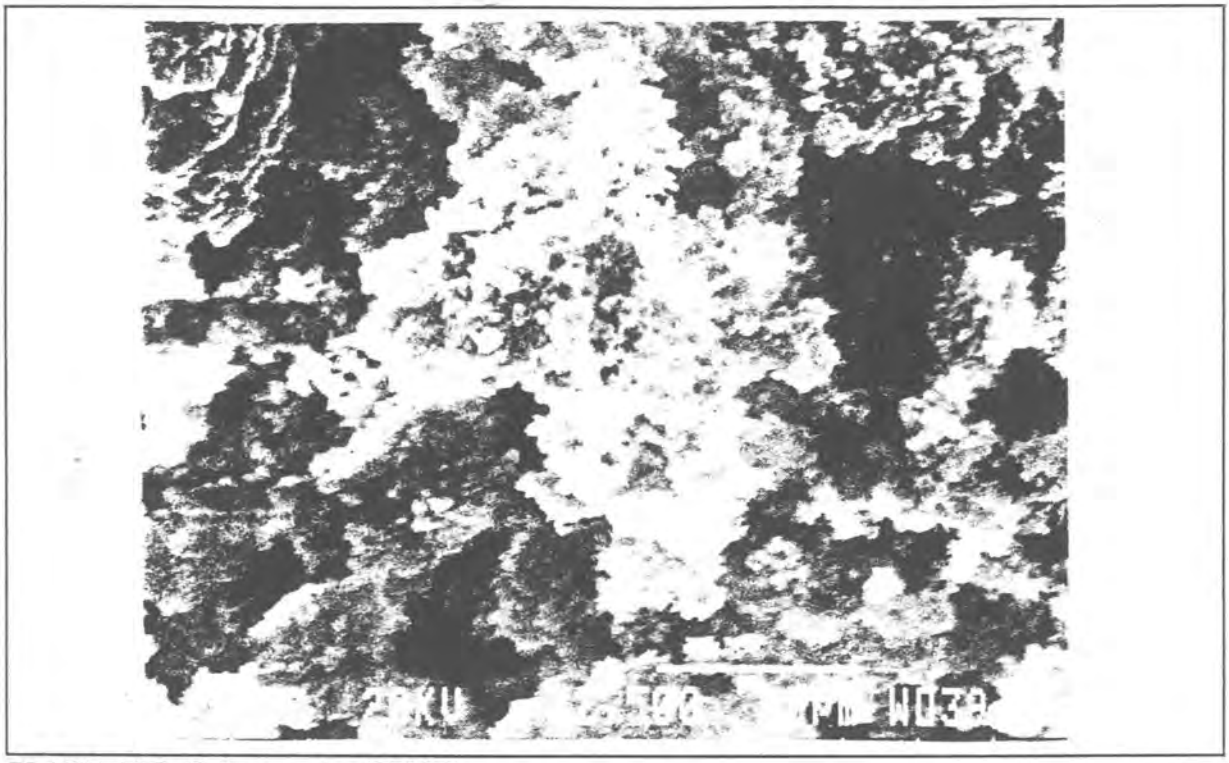

PLATE 14.7: SrO_2 powder (2500X)

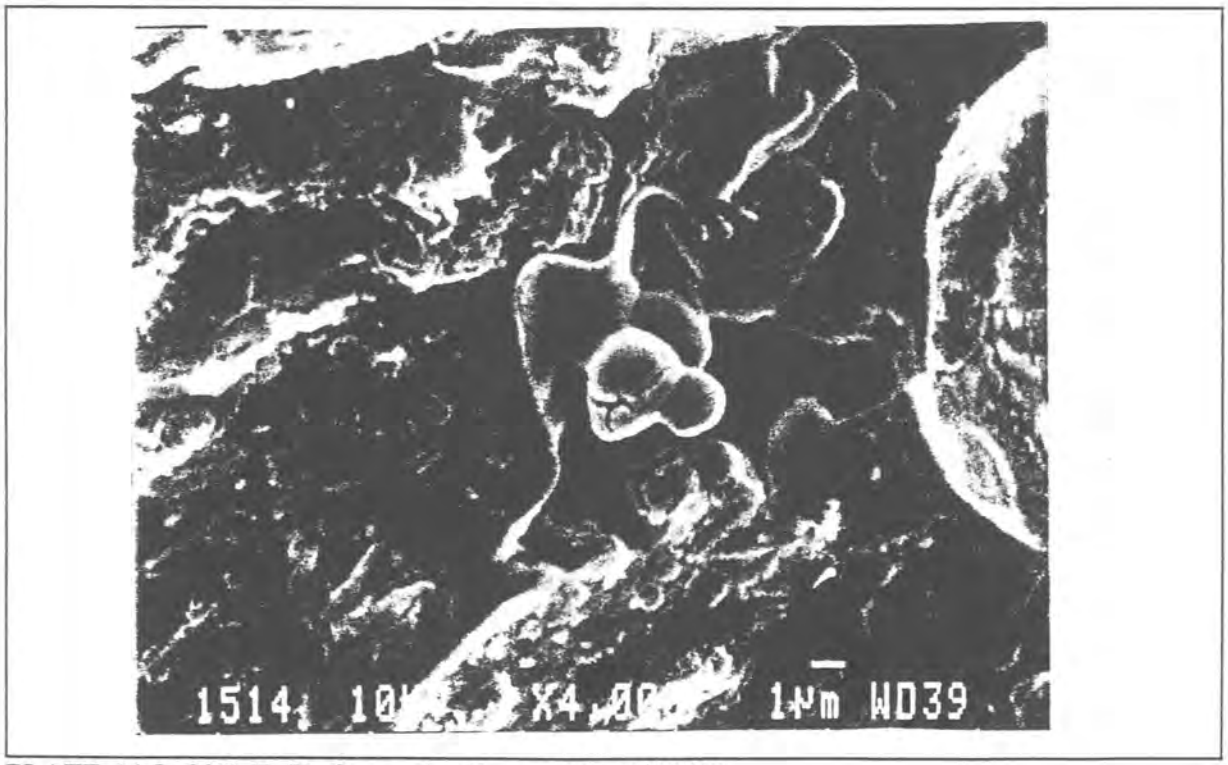

PLATE 14.8: 20% Fe/BaO_2 combustion residue (4000X)

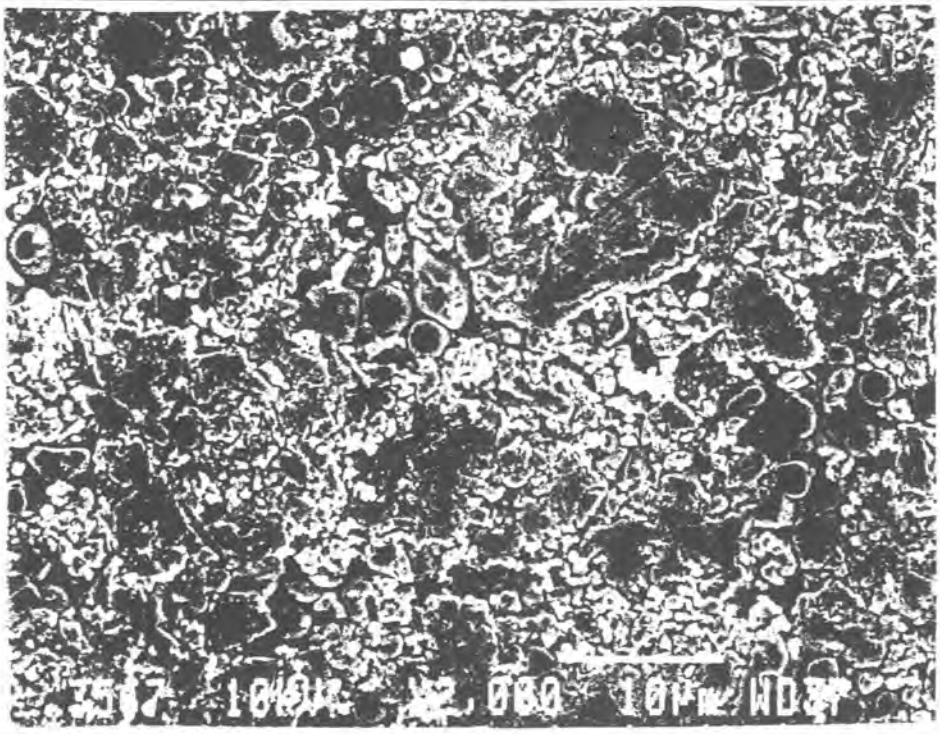

PLATE 14.9: Unreacted Fe/BaO_2 (2000X)

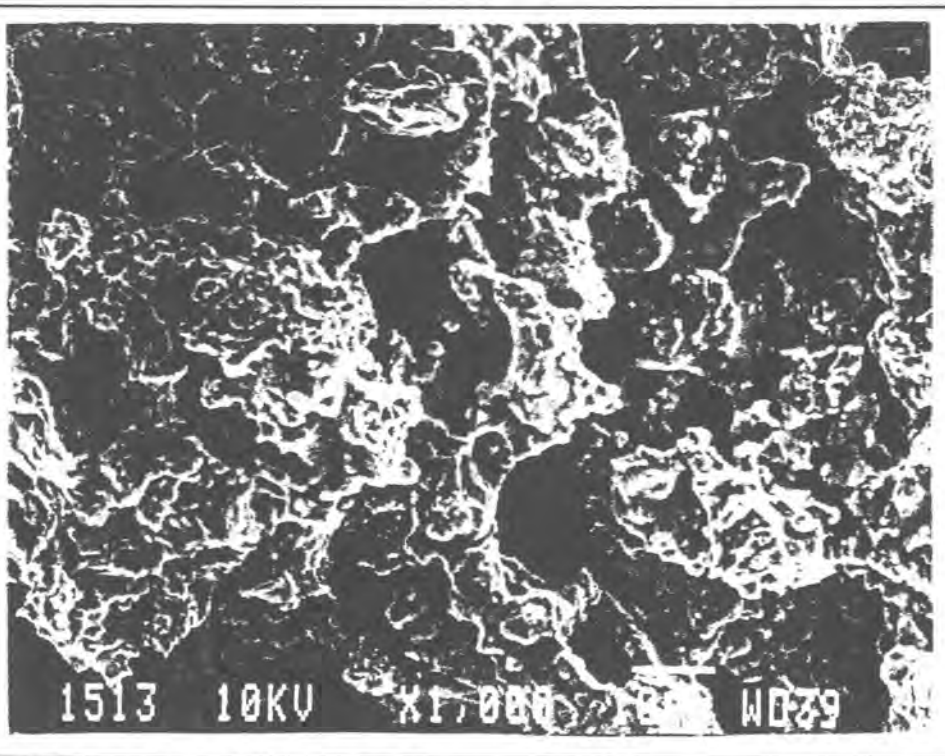

PLATE 14.10: Residue of the 50% Fe/BaO_2 system (1000X)

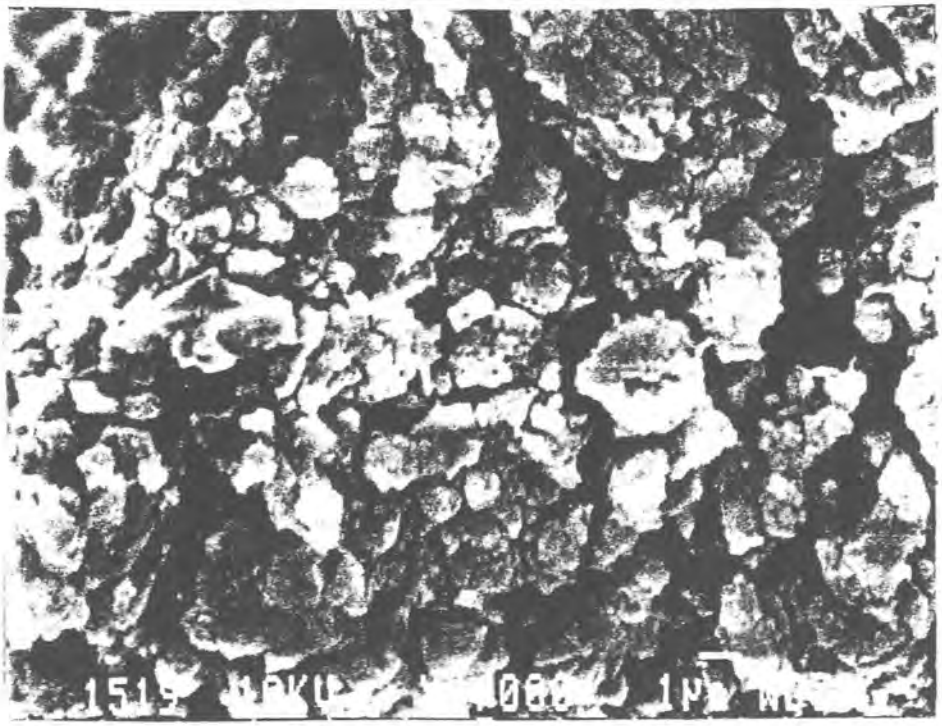

PLATE 14.11: 25% Fe/SrO_2 combustion residue (4000X)

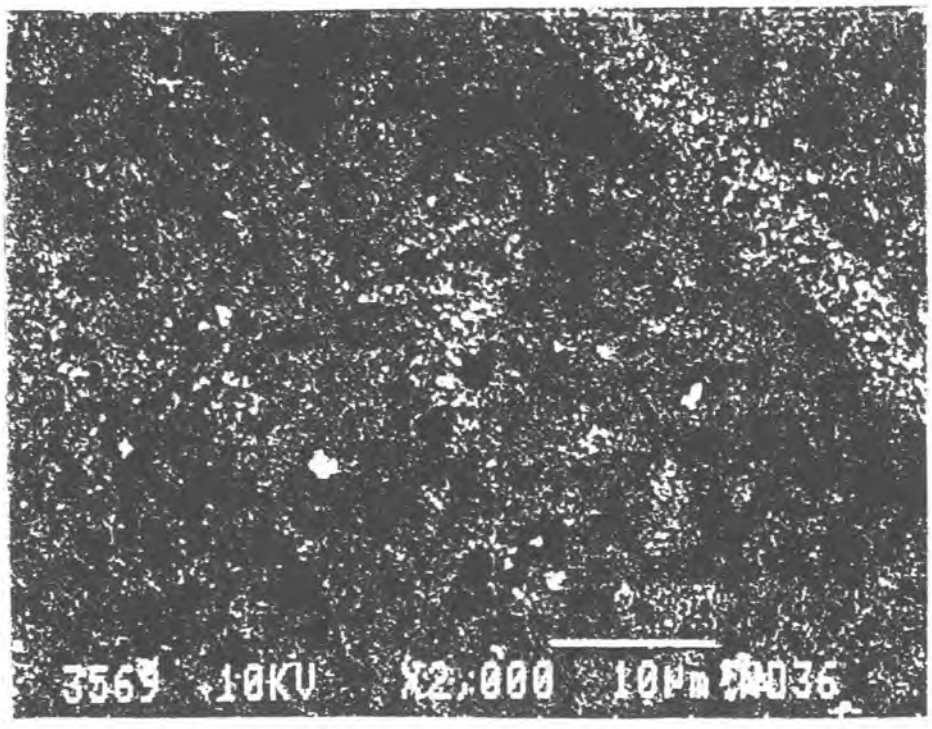

PLATE 14.12: Unreacted Fe/SrO_2 pellet (2000X)

14.1.4.3 Zn/BaO_2:

The stoichiometric ratio for the formation of ZnO and BaO from 94% zinc and 85% pure BaO_2 is 25.9% zinc. Temperature profiles give a maximum temperature of 1500°C. This temperature is far above the melting point of zinc (420°C), but considerably lower than the melting points of the possible oxide products of ZnO (m.p. 1975°C) and BaO (m.p. 1918°C). The micrograph of the residue of the 30% Zn/BaO_2 system is shown in Plate 14.13, and the residue from the combustion of 50% Zn/BaO_2 in Plate 14.14 (considerable excess of zinc). Both pictures show particles (of oxidant, product of oxidant decomposition, or reaction product) embedded in a matrix of solidified liquid. Most of the embedded particles have the size and shape of the original BaO_2 particles, but there are some spherical particles which could be isolated zinc droplets which have oxidised as spheres.

14.1.4.4 Zn/SrO_2:

The stoichiometric ratio for formation of ZnO and SrO from 94% pure zinc and 85% pure SrO_2 is 36.3% zinc. Temperature profiles give a maximum temperature of 1500°C. The residue from combustion of 30% Zn/SrO_2 (Plate 14.15) (slight fuel deficit) shows melting of the zinc and some patches of the oxidant that have not been reached by the liquid. There is a spherical sub-structure to some of the melted regions which suggests either only surface melting and sintering of zinc particles during passage of the combustion front, or that isolated zinc droplets have reacted to form a ZnO layer before being engulfed by molten zinc.

The residue of combustion of a richer zinc composition (50% Zn/SrO_2) (Plate 14.16) also shows signs of extensive melting. Although residue particles are generally rounded, the surfaces suggest some recrystallisation of products.

14.1.4.5 Discussion:

The above results all show the heterogeneous nature of the decomposition products and hence the heterogeneous nature of the combustion process. This situation arises from the passage of the burning front through the fuel/oxidant mixture, which may contain clusters of fuel and/or oxidant particles which are too large for complete reaction to occur throughout. This emphasizes the importance of mixing to give reproducible burning, and the difficulties of analysing combustion residues. The associated problem of obtaining a uniform product by self-propagating high-temperature synthesis (Section 3.11) is also notable.

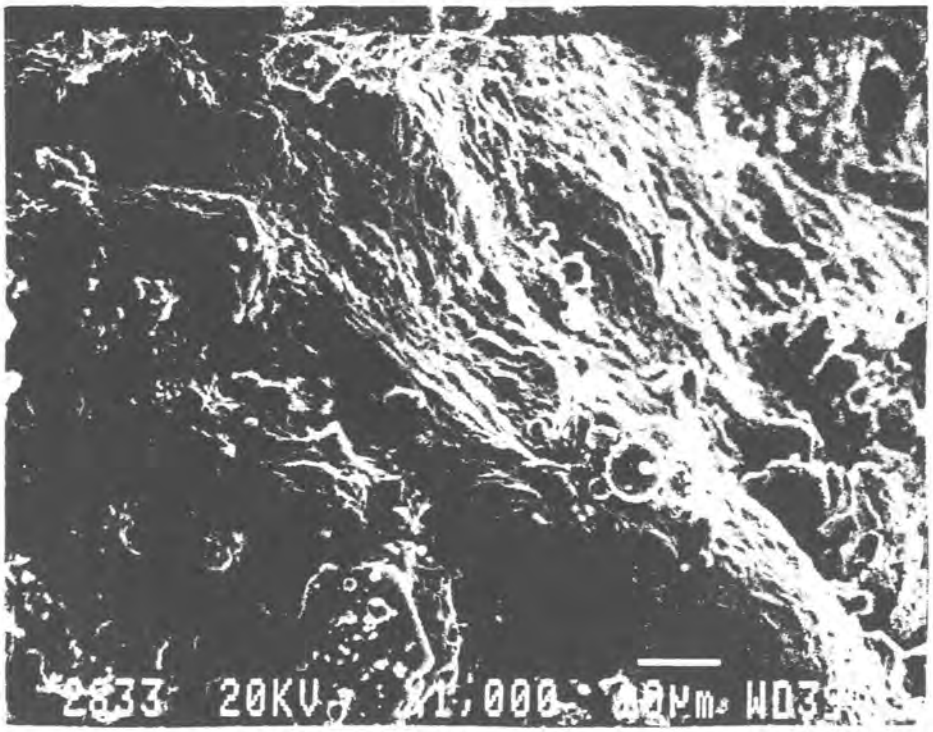

PLATE 14.13: 30% Zn/BaO_2 combustion residue (1000X)

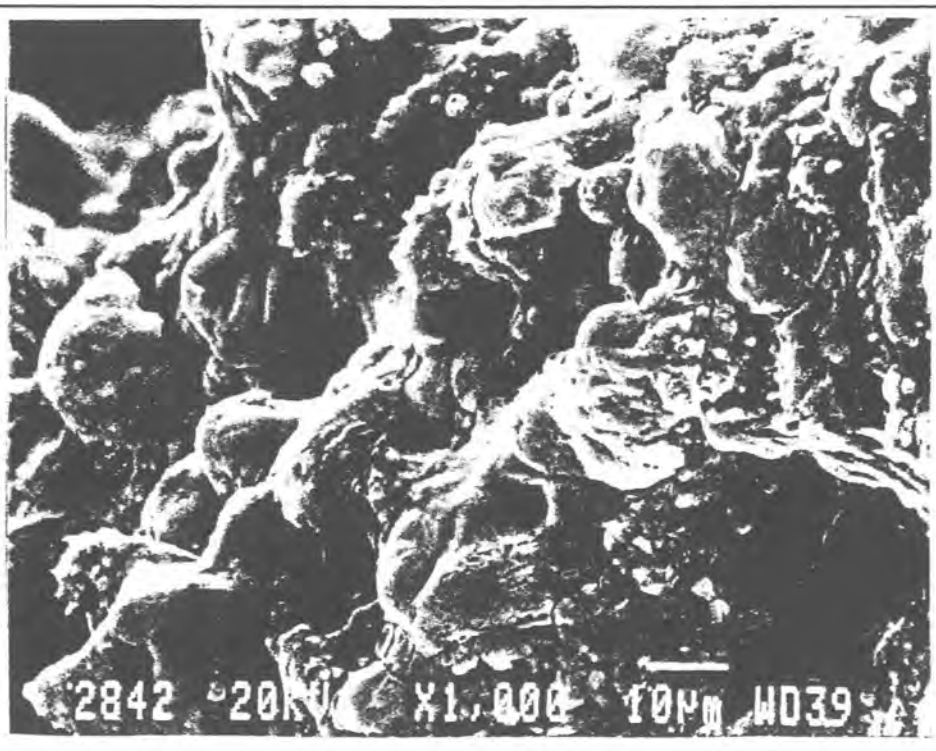

PLATE 14.14: 50% Zn/BaO_2 combustion residue (1000X)

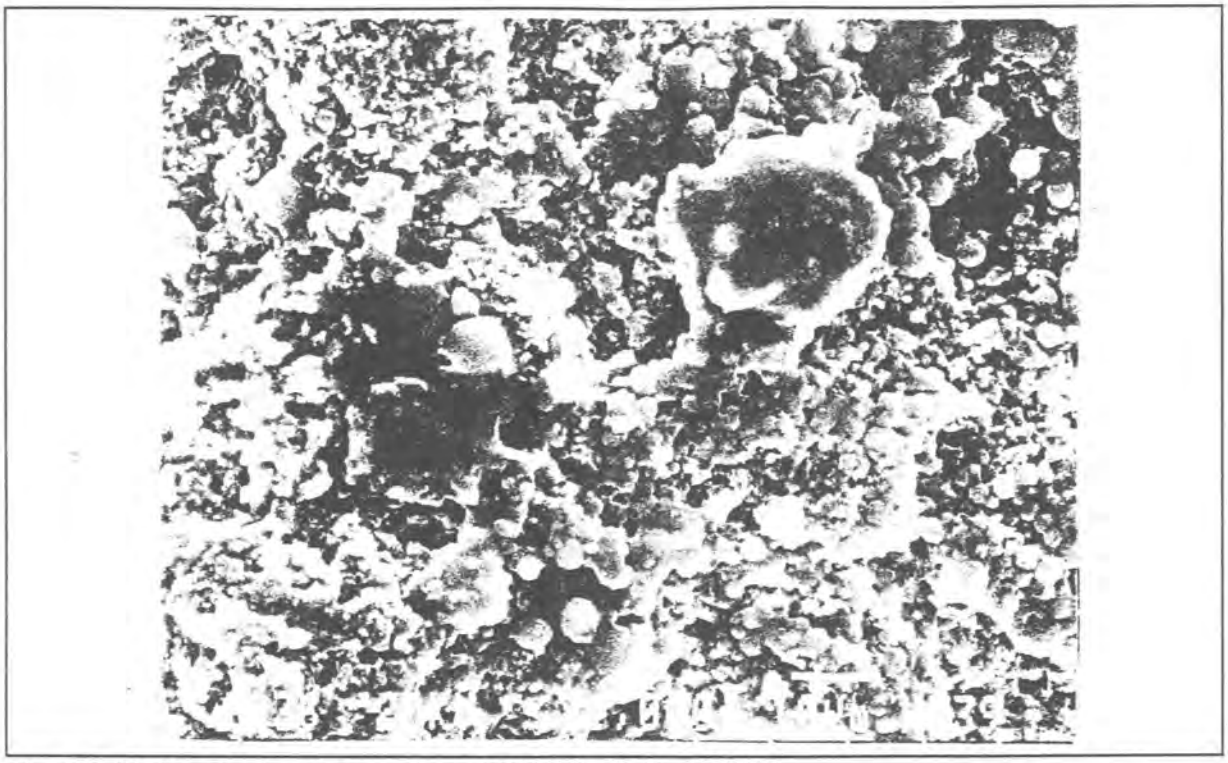

PLATE 14.15: Combustion residue of 30% Zn/SrO_2 (1000X)

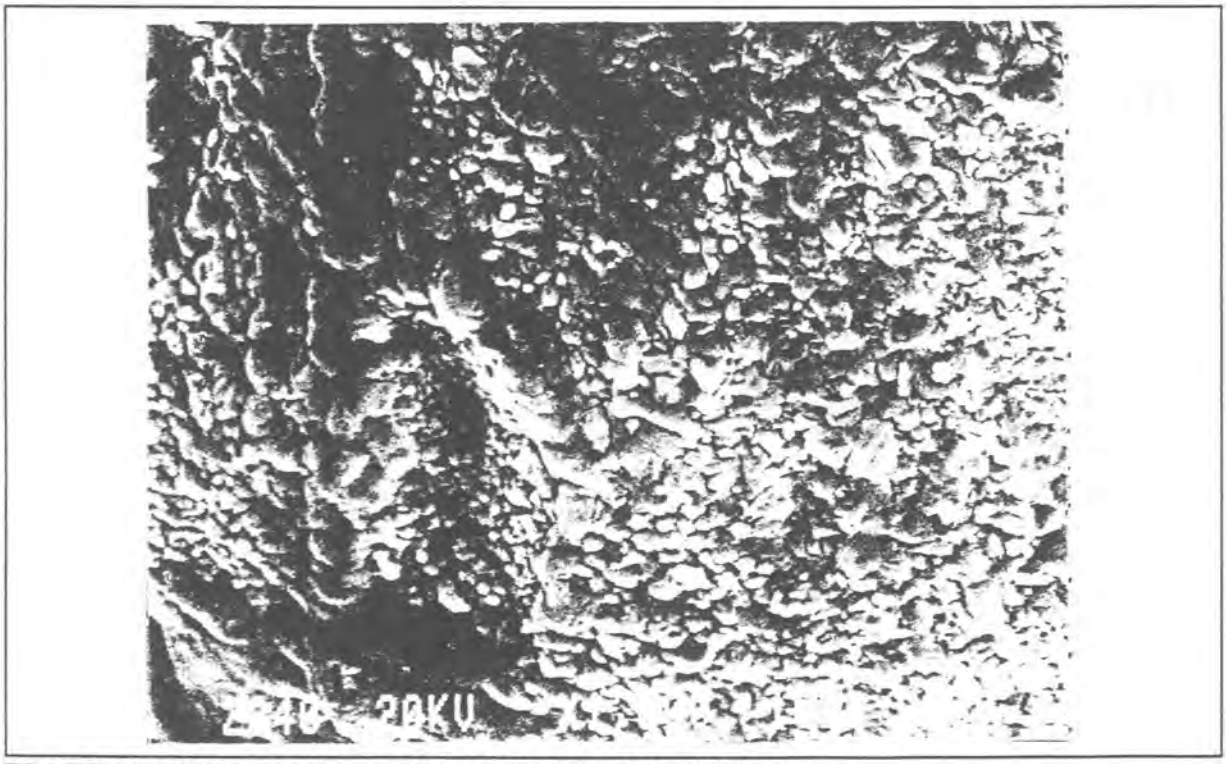

PLATE 14.16: Combustion residue of 50% Zn/SrO_2 (1000X)

14.1.4.6 Backscattered images:

Some attempts were made to obtain backscattered electron images of Fe/BaO_2 and Fe/SrO_2 residues using a Jeol 840 SEM. The technique is more powerful when applied to the BaO_2 systems, rather than SrO_2, since the Ba has a mass number much greater than Sr, relative to Fe and Zn. The photographs obtained (Plates 14.17 to 14.20) confirmed the non-uniform composition of the residues. The backscattered photographs show dual images. The photographs on the left are the conventional scanning electron images, while the photographs on the right are the backscattered images. In the backscattered images, regions of elements of large atomic mass appear darker, while the lighter regions are the lighter elements. Consequently the Ba or Sr appear dark, while the Fe regions appear light. The zinc systems were not examined by backscattered imaging since the low level of compaction of the samples and residues had the result that both reactants and products were powders, without definite form. Since the aim of using backscattered imaging was to obtain a sharper image of elemental distribution in the compacted samples before and after combustion, the zinc systems were found unsuitable for study by this approach. The photographs show, however, that the random distribution of Fe in the samples before combustion become isolated unreacted Fe particles in an amorphous mass of product.

14.1.5 Iron wire/oxidant experiments:

14.1.5.1 Introduction:

Several experiments were carried out (as described in Section 4.9) in which fine (0.4 mm diameter) iron wire was heated electrically while surrounded by either air, or BaO_2 powder, or SrO_2 powder. The original surface of the iron wire is relatively smooth (Plate 14.21) with some extrusion marks and a few shallow pits. A sample of wire subjected to burnthrough in air (Plate 14.22) shows melting and formation of surface layers of oxide which are not very adherent under these conditions.

The temperature of the wire surface was determined from temperature-current calibration curves (see Section 4.9). Four temperatures were selected for the study in air and the peroxides, viz. 100, 300, 500 and 700°C, the uncertainty in the temperatures being about 5°C. These experiments were performed individually in air, barium peroxide and strontium peroxide. As expected, higher currents were used in the peroxide systems due to the higher thermal conductivities (0.33 W m^{-1} K^{-1} for BaO_2 and 0.21 W m^{-1} K^{-1} for SrO_2) relative to air (0.026 W m^{-1} K^{-1}), which resulted in heat loss from the wire.

Due to the electrical heating imposed on the wire, and the corrosive nature of oxygen on the surface, breakdown of the wire occurred when the metal attained temperatures in excess of 800°C. The decrease in wire diameter due to surface oxidation resulted in a smaller electrically-conductive

cross-section. This effectively raised the resistance and exceeded the factor by which the resistance of the wire was lowered by temperature increase. Since the current was kept constant, the result was a surge in power and uncontrolled heating of the wire, causing burnthrough.

After obtaining a current versus surface-temperature relationship for the iron wire both in air and in the two oxidants, 100 mm lengths of wire were placed in separate samples of both oxidants (compacted by hand) and were electrically heated to pre-determined temperatures which were maintained for 30 seconds. As surface effects were under consideration, heating was performed by a 50Hz ac circuit, the resulting skin-effect having the advantage that excessive heating of the bulk and possible burn-through was avoided. The wire samples were cooled, removed, stored under dry conditions, and the surfaces examined directly after the experiment.

14.1.5.2 Wire heated in BaO_2:

Even at temperatures as low as a calculated 100°C, the surface of the wire appears to have reacted with the formation of poorly adherent surface layers. At a calculated 300°C, there is evidence of some surface melting with incorporation of oxidant particles. The scale on some regions of the surface appears more dense and adherent than at 100°C. At 500°C surface melting is more extensive. Some parts of the surface are smooth and there appears to have been a flow of molten material over the scale-covered surface regions. At 700°C (Plates 14.23 and 14.24) this flow has engulfed most of the non-molten surface features. There are only a few holes suggesting evolution of gas from some of the particles.

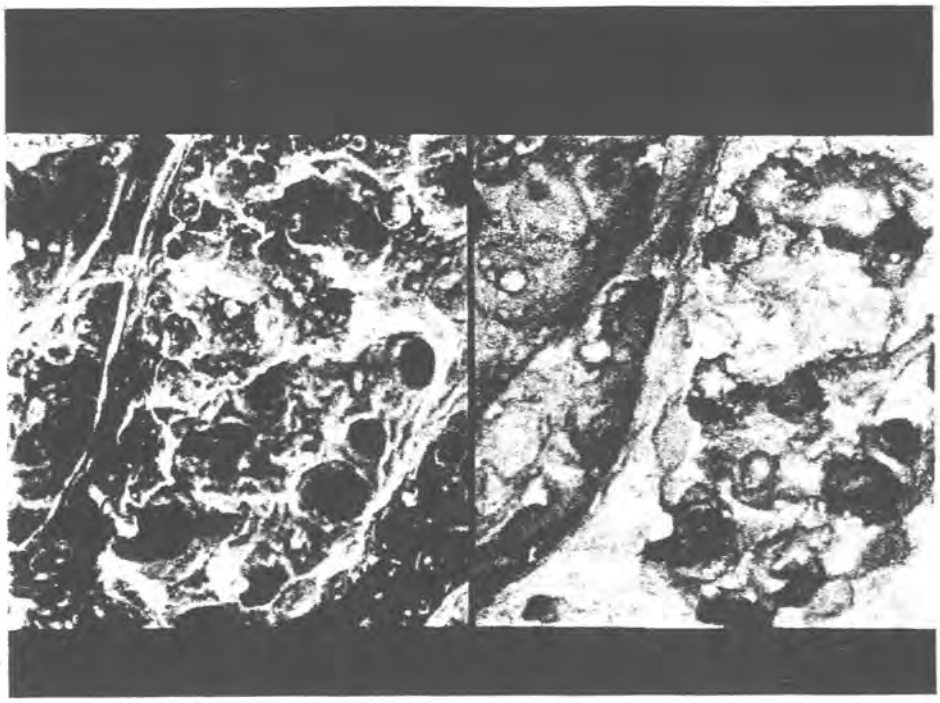

PLATE 14.17: Backscattered image of 20% Fe/BaO_2 residue (100X)

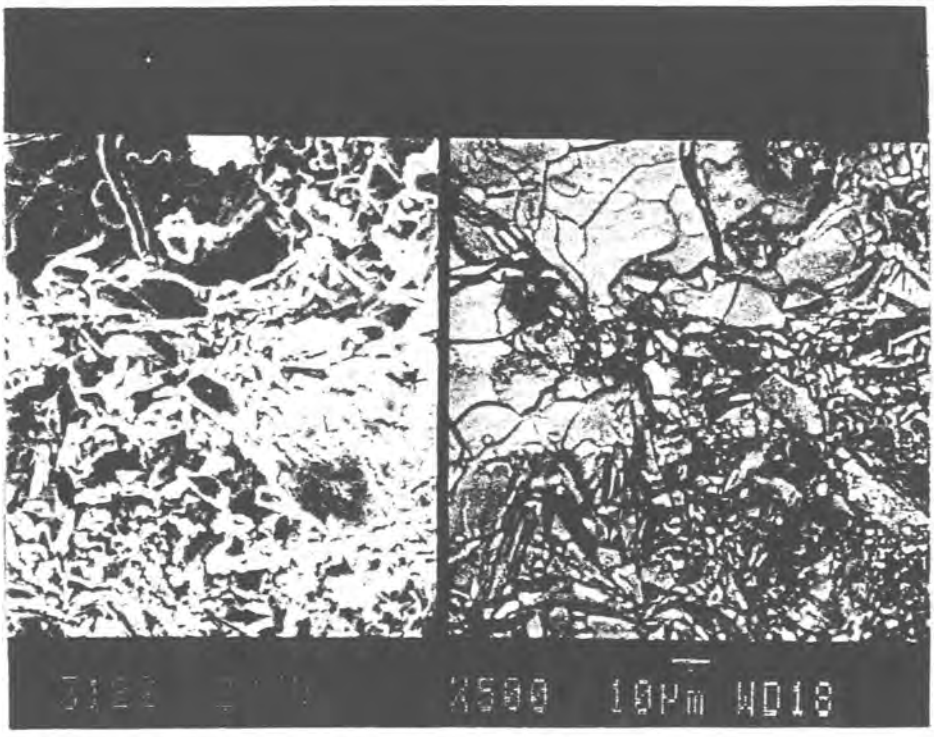

PLATE 14.18: Backscattered image of 20% Fe/SrO_2 (500X)

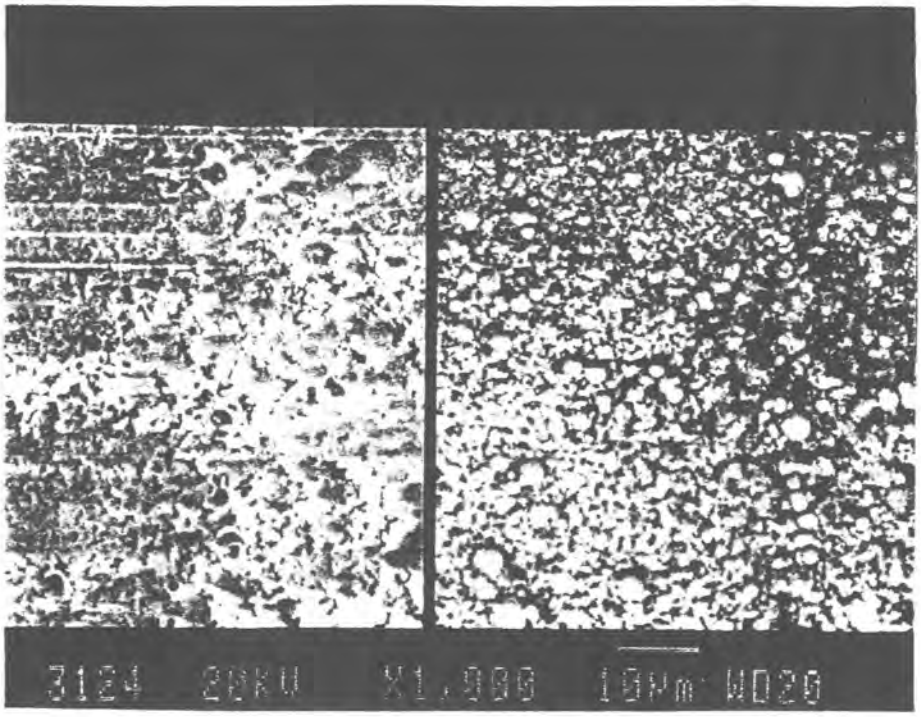

PLATE 14.19: Backscattered image of unreacted 20% Fe/BaO_2 (1000X)

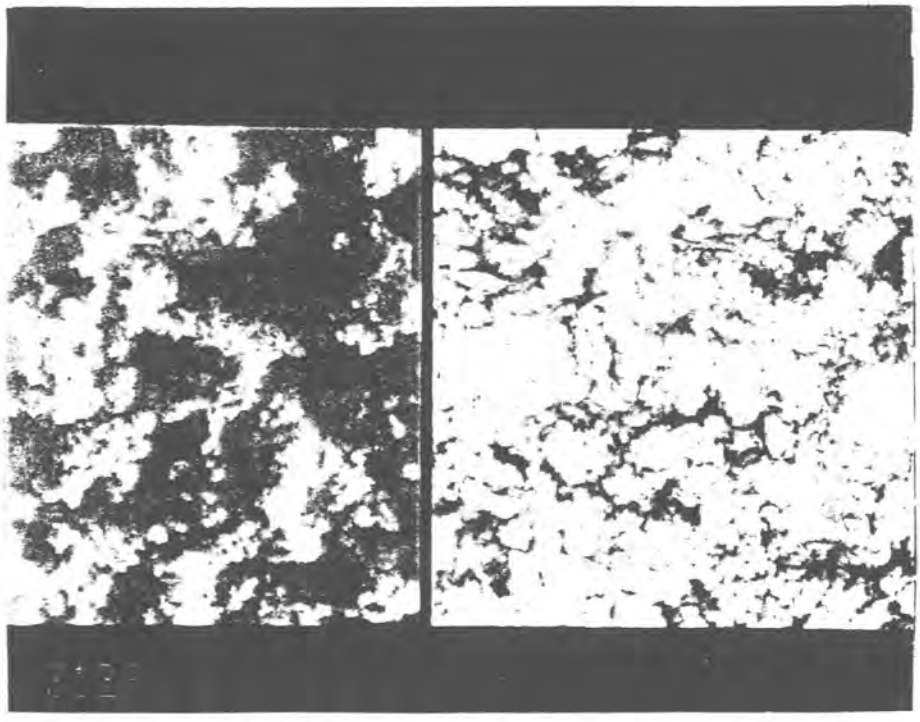

PLATE 14.20: Backscattered image of unreacted 20% Fe/SrO_2 (500X)

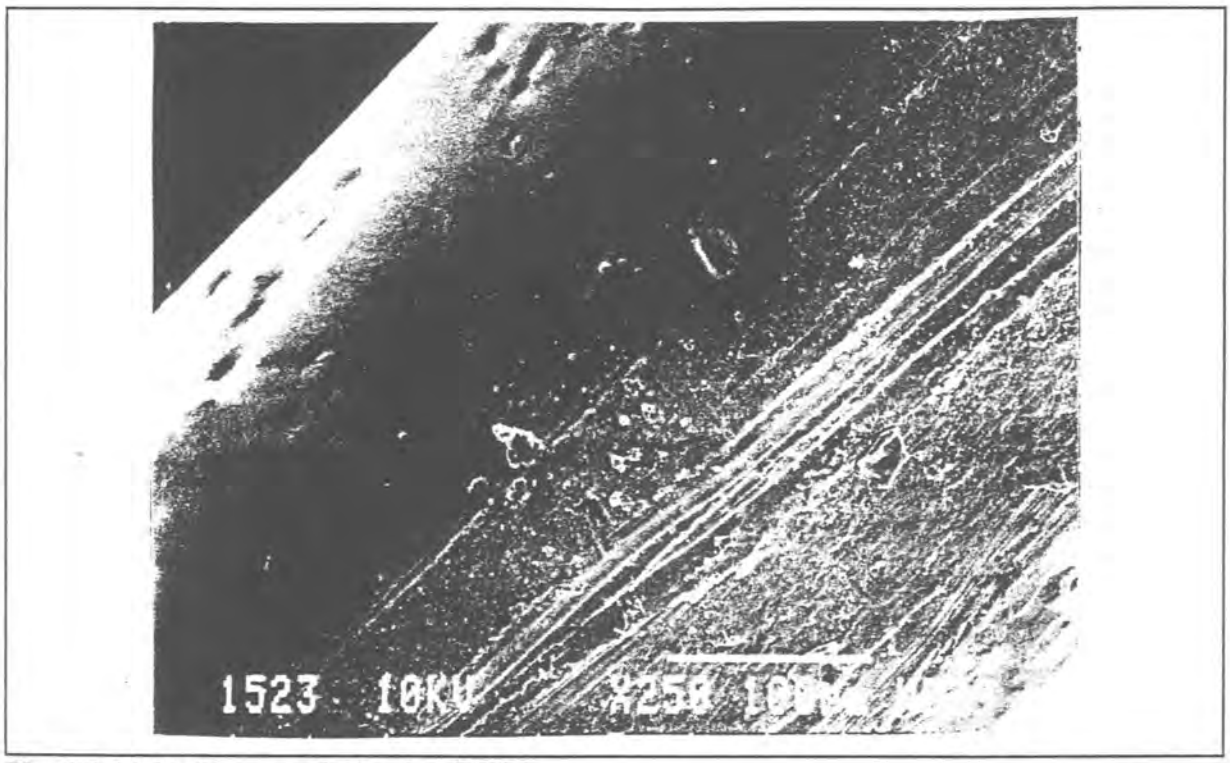

PLATE 14.21: Unreacted Fe wire (250X)

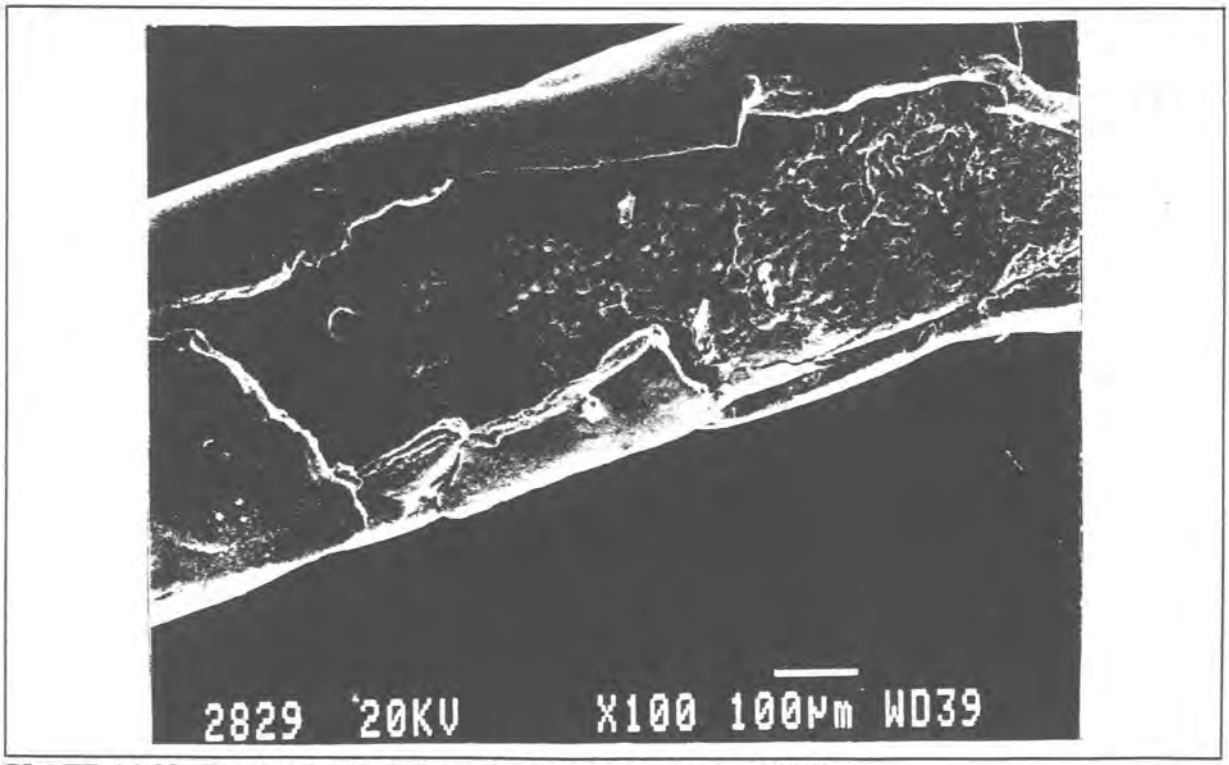

PLATE 14.22: Fe wire burned-through electrically in air (100X)

14.1.5.3 Wire heated in SrO_2:

No significant reaction had occurred by 100°C. By 300°C, some melting and partial submerging of particles had occurred. By 500°C, few areas of smooth surface remained (Plate 14.25). The surface consisted mainly of layers of scale (cooling of the wire apparently causes cracking of surface layers). By 700°C, there are some areas of surface with a ripple-like structure formed by cooling of molten material (Plate 14.26). Some embedding of product (possibly SrO) has begun to occur on a small scale on the wire, yet the most dominant feature is the effect the peroxide has had on the surface - pitting, yet no large clusters of product have formed as for the BaO_2.

14.1.5.4 Wire positioned in pyrotechnic mixtures:

In some experiments, approximately 40 mm lengths of 0.4 mm diameter iron wire were spanned first along, and then across a channel (see combustion study) of iron-fuelled pyrotechnic mixture. The mixtures were ignited, and the wire surfaces studied for signs of reaction.

Both Fe/BaO_2 (Plate 14.27) and Fe/SrO_2 (Plate 14.28) systems showed interaction between the pyrotechnic and the wire, with particles sinking into the molten surface, some more deeply than others. "Wetting" by liquid iron is seen, with lumps of product fusing to the wire. It is noticeable that major portions of the wire are recognisably intact and that only surface melting has occurred. The way in which particles are imbedded in the wire suggests that this process is accompanied by further exothermic reaction at the regions of contact, providing heat for further melting. No significant differences in the appearance of the wire were found for the different orientations (i.e. perpendicular or parallel) of the wire relative to the burning front.

14.1.6 Conclusions:

It is important in industrial applications to ascertain whether reactions occur in the condensed phase, or with participation of gas formed by prior decomposition of the oxidant. The use of SEM to study the effects of contact with oxidant on a relatively uniform surface of fuel, namely iron wire, yields useful information about the temperatures at which important events occur.

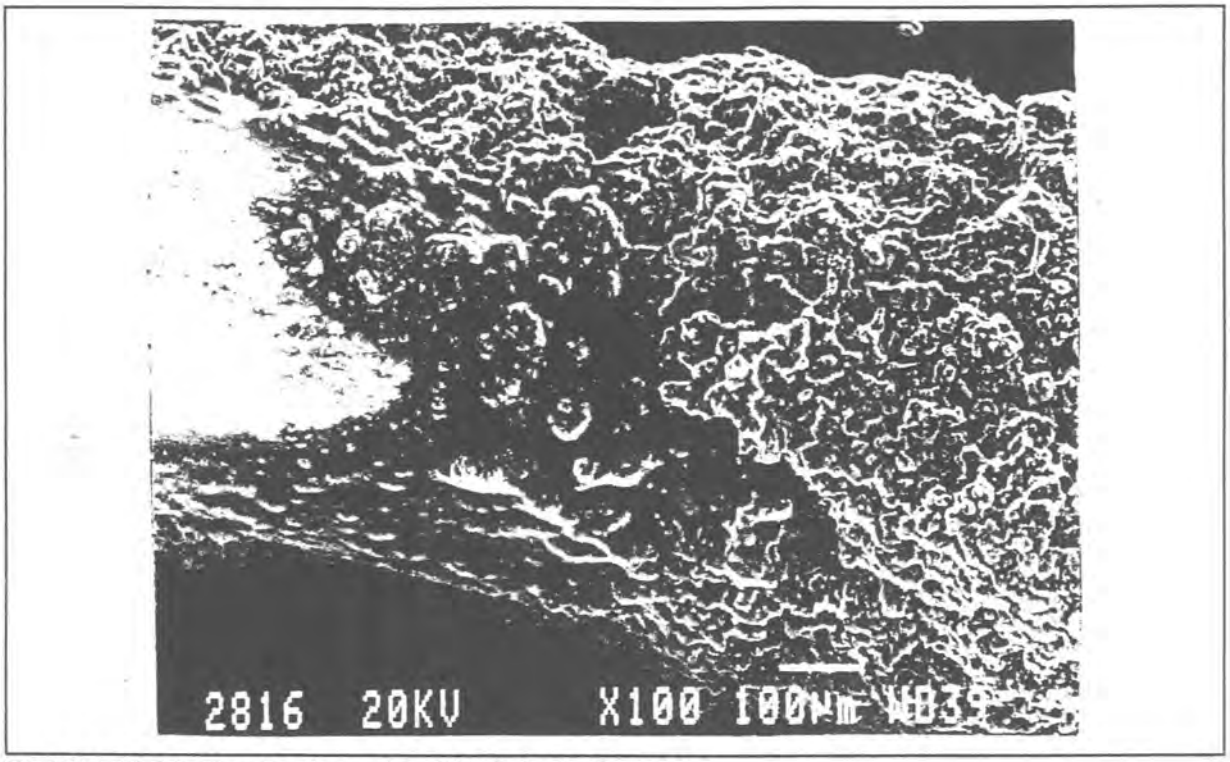

PLATE 14.23: Fe wire heated to 700°C in BaO_2 (100X)

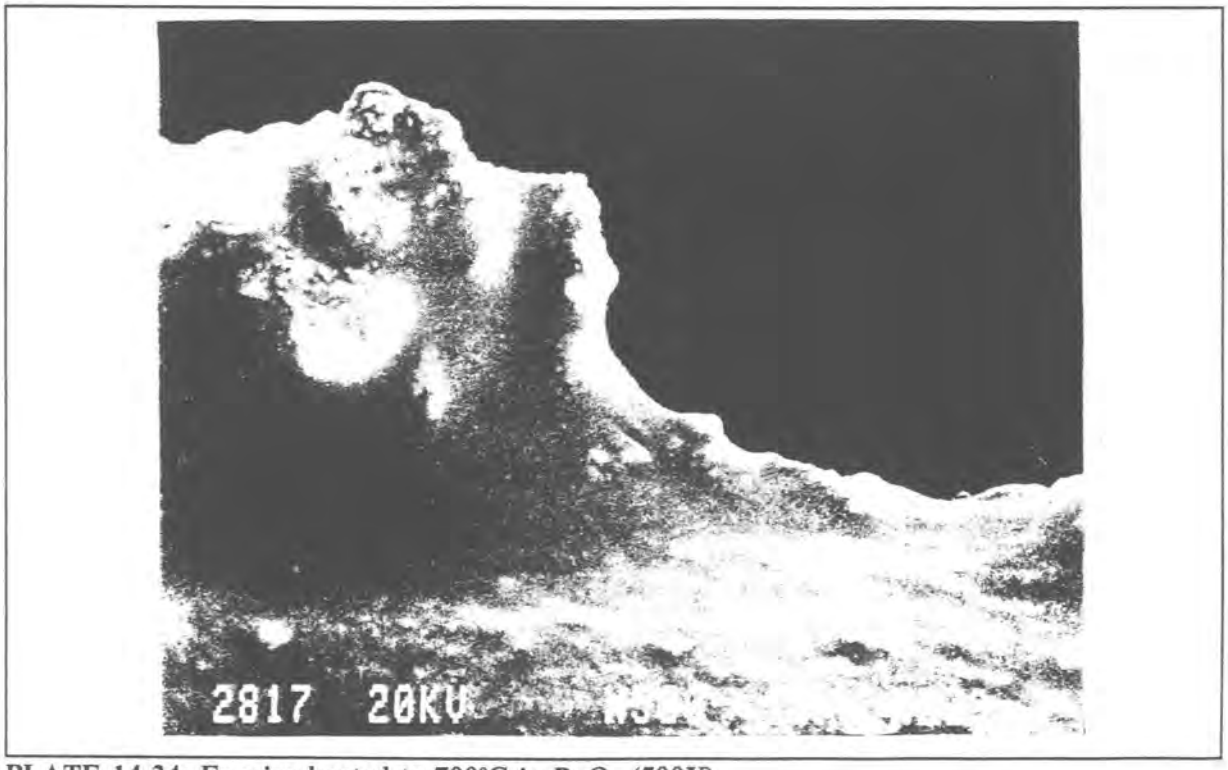

PLATE 14.24: Fe wire heated to 700°C in BaO_2 (500X)

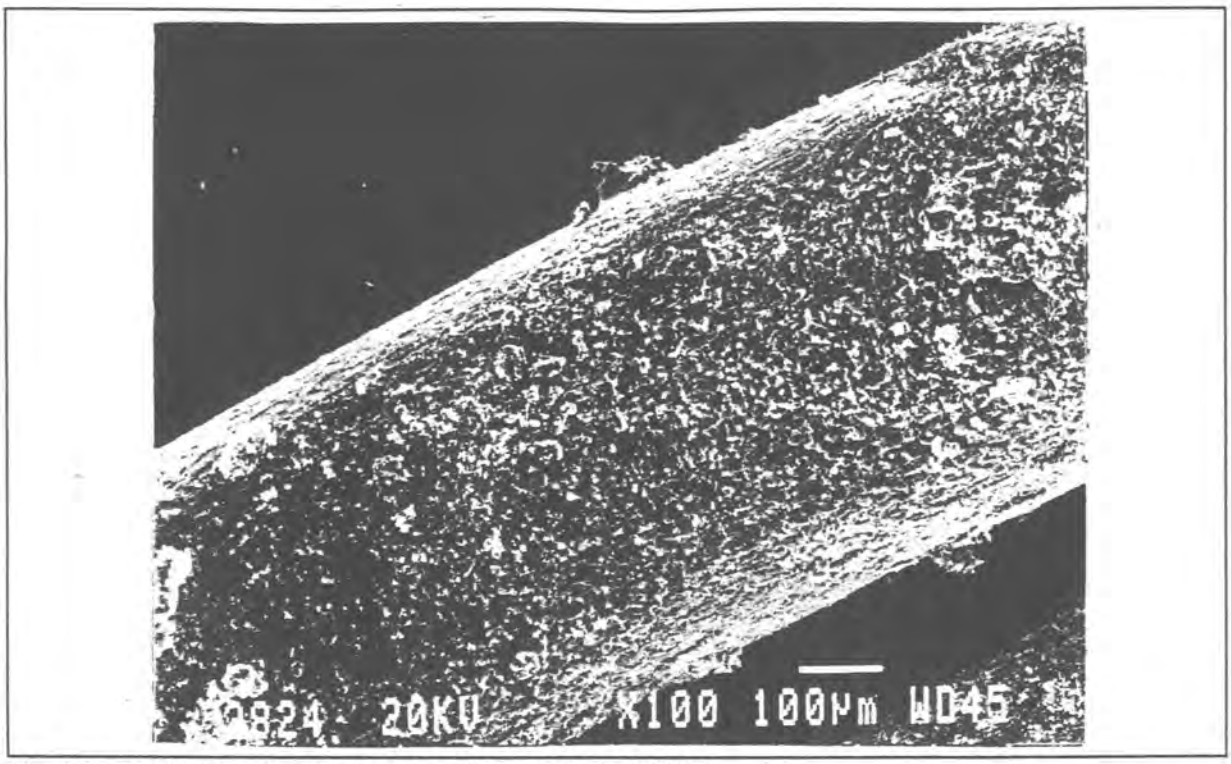

PLATE 14.25: Fe wire heated to 500°C in SrO_2 (100X)

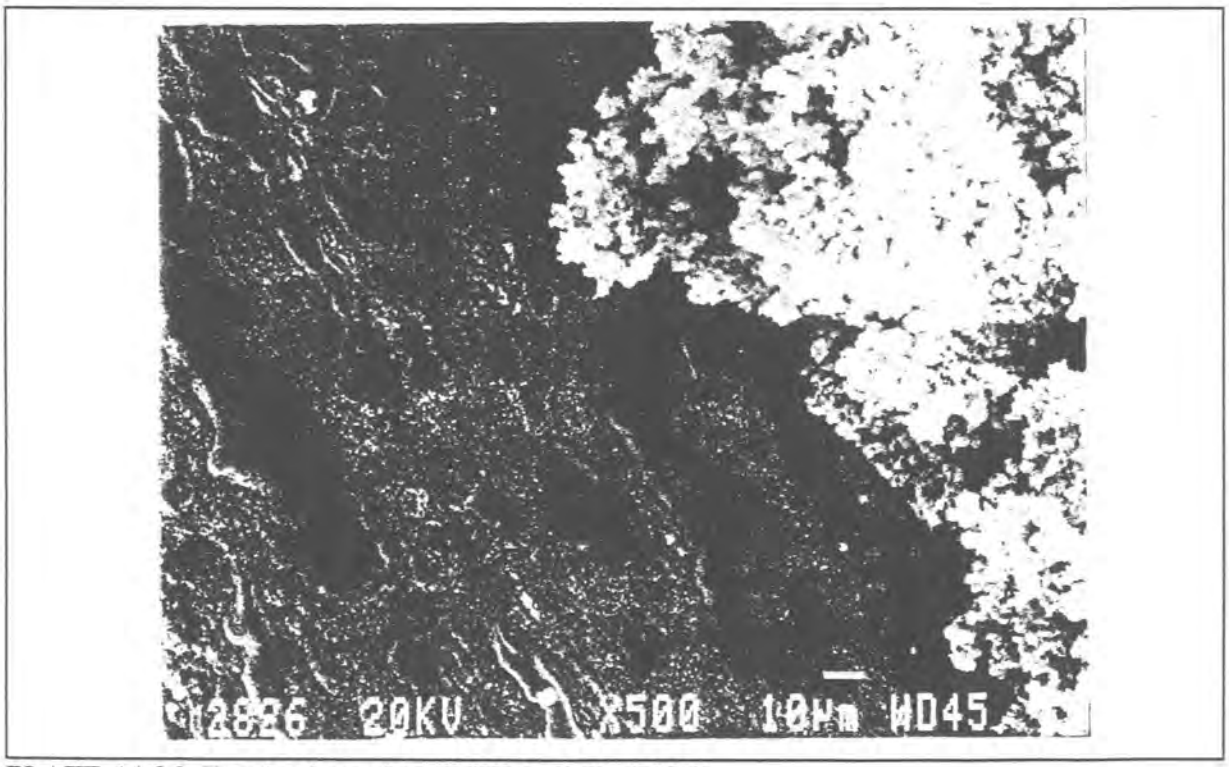

PLATE 14.26: Fe wire heated to 700°C in SrO_2 (500X)

14.2 Infrared spectra:

14.2.1 The reactants:

The IR spectra of the BaO_2 and SrO_2 samples exhibited similar carbonate absorptions to those documented in Drennan's study [6]. Some researchers claim that no characteristic absorption bands exist for peroxides [177], but the existence of a weak bands, including an O-O stretch at 1119.5 cm^{-1}, a 571.8 cm^{-1} band from the interionic stretch mode of BaO_2, and 401-520 cm^{-1} bands assigned to the stretch mode of BaO, have been documented [178]. Further mention is made of an interatomic vibration mode of SrO_2 at 474 cm^{-1}, and the SrO band at 423 cm^{-1}. However, none of these bands were positively identified.

14.2.2 Reaction products:

14.2.2.1 The Fe/BaO_2 system:

The infrared absorption bands for bond vibrations in Fe_3O_4 and Fe_2O_3 occur around 570 cm^{-1} [179], as do those of BaO_2. The only difference noted in the product spectra was the disappearance of the bands at 1420 and 3570 cm^{-1} (Ba-O stretch) attributed to the loss of oxygen.

14.2.2.2 The Fe/SrO_2 system:

Differences noted between the spectra of the residue and that of the starting material were the apparent loss of the Sr-O stretch at 3490 cm^{-1} due to the decomposition of SrO_2, and decreases in the peaks at 1450, 1020 and 850 cm^{-1} (formation of $SrCO_3$) [180].

14.2.2.3 The Zn/BaO_2 system:

The absorption bands at 3570, 1750, 1430 and 850 cm^{-1} observed in the BaO_2 spectrum were decreased in intensity or removed, while a new peak appeared at 730 cm^{-1} due to the formation of ZnO.

14.2.2.4 The Zn/SrO_2 system:

As for the iron system, the spectra of the residue and that of the starting material differed by the loss of the Sr-O stretch at 3490 cm^{-1} and decreased intensities of the peaks at 1450, 1020 and 850 cm^{-1}. No trace of the ZnO absorption was apparent at 730 cm^{-1}.

14.2.2.5 Discussion:

IR spectra do not provide much useful information on the possible formation of complex oxide or ferrate systems, since the reactants and products have absorptions in similar regions in the spectrum between 800 and 400 cm^{-1}.

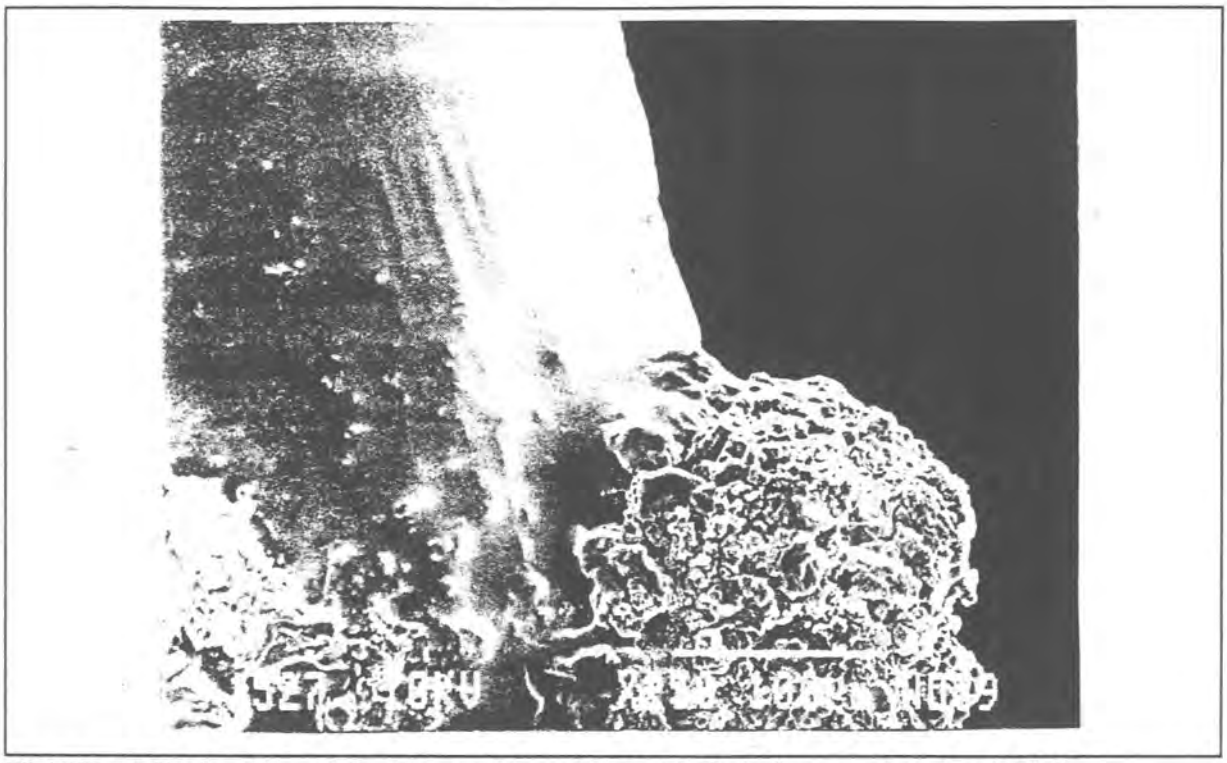

PLATE 14.27: Residue of Fe wire positioned in Fe/BaO_2 before combustion (250X)

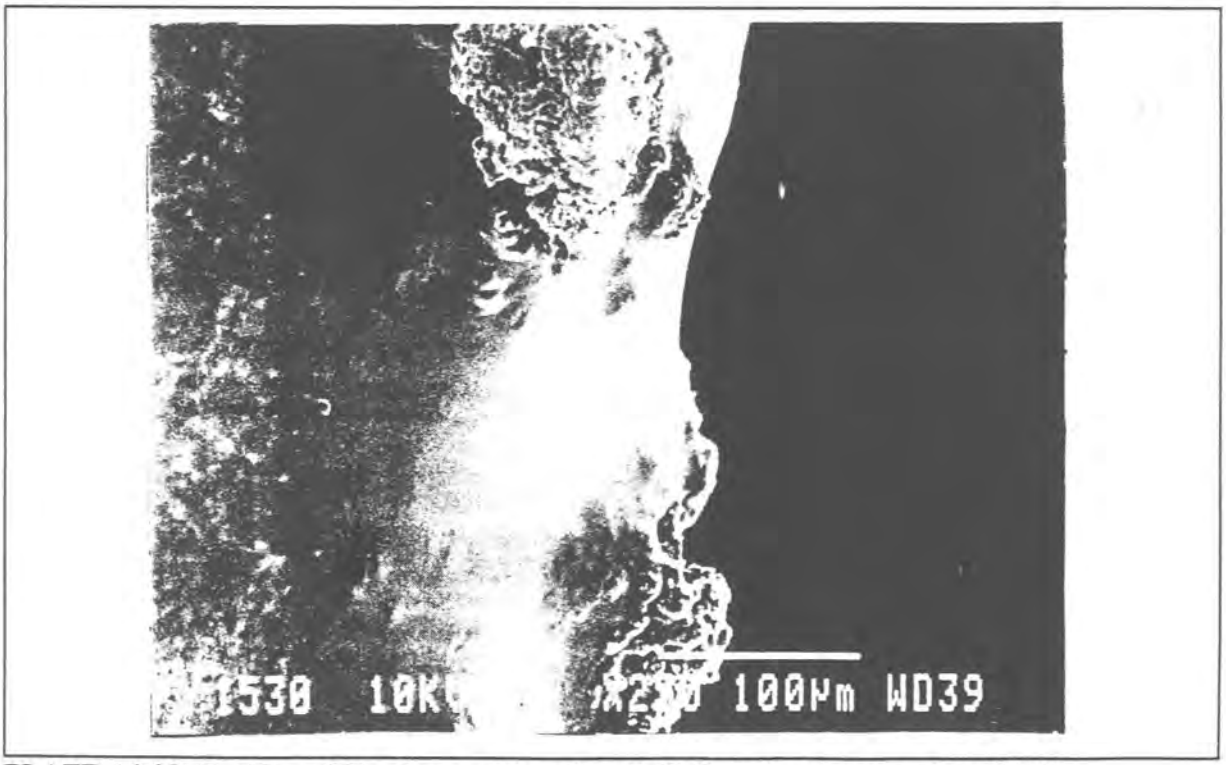

PLATE 14.28: Residue of Fe wire positioned in Fe/SrO_2 before combustion (250X)

14.3 X-ray powder diffraction patterns:

14.3.1 Introduction

The XRD patterns of the reagents used in the study are presented in Figures 14.1 (Fe), 14.2 (Zn), 14.3 (BaO_2) and 14.4 (SrO_2). I/I_1 values ≤ 10 have been omitted from the tables and figures.

A comparison was made between experimental diffraction patterns and catalogued patterns for the reactants. Impurities noted in the zinc used included a minor peak at d=2.90 Å, due to ZnO; and in the control ZnO, a minor peak at d=3.70 Å, due to $ZnCO_3$.

The diffraction patterns of the products resulting from the combustion of the 20% and 50% Fe/BaO_2 systems are shown in Figures 14.5 and 14.6 (d-spacings have been tabulated in Appendix 11). It was not possible to prevent reaction of the combustion products with the surrounding atmosphere during handling and so allowance for the possible combination of oxides with CO_2 to form carbonates and oxides with water to form hydroxides and/or hydrates has to be made.

The primary product formed in the combustion was $Ba_3Fe_2O_6$ (Figure 14.7), with minor peaks from impurities. Much unreacted iron exists in the residue of the 50% system as expected, along with a phase which could not be identified. Surprisingly, little or no Fe_2O_3 was found.

Combustion of the 25% Fe/SrO_2 system gave a product (Figure 14.8) which corresponded to a combination of $Sr_3Fe_2O_{6.16}$ (Figure 14.9) and $Sr_3Fe_2(OH)_2$ (not shown) together with an unidentified phase also apparent in the SrO_2 starting material. Little Fe and Fe_2O_3 existed in the product. As expected, some unreacted Fe was found in the residue of the 50% system (Figure 14.10), along with $Sr_3Fe_2O_{6.16}$. SrO, SrO_2, $SrCO_3$, iron oxides and hydroxides do not account for the same unidentified phase as seen in the 20% Fe/SrO_2 system above.

Combustion of the 30% Zn/BaO_2 mixture was very gassy and material was ejected from the channel. The residue remaining was unreacted Zn/BaO_2 (Figure 14.11). Consequently a less reactive system (50% Zn/BaO_2) was used for product generation, which yielded the pattern shown in Figure 14.12. This pattern showed that the products formed in the reaction included ZnO and BaO, although the bulk of the products were amorphous to X-rays, and are thought to be mixed oxides. The residue resulting from the combustion of the 30% Zn/SrO_2 system is shown in Figure 14.13, which reacted with the atmosphere to become the product shown in Figure 14.14 on ageing under laboratory conditions for 4 weeks. Small amounts of ZnO and alkaline-earth oxides were present in the residues, but no traces of hydrated $BaZnO_2$ or $SrZnO_2$, as reported in the literature [136], could be found. No appreciable amounts of carbonates or hydroxides were found.

14.3.2 Discussion:

Use of XRD to examine the products of combustion has several drawbacks: (i) products are formed at high temperatures, but could only be examined after cooling, and room temperature phases usually differ markedly from high-temperature phases; (ii) the rapid cooling involved can result in solidification of phases which are amorphous to X-rays; and (iii) reaction of product phases with the surrounding atmosphere is impossible to prevent. X-ray powder diffraction results indicate that the main crystalline substances in the cooled products of combustion of the Fe/peroxide systems were mixed oxides, with little or no trace of the simple products predicted (Section 3.1).

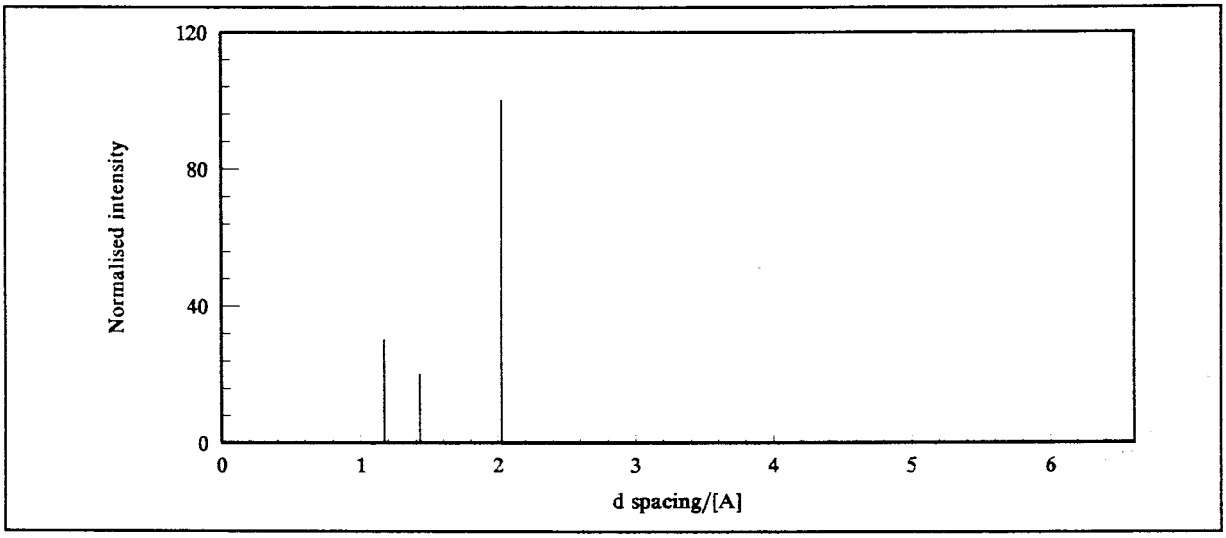

FIGURE 14.1: XRD pattern of Fe

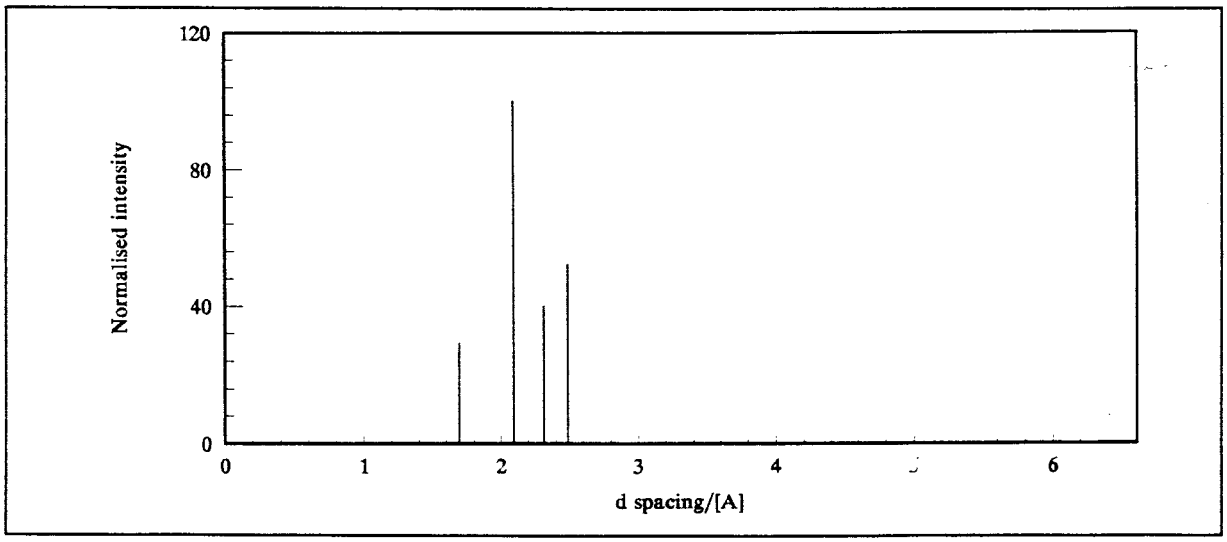

FIGURE 14.2: XRD pattern of Zn

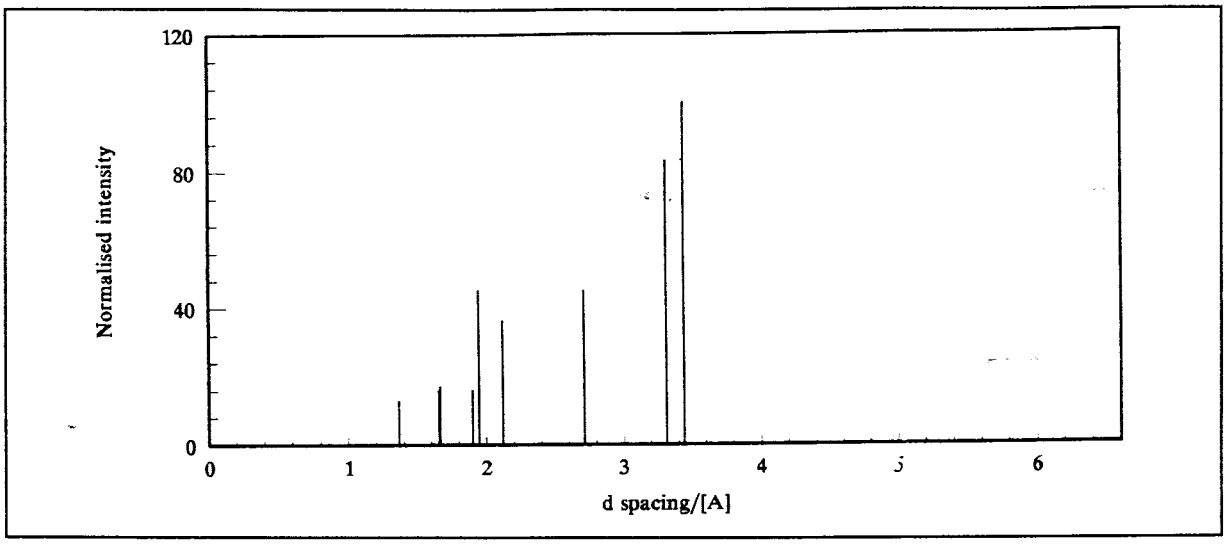

FIGURE 14.3: XRD pattern of BaO_2

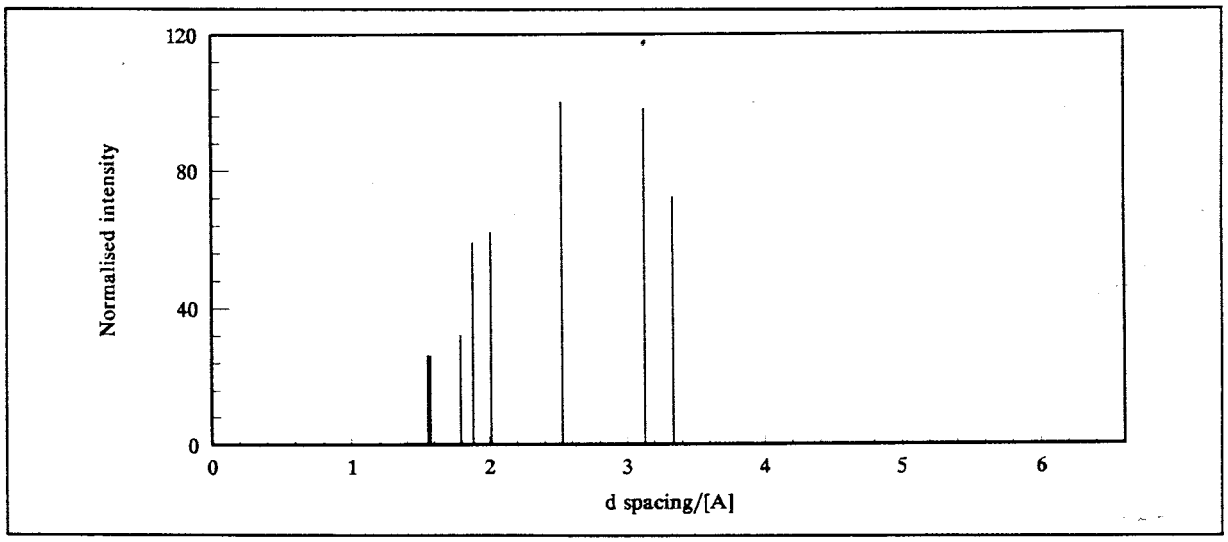

FIGURE 14.4: XRD pattern of SrO_2

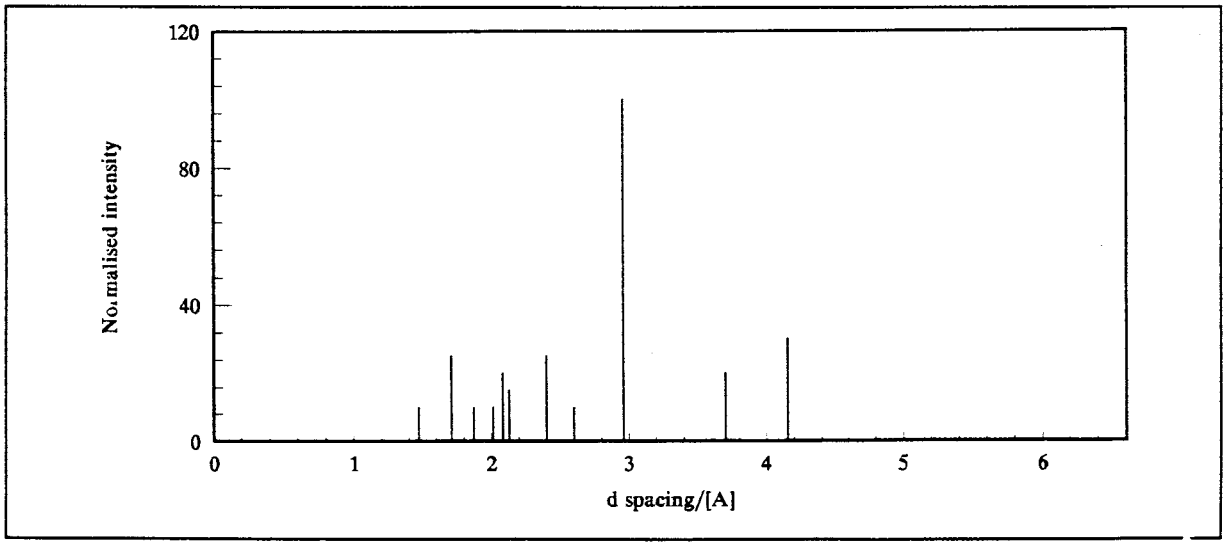

FIGURE 14.5: XRD pattern of 20% Fe/BaO_2 combustion residue

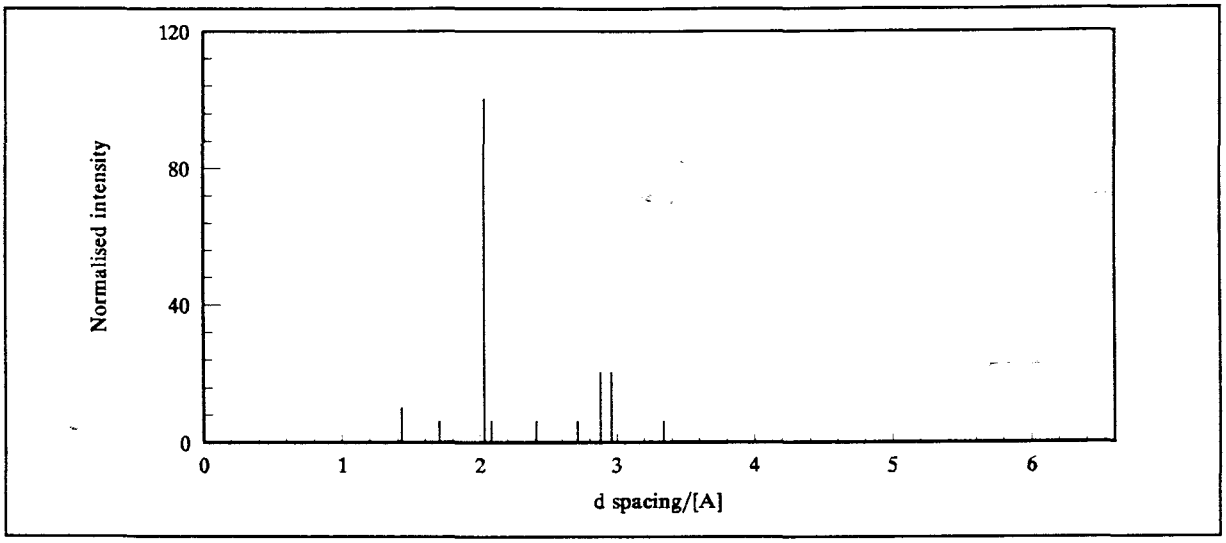

FIGURE 14.6: XRD pattern of 50% Fe/BaO_2 combustion residue

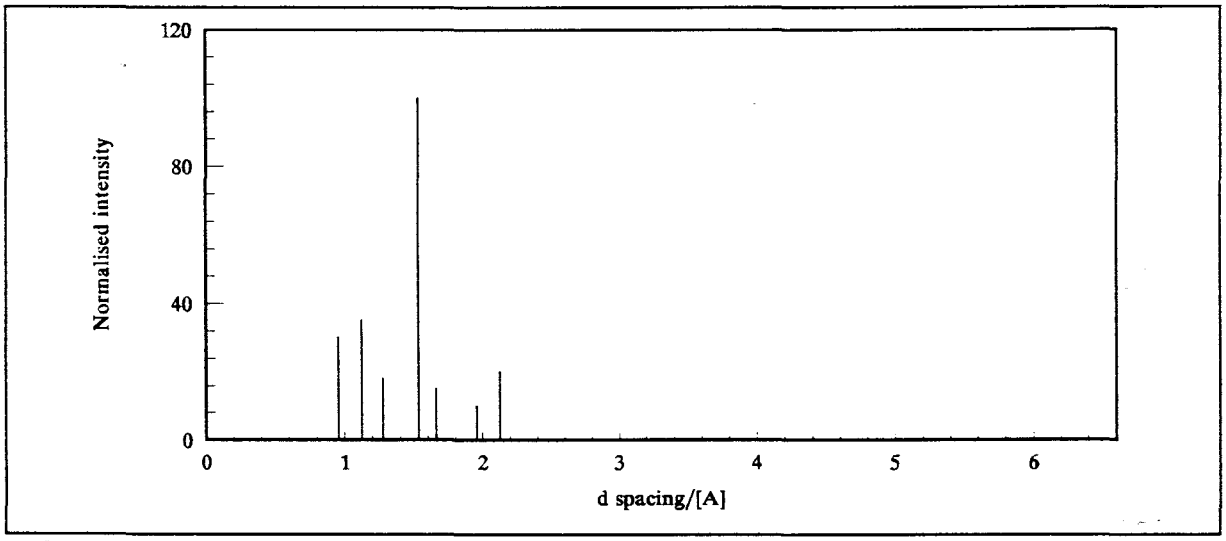

FIGURE 14.7: XRD pattern of $Ba_3Fe_2O_6$

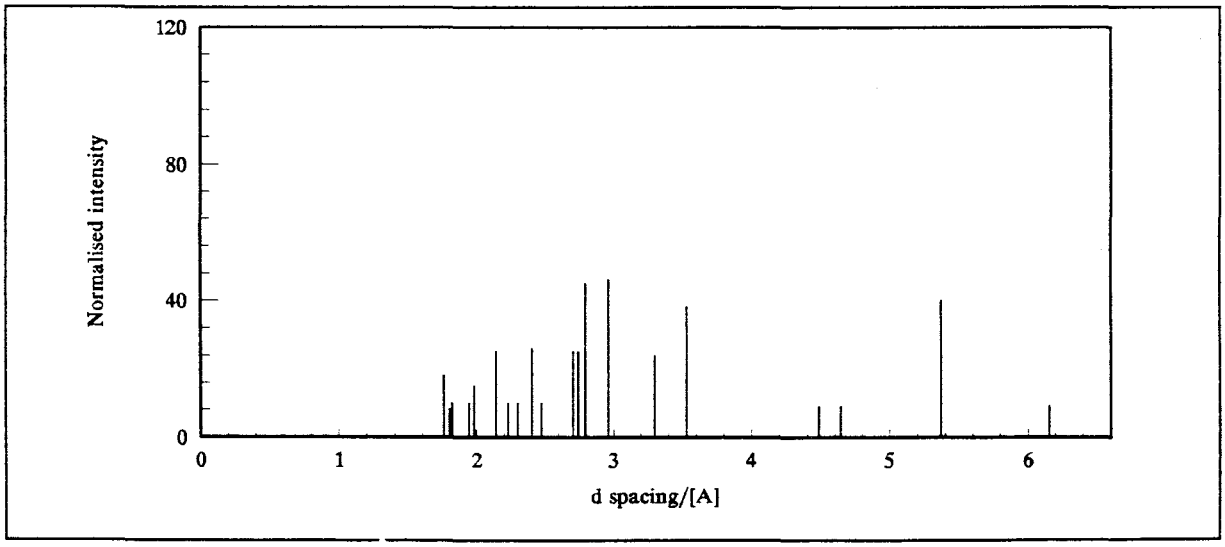

FIGURE 14.8: XRD pattern of 25% Fe/SrO_2 combustion residue

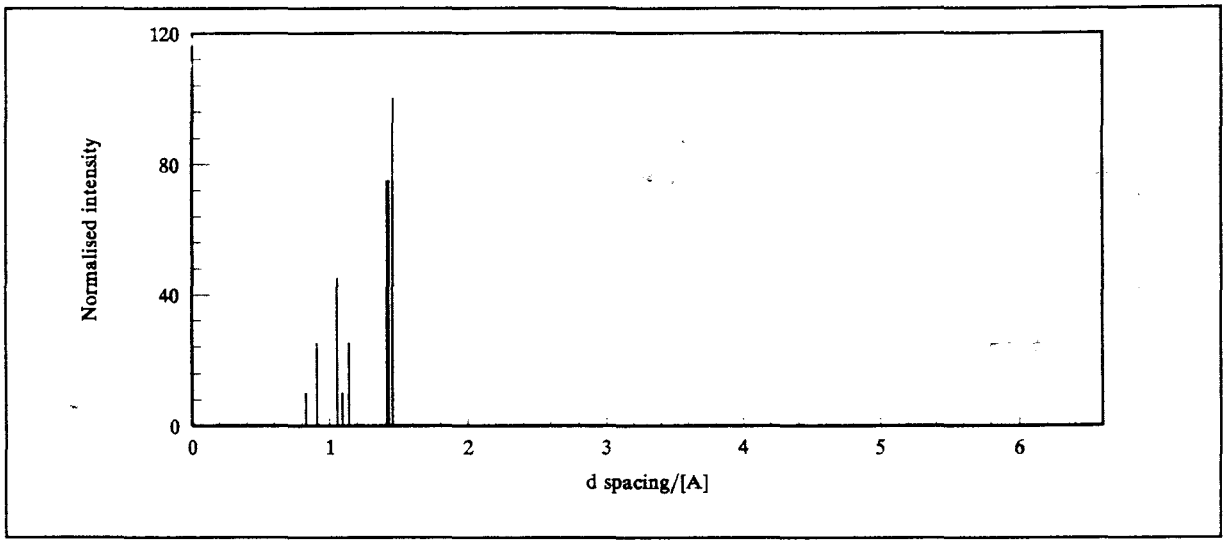

FIGURE 14.9: XRD pattern of $Sr_3Fe_2O_{6.16}$

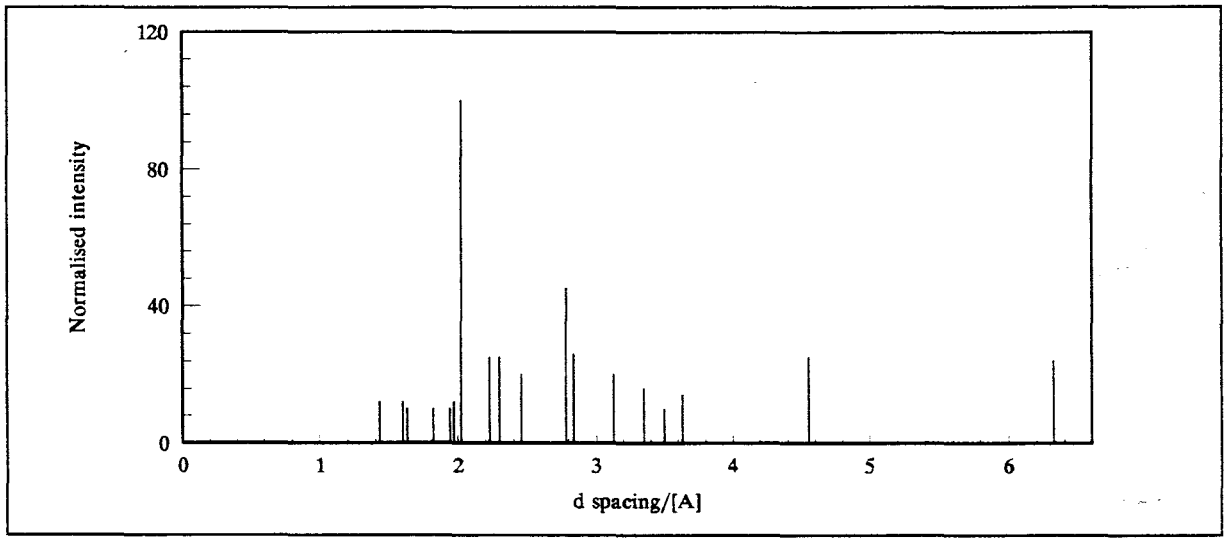

FIGURE 14.10: XRD pattern of 50% Fe/SrO_2 combustion residue

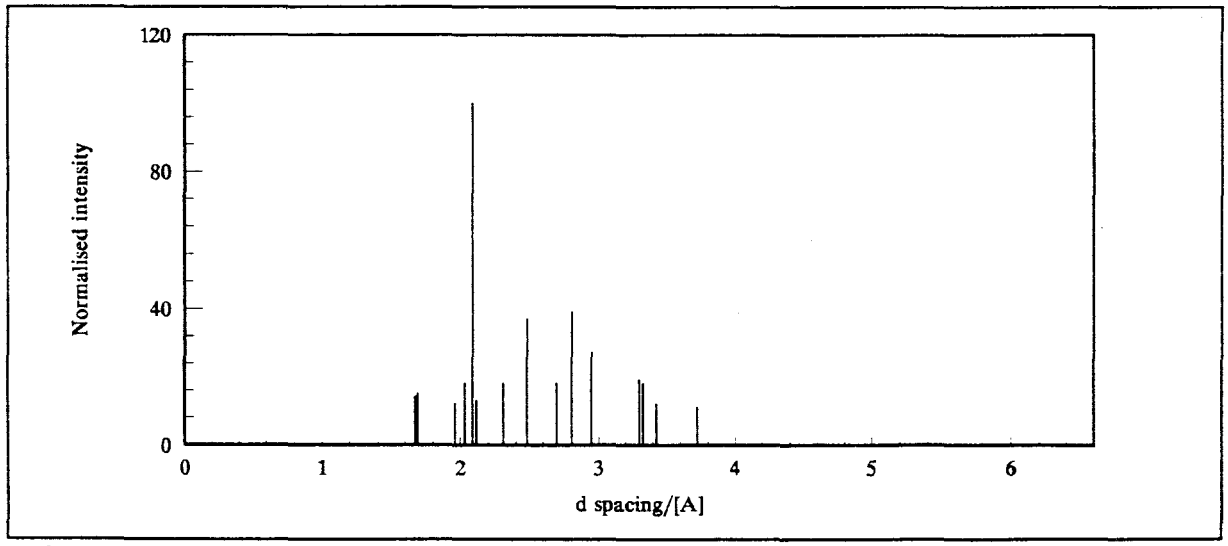

FIGURE 14.11: XRD pattern of 30% Zn/BaO_2 combustion residue

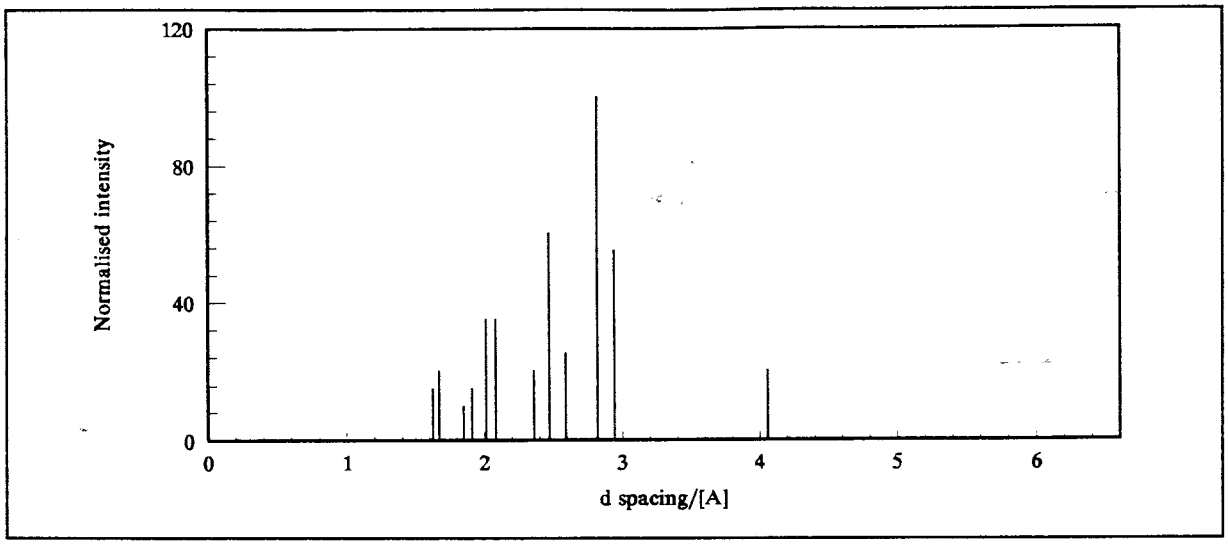

FIGURE 14.12: XRD pattern of 50% Zn/BaO_2 combustion residue

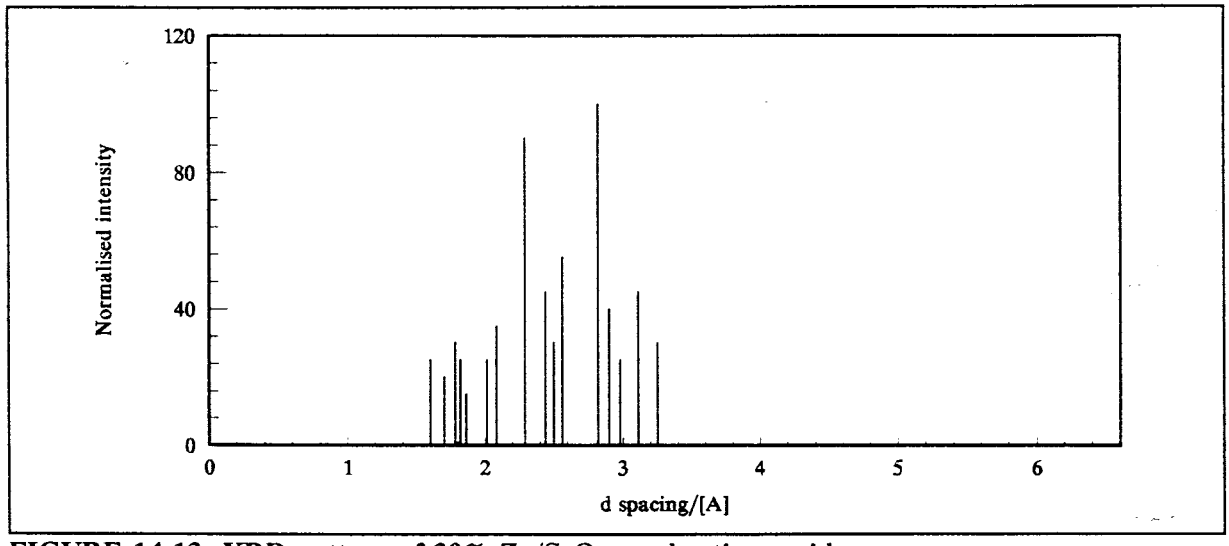

FIGURE 14.13: XRD pattern of 30% Zn/SrO_2 combustion residue

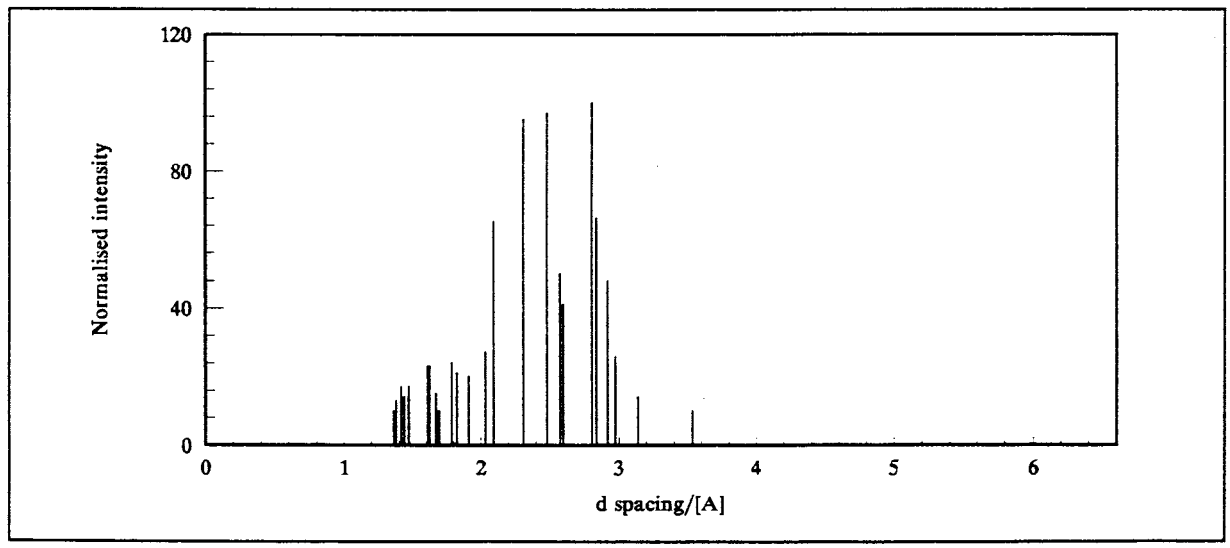

FIGURE 14.14: XRD pattern of aged 30% Zn/SrO_2 combustion residue

14.3.3 Results of an XRD study of the product variation in the Fe/peroxide system:

The study of products formed in the Fe/peroxide pyrotechnic systems was extended to investigate the variations in the products caused by variation of the starting proportions of reagent. The stability of these products was investigated by comparing two-year old samples (which had been stored under laboratory conditions) with the residues of freshly combusted material. The samples are subsequently distinguished from each other using the terms "old" and "fresh". The findings of the study are tabulated below. Intensities indicated are as a percentage of the major peak in the spectrum.

14.3.4 Discussion:

The XRD patterns of fuel-rich compositions were dominated, as expected, by patterns of unreacted fuel. The major products formed in the Fe/BaO_2 reaction (identified using the JCPDS 1989 database tables [136]), were $Ba_3Fe_2O_6$, $Ba_2Fe_2O_5$ and $Fe_2O_3.H_2O$ (the last possibly being generated as Fe_2O_3 + H_2O during handling). These products will subsequently be referred to as [a], [b] and [c], respectively, in the column graphs which follow (Figures 14.15 and 14.16). BaO was only found across the composition range as a minor product. The Fe/BaO_2 reaction products which had been aged under laboratory conditions (25°C) for 2 years showed the existence of $BaCO_3$ in large quantities (relative to the other reaction products) especially in oxidant-rich compositions. The levels of the major products (relative to one another in each composition) across the composition range are shown below (Figures 14.15 and 14.16). Comparison of the peak intensities to a reference level across the composition range was not possible as the amount of amorphous material was not determinable, yet the particle size range of the reagents suggested that levels of compounds could be determined in the product residue relative to each other [181]. The effect of compaction pressure on the products formed during combustion of the Fe/BaO_2 system appeared to be small.

The products of combustion of the Fe/SrO_2 were a wide variety of mixed oxides. The chief products were $Sr_3Fe_2O_{6.16}$ and Sr_3FeO_{3-x}, together with $SrFe_2O_4$. These products are referred to as [a], [b] and [c], respectively, in Figures 14.17 and 14.18. The simple oxides (Fe_2O_3 and SrO) did not occur in significant quantity in the product in crystalline form. The variation of products across the composition range is shown in Figure 14.17 for the freshly combusted sample and in Figure 14.18 for the aged sample. The aged compositions (2 years under laboratory conditions), showed the existence of $Sr_3Fe_2(OH)_{12}$ and some $SrCO_3$. The effect of compaction on the products was seen in that $SrFeO_{3-x}$ dominated in the uncompacted mixture, while $Sr_3Fe_2O_{6.16}$ dominated in the 50-150 MPa compacted mixture.

Some unidentified phases (not present in the JCPDS 1989 diffraction data file [154]) were found in the residues of combustion of both systems (Fe/BaO_2 and Fe/SrO_2).

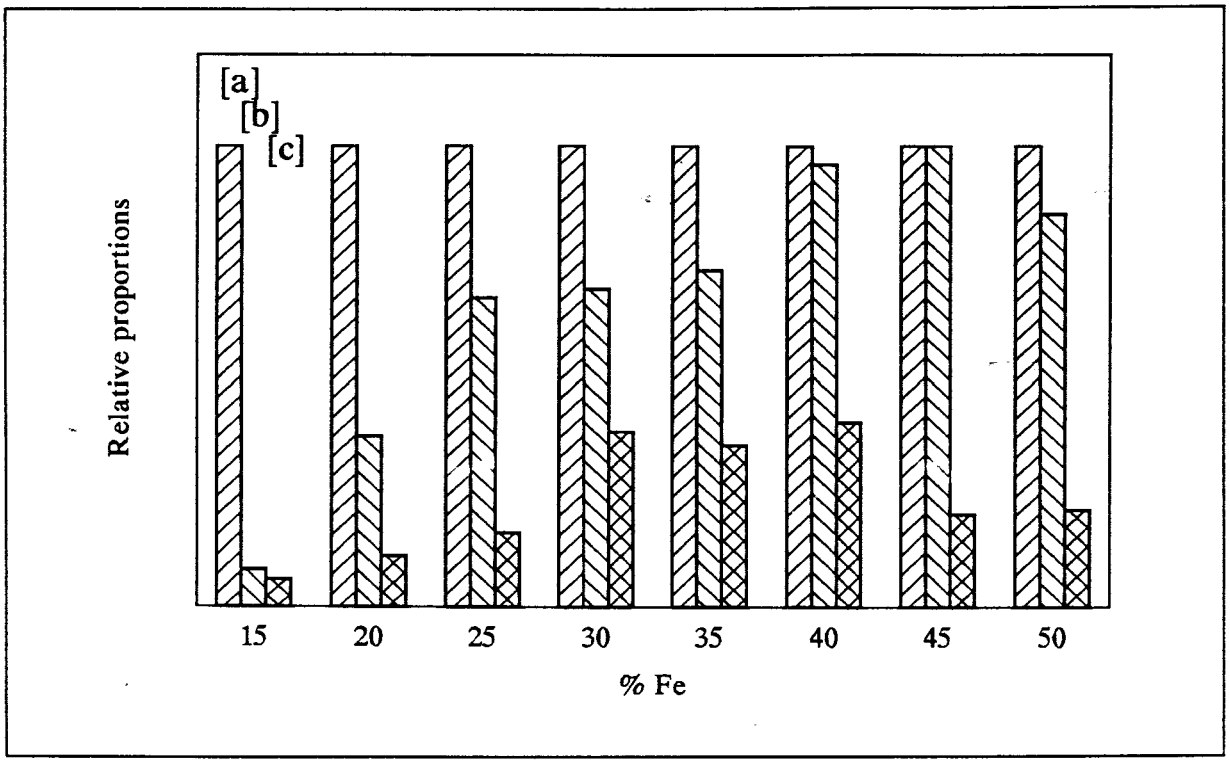

FIGURE 14.15: Stoichiometry of freshly prepared combustion products of Fe/BaO_2 [a]: $Ba_3Fe_2O_6$, [b]: $Ba_2Fe_2O_5$ and [c]: $FeO_3.H_2O$

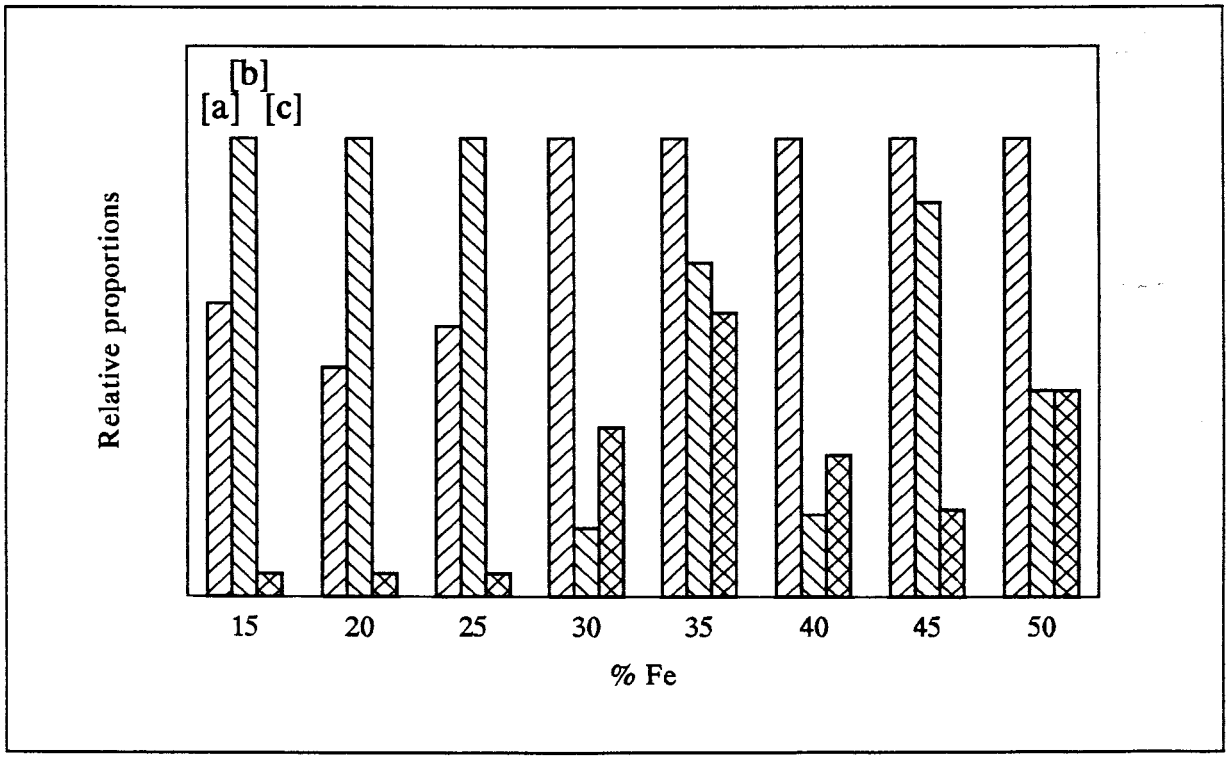

FIGURE 14.16: Stoichiometry of two-year old combustion products of Fe/BaO_2 [a]: $Ba_3Fe_2O_6$, [b]: $BaCO_3$ and [c]: $Fe_2O_3.H_2O$

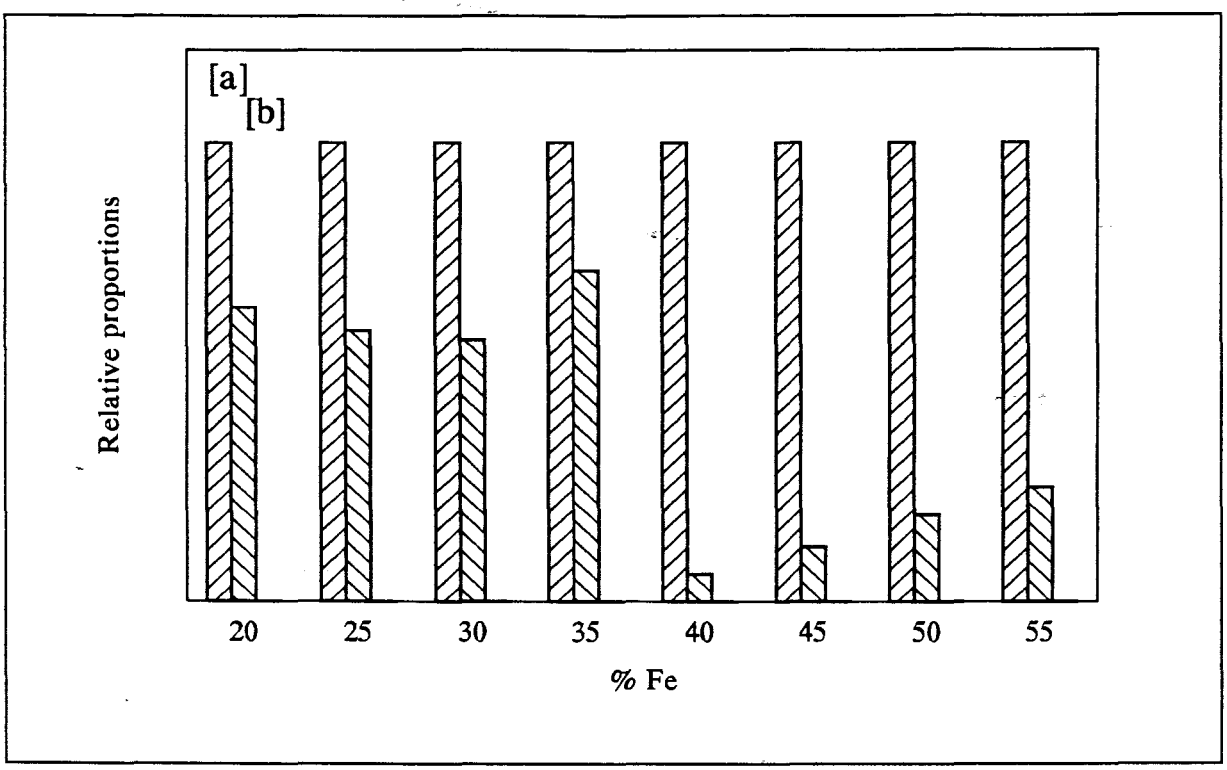

FIGURE 14.17: Stoichiometry of freshly prepared combustion products of Fe/SrO_2 [a]: $Sr_3Fe_2O_{6.16}$ and [b]: Fe_2O_3

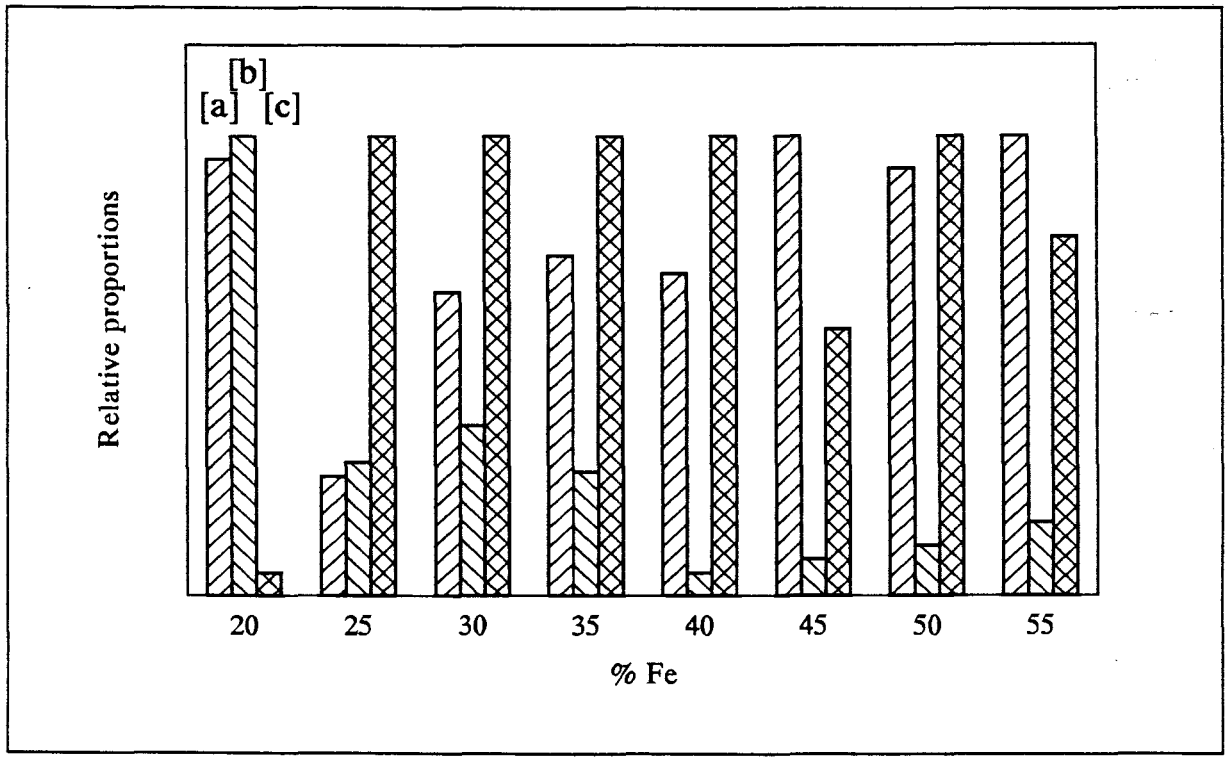

FIGURE 14.18: Stoichiometry of two-year old combustion products of Fe/SrO_2 [a]: $Sr_3Fe_2O_{6.16}$, [b]: $SrFeO_{3-x}$ and [c]: $Sr_3Fe_2(OH)_{12}$

14.4 Electron probe micro-analysis:

14.4.1 Introduction:

The electron probe apparatus (detailed in Section 4.7) was used to study the elemental distribution in three varieties of sample, to establish whether the distribution of material in the sample changed during reaction. The probe was calibrated using samples of pure Fe, BaO_2 or SrO_2. An electron beam-width of 50 μm, and an acceleration voltage of 10 kV were used. The photographs shown below the distribution graphs indicate the actual surface traversed in the study. Since SEM images have been used, dark regions correspond to cracks and hollows in the surface, and not different materials.

14.4.2 Combustion residues:

The study of combustion residues was performed on the fuel-rich mixtures of 50% Fe/BaO_2 and 50% Fe/SrO_2, to avoid the problems associated with beam scatter from irregular surfaces in residues, created by the formation of gas pockets generated by decomposition of excess peroxide. Samples were combusted as outlined in Section 4.2, after being compacted at 55 MPa for 1 minute. To avoid reaction of the reactive oxides, produced on heating, with CO_2 and H_2O, the residues formed were carefully removed from the channel and mounted in polyester resin, in such a manner as to allow study of a vertical cross-section of the residue. Four separate regions were studied, each study comprising twenty samples taken in 25 μm steps, measuring the relative levels of Fe and Ba or Sr at each step. A further experiment was performed by extending the step size to 100 μm intervals, in an attempt to compare short-range and longer-range distribution effects (Figure 14.19). The data obtained were normalised relative to the calibration levels, and examined to determine the stoichiometry of the products in the residue.

Combustion residues showed distinctive zoning. The smaller step samples showed definite distribution trends down the residue (either an increase or decrease in the level of the fuel), and the larger step samples showed a definite increase in Fe distribution towards the lower side of the residue (corresponding to the bottom of the combustion channel). This behaviour was found in both the Fe-Ba and the Fe-Sr systems, as shown in Figure 14.20 and Figure 14.21. The feature of one element "settling-out" of the mixture relative to another during reaction is well documented in SHS reactions (Section 3.10) and thus was not unexpected for the system studied. SEM examination of the Fe/SrO_2 residue sample showed formation of $\sim$30 μm pockets, probably due to the tendency of the SrO_2 to coalesce during mixing, and subsequent reaction in that state. The expected elemental levels for the 50% Fe/BaO_2 residue are Fe: 59% and Ba: 41%; and for the 50% Fe/SrO_2 system, Fe: 62% and Sr: 38%, respectively.

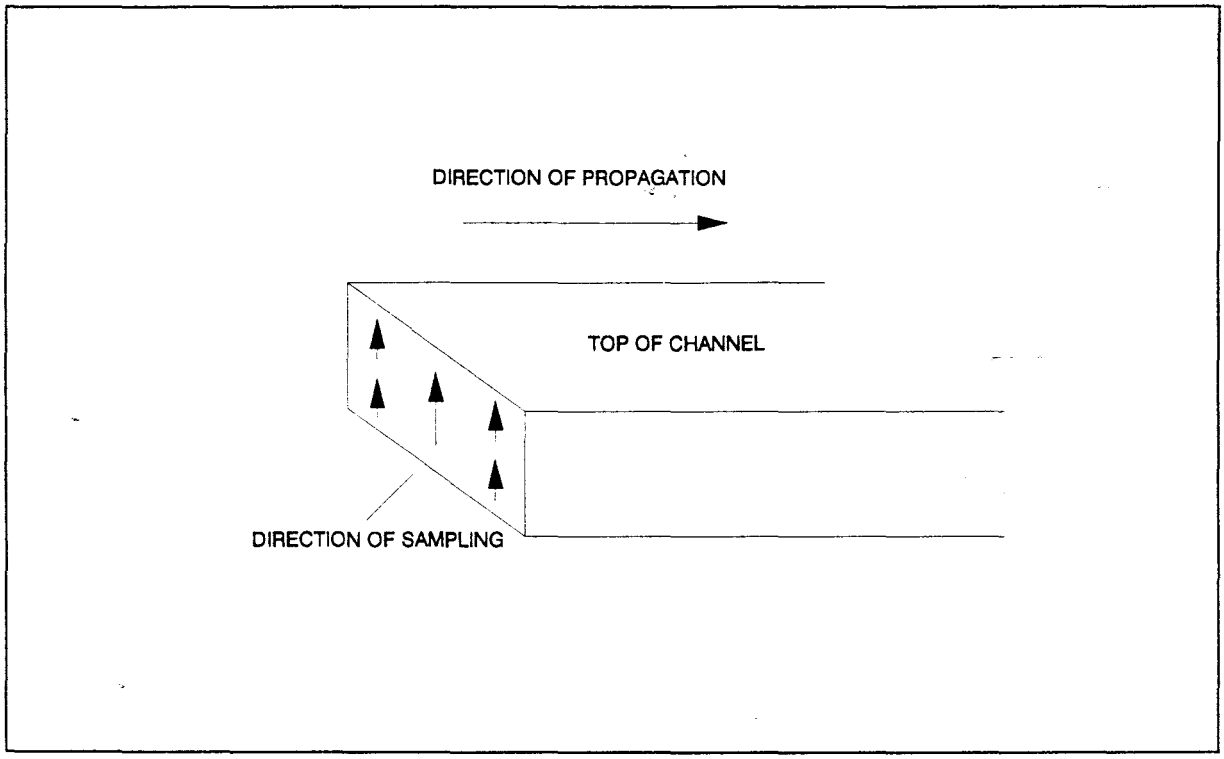

FIGURE 14.19: Schematic of the sampling orientation used to study combustion residues

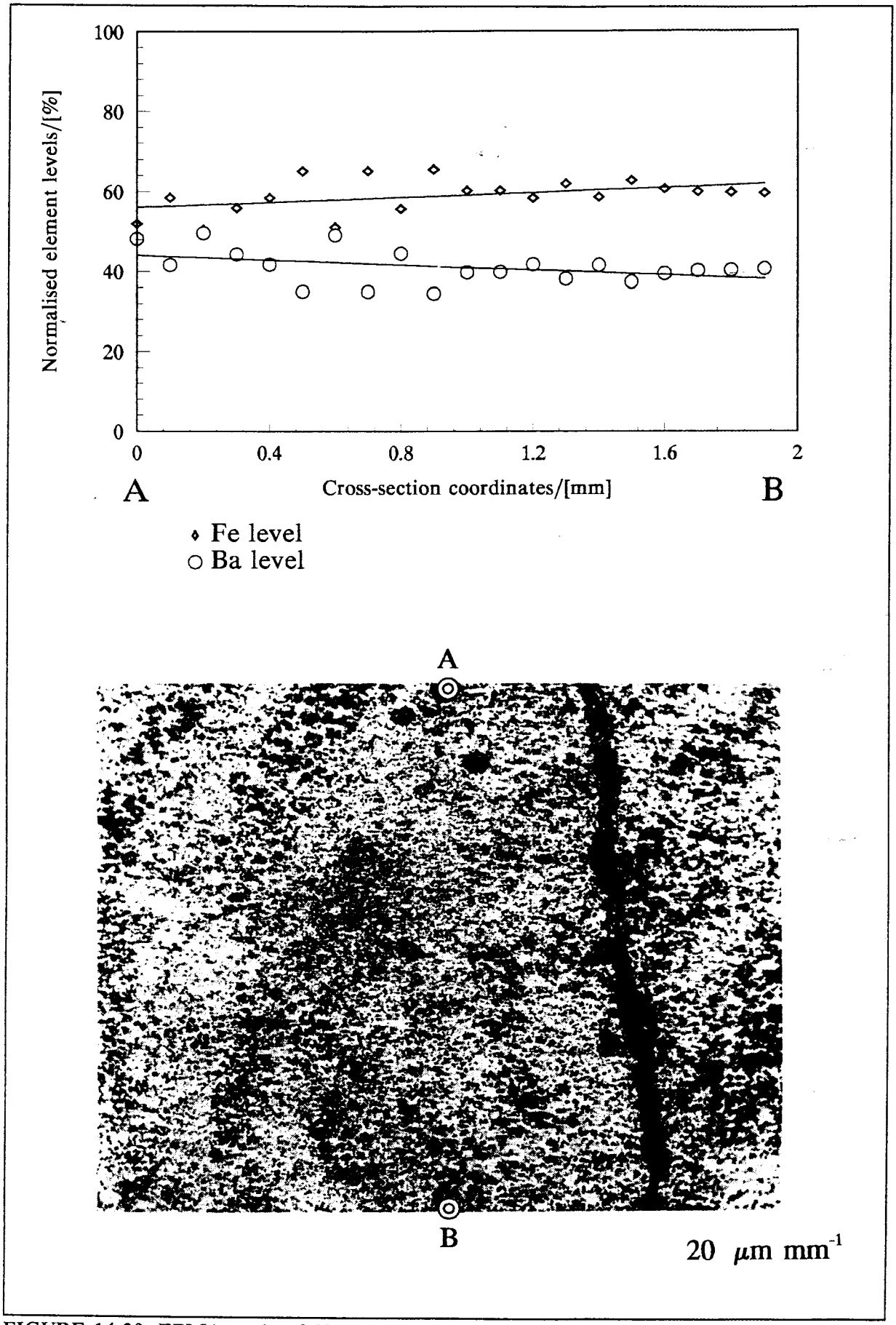

FIGURE 14.20: EPMA study of 50% Fe/BaO_2 combustion residue

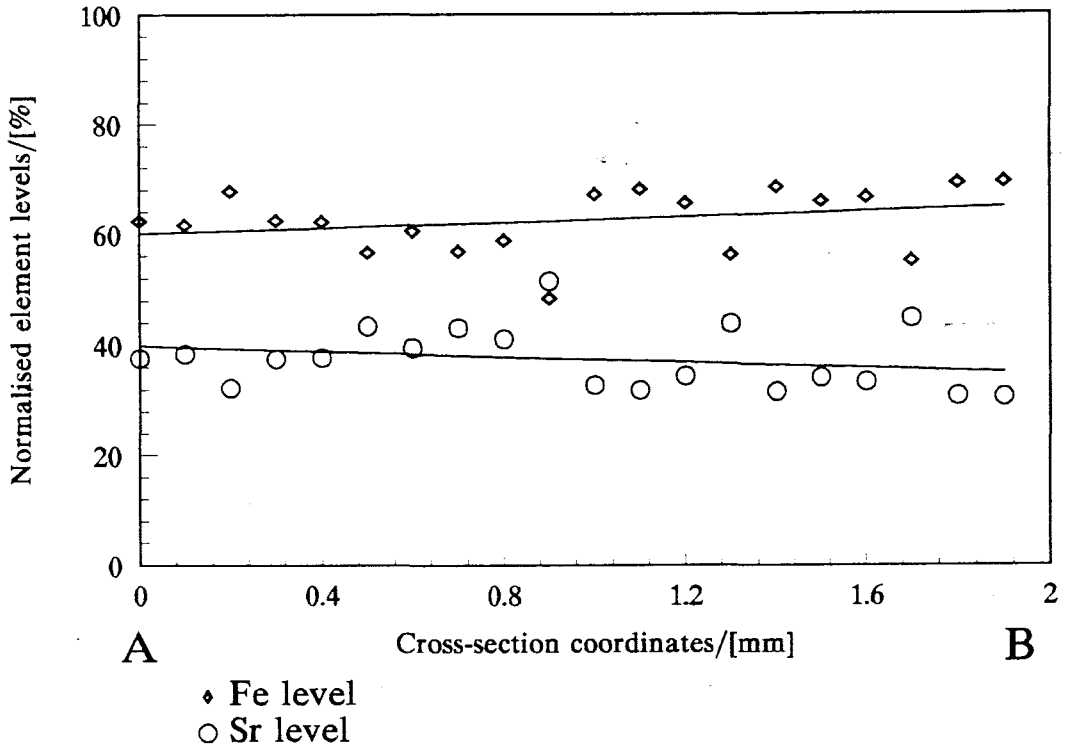

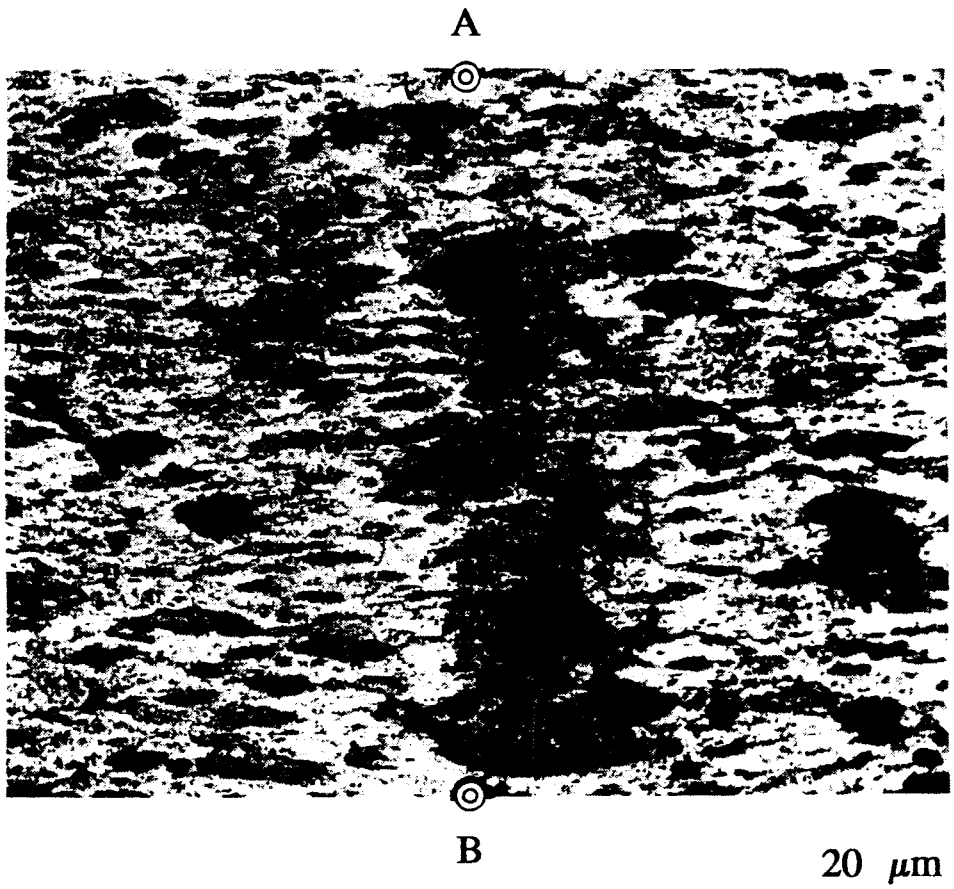

FIGURE 14.21: EPMA study of 50% Fe/SrO_2 combustion residue

14.4.3 Interaction of iron wire with pyrotechnic compositions:

Samples were prepared in the same manner as those in the above study, and were packed into the channel, along with a length of thin (0.4 mm diameter) Fe wire embedded longitudinally down the centre of the pyrotechnic composition in the channel before compaction of the sample. The samples were combusted and the residues of combustion were mounted in resin and orientated for a cross-section analysis. The radial distribution of element levels outward from the wire core was determined. Sampling during analysis was done horizontally (in the context of the combustion channel) to avoid the effects of vertical settling of material during combustion (mentioned above). 60 steps of 5 μm, and a 20 μm electron beam were used (Figure 14.22). These values were selected to avoid beam scatter caused by the coarse surface, and to avoid studying single particles (as a beam width of 5 μm is of the same magnitude as Fe particles). The sample step of 5 μm was used to provide a smooth transition from regions of high concentration to regions of low concentration (such as cracks in the surface). The appearance of the wire cross-section in the electron micrograph gives no indication of bulk melting.

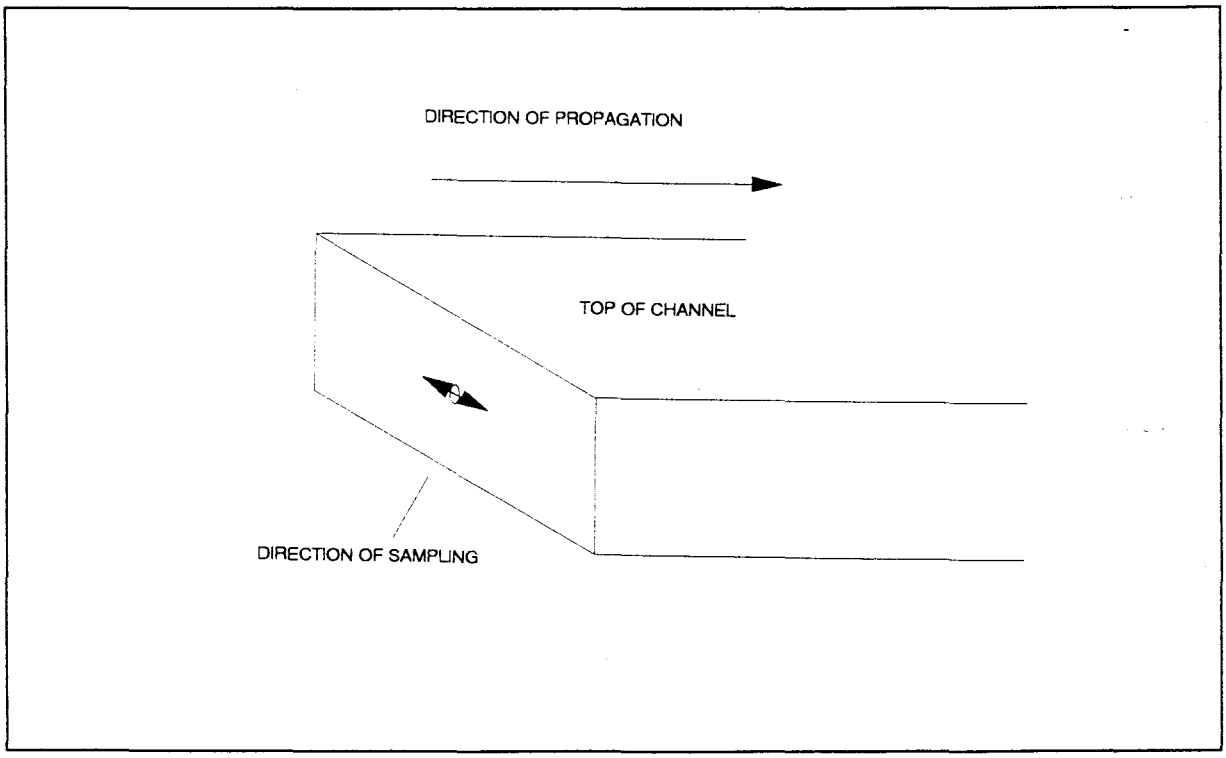

FIGURE 14.22: Schematic of the sample orientation used in the core-wire study

The transects of a cross-section of the pyrotechnic residue, with Fe wire embedded longitudinally, showed that zoning (whereby the Fe is coalescing and forming layers) is occurring near the boundary of the wire. The boundary is readily discernible in the Fe-Ba system (Figure 14.23) and in the immediate vicinity of the wire there is a slight decrease in Fe content and corresponding increase in Ba content. Possible explanations include formation of a relatively stoichiometric compound in the

neighbourhood of the iron surface, or a surface tension effect involving some melting of Fe particles near the wire surface followed by adherence to the surface, thus depleting the immediate neighbourhood. In the Fe-Sr system, the distribution shows flow of Fe into the strontium peroxide across the wire boundary, as shown by the high levels of Fe beyond the boundary in the combusted mixture (Figure 14.24). Significant spreading of the Fe was found in the Sr sample with less occurring in the Ba sample.

14.4.4 Interaction of fuel-peroxide surfaces:

Four control pellets, comprising separate layers of Fe and BaO_2; Fe and SrO_2; Zn and BaO_2; and Zn and SrO_2; were prepared (as outlined in Section 4.4) and set in resin. A further four identical pellets were prepared and heated in the TG balance in N_2 at a heating rate of 20°C up to 470°C for the zinc systems, or 900°C for the Fe systems. The temperature was then held constant at these values for five minutes. The mass variation measured was less than 0.1%, showing that little reaction of the bulk of the pellet was occurring with the atmosphere in the furnace. These pellets were cooled (in N_2) and immediately set in resin to avoid reaction with water from the surroundings. Analysis of the pellets was performed by sampling a series of points in 10 μm steps, using a 20 μm beam, perpendicularly across the interface between the two materials, shown schematically in Figure 14.25.

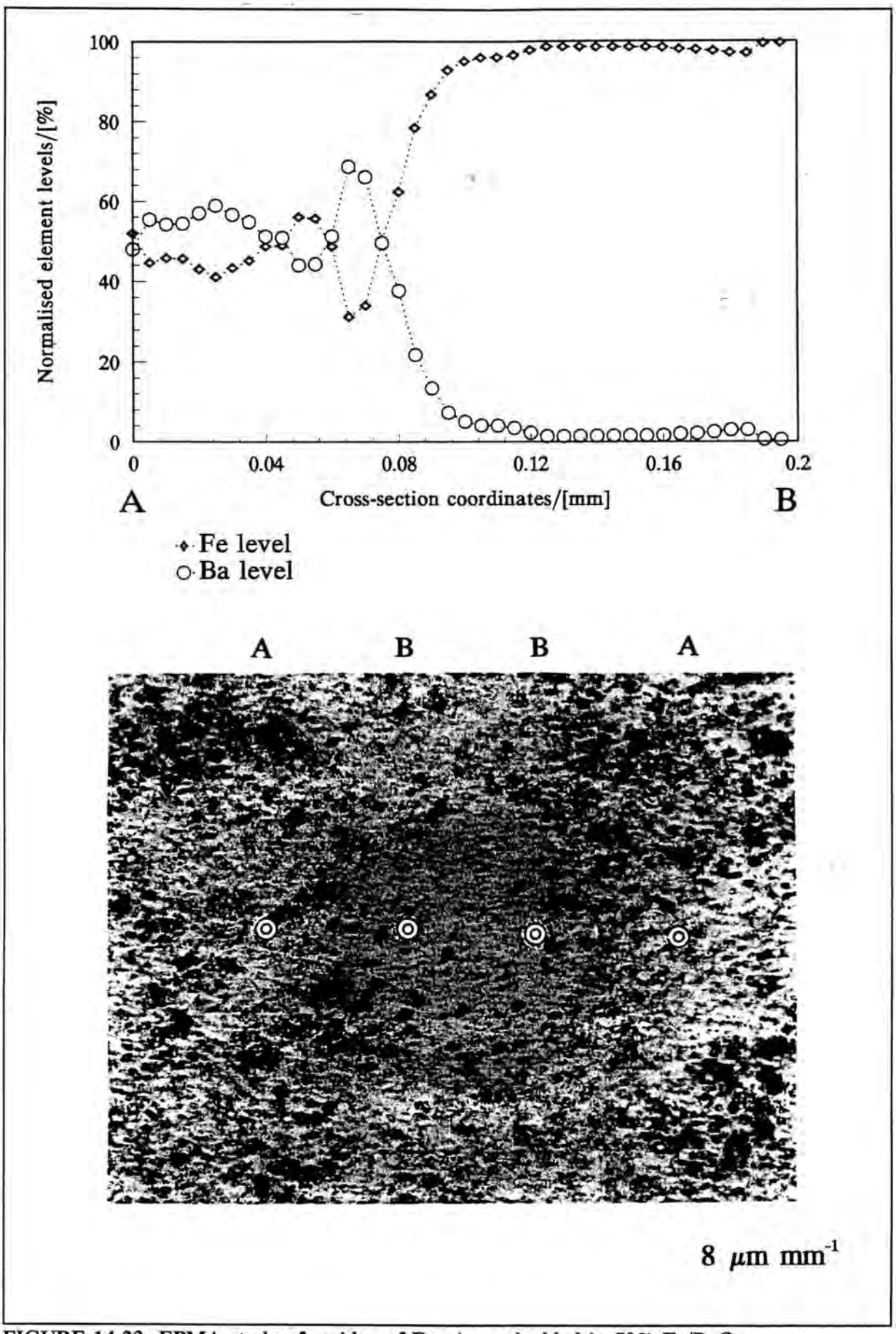

FIGURE 14.23: EPMA study of residue of Fe wire embedded in 50% Fe/BaO_2

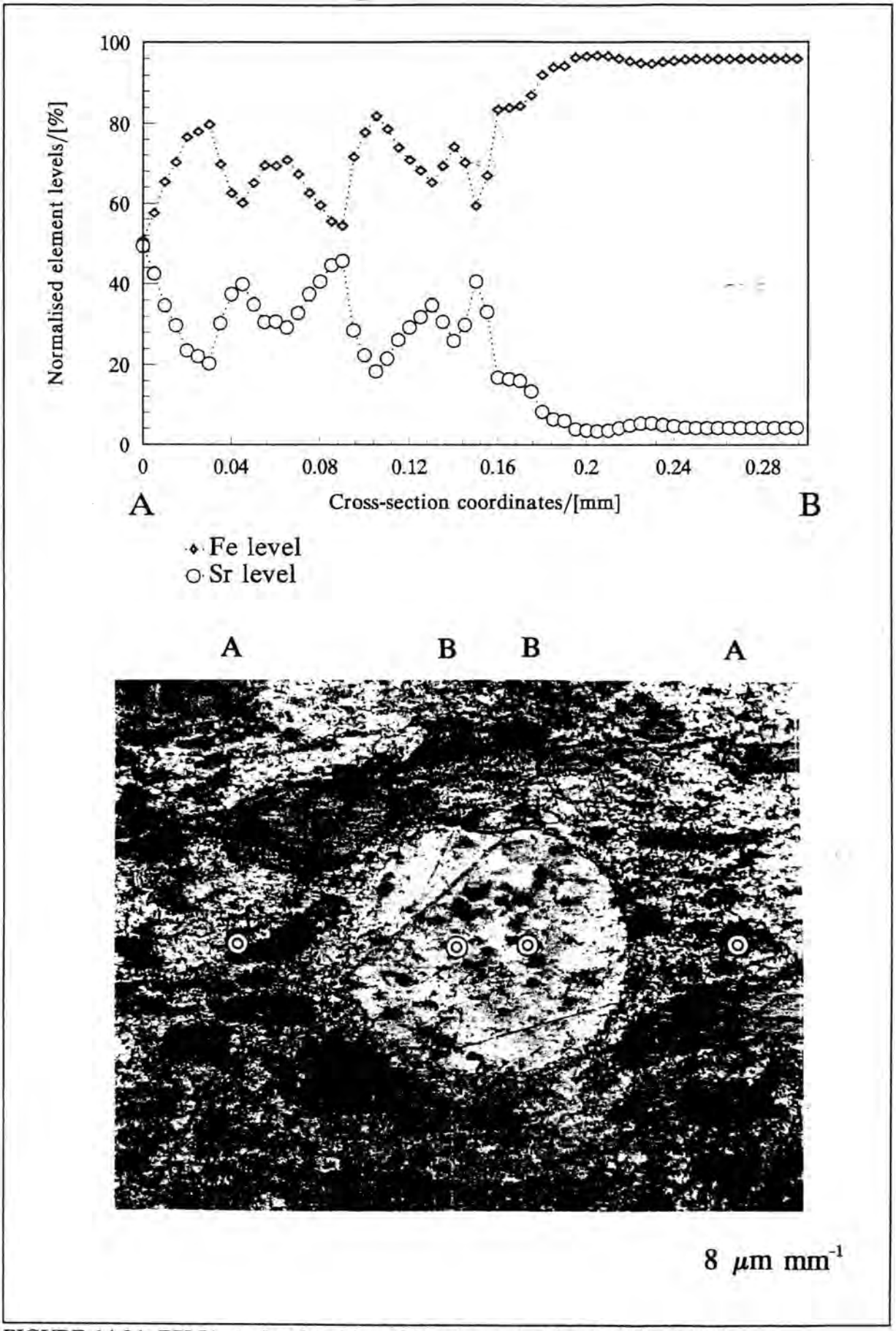

FIGURE 14.24: EPMA study of residue of Fe wire embedded in 50% Fe/SrO_2

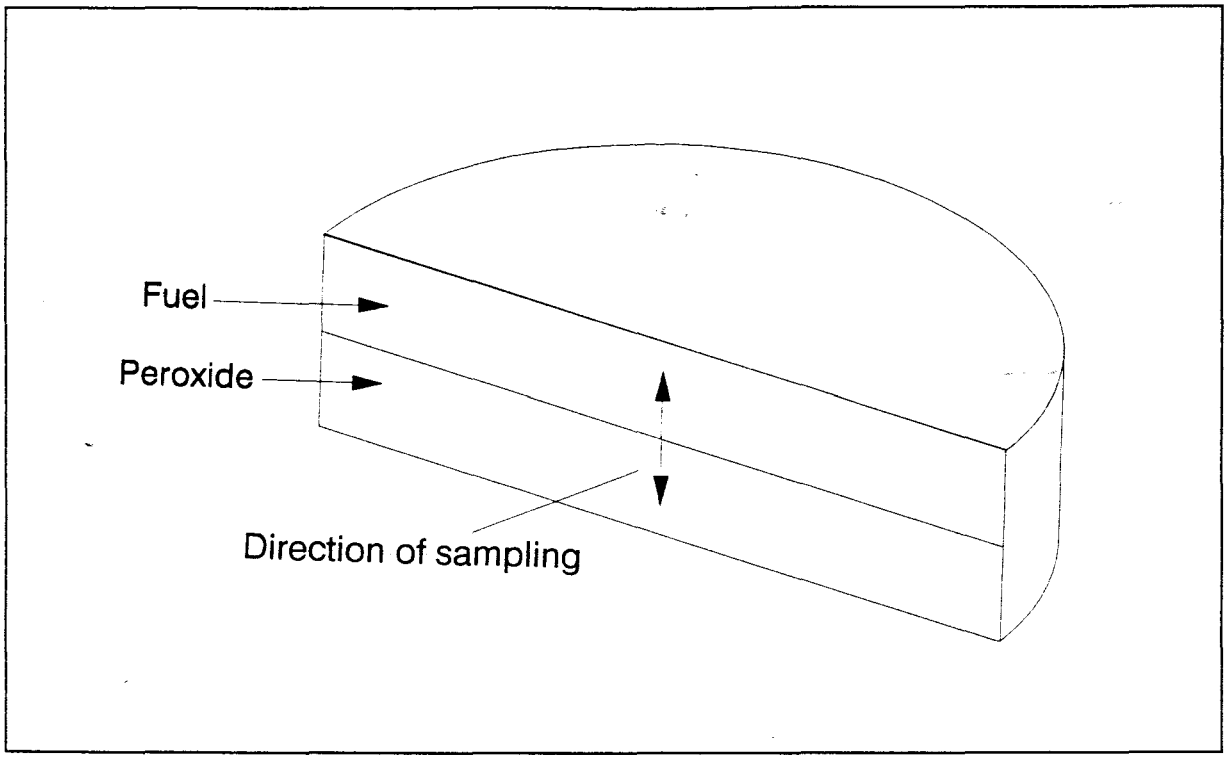

FIGURE 14.25: Schematic of sample orientation used in the layered pellet study

In the figures for the layered pellet study, only the variations in Fe levels across the boundary are depicted. In the Fe/BaO_2 system, distinct spreading of Fe occurs across the boundary in the heat treated pellet, compared to the control pellet, as shown in Figure 14.26. Regions of stable stoichiometry indicated the formation of oxides or ferrates of general formula Fe_4BaO_x and $Fe_2Ba_3O_y$. The Fe/SrO_2 system shows similar behaviour (Figure 14.27), with regions developing along the boundary of composition Fe_4SrO_x and $Fe_2Sr_3O_y$. The Zn/BaO_2 and Zn/SrO_2 layered pellet systems (Figures 14.28 and 14.29) show no significant compositional changes along the boundary, with minimal reaction occurring until the bulk of the zinc was in the liquid state (unlike the Fe/peroxide systems which rely on diffusion for reaction to occur). Only the element levels of zinc are shown in the zinc/peroxide graphs. Possible reaction mechanisms are discussed in detail in Section 15.

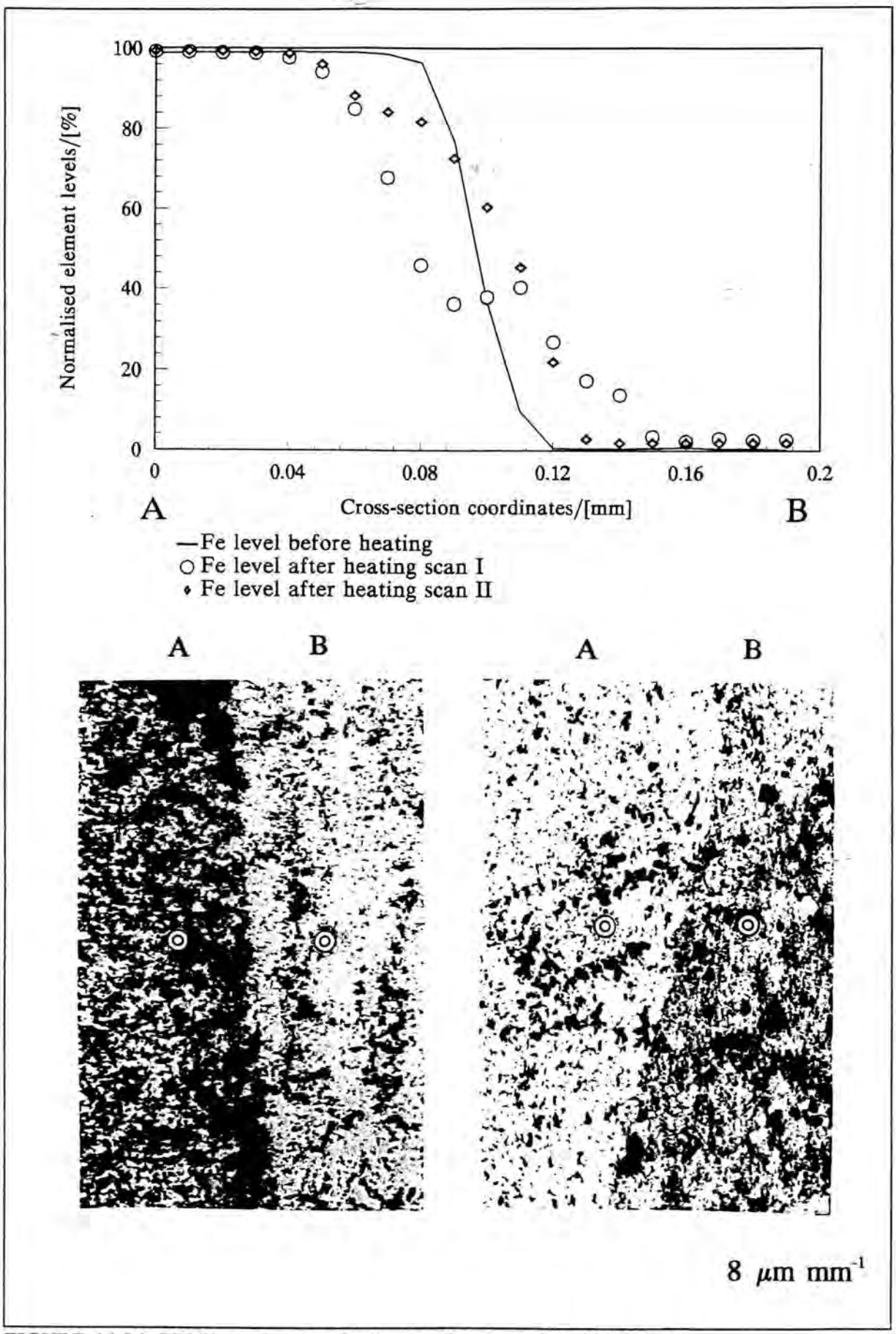

FIGURE 14.26: EPMA study of Fe/BaO_2 interface heated to 900°C in N_2

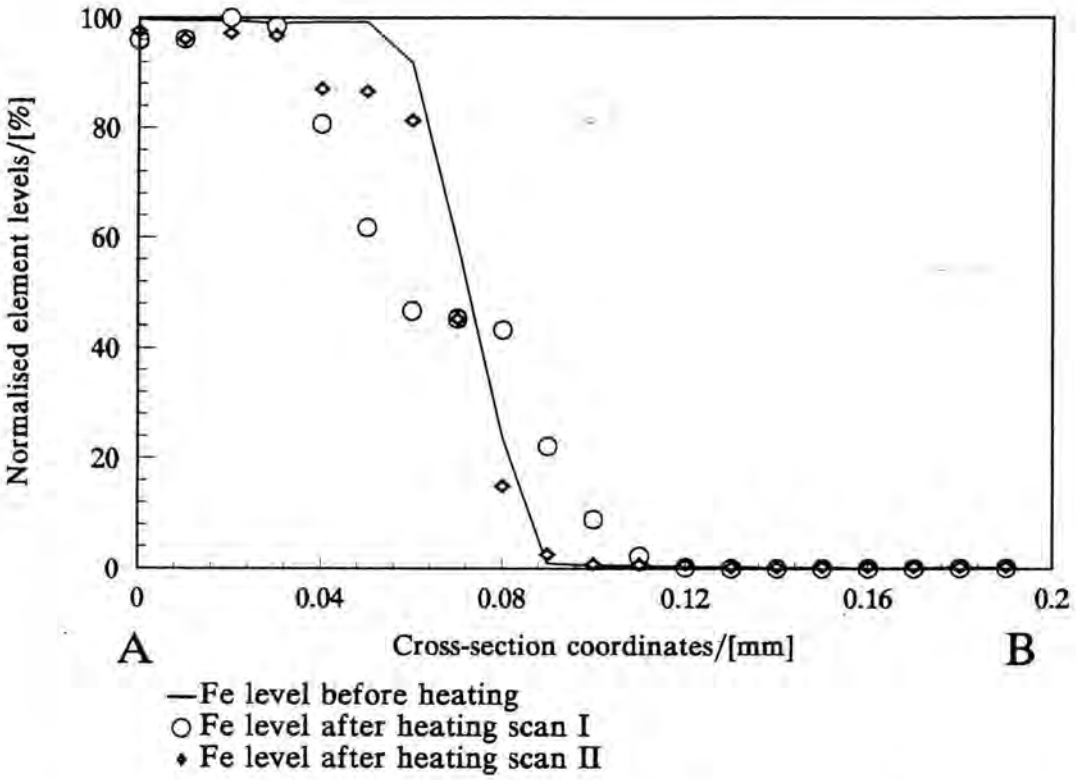

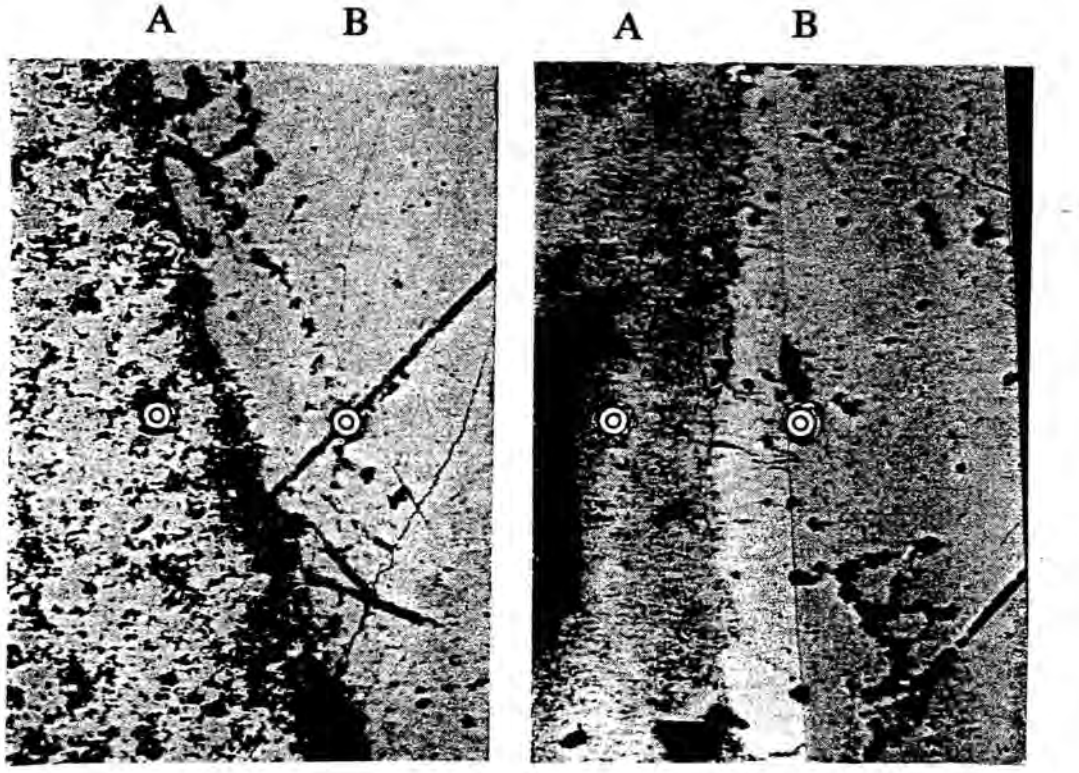

8 μm mm^{-1}

FIGURE 14.27: EPMA study of Fe/SrO_2 interface heated to 900°C in N_2

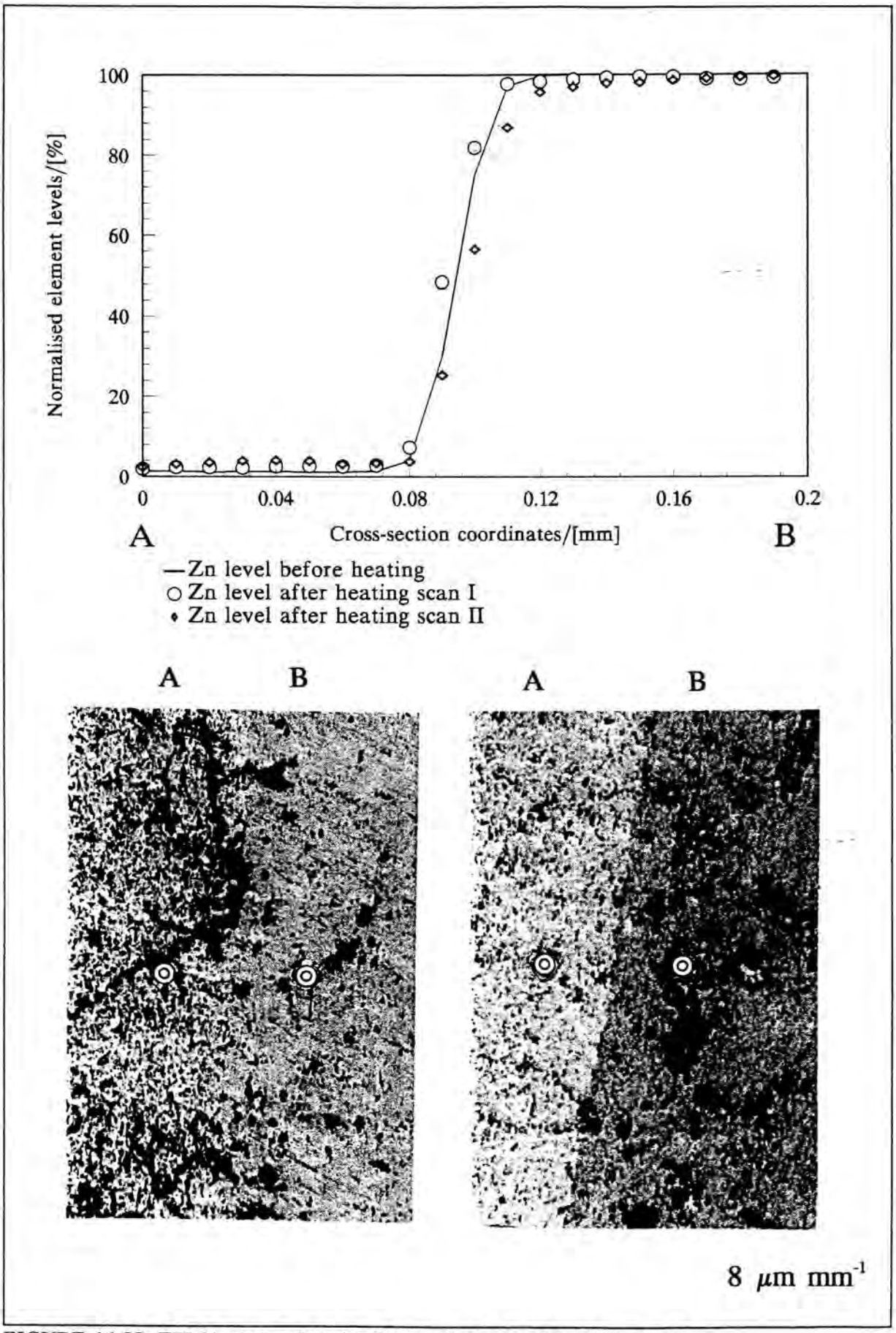

FIGURE 14.28: EPMA study of Zn/BaO_2 interface heated to 470°C in N_2

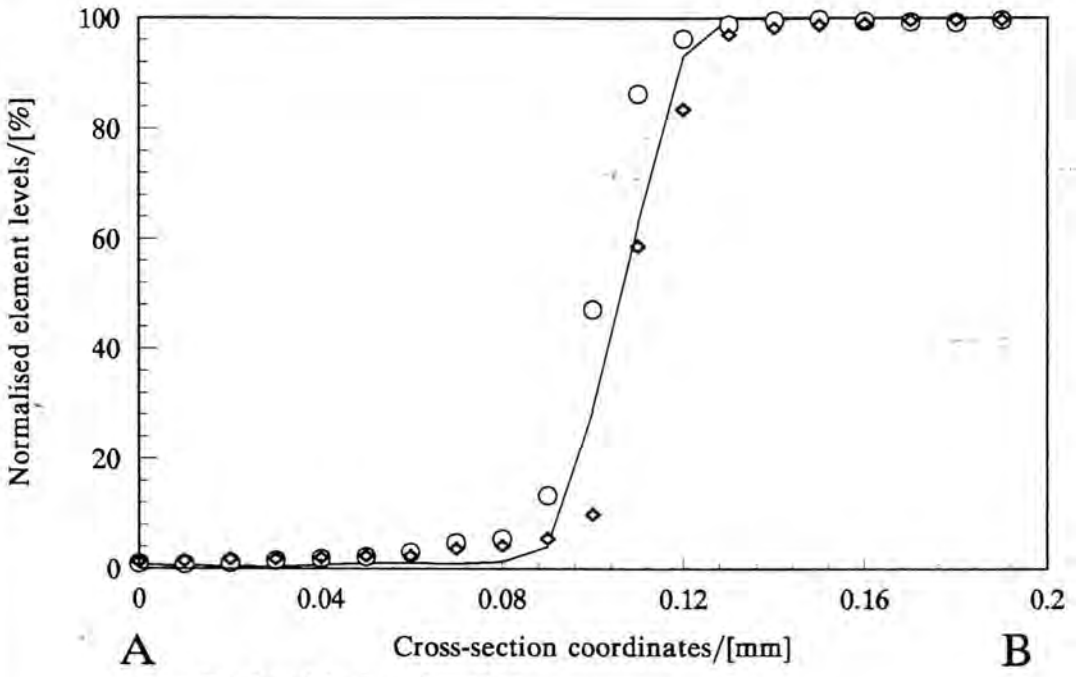

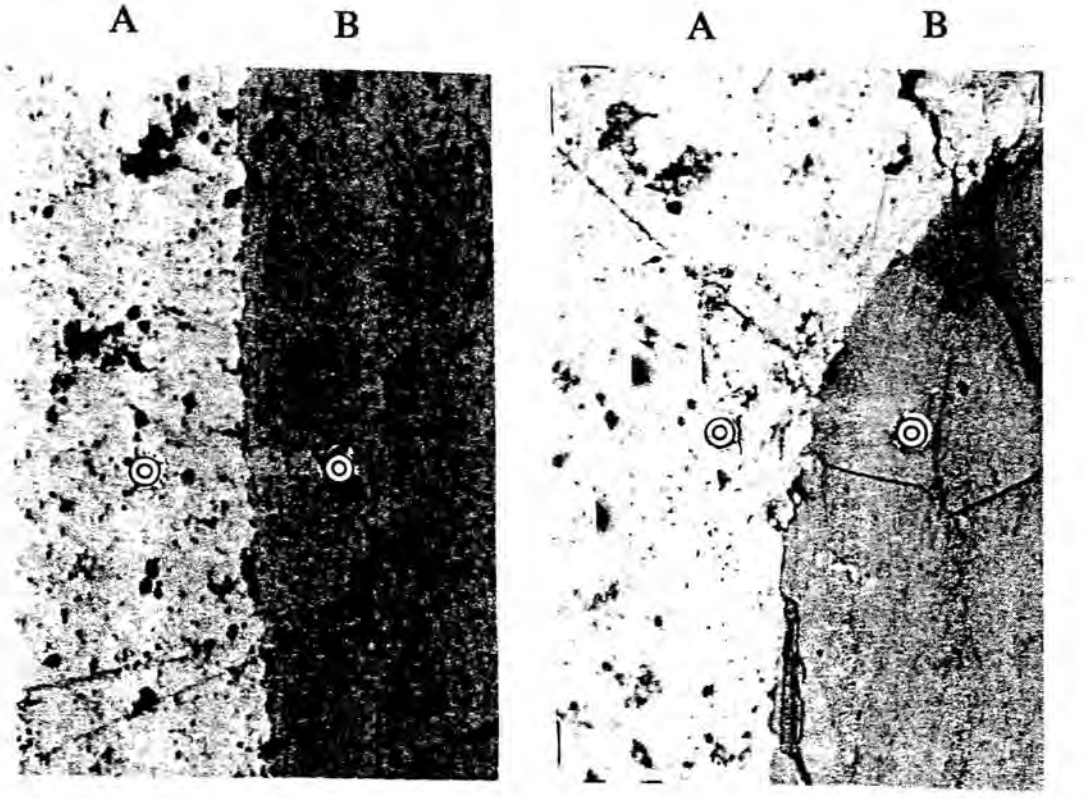

8 μm mm^{-1}

FIGURE 14.29: EPMA study of Zn/SrO_2 interface heated to 470°C in N_2

15. DISCUSSION

15.1 Introduction:

Discussion of the finer details of the results has been included in the sections in which the results are presented. In this section a broader overall discussion is presented under several general headings:

(1) fuel/oxidant contact

(2) structure and diffusion

(3) mechanistic information from thermal analysis

(4) combustion characteristics

(5) kinetic information

This discussion is followed by some brief conclusions in Section 16.

15.2 Fuel/oxidant contact

For reaction to be initiated between fuel (A) and oxidant (B) there must be some form of contact between A and B. The nature of this initial contact is discussed further below.

Hao and Tanaka [182,183] have proposed that the reactivity of two components in a solid-solid system is a function of the number of contact points, determined (assuming spherical particles) from values of the particle-size ratio, molar ratio and molar density ratio. Brown [184] has recently shown that a qualitative connection exists for several pyrotechnic systems, between the calculated number of contact points and the linear burning-rates recorded across the composition range. Such comparisons have been made for the Fe/peroxide systems and fair agreement of the trends was obtained (Figures 15.1 and 15.2).

SEM (Section 14.2) of pellets of pyrotechnic material compacted at 55 MPa (Plates 15.1 and 15.2) show the actual packing of peroxide particles around the fuel particles (10 000X). The contact between fuel and oxidant is far from the ideal model assumed in the calculations, but the general trends of burning-rate and contact points are similar. Details of the calculation of the number of contact points, N_R, are given in Appendix 10. In both of the Fe/peroxide systems, the maximum burning rates occur at compositions lower in fuel than predicted. This may result from the non-ideality of the particles or could indicate deviation from a totally solid-solid mechanism. It is also of interest that the apparent proportionality factor between N_R and v differs in the two systems (Fe/BaO_2: $40x10^7 \approx K_1$ x 20 mm s^{-1}; Fe/SrO_2: $100x10^7 \approx K_2$ x 4 mm s^{-1}) so $K_2 \approx 13 \times K_1$. Similar comparisons were not done for the Zn/peroxide systems, since Zn has been shown (Section 6) to melt prior to reaction.

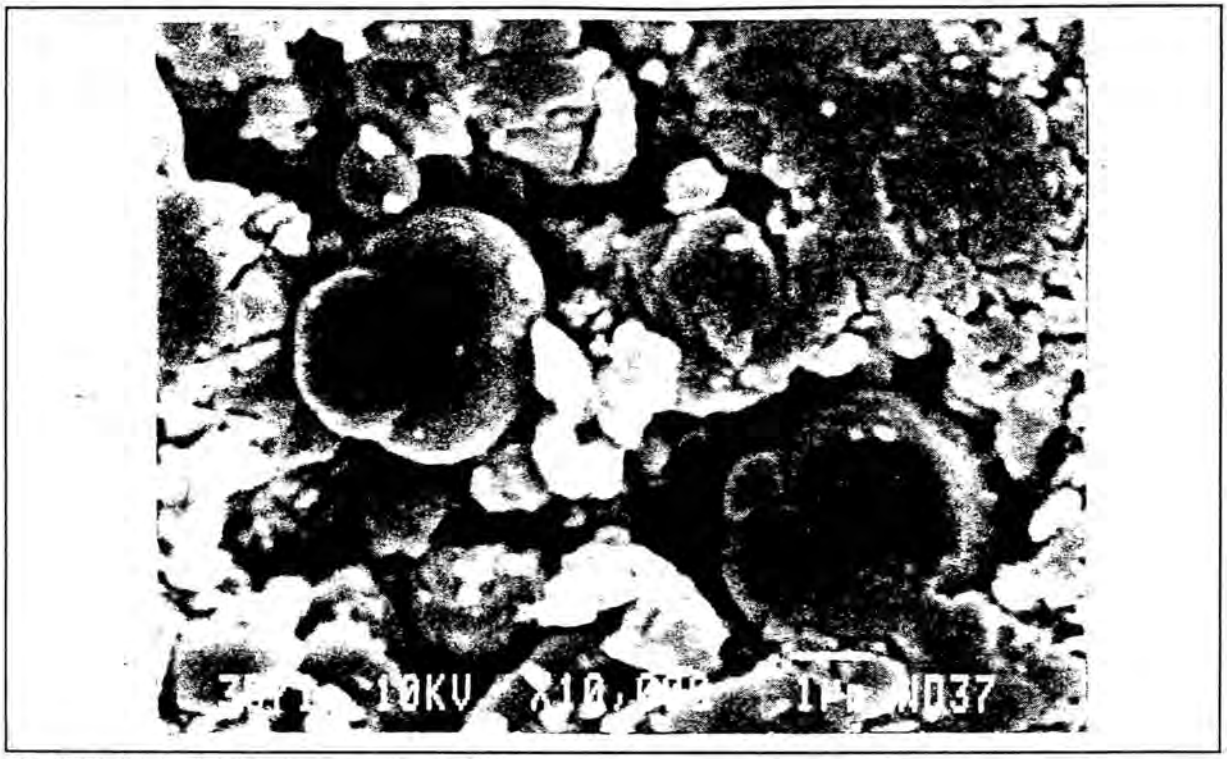

PLATE 15.1: SEM micrograph of 50% Fe/BaO_2 compacted at 55 MPa

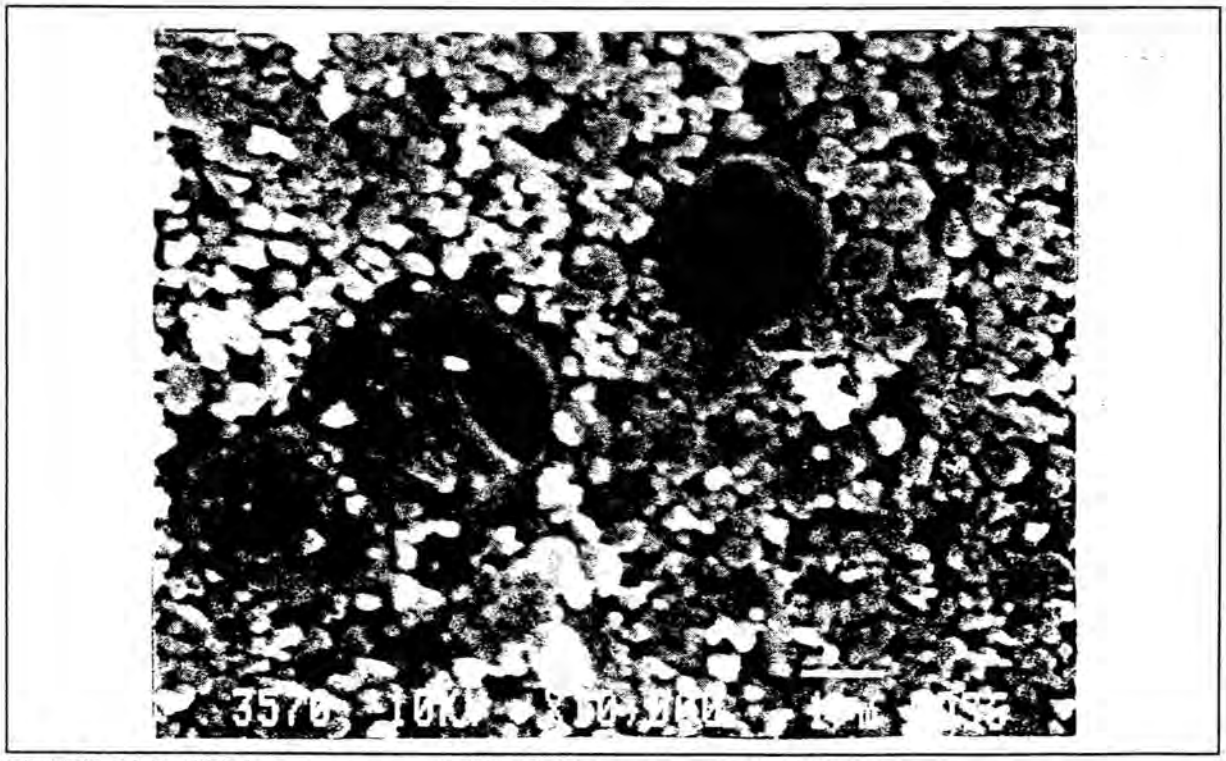

PLATE 15.2: SEM micrograph of 50% Fe/SrO_2 compacted at 55 MPa

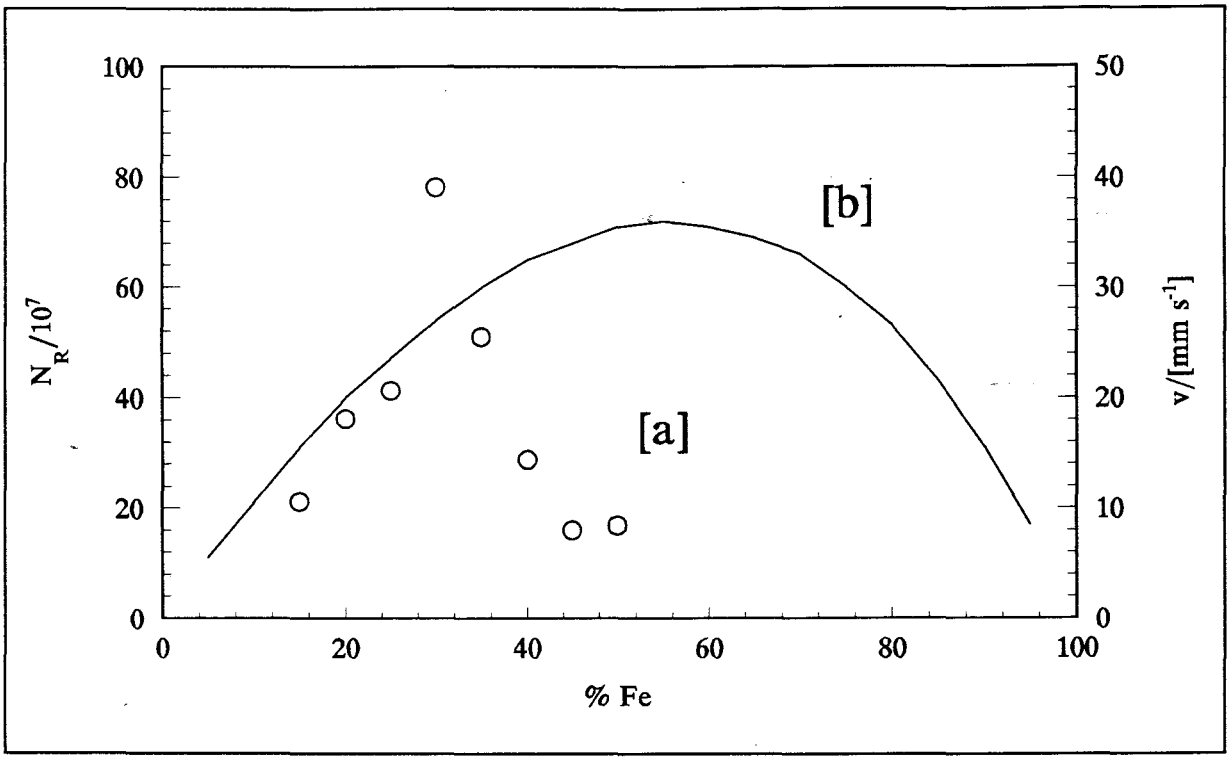

FIGURE 15.1: Correlation between [a]:burning-rates and [b]:contact points for the Fe/BaO_2 system

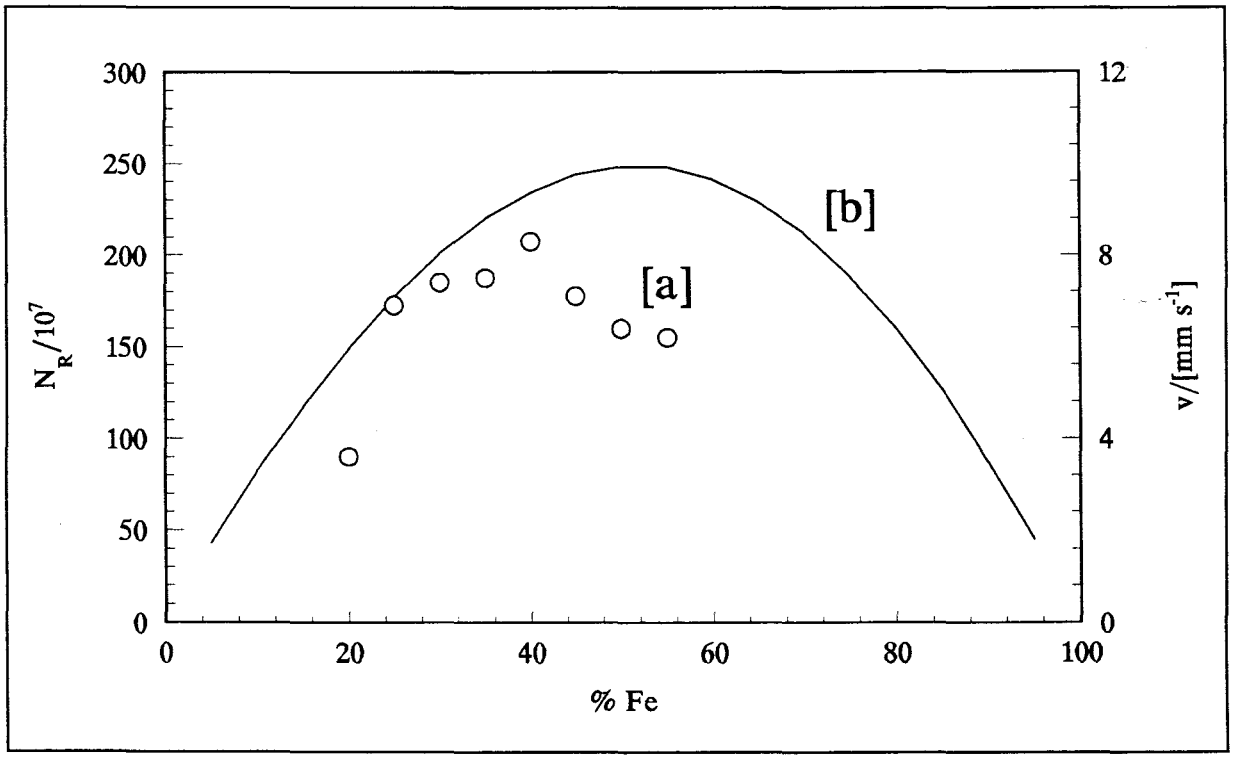

FIGURE 15.2: Correlation between [a]:burning-rates and [b]:contact points for the Fe/SrO_2 system

15.3 Structure and diffusion

Once fuel/oxidant contact is present, one or more of several possibilities has to occur:

(1) Atoms or ions derived from A have to move across the A/B interface into the B lattice.

(2) Atoms or ions derived from B have to move across the B/A interface into the A lattice.

(3) Species derived from both A and B diffuse simultaneously in opposite directions.

Once exothermic reaction has been initiated, the temperature will rise rapidly, at least in the neighbourhood of the sites of initiation. Such temperature rises can produce phase changes and/or oxidant decompositions which can significantly alter the mechanisms and overall course of reaction.

Where the fuel is a metal, the oxidant is an oxide or peroxide, and the reaction product is a complex metal oxide, even if usually amorphous in structure, it is most probable that atoms of the metal fuel will diffuse into the oxide or peroxide lattice (with the appropriate electron transfer processes taking place as required). This should occur most readily in excess-metal type oxides. Hill [9] has proposed that this type of mechanism accounts for the two-stage temperature profiles observed for the combustion of several metal/$KMnO_4$ systems. The two stages are proposed to arise from diffusion of metal fuel through (a) structurally defective oxidant, and (b) the bulk of the oxidant of more regular structure. For the finely-ground powders used in pyrotechnic systems, a fairly high proportion of oxidant is likely to be defective in structure, but it is of interest to examine initially the possibilities of diffusion of fuel into the regular structures of the oxidants.

The ideal path would be:

fuel A + oxidant B (regular structure) → solid product C (regular structure)

but this will undoubtedly be accompanied (and probably dominated) by the alternative paths:

fuel A + oxidant B (regular structure) → product C (amorphous)

fuel A + oxidant B (defective structure) → product C (regular structure)

fuel A + oxidant B (defective structure) → product C (amorphous)

Several complicating factors can intervene:

a) the oxidant may undergo solid phase changes, melting or decomposition, for example:

oxidant B (regular structure) → product D (usually defective structure) + gases

b) the fuel A may melt (or even vaporise at high temperatures).

As an initial simplification, the oxidant B will be assumed to be of regular structure and the structure will be approximately maintained during the initial stages of reaction. Whether the fuel A is then present as solid, liquid, or even vapour, will then only influence the ease with which the concentration of A on the surfaces of solid particles of B is maintained.

The unit cell parameters of the reactants and some possible intermediates or products of the binary pyrotechnic reactions studied are listed in Table 15.1.

TABLE 15.1 : Lattice parameters of reaction materials

System	Space group	a_o/[nm]	b_o/[nm]	c_o/[nm]	α	β	γ	Ref
Fe α	Im3m	0.2866	2.866	2.866	90	90	90	[186]
Fe γ	Fm3m	0.2910	2.910	2.910	90	90	90	[186]
Fe δ	Im3m	0.2940	2.940	2.940	90	90	90	[186]
FeO	Fm-3m	0.4332	0.4332	0.4332	90	90	90	[107]
Fe_3O_4	Immm	0.5912	0.5945	0.8394	90	90	120	[189]
Fe_2O_3	R3c	0.503	0.503	1.375	90	90	120	[185]
Zn	P6/mmc	0.2665	0.2665	0.4947	90	90	120	[186]
ZnO	P6/mmm	0.3249	0.3249	0.5205	90	90	120	[190,191]
$BaFe_2O_4$	$Bb2_1m$	0.8448	1.905	0.539	90	90	90	[187,188]
BaO	Fm3m	0.552	0.552	0.552	90	90	90	[87]
BaO_2	F4/mmm	0.5384	0.5384	0.6841	90	90	90	[87,192]
SrO	Fm3m	0.5144	0.5144	0.5144	90	90	90	[87]
SrO_2	F4/mmm	0.5044	0.5044	0.655	90	90	90	[87,193]

Radii of the relevant atoms and ions are given in Table 15.2.

TABLE 15.2: Radii of atoms or ions involved in possible diffusion [8,161]:

Element	Valency	Ionic radius/[nm]
Ba	+1	0.153
Ba	+2	0.134
Fe α	0	0.124
Fe γ	0	0.129
Fe δ	0	0.127
Fe	+2	0.074
Fe	+3	0.064
O	-2	0.132
O	-1	0.176
Sr	+2	0.112
Zn	0	0.133
Zn	+1	0.088
Zn	+2	0.074

The BaO_2 and SrO_2 structures have the same space group, shown in Figure 15.3, with slightly different lattice parameters (Table 15.1). The stoichiometry of the peroxide decompositions indicates the formation of the oxides, BaO and SrO, and O_2 gas. The structures of BaO and SrO are the same (Figures 15.4), again with slightly different lattice parameters (Table 15.1). Loss of oxygen results in a contraction of the unit cells of both oxidants in the c-dimension, accompanied by slight expansions in the a- and b- dimensions. Partial loss of oxygen could create considerable space within the oxidant structure for accommodation of atomic or ionic species derived from the fuel. Using the ionic radii given in Table 15.2, the fcc unit cell parameters of BaO and SrO indicate virtual ionic "contact" along cell edges: BaO has a possible packing size of $2r_{Ba2+} + 2r_{O2-} = 0.532$ nm, with a cell edge of 0.552 nm; while SrO has $2r_{Sr2+} + 2r_{O2-} = 0.488$ nm, with a cell edge of 0.514 nm. The well-documented formation of complex oxides, using alkaline-earth peroxides as reactants with other simple metal oxides, confirms the ease of movement of cations in a matrix of oxide ions.

Static models do not account for the vibrations of solid particles associated with high temperatures, nor do spheres accurately represent the behaviour of complex ions such as peroxides. The diagrams do, however, illustrate the relative ionic sizes of ions involved in the reactions and thus it is possible to speculate on the species which are most likely to diffuse in the event of diffusion reactions occurring.

X-ray powder diffraction studies (Section 14.3) of the products of the Fe/BaO_2 and Fe/SrO_2 reactions indicate the formation of some $Ba_3Fe_2O_6$ and $BaFe_2O_4$, and $Sr_3Fe_2O_{6.16}$, respectively (along with unreacted reactants and some BaO and SrO). In the $Ba_3Fe_2O_6$ structure, Fe has an oxidation state of +3. A starting point for consideration then, would be the movement of an Fe^{3+} ion into the BaO_2 structure. From Table 15.2, the radius of an Fe atom is 0.126 nm and of an Fe^{3+} ion is 0.055 nm. The Ba^{2+} ion has a radius of 0.134 nm, so an Fe atom could be accommodated in a Ba^{2+} vacancy. The radius of an Sr^{2+} ion is 0.112nm, so accommodation of an Fe atom in an Sr^{2+} vacancy would be more difficult. It is thus likely that either Fe^{3+} is formed by surface oxidation of iron particles and that these ions can then transfer to oxidant particles, or that Fe atoms may be accommodated initially in cation vacancies at the oxide surface, undergo electron transfer and then move into the structure as Fe^{3+}.

The activation energies recorded for the Fe/BaO_2 and Fe/SrO_2 systems (Table 15.3) are both relatively low, in accordance with the values expected for diffusion-based reactions. The values of the BaO_2 system vary between 10 and 16 kJ mol^{-1}, while the values of SrO_2 are slightly higher at 20 kJ mol^{-1} to 42 kJ mol^{-1}. The lower activation energies recorded for the Fe/BaO_2 system could support the suggestion that diffusion of Fe in the BaO_2/BaO lattice occurs more readily than in the SrO_2/SrO lattice.

By comparison, the activation energies found [6] for the Mn/BaO_2, Mo/BaO_2 and Mn/SrO_2 systems at 20% by mass of fuel were between 16 and 22 kJ mol^{-1}, and that of Mo/SrO_2, 38 kJ mol^{-1} at 40% fuel.

For the zinc/peroxide systems, X-ray powder diffraction did not indicate any mixed oxide formation, although such oxide products could be amorphous to X-rays. The radii of the zinc atom (0.137 nm) and Zn^{2+} ion (0.075 nm) are larger than the species expected in the Fe systems (Table 15.1).

Drennan and Brown [195-197] have reported on studies of the combustion of the Mn/BaO_2, Mo/BaO_2, Mn/SrO_2 and Mo/SrO_2 systems. The relevant radii are: Mn metal, 0.137 nm; Mo metal, 0.140 nm; Mn^{2+}, 0.067 nm; Mn^{3+}, 0.058 nm; Mn^{7+}, 0.026 nm; Mo^{3+}, 0.067 nm; Mo^{4+}, 0.065 nm; Mo^{6+}, 0.060 nm; Ba^{2+}, 0.136 nm; and Sr^{2+}, 0.113 nm. Diffusion via cation vacancies in the oxidant structure should thus be favoured in the BaO_2 lattice relative to the SrO_2 lattice, but, for comparable oxidation states, differences between the behaviour of Mn and Mo, based on geometry, should be slight. Based on the same mass percentage of fuel, or on the same mole ratio, the binary fuel/peroxide systems had burning-rates in the following order [194]:

$$Mn/SrO_2 > Mn/BaO_2 > Mo/BaO_2 > Mo/SrO_2.$$

Inclusion of the Fe- and Zn-fuelled systems, which all had greater rates of burning than the Mn- and Mo-fuelled systems, gave the following series of maximum rates of burning:

$$Zn/BaO_2 > Fe/BaO_2 > Zn/SrO_2 > Fe/SrO_2 > Mn/SrO_2$$

Activation energies derived from combustion studies were in the order:

$$Fe/BaO_2 < Zn/SrO_2 < Mn/BaO_2 < Zn/BaO_2 < Mn/SrO_2 \approx Mo/BaO_2 < Mo/SrO_2 < Fe/SrO_2,$$

so these results do not follow the predictions based on cation diffusion. In a trend opposite to the Si/oxidant systems studied by Rugunanan [198], lower activation energies are associated with slower burning-rates in the Mo- and Mn-fuelled systems. Although Mn and Mo appear at the extremes of the above set of Mn/ and Mo/peroxide systems, the suggestion that the properties of the fuels are more important than the properties of the oxidants in the above systems only appears to apply to the specific studies, since the effect of the peroxide can clearly be seen in studies on the Fe- and Zn-fuelled systems. The melting point of Mn (1244°C) is far lower than that of Mo (2610°C), so that Mn is likely to be molten at the combustion temperatures (1350°C to > 1800°C). Similarly, Fe melts at 1535°C, approximately the maximum temperature attained in the Fe/peroxide systems, but Zn melts at 419°C, well below the reaction temperature of Zn/peroxide systems. Examination of the products of combustion showed that oxidation of the metals was generally incomplete, probably because of the formation of protective layers of oxide. Both the temperature and the energy requirements for dissociation are lower for SrO_2 than for BaO_2, so the trends above could be explained on the basis of some preliminary dissociation of the peroxides, followed by metal + $O_2(g)$ → metal oxide. Oxidation of Mn powder, heated alone in $O_2(g)$, began at lower temperatures than for Mo powder

under the same conditions, but oxidation of Mo was complicated by sublimation of product. Fe powder was found to oxidise at temperatures roughly 100°C lower than those of zinc, since the oxidation of zinc was only noticeable above the melting point of 419°C, under controlled heating conditions.

From the above discussion, it may be concluded that fuel/oxidant interactions may fit into one of several patterns lying between the extremes of solid-solid reactions involving diffusion of species derived from the fuel into the structure of the oxidant, oxidation of the fuel by gaseous products of oxidant decomposition, or even liquid-solid or liquid-vapour reactions. Detailed knowledge is needed of the thermal behaviour of the fuel in oxygen and of the structural and thermal characteristics of possible oxidation products, as well as of the thermal stability of the oxidant and any likely decomposition products. The participation of liquid and/or gaseous phases may be difficult to detect, but is of great practical importance.

15.4 Reaction mechanisms:

Although binary pyrotechnic systems are initially solid-solid mixtures, much effort [4,7] has been directed at determining whether the major contribution to the combustion reaction occurs in the condensed phase as a solid-solid, solid-liquid or liquid-liquid reaction, or whether gaseous intermediates are involved. Pyrotechnic delay systems for use in sealed detonator tubes must be essentially gaseous. The Fe/BaO_2 system was identified almost 40 years ago, by Spice and Staveley [4,7], as such a system. In this study, new thermal analysis techniques, including thermomagnetometry (TM) have been used to provide additional information about the system.

Thermomagnetometry (TM) can provide information on the mechanism if the magnetic properties of some of the materials change during the course of reaction. The TG curves for the oxidation of Fe show a final mass gain corresponding to the formation of Fe_2O_3 as expected. TM shows the Curie point of Fe_3O_4 around 580°C. A magnetic event at ~340°C probably arises from the surface formation of some ferromagnetic γ-Fe_2O_3, which converts to paramagnetic α-Fe_2O_3 at about this temperature. TG curves for both Fe/oxidant systems, heated in powder form at 20 °C min^{-1} in N_2, showed superimposition of the oxidation of Fe on the decompositions of the oxidants. DTA traces showed strongly exothermic processes corresponding to ignition. The TM traces showed the same features as that of Fe in air, suggesting that reaction under these conditions is solid-gas with little or no interaction between Fe and the solid oxidants. In some mixtures the presence of unreacted Fe was apparent from the Curie point of Fe at 780°C. Fe/oxidant pellets behaved differently from loose powders, but there was no conclusive evidence for solid-solid reaction mechanisms. Most of the observations could be explained by trapping of the gaseous products of oxidant decomposition within

the pellets.

The physical properties of the SrO_2 particles, including the mean particle size (~ 3 μm vs < 20 μm for BaO_2) resulted in a tendency for these particles to coalesce. This may affect the degree of mixing with fuels during preparation of pyrotechnic mixtures, ultimately affecting the degree of completion of reaction. The differences between the behaviour of BaO_2 and SrO_2 with the same fuel must arise mainly from chemical factors. The decompositions, $SrO_2 \rightarrow SrO + \frac{1}{2}O_2$ and $BaO_2 \rightarrow BaO + \frac{1}{2}O_2$, (Section 7.1) are considerably different so that availability of oxygen for a solid-gas reaction would be different in the two combinations. The role of diffusion of ions in any solid-solid reaction contribution has been discussed above. The degree of wettability of peroxide surfaces by liquid zinc may also play a part in the Zn/peroxide systems.

The Fe/oxidant reactions appear to be more vigorous than $Fe/O_2(g)$. Reasons for this could be: (i) local high pressure pockets of $O_2(g)$ formed by decomposition of the oxidant and trapped within the powder, and/or (ii) some kind of surface process where the partially-oxidised surface of the Fe particles may be activated by reaction with neighbouring oxidant particles or a gaseous species (for example H_2O) generated on heating the oxidant. Water in relatively large amounts inhibits reaction, due to the reactivity of both the fuels and the peroxides with H_2O.

Differences in behaviour of the M/BaO_2 system for M=Fe and M=Zn are to be expected on account of the differences in the melting points (Fe:1535°C, Zn:419°C), and hence in mechanisms of reaction. The oxidation of zinc in air begins immediately upon the fusion of the metal at 420°C. Although the standard boiling point of zinc is 908°C, the vaporisation of zinc occurs readily above 700°C in nitrogen. Reactions of zinc with the solid oxidants, under the controlled heating rate conditions of thermal analysis, all show prior melting of the zinc. Under the uncontrolled conditions of combustion it is probable that reaction involves both molten and gaseous zinc.

Contact between a molten fuel and a solid oxidant will be better than between two solids. The surface tension [161] of liquid zinc (816 mN/m at 440, decreasing to 774 mN/m at 600°C in N_2) may be sufficiently low (compared to 73.1 mN/m of H_2O at 18°C [161]) to allow wetting of surfaces by molten zinc. In ternary Fe,Zn/peroxide systems, wetting of Fe particles by Zn is similar to the hot-dip galvanising process, where Fe is placed in liquid zinc at 440-445°C [199]. In the process, zinc is alloyed with Fe in intermediate layers between Fe and Zn. These alloys are harder than the pure metals and result in Fe being protected sacrificially by the zinc [200]. The formation of Zn^{2+} is favoured relative to the formation of Fe^{2+} or Fe^{3+}, and so reaction of the peroxide with Zn will be complete before the reaction of Fe with the peroxide.

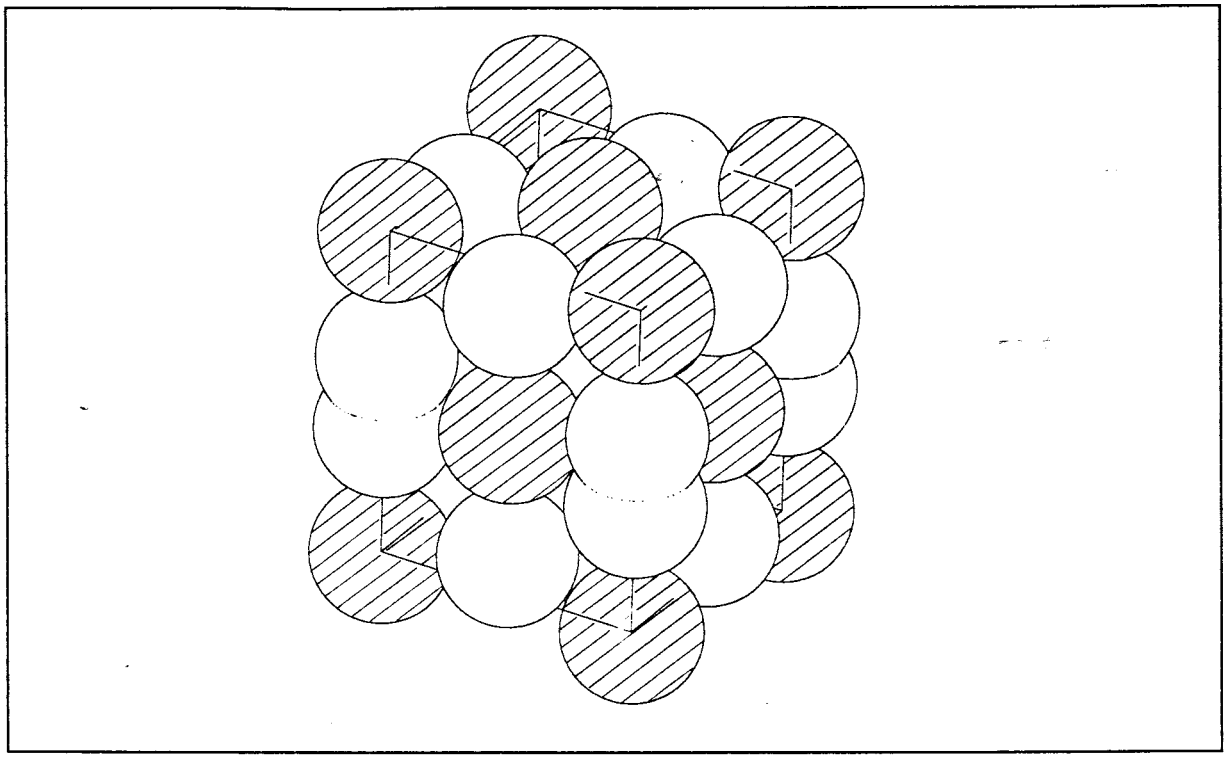

FIGURE 15.3: The BaO_2 structure, showing Ba^{2+} as shaded spheres

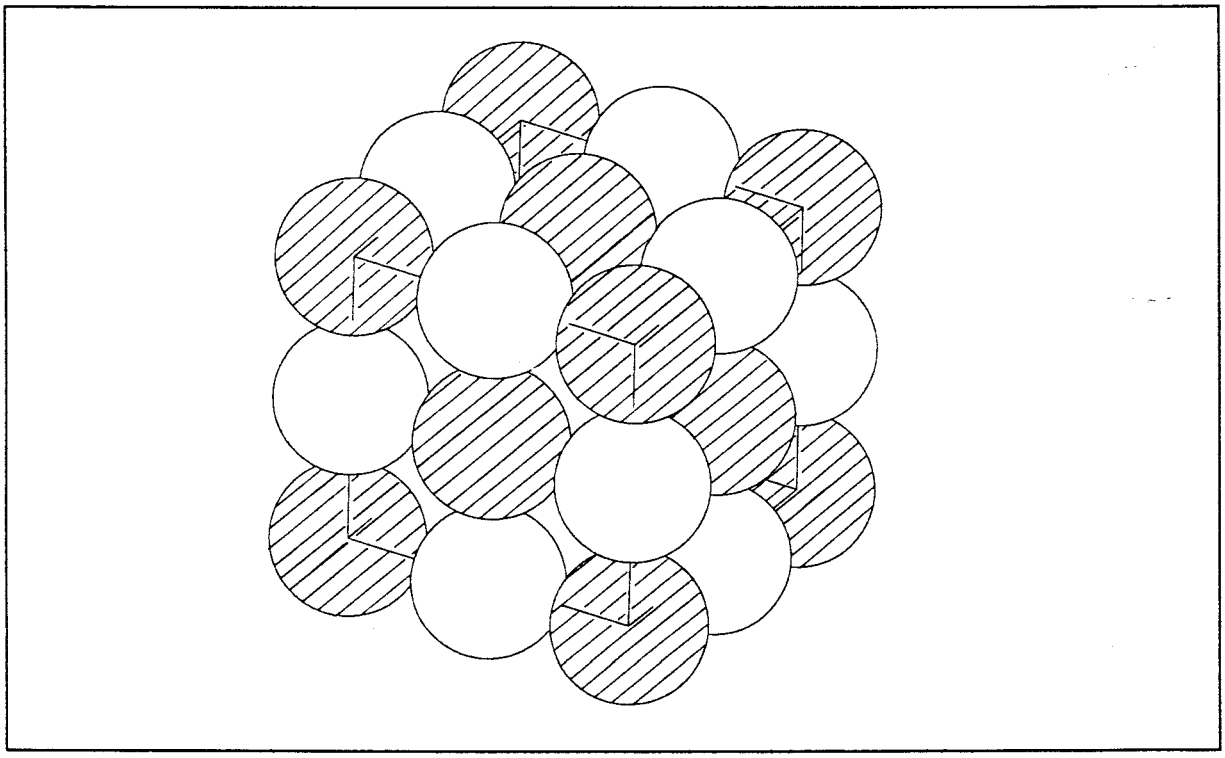

FIGURE 15.4: The BaO structure, showing Ba^{2+} as shaded spheres

Zn(l)/oxidant behaviour [203] is markedly different from Zn(l)/O_2(g) behaviour in that complex exotherms are observed. Pelleting did not have much effect as would be expected when a liquid fuel is formed. Vaporization of zinc is another complicating factor. Mass losses in TG may be made up of

$$BaO_2(s) \rightarrow BaO(s) + \tfrac{1}{2}O_2(g) \quad \text{(i)}$$

and

$$Zn(l) \rightarrow Zn\ (g) \quad \text{(ii)}$$

The DTA of Zn/SrO_2 shows considerable decomposition of SrO_2 before or during oxidation of Zn.

15.5 Combustion:

The characteristics of combustion of the metal/peroxide systems studied [134,194-197,203,204] are summarized in Table 15.3.

Table 15.3: Combustion data of the metal/peroxide pyrotechnic systems

System	Range of compositions/[%]	Range of v/[mm s^{-1}]	U_{ad}/[°C]	E_a/[kJ mol^{-1}]
Mn/BaO_2	15-65 (55 MPa)	2-12 (Max: 20%)	700-1760	16 (20%)
Mo/BaO_2	20-70 (55 MPa)	3-10 (Max: 45%)	860-1710	22 (20%)
Fe/BaO_2	15-50 (55 MPa)	8-39 (Max: 30%)	1050-1500	7-16 (35%)
Zn/BaO_2	15-65 (0 MPa)	4-75 (Max: 45%)	700-1300	7-19 (40%)
Mn/SrO_2	20-80 (55 MPa)	5-12 (Max: 75%)	620-1730	20 (20%)
Mo/SrO_2	40-45 (55 MPa)	2-3 (Max: 40%)	1410-1600	38 (40%)
Fe/SrO_2	20-55 (55 MPa)	4-8 (Max: 40%)	900-1350	20-44 (40%)
Zn/SrO_2	30-80 (0 MPa)	5-25 (Max: 50%)	1100-1500	10-16 (50%)

Of all the binary systems, the Fe/BaO_2 system burned the fastest in the compacted state, while the Zn/BaO_2 system burned most rapidly in the uncompacted state. Lower burning-rates were observed in the corresponding SrO_2 systems. The Zn-fuelled systems should be classified separately on account of their high vapour pressure and susceptibility to compaction.

The maximum excess temperatures recorded for all systems was high at the fuel-rich extremes of the composition range. The E_a values of systems in which combustion was propagated with difficulty are high.

The introduction of small proportions of a second fuel into a binary composition [6,144] generally decreases the burning-rate of the ternary composition until a minimum is reached whereafter the reaction of the second fuel with the oxidant begins to dominate and the burning-rate increases. Since

very few reactions occur in similar temperature ranges, the reaction temperature is either lowered by the presence of the second fuel in the high temperature reaction; or, the presence of the second fuel decreases the effective interparticle contact, as for an inert additive, and affects the low temperature reaction. The oxidants used in this study showed no interaction [195], and hence ternary systems composed of two oxidants were not investigated.

15.6 Kinetic information

Kinetic analysis of the temperature profiles gave low values for the activation energy (<40 kJ mol^{-1}) and such low values are explained [170] in terms of diffusion mechanisms. Diffusion processes have been described above.

Kinetic data may only be determined from relatively simple thermal analysis curves. The thermal analysis curves obtained (using TG, DSC and DTA) were analysed using the Borchardt and Daniels method to obtain the Arrhenius parameters for: the oxidations of Fe and of Zn; the decompositions of BaO_2 and of SrO_2; and the reactions of the pyrotechnic mixtures of Fe/BaO_2, Fe/SrO_2, Zn/BaO_2 and Zn/SrO_2. All mixtures were studied at both the fuel-deficient and fuel-rich extremes of their combustion ranges as established in Sections 9 to 12.

The kinetic parameters determined from temperature profiles (k_{TP}) using the Leeds' approach, along with the values determined from thermal analysis (k_{TA}), are compared in Table 15.4.

Activation energies determined from thermal analysis are presumed to be more representative of the chemical processes occurring and, as found in all such studies, are much higher than the values determined under combustion conditions. As discussed by Boddington and Laye [201], the values obtained from temperature profiles predict unreasonably high rates of reaction at lower temperatures. They thus suggested a more complicated temperature dependence of the rate constant for pyrotechnic reactions (see Appendix 14).

Graphs of the modified rate constant [201]:

$$\frac{1}{k_{TP}} = \frac{1}{k_{TA}} + \frac{1}{BT^m}$$

are shown in Figures 15.5 (Fe/BaO_2) and 15.6 (Fe/SrO_2) and values of the constants B and m are listed in Table 15.4. These values are similar for all the systems considered, except the value of B for the Fe/SrO_2 system.

Table 15.4: Parameters used to calculate the modified rate constants

System	Thermal analysis		Temperature profiles		B	m
	E_a/[kJ mol^{-1}]	A/[s^{-1}]	E_a/[kJ mol^{-1}]	A/[s^{-1}]	[s^{-1} K^{-m}]	[]
20% Fe/BaO_2	132.2	$3.73x10^{7}$	13.8±1.8	165	0.012	1.15
20% Fe/SrO_2	210.0	$88.3x10^{10}$	20.1±2.3	196	$5.4x10^{-4}$	1.53
30% Zn/BaO_2	127.9	$17.5x10^{7}$	16.0±3.5	241	0.016	1.14
30% Zn/SrO_2	302.7	$18.3x10^{19}$	10.8±0.8	96	0.013	1.10
40% Mn/SrO_2 [6]	434.0	$2.0x10^{42}$	13.9±1.5	1379	0.013	1.75

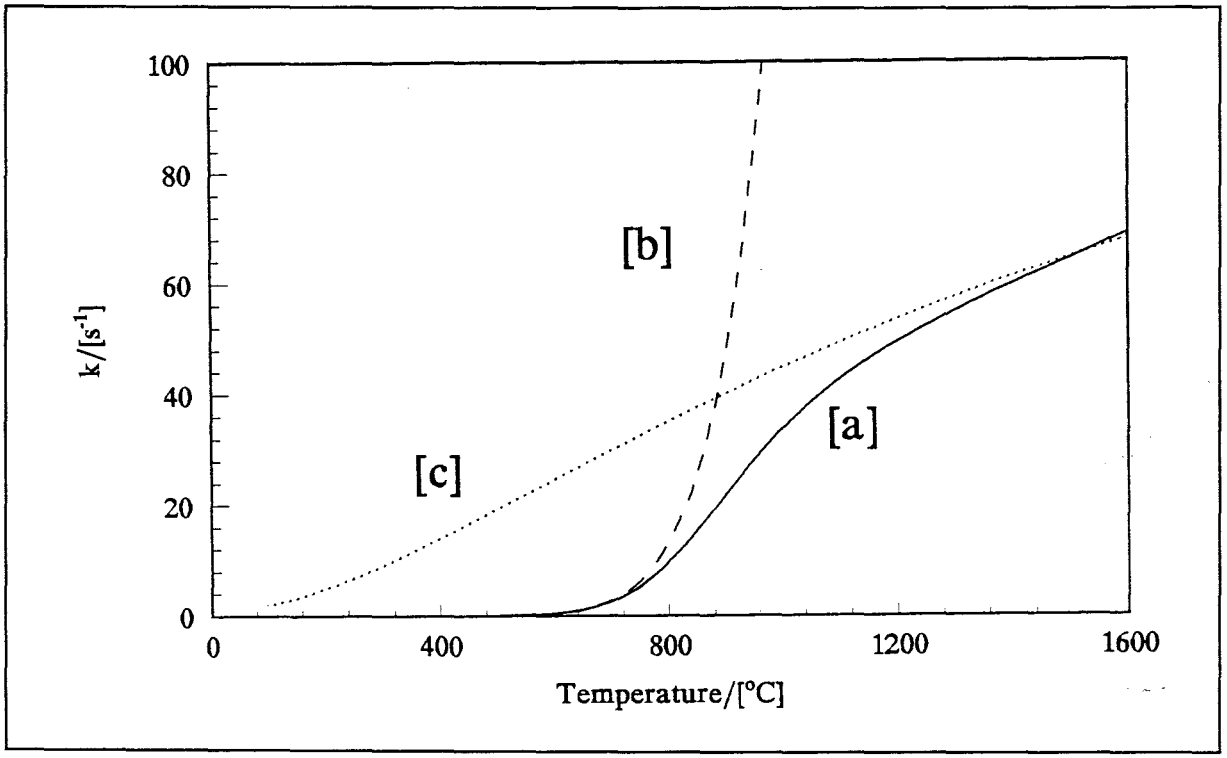

FIGURE 15.5: The modified Leeds equation [a], k_{TA} [b] and k_{TP} [c] for the 20% Fe/BaO_2 system

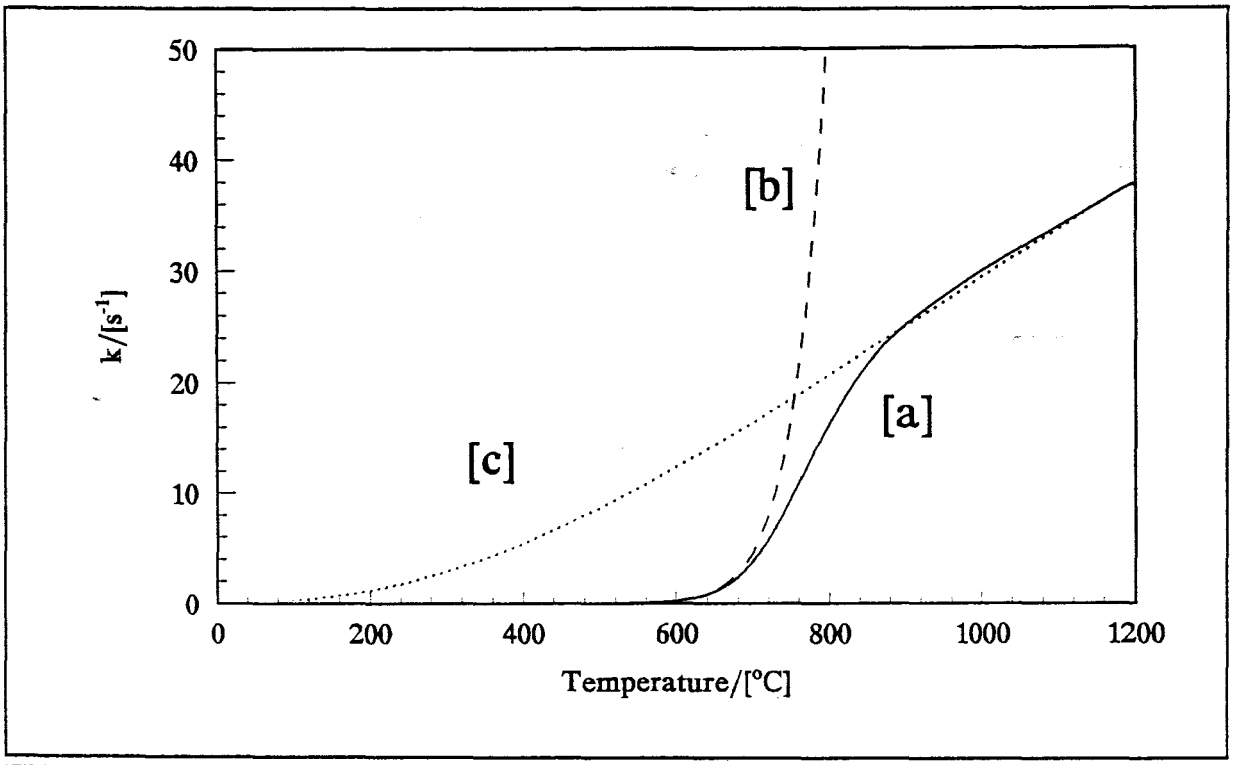

FIGURE 15.6: The modified Leeds equation [a], k_{TA} [b] and k_{TP} [c] for the 20% Fe/SrO_2 system

16. CONCLUSIONS AND SUGGESTIONS FOR FUTURE WORK:

The aim of this and several other recent studies [197,198] has been to examine the thermal behaviour of a series of binary pyrotechnic systems, to identify some of the chemical factors which influence combustion. Even though the fuel/oxidant combinations used in this study were chosen from a chemical perspective, in the hope of obtaining useful mechanistic information on the combustion of pyrotechnic systems, there was also the hope of finding desirable systems for commercial use.

The series which have been examined have had (a) a single fuel (silicon) in a binary combination with a variety of oxidants [198]; and (b) several metal fuels in combination separately with barium peroxide and with strontium peroxide. This study forms part of (b) above and adds two very different fuels, iron and zinc, to the molybdenum and manganese systems studied by Drennan [195-197].

The Zn/BaO_2 and Zn/SrO_2 systems did not burn under compaction and combustion of uncompacted powders was erratic. Zinc liquid (and probably zinc vapour) takes part in the reaction and the gaseous nature of the combustion of uncompacted mixtures gave temperature profiles which were noisy and irreproducible, and burning-rates were unreliable. Even if they have desirable environmental properties, zinc-fuelled pyrotechnic systems are unlikely to prove suitable for delay applications.

Any potential use which the Fe/peroxide systems may have as delay compositions, with burning-rates of from 3-30 mm s^{-1}, is offset by the susceptibility of the oxidants to reaction with water and CO_2 in the atmosphere. Combustion of the Fe/peroxide systems was very susceptible to the presence of added or absorbed water.

An additional aim of this study was to determine whether processes could lead to the formation of useful solid residues. For example, combustion of the iron/peroxide systems could be considered as a self-propagating high-temperature synthesis (SHS) route to the production of ferrites with their useful electronic applications. All the techniques used (SEM, XRD, EPMA) showed, however, the heterogeneity of the solid residues of combustion. Hence, even if SHS was suitable as a first stage in the production of ferrite materials (or other complex oxides), there would still have to be a more conventional treatment involving grinding of the residue, possible adjustment of compositions, and calcining.

Although studies in the field of the pyrotechnic systems have far from exhausted all the possible fuel/oxidant permutations, the existence of truly gasless solid-solid pyrotechnic reactions is uncertain.

The techniques available for the study of pyrotechnic combustion are limited and there is a need for some technique which can provide more direct information on the processes occurring at a fundamental level.

Parallel studies [206] are taking place using finite-element codes, such as TOPAZ, to simulate pyrotechnic combustion. Such studies are very dependent upon the data collected in studies such as those reported in this thesis, for establishment of suitable models, from which predictions to untried systems may eventually be made.

Much of the effort into the use of chemical delays is threatened by the development of totally electronic delay detonators, with their superior performance at much greater expense.

17. REFERENCES:

1. A. Bailey and S. G. Murray, *Explosives, Propellants and Pyrotechnics*, Brassey's Ltd., 1989.
2. J. A. Conkling, *Chemistry of Pyrotechnics*, Marcel Dekker Inc., New York, 1985.
3. J. H. McLain, *Pyrotechnics from the Viewpoint of Solid-State Chemistry*, The Franklin Institute Press, Philadelphia, 1980.
4. J. E. Spice and L. A. K. Staveley, J. Soc. Chem. Ind., 68 (1949) 313.
5. J. Subrahmanyam and M. Vijakumar, J. Mater. Sci., 27 (1992) 6249.
6. R. L. Drennan, *Binary and Ternary Pyrotechnic Systems Containing Manganese, Molybdenum, Barium Peroxide and Strontium Peroxide*, Ph.D. Thesis, Rhodes University, 1991.
7. J. E. Spice and L. A. K. Staveley, J. Soc. Chem. Ind., 68 (1949) 348.
8. R. C. Weast, *Handbook of Chemistry and Physics*, CRC Press, Boston, 64th ed., 1984.
9. R. A. W. Hill, L. E. Sutton, R. B. Temple and A. White, Research, 3 (1950) 877.
10. F. Booth, Trans. Faraday Soc., 49 (1953) 272.
11. V. D. Hogan and S. Gordon, J. Phys. Chem., 61 (1957) 1401.
12. T. J. Barton, N. Williams, E. L. Charsley, J. Rumsey and M. R. Ottaway, 8th Int. Pyrotech. Sem., (1982) 99.
13. S. Nakahara and T. Hikita, J. Ind. Expl. Soc. Japan, 21 (1960) 2.
14. S. Nakahara and T. Hikita, J. Ind. Expl. Soc. Japan, 20 (1959) 356.
15. L. B. Johnson, Ind. Eng. Chem., 52 (1960) 241.
16. S. Yoshinaga, K. Watanabe, M. Matsumoto and T. Nagaishi, Kyushu Sangyo Daigaku Kogakubu Kenkyu Hokoku, 21 (1984) 47.
17. D. Beyens and E. Dubois, 10th Int. Pyrotech. Sem., (1985) 17-1.
18. R. A. W. Hill and A. A. Wallace, Nature, 178 (1956) 692.
19. E. Martinez-Tamayo, A. Beltran-Porter and D. Beltran-Porter, Thermochim. Acta, 91 (1985) 249.
20. E. Martinez-Tamayo, A. Beltran-Porter and D. Beltran-Porter, Thermochim. Acta, 98 (1986) 167.
21. S. Gordon and C. Campbell, Proc. 5th Symp. Comb., Reinhold, New York, (1955) 277.
22. G. Krien, Explosivstof., 13 (1965) 205.
23. S. Nakahara, J. Ind. Expl. Soc. Japan, 22 (1961) 259.
24. D. Nicholls, *Comprehensive Inorganic Chemistry*, Pergamon, London, 1973.
25. D. R. Stull and G. C. Sinke, *Thermodynamic Properties of the Elements*, American Chemical Society, 1956.

26. D. E. Davies, U. R. Evans and J. N. Agar, Proc. Roy. Soc. (London), A225 (1954) 443.

27. N. P. Zhuk and B. V. Linchevskii, Zh. Fiz. Khim., 28 (1954) 440.

28. M. Wyn-Roberts, Trans. Faraday Soc., 57 (1961) 99.

29. E. Karmazsin, P. Satre and P. Vergnon, J. Therm. Anal., 28 (1983) 279.

30. K. H. Hellwege (chief ed.) and A. M. Hellwege, *Numerical Data and Functional Relationships in Science and Technology*, New series III, Springer-Verlag, Berlin, 4a (1970).

31. S. St. J. Warne, H. J. Hurst and W. I. Stuart, Therm. Anal. Abstr. Rev. 6, 17 (1988) 1.

32. A. G. Zhigotskii, S. I. Radoshinskaya and T. M. Shvets, Poroshkovaya Metallurgiya 293(5) (1987) 78.

33. O. Kubaschewski and B. E. Hopkins, *Oxidation of Metals and Alloys*, 2nd ed., Butterworths, Oxford, 1967.

34. A. Rahmel and H. J. Engell, Arch. Eisenhüttenw., 30 (1959) 743.

35. K. Hauffe and B. Ilschner, Z. Elektrochem., 58 (1954) 382.

36. K. Heindlhofer and B. M. Larsen, Trans. Amer. Soc. Steel Treat., 21 (1933) 865.

37. W. W. Smeltzer and D. J. Young, Prog. Solid State Chem., 10 (1975) 17.

38. N. W. Grimes, Phil. Mag., 25 (1972) 67.

39. W. E. Boggs, R. H. Kachik and G. E. Pellissier, J. Electrochem. Soc., 112(6) (1965) 539.

40. N. V. Sidgwick, *Chemical Elements and their Compounds*, Volume II, Clarendon Press, Oxford, 1950.

41. I. Gaballah, C. Gleitzer and J. Aubry, *8th Int. Symp. React. Solids*, Plenum Press, New York, 1977, 391.

42. D. D. Wagman, *Selected Values of Chemical Thermodynamic Properties*, American Chemical Society, 1969.

43. P. K. Gallagher, E.M. Gyorgy and H. E. Bair, J. Chem. Phys., 71 (1979) 830.

44. M. H. Davies, M. T. Simnad and C. E. Birchenall, J. Met., 3 (1951) 889.

45. M. H. Davies, M. T. Simnad and C. E. Birchenall, J. Met., 5 (1953) 125.

46. T. Yamaguchi and T. Kimura, J. Am. Ceram. Soc., 59 (1976) 333.

47. U. Colombo, G. Fagherazzi, F. Gazzarrini, G. Lanzavecchia and G. Sironi, Nature (London), 202 (1964) 175.

48. C. H. Mathewson, *Zinc*, Hafner, New York, 1959.

49. J. K. Stanley, J. Von Hoene and R. T. Huntoon, Trans. Amer. Soc. Metals, 43 (1951) 426.

50. J. Paidassi and D. Fuller, Acta Metall., 4 (1956) 227.

51. J. Paidassi, Acta Metall., 6 (1958) 184.

52. N. Cabrera and N. F. Mott, Rep. Progr. Metal Physics, 12 (1949) 163.

53. P. K. Gallagher and S. St.J. Warne, Thermochim. Acta, 43 (1981) 253.

54. P. K. Gallagher and S. St. J. Warne, Mat. Res. Bull., 16 (1981) 141.

55. E. Karmazsin, P. Satre, M. Romand and B. Durand, Thermochim. Acta, 55 (1982) 287.

56. P. K. Gallagher, E. M. Gyorgy, F. Schrey and F. Hellman, Thermochim. Acta, 121 (1987) 231.

57. H. Watanabe, J. Phys. Soc. Japan, 12 (1957) 515.

58. C. T. Peters, Nature Phys. Sci., 244 (1973) 79.

59. M. W. Rowe, S. M. Lake and R. Fanick, Nature, 266 (1977) 612.

60. R. F. Barrow, P. G. Dodsworth, A. R. Downie, E. A. N. S. Jeffries, A. C. P. Pugh, F. J. Smith and J. M. Swinstead, Trans. Faraday Soc., 51 (1955) 1354.

61. M. E. Derevyaga, L. N. Stesik and E. A. Fedorin, Fizika Goreniya i Vrzryva, 13(6) (1977) 852.

62. J. O. Cope, Trans. Faraday Soc., 57 (1961) 493.

63. H. G. Von Schnering and R. Hoppe, Z. Anorg. Allg. Chem., 312 (1961) 87.

64. U. Spitsbergen, Acta Cryst., 13 (1960) 197.

65. H. G. Von Schnering, R. Hoppe and J. Zemann, Z. Anorg. Allg. Chem., 305 (1960) 241.

66. B. J. Aylett, *Comprehensive Inorganic Chemistry*, Pergamon, London, 1973.

67. U. R. Evans, Electrochem. Soc. Trans., 83 (1943) 337.

68. C. D. S. Tuck, M. E. Whitehead and R. E. Smallman, Corrosion Sci., 21 (1981) 333.

69. W. J. Moore and J. K. Lee, Trans. Faraday Soc., 47 (1951) 501.

70. D. G. Thomas, J. Phys. Chem. Solids, 3 (1957) 229.

71. N. V. Parish, *The Metallic Elements*, Longman, London, 1977.

72. V. Averbuh and G. Chufarov, Zh. Obsthei Khimii, 21 (1951) 626.

73. S. Makarov and M. Grigorieva, Isv. AN USSR, 7 (1959) 1168.

74. M. Tzentnershver and M. Blumenthal, Bull. Inorg. Acad. Pol., Series A (1935) 540.

75. Y. Azuma, M. Mizuide and K. Suehiro, Gyp. Lim., 162 (1979) 175.

76. S. Tamaru and K. Shiomi, Z. Phys. Chem., A171 (1935) 221.

77. S. Tamaru and K. Shiomi, Z. Phys. Chem., A171 (1935) 229.

78. V. Dolgov and A. Basharin, Vesti AN BSSR, 2 (1978) 10.

79. J. A. Hedvall, Z. Anorg. Allg. Chem., 104 (1918) 163.

80. M. Blumenthal, Roczniki Chem., 13 (1933) 5.

81. M. Blumenthal, J. Chem. Phys., 31 (1934) 489.

82. V. Osika, V. Annopolskii and V. Karpenko, Tr. NIPI Osnov. Khimii, 51 (1979) 17.

83. Y. Pelovsky, V. Raynova, I. Gruncharov and I. Dombalov, J. Therm. Anal., 37 (1991) 841.

84. M. Blumenthal, Roczniki Chem., 14 (1934) 598.

85. I. I. Volnov, Doklady Akad. Nauk SSSR, 94 (1954) 477.

86. I. I. Volnov, Zh. Neorg. Khim., 3 (1958) 402.

87. H. G. Wiedemann and G. Bayer, Proc. 1st Europ. Symp. on Therm. Anal., (1976) 295.

88. M. A. Fahim and J. D. Ford, J. Chem. Eng., 27 (1983) 21.

89. L. Till, J. Therm. Anal., 3 (1971) 177.

90. A. F. Mayorova, S. N. Mudretsova, M. N. Mamontov, P. A. Levashov and A. D. Rusin, Thermochim. Acta, 217 (1993) 241.

91. V. J. Brunere and A. N. Dokuchaeva, Iz. Akad. Nauk. Latvijskoj SSR, Serija Chimiceskaja, 3 (1990) 332.

92. J. B. Holt and S. D. Dunmead, Ann. Rev. Mater. Sci., 21 (1991) 305.

93. W. L. Frankhouser, K. W. Brendley, M. C. Kieszek and S. J. Sullivan, *Gasless Combustion Synthesis of Refractory Compounds*, Noyes Publications, New Jersey, 1985.

94. A. M. Kanury, AIChE Symp. Heat Transfer, Houston, 84 (1988) 44.

95. E. A. Nekrasov, Y. M. Maksimov, M. K. Ziatdilov and A. S. Shteinberg, Dokl. Phys. Chem., 14 (1978) 575.

96. T. S. Azatyan, V. M. Maltsev, A. G. Merzhanov and V. A. Seleznev, Dokl. Phys. Chem., 13 (1977) 156.

97. T. Kottke, L.J. Kecskes and A. Niiler, Report 3793, Ballistic Research Laboratory, Maryland, USA, (1989).

98. A. G. Merzhanov, Archivum Combustionis, 1 (1981) 23.

99. T. Boddington, A. Cottrell and P. G. Laye, 11th Int. Pyro. Sem., Vail, Colorado, (1986) 419.

100. G. J. Rees, Fuel, 52 (1973) 138.

101. Z. A. Munir and J. B. Holt (ed.), *Combustion and Plasma Synthesis of High-Temperature Materials*, VCH Publishers, New York, 1990.

102. A. P. Hardt, P. V. Phung and F. J. Valenta, 5th Int. Pyrotech. Sem., Denver, Colorado, (1976) 223.

103. I. G. Kokarovtseva, I. N. Belyaev and L. V. Semenyakova, Russ. Chem. Rev., 41(11) (1972) 929.

104. JCPDS International Centre for Diffraction Data, *Powder Diffraction File*, Swarthmore, Philadelphia, 1989.

105. H. J. Van Hook, J. Phys. Chem., 68 (1964) 3786.

106. S. W. Derbyshire, A. C. Fraker and H. H. Stadelmaier, Acta Cryst., 14 (1961) 1293.

107. R. W. G. Wyckoff, *Crystal Structures*, Volume II, Interscience, 1960.

108. J. Beretka and M. J. Ridge, J. Chem. Soc., A3 (1968) 2463.

109. J. Beretka, M. J. Ridge and T. Brown, Trans. Faraday Soc., 67 (1971) 1453.

110. J. Beretka and M. J. Ridge, Aust. J. Chem., 26 (1973) 1353.

111. M. Erchak, I. Fankuchen and R. Ward, J. Am. Chem. Soc., 68 (1946) 2085.

112. H. Stäblein and J. Willbrand, 7th Symposium Reactivity of Solids, Chapman and Hall, London, (1972) 589.

113. E. Martinez, E. Sanchez-Viches, A. Beltran-Porter and D. Beltran-Porter, Mat. Res. Bull, 21 (1986) 511.

114. Y. Pelovski, V. Petkova, I. Dombalov and I. Gruncharov, J. Therm. Anal., 36 (1990) 1727.

115. G. H. Jonker, H. P. J. Wijn and P. B. Braun, Philips Tech. Rev., 18 (1956) 145.

116. E. Lucchini, S. Meriani, F. Delben and S. Paoletti, J.Mater. Sci., 19 (1984) 121.

117. S. Kulkarni, J. J. Shrotri, C. E. Deshpande and S. K. Date, J. Mater. Sci., 24 (1989) 3739.

118. J. Beretka and T. Brown, Austral. J. Chem., 24 (1971) 237.

119. A. Tawfik and M. M. Barakat, J. Mater. Sci., 7 (1988) 1098.

120. J. B. MacChesney, R,C. Sherwood and J. F. Potter, J. Chem. Phys., 43 (1965) 1907.

121. S. D. Kulkarni, C. E. Deshpande, J. J. Shrotri, V. G. Gunjikar and S. K. Date, Thermochim. Acta, 153 (1989) 47.

122. B. C. Tofield, 8th Symp. Reactivity of Solids, Plenum, New York, (1976) 253.

123. A. C. Fraker, J. Phys. Chem., 69 (1965) 4395.

124. J. L. Snoek, Physica, 3 (1936) 463.

125. K. R. Krishnamurthy, B. Viswanathan and M. V. C. Sastri, Indian J. Chem., 15A (1977) 205.

126. M. Erchak and R. Ward, J. Am. Chem. Soc., 68 (1946) 2093.

127. D. E. Speliotis, IEEE Trans. Magnet., 28 (1992) 2394.

128. H. J. Masterson, J. G. Lunney, J. M. D. Coey, R. Atkinson, I. W. Salter and P. Papakonstantinou, J. Appl. Phys., 73 (1993) 3917.

129. C. M. van der Burgt, Electronic Tech., 37 (1960) 330.

130. R. Klein, M. Menster, G. von Elbe and B. Lewis, J. Phys. Chem., 54 (1950) 877.

131. T. Boddington, P. G. Laye, J. R. G. Pude and J. Tipping, Comb. Flame, 47 (1982) 235.

132. T. Boddington, P. G. Laye, J. Tipping and D. Whalley, Comb. Flame, 63 (1986) 359.

133. M. W. Beck, ICI progress report, Ardeer, Scotland, 1989.

134. M. E. Brown, M. J. Tribelhorn and M. G. Blenkinsop, J. Therm. Anal., 40 (1993) 1123.

135. S. St. J. Warne and P. K. Gallagher, Thermochim. Acta, 110 (1987) 269.

136. J. V. Smith (ed.), *X-ray Powder Data File*, ASTM Publication 48-J, Philadelphia, 1960.

137. J. D. H. Donnay (ed.), *Crystal Data Determinative Tables*, 2nd ed., Amer. Cryst. Assoc. Monograph 5, 1963.

138. S. Motherwell, Pluto 78 User Manual, University of Cambridge Press, Cambridge, 1978.

139. User support services: University of Cape Town, *Introduction to Vax/VMS*, Cape Town, RSA, 1988.

140. C. M. Wilson, G. C. Bye, C. R. Howard, J. H. Sharp, D. M. Tinsley and S. A. Wentworth-Rossi, 7th Int. Symp. React. Solids, Chapman and Hall, London, (1972) 598.

141. T. Hahn, *International Tables for Crystallography*, Reidel Publ., USA, A (1983).

142. R. A. W. Hill and T. L. Cottrell, 4th Symp. on Comb., Baltimore, (1953) 349.

143. M. W. Beck, *Intersolid Combustion Reactions in Pyrotechnic Systems*, Ph.D. Thesis, Rhodes University, 1984.

144. R. A. Rugunanan, *Intersolid Pyrotechnic Reactions of Silicon*, PhD Thesis, Rhodes University, Grahamstown, 1991.

145. R. L. Powell, W. J. Hall, C. H. Hyink and L. L. Sparks, *Thermocouple Reference Tables Based on the IPTS-68*, Omega Press, Washington, (1975) 219.

146. A. Savitsky and M. J. E. Golay, Anal. Chem., 36 (1964) 1627.

147. P. A. Gorry, Anal. Chem., 62 (1990) 570.

148. K. Ebert, H. Ederer and T. L. Isenhour, *Computer Applications in Chemistry*, VCH Verlag, Weinheim, (1989) 337.

149. J. Steinier, Y. Termonia and J. Deltour, Anal. Chem., 44 (1972) 1906.

150. W. J. Dixon (ed.), *BMDP Statistical Software Manual*, University of California Press, Berkeley, 2 (1985) 843.

151. H. E. Kissinger, Anal. Chem., 29 (1957) 1702.

152. M. Selvaratnam and P. D. Garn, J. Am. Ceram. Soc., 59 (1976) 376.

153. J. A. Augis and J. E. Bennet, J. Therm. Anal., 13 (1978) 283.

154. N. Sbirrazzuoli, D. Brunel and L. Elegant, J. Therm. Anal., 38 (1992) 1509.

155. G. M. Kerch and L. A. Irgne, J. Therm. Anal., 36 (1990) 129.

156. A. V. Khabenko and S. A. Dolmatov, J. Therm. Anal., 36 (1990) 45.

157. C. Rozycki and M. Maciezewski, Thermochim. Acta, 91 (1985) 91.

158. J. M. Criado and J. Morales, Thermochim. Acta, 16 (1976) 382.

159. H. J. Borchardt and F. Daniels, J. Am. Chem. Soc., 79 (1957) 41.

160. Y. S. Yang and L. J. Lee, Calorim. Anal. Therm., 19 (1988) 3-1.

161. D. R. Lide (ed.), *Handbook of Chemistry and Physics*, 72nd ed., CRC Press Inc., Boston, U.S.A., 1991.

162. O. Kubaschewski, E. L. I. Evans and C. B. Alcock, *Metallurgical Thermochemistry*, Pergamon, Oxford, 1967.

163. M. E. Brown and R. L. Drennan, 14th Int. Pyrotech. Sem., (1989) 423.

164. A. Dokuchaeva, Latv. Khim. Z., 1 (1991) 32.

165. A. Dokuchaeva, Latv. Khim. Z., 1 (1991) 37.

166. U.S. Pat. 3.812.048/21.05.1974

167. U.S. Pat. 3.310.381/21.03.1967

168. J. Hedvall and N. Zweigbergk, Z. Anorg. Allgem. Chem., 108 (1919) 119.

169. B. J. Erofeev and N. D. Sokolova, *Topokinetic Equation Tables*, Akad. Nauk. BSSR, Minsk, (1963) 3.

170. M. E. Brown, D. Dollimore and A. K. Galwey, *Comprehensive Chemical Kinetics: Volume 22: Reactions in the Solid State*, Elsevier, Amsterdam, (1980).

171. G. M. Habashy and G. A. Kolta, J. Inorg. Nucl. Chem., 34 (1972) 57.

172. K. H. Stern and E. L. Weise (ed), *High Temperature Properties and Decomposition of Inorganic Salts*, Government Printing Unit, Washington, 2 (1969) 12.

173. W. L. Wanmaker and D. Radielovic, 5th Int. Symp. Reactivity Solids, Plenum, New York, (1964) 529.

174. R. Furuichi, T. Ishii, Z. Yamanaka and M. Shimokawabe, Thermochim. Acta, 51 (1981) 245.

175. J. J. Gilman, *Inventivity*, Van Nostrand Reinholdt, New York, (1992) 116.

176. D. Kunii and J. M. Smith, J. Am. Inst. Chem. Eng., 6 (1969) 71.

177. E.G. Brame, J.C. Margrave and V.W. Meloche, J. Inorg. Nucl. Chem., 5 (1957) 48.

178. B.S. Ault and L. Andrews, J. Chem. Phys., 62 (1975) 2312.

179. R. D. Waldron, Phys. Rev. 2nd series, 99 (1955) 1727.

180. K. Nakamoto, *IR Spectra of Inorganic and Coordination Compounds*, Wiley, USA, 1970.

181. W. Parrish (ed.), *Advances in X-ray Diffractometry and X-ray Spectrography*, Centrex, Eindhoven, (1962) 103.

182. Y. Hao and T. Tanaka, Canad. J. Chem. Eng., 66 (1988) 761.

183. Y. Hao and T. Tanaka, Solid State Ionics, 38 (1990) 213.

184. M. E. Brown, in preparation.

185. L. W. Finger and R. M. Hazen, J. Appl. Phys., 51 (1980) 5362.

186. A. F. Wells, *Structural Inorganic Chemistry*, Oxford Press, Oxford, 1962.

187. H. Mitsuda, S. Mori and C. Okazaki, Acta. Cryst., B27 (1971) 1263.

188. S. Meriani, Acta Cryst., B28 (1972) 1241.

189. S. C. Abrahams and B. A. Calhoun, Acta. Cryst., 6 (1953) 105.

190. F. Donald Bloss, *Crystallography and Crystal Structure - An Introduction*, Holt Inc., New York, (1971) 230.

191. G. P. Mohanty and L. V. Azaroff, J. Chem. Phys., 35 (1961) 1268.

192. J. D. Bernal, E. Diatlowa, J. Kasarnowsky, S. Reichstein and A. G. Ward, Z. Krist., 90A (1935) 374.

193. J. D. Bernal, E. D'yatlova, J. Kasarnovskii, S. Raikhstein and A. G. Ward, Z. Krist., 92 (1935) 344.

194. M. E. Brown, M. W. Beck, R. L. Drennan, R. A. Rugunanan, M. J. Tribelhorn and M. G. Blenkinsop, Proc. 4th Int. Symp. Expl. Tech. and Ballistics, Pretoria, (1992) 391.

195. R. L. Drennan and M. E. Brown, Thermochim. Acta, 208 (1992) 201.

196. R. L. Drennan and M. E. Brown, Thermochim. Acta, 208 (1992) 223.

197. R. L. Drennan and M. E. Brown, Thermochim. Acta, 208 (1992) 247.

198. R. A. Rugunanan and M. E. Brown, Combust. Sci. and Tech., 20 (1993) 1.

199. R. J. McKay and R. Worthington, *Corrosion Resistance of Metals and Alloys*, ACS Monograph Series, Reinhold Publishing, New York, (1937) 157.

200. L. L. Shreir (ed.), *Corrosion: Volume 2: Corrosion Control*, Newnes-Butterworths, London, (1976) 14:36.

201. T. Boddington, A. Cottrell and P. G. Laye, Combustion and Flame, 79 (1990) 234.

202. P. G. Laye and E. L. Charsley, Thermochim. Acta, 120 (1987) 325.

203. M. J. Tribelhorn, D. S. Venables and M. E. Brown, in preparation.

204. M. J. Tribelhorn, D. S. Venables and M. E. Brown, in preparation.

205. A. de La Croix, MSc Thesis, Rhodes University, in preparation.

206. S. J. Taylor, PhD Thesis, Rhodes University, in preparation.

18. APPENDICES:

APPENDIX 1: Optimisation of kinetic parameters:

Three columns of data, G_{exp}, 1-α and 1/T were extracted from the worksheet and printed as an unformatted data file to disk.

Outline of procedure using the SunOS UNIX system:

The "filename.prn" files, containing three columns of data (G_{exp}, 1-α and 1/T), were placed in the local directory of the PC, prior to network linking. The KERMIT 3.1 communications package was used to connect to the Microvax 3100 midi-computer (Digital Electronics, operating in VMS format), which in turn was linked via a LAN to the SunOS UNIX system (no direct link to the Sun was available). Stage one of the file transfer was to the Vax via the KERMIT system (both on the local server and remote server, MS-KERMIT and KERMIT-32), followed by logging on to the Sun system and FTP transfer (ascii mode) of the files from the Vax to the Sun. On the Sun (Hippo), files were moved/renamed to chmb1 prior to processing, whereafter the linear BMDP analysis was carried out by typing BMDP <enter>, followed by "1R" when prompted for the program to run; "BROWN" when prompted for the instruction language file; and "fnameout" when prompted for an output file. On program termination, the output file was viewed/edited using the "vi" editor, and the relevant output used in the "BROWN3R" programme (also edited using the vi editor). When this information had been entered in the listing and the file saved, the non-linear optimisation program was run by typing BMDP and entering "3R" as the program and "BROWN3R" as the instruction language file. Again an output file was selected, which was viewed to determine the optimised non-linear parameters.

The instruction language files Brown and Brown3r, being the linear and non-linear routines, respectively, are listed overleaf.

Instruction language file "BROWN":

```
/PROBLEM        TITLE IS 'OPTIMISING A, B, & N  - LINEAR MODEL'.
/INPUT          FILE = chmb1.
                VARIABLES ARE 3.
                FORMAT IS FREE.
/VARIABLES      NAMES ARE Y,X,Z.
/TRANSFORM      TY=LN(Y).  TX=LN(X).
                W=(EXP(4.25935))*(X**0.5621)*(EXP(-1613.7773*Z)).
Comment:  This line (↑) holds ln a, n and b, respectively, when the program is terminated.
/REGRESS        DEPENDENT=TY.
                INDEPENDENT=TX,Z.
/PRINT          DATA.
/REGRESS        DEPENDENT=Y.
                INDEPENDENT=W.
                TYPE = ZERO.
/END
```

Instruction language file "BROWN3R":

```
/PROBLEM        TITLE IS 'OPTIMISING A, B, & N'.
/INPUT          FILE = chmb1.
                VARIABLES ARE 3.
                FORMAT IS FREE.
/VARIABLES      NAMES ARE Y,X,Z.
/REGRESS        DEPENDENT=Y.
                PARAMETERS=3.
/PARAM          INITIALS ARE 150.6553,0.4506,1698.2
Comment:  This line (↑) holds a, n and b, respectively, when the program is terminated.
/FUN            F=P1*(X**P2)*EXP(P3*(-1.0*Z)).
/END
```

APPENDIX 2: Programs used:

A) Profile.pas was used to capture temperature profiles via a PC-26 A-to-D card.

```
PROGRAM PROFILE;

uses dos,crt,general,inter,turbo3,graph, ghutils,
    globals,plot_graph,collect_,file_, init_sys;

{ ********************************************************************************* }
{ *                                                                               * }
{ *  Tempe ature Profile software written in TURBO PASCAL V3.1                    * }
{ *  for the PC-26 A/D card for the IBM-PC and Compatibles.                       * }
{ *                                                                               * }
{ *  The PC-26 card must be set to 0v to +10v mono-polar,                         * }
{ *  with a base-address of $700 (Hex) !                                          * }
{ *                                                                               * }
{ *  Created by Barry Guthrie, RHODES UNIVERSITY, January 1988.                   * }
{ *  Some original code by Mattias H. Popp, April 1986.                           * }
{ *                                                                               * }
{ *  Modified by David Williams RHODES UNIVERSITY December 1989                   * }
{ *       - proposed modifiation = accept the first 256                           * }
{ *          points prior to the burn                                             * }
{ *                                                                               * }
{ ********************************************************************************* }

BEGIN
  for count := 0 to 30720 do
    values[count] := 0;
  GetDir(0,Help_drive);  (* drive containing program disk *)
  key := '0';
  Sample_No := 0;
  Text_Normal;
  Define_System;
  WHILE NOT (key = 'E') DO
  BEGIN
    MARK (heap_top);
    Process_Data;
    RELEASE (heap_top);
  END;
  CLRSCR;
  ChDir(Help_drive);  (* drive containing program disk *)
END.
```

B) Twinold.pas was used to capture two separate temperature profiles in succession, and was based on a routine written previously [184] for this purpose.

```
PROGRAM FAST;
 {This program rapidly monitors two sequential thermocouple outputs      }
 {M W Beck ICI EGTC, slightly modified for faster CPU's by M J Tribelhorn}
 {RU Chemistry Department, 1993...  }

  TYPE
    range=array[0..5000] of integer;
    names=string[15];
  VAR
    time1,time3,interval: real;
    filename:names;
    record_length,level,rate1,rate2,start_1,start_2,datalength,datalength2,
    flag,exitval,channel,i: integer;
    volt1,volt2,voltm: range;
    reply: char;
{*************************************************************************}
 PROCEDURE BEEP;

   begin
     sound(500);
     delay(200);
     nosound;
   end;
{*************************************************************************}

  FUNCTION ADSAMPLE (channel:integer):integer;

  { Function reads the A/D channel specified }
   var i:integer;
   begin
     port[$702]:=(channel shl 4)+2;
     port[$702]:=(channel shl 4)+3;
     for i:=1 to 26 do
       begin          { loop until end of conversion }
       end;
     ADSAMPLE:=((port[$701] and $0f) shl 8)+port[$700];
   end;

{*************************************************************************}


PROCEDURE FASTSAMPLE (var record_length,level,channel,exitval,datalength:integer;
                      var interval:real;
                      var voltm: range );
  VAR
    j,k,i: Integer;
  begin
    exitval:= -2;
    k:=-1;interval:=0;
    for j:=0 to datalength do voltm[j]:=0;
      repeat
        k:=(k+1) mod datalength;
        interval:=interval+1;
        PORT[$702]:=(channel SHL 4) + 2;
        PORT[$702]:=(channel SHL 4) + 3;
        for j:=0 to 96 do
          begin                 { loop until end of conversion }
```

```
        end;
      voltm[k]:=((PORT[$701] and $0F) SHL 8) + PORT[$700];
      if (voltm[k]>level) and (exitval=-2) then
        begin
          exitval:=(k+record_length) mod datalength;
        end
    until k=exitval;
end;

{*************************************************************************}


PROCEDURE SLOWSAMPLE (channel,datalength2:integer;var voltm: range);

  VAR  j,k: Integer;
  begin
    for j:=0 to (datalength2-1) do voltm[j]:=0;
    gotoxy(28,24);write('recording...');
     for j:=0 to (datalength2-1) do
       begin
         delay(50);
         PORT[$702]:=(channel SHL 4) + 2;
         PORT[$702]:=(channel SHL 4) + 3;
         for k:=0 to 480 do
           begin
           end;
         voltm[j]:=((PORT[$701] and $0F) SHL 8) + PORT[$700];
       end;
    writeln(' ');
  end;
{*************************************************************************}

PROCEDURE TEMP_CONVERT(start_1,datalength:integer;var volt1:range);

    { procedure to convert A/D data into temperature*10 values }
  var
    i:integer;
    temp:real;
  begin
    i:=start_1;
    repeat
      i:=((i+1) mod datalength);
      temp:=(volt1[i]/(409.5*400))*1000;
      temp:=10.637+134.172*temp-5.1291*temp*temp+0.23513*temp*temp*temp
       -0.00412027*temp*temp*temp*temp;
      volt1[i]:=ROUND(temp*10);
    until i=start_1;
  end;
{*************************************************************************}

PROCEDURE FILED (filename:names;time1,interval:real;
                 start_1,datalength:integer;volt1:range);

  { procedure for writing captured data to a file }

  VAR i:integer;
      filvar:text;

   begin
      filename:='a:'+ filename +'.dat';
      assign(filvar,filename);
      rewrite(filvar);
      writeln(filvar,interval:7:1);
```

```
      writeln(filvar,time1*1000:12:5);
       i:=start_1;
       repeat
         i:=((i+1) mod datalength);
         writeln(filvar,(volt1[i]/10):5:1);
       until i=start_1;
      close(filvar);
   end;
{*************************************************************************}

 PROCEDURE VALUES(level,record_length,datalength,datalength2,flag:integer;
                  time1,time3:real);
    var volt:range;
    begin
      volt[0]:=level;
      TEMP_CONVERT(0,1,volt);
      volt[0]:=ROUND(volt[0]/10);
      gotoxy(41,10);write(level:4,'      ',volt[0]:4,' oC');
      gotoxy(41,12);write(datalength:4,round(datalength*time1*1000):9,' ms');
      gotoxy(41,14);write(datalength2:4,round(datalength2*time3):9,' s');
      gotoxy(41,16);write(datalength-record_length-1:4);
      gotoxy(44,18);writeln(flag);
    end;
{*************************************************************************}

 PROCEDURE STORE_VALUES(level,record_length,datalength,datalength2,flag:integer);

   var filvar:text;
   begin
     assign(filvar,'TEMPOLD.VAL');
     rewrite(filvar);
     writeln(filvar,level);
     writeln(filvar,record_length);
     writeln(filvar,datalength);
     writeln(filvar,datalength2);
     writeln(filvar,flag);
     close(filvar);
   end;
{*************************************************************************}

 PROCEDURE ALTER_VALUES(var level,record_length,datalength,datalength2
                        ,flag:integer);
  var number,result:integer;
      reply:char;
      value:string[4];
      volt:range;
  label mark;
  begin
    mark:gotoxy(1,24);writeln('                                                  ');
    gotoxy(1,24);write('Enter trigger level (0 - 2900) ');
    number:=level;read(value);
    VAL(value,number,result);
    if result=0 then
       begin
         if (number<2901) and (number>-1) then level:=number;
         volt[0]:=level;
         TEMP_CONVERT(0,1,volt);
         volt[0]:=ROUND(volt[0]/10);
         gotoxy(41,10);writeln(level:4,'      ',volt[0]:4);
       end;
    gotoxy(1,24);write('Enter number of datapoints {fast} (100 - 5000) ');
    number:=datalength;read(value);
    VAL(value,number,result);
```

```
    if result=0 then
       begin
         if (number<5001) and (number>100) then datalength:=number;
         gotoxy(41,12);writeln(datalength:4,round(datalength*time1*1000):9);
       end;
    gotoxy(1,24);write('  Enter number of datapoints  {slow}  ( Max 5000 ) ');
    number:=datalength2;read(value);
    VAL(value,number,result);
    if result=0 then
       begin
         if (number<5001) and (number>0) then datalength2:=number;
         gotoxy(41,14);writeln(datalength2:4,round(datalength2*time3):9);
       end;
    gotoxy(1,24);writeln('                                                    ');
    gotoxy(1,24);write('Enter number of pre-trigger data points (< ',datalength,' ) ');
    number:=(datalength-record_length-1);read(value);
    VAL(value,number,result);
    if result=0 then
       begin
         if (number<datalength) and (number>=0) then record_length:=datalength-number-1;
         if record_length+1 > datalength then record_length:=datalength-1;
         gotoxy(41,16);writeln(datalength-record_length-1:4);
       end;
    gotoxy(1,24);writeln('                                                    ');
    gotoxy(1,24);write('Enter number of thermocouples (1 or 2 ) ');
    number:=2;read(value);
    VAL(value,number,result);
    if result=0 then
        begin
          if (number=1) or (number=2) then flag:=number;
          gotoxy(44,18);writeln(flag);
        end;
    gotoxy(1,24);write(' Press ESCAPE to alter values or RETURN to continue...');
    repeat until keypressed;
    read(kbd,reply);
    writeln(' ');
    if reply=#27 then goto mark;
    gotoxy(1,24);writeln('                                                    ');
    gotoxy(1,24);write(' Save these values as defaults? ');
    repeat until keypressed;
    read(kbd,reply);
    writeln(' ');
    if (reply='Y') or (reply='y') then
      STORE_VALUES(level,record_length,datalength,datalength2,flag);
  end;
{*********************************************************************}

  PROCEDURE DISPLAY(var rate1,rate2,record_length,level,datalength,
                    datalength2,flag:integer;time1,time3:real);
 var
    reply:char;
    filvar:text;
 begin
   assign(filvar,'TEMPOLD.VAL');
   reset(filvar);
   read(filvar,level);
   read(filvar,record_length);
   read(filvar,datalength);
   read(filvar,datalength2);
   read(filvar,flag);
   close(filvar);
   ClrScr;
   writeln(' ************************************************************************');
```

```
  gotoxy(13,4);
  writeln('     THERMOCOUPLE DATA COLLECTION ROUTINE ');
  gotoxy(1,7);
  writeln(' ************************************************************************');
  gotoxy(1,10);
  writeln('   Trigger level ');writeln(' ');
  writeln('   No. of data points  {Fast}');writeln(' ');
  writeln('   No. of data points  {Slow}');writeln(' ');
  writeln('   No. of pre-trigger data points');writeln(' ');
  writeln('   No. of thermocouples ');writeln(' ');
  writeln('   Sample rate {Fast} (Hz)              ',rate1);writeln(' ');
  writeln('   Sample rate {Slow} (Hz)               ',rate2);
  VALUES(level,record_length,datalength,datalength2,flag,time1,time3);
  writeln(' ');writeln(' ');
  writeln(' ');writeln(' ');writeln(' ');
  write(' Press ESCAPE to alter values or RETURN to continue... ');
  repeat until keypressed;
  read(kbd,reply);
  writeln(' ');
  if (reply=#27) then ALTER_VALUES(level,record_length,datalength,datalength2,flag);
end;
{*********************************************************************}

          {            main program            }

begin
  PORT[$703]:=$92;
  channel:=0;
  rate1:= 5000; { oscilloscope 1 kHz }
  rate2:= 375;  { oscilloscope 100 Hz }
  time1:=1/rate1;
  time3:=1/rate2;
  DISPLAY(rate1,rate2,record_length,level,datalength,datalength2,flag,time1,time3);
  gotoxy(1,24);writeln('                                                    ');
  gotoxy(1,24);write('Press RETURN to activate data capture ');
  gotoxy(60,18);writeln('No.1   No.2');
  gotoxy(60,19);writeln('----   ----');
   repeat
     gotoxy(60,20);writeln(ADSAMPLE(0):4,ADSAMPLE(1):7);gotoxy(40,24);
     if (ADSAMPLE(0)>50) or (ADSAMPLE(1)>50) then beep;
     delay(1000);
   until keypressed;
  gotoxy(60,20);writeln('            ');
  gotoxy(1,24);writeln('                          ARMED       ');
  FASTSAMPLE(record_length,level,channel,start_1,datalength,interval,volt1);
  if flag=2 then
     begin
       channel:=1;
       FASTSAMPLE(record_length,level,channel,start_2,datalength,interval,volt2);
       interval:=interval*time1*1000;
       gotoxy(1,24);
       writeln('Delay time = ',interval:7:1,' ms      ');
     end;
   if flag<>2 then interval:=0.0;
   SLOWSAMPLE(channel,datalength2,voltm);
   gotoxy(28,24);write('Converting 1st profile to temperatures...');
   TEMP_CONVERT(start_1,datalength,volt1);
   writeln(' ');gotoxy(39,24);
   writeln('2nd');gotoxy(69,24);
   if flag=2 then
         begin
           TEMP_CONVERT(start_2,datalength,volt2);
           gotoxy(39,24);writeln('3rd');gotoxy(69,24);
```

```
        end;
  TEMP_CONVERT(datalength2-1,datalength2,voltm);
  BEEP;
 write('Enter file name for 1st thermocouple data: ');
 readln(filename);
  FILED(filename,time1,interval,start_1,datalength,volt1);
 if flag=2 then
     begin
        write('Enter file name for 2nd thermocouple data: ');
        readln(filename);
        FILED(filename,time1,interval,start_2,datalength,volt2);
     end;
 write('Enter file name for cooling profile: ');
 readln(filename);
  FILED(filename,time3,interval,datalength2-1,datalength2,voltm);
end.
```

C) Modtwin.pas was based on the routine "tempold.pas", but was extended to allow simultaneous capture on two separate channels of two profiles.

```
PROGRAM FAST;

{*************************************************************************
 Description : This program rapidly monitors two thermocouple outputs.
 Author      : M W Beck ICI EGTC
  Subsequently modified for simultaneous data capture.
  Mike Tribelhorn RU Chem 1991, 1992, 1993.
  And fiddled by Andre Ferreira, 1991.

*************************************************************************}

  {$I [illegible]hX.pas'     { use a: if running on floppy }


  TYPE
    range=array[0..5000] of integer;
    names=string[15];

  VAR
    time1,time3,interval: real;
    filename:names;
    record_length,level,rate1,rate2,start_1,start_2,datalength,datalength2,
    flag,exitval,channel,i: integer;
    volt1,volt2,voltm,voltn: range;
    reply: char;

{************************************************************************}

 PROCEDURE BEEP;

   begin
     sound(20);
     delay(10);
     sound(20);
     nosound;
   end;

{************************************************************************}

  FUNCTION ADSAMPLE (channel:integer):integer;

  { Function reads the A/D channel specified }

  var i:integer;

  begin
    port[$702]:=(channel shl 4)+2;
    port[$702]:=(channel shl 4)+3;
    for i:=1 to 26 do
      begin          { loop until end of conversion }
      end;
    ADSAMPLE:=((port[$701] and $0f) shl 8)+port[$700];
  end;

{************************************************************************}

PROCEDURE FASTSAMPLE (var record_length,level,exitval,datalength:integer;
                      var interval:real;
                      var voltm,voltn: range );
```

```
VAR
  j,k,i: Integer;

begin
   channel:=0;
   exitval:= -2;
   k:=-1;interval:=0;
   for j:=0 to datalength do
      begin
       voltm[j]:=0;
       voltn[j]:=0;
      end;
      repeat
        k:=(k+1) mod datalength;
        interval:=interval+1;
        PORT[$702]:=((0) SHL 4) + 2;
        PORT[$702]:=((0) SHL 4) + 3;
        for j:=0 to 26 do
          begin                { loop until end of conversion }
          end;
        voltm[k]:=((PORT[$701] and $0F) SHL 8) + PORT[$700];
        PORT[$702]:=((1) SHL 4) + 2;
        PORT[$702]:=((1) SHL 4) + 3;
        for j:=0 to 26 do
          begin
          end;
        voltn[k]:=((PORT[$701] and $0f) SHL 8 ) + PORT[$700];
        if ((voltm[k]>level) and (exitval=-2)) or ((voltn[k]>level) and (exitval=-2)) then
           begin
             exitval:=(k+record_length) mod datalength;
           end
      until k=exitval;
end;

{*********************************************************************}


PROCEDURE SLOWSAMPLE (datalength2:integer;var voltm,voltn: range);

 VAR  q,j,k: Integer;

 begin
   channel:=0;
   for j:=0 to (datalength2-1) do voltm[j]:=0;
   gotoxy(28,24);write('recording...');
    for j:=0 to (datalength2-1) do
       begin
        Delay (5);
        For q:=1 to 10 do  { loop to sample tenth value }
         Begin
          PORT[$702]:=((0) SHL 4) + 2;
          PORT[$702]:=((0) SHL 4) + 3;
          for k:=0 to 26 do
             begin
             end;
          if q=10 then
             begin
              voltm[j]:=((PORT[$701] and $0F) SHL 8) + PORT[$700];
             end;
          PORT[$702]:=((1) SHL 4) + 2;
          PORT[$702]:=((1) SHL 4) + 3;
          for k:=0 to 26 do
             begin;
```

```
            end;
          if q=10 then
            begin
             voltn[j]:=((PORT[$701] and $0F) SHL 8) + PORT[$700];
            end;
         end;
       end;
   writeln(' ');gotoxy(28,24);write('              ');
 end;

{*********************************************************************}

PROCEDURE TEMP_CONVERT(start_1,datalength:integer;var volt1,volt2:range);

{ procedure to convert A/D data into temperature*10 values }

 var
   i:integer;
   temp1,temp2:real;

 begin
   i:=start_1;
   repeat
     i:=((i+1) mod datalength);
     temp1:=(volt1[i]/(409.5*400))*1000;
     temp2:=(volt2[i]/(409.5*400))*1000;
     temp1:=10.637+134.172*temp1-5.1291*temp1*temp1+0.23513*
       temp1*temp1*temp1-0.00412027*temp1*temp1*temp1*temp1;
     temp2:=10.637+134.172*temp2-5.1291*temp2*temp2+0.23513*
       temp2*temp2*temp2-0.00412027*temp2*temp2*temp2*temp2;
     volt1[i]:=ROUND(temp1*10);
     volt2[i]:=ROUND(temp2*10);
   until i=start_1;
 end;

{*********************************************************************}

PROCEDURE FILED (filename:names;time1,interval:real;
                 start_1,datalength:integer;volt1,volt2:range);

{ procedure for writing captured data to a file }

 var
  i:integer;
     filvar:text;

  begin
     filename:='a:'+ filename +'.dat';
     assign(filvar,filename);
     rewrite(filvar);
     writeln(filvar,interval:7:1);
     writeln(filvar,time1*1000:12:5);
      i:=start_1;
      repeat
        i:=((i+1) mod datalength);
        write(filvar,(volt1[i]/10):5:1);
        write(filvar,(' '));
        writeln(filvar,(volt2[i]/10):5:1);
       until i=start_1;
     close(filvar);
  end;

{*********************************************************************}
```

```
PROCEDURE VALUES(level,record_length,datalength,datalength2,flag:integer;
                 time1,time3:real);

  var
   volt1,volt2:range;

  begin
    volt1[0]:=level; { set at same level for simplicity in capture }
    volt2[0]:=level;
    TEMP_CONVERT(0,1,volt1,volt2);
    volt1[0]:=ROUND(volt1[0]/10);
    volt2[0]:=ROUND(volt2[0]/10);
    gotoxy(41,7);write(level:4,'      ',volt1[0]:4,' oC');
    gotoxy(41,8);write(level:4,'      ',volt2[0]:4,' oC');
    gotoxy(41,10);write(datalength:4,round(datalength*time1*1000):9,' ms');
    gotoxy(41,12);write(datalength2:4,round(datalength2*time3):9,' s');
    gotoxy(41,14);write(datalength-record_length-1:4);
    gotoxy(44,16);writeln(flag);
  end;

{*************************************************************************}

PROCEDURE STORE_VALUES(level,record_length,datalength,datalength2,
                       flag:integer);

  var
   filvar:text;

  begin
    assign(filvar,'a:\TEMPAF.VAL');
    rewrite(filvar);
    writeln(filvar,level);
    writeln(filvar,record_length);
    writeln(filvar,datalength);
    writeln(filvar,datalength2);
    writeln(filvar,flag);
    close(filvar);
  end;

{*************************************************************************}

PROCEDURE ALTER_VALUES(var level,record_length,datalength,datalength2,
                       flag:integer);

  var
   number,result:integer;
   reply:char;
   value:string[4];
   volt1,volt2:range;

  label mark;

  begin
    mark:gotoxy(1,22);writeln('                                                ');
    gotoxy(1,22);write('Enter trigger level (0 - 2900) ');
    number:=level;read(value);
    VAL(value,number,result);
    if result=0 then
       begin
         if (number<2901) and (number>-1) then level:=number;
         volt1[0]:=level;
         volt2[0]:=level;
         TEMP_CONVERT(0,1,volt1,volt2);
```

```
        volt1[0]:=ROUND(volt1[0]/10);
        volt2[0]:=ROUND(volt2[0]/10);
        gotoxy(41,7);writeln(level:4,'      ',volt1[0]:4);
        gotoxy(41,8);writeln(level:4,'      ',volt2[0]:4);
      end;
  gotoxy(1,22);write('Enter number of datapoints {fast} (100 - 5000) ');
  number:=datalength;read(value);
  VAL(value,number,result);
  if result=0 then
     begin
       if (number<5001) and (number>100) then datalength:=number;
       gotoxy(41,10);writeln(datalength:4,round(datalength*time1*1000):9);
     end;
  gotoxy(1,22);write('  Enter number of datapoints  {slow}  ( Max 5000 ) ');
  number:=datalength2;read(value);
  VAL(value,number,result);
  if result=0 then
     begin
       if (number<5001) and (number>0) then datalength2:=number;
       gotoxy(41,12);writeln(datalength2:4,round(datalength2*time3):9);
     end;
  gotoxy(1,22);writeln('                                                    ');
  gotoxy(1,22);write('Enter number of pre-trigger data points ( < ',datalength,' ) ');
  number:=(datalength-record_length-1);read(value);
  VAL(value,number,result);
  if result=0 then
     begin
       if (number<datalength) and (number>=0) then record_length:=datalength-number-1;
       if record_length+1 > datalength then record_length:=datalength-1;
       gotoxy(41,14);writeln(datalength-record_length-1:4);
     end;
  gotoxy(1,22);writeln('                                                    ');
  {gotoxy(1,22);write('Enter number of thermocouples ( 2 ) ');
  number:=2;read(value);
  VAL(value,number,result);
  if result=0 then
      begin
        if (number=1) or (number=2) then flag:=number;
        gotoxy(44,16);writeln(flag);
      end;}
  gotoxy(44,16);writeln(flag);
  gotoxy(1,22);writeln('                                                    ');
  gotoxy(1,22);write(' Press ESCAPE to alter values or RETURN to continue...');
  repeat until keypressed;
  read(kbd,reply);
  writeln(' ');
  if reply=#27 then goto mark;
  gotoxy(1,22);writeln('                                                    ');
  gotoxy(1,22);write(' Save these values as defaults? ');
  repeat until keypressed;
  read(kbd,reply);
  writeln(' ');
  if (reply='Y') or (reply='y') then
    STORE_VALUES(level,record_length,datalength,datalength2,flag);
end;

{*********************************************************************}

PROCEDURE DISPLAY(var rate1,rate2,record_length,level,datalength,
                  datalength2,flag:integer);

var
 reply:char;
```

```
 filvar:text;

begin
  assign(filvar,'a:TEMPAF.VAL'); { use a: if required }
  reset(filvar);
  read(filvar,level);
  read(filvar,record_length);
  read(filvar,datalength);
  read(filvar,datalength2);
  read(filvar,flag);
  close(filvar);
  ClrScr;
  writeln(' ********************************************************************************');
  gotoxy(13,3);
  writeln('     THERMOCOUPLE DATA COLLECTION ROUTINE ');
  gotoxy(1,5);
  writeln(' ********************************************************************************');
  gotoxy(1,7);
  writeln('   Trigger level : 1');writeln('                 : 2'); { fixed }
  writeln(' ');
  writeln('   No. of data points  {Rise}');writeln(' ');
  writeln('   No. of data points  {Cool}');writeln(' ');
  writeln('   No. of pre-trigger data points');writeln(' ');
  writeln('   No. of thermocouples ');writeln(' ');
  writeln('   Sample rate {Rise} (Hz)          ',rate1);writeln(' ');
  writeln('   Sample rate {Cool} (Hz)          ',rate2);
  VALUES(level,record_length,datalength,datalength2,flag,time1,time3);
  writeln(' ');writeln(' ');
  writeln(' ');writeln(' ');writeln(' ');
  write(' Press ESCAPE to alter values or RETURN to continue... ');
  repeat until keypressed;
  read(kbd,reply);
  writeln(' ');
  if (reply=#27) then ALTER_VALUES(level,record_length,datalength,datalength2
                                   ,flag);
end;

{*********************************************************************}

          {          main program          }

begin
  PORT[$703]:=$92;  { set system trigger }
  channel:=0;
  rate1:= 5400; { set from 1 kHz signal }
  rate2:= 215; { set from 100 Hz signal }
  time1:=1/rate1;
  time3:=1/rate2;
  DISPLAY(rate1,rate2,record_length,level,datalength,datalength2,flag);
  gotoxy(1,22);writeln('                                                    ');
  gotoxy(1,22);write('Press RETURN to activate data capture ');
  gotoxy(60,18);writeln('No.1   No.2');
  gotoxy(60,19);writeln('----   ----');
   repeat
     gotoxy(60,20);writeln(ADSAMPLE(0):4,ADSAMPLE(1):7);gotoxy(40,24);
     if (ADSAMPLE(0)>50) or (ADSAMPLE(1)>50) then beep;
     delay (50);
   until keypressed;
  gotoxy(60,20);writeln('          ');
  gotoxy(1,22);writeln('                          ARMED       ');
  FASTSAMPLE(record_length,level,start_1,datalength,interval,
          volt1,volt2);
   SLOWSAMPLE(datalength2,voltm,voltn);
```

```
  gotoxy(28,22);writeln('Converting rise profiles to temperatures...');
  TEMP_CONVERT(start_1,datalength,volt1,volt2);
  writeln(' ');gotoxy(39,22);
  writeln('cool');
  TEMP_CONVERT(datalength2-1,datalength2,voltm,voltn);BEEP;
  gotoxy(28,22);writeln('                                    ');
  gotoxy (0,23);
 write('Enter file name for rise region data: ');
 readln(filename);
  FILED(filename,time1,interval,start_1,datalength,volt1,volt2);
 write('Enter file name for cool region data: ');
 readln(filename);
  FILED(filename,time3,interval,datalength2-1,datalength2,voltm,voltn);
end.
```

D) Program.pas was written to generate a table of Savitsky Golay factors, for use in Savitsky Golay smoothing and differentiation, specifically when few points were available and loss of peripheral points could not be afforded [147]. The factors generated by this routine allowed end-points of the data sets to be retained.

```
Program Table;
{ Generation of a table of Gram Polynomial/Savitzky-Golay      }
{ factors for use in smoothing and differential programs.      }
{ Function code by P. A. Gorry, program by M. J. Tribelhorn 1991.}

Var
  aa,bb,cc,dd,ee:integer;
  xy:real;

 Function GramPoly(i,m,k,s :integer):real;
 { Calculates the Gram Polynomial (s=0), or its s'th     }
 { derivative evaluated at i, order k, over 2m+1 points  }
 begin
  if k>0 then
    GramPoly := (4*k-2)/(k*(2*m-k+1))*(i*GramPoly(i,m,k-1,s)+
    s*GramPoly(i,m,k-1,s-1))-((k-1)*(2*m+k))/(k*(2*m-k+1))*GramPoly(i,m,k-2,s)
   else
    if (k=0) and (s=0) then GramPoly:=1 else GramPoly:=0;
 end;

 Function GenFact(a,b:integer):real;
 { Calculates the generalised factorial (a)(a-1)...(a-b+1) }
  var
   j:integer;
   gf:real;
 begin
  gf:=1;for j:=(a-b+1) to a do gf:=gf*j;GenFact:=gf;
 end;

 Function Weight(i,t,m,n,s:integer):real;
 { Calculates the weight of the i'th data point for the t'th Least-Square  }
 { point of the s'th derivative, over 2m+1 points, order n.                }
  var
   k:integer;
   sum:real;
 begin
  sum:=0;
  for k:=0 to n do sum:=sum+(2*k+1)*(GenFact(2*m,k)/GenFact(2*m+k+1,k+1))
        *GramPoly(i,m,k,0)*GramPoly(t,m,k,s);
  Weight:=sum;
 end;

begin
 Write('Value for m (2m+1 smoothing): ');Readln(cc);
 Write('Value for n (order of derivative): ');Readln(dd);
 Write('Derivative (0 for Gram Poly): ');Readln(ee);
```

```
 begin
  Writeln(lst,'Smooth points=',2*cc+1);
  Writeln(lst,'Order=',dd);
  Writeln(lst,'Derivative=',ee);
  Writeln(lst);
  For aa:=-cc to cc do
   begin
    For bb:=-cc to cc do
     begin
      Write(lst,'i=',aa,' t=',bb,' :  ');xy:=Weight(aa,bb,cc,dd,ee);
      Writeln(lst);Write(lst,xy);writeln(lst);
     end;
     Writeln(lst);
   end;
   Writeln(lst);
 end;
end.
```

E) Mspline.bas is based on a cubic-spline smoothing routine [148], and was used extensively in smoothing raw temperature profile data.

```
REM "REGSPL1 "        EBERT/EDERER          910207
1 REM ***********************************************
2 REM *** A regression - spline function is          ***
3 REM *** calculated. Equidistant grid points       ***
4 REM *** are needed.                               ***
5 REM *** The algorithm is taken from:              ***
6 REM *** Lawson/Hanson: Solving Least Squares      ***
7 REM *** Problems. Prentice Hall 1974.             ***
9 REM ***********************************************
100 DIM X(500),Y(500),Z(500)
110 DIM A(552,5),D(552,7)
120 DIM B(500),C(500)
130 DIM YS(500)
200 DEF FNP(T)=.25*T*T*T
210 DEF FNQ(T)=1-.75*(1+T)*(1-T)*(1-T)
215 PRINT
216 CL$
220 PRINT "+++ MSPLINE SMOOTHING PROGRAM +++"
230 PRINT
300 PRINT "Using 12 grid points, line300":N=12
303 PRINT
305 PRINT "MAXIMUM NO. OF DATA POINTS = 500 "
310 TOT=500
320 GOSUB 10000 : REM Reading data in X() and Y()
325  PRINT:PRINT"PLEASE WAIT - SMOOTHING TAKES ABOUT 1 MINUTE FOR 300
POINTS"
330 GOSUB 11000 : REM Sorting data ascending in X()
360 IF N>=M-2 THEN N=M-2
400 B(1)=X(1) : B(N)=X(M)
410 H=(B(N)-B(1))/(N-1)
420 FOR I=2 TO N-1
430   B(I)=B(1)+H*(I-1)
440 NEXT I
460 GOSUB 12000 : REM Filling of matrix A
480 GOSUB 13000 : REM Filling of band matrices
481             REM D=At*A und Z=At*Y
500 GOSUB 14000 : REM Solving equation D*C=Z
550 GOSUB 20000 : REM Calculating spline
560 GOSUB 24000
9900 PRINT:PRINT"Run ended - data in file ",FILE2$
9999 END
10000 REM ******************************************
10001 REM *** Reading data in X() and Y()          ***
10002 REM ******************************************
10003 PRINT:PRINT "ENTER THE NAME OF THE RAW DATA FILE"
10004 PRINT"FORMAT;  drive:filename":INPUT FILE$
10006 OPEN"I",#1,FILE$
10008 FOR I=1 TO TOT
10010 IF EOF(1) THEN 10026
10012 INPUT#1,X(I),Y(I)
```

```
10020 NEXT I
10026 CLOSE#1
10028 M=I-2
10030 RETURN
11000 REM ******************************************
11001 REM ***  Data are sorted ascending in x.      ***
11002 REM ***  The minima and maxima in x and y     ***
11003 REM ***  are determined.                      ***
11005 REM ******************************************
11020 X0=X(1) : Y0=Y(1) : XM=X0 : YM=Y0
11040 FOR I=2 TO M
11060   IF X0>X(I) THEN X0=X(I)
11080   IF XM<X(I) THEN XM=X(I)
11100   IF Y0>Y(I) THEN Y0=Y(I)
11120   IF YM<Y(I) THEN YM=Y(I)
11140 NEXT I
11200 D=INT(LOG(M)/LOG(2)):D=2^D-1
11220 FOR I=1 TO M-D
11240   FOR J=I TO 1 STEP -D
11260     IF X(J)<=X(J+D) THEN 11300
11270     HY=Y(J) : Y(J)=Y(J+D) : Y(J+D)=HY
11280     HX=X(J) : X(J)=X(J+D) : X(J+D)=HX
11290   NEXT J
11300 NEXT I
11320 D=INT(D/2) : IF D>0 THEN GOTO 11220
11900 RETURN
12000 REM ******************************************
12001 REM ***  Filling of the matrix A             ***
12002 REM ******************************************
12010 IB=1 : REM Index for grid points
12020 IX=1 : REM Index for data points
12050 IF X(IX)>B(IB+1) THEN GOTO 12150
12060 T=(X(IX)-B(IB))/H
12070 A(IX,1)=FNP(1-T)
12080 A(IX,2)=FNQ(1-T)
12090 A(IX,3)=FNQ(T)
12100 A(IX,4)=FNP(T)
12110 A(IX,5)=IB
12120 IF IX=M THEN GOTO 12200
12130 IX=IX+1 : GOTO 12050
12150 IB=IB+1 : GOTO 12050
12200 RETURN
13000 REM ******************************************
13001 REM *** Filling of the band matrices          ***
13002 REM *** D=At*A and Z=At*Y                     ***
13003 REM ******************************************
13060 FOR I=1 TO N+2
13080   FOR J=1 TO 7 : D(I,J)=0
13100   NEXT J : Z(I)=0 : NEXT I
13140 FOR K=1 TO M
13160   FOR I=1 TO 4 : FOR J=1 TO I
13200       I0=I+A(K,5)-1 : J0=J+A(K,5)-1
13220       D(I0,J0-I0+4)=D(I0,J0-I0+4)+A(K,I)*A(K,J)
```

```
13240      NEXT J : Z(I0)=Z(I0)+A(K,I)*Y(K)
13260   NEXT I : NEXT K
13300 FOR I=1 TO N+2 : FOR J=1 TO 3
13320     IF D(I,J)=0 THEN GOTO 13400
13340     D(J+I-4,8-J)=D(I,J)
13400 NEXT J : NEXT I
13900 RETURN
14000 REM ******************************************
14001 REM *** Solving equation system D*C=Z        ***
14002 REM ******************************************
14040 FOR I=1 TO N+2 : D4=D(I,4) : FOR J=1 TO 7
14060     D(I,J)=D(I,J)/D4 : NEXT J : Z(I)=Z(I)/D4
14080   J=I+3 : IF J>(N+2) THEN J=N+2
14100   IF I=N+2 THEN GOTO 14400
14140   FOR K=I+1 TO J
14150     L3=D(K,4 -(K-I))
14160     FOR L=1 TO 4
14180       L1=L+3 : L2=L+3-(K-I)
14200       D(K,L2)=D(K,L2)-L3*D(I,L1)
14220     NEXT L : Z(K)=Z(K)-L3*Z(I)
14240   NEXT K
14400 NEXT I
14500 FOR I=1 TO N+5 : C(I)= 0 : NEXT I
14520 FOR I=N+2 TO 1 STEP -1
14540 C(I)=Z(I)-D(I,5)*C(I+1)-D(I,6)*C(I+2)-D(I,7)*C(I+3)
14560 NEXT I
14900 RETURN
20000 REM ******************************************
20001 REM *** Calculating the spline function    ***
20002 REM ******************************************
20020 FOR I=1 TO M
20030   X=X(I)
20040   GOSUB 21000 : REM determining spline interval j
20060   T=(X-B(J))/H
20080   Y=C(J)*FNP(1-T)+C(J+1)*FNQ(1-T)+C(J+2)*FNQ(T)
20090   Y=Y+C(J+3)*FNP(T)
20110 YS(I)=Y
20200 NEXT I
20990 RETURN
21000 REM ******************************************
21001 REM *** Determining spline interval j       ***
21002 REM ******************************************
21010 J=0
21020 IF X<=B(1) THEN : J=1 : RETURN
21040 IF X>=B(N) THEN : J=N-1 : RETURN
21060 J=J+1
21080 IF X>B(J) THEN GOTO 21060
21100 J=J-1
21200 RETURN
22000 REM ******************************************
22001 REM ***  Evaluating the spline function     ***
22002 REM ******************************************
22040 GOSUB 21000 : REM determining spline interval j
```

```
22060 T=(X-B(J))/H
22070 Y=C(J)*FNP(1-T)+C(J+1)*FNQ(1-T)+C(J+2)*FNQ(T)
22080 Y=Y+C(J+3)*FNP(T)
22900 RETURN
24000 REM ****************************************
24010 REM     OUTPUT TO FILE
24020 REM ****************************************
24025 PRINT:PRINT"Smoothed data to be written to filename ?":INPUT FILE2$
24030 OPEN"O",#2,FILE2$
24040 FOR J=1 TO M
24050 WRITE#2,X(J),YS(J)
24060 NEXT J
24100 CLOSE#2
24200 RETURN
63999 END
```

F) PLUTO source files, written for the VAX fortran PLUTO78 package, were used to generate space-filling structural diagrams of some of the reactants, possible intermediates and products of combustion.

These included the structures of BaO_2, BaO, SrO_2, SrO, Fe_2O_3, Fe_3O_4, $BaFe_2O_4$ and various other possible intermediate and product lattices.

An example of a Fortran input file, used to generate a space-filling diagram of $BaFe_2O_4$, as viewed along the z-axis, is shown here:

```
DATA BaFe2O4
CELL 0 8.448 19.05 5.39 90 90 90
SYMM X, Y, Z
SYMM -X,-Y,.5+Z
SYMM X,-Y,.5+Z
SYMM -X,Y,Z
SYMM .5+X,.5+Y,Z
SYMM .5-X,.5-Y,.5+Z
SYMM .5+X,.5-Y,.5+Z
SYMM .5-X,.5+Y,Z
BA1 1 0 .1307 .25
BA2 1 0 .6173 .227
FE1 1 .2776 .0424 .732
FE2 1 .2913 .2084 .774
O1 1 .243 .037 .403
O2 1 .225 .123 .917
O3 1 .281 .209 .417
O4 1 0 .453 .226
O5 1 0 .28 .226
OPT SOLID PACK VIEWZ CELLPLOT NOLABEL
RAD ATOMS FE .64 O 1.32 BA 1.34
PLOT
```

Towards completion of the study, the software was adapted to accept a space group instead of the symmetry positions. For the $BaFe_2O_4$ system, the symmetry operator lines of code were replaced by the command:

```
SYMM C M C 21
```

which represented the orthorhombic Cmmm space group (#36) in which $BaFe_2O_4$ crystallises.

APPENDIX 3: Macros used during spreadsheet manipulation of data:

A) Temperature profile analysis macro converting the output of the PC-28 thermocouple monitoring routine to T,t values, including a 9-point Savitsky Golay convolution cubic-spline smoothing routine.

```
Worksheet cleanup        /wdca1..c1~                                    EXECUTE BY ALT Q
                         /wica1..c1~

Data processing:         {HOME}{GOTO}a4~~                               EXECUTE BY ALT T
Import file              /FIN {ESC}{?}~
Thermocouple corrections: {goto}b4~
Counts to millivolts     +2.44259*$a4/253.92~
                         /c~.{left}{end}{down}{right}~
                         {goto}c4~
Millivolts to temperature +32.1105+120.18*$b4-2.4578*$b4^2+.041*$b4^3+.000636838*$b4^4~
                         /c~.{left}{end}{down}{right}~
                         {goto}a4~/wgrm~
                         /wdc~
                         /wdc~
                         {goto}b4~
Arithmetic averaging     +($a2+$a3+$a4+$a5+$a6)/5~
                         /c~.{left}{end}{down}{right}~
Savitsky-Golay           {goto}c8~
Smoothing                +((-78*$b1-13*$b2+42*$b3+87*$b4+122*$b5+147*$b6+162*$b7+167*$b8 > > >
                         +162*$b9+147*$b10+122*$b11+87*$b12+42*$b13-13*$b14-78*$b15)/1105)~
                         /c~.{left}{end}{down}{right}~
                         /c~.{left}{end}{up}{right}~
                         {goto}b4~
                         /wdc~
                         {goto}h1~
                         /wic{right}~
                         {goto}c4~
Produce time values      /dfc4..c4~~~~
                         /df.{left}{end}{down}{right}~~
                         {?}~{?}~
                         {goto}e4~
                         /wic{right 2}~
                         {goto}c4~
Draw graph (optional)    /grx~a~{esc}
                         tXx.{end}{down}~
                         a{left}.{end}{down}~
                         ofgl{esc}
                         TF {ESC}TEMPERATURE PROFILE~
                         TX {ESC}TIME / [ms]~
                         TY {esc}TEMPERATURE / [degrees C]~
                         ts {esc} {?}~
                         {esc}v
Save graph (optional)    S
                         {?}~
                         {esc}{esc}
```

B) File condensing series of macros for modifying (Y,t) data sampling intervals

Example:

A set of data in a LOTUS-123° spreadsheet has been sampled every 2.4 seconds (series 1) instead of every 2.8 seconds (series 2). The first list is thus 2.8/2.4 times longer than the second and must be reduced by a factor of 2.4/2.8=6/7.

For convenience and generality, let the numerator N=6 and the denominator D=7. (All macro's are assumed to be positioned at address C1).

STEP 1: Expansion of the existing series 1.

Macro: {down}/wir{down (N-2)}~{down (N-1)}~
{branch C1}~

STEP 2: Filling the vacancies generated with formulae calculating the mean between the existing points. (In the example original data is found at A1 and A7).

A1
(A1*5+A7*1)/6
(A1*4+A7*2)/6
(A1*3+A7*3)/6
(A1*2+A7*4)/6
(A1*1+A7*5)/6
A7

Macro: {down}/c.{down (N-2)}~{down (N)}~{down (N-1)}~
{branch c1}~

STEP 3: Convert the series to values prior to reduction with the "Range Values" command.

STEP 4: Reduction of the series.

Macro: {down}/wdr{down (D-2)}~
{branch C1}~

STEP 5: Series 1 is now on a time-base compatible with series 2.

STEP 6: (Optional). A column of data may be fragmented at specific levels to hasten processing by rearranging into numerous adjacent columns. Care must be taken to ensure no data corruption takes place by the choice of the sectioning positions.

C) Trimming extraneous points was achieved by filtering rapid changes in the profiles, due to electrical shorting of the thermocouple or for other reasons discussed below.

If extremely noisy data was encountered (with drop-out points), for example noisy combustion (accompanied by a gas phase), or the response of thin thermocouples (less than 0.1 mm), it was necessary to replace the value of extraneously low points with those of the neighbouring point values. This technique differed from Savitsky-Golay convolution in that extraneous points were discarded in favour of earlier points. This was achieved with the following macro routine (designed specifically for rise regions of profiles and decay regions with high sampling rates (usually 0.5 ms) and decay regions having a T_d of more than 1000 ms). The routine compared the $f(x+1)$ value with $f(x)$, and replaced $f(x+1)$ with $f(x)$ if $f(x+1) < f(x)+5$. The value 5 may be replaced with a suitable factor depending on the severity of the elimination process, but the factor proved most successful at the value indicated.

If data is assumed to be in column B, execution of the following routine enables smoothing of extraneously low values:

```
@IF(@VALUE(B4)<@VALUE(B3-5),@VALUE(B3),@VALUE(B4))
      ↑              ↑              ↑        ↑
    f(x+1)         f(x)        Make f(x+1)=f(x)
```

APPENDIX 4: Thermocouple conversion factors:

The raw data captured from the A/D interface during temperature profile capture represents a set of counts in a specific time interval. A meaningful set of temperature versus time data may only be determined once these counts have been converted to mV,

$$mV = counts*2.44259/253.92.$$

The factors used represent a decrease in the intensity of the signal by the amplification factor of the DC amplifier, and an increase determined from the operating conditions of the 16-bit A/D board, including the counts/mV rating of the A/D board of 2.44259.

The mV values have to be converted to temperature values by thermocouple correction factors for S-type thermocouples, which are based on the following mathematical series [145]:

$$T = 32.1108 + (120.180 \times mV) - (2.45780 \times (mV)^2) + (0.0410001 \times (mV)^3) + (0.000636830 \times (mV)^4)$$

APPENDIX 5: The Borchardt and Daniels kinetic analysis of DTA and TG data:

The Borchardt and Daniels method [159] requires calculation of the fractional extent of reaction, α, and the first derivative of α, $d\alpha/dt$, to give the rate constant:

$$k=\frac{\frac{d\alpha}{dt}}{(1-\alpha)^n}$$

The "order" of reaction, n, is then varied through values corresponding to different kinetic models, until a plot of ln k against 1/T yields an approximately straight line. The relationship used is

$$\frac{d\alpha}{dt}=k(1-\alpha)^n=A(1-\alpha)^n e^{\frac{-E_a}{R}\cdot\frac{1}{T}}$$

The TG data require normalisation of mass changes from the initial mass, by division by the overall mass change, to determine α, followed by determination of $d\alpha/dt$ using a 9-pt Savitsky-Golay first derivative convolution.

The DTA is treated differently to calculate α. The total area under a thermal peak is determined initially, and the partial area at any given T, as a fraction of the total area, gives a measure of α at that temperature. These values of α are then used, as above, to obtain $d\alpha/dt$ values.

The data obtained from both TG and DTA is, however, in the α,T format. Based on the assumption that $d\alpha/dt = d\alpha/dT \cdot dT/dt = d\alpha/dT \cdot \phi$, where ϕ is the constant heating rate for the temperature program experiments, results in ϕ being incorporated in the relationship shown above, which now becomes:

$$\frac{d\alpha}{dT}=\frac{k}{\phi}(1-\alpha)^n=\frac{A}{\phi}(1-\alpha)^n e^{\frac{-E_a}{R}\cdot\frac{1}{T}}$$

The intercept of the Arrhenius plot is ln A - ln ϕ and the slope $-E_a/R$.

APPENDIX 6: Thermodynamic data:

Thermodynamic data used for the systems studied have been included below:

The temperature dependence of heat capacities was calculated using the following [8] mathematical series:

Fe: $C_p=(3.37+(0.00710)T+43000T^{-2})x4.184$ J K^{-1} g^{-1}

Zn: $C_p=(5.35+(0.00240)T)x4.184$ J K^{-1} g^{-1}

BaO_2: $C_p=(13.6+(0.0020)T)x4.184$ J K^{-1} g^{-1}

SrO_2: $C_p=(16.8+(0.0022)-300000T^{-2})x4.184$ J K^{-1} g^{-1}

Temperature dependence of the enthalpy of formation of Fe oxides [8]:

Temperature Range/[K]		$Fe_{0.947}O$ /[kJ mol^{-1}]		Fe_3O_4 /[kJ mol^{-1}]		Fe_2O_3 /[kJ mol^{-1}]	
298	900	-273.3	α	-1122.6	α	-836.8	α
900	950	-273.3	α	-1139.3	α	-836.8	α
950	1033	-273.3	α	-1139.3	α	-849.2	α
1033	1050	-261.0	β	-1100.4	β	-823.2	β
1050	1179	-261.0	β	-1100.4	β	-808.3	β
1179	1650	-279.3	γ	-1158.9	γ	-847.4	γ
1650	1674	-279.3	γ	-1158.9	γ	-847.4	γ
1674	1800	-279.3	γ	-1098.6	δ	-807.2	δ

Thermodynamic data for reactants and products (298 K and 1 atm pressure) [8]:

Compound	ΔH_f°	Molar mass	Specific heat capacity	Molar heat capacity
Fe	-	55.85	0.4473	24.98
FeO	-273.2	71.85	0.6232	44.78
Fe_3O_4	-1122.6	231.55	0.2247	52.03
Fe_2O_3	-836.8	159.70	0.9495	151.64
Zn	-	65.39	0.3849	25.17
ZnO	-354.2	81.39	0.4946	40.25
BaO_2	-647.8	169.33	0.3508	59.40
BaO	-563.1	153.33	0.4171	63.95
SrO_2	-650.6	119.62	0.4924	58.90
SrO	-595.8	103.62	0.5939	61.54

Zinc oxidation thermochemistry [48]:

	$\Delta H_{reaction}$/ [kJ mol^{-1}]:				
Temperature/[°C]	25	419	907	1527	1730
$Zn_{(s)} + \frac{1}{2}O_{2(g)} \rightarrow ZnO_{(s)}$	-318.4	-279.5			
$Zn_{(l)} + \frac{1}{2}O_{2(g)} \rightarrow ZnO_{(s)}$		-279.5	-227.4		
$Zn_{(g)} + \frac{1}{2}O_{2(g)} \rightarrow ZnO_{(s)}$		-328.1			-64.8
$Zn_{(s)} \rightarrow Zn_{(g)}$	+94.5	+48.7			
$Zn_{(l)} \rightarrow Zn_{(g)}$		+48.7	0.0	-58.8	

APPENDIX 7: Equations used for exponential regression in "Graftool":

The current-temperature (I,t) calibration curve for estimating wire surface temperatures was generated using the exponential regression routine in "GRAFTOOL". The exponential regression was chosen as it provided the most satisfactory fit to the calibration data. The polynomial regression provided less satisfactory results.

The data were considered to be of the form:

$$y = a(b^x)$$

where y is the current, b^x a function of temperature where x is f(T) and b is the exponential constant, while a is a scaling constant.

Assuming a set of data $\{(x_1,y_1),(x_2,y_2),\ldots,(x_m,y_m)\}$, solution of the normal equations:

$$\sum_{i=1}^{M} \log(y_i) = M \log(a) + \sum_{i=1}^{M} x_i \log(b)$$

$$\sum_{i=1}^{M} x_i \log(y_i) = \sum_{i=1}^{M} x_i \log(a) + \sum_{i=1}^{M} x_i^2 \log(b)$$

results in the following constants for a and b:

$$a = \exp\left[\frac{\sum_{i=1}^{M} \log(y_i) \sum_{i=1}^{m} x_i^2 - \sum_{i=1}^{M} x_i \sum_{i=1}^{M} x_i \log(y_i)}{M \sum_{i=1}^{M} x_i^2 - \left[\sum_{i=1}^{M} x_i\right]^2}\right]$$

$$b = \exp\left[\frac{M \sum_{i=1}^{M} x_i \log(y_i) - \sum_{i=1}^{M} x_i \sum_{i=1}^{M} \log(y_i)}{M \sum_{i=1}^{M} x_i^2 - \left[\sum_{i=1}^{M} x_i\right]^2}\right]$$

These constants were used to generate the calibration curves.

APPENDIX 8: Perkin-Elmer file workup (Copyright, PE Corporation 1992):

The data files generated by the software supplied with the Perkin-Elmer thermal analysis equipment is stored in the format shown, and may be converted for use in LOTUS spreadsheets by generating suitable abscissa and ordinate data as shown below:

PERKIN-ELMER PC SERIES TGA7 STANDARD THERMAL ANALYSIS FILE FORMAT ("*.G7")

The first line of the data file consists of:

1) Sample ID (30 characters)
2) Operator ID (20 characters)
3) Date and time of run (19 characters)
4) name of baseline file (8 characters)

Line 1:	e.g. 659.6993	Actual Final Temp (°C)
Line 2:	e.g. 440	Minimum Temp for display (°C)
Line 3:	e.g. 3.684	Sample Weight (mg)
Line 4:	e.g. 0	Curve type (0 for data file)
Line 5:	e.g. 2.2	Data Rate (sec/point)
Line 6:	e.g. 440.066	Actual Starting Temp (°C)
Line 7:	e.g. 1199	Number of data points
Line 8:	e.g. 5	Scanning rate (°C/min)
Line 9:	e.g. 200	Data Point Scaling Factor
Line 10:	e.g. 22	Temp Increment (for display) (°C)
Line 12:	e.g. 660	User Input Final Temp (°C)
Line 13:	e.g. 100	Y Range (in %)
Line 15:	e.g. 0	Temperature (°C) when instrument first entered control
Line 16:	e.g. 20	Load Temperature (°C)
Line 17:	e.g. 200	Goto Temp Rate (°C/min)
Line 18:	e.g. 4	End Condition: 4=Start temp;8=Hold;1=Load temp
Line 20:	e.g. .5	Delay time (min)
Line 21:	e.g. 440	User Input Starting Temp
Line 23:	e.g. 0	Valve 1 time (min)
Line 24:	e.g. 0	Valve 2 time (min)
Line 25:	e.g. -42.36934	Ordinate offset from height calibration
Line 27:	e.g. 0	Scaling offset (= 100 - Y Range) (in %)
Line 31:	e.g. 2	Flag used for multitasking
Line 32:	e.g. 1	Instrument Type (1 = TGA)
Lines 33-56:	e.g. 1	Results from calculations #1 to #4 (6 lines each)
Line 57:	e.g. 20027	Beginning of Ordinate data

If a Version 3.1 file is to be processed, the second column is temperature data; columns are separated by comma

See Line 7 for the number of data points

Weight/mass (%) = Data / (20000! / Y Range(Line 9)) + Offset(Line 27)

Example: Data point #1

Weight (%) = 20027 / (20000! / 100) + 0 = 100.135

To generate temperature data:
Temp 1 = Line 21 User Input Starting Temp

Subsequent temperatures are found by incrementing
Temp 1 by the number of degrees / point:
degrees/point = (Data rate) / 60 * (Scanning rate)
degrees/point = (Line 5) / 60 * (Line 8)
In this file:
degrees/point = 2.2 / 60 * 5 = .18333

Lines omitted above have zero value in the output file.

PERKIN-ELMER PC SERIES DTA 1700 THERMAL ANALYSIS FILE FORMAT ("*.E7")

Similar to that above, the first line consists of:

1) Sample ID (30 characters)
2) Operator ID (20 characters)
3) Date and time of run (13 characters)

Line 1:	e.g. 659.6993	Right Temperature (Maximum reached)
Line 2:	e.g. 440	Minimum Temp for display during run
Line 3:	e.g. 3.684	Sample Weight (mg)
Line 4:	e.g. 0	Convention status word Bit 4: set if Y units are degrees; clear otherwise Bit 2: Temp scale 0=deg C; 1=deg K Bit 0: Y units 0=English; 1=metric;clear if bit 4 set
Line 5:	e.g. 2.2	External Data Rate (Sec/point)
Line 6:	e.g. 440.066	Left Temperature (Minimum during run)
Line 7:	e.g. 1199	Number of data points
Line 8:	e.g. 5	Scanning rate
Line 9:	e.g. 200	Data Point Scaling Factor
Line 10:	e.g. 22	Temp Increment (for display)
Line 12:	e.g. 660	Final Temp (user input)
Line 13:	e.g. 100	Y Range
Line 14:	e.g. 0	Heating Rate
Line 15:	e.g. 0	Cooling Rate
Line 16:	e.g. 20	End Condition: 0=Heat;1=Iso;2=Cool
Line 17:	e.g. 200	Delay Time
Line 18:	e.g. 4	Dwell Time
Line 19:	e.g. 0	Zero Offset:-1=down;0=none;1=up
Line 20:	e.g. .5	Flow Rate
Line 21:	e.g. 440	Calibration Factor
Line 22:	e.g. 0	Option Flag for Peak Search and Plot during run
Line 23 to 32:	e.g. 0	Not used
Line 33:	e.g. 0	Results (56 values)
Line 89:	e.g. 20027	Beginning of ordinate data Ordinate data

Ordinate = Data / Data point scaling factor (Line 9)

Example: Data point #1

Ordinate = 20027 / 200 = 100.135

Temperature data are determined as shown above (TGA)

PERKIN-ELMER PC SERIES DSC7 STANDARD THERMAL ANALYSIS FILE FORMAT ("*.D7")

As above, the first line consists of:

1) Sample ID (30 characters)
2) Operator ID (20 characters)
3) Date and time of run (19 characters)
4) name of baseline file (8 characters)
5) empty string (30 characters)

Line 1:	e.g. 659.6993	Actual Highest Temp(°C)(Heating: T final;Cooling: T start)
Line 2:	e.g. 440	Minimum Temp for display (°C)
Line 3:	e.g. 3.684	Sample Weight (mg)
Line 4:	e.g. 0	Curve type (0 for data file)
Line 5:	e.g. 2.2	External Data Rate (Sec/point) ($R)
Line 6:	e.g. 440.066	Actual Lowest Temp (°C)(Heating: T start;Cooling: T final)
Line 7:	e.g. 1199	Number of data points
Line 8:	e.g. 5	Scanning rate (°C/min)
Line 9:	e.g. 200	Data Point Scaling Factor
Line 10:	e.g. 22	Temp Increment (for display) (°C)
Line 11:	e.g. 0	Time at T Final (°C)
Line 12:	e.g. 660	User Input Final Temp (°C)
Line 13:	e.g. 100	Y Range (in mW)
Line 14:	e.g. 0	Time at T Start (°C)
Line 15:	e.g. 0	Temperature (°C) when instrument first entered control
Line 16:	e.g. 20	Load Temperature (°C)
Line 17:	e.g. 200	Goto Temp Rate (°C/min)
Line 18:	e.g. 4	End Condition: 4=Start temp;8=Hold;1=Load temp
Line 19:	e.g. 0	Y Initial value (mW)
Line 20:	e.g. .5	Delay time (min)
Line 21:	e.g. 440	User Input Starting Temp
Line 22:	e.g. 0	Calibration Offset
Line 23:	e.g. 0	Event 1 time (min)
Line 24:	e.g. 0	Event 2 time (min)
Line 25:	e.g. 156.6	Calibration Expected onset 1
Line 26:	e.g. 157.1	Calibration Measured onset 1
Line 27:	e.g. 419.47	Calibration Expected onset 2
Line 28:	e.g. 422	Calibration Measured onset 2
Line 29:	e.g. 1.0	Calibration constant
Line 30:	e.g. 0	(?)
Line 31:	e.g. 2	Flag used for multitasking
Line 32:	e.g. 1	Instrument Type (4 = DSC)
Line 33-56:	e.g. 1	Results from calculation #1 to #4 (6 lines each)
Line 57:	e.g. 20027	Beginning of Ordinate data

If it's Version 3.1 file, second column is temperature data;
columns separated by comma

mW = Data / Data point scaling factor (Line 9)

Example: Data point #1

mW = 20027 / 200 = 100.135

PERKIN-ELMER PC SERIES TGA7 MULTI-RAMP THERMAL ANALYSIS FILE FORMAT ("*.P7")

First line consists of:

1) Sample ID (30 characters)
2) Operator ID (20 characters)
3) Date and time of run (19 characters)

Line 1:	e.g. 15.28	Actual Final Time (min)
Line 2:	e.g. 0	Scaling offset (= 100 - Y Range) (in %)
Line 3:	e.g. 14.7613	Sample Weight (mg)
Line 4:	e.g. 0	Curve type (0 for data file)
Line 5:	e.g. 1.2	Data Rate (sec/point)
Line 6:	e.g. 0	Not used
Line 7:	e.g. 765	Number of data points
Line 8:	e.g. 0	Temperature when instrument entered control
Line 9:	e.g. 200	Data Point Scaling Factor
Line 10:	e.g. 16.065	Temp Increment (for display) (°C)
Line 11:	e.g. 0	Delay time (min)
Line 12:	e.g. 37.6195	Ordinate offset from weight calibration
Line 13:	e.g. 100	Y Range (in %)
Line 14:	e.g. 8.6	Valve 1 time (min)
Line 15:	e.g. 20	Valve 2 time (min)
Line 16:	e.g. 20	Load Temperature (°C)
Line 17:	e.g. 200	Goto Temp Rate (°C/min)
Line 18:	e.g. 1	End Condition: 4=Start temp;8=Hold;1=Load temp
Line 19-:	e.g. 20	(19) Temp 1 (20) Time 1 (21) Rate 1
Line -42:	e.g. 0	(40) Temp 8 (41) Time 8 (42) Rate 8
Line 43:	e.g. 2	Flag used for multitasking
Line 44:	e.g. 1	Instrument Type (1 = TGA)
Line 45:	e.g. 11	Flag for end of temp program

where: 4 - Temp 1; 5 - Time 1; 6 - Rate 1 was last item entered
25 - Temp 8; 26 - Time 8; 27 - Rate 8 was last item entered

Line 46-60:	e.g. 1	Results from calculation #1 to #4
Line 61:	e.g. 20027	

Beginning of Ordinate and Temperature data
See Line 7 for number of data points

Weight/mass(%) = Data / (20000! / Y Range(Line 9)) + Offset(Line 2)

Example: Data point #1
Weight/mass(%) = 20027 / (20000! / 100) + 0 = 100.135

To generate time data:
Time 1 = 0
Subsequent times are found by incrementing
Time 1 by the number of sec/point:
In this file:
sec/point = 1.2
The time at the 20th data point is:
Time = data rate * data point #
Time = 2.2 * 20 = 24 sec

APPENDIX 9: Algorithms used in spreadsheets:

Calculation of derivatives by the Savitsky-Golay convolution procedure and areas by the trapezoidal rule.

Integration:

Area determination was required in various aspects of the study, including the calculation of area under G-function graphs in the temperature profile study and areas under DTA graphs in the thermal analysis study.

The cumulative area was calculated by the trapezoidal rule as follows:

$|(y_1-y_0)*.5*\delta t| = a$

$|(y_2-y_1)*.5*\delta t| + (y_1-y\$_0)*\delta t + a = b$

$|(y_3-y_2)*.5*\delta t| + (y_2-y\$_0)*\delta t + b = c$

etc.

Differentiation:

First derivatives were obtained by Savitsky-Golay convolution [146,147,149] (9-point), with a normalising constant of 60:

$$\frac{dy}{dt} = \frac{-4y_o - 3y_1 - 2y_2 - y_3 + y_5 + 2y_6 + 3y_7 + 4y_8}{60\Delta t}$$

shown here acting on point y_4. In specific cases where endpoints could not be omitted, special factors were generated by the recursive properties of Gram polynomials, by the Pascal program (shown in Appendix 2, section D) for generating tables of factors. In the code, the order of the polynomial is given by k, the position fixed is t, and the factors ranged over 2m+1 points.

APPENDIX 10: Calculation of contact points [182,183,184]:

The calculation of the number of contact points, N_R, as discussed in Section 15, was performed by the following routine. The variables MMA, MMB and MMC represent the molecular masses of the three species, where A is the metal and B or C the oxide. The variables RA, RB and RC are the radii of the atoms; PA, PB and PC the molar densities; MA, MB and MC are arrays storing the number of moles of the material; RRB and RRC are the radius ratios of metal to oxide; RPB and RPC are the molar density ratios of metal to oxide; RMB and RMC are the mole ratios of metal to oxide; and EA is the porosity constant. The calculation provides an estimate of the theoretical number of contact points, based on the size, mole and density ratios of the components present. The program which follows performs the calculation for two binary systems which have the same metal, A.

```
0 REM Program to generate number of contact points of a binary material
10 CLS : DIM MA(100): DIM MB(100): DIM MC(100)
15 MMA = 55.85: MMB = 169.33: MMC = 119.62
20 RA = .0000026: RB = .0000051: RC = 1.75E-06: REM Radii of ABC
30 PA = 7860000 / MMA: PB = 4960000 / MMB: PC = 4560000 / MMC: REM Molar density
40 PI = 3.1415926535#
50 REM Mole equivalents determined from masses
60 N = 0
70 FOR N = 5 TO 95 STEP 5: REM Percentage fuel
80 MA(N) = (N / 100) / MMA
90 MB(N) = ((100 - N) / 100) / MMB
100 MC(N) = ((100 - N) / 100) / MMC
110 NEXT N
120 EA = .35: REM Porosity
130 LPRINT : LPRINT "% FE |    BAO2      |    SRO2     |"
140 RRB = RB / RA: RRC = RC / RA
150 RPB = PB / PA: RPC = PC / PA
160 FOR N = 5 TO 95 STEP 5
170 RMB = MB(N) / MA(N)
180 RMC = MC(N) / MA(N)
190 PHIB = ((RRB) ^ 3) * RPB / RMB
200 PHIC = ((RRC) ^ 3) * RPC / RMC
210 X = (3 * (1 - EA) * MA(N)) / (PI * PA * (RA ^ 3))
220 YB = (1 + RRB + 2 * PHIB) ^ 2 * (2 * RRB + (1 + RRB) * PHIB) ^ 2
230 YC = (1 + RRC + 2 * PHIC) ^ 2 * (2 * RRC + (1 + RRC) * PHIC) ^ 2
240 ZB = (1 + PHIB) * (RRB + PHIB) ^ 2 * (3 * (RRB + PHIB) ^ 2 + (1 + PHIB) * (RRB ^
2 + PHIB))
250 ZC = (1 + PHIC) * (RRC + PHIC) ^ 2 * (3 * (RRC + PHIC) ^ 2 + (1 + PHIC) * (RRC
^ 2 + PHIC))
260 NRB = (X * YB) / ZB
270 NRC = (X * YC) / ZC
280 PRINT N; " "; NRB; "    "; NRC
290 LPRINT N; " "; NRB; "    "; NRC
300 NEXT N
310 END
```

APPENDIX 11: X-ray powder diffraction data for substances used and formed in the study (Section 14.3):

Fe powder:

d/[Å]	I/I_1
2.02	52.5
1.43	77.5

Zn powder:

d/[Å]	I/I_1
2.49	52
2.31	40
2.09	100
1.69	29

BaO_2:

d/[Å]	I/I_1	d/[Å]	I/I_1
3.44	100	1.90	16
3.31	83	1.66	17
2.71	45	1.65	16
2.12	36	1.37	13
1.95	45		

SrO_2:

d/[Å]	I/I_1	d/[Å]	I/I_1
3.34	72	1.88	59
3.13	98	1.79	32
2.53	100	1.57	26
2.01	62	1.55	26

20% Fe/BaO_2 combustion product:

d Å	I/I_1	d Å	I/I_1	d Å	I/I_1
4.15	30	2.40	25	1.87	10
3.70	20	2.13	15	1.71	25
2.96	100	2.08	20	1.47	10
2.60	10	2.01	10		

50% Fe/BaO_2 combustion product:

d Å	I/I_1	d Å	I/I_1
3.34	6	2.08	6
2.96	20	2.03	100
2.88	20	1.70	6
2.71	6	1.43	10
2.41	6		

20% Fe/SrO_2 combustion product:

d Å	I/I_1	d Å	I/I_1	d Å	I/I_1
13.58	100	2.96	46	2.14	25
7.02	12	2.79	45	1.98	15
6.15	9	2.74	25	1.94	10
5.37	40	2.70	25	1.82	10
4.64	9	2.47	10	1.80	8
4.48	9	2.40	26	1.76	18
3.53	38	2.30	10		
3.30	24	2.23	10		

50% Fe/SrO_2 combustion product:

d Å	I/I_1	d Å	I/I_1	d Å	I/I_1
6.32	24	2.84	26	1.97	12
4.55	25	2.78	45	1.94	10
3.63	14	2.46	20	1.82	10
3.50	10	2.30	25	1.63	10
3.35	16	2.23	25	1.60	12
3.13	20	2.02	100	1.43	12

50% Zn/BaO_2 combustion product:

d Å	I/I_1	d Å	I/I_1	d Å	I/I_1
4.06	20	2.47	60	1.91	15
2.94	55	2.36	20	1.85	10
2.82	100	2.08	35	1.67	20
2.59	25	2.01	35	1.62	15

30% Zn/SrO_2 combustion product:

d Å	I/I_1	d Å	I/I_1	d Å	I/I_1
3.25	30	2.50	30	1.82	25
3.11	45	2.44	45	1.78	30
2.98	25	2.29	90	1.70	20
2.90	40	2.08	35	1.60	25
2.82	100	2.01	25		
2.56	55	1.86	15		

APPENDIX 12: Temperature profile analysis based on the publications of Boddington and Laye (University of Leeds) [131,132]:

The starting point is the general energy-balance equation,

$$\lambda\frac{\partial^2 T}{\partial z^2} = \rho[c\frac{\partial T}{\partial t} - q\frac{\partial \alpha}{\partial t}]+h(T-T_o)$$

Assuming that u=z+vt (i.e that the time of ignition is based on a frame of reference) and

$$\frac{\partial^2}{\partial u^2} = \frac{1}{v^2}\frac{\partial^2}{\partial t^2}$$

the term

$$\lambda\frac{d^2T}{dz^2} = \frac{\lambda}{v^2}\frac{d^2T}{dt^2}$$

may be substituted in the equation, which becomes

$$\frac{\lambda}{v^2}\frac{d^2T}{dt^2}-\rho c\frac{dT}{dt}+\rho q\frac{d\alpha}{dt}-h(T-T_o)=0$$

where the terms in the expression represent the heat loss by conductivity, the loss by convection, the total heat generated and the heat loss by lateral heat transfer, respectively. Dividing through by ρc,

$$\frac{\lambda}{\rho c v^2}\frac{dT}{dt}+\frac{q}{c}\frac{d\alpha}{dt}-\frac{h}{\rho c}(T-T_o)=0$$

and substituting $U=T-T_0$ (the excess temperature above ambient), $D=\lambda/(c\rho)$, the thermal diffusivity, and $t_{th}=(c\rho/h)$, the thermal relaxation time due to lateral heat loss, the equation becomes

$$\frac{D}{v^2}\frac{d^2U}{dt^2}-\frac{dU}{dt}+\frac{1}{c}q\frac{d\alpha}{dt}-\frac{1}{t_{th}}U=0$$

Finally the term $G=dq/dt=(1/c)q(d\alpha/dt)$ is substituted into the equation, being the rate of heat generated in an adiabatic system, along with $t^*=D/(v^2)$, giving

$$t^*\frac{d^2U}{dt^2}-\frac{dU}{dt}+G-\frac{U}{t_{th}}=0$$

Boddington *et al.* [131,132] showed that $t^* \approx t_r$ in the rise portion of the profile and $t_{th} \approx t_d$ in the decay region of the profile where little axial conduction of heat occurs. In practice $1/t_r$ is obtained from a plot of d(lnU)/dt vs U in the rise region, and $1/t_d$ from a plot of -d(lnU)/dt vs U in the decay region. The kinetic parameters obtained by using this approach have proven [6,144] superior to those obtained

by the more conventional "Hill approach" [9], which assumes no lateral heat loss term. As discussed briefly in Section 5, an iterative routine is used to minimise the sum:

$$\Sigma[(G_{exp}) - (G_{calc})]^2$$

from which kinetic parameters were obtained. The substitutions $y_i=(G_{exp})_i$; $x_i=1-\alpha_i$; $z_i=1/T$; $a=U_{ad}A$ and $b=E_aR$ were made in equation for G in Section 5, such that $f=y_i-a(x_i)^n \exp(-bz_i)$. a, b and n are adjusted until the sum is minimised. The output of the linear routine includes ln a, -b and n.

APPENDIX 13: The Kunii-Smith model for thermal conductivity determination:

The Kunii-Smith [176] model was used to estimate the thermal conductivity of materials used in the study. The model is based on the thermal transfer characteristics of porous rocks in packed beds. The ratio of λ_{eff}/λ_g is determined using the following expression:

$$\frac{\lambda_{eff}}{\lambda_g} = \epsilon + \frac{\beta(1-\epsilon)}{\phi+\gamma(\frac{\lambda_g}{\lambda_s})}$$

where $\epsilon=(\rho_{solid}-\rho_{eff})/(\rho_{solid}-\rho_{gas}) \approx 1-(\rho_{eff}/\rho_{solid})$; β=ratio of distance between centres of two neighbouring particles in direction of heat flow (ΔL) to the diameter of original particles (D_p), and may be estimated as $0.9 \rightarrow 1.0$. ϕ, which is proportional to the thermal resistance, is a measure of the effective thickness, l_r, of the fluid film adjacent to the contact surface of two solid particles.

$$\phi = \frac{1}{2}\frac{(\frac{K-1}{K})\sin^2\theta_o}{\ln(K-(K-1)\cos\theta_o)-(\frac{K-1}{K})(1-\cos\theta_o)} - \frac{2}{3K}$$

where $K=\rho_{solid}/\rho_{gas}$ and $\sin^2\theta_o=1/n$, where n is the number of contact points on the semi-spherical surface of one solid particle. However, it has been shown [176] that ϕ agrees well with the ratio of ρ_s/ρ_g, allowing ϕ to be estimated from this ratio. θ corresponds to the angle of orientation relative to the boundary of the heat flow region. The number of contact points on a semi-spherical surface, n, lies between $n_2 = 4(3)^{1/2}$ for close packed spheres and $n_1 = (2)^{1/2}$ for cubic packing. The porosities corresponding to these extremes are $\epsilon_2=0.260$ and $\epsilon_1=0.476$. ϕ_2 and ϕ_1 may be calculated using ρ_s and ρ_g, and these ϵ_2 and ϵ_1 values. This allows determination of ϕ for any system with an intermediate ϵ value, by the following relationship:

$$\phi = \phi_2+(\phi_1-\phi_2)\frac{(\epsilon-\epsilon_2)}{(\epsilon_1-\epsilon_2)}$$

γ=ratio of the effective thickness of the fluid film adjacent to the surface of two solid particles (l_r) to D_p, and may be estimated as ⅔.

APPENDIX 14: The Boddington and Laye [201] modified kinetic equation:

The application of Arrhenius kinetics to reactions involving solids has often been questioned. Boddington *et al* found [201] that the reaction rate predicted by Arrhenius parameters was far greater than that expected at low temperatures. Consequently a modified rate equation, which combined the temperature dependent Arrhenius rate equation with a diffusion dependent kinetic term, has been used to give a more accurate description of the kinetic behaviour of the pyrotechnic reactions across the temperature range.

The low-temperature kinetic behaviour is satisfactorily described by the kinetic behaviour derived from thermal analysis experiments,

$$k_{TA} = k_{AR} = A_{AR}\, e^{-\frac{E_{AR}}{RT}}$$

while the high-temperature diffusion behaviour is described by the kinetic information determined from the analysis of temperature profiles, k_{TP}.

The modified form of the rate equation suggested was:

$$k_{TP}^{-1} = k_{TA}^{-1} + [BT^m]^{-1}$$

where B is a diffusion coefficient. The determination is performed by estimating values of k_{AR} and m from the rate function:

$$k^{-1} = k_{AR}^{-1} + [BT^m]^{-1}$$

compared to the experimental values beyond T_{ign}, where B is calculated from:

$$B^{-1} = T^m(k_{TP}^{-1} + k_{AR}^{-1})$$

The corresponding values of E_{AR} and A_{AR} are calculated using:

$$A_{AR} = k_{AR}\, e^{\frac{E_{AR}}{RT}}$$

and

$$E_{AR} = \frac{k_{AR}}{k_{TPA}}(E - nRT) + nRT$$

allowing optimised values to be found.

APPENDIX 15: X-Ray powder data of product variation in the Fe-fuelled systems:

The study of products formed in the Fe/peroxide pyrotechnic systems was extended to investigate product control by variation of the starting proportions of reagent. The findings of the study are tabulated below.

Values indicated are as a percentage of the major peak in the spectrum.

	% Fe/BaO_2							
d/[Å]	15	20	25	30	35	40	45	50
4.17	28	15	14	10	16	10	10	10
4.11	<5	12	22	17	21	16	14	9
3.40	<5	<5	11	<5	<5	<5	<5	5
3.31	11	<5	15	10	7	10	8	8
3.21	10	<5	<5	<5	6	<5	<5	<5
2.94	100	100	100	100	100	84	64	48
2.88	12	41	70	64	75	78	62	45
2.68	11	<5	12	7	<5	<5	<5	<5
2.41	12	15	15	11	13	12	11	7
2.37	5	6	11	9	13	13	12	7
2.09	25	19	17	17	25	16	15	10
2.04	<5	<5	16	14	25	20	18	10
2.02	<5	18	53	59	82	100	100	100
1.87	6	<5	<5	<5	10	11	7	6
1.70	17	23	27	17	24	20	17	10
1.67	<5	7	10	8	13	13	10	7

	% Fe/BaO_2 - Two-year old sample							
d/[Å]	15	20	25	30	35	40	45	50
4.49	14	13	9	<5	<5	<5	<5	7
4.17	36	18	24	<5	<5	<5	14	<5
4.11	<5	<5	<5	37	31	17	8	<5
3.70	100	100	100	15	37	10	36	<5
3.40	18	9	<5	<5	<5	<5	<5	<5
3.31	43	10	<5	<5	<5	6	<5	15
3.21	<5	12	12	<5	11	<5	<5	<5
2.94	64	50	59	100	71	55	42	11
2.88	<5	<5	<5	<5	<5	45	23	8
2.68	20	<5	9	<5	<5	<5	<5	11
2.59	51	34	43	<5	14	<5	12	<5
2.52	29	<5	<5	<5	<5	5	<5	<5
2.41	<5	13	18	32	26	13	10	<5
2.32	<5	<5	7	<5	<5	<5	<5	7
2.14	43	21	26	<5	17	10	<5	<5
2.11	57	15	24	20	<5	<5	9	7
2.09	<5	16	18	26	<5	<5	<5	5
2.04	<5	<5	<5	<5	<5	<5	<5	<5
2.02	36	26	48	62	100	100	100	100
1.93	27	21	20	<5	<5	<5	<5	6
1.87	<5	<5	<5	<5	10	<5	<5	<5
1.70	<5	9	<5	15	14	<5	<5	<5
1.67	<5	8	<5	<5	<5	<5	<5	<5

	% Fe/SrO2							
d/[Å]	20	25	30	35	40	45	50	55
6.13	<5	<5	<5	<5	<5	<5	7	5
5.16	<5	<5	5	<5	9	8	7	6
4.92	20	11	8	<5	8	7	6	5
4.53	<5	<5	<5	<5	<5	<5	8	7
3.81	12	15	10	14	9	9	<5	<5
3.51	6	<5	<5	<5	<5	<5	<5	<5
3.31	14	13	11	15	17	16	10	8
3.12	13	14	14	21	28	26	19	14
2.95	6	<5	7	13	16	25	6	<5
2.77	100	100	100	100	85	41	27	20
2.74	64	59	57	72	<5	<5	20	18
2.56	8	<5	10	11	13	23	10	8
2.50	14	<5	9	9	14	14	<5	<5
2.46	6	<5	<5	6	10	8	7	6
2.34	8	<5	<5	<5	<5	10	<5	<5
2.29	11	9	9	<5	<5	<5	<5	<5
2.16	20	<5	<5	<5	<5	7	<5	<5
2.12	<5	17	14	15	<5	<5	<5	<5
2.03	25	20	36	58	100	100	100	100
2.01	<5	24	14	<5	<5	<5	6	<5
1.94	39	26	25	34	24	15	12	10
1.88	<5	<5	<5	<5	<5	5	6	<5
1.82	<5	<5	<5	<5	<5	12	7	<5
1.65	<5	<5	<5	<5	<5	<5	<5	<5
1.61	11	11	11	9	11	7	5	<5
1.59	19	24	22	26	20	8	6	<5

% Fe/SrO_2 - Two-year old sample

d/[Å]	20	25	30	35	40	45	50	55
7.68	<5	<5	7	6	7	<5	<5	<5
6.96	18	<5	<5	<5	<5	<5	<5	<5
6.13	<5	<5	11	11	9	19	<5	<5
5.73	<5	<5	<5	11	7	<5	<5	<5
5.37	<5	88	100	66	28	24	6	<5
5.16	<5	<5	<5	<5	<5	<5	<5	<5
4.92	16	<5	<5	<5	<5	<5	<5	<5
4.53	<5	<5	12	10	8	23	<5	<5
4.27	<5	<5	<5	17	14	<5	<5	5
3.81	18	<5	<5	<5	<5	<5	<5	<5
3.51	14	100	84	100	91	35	84	50
3.44	<5	22	<5	32	36	35	41	23
3.31	<5	33	40	26	17	12	<5	<5
3.21	19	<5	<5	<5	<5	<5	<5	<5
3.12	29	<5	9	<5	<5	14	<5	<5
2.95	<5	75	89	62	26	21	8	<5
2.82	<5	<5	30	27	24	24	17	11
2.77	95	26	66	74	64	60	42	32
2.74	100	29	37	27	<5	<5	<5	<5
2.56	10	<5	<5	17	14	<5	9	7
2.50	11	<5	<5	<5	<5	<5	<5	<5
2.46	14	15	10	22	23	19	30	19
2.43	10	48	56	41	18	13	<5	<5
2.34	19	<5	<5	<5	<5	<5	<5	<5
2.29	13	<5	10	11	10	22	6	4
2.19	<5	<5	<5	<5	9	<5	<5	6
2.16	9	52	60	41	20	17	10	8
2.12	22	<5	<5	<5	<5	<5	<5	<5
2.04	<5	12	<5	<5	22	<5	26	16
2.03	<5	<5	37	75	100	100	100	100
2.01	21	<5	<5	<5	<5	<5	<5	<5
1.97	<5	<5	16	19	16	19	14	11
1.94	71	9	<5	<5	13	11	14	10
1.91	20	18	12	22	16	<5	17	11
1.82	8	31	33	27	18	16	20	10
1.80	8	20	22	16	<5	<5	<5	<5
1.77	<5	37	46	30	16	14	5	<5
1.65	<5	11	10	10	<5	<5	<5	<5
1.61	18	<5	<5	<5	<5	12	<5	<5
1.59	29	7	10	14	11	14	9	8

Effect of compaction on product of 20% Fe/BaO_2 combustion

d/[Å]	0 MPa	50 MPa	100 MPa	150 MPa
4.17	<5	15	15	16
4.11	17	12	13	12
3.40	<5	<5	<5	<5
3.31	<5	<5	<5	8
3.21	<5	<5	<5	<5
2.94	100	100	100	100
2.88	58	41	52	48
2.68	<5	<5	<5	<5
2.41	9	15	<5	14
2.37	<5	<5	10	8
2.09	19	19	23	21
2.04	16	<5	10	10
2.02	<5	18	11	15
1.87	7	<5	<5	<5
1.70	23	23	30	24
1.67	10	7	11	8

Effect of compaction on product of 25% Fe/SrO_2 combustion

d/[Å]	0 MPa	50 MPa	100 MPa	150 MPa
4.92	8	11	10	17
3.81	10	15	12	11
3.31	10	13	12	19
3.12	8	14	13	21
2.95	10	9	10	8
2.77	87	100	100	100
2.74	100	59	56	81
2.56	10	6	10	9
2.50	<5	<5	9	12
2.29	6	9	6	7
2.23	12	<5	<5	<5
2.12	17	17	19	22
2.03	12	20	21	29
2.01	14	24	14	30
1.94	34	26	29	31
1.61	11	11	11	11
1.59	18	24	25	30
1.57	15	<5	<5	<5

The above data represents the findings of the XRD study which aimed to determine product variation by varying the initial conditions for the reactions. The findings are discussed in Section 14.3.4.